

Advanced photonic sensors for industrial applications

Josu Amorebieta Herrero



2021

Advanced photonic sensors for industrial applications

by

Josu Amorebieta Herrero

PhD in Engineering

at the

eman ta zabal zazu



Universidad
del País Vasco

Euskal Herriko
Unibertsitatea

University of the Basque Country UPV/EHU

Department of Communications Engineering

Advisors

Gaizka Durana Apaolaza

Agustín Joel Villatoro Bernardo

Bilbao, 2021

A los que estáis,

Y especialmente a los que no estáis ya con nosotros.

Después de todo lo que nos ha pasado,
¿quién se hubiera imaginado que llegaríamos hasta aquí?

Soy feliz por encima de mis posibilidades

ACKNOWLEDGMENTS

I would like to express my gratitude for the support and confidence provided by all the people and institutions I have been involved with during my thesis. In first place, I would like to thank Professor Joseba Zubia for giving me the opportunity to be part of the Applied Photonics Group APG-FAT and for the optimism and encouragement he conveyed to me. In second place, I would like to thank my advisors Gaizka Durana and Joel Villatoro for the combination of guidance and freedom they have provided me during my research, which I believe has helped significantly in the improvement of my skills. Lastly, but equally important to me, I want to thank especially the members of the Applied Photonics Group APG-FAT with which I have spent these last years. They have helped and advised me always in a selfless manner and in the right direction. I have always felt supported by them and they have made me feel part of their family.

I would like to thank Professor Walter Margulis for letting me work at RISE even under the tough circumstances caused by the pandemic. It was a very constructive period of time to me where I learnt hugely about different working methodologies and cultures, and where I met very special people.

Additionally, I would like to thank my immediate family for letting me have the opportunity to get up to this point. We know the problems and obstacles that we have had to overcome to get here. Problems that have delayed or made me lose so many things in my life, and that have made us live through experiences that made me think about giving up more than once or twice. It looks like we are

finally seeing the light at the end of the tunnel, which seemed impossible not that long ago. Thank you from the bottom of my heart.

Finally, I cannot end without mentioning my friends, who have always been there for me, even in the worst moments, and have helped me not to drown. This work belongs to them as well.

SUMMARY

Photonic sensors, and especially optical fiber-based ones, have reached a maturity in which they have become a realistic alternative for certain industrial environments thanks to their higher versatility and performance compared to traditional sensors. As a result, the demand for highly sensitive and reliable optical sensors for a wide and diverse variety of fields such as biomedicine, car industry, aeronautics, gas and oil industry, etc. has increased significantly.

In this work, several optical sensors for industrial applications are shown. These sensors are designed especially for aeronautical applications but not limited to them, and are based on different operating principles depending on the nature of the measurand. The process that involves the design, fabrication and testing of each device is explained in detail in this work.

This thesis is presented as a compendium of published articles. Its structure consists of a first Section of synthesis that includes an introduction to the topic of the research, the description of the theoretical framework and the methodological tools used to that end, the definition of the hypothesis and the objectives that are pursued by it, and lastly, a summary and discussion of the results.

The research described in this first part is divided in two different lines: In the first, the process to develop an optical fiber-based displacement sensor for aeronautical turbines is explained. Such research and its results are included in **Article 1** in the Appendix. In the second part, several sensors based on strongly coupled multicore fibers and designed for the measurement of diverse parameters (such as temperature or vibrations) are described. The process to reach up to each device and their respective results are included in **Articles 2, 3 and 4** in the Appendix.

In Section 2, the conclusions regarding the research carried out during the thesis are summarized, as well as the future lines of research that have been opened as a result of it. Additionally, the contributions during the thesis, including published papers and conferences, are included as well.

In the Appendix, the published Articles that have allowed this thesis to be presented as a compendium of articles are included.

Content Index

Synthesis	1
1.1 Introduction.....	3
1.1.1 Context of the research.....	3
1.1.2 Optical fiber sensors	5
1.1.1.1 Overview	5
1.1.1.2 Classifications.....	7
1.1.3 Motivation of the thesis.....	10
1.2 Optical fiber-based displacement sensor (OFDS)	11
1.2.1 Introduction and context of the research	11
1.2.2 Theoretical framework and methodological tools	14
1.2.2.1 Definition of Tip Clearance (TC) and Tip Timing (TT).....	14
1.2.2.2 TC and TT sensing technologies	17
1.2.2.3 Optical fiber-based TC and TT sensors.....	18
1.2.2 Hypothesis and objectives.....	20
1.2.2.1 Performance requirements	20
1.2.2.2 Mathematical approach.....	25
1.2.3 Summary and results.....	29
1.2.3.1 Aiming at the sealing land of the blades.....	29
1.2.3.2 Aiming at the datum of the blades.....	35
1.3. Strongly coupled multicore fiber-based (MCF) sensors.....	43
1.3.1 Introduction and context of the research	43
1.3.1.1 Parameters of interest for the industry.....	43
1.3.1.2 Extrinsic optical sensors	44
1.3.2 Theoretical framework and methodological tools	47
1.3.2.1 Operating principle of strongly coupled MCFs	47
1.3.2.2 Manufacturing equipment and interrogation setup .	54
1.3.3 Hypothesis and objectives.....	55
1.3.4 Summary and results.....	56
1.3.4.1 Temperature sensors.....	56

1.3.4.1.1 Highly sensitive packaged 7cMCF-based sensor	56
1.3.4.1.2 Highly sensitive ruggedized 3cMCF-based sensor	62
1.3.4.2 Omnidirectional vector bending sensor.....	72
1.3.4.3 Accelerometer.....	80
1.3.4.4 Direction sensitive curvature sensor	89
Bibliography.....	93
Conclusions	103
2.1 OFDS	105
2.1.1 Conclusions.....	105
2.1.2 Improvement/Evolution of the developed devices	106
2.1.3 New lines of investigation	107
2.2 MCF-based sensors	108
2.2.1 Conclusions.....	108
2.2.2 Improvement/Evolution of the developed devices	109
2.2.3 New lines of investigation	110
2.3 Contributions of the thesis.....	111
2.3.1 Publications.....	111
2.3.2 Conferences	112
Appendix: Published papers	115
Article 1	117
Article 2	133
Article 3	143
Article 4	157

Index of Figures

Figure 1: Operating principle of an optical fiber.....	6
Figure 2: Schematic of an optical fiber-based sensing system.	6
Figure 3: Schematic of the stages of a jet engine. Courtesy Jeff Dahl, CC BY-SA 4.0, via Wikimedia Commons.	13
Figure 4: a) Blik of a compressor with the direction of the airflow and the vibrations suffered by the blades indicated in it and b) front and side views of a blade from a low-pressure turbine with the direction of the vibrations indicated in it.	14
Figure 5: Detail of the TC of a low-pressure turbine stage once it is assembled in the casing.	15
Figure 6: Schematic representation of the definition of TT.	16
Figure 7: Typical response curves for the different fiber arrangements of intensity-modulated sensors. Red and blue colours indicate transmitting and receiving fibers, respectively.....	19
Figure 8: a) Wind tunnel where the tests were carried out. The position of the rotor under test is indicated by the red dotted rectangle. b) Detail of how turbine stages are installed in the wind tunnel.....	21
Figure 9: a) 3D model of a rotor. The point where the hole in the casing was done to insert the probe is indicated by the red circle. The black dotted line indicates the direction to which the sensor is pointing. b) Detail of how the probes are inserted in the holes and installed in the casing in the wind tunnel.....	22
Figure 10: 3D model of the generic shape of a blade tip of a turbine.	22
Figure 11: Generic geometry of the developed OFDSs in this work for TC measurements.	24
Figure 12: Schematic of the optic ray geometry.	26

Figure 13: Schematic representation of the measurement conditions.	30
Figure 14: Photograph of the end face of the probe tip and schematic of the manufactured fiber bundle.	31
Figure 15: Simulated and measured calibration curves for Region 1.	32
Figure 16: a) Micropositioner used for the tests. b) Detail of the fiber bundle end in the micropositioner.	32
Figure 17: Schematic of the optical probe placement within the casing and the TC calculation.	33
Figure 18: Example of the acquired signal during the tests. The blade highlighted in red was used as reference due to its particular reflection pattern.	34
Figure 19: TC values and the corresponding standard deviation of each blade at 4258 rpm over 1100 turns.	35
Figure 20: Photograph of each of the ends and schematic of the of the upgraded manufactured fiber bundle.	37
Figure 21: Schematic of the OFDS with the real hardware components that conform it.	37
Figure 22: Schematic and scaled representation of the cross-sections of the devices used in this test.	38
Figure 23: Schematic representation of the deployment of the sensors along the casing.	38
Figure 24: Response curves of the sensors and the expected region of the TC in this turbine.	39
Figure 25: Comparison between the signals from blade 55 with the three sensors and the ideal signal.	40
Figure 26: Example of waveforms with abnormal behaviors that indicated some anomaly in the blades. The inspection of the	

corresponding blades after the tests showed that a) black paint and b) a scratch caused them.....	41
Figure 27: TC value and the corresponding standard deviation of each blade at 3627 rpm over 20000 turns.	41
Figure 28: Photographs taken with a microscope after the tests of the end face of a) the upgraded OFDS and b) the OFDS from Article 1	42
Figure 29: Schematic of two decoupled waveguides.....	47
Figure 30: Schematic of two coupled waveguides.....	48
Figure 31: Schematic of a generic structure of the MCFs under study.	51
Figure 32: Evolution of the normalized coupled power in the central and one of the adjacent cores as a function of the emitted wavelength for a generic MCF.	53
Figure 33: Schematic of n MCF segments in series along the same SMF.....	53
Figure 34: Schematic of the interrogation setup.	55
Figure 35: a) Photograph of the cross-section of the 7cMCF and b) schematic of the temperature sensor.....	57
Figure 36: a) SP_{01} and b) SP_{02} orthogonal coupled supermodes for the 7cMCF.....	57
Figure 37: Spectra of the manufactured and simulated devices. ...	59
Figure 38: Photograph of the manufactured device after the temperature tests.	60
Figure 39: Evolution of the spectra as a function of temperature. 61	
Figure 40: Calibration curves and linear fitting of the packaged MCF sensor and the bare 7cMCF.....	61
Figure 41: Cross-section of the 3cMCF.....	63

Figure 42: a) SP_{01} and b) SP_{02} orthogonal coupled supermodes for the 3cMCF.....	63
Figure 43: Schematics of the manufactured samples and their corresponding spectra at room temperature ($T=25\text{ }^{\circ}\text{C}$).....	65
Figure 44: Simulations of Δn as a function of temperature for the 7cMCF (black triangles) and 3cMCF (black circles).	67
Figure 45: a) Evolution of the spectrum as a function of temperature and b) calibration curve of the packaged device with 25 mm of 3cMCF.....	68
Figure 46: Photograph of the upgraded device (up) and the device in Article 2 (down) after the tests.....	70
Figure 47: Evolution of the spectrum as a function of temperature of the devices with a) the 3cMCF and b) the 7cMCF.	70
Figure 48: Calibration curves for the ruggedized 3cMCF (black circles) and 7cMCF devices (black triangles).....	71
Figure 49: Schematic of the structure of the sensor.....	72
Figure 50: Spectra of the manufactured and simulated devices of 8 mm of 3cMCF.....	75
Figure 51: Schematics of a) the setup to apply the bending and b) the direction of rotation of the 3cMCF, the evaluated points and the applied bending direction.	77
Figure 52: Spectra and two cycles of the time evolution of the measured parameters when the device is bent in the direction indicated by the arrow and the 3cMCF is rotated a) b) 90° and c) d) 270° with respect to the initial 0° position, respectively.	78
Figure 53: Spectra and two cycles of the time evolution of the measured parameters when the device is bent in the direction indicated by the arrow and the 3cMCF is rotated a) b) 180° and c) d) 360° with respect to the initial 0° position, respectively.....	78

Figure 54: Wavelength shift and light power variation sensitivities and their respective standard deviations at each fiber position.....	79
Figure 55: Polar representation of the normalized bending sensitivities and standard deviations in absolute value.....	80
Figure 56: Schematic of the device.....	81
Figure 57: Simulated spectra of each of the 3cMCF segments and the resulting spectra for the cases where the structure is a) straight, b) bent upwards and c) bent downwards by its fusion splice point. The arrow indicates the bending direction, the wavelength shift or the power variation in each case. The cores of MCF1 are in a V-like configuration, whereas the ones in MCF2 are in an inverted V-like configuration.....	82
Figure 58: Normalized spectra of the simulated (black dashed line) and manufactured devices (black continuous line). Notice that the maxima of both curves is around 1554 nm and there are no secondary lobes. Simulated spectra of MCF segments of 11.4 mm (red dashed line) and 12.2 (blue dashed line) are shown as well. As indicated in Eq. 44 their product results in the black dashed line.....	83
Figure 59: Schematic lateral and top views of the experimental setup. The close-up shows how the manufactured optical accelerometer was surface bonded to the plate. Red cores belong to MCF1 whereas blue cores belong to MCF2. The red central core indicates MCF1 is in front of MCF2, as they share common central core.....	84
Figure 60: Results of the power measurements in the manufactured optical device. a) Time response of three representative cases. b) FFT amplitudes for frequencies from 30 Hz down to 1 mHz for a sinusoidal signal of 1 Vpp. The Measured frequency axis is in logarithmic scale.	85
Figure 61: Results of the wavelength shift measurements in the manufactured optical device. a) Time response of three representative cases. b) FFT amplitudes for frequencies from 30 Hz	

down to 1 mHz for a sinusoidal signal of 1 Vpp. The Measured frequency axis is in logarithmic scale.....	85
Figure 62: Results of the acceleration measurements in the electronic accelerometer. a) Time response of three representative cases. b) FFT amplitudes for frequencies from 30 Hz down to 1 mHz for a sinusoidal signal of 1 Vpp. The Measured frequency axis is in logarithmic scale.	86
Figure 63: Results of the power variation measurements in the manufactured optical device. a) Time response of three representative cases, and b) FFT amplitudes for sinusoidal signals of 6 Hz and amplitudes from 1 Vpp down to 10 mVpp.	87
Figure 64: Results of the wavelength shift measurements in the manufactured optical device. a) Time response of three representative cases, and b) FFT amplitudes for sinusoidal signals of 6 Hz and amplitudes from 1 Vpp down to 10 mVpp.	87
Figure 65: Results of the acceleration measurements in the electronic accelerometer. a) Time response of three representative cases, and b) FFT amplitudes for sinusoidal signals of 6 Hz and amplitudes from 1 Vpp down to 10 mVpp.....	87
Figure 66: Calibration of the manufactured optical accelerometer.	88
Figure 67: Spectra of the manufactured device in Article 3 (blue line) and the one in Article 4 (black line).	90
Figure 68: Schematic diagram of the measuring setup.....	91
Figure 69: Spectra at different curvatures observed when the position of the device was at a) 0° and b) 90°, respectively.	91
Figure 70: Polar representation of the averaged curvature sensitivity in terms of a) wavelength shift and b) intensity changes.....	92

Index of Tables

Table 1 : Summary of the results	66
Table 2: Summary of the results	71

Section 1

Synthesis

In this section, an overview of the research is shown. It includes an introduction to the frame and motivation of the thesis and the detailed description of the two research lines carried out during it: The development of an optical fiber-based displacement sensor for aeronautical turbines and the development of strongly coupled multicore fiber-based sensors for the measurement of parameters of interest for the industry.

1.1 Introduction

1.1.1 Context of the research

The continuous quest of the industry for designing and producing goods with improved performance at lower costs has generated a great interest in mechanisms to optimize their productions. To that end, every step of the process, starting from prototype testing to mass production, is subjected to exhaustive quality control tests. In order to carry out such quality tests, the industry demands robust, reliable and highly sensitive sensors with the aim of monitoring several parameters of interest in real time. Thanks to them, critical information about the entire fabrication process can be obtained, as it can be monitored and characterized precisely. For instance, they can be used to detect and correct design failures in prototypes before reaching mass production, to verify that all the items in the production chain are subjected to identical conditions during their fabrication, or to certify that the rigorous standards that are specific for each of the industrial sectors are fulfilled. Thus, the potential benefits of the deployment of a reliable and sensitive sensing system in terms of quality improvements and economy savings seem evident.

In the industry, it is common to find sensing solutions based on mature technologies to monitor such processes, as they have proven to be reliable, long lasting and cost-effective through years. Those mature technologies usually have an electric or electronic nature, which indicates that their operating mechanism is based on measuring a physical input from the environment and convert that information into an electrical signal that can be interpreted by either a human or a machine, as it is the case of thermocouples and gauges, among others [1]. This characteristic may not be an issue in some circumstances, but it can represent a major concern if such sensors are deployed in certain environments that require strict security

measures such as gas and oil facilities, nuclear plants, aeronautical structures, etc. in which there may be flammable gases or high voltage lines, for instance. Moreover, these sensors may struggle to perform in environments with high radiation or electromagnetic fields due to interferences, or their reliability may be affected under extreme temperatures.

With the aim of overcoming such limitations, photonic technology emerged as appealing alternative to replace or be combined with the aforementioned sensors. Photonic sensors are based on the study or application of the electromagnetic energy whose basic unit is the photon, which is commonly known as light. From a physics point of view, photons do not have mass, do not interfere with electrons and only interfere with other photons under specific conditions. Therefore, their behavior is predictable and controllable according to basic physical laws, even within high electromagnetic, magnetic and radiation fields, and extreme temperature environments [2]. Photonic sensors have proven to be highly sensitive to a wide range of parameters such as strain, pressure, temperature, etc. This combination of performance makes them have a great potential, as these are much-demanded characteristics for harsh environment sensing [3]. To guide the light, photonic sensors make use of technologies such as optics, lasers and optical fibers, for instance; and by studying the perturbation or changes in the characteristics of the light, the physical effect applied to it can be detected and measured with high precision. Even though the aforementioned components were expensive when they first appeared, their continuous evolution and improvement has caused a progressive lowering of their cost up to a point in which they are an economically viable alternative. This fact has allowed a significant progress in photonics and has permitted its expansion to fields of application of different nature apart from sensing, as communications, information storage and data processing, for instance. As a result, photonic-based devices have gained much relevance in the industry, and nowadays it is possible to find

commercial sensing systems based on this technology deployed in several production processes, as for example precision metrology and laser-based calibration systems [4].

Among photonic-based sensing solutions, those based on optical fiber technology should be highlighted. Historically, this technology has been used to enhance the capabilities of communication networks. However, as many of the innovations stemming from that industry can be directly applied to sensing, a significant increase in the interest for developing optical fiber-based sensing solutions has taken place. In fact, nowadays, optical fiber sensing technology has reached a maturity in which it offers a good compromise between cost-effectiveness and performance at the same time that overcomes many of the aforementioned limitations of traditional sensors to operate in harsh environments. As a result, the industry has shown great interest in integrating them in their production processes or quality control tests, as they allow solutions that without the capability of optical fibers would not be possible or would be bulky to realize.

1.1.2 Optical fiber sensors

1.1.1.1 Overview

Briefly, an optical fiber is a flexible circular dielectric waveguide whose diameter is slightly thicker than that of a human hair, and commonly made of silica or polymer. Commonly, its structure consists of a core and a cladding surrounding it, and its operating principle is based on total internal reflection, which permits the light that is launched into the core from a laser or a LED to propagate along its axis (see Fig. 1). To obtain such confinement of the optical signal in the core, the refractive index of the latter (n_{core}) must be greater than that of the cladding (n_{cladding}) [5].

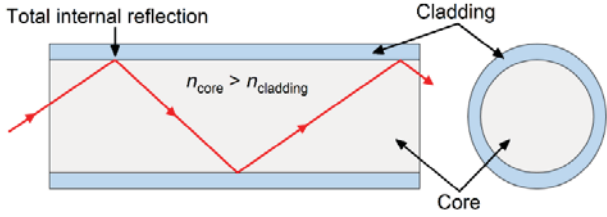


Figure 1: Operating principle of an optical fiber.

Thanks to these properties, optical fibers have been widely used to transmit light between their ends in a very efficient manner, as they provide higher bandwidth with less losses or interferences than those in electrical cables. Additionally, they have proved to be very useful as sensing elements as well, as they are very sensitive to diverse parameters that affect the characteristics of the light propagating through it (such as intensity, phase, etc.) or its transit time.

In its simplest configuration, apart from the optical fiber itself, a sensor based on optical fiber only requires a light source and an interrogator to operate. After the light is launched into the core of the fiber, its properties are modulated or altered in proportion to the physical effect applied to the fiber. Then, this altered light reaches the interrogator, which translates the received optical signal or signals into electronic quantities in analog or digital form, and acts as the interface to the control equipment (see Fig. 2). Starting from this point, the setups for optical fiber sensing can become more complex to make it possible to multiplex several sensors or to measure different parameters simultaneously, for instance.

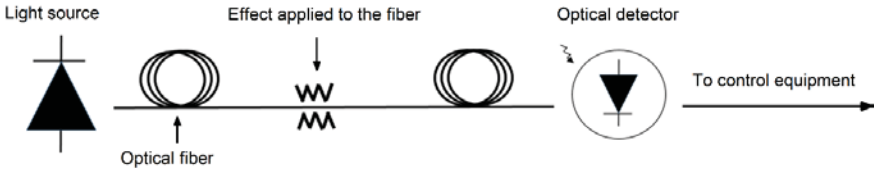


Figure 2: Schematic of an optical fiber-based sensing system.

Hence, for sensing purposes, optical fiber sensors have many advantages, such as small size and weight, deployment ease, setup simplicity, embedding or surface bonding possibility and electromagnetic immunity. Additionally, they can transmit signals over long distances without significant losses and without the requirement of any power supply, be multiplexed to enable large sensor counts and suitable for extreme environments (as environments with high voltage lines, radioactivity, high temperatures or corrosive substances, for example).

However, they tend to be more expensive than electronic sensors and their interrogation equipment is usually more complex than that for electronic sensors, although this characteristic has been significantly improved in the last decades. Moreover, depending on the intended measurement, they require precise installation methods and procedures to avoid the optical fiber getting damaged or broken, and the interrogation systems require basic training before the user can start using them.

Thus, when planning a sensing system, selecting the right sensor and the right sensor technology is fundamental and has to be studied for each case independently. For the frame of the research of this thesis, optical fiber sensing provides many powerful advantages, as it will be demonstrated in throughout this document.

1.1.2.2 Classifications

Optical fiber-based sensors can be classified in many different manners. Some of the most typical classifications are briefly summarized below.

They can be classified according to the nature of the magnitudes that are going to be measured: mechanical, electromagnetic, chemical, fluid flows, thermal or biomedical, for instance [6].

Another classification can be done by separating intrinsic and extrinsic sensors [7]. On the one hand, in intrinsic sensors, the alteration or modulation of the light is caused by an internal effect inside the fiber. Commonly, these effects are absorption, dispersion or fluorescence [8]. On the other hand, in extrinsic sensors, the alteration or modulation of the light is caused by an effect (or effects) from outside the fiber. By means of these sensors, parameters such as vibration, rotation, displacement, velocity, acceleration, torque, and torsion can be measured precisely [9].

According to their spatial distribution, optical sensors can be classified in three different types. Single point sensors provide the measurement in a discrete point of the fiber whereas distributed sensors are capable of providing measurements along the entire fiber [10]. As an intermediate solution, the quasi-distributed or multi-point sensors can be found [11]. These sensors are based on multiplexing several sensors so that the measurement of each individual sensor can be obtained unequivocally. In some cases, when the requirements of the measurement in terms of spatial resolution are not very demanding, multi-point sensors provide a better solution than distributed sensors, as they are cheaper and easier to operate.

Regarding the parameter of the light that is being modulated, the following classification can be done:

1. Sensors based on the modulation of the intensity: The changes in the intensity of the light in the fiber are caused by different effects such as bending or curvature, and are proportional to their magnitude. These sensors are commercially appealing as they provide a good combination of cost-effectiveness and simplicity [12].
2. Sensors based on the modulation of the wavelength: These sensors are based on the study of the shift of the wavelength caused by different factors that affect the fiber. The main advantage of these

sensors is that they can be multiplexed along a single fiber, and easily deployed and/or embedded in large structures such as dams, aircrafts, bridges, etc., which makes them appealing for structural health monitoring (SHM) [13]. Probably, the most popular solution among these sensors is the one based on fiber Bragg gratings (FBGs), which is a very mature technology that has been commercially available for years.

3. Sensors based on the modulation of the phase: Interferometric techniques are used in order to make two beams of light interfere with each other and detect the change in the phase of the light. In such sensors, one of the beams is used as reference whereas the other beam is exposed to the effect that is intended to be measured. In this manner, high sensitivity may be achieved in the measurement, although complex setups and exhaustive alignments are required in order to perform correctly [14]. The most common solutions are based on Mach-Zehnder, Michelson, Fabry-Perot and Sagnac interferometers.
4. Sensors based on the modulation of the polarization: These sensors are based on measuring the change of the polarization of the light within the fiber due to effects such as the Faraday Effect. They are commonly used to measure magnitudes as current or pressure [15].
5. Sensors based on the modulation of the spectrum: These sensors are based on spectroscopy, and their operating principle is based on analyzing the variations in the transmitted spectrum [16].
6. Sensors based on the modulation of the dispersion of light: The detection of the amplitude and position of the measurand is carried out by the study of the scattered light due to scattering effects such as Raman, Brillouin or Rayleigh [17].

1.1.3 Motivation of the thesis

The aim of the research of this thesis is to design and manufacture novel optical fiber-based sensors that are simple, robust, easy to operate and capable to offer better performance than actual optical or electronic solutions. The devices described in this work can be configured to operate as single-point or multi-point sensors with the aim of making them as versatile as possible for their deployment in industrial environments.

Such sensors have been conceived according to the exhaustive requirements of each specific case, which have determined their characteristics. As a result of that, the sensors appearing in this work are based on different operating principles and have different configurations depending on the magnitude to measure, the context in which they are going to be deployed and in order to optimize their performance.

Two different types of sensors were designed, manufactured and tested for this thesis. On the one hand, a displacement sensor designed to operate in aeronautical turbines. As the measurement required a non-contact system, a sensor based on the intensity of the reflected light was developed. On the other hand, several sensors conceived to measure parameters of interest for the industry such as temperature, vibrations, curvature, etc. All the sensors in the second part share identical operating principle, but their configuration was particularized and optimized for each measurand.

1.2 Optical fiber-based displacement sensor (OFDS)

In this section, the entire process regarding the development of a custom-designed optical fiber-based displacement sensor (OFDS) for the measurement of Tip Clearance in real time in aeronautical engines is presented: starting from the definition of the requirements for this application, to its results when it is installed and tested in a real turbine stage in a wind tunnel. Additionally, this section includes the mathematical approach of the operating principle of the sensor and the comparison of its performance under different working conditions and against a commercial solution.

1.2.1 Introduction and context of the research

The aim of the research exposed in this section is to develop a highly sensitive, simple and robust optical sensor capable of measuring distance and/or displacement with high resolution. Such measurement is very relevant in many industrial sectors in which these sensors are commonly deployed for metrology and calibration purposes as part of the Industry 4.0 [18, 19]. Examples of their application can be found from pre to post production processes in which they are used for multiple quality validation procedures. For instance, in the car industry or in the machine-tool sector, where they are applied to compare the dimensions of manufactured items with their respective simulation models. Apart from the significant performance provided by OFDSs regarding the quality of the measurement itself [20], they offer some other significant advantages that are interesting for the industrial environment in which they are meant to be deployed, such as high-speed measurements, wide temperature operation ranges and adaptability. The combination of such characteristics make OFDSs appealing towards the desired “zero defects” production [21].

Among the sectors in which metrology plays a major role, the aeronautical industry is probably the benchmark as it has the most demanding requirements in terms of performance and reliability. Such sector tends to be very strict regarding manufacturing and validation processes, and as a result, they use mature technologies whose reliability and performance have been verified through years, as thermocouples or strain gauges, among others. These sensors are commonly used to characterize or verify aeronautical components and their structural health, as these elements are designed in a manner in which they can withstand certain levels of damage without affecting their performance [22]. Due to that, meticulous inspections are required to keep these possible damages within the safety margins. In this context, sensors capable of reaching the quality standards of the inspection at the same time that are capable of reducing the time to perform those maintenance or inspection processes are pursued. The reason for the latter is the increase of the profit of airlines and manufacturers accordingly as the time required for the validation of the components and/or the time the aircrafts are on the ground is shortened. Hence, developing an OFDS capable to fulfill such demanding requirements and become a realistic alternative in such a conservative industry as the aeronautical is a very challenging objective.

Among the many of components with which an aircraft is comprised, the engines are likely to be the most critical and expensive components. As it can be noticed in Fig. 3, they consist of several cascaded stages. If we attend to the direction of the airflow, the first stage is the fan, whose purpose is to guide part of the air driven by it into the core of the engine through the low-pressure compressor. The low-pressure and high-pressure compressors conform the second stage, and their function is to increase the pressure of the air through it so that the efficiency of the combustion is increased proportionally. The third stage is the combustion chamber, where the fuel and pressurized incoming air are mixed; and at the exit of it is where the

fourth stage is located. It consists of the high and low-pressure turbines, which are in charge of extracting the energy from the airflow to make the fan and compressors rotate.

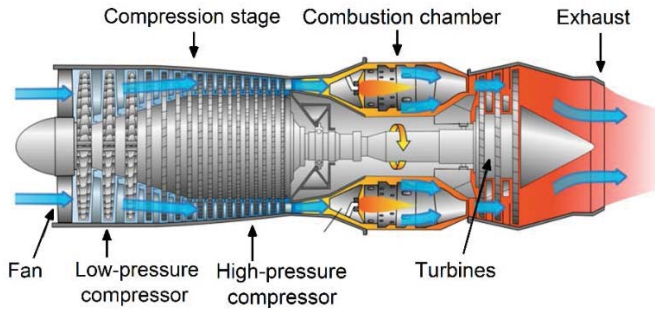


Figure 3: Schematic of the stages of a jet engine. Courtesy Jeff Dahl, CC BY-SA 4.0, via Wikimedia Commons.

Commonly, turbine and compressor stages consist of blisks, which is the name given to a rotor formed by the assembly of a disk and a series of blades integrated into it (blades + disk). During the operation of an engine of this nature, there are multiple parameters that require to be monitored, such as temperature, vibration, pressure, rotation speed, etc. [23]. Among them, the characterization of the vibrations in the blades of the blisks is of vital importance as they are directly linked to the efficiency and safety of the engine, and currently, a technology that fully meets the needs of engine manufacturers regarding this topic does not exist.

When a blisk is rotating at high speed, the vibrations suffered by the blades can be of three types: radial, tangential and axial (see Fig. 4). Radial vibrations will induce changes in the length of each blade, which will cause the blades to be closer or further from the engine casing. This distance is defined as Tip Clearance (TC), which is a very significant parameter for engine safety and efficiency. The tangential vibrations of the blades occur in the plane perpendicular to the airflow in which the rotor is located, and may be characterized by the technique named Tip Timing (TT) [24]. By using this method,

it is possible to calculate the amplitude and frequency of the vibration of each blade individually. To that end, the differences between the real and theoretical times of arrival of each blade at a certain point are analyzed. Due to the nature of TC and TT, the same sensor could be used for the measurement of both parameters [25]. Lastly, axial vibrations take place in the same direction as the airflow. Even though these vibrations are relevant for the performance of engines, they are out of the scope of this work.

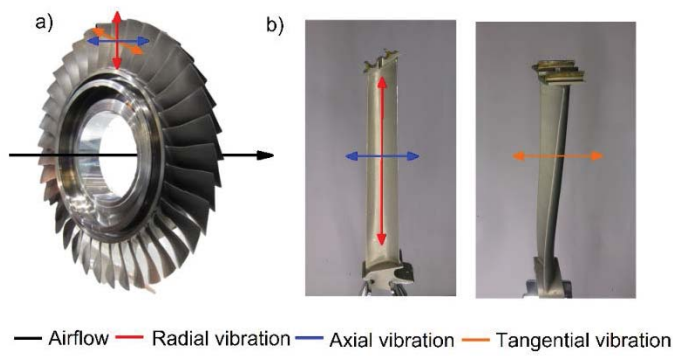


Figure 4: a) Blisk of a compressor with the direction of the airflow and the vibrations suffered by the blades indicated in it and b) front and side views of a blade from a low-pressure turbine with the direction of the vibrations indicated in it.

1.2.2 Theoretical framework and methodological tools

1.2.2.1 Definition of Tip Clearance (TC) and Tip Timing (TT)

As it has been mentioned in the previous section, the TC of a blade in a blisk is defined as the distance from the blade to the casing of the engine. This gap, shown in Fig. 5, generates a leak in the airflow that does not contribute to the operation of the engine and therefore, reduces its efficiency [26]. The relevance of this parameter is such

that if it decreases by 0.25 mm, it causes a decrease in the fuel consumption of 1% and a decrease in the temperature of the exhaust gases of 10 °C, which would increase the life span of its components [27]. Even though these figures may seem small at first sight, if we attend to the global air traffic prior to the pandemic, it could cause savings of up to 167 million dollars per year [28]. Considering the delicate economic situation of many airlines as a result of the aforementioned pandemic and the progressive but slow coming back to pre-pandemic figures, such figures are worth be taken into account. Apart from the economic benefits, there would also be environmental benefits as gas and acoustic emissions would be decreased accordingly.

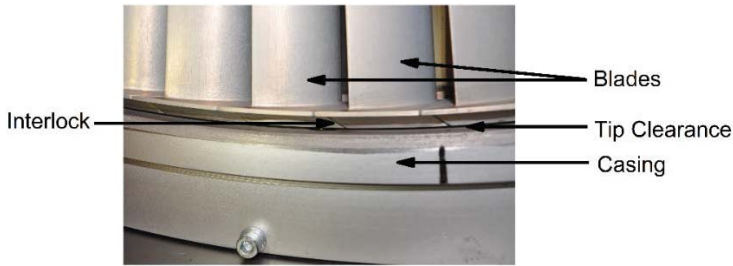


Figure 5: Detail of the TC of a low-pressure turbine stage once it is assembled in the casing.

Due to the combination of the characteristics mentioned above, it is highly interesting for the industry to integrate a system to keep the TC as low as possible but always above a minimum safety operation gap to avoid a fatal accident caused by a blade break due to scratching excessively the casing. Such systems are known as Active TC Control Systems, and they allow modifying the value of the TC by controlling the thermal expansion of the casing. In order to do that, part of the airflow is redirected to the casing by means of valves so that the TC can be optimized and therefore, the efficiency of the engine increased [29].

While TC values from 2 to 8 mm are typical for power generation turbines, TC values for aeronautical engines rarely exceed 3 mm [30].

Such TC values depend mainly on the operating regime of the engine (takeoff, cruise or landing), and as a general rule, it can be considered that the TC values are inversely proportional to the rotational speed of the engine: as its speed increases, TC decreases and vice versa. However, this is not the only factor affecting TC, as it also depends on the aging of its components [31, 32].

While TC is more related to the efficiency of the engine, the technique known as TT provides information about the structural health of the blisks [24]. In order to do that, such technique characterizes the tangential vibrations of the blades, which allow predicting potential failures in them caused by fatigue [33] and provides crucial information for the design and development of more reliable and safe engines. TT allows determining the amplitude and frequency of the deflections of the blades by means of measuring their arrival time to the position of the sensor and comparing such measurements with their theoretical time of arrival to that point, which is the expected time of arrival if the blades did not suffer any vibration (Fig. 6).

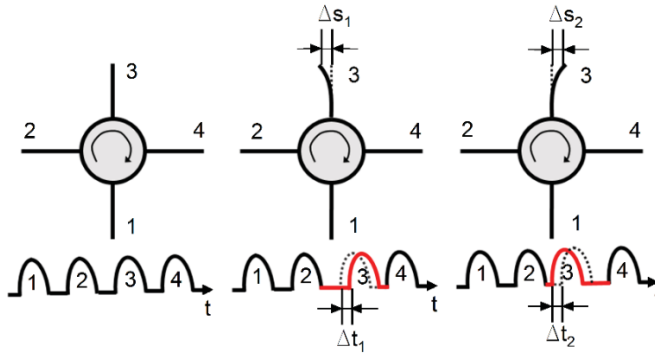


Figure 6: Schematic representation of the definition of TT.

To that end, several sensors must be deployed consecutively in the casing following the direction of rotation, in order to track the vibration of each blade along a section of their rotation path [34]. Once the difference between the measured and theoretical times of

arrival is known, as well as the rotational speed and the radius of the turbine, the amplitude of the vibration of each blade can be calculated. By processing this data, some other relevant parameters of the engine can be known as well, such as the frequency of vibration of the blades, number of nodal diameters of the blisk, etc.

1.2.2.2 TC and TT sensing technologies

TC and TT measurements have to be carried out in a context in which the blades are rotating at high speed. Thus, sensors capable of providing non-contact measurements are required in order not to affect or condition the natural movement of the blades. To that end, aeronautical engine manufacturers have developed several non-contact measurement solutions based on different technologies. Among them, capacitive, inductive, microwave and optical fiber-based sensors should be highlighted.

Capacitive sensors are probably the most spread TC sensors thanks to their simplicity, robustness and cost-effectiveness. Their main drawbacks rely on the facts that they provide low spatial resolution, bandwidth and short operating range. Moreover, they require the blades to be made of electrically conductive materials in order to operate [35]. Inductive sensors are lightweight and cost-effective, and are able to operate even if the blade is out their sight. However, their measurement setup tends to be complex, as their calibration depends on many factors that have to be known in advance such as temperature, shape of the blade or rotational speed of the shaft, for instance [36]. Discharging probe sensors are a common variant of the latter technology. Such sensors require the blades to be electrically conductive and they only provide the lowest TC value in the blisk [37]. Microwave sensors are capable of operating at high temperatures with high precision, and are not affected by the combustion residues inside the turbine. The main drawback of this

technology is the price, as it requires complex and heavy signal processing setups to perform properly [38, 39]. Many of the aforementioned drawbacks may be overcome by optical fiber-based sensors, which provide wide bandwidth, high resolution and high sensitivity [25]. Moreover, they are very versatile and do not require complex setups to operate. However, their main drawback is that they are very sensitive to combustion residues, as they operate by analyzing light. Thus, if the sensor head is contaminated, it may affect its performance. This obstacle must be solved so that they can be used in turbines for long periods. However, for tests included in this work, that have been carried out in a wind tunnel, optical sensors are the best fitting sensing solution, as there are no combustion residues inside it that may affect the performance.

1.2.2.3 Optical fiber-based TC and TT sensors

Among optical fiber-based sensors, there are three common configurations for precise distance measurements: Interferometric sensors, sensors based on Doppler Effect and sensors based on the modulation of the intensity of the reflected light. Interferometric sensors provide high resolution and sensitivity, although they usually require a coherent light and a very stable optical setup [40], which complicates its implementation in turbines that are subjected to vibrations. Sensors based on Doppler Effect consist in analyzing the frequency change in the reflected light caused by the movement of the target, which can be translated into distance after processing the signal [41]. They provide high resolution and sensitivity, although the components of such devices, as the highly coherent laser, are expensive. Lastly, those based on the modulation of the intensity of the reflected light consist of two type of fibers (emitting and receiving fibers) or a single fiber that acts as emitter and receiver at the same time by means of a circulator or a splitter. Transmitting fiber/s send/s light to the target, which is reflected in it and then gathered

by the receiving fibers. By analyzing its intensity, the relation between the distance from the sensor to the target and intensity can be accurately established [42]. These sensors are very simple and versatile, as in order to optimize their performance or to obtain a specific response curve, they can be easily customized just by modifying the arrangement of the transmitting and receiving fibers in it. In Fig. 7, a summary of the most common configurations of sensors of this type along with their respective typical response curves are shown. Except for the case of a single fiber acting as transmitter and receiver, two different regions of quasi-linear behavior can be acknowledged in the response curves: the first region (Region 1) has a positive slope, whereas the second region (Region 2) has a negative slope. Region 1 shows higher sensitivity and linearity compared to those in Region 2, although the range of distances in which it works is significantly shorter.

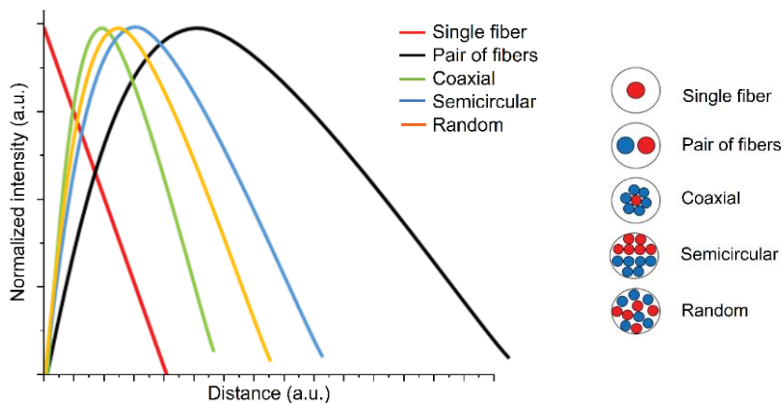


Figure 7: Typical response curves for the different fiber arrangements of intensity-modulated sensors. Red and blue colours indicate transmitting and receiving fibers, respectively.

Selecting one of the aforementioned optical configurations will depend on the measurement requirements. For the case of this work, such conditions are explained below.

1.2.2 Hypothesis and objectives

1.2.2.1 Performance requirements

The OFDS was designed according to the specifications determined by of our partner in this research, Centro de Tecnologías Aeronáuticas (CTA). The facilities of CTA are located at the Bizkaia Science and Technology Park in Zamudio (Biscay), which is around 20 km away from those of the Applied Photonics Group APG-FAT. This fact facilitated significantly the communication and feedback between us. In such facilities, there is a wind tunnel where scaled stages of turbines for aeronautical engines are tested.

Such wind tunnel is a transonic testing bench with continuous airflow, where parameters such as pressure, temperature and mass flow can be individually controlled. In this manner, Mach and Reynolds numbers can be modified independently to simulate as close as possible takeoff, cruise and landing conditions of the engine. The wind tunnel has a cross-section of one meter and has a single shaft capable of rotating up to 7800 rpm (see Fig. 8). In order to supply the air in the wind tunnel, two electric power compressors of 3.7 and 5 MW are used. These compressors are capable to provide a maximum mass flow of 18 kg/s and a maximum pressure of 4.5 bar. Temperature inside the tunnel can be adjusted as well from room temperature to 160 °C. It is also worth mentioning that the wind tunnel is prepared to acquire up to 800 pressure and 200 temperature signals, as well as a Once Per Revolution (OPR) signal that allows knowing the rotational speed of the shaft [43]. As said before, in the wind tunnel in which the sensors were tested there is no combustion. Thus, optical sensing technology is the best fitting solution for TC measurements in this context, as it provides all the benefits of using optical fibers without the critical drawback of the possible contamination of the tip of the sensor. It is important to point out

that the OFDS has to be made of glass fiber, as 160 °C is close to the thermal limit of the operating range of polymer optical fibers. Moreover, an additional reason for choosing glass fibers is the aim is to develop an OFDS suitable for this environment but upgradeable to environments with higher temperatures.

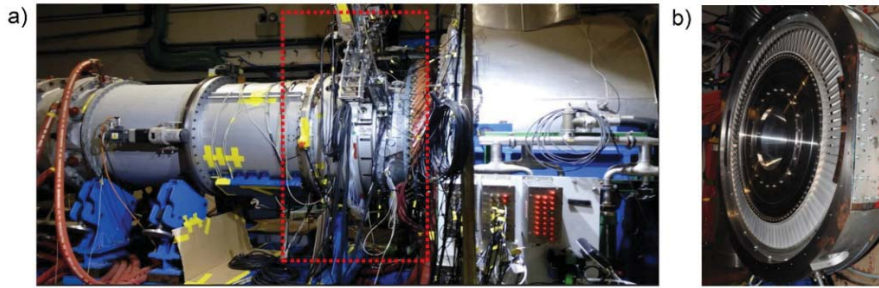


Figure 8: a) Wind tunnel where the tests were carried out. The position of the rotor under test is indicated by the red dotted rectangle. b) Detail of how turbine stages are installed in the wind tunnel.

The turbine of an aeronautical engine consists of several cascaded stages, each of them consisting in a couple formed by a rotor and a stator. The stator is fixed to the casing and consists of blades whose aim is to redirect the airflow to the rotor and increase its speed. The rotor is fixed to the shaft and consists of multiple blades that are rotating at high speed. Its aim is to extract the energy from the incoming airflow from the stator. The turbine stages are installed in a casing that has an abradable material in its inner part. The latter is a soft protective wear material that is mounted on the wall and aligned with the blades. In fact, the turbine blades are designed to rotate as close as possible or even scratch it slightly to create a good sealing between them to improve combustion efficiency without being damaged in the process.

In the wind tunnel at CTA, one stage of such turbines is tested each time. For TC measurements, the sensors are installed radially in the casing in a manner in which they are aiming at the center of the rotor and aligned with the rotating blades (see Fig. 9). Considering

the vibrations suffered by the blades, the small holes in the casing to install the sensors have to be made precisely in order to ensure the alignment and optimize the performance of the sensor.

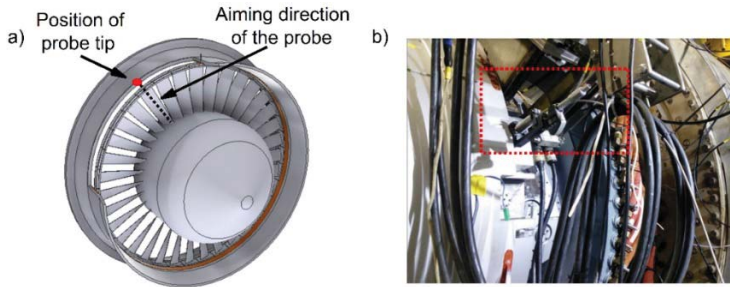


Figure 9: a) 3D model of a rotor. The point where the hole in the casing was done to insert the probe is indicated by the red circle. The black dotted line indicates the direction to which the sensor is pointing. b) Detail of how the probes are inserted in the holes and installed in the casing in the wind tunnel.

The designs of the blade tips are specific for each turbine and are even specific for each stage of the turbine. Thus, it is habitual to have different blade tips in terms of size and shape at different stages within the same turbine. Commonly, their tip consists of a thin flat surface sandwiched between two sealing lands. The latter are two sharp and thin edges (below 1 mm wide) that are designed to be as close as possible to the abradable or even scratching it, whereas the flat platform between them contains a datum in it that acts as a marker to evaluate the quality of the manufacturing process of the blades (see Fig. 10).

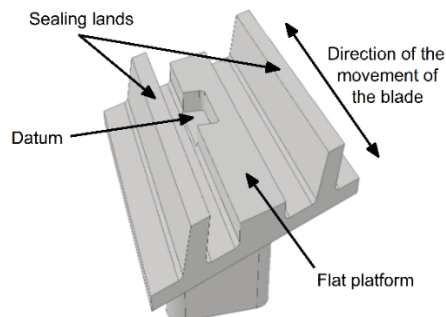


Figure 10: 3D model of the generic shape of a blade tip of a turbine.

For the measurements provided by the OFDS to be valid and useful for CTA, they determined some performance requirements that had to be fulfilled in all the tests:

- Provide a non-contact measurement in order not to interfere with the mechanical behavior of the blades.
- A precision in the measurement of TC of 25 μm at least.
- High resolution. The sensor has to be capable of detecting the blades individually in order to make it possible to analyze them one by one and identify unequivocally those with abnormal values.
- High sensitivity and resolution in the measurement so that any imperfection or defect in the blades could be detected.
- A linear region of operation that covers a range of distances of 1 mm at least. The definitive range of interest is defined by the turbine under test.
- Robustness of the sensor in order to withstand the aggressive environment in which the measurements are going to be carried out, especially according to vibrations.
- Simplicity and implementation easiness to be deployed in real-field testing. Apart from the fiber bundle, the rest of the hardware should be as off-the-shelf as possible to make it possible to replace it easily and fast in case it gets damaged or broken.
- Cost-effectiveness in order to make it economically viable towards the development of a commercial product. Apart from the fiber bundle, there should not be any other ad-hoc hardware, and even the fiber bundle should be made of standard fibers.

Considering all the aforementioned requirements, it was decided that the best fitting optical solution for the design of an OFDS for TC measurements was the one based on the modulation of the intensity of the reflected light. Among the multiple possible configurations

within this type of sensors (see Fig. 7), the coaxial fiber distribution was selected. Even though this configuration is not the best in terms of measurement range [44], thanks to its circular symmetry, it avoids major alignment issues with the blades of the rotor. This is a very relevant characteristic, as it would facilitate its installation in the casing significantly, which was one of the requirements of our partner CTA. Moreover, a configuration based on two independent concentric receiving fiber rings was chosen (see Fig. 11). In this manner, by obtaining a differential signal from both of the rings, it is possible to attenuate or minimize the effects of possible variations in the reflectivity of the blades, fluctuations in the light source or losses of optical power, for instance. Such fact is demonstrated mathematically below.

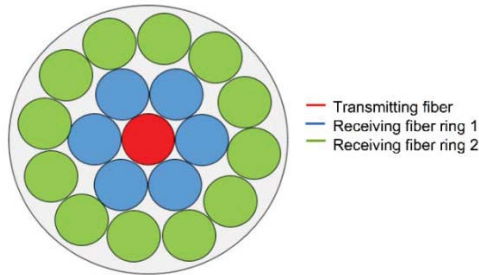


Figure 11: Generic geometry of the developed OFDSs in this work for TC measurements.

In the literature, it is easy to find many sensors of this type for distance measurements [45-48]. Most of these sensors have been tested in a laboratory using a mirror as a target, and some of them have been specifically adapted for turbine simulators that operate in controlled environments [49-51]. However, very few have been tested in real engine conditions. In those few cases, they operated in Region 2, which is longer than Region 1 but provides less resolution and sensitivity [25]; or in Region 1 in very specific and special situations where very low TC variations were expected [52]. Moreover, in such cases, the measurements were not made in real time and the signal required being post processed offline to obtain results, which limited

their potential application as online and real-time preventive maintenance system significantly.

To overcome such limitations, in this work, an OFDS for TC measurements designed to operate in Region 1, and capable to provide TC values in real time is shown, leaving the use of Region 2 for exceptional cases as less demanding situations or for comparison purposes. The mathematical approach for the design of the optical fiber bundle is explained in the section below as well as the hardware configuration for the OFDS. The complete information regarding this research and the summary of its results can be found in **Article 1** in the Appendix, in section 1.2.3 and in [53], respectively.

1.2.2.2 Mathematical approach

In order to get the most accurate performance prediction of the fiber bundle of the OFDS, the key parameter is the beam propagation model of the transmitting fiber (TF). For intensity modulated OFDSs where the fibers are axially aligned and fully illuminated during the measurement, the Gaussian beam propagation model fits for an accurate prediction. However, for OFDSs where the illumination of the receiving fibers is partial, as it happens in the ones in this work, the Gaussian beam does not offer such accuracy and a quasi-Gaussian beam model approach is required [44, 54]. The latter modifies the Gaussian model to include the so-called perturbation parameters [55], which denote the divergence between the two beam models.

The mathematical expression for the beam propagation model defines the effective radius of the output optical field as a function of distance ($q(d)$). Considering that both TF and receiving fiber (RF) ends are at the same level, it can be assumed, by optic ray geometry, that the reflected gathered light for a certain distance d is equivalent

to the one gathered by a single fiber located at twice the distance ($2d$) (see Fig. 12).

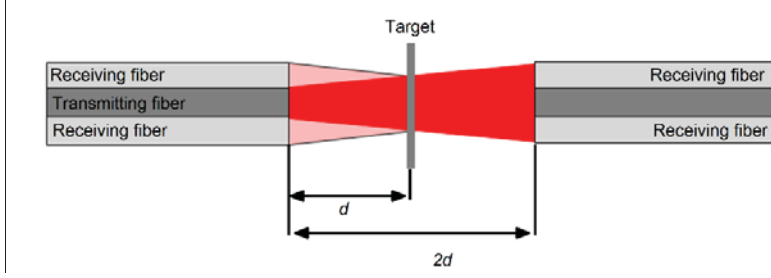


Figure 12: Schematic of the optic ray geometry.

Therefore, the effective radius of the output optical field can be expressed as:

$$q(2d) = \sigma r_T \left[1 + \zeta \left(\frac{2d}{r_T} \right)^\eta \tan(\arcsin(NA)) \right] \quad (1)$$

where r_T and NA are the core radius and the numerical aperture of the TF, respectively, and σ , ζ and η are three regulating parameters of light intensity distribution relative to the characteristics of the light source and TF [44]. For a case of a single TF and RFs, by integrating the received light intensity along the core area of the RF, the received power can be expressed as:

$$P(d) = \frac{\delta P_0 r_R^2}{q^2(2d)} \exp \left[\frac{-\rho^2}{q^2(2d)} \right] \quad (2)$$

If we call $f = [r_R^2/q^2(2d)] \exp[-\rho^2/q^2(2d)]$ the modulation characteristic function of a fiber pair, we can express Eq. 2 as:

$$P(d) = \delta P_0 f(r_T, r_R, NA, \rho, d) \quad (3)$$

where δ stands for the target surface reflectivity, P_0 is the power exiting the TF, r_R is the core radius of the RF and ρ is the gap between the axes of the RF and TF. As it has been explained

previously, due to the coaxial distribution that has been chosen to design the fiber bundle, each RF ring has a finite number of identical fibers (n_R) and there is only one TF (see Fig. 11). As a result, a model in which a summation of each individual TF-RF interaction within the same ring needs to be considered.

$$P(d) = \sum_{i=1}^{n_R} P_{i(d)} = \delta P_0 \sum_{i=1}^{n_R} f(r_T, r_R, NA, \rho_i, d) = \delta P_0 F(r_T, r_R, n_R, NA, \rho, d) \quad (4)$$

where $F = \sum_{i=1}^{n_R} f(r_T, r_R, n_R, \rho_i, NA, d)$ is defined as the modulation characteristic function of a fiber bundle. As it can be deduced from Eq. 4, the received power has a strong dependence on the surface reflectivity and the emitted power in a configuration of a single TF and one RF ring. To minimize or even avoid this dependence, a distribution based on two concentric fiber rings was implemented in order to obtain the ratio between the gathered light from each RF ring.

$$Ratio = \frac{P_1}{P_2} = \frac{\delta P_0 F_1}{\delta P_0 F_2} = \frac{F_1}{F_2} \quad (5)$$

where the terms with subindex 1 and 2 are related to the inner and outer rings, respectively. As it can be deduced from Eq. 5, by using this configuration, the dependence on the reflectivity and the emitted power is avoided. Moreover, considering that the parameters r_T , r_R , n_R and NA included in F are fixed by the fibers that comprise the fiber bundle, the modulation function will only depend on the difference between fiber axes ρ and the distance to the target d . As d is the value intended to be measured in TC, the key parameter of the design of the fiber bundle is ρ . Once ρ is fixed, the ratio of the received power will only depend on the distance to the target (d).

The gathered light power from each of the rings is then amplified and converted into voltage by means of a switchable gain (G)

photodetector (PD) connected to each of the RF rings. PD1 was connected to the inner RF ring and PD2 to the outer RF ring, respectively. Each PD has a responsivity value that depends on the emitted wavelength ($R(\lambda)$) and a transimpedance value that depends on the selected gain ($T(G)$).

$$V_{PD} = R(\lambda) * T(G) * P(d) \quad (6)$$

Thus, for a distribution of two concentric rings, the ratio of the voltage between the two RF rings can be expressed as:

$$Ratio = \frac{R(\lambda) * T_2(G) * F_2(d)}{R(\lambda) * T_1(G) * F_1(d)} = \frac{T_2(G) * F_2(d)}{T_1(G) * F_1(d)} = K * \frac{F_2(d)}{F_1(d)} \quad (7)$$

where the terms with subindex 1 and 2 are related to the inner and outer rings, respectively. The term regarding the responsivity ($R(\lambda)$) can be simplified as the emitted wavelength is the same for both rings. From Eq. 7, it can be concluded that the ratio will depend on the quotient between the gains of the PDs connected to each RF ring (K), and on a quotient between two functions (F) that depend only on the distance from the fibers to the target (d). This means that the output ratio is going to be unaffected by light source fluctuations, fiber losses or changes in the reflectivity of the blades [49, 56], as it was intended. Thus, a relation between the ratio of the measured voltages and distance can be easily determined.

The aforementioned mathematical approach was implemented in Matlab MathWorks to simulate the response curve of OFDSs with different fibers, fiber arrangements and PD gains in order to obtain a configuration that fulfilled the requirements of our partner CTA and that could be manufactured and used in real-life measurements in the wind tunnel. To that end, certain OFDS properties were fixed, such as using a laser at 660 nm, all the fibers in the bundle to be step index ($\sigma = 1$) and the TF to be a SMF ($NA = 0.12$ and $r_T = 2.15$

μm) at 660 nm. These characteristics were decided for practical purposes: using a SMF as TF avoids the appearance of any modal or speckle noise that could affect the power distribution [42], and using a wavelength in the visible range makes it possible to verify the spot at which the sensor is aiming. Moreover, the prize of components with such characteristics is lower compared to those for longer wavelengths, which makes the sensing system more cost-effective.

As it will be shown in the following section, such simulation program demonstrated to be a very powerful and useful tool to design fiber bundles and predict their response curves before manufacturing them, as the results provided by it were close to those provided by the physical devices manufactured according to the specifications provided by it.

Regarding the rest of the measurement system, it consisted of: a fiber-coupled laser source at 660nm (Thorlabs S4FC), one switchable gain PD for each RF ring (Thorlabs PDA100A-EC), an acquisition board that operates at high speed (National Instruments 6366 USB, 2 MS/s) that was connected via USB to a laptop (HP Elitebook 840 g3). To process the data, a custom-made LabVIEW program was developed. This program allowed monitoring the TC values in real time and storing the raw signal in a hard drive. The latter is a relevant characteristic for long lasting tests in which an amount of data in the order of terabytes is created.

1.2.3 Summary and results

1.2.3.1 Aiming at the sealing land of the blades

In this point, a summary of the article “Design, Fabrication and Testing of a High-Sensitive Fibre Sensor for Tip Clearance Measurements” is shown. This article was published in Sensors in

*August 2018 and it is included in the Appendix section of the thesis as **Article 1** to be consulted for further details.*

The first OFDS operating in Region 1 that was configured according to the results and characteristics provided by the simulation program was implemented in a turbine consisting of 92 blades which was expected to have TC variations below 1 mm and to spin at a maximum of 6000 rpm. The design of the holes in the casing forced the fiber bundle to be installed in the turbine rig aiming at the sealing lands of the blade tips (around 0.7 mm in width and designed to be close or even scratch the abradable material), which yielded a very low reflected signal, instead of the preferred flat platform (see Fig. 13). These factors were critical for the design of the fiber bundle, the emitted power and gain configuration of the PDs. For instance, to guarantee a safe operation without compromising the physical integrity of the rotor and the fiber bundle, the latter was designed with a Region 1 that started at 2.8 mm, so it could be placed further from the blade tips.

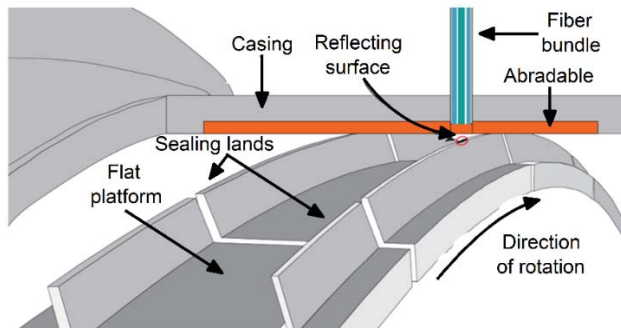


Figure 13: Schematic representation of the measurement conditions.

The best fitting OFDS configuration for these measurements was as follows: Regarding the fiber bundle, the inner ring of RFs was located at a radius of 200 μm from the center of the bundle and consisted of 5 optical fibers, whereas the outer ring of RFs was located at a radius of 930 μm and consisted of 17 optical fibers. All the RFs were

multimode with a NA of 0.2. The diameters of those from the inner and outer RFs were 200 μm and 300 μm , respectively (see Fig. 14). According to the emitted power, it was set to 50 mW to guarantee that enough light was going to be reflected back to the device. The gain configuration of the PDs was set to 10 and 40 dB for the inner and outer rings, respectively, to keep them below the saturation value and create voltage values spanned over the full voltage scale (0–5V) of the acquisition board to optimize its performance.



Figure 14: Photograph of the end face of the probe tip and schematic of the manufactured fiber bundle.

The calibration of the OFDS was carried out in the laboratory aiming at the sealing land of a spare blade of the turbine to simulate as close as possible the measurement conditions that were going to take place in the turbine rig. The reason for carrying the calibration in the laboratory was that the fiber bundle and the sealing lands were going to be aligned only when the turbine was rotating at high speed. In idle state, there was no alignment, which made it impossible to calibrate the sensor in-situ once it was installed in the casing. The small difference between the experimental calibration curve and the one provided by the simulation program in Region 1 is shown in Fig. 15, where it can be noticed that they never diverge more than 1.5%.

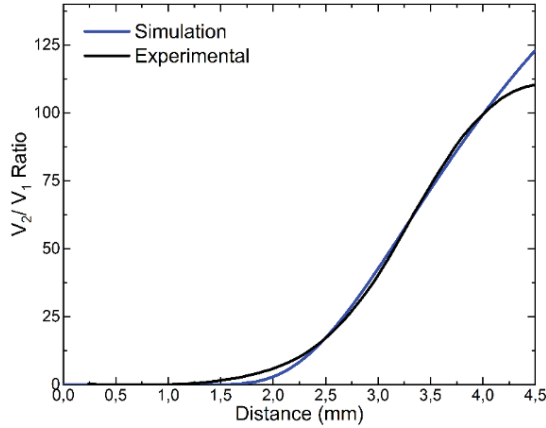


Figure 15: Simulated and measured calibration curves for Region 1.

The linear fit of the experimental response curve shown in Fig. 15 starts at 2.8 mm and has a Pearson's correlation of 0.997 in the range of interest (from 2.8 mm to 4 mm, larger than the expected 1 mm TC variation) with a sensitivity slope of 61.73 mm^{-1} , which are characteristics beyond the requirements of our partner.

To install the fiber bundle in the turbine, it was introduced in a micrometer-driven adapter (see Fig. 16) in a manner in which the fiber bundle end and that of the micrometer were at the same level. Then, the micrometer was inserted and fixed in a radial hole that was made in the casing to that purpose (see Fig. 9b).

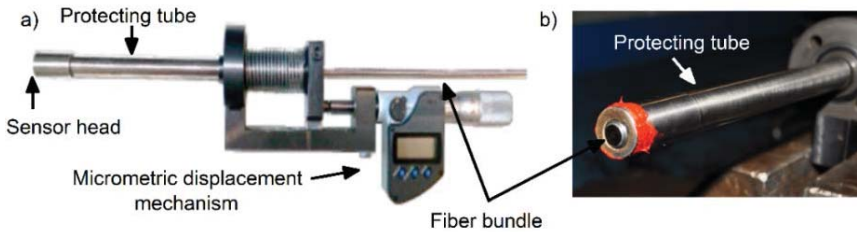


Figure 16: a) Micropositioner used for the tests. b) Detail of the fiber bundle end in the micropositioner.

By means of this tool and thanks to the fact that Region 1 started at 2.8 mm, it was possible to place the sensor within the abradable layer at a distance of 3.2 mm from the tip of the blades. This distance

was selected for being the center of the Region 1 of the response curve of the fiber bundle (see Fig. 15). In this manner, it was guaranteed to operate in the linear region all the time during the tests, and the possibility of damaging the blades or the sensor head was avoided. As TC values are commonly referenced to the end of the abradable coating, the TC value was obtained subtracting 2.74 mm to the sensor measurement (distance from probe tip to reflecting surface), as shown in Fig. 17.

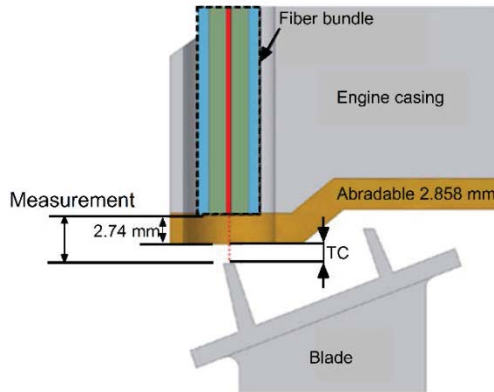


Figure 17: Schematic of the optical probe placement within the casing and the TC calculation.

The tests were carried out at different Working Points (WP) of the turbine and were repeated during several days. For each WP, parameters such as rotational speed, pressure, etc. in the wind tunnel were modified by the crew of CTA to simulate specific situations of their interest. Each engine revolution was identified with two methods for blade identification purposes: with a blade of a particular reflection pattern that was taken as reference, and with a stable and non-vibrating Once per Revolution (OPR) signal obtained from the shaft. During the entire tests, the signal pattern of each of the 92 blades in the rotor was easily identifiable, and even the spacing between them (interlocks) were acknowledged (see Fig. 18).

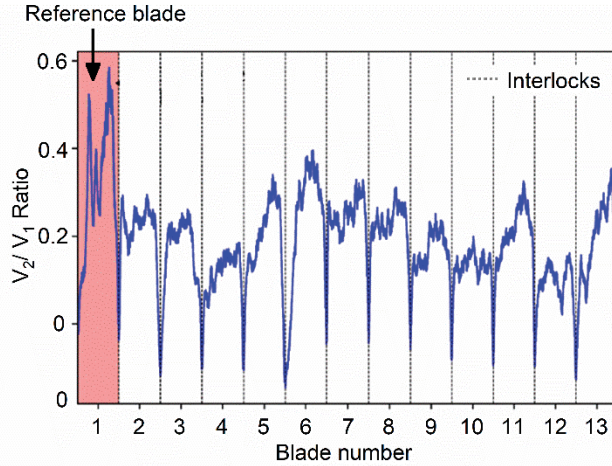


Figure 18: Example of the acquired signal during the tests. The blade highlighted in red was used as reference due to its particular reflection pattern.

To study each blade individually, the TC was defined as the average value of the corresponding dataset of each blade at the 50% selection level around their central sample. According to this definition, even in the worst case, the TC variability was approximately of $20\ \mu\text{m}$ within the same WP, and the average value over the 92 blades was below $5\ \mu\text{m}$. Moreover, it was possible to identify blades with very small or abnormal TC values, which could indicate that there was a defect in their manufacturing or installation process that could be dangerous for the integrity of the turbine. Fig. 19 is an example of the latter, as for the WP of 4258 rpm, the TC values of blades number 16, 38, 43, 51 and 69 indicated that they were close to the abradable surface and they should be monitored carefully.

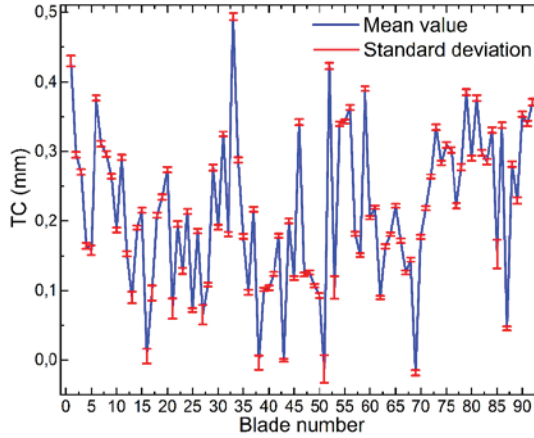


Figure 19: TC values and the corresponding standard deviation of each blade at 4258 rpm over 1100 turns.

By means of the high resolution and sensitivity provided by this OFDS, it was possible to carry out an individualized analysis of the blades, and it was demonstrated that TC and the rotational speed of the rotor are inversely proportional: as one increases, the other decreases and vice versa. This fact can be attributed to the centrifugal and thermal loads acting on static and rotating components of the turbine.

Moreover, the results from this work were useful for our partner CTA to characterize the TC of the turbine, and for ourselves to validate the simulation program, as the calibration curves of the simulated and manufactured devices came together, confirming its accuracy and reliability. This fact opened the possibility to design ad-hoc highly sensitive OFDSs for specific contexts, as the one shown below.

1.2.3.2 Aiming at the datum of the blades

In this point, a summary of the article “Performance Comparison of Three Fibre-Based Reflective Optical Sensors for Aero Engine Monitorization” is shown. This article was published in Sensors in May 2019 and it is reference [53] to be consulted for further details.

As a step forward from the device described in the previous section and to confirm the validity of the simulation program, an upgraded OFDS was designed in order to measure the TC of a new turbine for CTA. As it is explained in detail in [53], the need for a new OFDS was caused by the fact that for this new turbine, that consisted of 94 blades, the TC range was expected to be larger than that in **Article 1**, which would force the OFDS in **Article 1** to operate in the less sensitive Region 2.

Taking advantage of this situation, the upgraded OFDS was designed with some characteristic improvements compared to its predecessor:

- Larger Region 1: In this manner, the OFDS will have a longer linear region to operate. This feature will make it be more versatile to perform in different turbines and with different ranges of TCs, avoiding the need of specific OFDS designs for each case.
- Region 1 that starts at longer distance: In this manner, the sensor head could be placed further from the blade tips and even outside the abradable material, avoiding any possible deposition of this soft material in the probe tip that could affect its performance.
- Region 1 of higher slope and dynamic range, which implies higher sensitivity to obtain the highest resolution and precision possible.
- The size of the OFDS had to be identical to that in **Article 1** to fit in the holes that were made in the casing for this purpose. Such holes were identical in size as those in **Article 1** and were made before knowing that the expected TC values for this turbine were larger. Therefore, the size of the fiber bundle in terms of diameter was restricted by this fact. In this manner, this OFDS would be able to operate in holes of standard size and provide enhanced performance at the same time.

The same simulation program used in **Article 1** was used to design this new sensor. According to it, the OFDS that fulfilled all the aforementioned requirements was identical to that used for the previous tests with the difference of the radius and number of fibers in the outer ring of the fiber bundle. In this OFDS, the outer ring had a radius of 1800 μm and consisted of 30 fibers (see Fig. 20).



Figure 20: Photograph of each of the ends and schematic of the of the upgraded manufactured fiber bundle.

Regarding the rest of the sensing system, the same hardware as for previous tests was used (laser source: Thorlabs S4FC, PDs: Thorlabs PDA100A-EC, acquisition board: National Instruments 6366 USB and laptop: HP Elitebook 840 g3) (see Fig. 21).

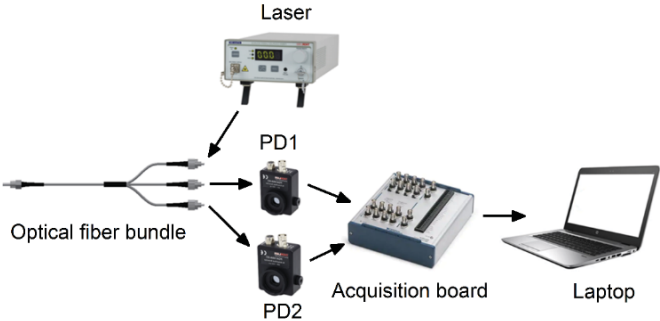


Figure 21: Schematic of the OFDS with the real hardware components that conform it.

For comparison purposes, in these tests another two OFDSs were installed in the casing of the turbine. The first was a commercial sensor (Philtec model RC171) that consisted of several transmitting and receiving fibers arranged in an adjacent semi-circular pattern where the fibers are distributed randomly. The second sensor was the

OFDS from **Article 1**, but forced to operate in Region 2 for the measurement conditions. The schematics of the cross-sections of the three OFDSs for these tests are shown in Fig. 22.

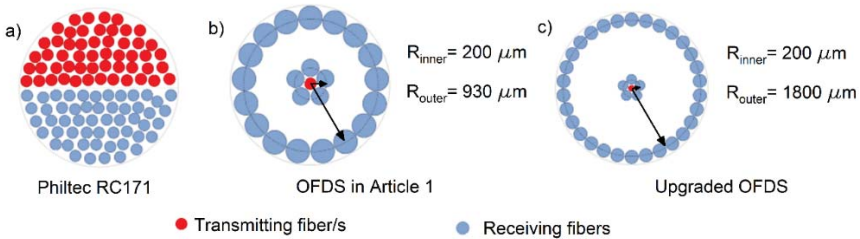


Figure 22: Schematic and scaled representation of the cross-sections of the devices used in this test.

The three sensors were inserted in micrometer-driven adapters as the one in Fig. 16 and installed in the casing as indicated in Fig. 23. Unlike in the operating conditions shown in **Article 1**, where the sensor was aiming at the sealing lands, in these tests, the holes in the casing were made so that the sensors could aim at the flat platform of the blade (see Fig. 10). This fact increased the reflected light significantly and allowed calibrating them in-situ once they were installed in the casing. Thanks to the increase of the reflected light, it was possible to share the laser source via a 50:50 splitter for both of the custom designed OFDSs as the commercial OFDS integrated its own source. The acquisition board was shared among the three devices.

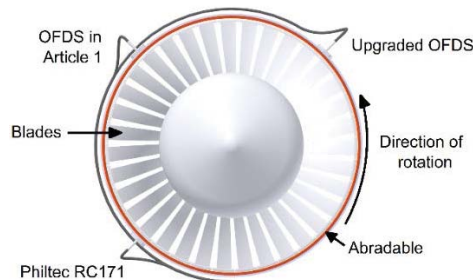


Figure 23: Schematic representation of the deployment of the sensors along the casing.

The calibration curves of each sensor are shown in Fig. 24, where it can be noticed that the upgraded OFDS operates in the Region 1 for the working region of interest whereas the previous OFDS is forced to operate in Region 2. Moreover, a larger and steeper Region 1 can be acknowledged in the upgraded OFDS. Regarding the commercial device, it operates in a less steep Region 1.

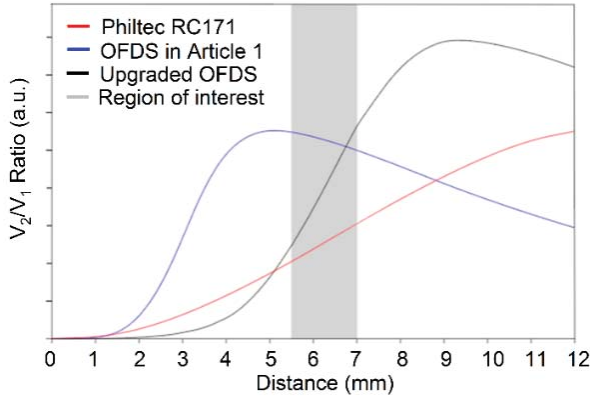


Figure 24: Response curves of the sensors and the expected region of the TC in this turbine.

The tests lasted from eight to ten continuous hours per day and were repeated for two weeks in consecutive days. As for the previous tests, every working point was recorded as well as the OPR signal for synchronization and blade identification purposes.

Results indicate that the custom designed OFDSs made it possible to determine the passage of each blade precisely and they were capable of detecting specific features such as the datum and inter-blade spacing. This fact did not happen in the commercial sensor, which provided a delayed and smoothed signal that made it hard to identify and synchronize events. As an example of this fact, in Fig. 25 the signal from blade 55 (which could be considered the standard signal of a blade) acquired in the three sensors and the comparison with the ideal signal are shown.

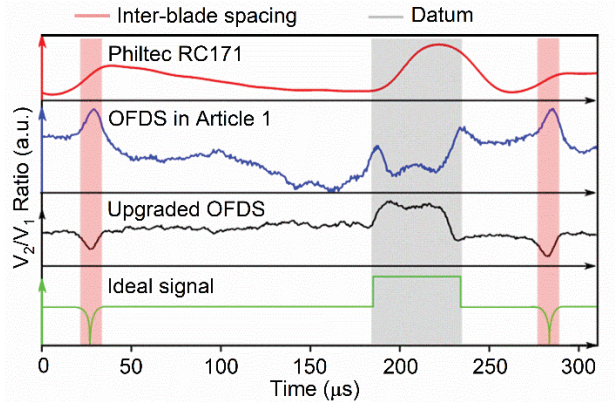


Figure 25: Comparison between the signals from blade 55 with the three sensors and the ideal signal.

Between the two custom designed OFDSs, the upgraded version provided higher sensitivity and resolution, and its signal was straightforwardly related to the physical shape of the blade and much closer to the ideal signal. The steep rising and falling edges in its waveform enabled determining precisely the boundaries of the datum, and ultimately, the arrival time of each blade, which could be an interesting feature for TT measurements (see Fig. 6). Moreover, thanks to this sensitivity enhancement, additional statistical parameters of the behavior of the turbine were obtained apart from TC, such as its instantaneous speed. It also allowed identifying unexpected features in blades just by comparing the shape of their signal with the one from a standard blade (as the one in Fig. 25), which is very relevant in order to prevent failures, malfunctions or to detect manufacturing defects (see Fig. 26).

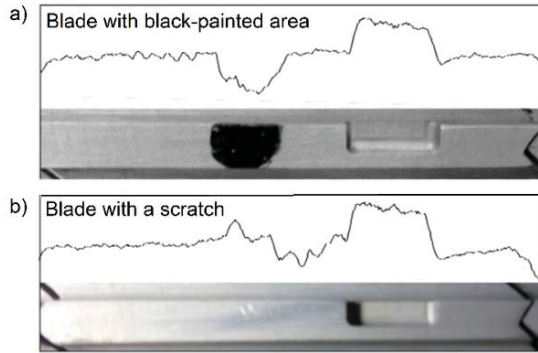


Figure 26: Example of waveforms with abnormal behaviors that indicated some anomaly in the blades. The inspection of the corresponding blades after the tests showed that a) black paint and b) a scratch caused them.

According to TC, this upgraded OFDS was capable of providing a very stable signal. For instance, Fig. 27 shows the TC values for a WP at 3627 rpm. The variability of the TC values over time (20000 engine revolutions), shown as vertical error bars, indicates a worst case of 20 μm within the same WP, and the average value of it over the 94 blades was below 7 μm .

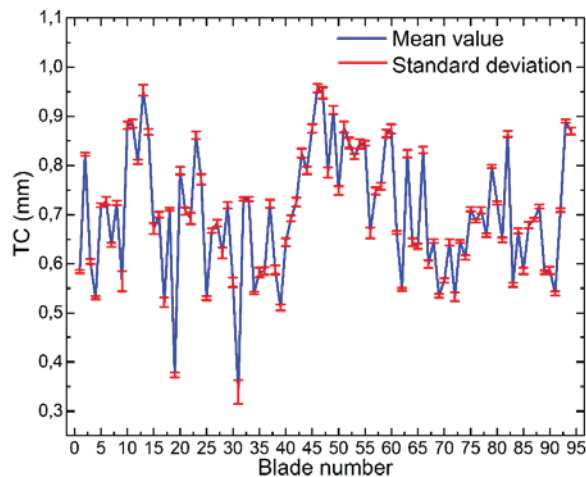


Figure 27: TC value and the corresponding standard deviation of each blade at 3627 rpm over 20000 turns.

The results from this work definitely confirmed the validity of the developed simulation program to design and manufacture highly

sensitive OFDSs for TC measurements. Moreover, this OFDS was designed to provide more versatility so that it could be used in different turbines thanks to its large Region 1 and its high dynamic range. These characteristics combined with the fact that Region 1 starts at longer distances, allows placing the sensor head further from the blade tips and even outside the abradable. This feature minimizes the risk of collisions between blade tips and sensor head, and minimizes the possibility of the probe head to get dirty due to any residue that could ruin its performance. To demonstrate the latter, both custom designed OFDS were examined in the microscope after the tests. The inspection showed that the end face of the upgraded OFDS remained without contamination residues, whereas the OFDS from **Article 1** showed abradable residues in some parts of its end face that could have ruined its performance as a result of having to place it within the abradable and closer to the blades (see Fig. 28).

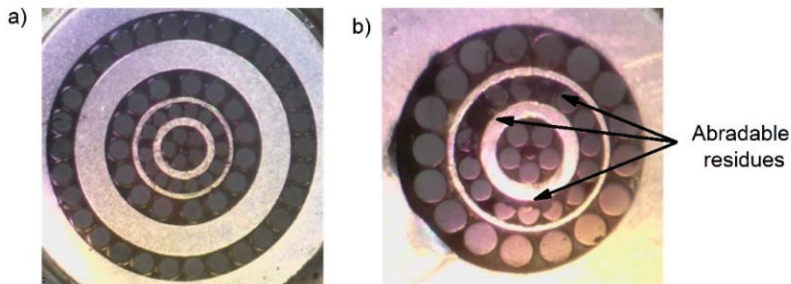


Figure 28: Photographs taken with a microscope after the tests of the end face of
a) the upgraded OFDS and b) the OFDS from **Article 1**.

1.3. Strongly coupled multicore fiber-based (MCF) sensors

In this section, several strongly coupled MCF-based optical sensors for sensing different parameters such as temperature, bending, acceleration, etc. are shown. To that end, the operating principle of such fibers is explained and exploited to develop highly sensitive devices.

1.3.1 Introduction and context of the research

1.3.1.1 Parameters of interest for the industry

As it was explained previously, in extrinsic sensors as the ones that are going to be described in this section, the alteration or modulation of some characteristics of the light are caused by an effect from outside the fiber. As a result of that, these types of sensors are used for the measurement of parameters such as temperature, bending or acceleration, for instance. The interest in the development of such sensors has remained unaltered through years, as all the aforementioned parameters are very relevant to monitor industrial processes or for SHM [57, 58], where it is common to find sensing solutions based on mature technologies that have proven to be reliable and cost-effective. Commonly, such solutions are based on devices of electronic nature, such as thermocouples, gauges, etc. However, considering that these sensors are usually deployed in harsh environments or in environments with high levels of radiation or radioactivity, they are prone to suffer from corrosion or interferences, which may lead to malfunctions or a decrease of their life span. Moreover, their electric or electronic nature may not be the best option for certain environments with flammable gases or liquids. A solution to this issue consists in protecting or shielding the devices, which may cause a loss in sensitivity.

The search for devices capable of overcoming such drawbacks and providing high sensitivity and resolution, deployment ease, cost-effectiveness, etc. has pushed towards the appearance of new technologies or sensing solutions. In this context, optical fiber sensing has arisen as an appealing option thanks to the characteristics that have been explained in detail in previous sections, and have started to gain visibility as a realistic alternative for industrial sensing and SHM [59, 60].

1.3.1.2 Extrinsic optical sensors

Among extrinsic optical sensors, those based on the alteration or modulation of the wavelength or the phase of the emitted light are the most spread solutions. In fact, several sensors based on these techniques have reached a maturity in which they can be found commercially.

One of the most spread and mature technique is the FBG. Briefly, it consists in creating a periodic variation in the refractive index of the core of the optical fiber so that it reflects only certain wavelengths of the emitted light and transmits the others. When the FBG is subjected to any external effect, the period of the grating changes, which causes the reflected wavelength to vary. Such wavelength shift can be directly and easily linked to the external effect. FBGs have been widely developed and have become very popular for temperature and strain sensing due to their high sensitivity, and nowadays they can be found in multiple configurations as tilted, phase-shifted, chirped, apodised, etc. depending on the application [61]. A variation of FBG technique, which could be considered as a category by itself, is the Long Period Grating (LPG). In LPGs, the period of the grating is much larger than the wavelength (on the order of 100 micrometers, to a millimeter), which can be used to achieve much broader responses. As a result, they are much easier to manufacture than FBGs [62]. The main drawbacks of FBG and LPGs

rely in the fact that both show intrinsic sensitivity to their surrounding medium, which forces proper isolation or compensation mechanisms to avoid crosstalk and be sensitive only to the parameter of interest, and that their setups require expensive lasers and interrogators.

Fabry-Perot interferometers (FPIs) are also a common solution to develop extrinsic sensors for the measurement of humidity, temperature, etc. [14]. Its operating principle is based on a small optical cavity made of two parallel reflecting surfaces whose length can be modified proportionally by the applied effect to it. As a result of that, optical waves can pass through the optical cavity only when they are in resonance with it, which means that if a broadband light source is used, only certain wavelengths of it are going to pass through it. Thus, the shift of the wavelengths that exit the cavity can be linked easily to the applied effect. FPIs are highly sensitive, although their main drawback is the difficulty to reproduce uniform cavities.

Mach Zehnder interferometry (MZI) and Michelson interferometers are used as well for sensing several parameters such as refractive indexes, temperature, gas, curvature, etc. [63, 64]. MZIs quantify the applied effect by measuring the relative phase shift between two collimated beams derived by splitting the light coming from a single source. One of the beams is used as reference, whereas the other is beam is subjected to the effect that is intended to be measured. In Michelson interferometers, the emitted light is split into two arms and, as in MZIs, one of them is used as reference and the other is used for measurements. Each of those light beams is reflected back towards the beam splitter, which then combines their amplitudes using the superposition principle. By analyzing the fringe pattern of the interference, the applied effect can be measured. Michelson interferometers have multiple applications, especially for stellar measurements, gravitational wave detectors, etc. [65]. Although

MZIs and Michelson interferometers are highly sensitive, their main drawback is their complex setups, as they require exhaustive alignments of the mirrors and very precise configurations in order to operate properly, which can represent a problem for their implementation in industrial facilities or outdoors.

In recent years, the development of specialty optical fibers has provided new alternatives for optical fiber sensing. This progress has been significant especially by the use of MCFs, which consist of multiple cores embedded in a common cladding. Depending on their geometrical arrangement, two groups can be acknowledged: weakly coupled and strongly coupled MCFs [66]. On the one hand, if the cores are far enough from each other, there is almost null crosstalk among them, and it can be assumed that they are decoupled. Such fibers are commonly used for telecommunication purposes, as they allow having multiple independent channels on the same physical medium [67]. On the other hand, when the cores are close enough to interact with each other, they are called strongly coupled MCFs, as there is a heavy crosstalk among the cores that results in a periodic coupling of light. Such coupling is extremely sensitive to several mechanical effects applied to the fiber and the reason why these type of fibers are exploited for sensing applications [68].

Compared with the optical solutions mentioned above, strongly coupled MCFs offer some significant advantages to develop extrinsic optical sensors. For instance, they do not require complex setups to operate (only a short segment of such fiber, a circulator, a spectrometer or a photodetector and a broadband light source), do not require exhaustive alignments nor expensive or ad-hoc components, and they are easy to handle. These reasons explain why this type of fibers has been chosen to develop the devices appearing in this thesis.

1.3.2 Theoretical framework and methodological tools

1.3.2.1 Operating principle of strongly coupled MCFs

The operating principle of strongly coupled MCFs can be described by the conventional Coupled Mode Theory (CMT), which has been widely developed in the literature [69-73]. According to it, in the simplest case, when there are two single mode waveguides (named 1 and 2) that are far enough to each other to interact (see Fig 29), the mode through each waveguide will propagate independently. For that case, the amplitude of the propagating mode through each of the waveguides can be expressed as:

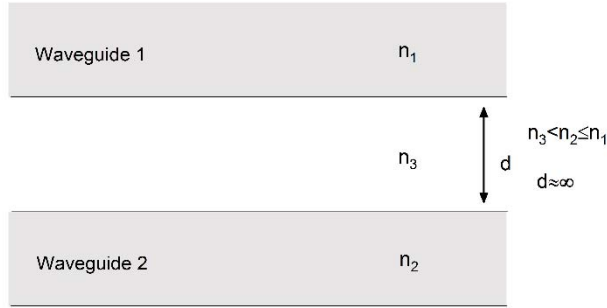


Figure 29: Schematic of two decoupled waveguides.

$$\frac{\partial a_1}{\partial z} = -j\beta_1 a_1 \quad (8)$$

$$\frac{\partial a_2}{\partial z} = -j\beta_2 a_2 \quad (9)$$

where a is the amplitude of the transverse electric field in each waveguide, β is the propagation constant of the mode, z is the direction of propagation and the subindexes 1 and 2 refer to each of the waveguides.

However, if the waveguides are close enough to each other so that the evanescent field from one guide penetrates into the other, there is a coupling between the two propagating modes (see Fig. 30). In such case, the amplitude of the modes can be expressed as:

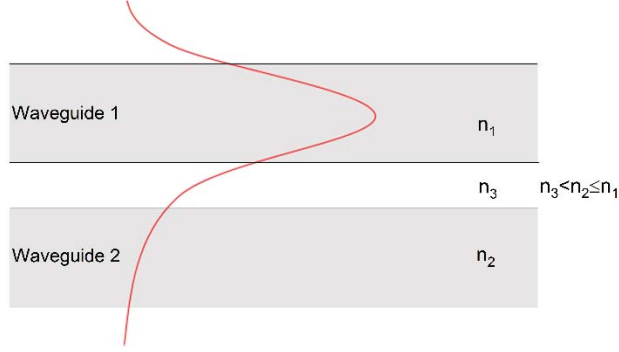


Figure 30: Schematic of two coupled waveguides.

$$\frac{\partial a_1}{\partial z} = -j(\beta_1 + k_{11})a_1 - jk_{12}a_2 \quad (10)$$

$$\frac{\partial a_2}{\partial z} = -j(\beta_2 + k_{22})a_2 - jk_{21}a_1 \quad (11)$$

where k parameters are the mutual and self-coupling coefficients between the orthogonal propagating modes in the waveguides 1 and 2, respectively. If we assume that we are in a lossless system and that the waveguides are uniform, the propagation constants and the coupling coefficients are independent of z [70], and the following simplifications can be applied:

$$P(z) = |a_1|^2 + |a_2|^2 \quad (12)$$

$$k_{12} = k_{21}^* = k \quad (13)$$

Moreover, if a common phase factor is taken from Eq. 10 and Eq. 11, they can be expressed as:

$$\frac{\partial \hat{a}_1}{\partial z} = -j\delta \hat{a}_1 - jk \hat{a}_2 \quad (14)$$

$$\frac{\partial \hat{a}_2}{\partial z} = -j\delta \hat{a}_2 - jk \hat{a}_1 \quad (15)$$

where

$$\delta = \frac{\beta_1 + k_{11} - \beta_2 - k_{22}}{2} \approx \frac{\beta'_1 - \beta'_2}{2} = \frac{\Delta\beta}{2} \quad (16)$$

As a result, the system formed by Eq. 14 and Eq. 15 can be written in matrix form:

$$\frac{dA}{dz} = -j\bar{H}A \quad (17)$$

where

$$A = \begin{bmatrix} \hat{a}_1 \\ \hat{a}_2 \end{bmatrix} \quad (18)$$

$$\bar{H} = \begin{bmatrix} \delta & k \\ k & -\delta \end{bmatrix} \quad (19)$$

In order to obtain the amplitudes of the modes as a function of the propagation axis z , which is the aim in order to be able to calculate the amount of coupled power in a certain waveguide at a certain distance, Eq. 17 can be arranged and expressed in terms of a transfer matrix as:

$$A(z) = T(z)A(0) \quad (20)$$

where the elements of matrix T are given by:

$$t_{11} = t_{22}^* = \cos(Sz) - j \cos(\eta) \sin(Sz) \quad (21)$$

$$t_{12} = t_{21} = -j \sin(\eta) \sin(Sz) \quad (22)$$

where

$$\tan(\eta) = \frac{k}{\delta} \quad (23)$$

$$S = \sqrt{\delta^2 + k^2} \quad (24)$$

$$\beta_0 = \frac{\beta_1 + k_{11} + \beta_2 + k_{22}}{2} \quad (25)$$

From Eq. 20, the normalized power in each of the waveguides can be obtained by applying the following expression:

$$P_i(z) = a_i(z) a_i^*(z) \quad (26)$$

Thus, for a situation in which only one of the waveguides is excited at $z=0$ ($a_1(0) = 1$ and $a_2(0) = 0$, for instance, according to Fig. 30), the normalized coupled power as a function of the propagation axis z in each of the waveguides can be expressed as:

$$P_1(z) = \cos^2(Sz) + \cos^2(\eta) \sin^2(Sz) \quad (27)$$

$$P_2(z) = \sin^2(\eta) \sin^2(Sz) \quad (28)$$

Let us now expand this model to a structure with a central waveguide and an undefined number N ($N > 1$) of identical and circularly distributed waveguides around it and close enough to interact. This

geometry is identical to that of the strongly coupled MCFs used to develop the devices in this document (see Fig. 31), and therefore, its conclusions are applicable [74].

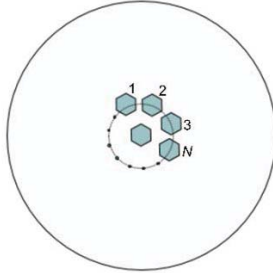


Figure 31: Schematic of a generic structure of the MCFs under study.

In such MCFs, all the cores are identical in size and physical properties, act as individual waveguides that support only the fundamental mode LP_{01} and are close enough to each other to induce the modes through each individual core to overlap among them, causing a cyclic power coupling among cores [75]. The resulting modes, which are called supermodes (SPs), are the linear combination of the modes propagating through each individual waveguide [76, 77]. When such MCFs are excited in their central core by the incoming LP_{01} mode from a standard SMF, as it has been done in this work, the two orthogonal supermodes that have power in the central core are coupled according to conventional CMT [73]. Such supermodes are named SP_{01} and SP_{02} , and are specific for each MCF geometry.

The analytical solution of this case is analogous to the one for the case of two waveguides shown in Eq. 17 but expanding it to include the interaction among all the cores taking part in the power coupling:

$$\frac{dA(z)}{dz} = -j\bar{H}A(z) \quad (29)$$

where $A(z) = [A_1(z) A_2(z) \dots A_N(z)]^T$ is a column vector, T denotes the transpose and H is a $N \times N$ matrix. After developing the system in Eq. 29 in analogous manner as the case of two waveguides described previously, the amplitudes of the propagating modes for the central (a_0) and the adjacent cores (a_i) can be expressed as:

$$a_0(z) = \frac{S \cos \frac{Sz}{2} + j\Delta\beta(z) \sin \frac{Sz}{2}}{S} e^{-j\beta_0 z} \quad (30)$$

$$a_i(z) = -j \frac{\Delta\beta}{S} e^{-j\beta_0 z} \sin\left(\frac{Sz}{2}\right) e^{\frac{-j\Delta\beta}{2z}} \quad (31)$$

where S can be defined as:

$$S = \sqrt{N\Delta\beta^2 + \Delta\beta^2} = \Delta\beta\sqrt{N+1} \quad (32)$$

where $\Delta\beta$ is defined as:

$$\Delta\beta = \frac{2\pi\Delta n}{\lambda} \quad (33)$$

where Δn is the difference between the effective refractive indices of the propagating coupled and orthogonal SPs and λ is the excitation wavelength. If this definition of $\Delta\beta$ is applied to Eq. 30 and Eq. 31, the generic normalized coupled power (calculated as indicated in Eq. 26) for the central (P_0) and in each of the adjacent cores (P_i) for MCFs can be expressed as:

$$P_0(z) = \cos^2\left(\sqrt{N+1} \frac{\pi\Delta n}{\lambda} z\right) + \frac{1}{N+1} \sin^2\left(\sqrt{N+1} \frac{\pi\Delta n}{\lambda} z\right) \quad (34)$$

$$P_i(z) = \frac{1}{N+1} \sin^2\left(\sqrt{N+1} \frac{\pi\Delta n}{\lambda} z\right) \quad (35)$$

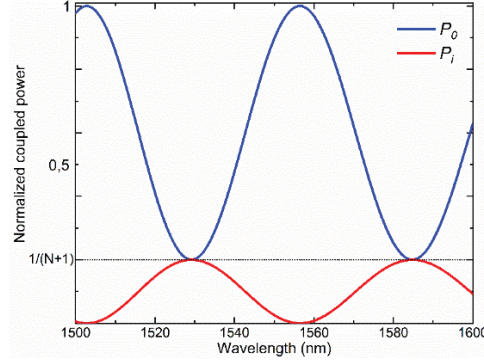


Figure 32: Evolution of the normalized coupled power in the central and one of the adjacent cores as a function of the emitted wavelength for a generic MCF.

From Eq. 34 and Fig. 32, it can be concluded that the power in the central core will vary periodically, with a maximum at certain values of z and/or λ , and minimum at others, but that there will be always a certain amount of light power oscillating in the range $[1/(N+1), 1]$. The latter means that in such MCFs $\delta \neq 0$. As all the cores are identical, and therefore, have identical β , it can be assumed that the core distribution is responsible for this phenomenon [70]. As mentioned before, this fact only takes place for $N > 1$, as for $N = 1$ the power is completely transferred from one core to the other, as explained in [78].

For the case in which there is an undefined number n of MCF segments of the same type in series along the same SMF (see Fig. 33), the normalized coupled power in the central core at the end of the chain is the product of the response of each MCF segment.



Figure 33: Schematic of n MCF segments in series along the same SMF.

$$P_{\text{cascade}}(z) = \prod_{j=1}^n P_j(z) \quad (36)$$

Thus, a cascaded structure will provide a narrower peak and higher visibility than a single segment due to the \cos and \sin raised to the $2n^{\text{th}}$ and the lower amount of light in the central core proportional to the number n of elements in series, respectively, which facilitate tracking any change in the spectrum. However, it will not enhance the sensitivity, as the phase remains unaltered.

Eq. 34 and Eq. 36 were used to design the MCF sensors in this work prior to manufacturing them. By adapting these equations to the different MCF geometries and configurations, it was possible to simulate the spectrum of the devices in order to optimize the value of the parameters that allow obtaining a pursued and specific shape of it, such as the length of the MCF segment.

1.3.2.2 Manufacturing equipment and interrogation setup

In order to manufacture all the devices shown in following sections, a precision fiber cleaver and splicer were used. The first, a Fujikura CT-105, allowed cutting MCF segments of specific lengths with 10 μm precision, which is a relevant feature in order to obtain specific spectral patterns, as mentioned above. The second, a Fujikura 100P+, can align the central core of the MCF with the unique of the SMF with high precision so that the insertion losses are typically 0,1 dB or below [79]. Moreover, it has a rotating mechanism and an imaging system that allows observing the end face of the fibers, which is a useful tool for the cases in which MCF-MCF splices with specific orientations are required.

Regarding the interrogation setup of the devices that are going to be described below, they all share the same setup. It is simple and carried out with commercial equipment in order to be as cost-effective as possible. It consists of a superluminescent light emitting diode (SLED) as the broadband light source (Safibra, s.r.o.) with its peak emission at 1550 nm and a FWHM of around 40 nm, and a

conventional fiber optic coupler (or circulator). In order to analyze the reflected light, a miniature spectrometer (Ibsen Photonics I-MON-512 High Speed, with an interrogation window from 1510 to 1595 nm) and/or an InGaAs PD (Thorlabs PDA30B2) were used depending on the device or the measurement requirements. In the cases in which wavelength shifts and power variations were required to be measured simultaneously, both detectors were connected by means of a fiber optic coupler (see Fig. 34).

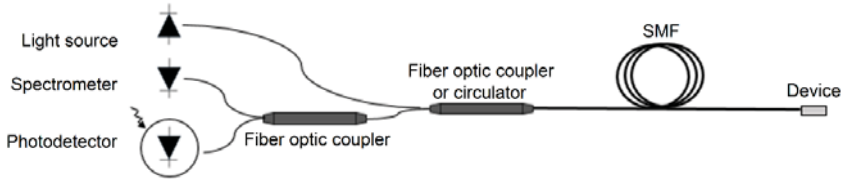


Figure 34: Schematic of the interrogation setup.

1.3.3 Hypothesis and objectives

The objective was to develop highly sensitive and novel optical MCF-based sensors for the measurement of different parameters that are of interest for the industry by means of exploiting the operating principle described above. To that end, each sensor shows a particular and unique configuration in order to optimize its performance. The result of this research is shown below and in **Articles 2, 3 and 4**.

1.3.4 Summary and results

1.3.4.1 Temperature sensors

1.3.4.1.1 Highly sensitive packaged 7cMCF-based sensor

*In this point, a summary of the article “Packaged multi-core fiber interferometer for high temperature sensing” is shown. This article was published in Journal of Lightwave Technology in March 2019 and it is included in the Appendix section of the thesis as **Article 2** to be consulted for further details.*

The first MCF-based device developed during the research period was a temperature sensor packaged accordingly to withstand and be deployed in harsh environments. The MCF in this device was fabricated at the University of Central Florida (Orlando, USA), and has a particular structure based on seven identical hexagonal cores (7cMCF) in which six of them are concentrically arranged in a ring-like shape around a central one. The mean diameter and distance among adjacent axes is $9.2\ \mu\text{m}$ and $11\ \mu\text{m}$, respectively, and the outer diameter of the fiber is $126\ \mu\text{m}$ (see Fig. 35a). All the cores are made of germanium doped silica glass and are inlaid in pure silica cladding. The NA of each of them is 0.14 at 1550 nm, which is the same NA of a typical SMF at that wavelength. A scheme of the MCF device is shown in Fig. 35b. Its structure is very simple, as it only consists of a short MCF segment (the temperature sensitive element in the device) fusion spliced by its central core to a conventional SMF.

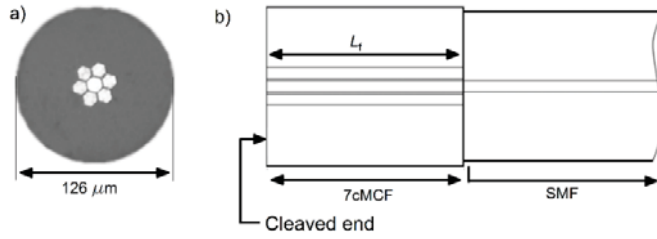


Figure 35: a) Photograph of the cross-section of the 7cMCF and b) schematic of the temperature sensor.

According to CMT [73], in this 7cMCF, the two orthogonal supermodes that are coupled are shown in Fig. 36:

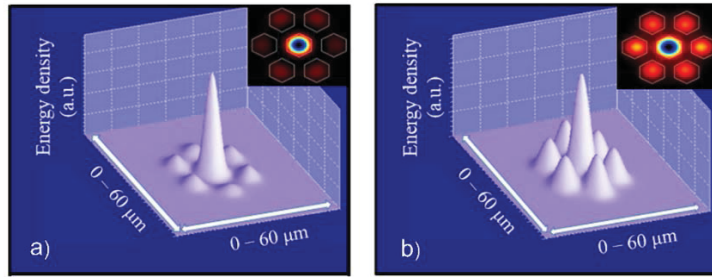


Figure 36: a) SP_{01} and b) SP_{02} orthogonal coupled supermodes for the 7cMCF.

For the particularization of Eq. 34 for this fiber, it has to be considered that the device operates in reflection mode, which implies that the light travels back and forth through the MCF. Thus, for a physical MCF segment of length L_f , the light travels $2L_f$. Taking into consideration this fact, the normalized coupled power of this device in the central core can be expressed as:

$$P_0(z = 2L_f) = \cos^2\left(\sqrt{7} \frac{\pi\Delta n}{\lambda} 2L_f\right) + \frac{1}{7} \sin^2\left(\sqrt{7} \frac{\pi\Delta n}{\lambda} 2L_f\right) \quad (37)$$

The maximum of the spectrum will take place when the phase of the \cos equals a multiple integer of 2π ($m2\pi$). Thus, the maxima will be located at the following wavelengths:

$$\lambda_m = \frac{\sqrt{7}}{m} \Delta n 2L_f \quad (38)$$

In general, in an optical fiber, the thermo-optic effect prevails over the thermal expansion effect. Thus, for temperature measurements, the simplification of considering only the changes in the refractive index of the fiber core (or cores) can be done [80, 81]. In our case, such changes induced a variation in the effective indices of the supermodes, and hence, a shift in the spectrum. As in this device the measurement of temperature is absolute because it is codified in wavelength, by monitoring λ_m , the temperature around the MCF can be known.

In order to measure the widest temperature range possible, the spectrum of the device had to fulfil two characteristics. On the one hand, the displacement of λ_m for this 7cMCF, whose thermal sensitivity is around 30 pm/°C without any packaging [81], must not overlap with adjacent maximums (located at λ_{m+1} or λ_{m-1}) in order to avoid any ambiguity in the measurement. On the other hand, λ_m must be within the interrogation window (from 1510 to 1595 nm) at any time. As according to Eq. 37, the length of the MCF is the only parameter that can be modified as the rest are fixed by the fiber itself, to obtain a length that fulfilled those requirements, Matlab MathWorks and PhotonDesign software programs were used. The best fitting length fulfilling them was calculated to be 2.545 cm. However, in order to make the fabrication faster and easier to reproduce, a length of 2.54 cm was decided to be used. The comparison between the spectra of the simulated and fabricated devices is shown in Fig. 37.

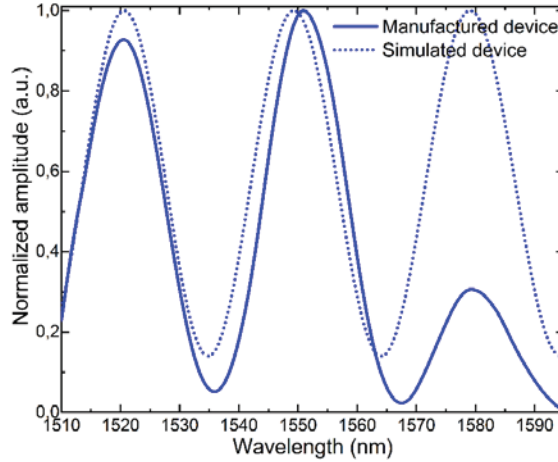


Figure 37: Spectra of the manufactured and simulated devices.

It can be noted that the wavelengths at which the peaks are located are very close in both simulated and manufactured spectra. As temperature increases, the peaks are expected to shift to longer wavelengths [82]. Hence, the peak located at 1520 nm (λ_m) was selected to be monitored and correlated with temperature. The difference in the amplitudes between both curves is caused by the envelope of the light source, which has different shapes in real-life and in the simulator.

In order to make the MCF sensor sensitive exclusively to temperature, it was packaged as follows: The bare SMF-MCF structure, whose total length was approximately 15 cm, was protected with a double shielding. The first layer was a thin ceramic tube (Omega Engineering TRX-005132-6) that had a bore with a diameter of 127 μm , whose purpose was to keep the bare SMF-MCF structure straight. In this manner, bending effects on the MCF were eliminated. The second layer was a stainless steel tube (Omega Engineering SS-116-6CLOSED) that covered the ceramic layer and provided protection against possible impacts or dirt. A photograph of the final sensor prototype is shown in Fig. 38. As it can be noticed, the sensitive part of the sensor is only 2.54 cm long and located close but separated enough from the edge of the shielding to avoid creating

a Fabry-Perot cavity. Thus, the sensor could be just about 3 cm long. The reason for the extra 12 cm that are protected with the metallic tube is the configuration of the furnace that was used for the tests (Isotech Pegasus Plus 1200). The latter had a vertical circular hole (slightly bigger than the sensor in diameter) of 15 cm in length that only in the deepest part reached temperatures of 1000 °C, which forced the packaged sensor to be vertically inserted completely.

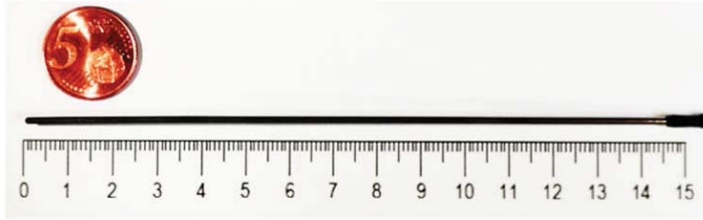


Figure 38: Photograph of the manufactured device after the temperature tests.

The tests were performed at the Aeronautical Technologies Centre (CTA) facilities located in the Alava Technology Park (Alava). Before running the calibration measurements, a mandatory curing process was carried out to eliminate as much as possible the hysteresis effect of the sensor [80]. Afterwards, the calibration was performed repeatedly in the range from 200 to 1000 °C, in steps of 50 °C that lasted 70 minutes each. Overall, each calibration lasted 100 hours approximately. During this process, λ_m was correlated with temperature, which was measured with a K-type thermocouple used for temperature calibration measurements (Herten, K-type, SN TCP187). The evolution of the spectrum of the MCF sensor with temperature is shown in Fig. 39.

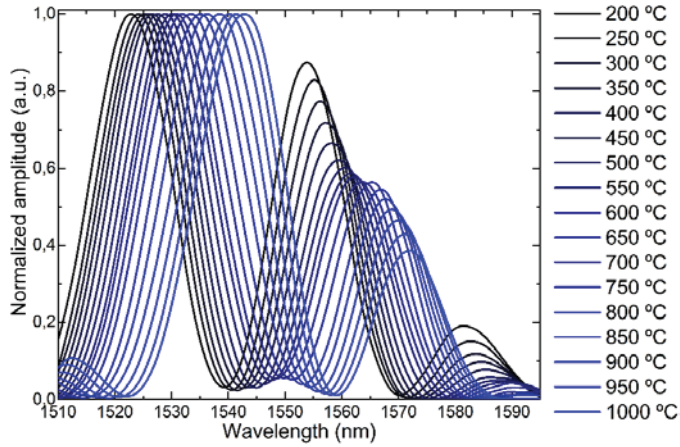


Figure 39: Evolution of the spectra as a function of temperature.

To evaluate the effect of the shielding on the temperature sensitivity, a device of 2.54 cm of bare MCF was subjected to an identical calibration process. The calibration curves of both MCF devices are shown in Fig. 40.

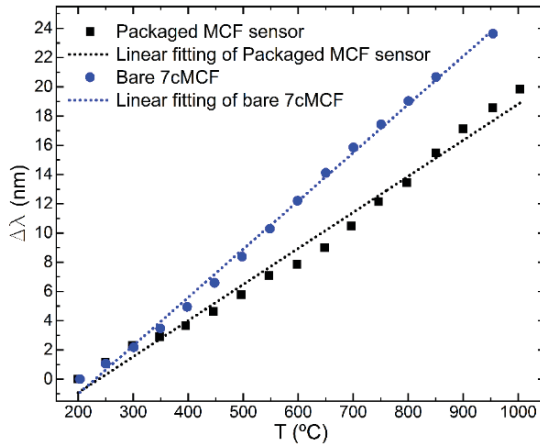


Figure 40: Calibration curves and linear fitting of the packaged MCF sensor and the bare 7cMCF.

For the packaged MCF sensor, the Pearson squared correlation coefficient was found to be $R^2 = 0.9856$. The correlation between temperature (in $^{\circ}\text{C}$) and λ_m (in nm) that was obtained from the experiments was:

$$T = 39,929\lambda_m - 60525 \quad (39)$$

This indicates that the temperature sensitivity of the packaged MCF sensor was 24.8 pm/°C. From the calibration curve of the 2.54 cm-long bare MCF shown in Fig. 40, a temperature sensitivity of 31.47 pm/°C was obtained. Therefore, it could be assumed that the packaging affects but does not compromise significantly the temperature sensitivity of the device with the advantage of providing the guarantee that this shift is caused exclusively by temperature. The latter does not happen for the bare 7cMCF, which is subjected to vibrations and bending that cause an additional shift apart from that from temperature.

This work showed a simple, inexpensive and easily reproducible MCF sensor that is highly sensitive, compact and robust. This sensor may represent an attractive solution in several applications that require high temperature sensing, high resolution and sensitivity, small dimensions and electromagnetic immunity, such as the ones for aeronautical engines, gas and oil facilities, etc.

1.3.4.1.2 Highly sensitive ruggedized 3cMCF-based sensor

As a step forward of the work reported in **Article 2**, an upgraded MCF-based thermometer was developed, which was capable of operating in even wider thermal ranges with a much more robust packaging and with higher sensitivity.

Two different MCFs were used in this work. Both were fabricated at the University of Central Florida. The first one was the 7cMCF used for **Article 2**, which has been described in the section above. The second MCF is an asymmetric strongly coupled MCF consisting of three cores (3cMCF): one of the cores is located at the geometrical

center of the fiber, whereas the other two are surrounding it and arranged adjacently in a V-like configuration (see Fig. 41). Each core is made of Germanium doped silica, and has a mean diameter of 9 μm and a NA of 0.14 at 1550 nm to match with that of the SMF. The cores are separated 11.5 μm from each other and embedded in a pure silica cladding of 125 μm of diameter.

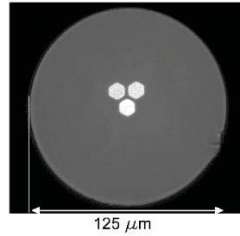


Figure 41: Cross-section of the 3cMCF.

According to Eq. 34, the particularization of the normalized power in the central core for this fiber can be expressed as:

$$P_0(z) = \cos^2\left(\sqrt{3} \frac{\pi\Delta n}{\lambda} z\right) + \frac{1}{3} \sin^2\left(\sqrt{3} \frac{\pi\Delta n}{\lambda} z\right) \quad (40)$$

And the two orthogonal supermodes that are coupled in it according to CMT [73] are shown in Fig. 42:

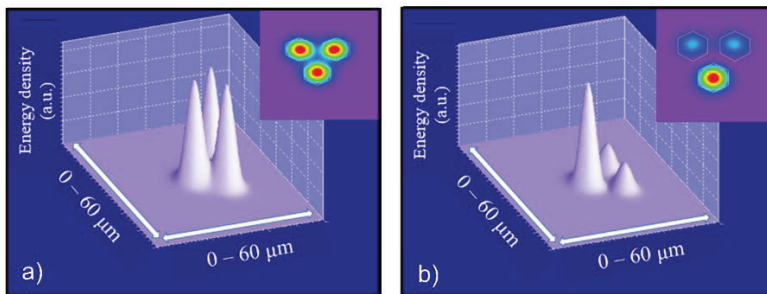


Figure 42: a) SP_{01} and b) SP_{02} orthogonal coupled supermodes for the 3cMCF.

To study the thermal sensitivity of the MCFs, the partial derivative with respect to temperature has to be applied to Eq. 34.

$$\frac{\partial \lambda_m}{\partial T} = \frac{L_f}{m} \sqrt{N+1} \left(\frac{\partial \Delta n}{\partial T} * (1 + \alpha \Delta T) + \Delta n \alpha \right) \quad (41)$$

where $L = L_f * (1 + \alpha \Delta T)$, L_f is the length of the MCF segment at room temperature ($T_r = 25 \text{ }^\circ\text{C}$), α is the thermal expansion coefficient and ΔT is the variation of temperature with respect to room temperature ($T - T_r$). From Eq. 41, it is assumed that the most significant parameters that have impact on thermal sensitivity are Δn and L_f , as α is related to the physical properties of the material of the MCF, which are identical and fixed for both MCFs under test. On the one hand, Δn , and therefore, $\partial \Delta n / \partial T$, are related to the SPs, and, therefore, to the geometry and physical properties of the MCF, such as the number of cores, their distribution, etc. On the other hand, L_f is the length at room temperature of the MCF segment. Although it can be noticed from Eq. 41 that the thermal sensitivity is proportional to L_f , it can be assumed that its impact on sensitivity is negligible, as the ratio L_f/m is fixed independently of the initial length of the MCF. Therefore, it can be concluded that the initial length of the MCF segment in the sensor has negligible impact on the thermal sensitivity.

To verify the fact that the initial length does not have any significant effect on thermal sensitivity, three devices consisting of segments of different lengths of 7cMCF were manufactured (see Fig. 43), and subjected to several temperature cycles from 200 $^\circ\text{C}$ to 500 $^\circ\text{C}$ and back to 200 $^\circ\text{C}$ in steps of 100 $^\circ\text{C}$. The fabricated and tested configurations were: 1) a sample with a 7cMCF segment of 12.5 mm (Fig. 43a), 2) a 7cMCF segment of 25 mm (Fig. 43b) and 3) a sample of twin cascaded 7cMCF segments of 12.5 mm (Fig. 43c).

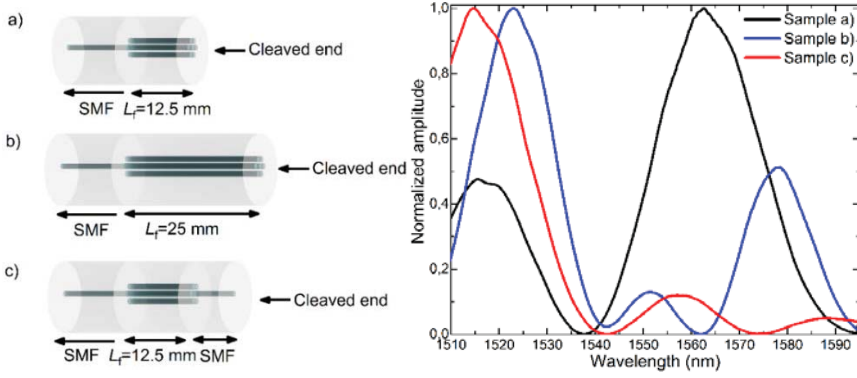


Figure 43: Schematics of the manufactured samples and their corresponding spectra at room temperature ($T=25$ °C).

Regarding the twin structure in Fig. 43c, it consists of a SMF-MCF-SMF structure. Due to its reflection mode configuration, the cleaved end of the SMF segment acted as a mirror. By means of this configuration, the light propagates forward and backward through the structure, passing twice through the MCF segment. Thus, with only one segment of MCF, a twin structure can be easily manufactured. For this operating configuration, Eq. 36 has to be particularized. As a result, normalized coupled power in the central core at the exit of this structure can be expressed as:

$$\begin{aligned}
 P_0(z = L_f) = & \cos^4\left(\sqrt{7} \frac{\pi\Delta n}{\lambda} L_f\right) + \frac{2}{7} \cos^2\left(\sqrt{7} \frac{\pi\Delta n}{\lambda} L_f\right) * \sin^2\left(\sqrt{7} \frac{\pi\Delta n}{\lambda} L_f\right) + \\
 & + \frac{1}{49} \sin^4\left(\sqrt{7} \frac{\pi\Delta n}{\lambda} L_f\right)
 \end{aligned} \tag{42}$$

To keep the MCF segments straight to be only sensitive to temperature, each specimen was introduced in a ceramic tube (Omega TRX-005132-6). After the annealing process, the devices were subjected to the aforementioned temperature cycles. The results of such tests are summarized in Table 1:

Table 1 : Summary of the results

MCF length (L_f)	12.5 mm	25 mm	Twin of 12.5 mm
Sensitivity (pm/°C)	20.38	22.22	21.16

From Table 1, it can be concluded that the initial length of the MCF and/or cascading such elements do have negligible impact on sensitivity for temperature measurements. This conclusion could have been deduced from the mathematical expressions in Eq. 34 and Eq. 36 as well, as the phase in them remains unaltered irrespective of the initial length or the configuration of the device (single or cascaded segments). However, this does not imply that L_f is a disposable parameter for the design of optical MCF-based thermometers, as it is still a relevant design factor that defines the shape of the spectrum and the position of λ_m , as it has been demonstrated in **Article 2** and in Fig. 43.

In order to study the impact of Δn on the thermal sensitivity, its variation with respect to the temperature was simulated by PhotonDesign for the two MCFs under study (Fig. 44). To that end, the refractive index of the material was defined as $n = n_f + \gamma\Delta T$ [83], where n_f is the refractive index of the cores at 25 °C, and γ is the thermo-optic coefficient [82]. The non-linearity of the latter in the range from -25 °C to 900 °C was taken into account for the simulations [84, 85].

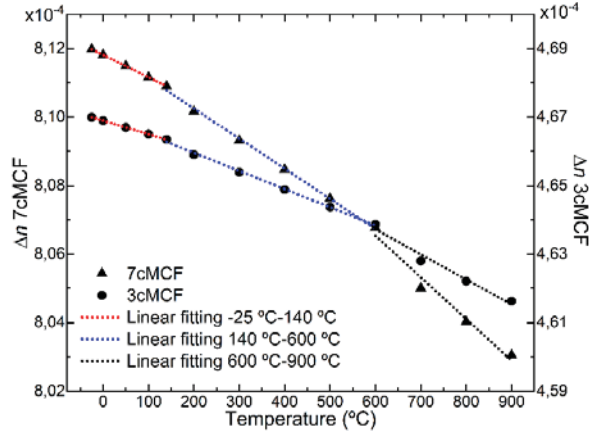


Figure 44: Simulations of Δn as a function of temperature for the 7cMCF (black triangles) and 3cMCF (black circles).

As demonstrated in **Article 2**, the expected proportional shift of λ_m with temperature (as the temperature increases, λ_m shifts to longer wavelengths, and vice versa) implies that the term $(\partial\Delta n/\partial T * (1 + \alpha\Delta T) + \Delta n\alpha)$ in Eq. 41 is positive. From Fig. 44, it can be noticed that Δn is always positive, but its slope (expressed as $\partial\Delta n/\partial T$) is negative in both MCFs under study. This indicates that $\partial\Delta n/\partial T * (1 + \alpha\Delta T) < \Delta n\alpha$, and as a result, it can be assumed that the thermal sensitivity increases as the difference between this two terms increases. Thus, the conclusion from Fig. 42 is that the thermal sensitivity of the 3cMCF is higher than that of the 7cMCF as Δn is lower and its slope is smaller in the 3cMCF for the temperature range under study.

To demonstrate such fact, a device with a packaging identical to that in **Article 2**, but with 25 mm of 3cMCF was manufactured and subjected to several stepped temperature cycles from -25 °C to 900 °C. Before running the tests, the device was subjected to an annealing process identical to that for the device in **Article 2** to avoid hysteresis. After that, the device was subjected to the aforementioned temperature cycles. The evolution of the spectrum as a function of temperature and its calibration are shown in Fig. 45.

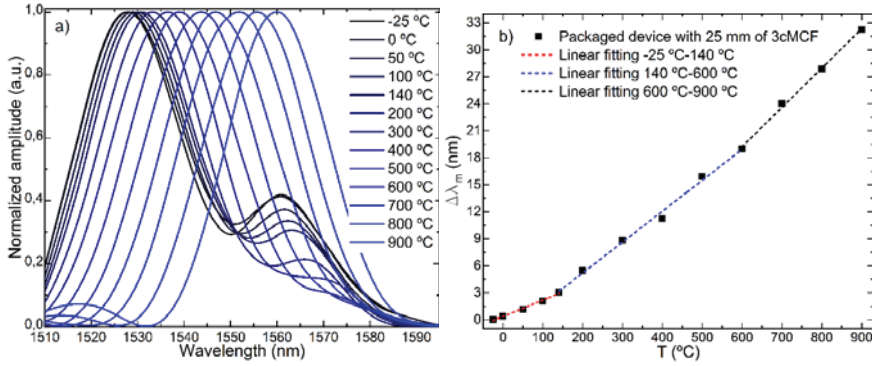


Figure 45: a) Evolution of the spectrum as a function of temperature and b) calibration curve of the packaged device with 25 mm of 3cMCF.

This device showed higher sensitivity than the one reported in **Article 2** with the same packaging and operating configuration, reaching a sensitivity up to 43.61 pm/°C for the range from 600 °C to 900 °C (the device in **Article 2** showed a sensitivity of 24.8 pm/°C). Hence, it can be concluded that the most significant parameter to design highly sensitive MCF thermometers is Δn , and that between the two MCFs under study, the 3cMCF is more thermal sensitive and therefore, the one that has to be chosen to manufacture this upgraded optical thermometer.

To manufacture the device, the requirements for the shape of the spectrum were identical to those for the device in **Article 2**. However, by using the 3cMCF, the best fitting MCF length fulfilling the requirements was found to be 12 mm, which is less than the half of the MCF needed in **Article 2** (2.54 cm), which is an additional advantage as the device as less material is required.

Regarding the packaging, one of the drawbacks of the device in **Article 2** is that the thin stainless steel metallic shielding tended to bend when it was subjected to extreme temperatures and did not return to its original shape. This is a potential problem to operate in harsh environments as it may lead to break the fiber inside it. To overcome such a critical drawback, a ruggedized packaging was developed in order to make it more robust to operate in harsh

environments and extreme temperatures. The packaging of this device consisted of three layers that covered the optical fiber. The first layer was the same as for previous devices and consisted of a ceramic tube (Omega TRX-005132-6) to keep the MCF straight and therefore, make it only sensitive to temperature. The second layer consisted of a thin Inconel tube (INC-116-6-OPEN) whose inner diameter is slightly bigger than the outer diameter of the ceramic tube. Its aim was to provide rigidity to the ceramic tube and avoid any possible fracture of it, as the latter shows high levels of fragility against impacts. The third layer consisted of a thick Inconel tube (INC-18-6CLOSED) to provide robustness. The reason for using Inconel instead of stainless steel as in **Article 2** was due to the fact that it is capable to withstand higher temperatures with higher structural integrity. With this ruggedized packaging, the final prototype was about 14 cm long (see Fig. 46). As it happened in **Article 2**, although the sensing part of the device was only 1.2 cm long and located at the tip of it but far enough to avoid creating a Fabry-Perot cavity, the 14 cm-long ruggedized packaging was caused by the configuration of the furnaces in which the device was tested (Fluke 9103 and Fluke 9150). The latter had a vertical hole of around 15 cm that only in their deepest part reach the desired temperature.

Finally, to make the device as robust as possible to be deployed in extremely harsh environments, the SMF from the device to the interrogation setup was protected as well with a double layer. The first one consisted of a tube (Thorlabs FT030) that contained an outer PVC jacket and Kevlar threads to provide protection. The second layer consisted of a stainless-steel jacket (Thorlabs FT05SS) which provided extra protection and avoided any visible or IR light entering through the length of the fiber.



Figure 46: Photograph of the upgraded device (up) and the device in **Article 2** (down) after the tests.

From Fig. 46, the benefits of this ruggedized packaging can be acknowledged. It is easily noticeable that the device from **Article 2** is bent significantly after being subjected to several temperature cycles, which may compromise its lifetime, whereas the upgraded device is still straight.

For comparison purposes, an identical device was manufactured with the same physical characteristics and packaging but with the 7cMCF. Prior to their calibration, both devices were subjected to an annealing process as the device in **Article 2** to avoid hysteresis. Afterwards, they were subjected to the same stepped temperature cycles as the device in Fig. 45. The evolution of their corresponding spectra is shown in Fig. 47.

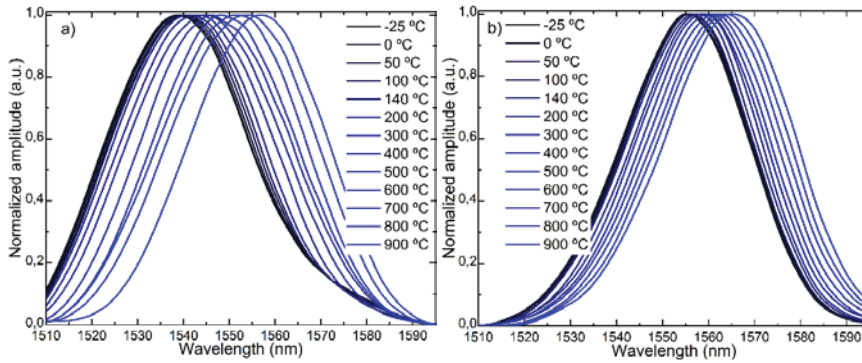


Figure 47: Evolution of the spectrum as a function of temperature of the devices with a) the 3cMCF and b) the 7cMCF.

The calibration curves for the ruggedized sensors are shown in Fig. 48 and are summarized in Table 2. Results demonstrate that the thermal sensitivity of the ruggedized device with 3cMCF is higher

than that in the device with 7cMCF in all the temperature ranges, obtaining almost twice the sensitivity in the range from 200 °C to 900 °C.

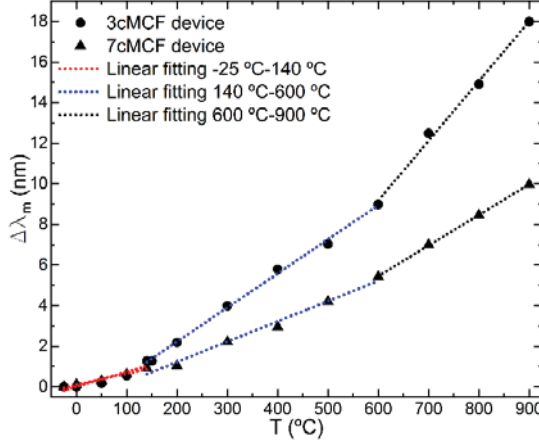


Figure 48: Calibration curves for the ruggedized 3cMCF (black circles) and 7cMCF devices (black triangles).

Table 2: Summary of the results

		-25°C-140°C	200°C-600°C	600°C-900°C
3cMCF	Correlation	$T=117.61 \lambda_m + 5.74$	$T=59.445 \lambda_m + 67.693$	$T=33.83 \lambda_m + 290.09$
	Sensitivity (pm/°C)	7.302	16.785	29.426
	R ²	0.926	0.9989	0.997
7cMCF	Correlation	$T=177.31 \lambda_m - 17.193$	$T=86.72 \lambda_m + 129.17$	$T=66.295 \lambda_m + 238.47$
	Sensitivity (pm/°C)	5.531	9.983	15.081
	R ²	0.99	0.992	0.999

The results reported here highlight the significance of understanding the fundamentals of strongly coupled MCFs, as exploiting them allows having higher sensitivity only by selecting adequately the MCF geometry in the device. In this work, this fact has been exploited for temperature sensing: It allowed a more robust shielding,

as the loss in sensitivity due to the ruggedized packaging was compensated by the increase in sensitivity provided by the MCF. Moreover, the fundamentals discussed here open the possibility to design and manufacture ad-hoc MCF structures and geometries with optimized and/or enhanced sensitivities to measure temperature or any other parameter such as strain or bending; or to design filters or switches, as the procedure for all those cases is analogous to the one exposed here.

1.3.4.2 Omnidirectional vector bending sensor

In this section, a simple and compact vector-bending sensor that is able to discern any direction and amplitude of the bending is shown. To manufacture this device, a short segment ($L_f=8$ mm) of the same 3cMCF shown in the previous work was used (see Fig. 41), which was fusion spliced at the distal end of a SMF (see Fig. 49), creating a simple SMF-MCF structure that operated in reflection mode. The device was interrogated in wavelength shift and light power variation simultaneously. In this manner, the amplitude and direction of the bending were unmistakably measured when the MCF was bent, as the spectrum shrank and shifted accordingly.

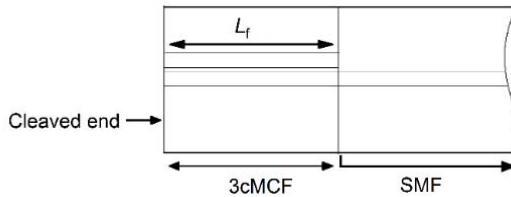


Figure 49: Schematic of the structure of the sensor.

For this structure and 3cMCF, the coupled power can be expressed as in Eq. 40 but particularized for $z=2L_f$:

$$P_0(z = 2L_f) = \cos^2\left(\sqrt{3} \frac{\pi\Delta n}{\lambda} 2L_f\right) + \frac{1}{3} \sin^2\left(\sqrt{3} \frac{\pi\Delta n}{\lambda} 2L_f\right) \quad (43)$$

The orthogonal coupled SPs for this device are identical to the ones shown in Fig. 42.

As it has been widely demonstrated, the refractive index of the core of an optical fiber changes it is bent [86-89]. For MCFs, certain core or cores are going to be more stressed than others when they are subjected to the same bending plane and amplitude, resulting in changes in the effective refractive indices of the propagating supermodes. According to Eq. 43, this effect implies changes in the normalized power coupling conditions, and therefore, in the resulting spectrum.

Among strongly coupled MCFs, for symmetric ones, the effect of the bending plane will be always the same irrespective of the bending direction. This is why such fibers are capable to distinguish the applied bending but not its direction [90]. However, for asymmetric MCFs, as the 3cMCF, the effect of bending in the spectrum will depend on the core orientation and the bending direction as well as on the arrangement and geometry of the cores. When these type of MCFs are bent, the variation in the refractive index of each core depends on the bending plane and its orientation with respect to it [91, 92]. As the cores are arranged asymmetrically, each of them suffers different levels of stress against the same bending plane and radius, causing the refractive index of each to vary independently. Such situation affects directly to the propagating supermodes, which modifies consequently the output spectrum of the normalized coupled power in Eq. 43. This is what makes asymmetric MCFs good candidates for direction-sensitive bending sensors, as the variation of the normalized coupled power will be specific for each bending case, giving rise to detectable changes in the spectrum of a SMF-MCF structure in terms of wavelength shift and/or light power variation depending on the applied bending direction.

In order to detect and measure the bending direction causing such changes in the spectrum, by monitoring only one of these two

variables, in principle, it could be possible to measure the bending direction and amplitude without ambiguity in 180° . In that range, the sensitivity of the measured variable will be unique for each bending plane and therefore, its measurement (shift to longer and shorter wavelengths, or increase and decrease of the reflected light power) could be linked to the applied bending unequivocally. However, for the remaining 180° , such measurements of the variable are going to be the same as for the previous 180° , giving as a result an ambiguity in which two bending directions provoke the same measured change in the monitored variable.

Such ambiguity can be eliminated by simultaneously measuring both variables (the wavelength shift and light power variation) as each of them shows unique sensitivity for each bending direction. In this manner, the measurement of the first variable will provide two possible solutions (two bending directions), whereas the second variable will be the key to resolve such ambiguity. For example, let us assume a case in which a certain wavelength shift has been measured. As it has been explained previously, such shift can be caused by two different bending directions. At this point, the measurement of light power will be the key to resolve the ambiguity, as in one of the possible solutions (one of the bending directions that cause such wavelength shift), the measured light power increases, whereas in the other bending direction, it decreases. This leads to a unique possible bending direction causing such changes in both variables at the same time. Identical procedure can be carried out by inverting the variables: using the light power measurement to provide two possible solutions and the wavelength shift to resolve the ambiguity. Therefore, by combining the simultaneous measurement of both variables, the ambiguity can be resolved and any bending direction can be unmistakably identified in 360° , making the device sensitive to any bending direction (omnidirectional). To that end, the interrogation setup shown in Fig. 34 was implemented, in order to measure both parameters simultaneously.

To demonstrate this behavior, a length of MCF segment (L_t) capable to provide a spectrum with one centered and well-defined maximum in the interrogation window (from 1510 to 1595 nm) of the spectrometer, and with no secondary maxima is required. The latter is mandatory to minimize any sensitivity loss that is caused by adjacent lobes with opposite trends (one increases whereas the other decreases) when measuring the reflected light power in the same interrogation window, as shown in [91]. To obtain an L_t that fulfilled the aforementioned requirements, PhotonDesign simulation software was used, and simulation results indicated that the best fitting MCF length was 8 mm. The great resemblance between the simulated and manufactured devices is shown in Fig. 50.

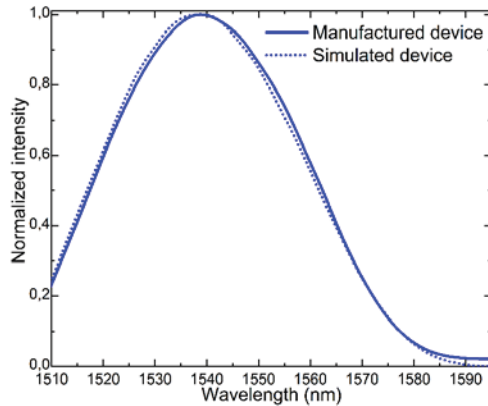


Figure 50: Spectra of the manufactured and simulated devices of 8 mm of 3cMCF.

The device was fixed horizontally on a fiber rotator (Thorlabs HFR007) in such a way that the MCF segment was set in a cantilever configuration (see Fig. 51a). This setup allowed selecting accurately the bending plane applied to the MCF. The latter was fixed on one end by the clap of the fiber rotator by the SMF-MCF fusion splice point and had its other end loose, as shown in Fig. 51a. As the length of the MCF in cantilever (L_t) was only 8 mm, it was straight in idle position. In that state, to set an initial core orientation that would be the reference position from which the fiber would be rotated (the 0° in Fig. 51b), a high-resolution camera (Dyno-Lite AM4116T) was

set in front of the MCF to record the orientation of the cores. The initial core orientation that was decided to be used as reference (the aforementioned 0° from which the fiber would be rotated) was when the cores were in an inverted V-like configuration, as indicated in Fig. 51b.

Once the MCF had its cores in that orientation, a thin ceramic tube (Omega Engineering TRX-005132-6), whose bore's inner diameter ($127\ \mu\text{m}$) is slightly bigger than the diameter of the MCF ($125\ \mu\text{m}$), was set in front of it, and by means of a micrometric displacement platform (Thorlabs RB13M), the MCF and the tube were aligned. This alignment allowed displacing the fiber forward in micrometric steps until $0.5\ \text{mm}$ of the loose end of the MCF were inserted in the ceramic tube. Thanks to the narrow difference between the diameter of the MCF and that of the ceramic tube, the MCF fitted tightly in it, avoiding any slack of the fiber during measurements.

Then, the ceramic tube was fixed to a precision travel stage (Thorlabs LTS150) in order to displace it vertically upwards and downwards with high precision, as this stage has a minimum achievable incremental movement of $0.1\ \mu\text{m}$, according to the manufacturer. In this manner, when the tube moved up and down, the fiber was bent and a triangle created, whose sides were the actual position of the fiber, its initial horizontal position (L_f) and the vertical displacement d , as indicated in Fig. 51a. This mechanism to apply bending to the fiber is similar to that used in [89, 91, 93, 94]. According to Fig. 51a, the degrees of the angle of bending were calculated as $\sin\theta = d/L_f$. According to it, as each step of d upwards or downwards was of $100\ \mu\text{m}$, it meant that the applied bending was of 0.716° at each step until reaching 3.583° . This process was repeated every 30° of rotation of the MCF in the direction indicated in Fig. 51b until completing a whole rotation around its axis 5 times.

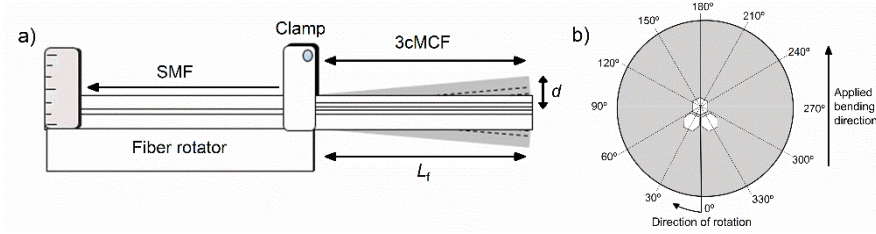


Figure 51: Schematics of a) the setup to apply the bending and b) the direction of rotation of the 3cMCF, the evaluated points and the applied bending direction.

The comparison of the gathered spectra and their corresponding measurement of wavelength shift and light power variation of the two most representative cases in which the 3cMCF has opposite orientations against the same bending plane is shown in Fig. 52 and Fig 53. Note that for the same applied bending direction and angles, the changes in the spectra go from mainly light power variations (see Fig. 52) to mainly wavelength shift (see Fig. 53) with a very stable signal from cycle to cycle. Such evolution took place progressively in clockwise direction of rotation. Thus, in each of the intermediate positions, a specific linear combination of shift and light power change was observed.

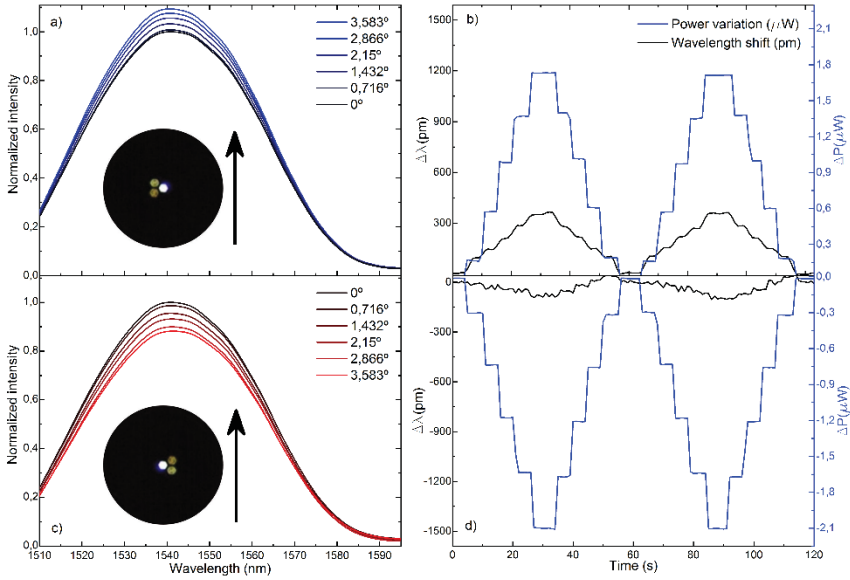


Figure 52: Spectra and two cycles of the time evolution of the measured parameters when the device is bent in the direction indicated by the arrow and the 3cMCF is rotated a) b) 90° and c) d) 270° with respect to the initial 0° position, respectively.

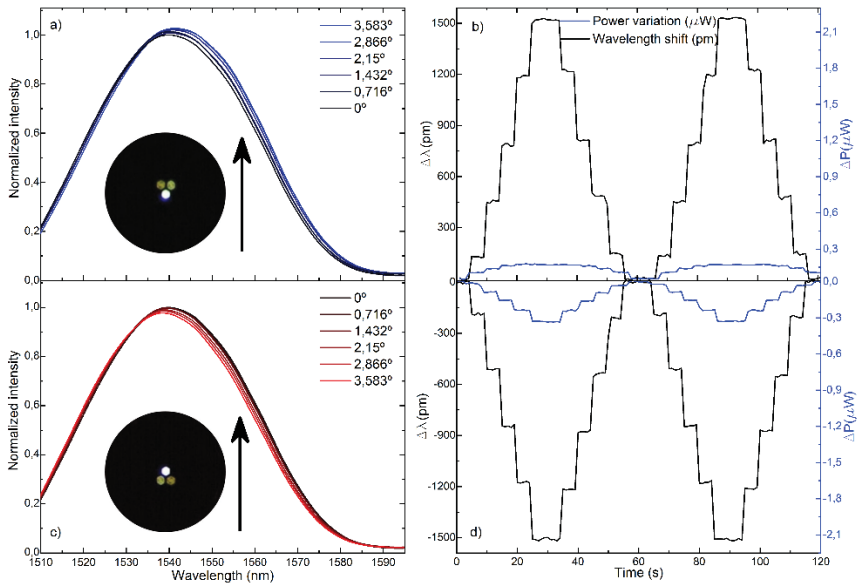


Figure 53: Spectra and two cycles of the time evolution of the measured parameters when the device is bent in the direction indicated by the arrow and the 3cMCF is rotated a) b) 180° and c) d) 360° with respect to the initial 0° position, respectively.

From the analysis of such spectral behavior, it can be concluded that by combining the measurement of both variables (wavelength shift and light power variations), this device is able to measure any bending direction in 360° and amplitude for bending angles up to 3.583° , as unique trends and sensitivities at each core orientation of the 3cMCF can be acknowledged. Moreover, such results suggest that an exhaustive alignment between cores and bending direction is not needed to devise such MCF-based vector bending sensor.

The bending sensitivities in terms of wavelength shift and light power variation and their respective standard deviation at the measured 3cMCF orientations with respect to the applied bending direction are summarized in Fig. 54. The maximum sensitivities and their respective standard deviations were found to be $506.72 \pm 5.5 \text{ pm}/^\circ$ and $587.5 \pm 11.08 \text{ nW}/^\circ$, for wavelength shift and light power variation measurements, respectively. These values represent an uncertainty in the measurement of 0.01° for wavelength shift and 0.018° for power variation. The combination of the trend and sensitivity of each parameter is unique at each point, which leads to an unambiguous detection of the bending direction and amplitude. It can be noticed that both curves are 90° out of phase between them as well, as expected from the results and the core orientations in Fig. 52 and Fig. 53.

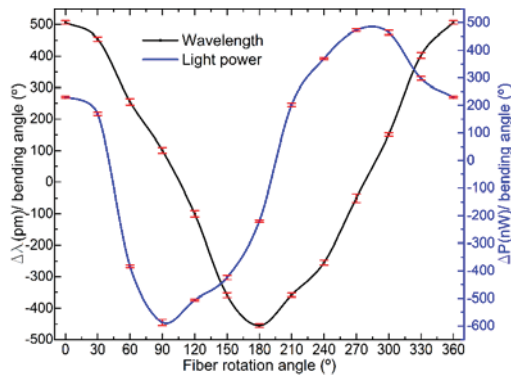


Figure 54: Wavelength shift and light power variation sensitivities and their respective standard deviations at each fiber position.

Fig. 55 is the normalized polar representation of the results in Fig. 54, in absolute value. When the shift in the reflection spectrum is maximum, the light power change is minimal, and vice versa, whereas in other orientations, a specific combination of power variation and wavelength shift can be acknowledged.

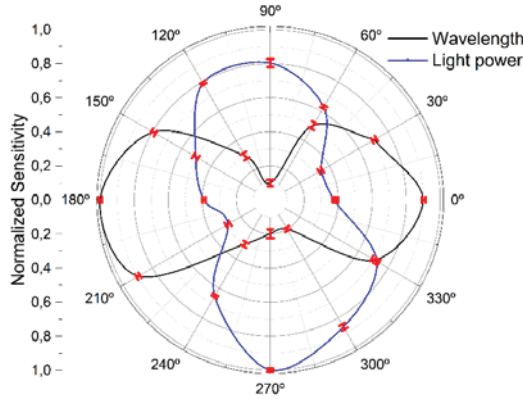


Figure 55: Polar representation of the normalized bending sensitivities and standard deviations in absolute value.

By combining simultaneous wavelength shift and light power variation measurements, a simple sensor consisting of 8 mm of 3cMCF capable of discerning bending direction and amplitude accurately in 360° was developed. This device does not require any specific alignment, and is capable to operate either for small and large bending angles, from below 1° up to 3.583° .

1.3.4.3 Accelerometer

*In this point, a summary of the article “Highly sensitive multicore fiber accelerometer for low frequency vibration sensing” is shown. This article was published in Scientific Reports in September 2020 and it is included in the Appendix section of the thesis as **Article 3** to be consulted for further details.*

In this section, an accelerometer based on cascading two segments of the 3cMCF (named MCF1 and MCF2) in Fig. 41 of different lengths

(L_1 and L_2 , respectively) and rotated 180° with respect to each other is shown. The 3cMCF segments are sandwiched between standard single mode fibers, creating a SMF-MCF1-MCF2-SMF structure that operates in reflection mode (see Fig. 56).

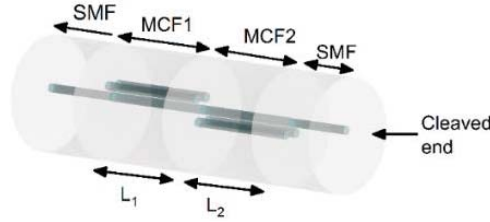


Figure 56: Schematic of the device.

For this 3cMCF cascaded configuration, the particularization of Eq. 36 allows expressing the normalized coupled power in the central core as the product of each of the segments, as follows:

$$\begin{aligned}
 P_0(L_1, L_2) = & \cos^2\left(\sqrt{3}\frac{\pi\Delta n}{\lambda}L_1\right) * \cos^2\left(\sqrt{3}\frac{\pi\Delta n}{\lambda}L_2\right) + \\
 & + \frac{1}{9}\sin^2\left(\sqrt{3}\frac{\pi\Delta n}{\lambda}L_1\right) * \sin^2\left(\sqrt{3}\frac{\pi\Delta n}{\lambda}L_2\right) + \frac{1}{3}\cos^2\left(\sqrt{3}\frac{\pi\Delta n}{\lambda}L_1\right) * \sin^2\left(\sqrt{3}\frac{\pi\Delta n}{\lambda}L_2\right) + \\
 & + \frac{1}{3}\cos^2\left(\sqrt{3}\frac{\pi\Delta n}{\lambda}L_2\right) * \sin^2\left(\sqrt{3}\frac{\pi\Delta n}{\lambda}L_1\right)
 \end{aligned} \quad (44)$$

Thus, as it was said before, a cascaded structure operating in reflection mode will provide a narrower peak and higher visibility than a single segment, which facilitate tracking any change in the spectrum.

Regarding the fiber arrangement, by rotating the two 3cMCF segments 180° with respect to each other, each of them will show contrary behavior in terms of wavelength shift and amplitude of the spectrum when they are bent due to their direction sensitive nature that has been explained in the previous section and is also explained in [91]. When the position of the cores of each 3cMCF segment and the applied bending are aligned as in Fig. 57, where one of the MCF segments has its cores oriented in a V-like configuration and the

other MCF segment has its cores oriented in an inverted V-like configuration (or rotated 180°), only amplitude variations will take place in the spectrum. In order the device to perform as shown in Fig. 57, MCF segments of different lengths are compulsory to avoid any ambiguity in the measurement. If the lengths were identical, the spectra of both segments would be overlapped in idle state, being that situation the point at which the maximum reflected light power would take place. Each spectrum would shift in opposite directions when the structure was bent, but only power decreases would be recorded, resulting in identical or similar power readings for opposite bending directions. Such ambiguity or loss in sensitivity is avoided by using segments of different lengths, as for this case, the measured power increases and decreases accordingly with the applied bending direction compared to the power measurement in idle state. Such amplitude variations in the spectrum are proportional to power variations, and therefore, only a PD will be necessary to interrogate the device. Such simplicity makes this SMF-MCF1-MCF2-SMF structure appealing as a very sensitive and cost-effective accelerometer, as it does not require high performance or ad-hoc equipment to operate.

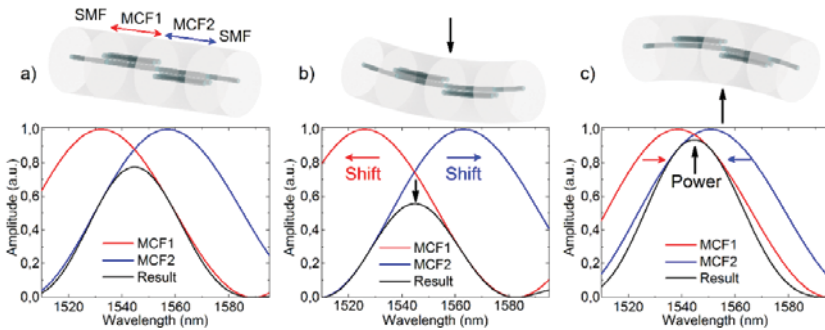


Figure 57: Simulated spectra of each of the 3cMCF segments and the resulting spectra for the cases where the structure is a) straight, b) bent upwards and c) bent downwards by its fusion splice point. The arrow indicates the bending direction, the wavelength shift or the power variation in each case. The cores of MCF1 are in a V-like configuration, whereas the ones in MCF2 are in an inverted V-like configuration.

To manufacture a device with such characteristics, some design constraints were required to be considered: Its spectrum had to be confined within the interrogation window (from 1510 to 1595 nm) at any time and it must have a unique and well-defined peak with no secondary lobes. Such requirements are mandatory to minimize any sensitivity loss when measuring the reflected light power that is caused by adjacent lobes with opposite trends (one increases whereas the other decreases) in the same interrogation window, as shown in [91]. The best fitting lengths for the MCF segments that fulfilled the requirements were 11.4 mm and 12.2 mm, resulting in a compact device of 23.6 mm. The spectra of the simulated and the manufactured devices are shown in Fig. 58, along with the simulation for each of the MCF segments that comprise the structure. Such simulations were carried out with PhotonDesign simulation software.

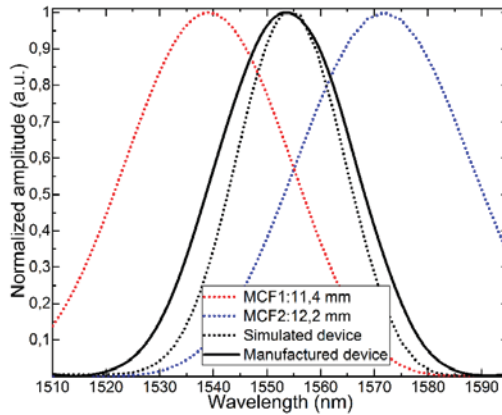


Figure 58: Normalized spectra of the simulated (black dashed line) and manufactured devices (black continuous line). Notice that the maxima of both curves is around 1554 nm and there are no secondary lobes. Simulated spectra of MCF segments of 11.4 mm (red dashed line) and 12.2 (blue dashed line) are shown as well. As indicated in Eq. 44 their product results in the black dashed line.

To test the device, a horizontally fixed rectangular methacrylate thin plate was used. Underneath and at the center of it, an amplified piezoelectric actuator (Thorlabs APFH720 combined with Thorlabs MDT694B amplifier) was fixed so that the plate could vibrate only in the vertical plane. The piezoelectric actuator was connected to a

function generator (Keysight Technologies 33220A) to generate signals of diverse amplitudes and frequencies. Then, the manufactured device was surface bonded with cyanoacrylate adhesive to the upper side of the plate, locating the MCF1-MCF2 splice just above the piezoelectric actuator, as it can be observed in the scheme of the experimental setup shown in Fig. 59. It was surface bonded with its cores oriented as in Fig. 57 to match the direction of vibration. Adjacent to the device, a commercial accelerometer (Pico Technology PP877 with Pico Technology TA096) was fixed for comparison and calibration purposes, as this electronic accelerometer provided the relation between the amplitude of the vibration and the acceleration. Its interrogation was carried out with the setup in Fig. 34.

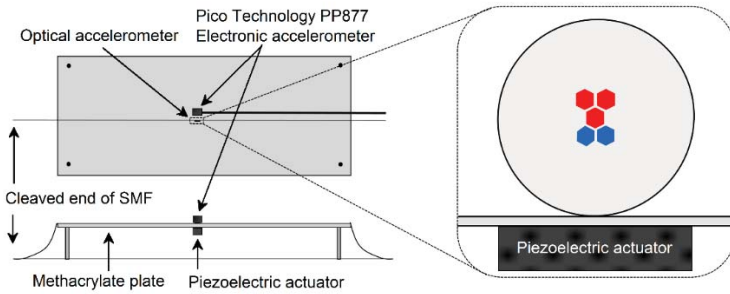


Figure 59: Schematic lateral and top views of the experimental setup. The close-up shows how the manufactured optical accelerometer was surface bonded to the plate. Red cores belong to MCF1 whereas blue cores belong to MCF2. The red central core indicates MCF1 is in front of MCF2, as they share common central core.

The first test consisted in emitting a sinusoidal signal of 1 V_{pp} amplitude and varying its frequency from 30 Hz down to 1 mHz (the lowest frequency provided by the function generator) in several steps so that the Limit of Detection (LoD) in terms of frequency of each device could be defined. The manufactured device detected every vibration clearly down to 1 mHz in wavelength shift and power variation (see Fig. 60 and Fig. 61). The small wavelength shift in Fig. 61 indicates that the device has been surface bonded with the

proper core orientation to the plate, and explains the fact that the FFT amplitudes are lower for the wavelength shift measurements than those for power variation. Nevertheless, even in this configuration aimed at maximizing the power variation, the device has detected such low vibrations by its wavelength shift as well, which is an indicator of its high sensitivity. According to the commercial accelerometer, it only detected vibrations of 2 Hz and above and with significantly noisier signal and with high level of harmonic components (see Fig. 62).

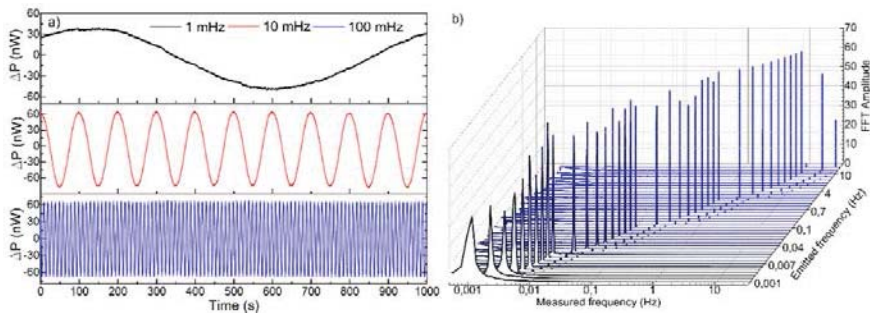


Figure 60: Results of the power measurements in the manufactured optical device. a) Time response of three representative cases. b) FFT amplitudes for frequencies from 30 Hz down to 1 mHz for a sinusoidal signal of 1 Vpp. The Measured frequency axis is in logarithmic scale.

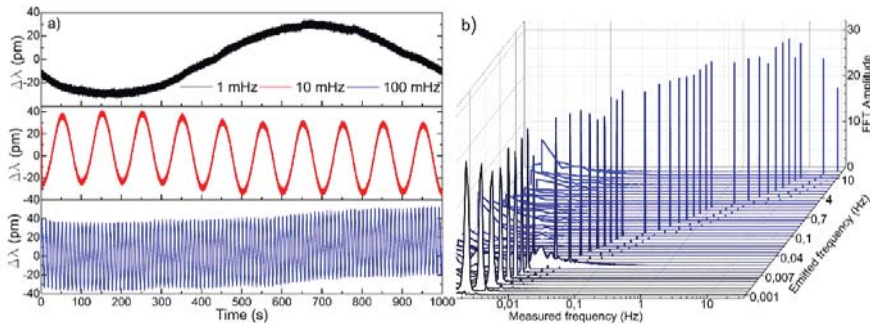


Figure 61: Results of the wavelength shift measurements in the manufactured optical device. a) Time response of three representative cases. b) FFT amplitudes for frequencies from 30 Hz down to 1 mHz for a sinusoidal signal of 1 Vpp. The Measured frequency axis is in logarithmic scale.

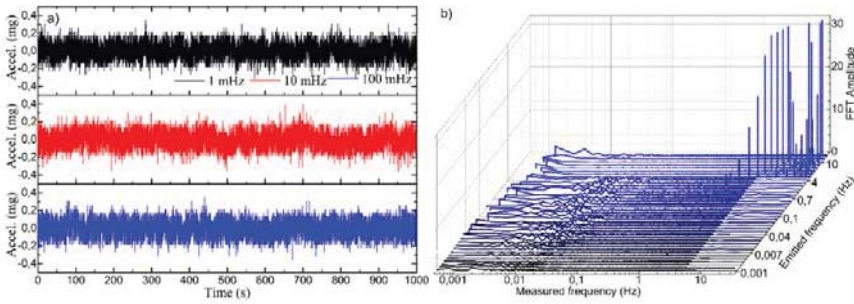


Figure 62: Results of the acceleration measurements in the electronic accelerometer. a) Time response of three representative cases. b) FFT amplitudes for frequencies from 30 Hz down to 1 mHz for a sinusoidal signal of 1 Vpp. The Measured frequency axis is in logarithmic scale.

The second test consisted in emitting a sinusoidal signal of a fixed frequency (6 Hz) and varying its amplitude from 1 Vpp down to 10 mVpp (the lowest amplitude provided by the function generator) to define the LoD of each device in terms of amplitude of vibration, which is related to the acceleration of the oscillation movement. The time responses and FFT amplitudes of both devices are shown from Fig. 63 to Fig. 65. The optical device detected vibrations down to 10 mVpp above the 3:1 SNR criteria that commonly is taken a rule [95]. The noticeable progressive decrease in the amplitude of the signals in the time domain (see Fig. 63a and Fig. 64a) and the FFT (see Fig. 63b and Fig. 64b) is proportional to the diminishment of the amplitude of the emitted signal. In both cases (wavelength shift and power variations), the emitted signal can be clearly detected and a low level of the harmonic components is noticeable. Regarding the commercial accelerometer, it detected signals down to 30 mVpp (see Fig. 65).

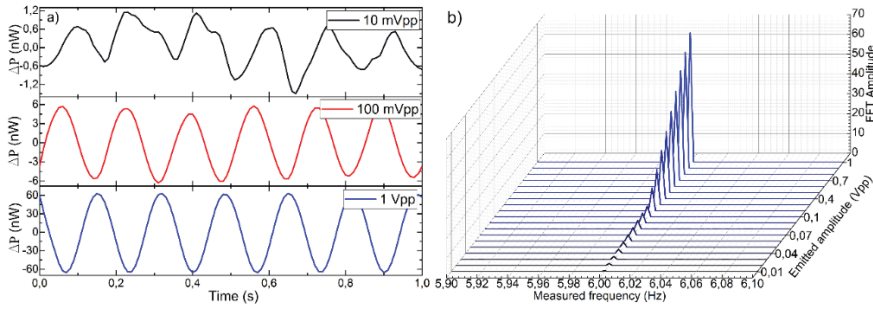


Figure 63: Results of the power variation measurements in the manufactured optical device. a) Time response of three representative cases, and b) FFT amplitudes for sinusoidal signals of 6 Hz and amplitudes from 1 Vpp down to 10 mVpp.

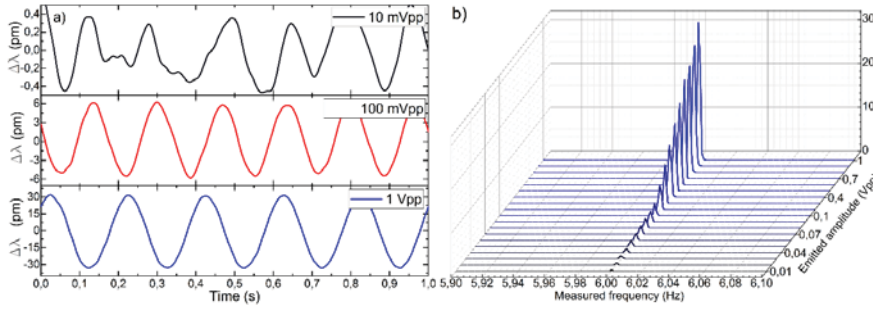


Figure 64: Results of the wavelength shift measurements in the manufactured optical device. a) Time response of three representative cases, and b) FFT amplitudes for sinusoidal signals of 6 Hz and amplitudes from 1 Vpp down to 10 mVpp.

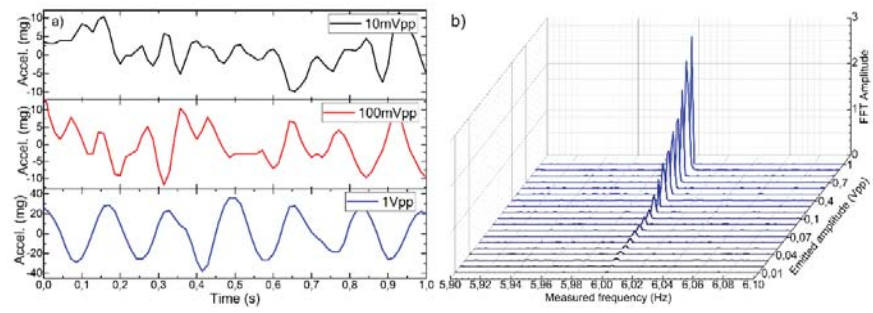


Figure 65: Results of the acceleration measurements in the electronic accelerometer. a) Time response of three representative cases, and b) FFT amplitudes for sinusoidal signals of 6 Hz and amplitudes from 1 Vpp down to 10 mVpp.

The calibration resulting from these tests is shown in Fig. 66.

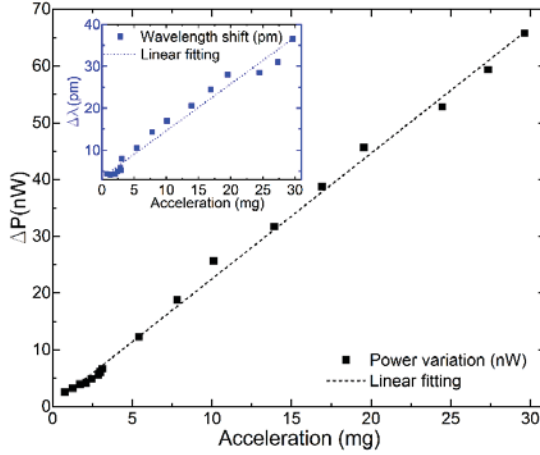


Figure 66: Calibration of the manufactured optical accelerometer.

The linear behavior of wavelength shift and power variations is significant, especially for the latter, where a sensitivity of 2.213 nW/mg with a Pearson squared correlation coefficient of $R^2 = 0.997$ and with a noise density of 1.083 $\mu\text{g}/\text{sqrt}(\text{Hz})$ was obtained. As a result, the correlation between the power variation (ΔP) and the acceleration (in mg) can be expressed as:

$$a = 0.450\Delta P - 0.143 \quad (45)$$

According to wavelength shift measurements, a sensitivity of 1.116 pm/mg with a Pearson squared correlation coefficient of $R^2 = 0.976$ was achieved. It should be pointed out that our MCF accelerometer was optimized to operate with power variation measurements, which implied low sensitivity in terms of wavelength shift. Thus, such result indicates that the device was surface bonded as close as possible as depicted in Fig. 59 and that it operates as intended.

In this work, a compact and highly sensitive all-fiber accelerometer is shown. Its structure is designed to optimize the change in the amplitude of the spectrum, which is related to power variation. This

configuration makes its interrogation to be very simple, made by few off-the-shelf equipment and cost-effective. The device was capable of detecting extremely low frequency vibrations down to 1 mHz with a sensitivity of 2.213 nW/mg, which makes it appealing for applications in which these characteristics are demanded, such as in seismology.

1.3.4.4 Direction sensitive curvature sensor

*In this point, a summary of the article “Composed multicore fiber structure for direction-sensitive curvature monitoring” is shown. This article was published in APL Photonics in July 2020 and it is included in the Appendix section of the thesis as **Article 4** to be consulted for further details.*

In this section, the same sensor architecture and interrogation setup as in **Article 3** was employed to measure curvature (see Fig. 56). However, in this case, the SMF-MCF1-MCF2-SMF structure was built with segments of $L_1 = 17.4$ mm and $L_2 = 18.2$ mm in order to obtain a sharper and narrower peak in the spectrum than that in **Article 3** (see Fig. 67). The expression for the coupled power in the central core is identical to the previous device (Eq. 44) as well as its interrogation setup (see Fig. 34).

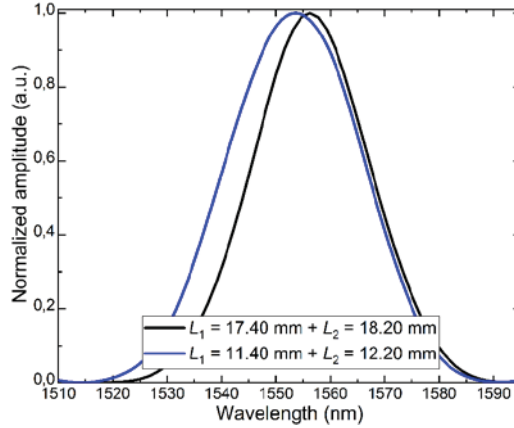


Figure 67: Spectra of the manufactured device in **Article 3** (blue line) and the one in **Article 4** (black line).

To subject the device to curvature, the device was held by the SMFs by means of two fiber chucks that were mounted on rotators (Thorlabs HFR001) and secured on an optical breadboard that was placed in a vertical position. Another fiber chuck was attached and used as a mass (20 g) in the lower SMF to keep the tension of the fiber constant by means of gravity. The measurements of curvature were carried out at different orientations of the 3cMCF segments in the device, between 0° and 180° in steps of 30° with respect to curvature (see Fig. 68) and a translation stage with micrometer resolution was used to bend the structure by its MCF1-MCF2 junction in a controlled manner. The value of curvature (C) on the device was calculated with the following equation: $C = 12h/d^2$ [96], where h is the displacement of the translation stage and d is the separation between the two fiber rotators.

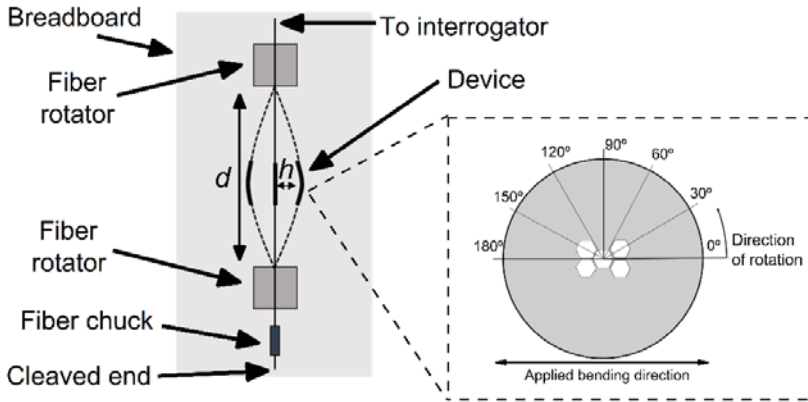


Figure 68: Schematic diagram of the measuring setup.

Fig. 69 shows the spectra observed when the curvature at two perpendicular directions was applied to the device (0° and 90° orientations according to Fig. 68). Note that when the wavelength shift is larger, the changes in intensity are minimal and vice versa. This behavior was expected due to the architecture of the device and the asymmetry of the 3cMCFs in it, as shown in **Article 3**.

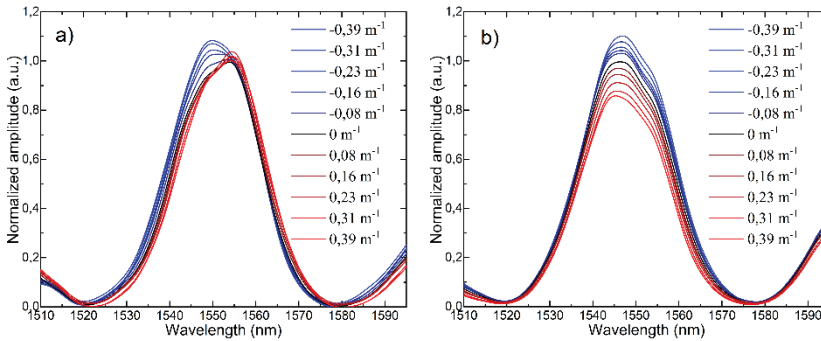


Figure 69: Spectra at different curvatures observed when the position of the device was at a) 0° and b) 90° , respectively.

Fig. 70 shows the averaged curvature sensitivities that were measured in the seven different orientations of the device indicated in Fig. 68.

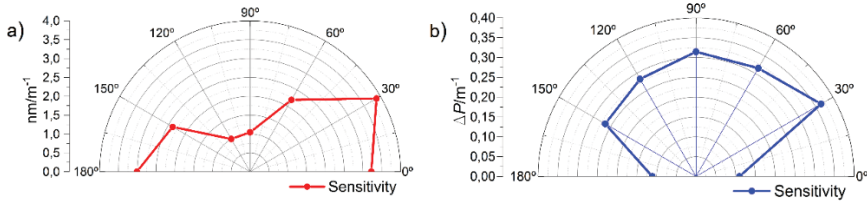


Figure 70: Polar representation of the averaged curvature sensitivity in terms of a) wavelength shift and b) intensity changes.

Thus, in this work, a highly sensitive device capable to provide the amplitude and the direction of curvature has been shown. The curvature sensitivity of the sensor reported here was found to be 4.66 dB/m^{-1} when intensity changes were correlated with curvature.

Bibliography

- [1] J. S. Wilson, *Sensor technology handbook*. Elsevier, 2004.
- [2] S. L. Chuang, *Physics of photonic devices*. John Wiley & Sons, 2012.
- [3] M. Zhang *et al.*, "photonic sensors review progress of optical fiber sensors and its application in harsh environment," vol. 1, no. 1, pp. 84-89, 2011.
- [4] G. E. J. P. E. Sommargren, "A new laser measurement system for precision metrology," vol. 9, no. 4, pp. 179-184, 1987.
- [5] E. Udd and W. B. Spillman Jr, *Fiber optic sensors: an introduction for engineers and scientists*. John Wiley & Sons, 2011.
- [6] J. M. López-Higuera, *Handbook of optical fibre sensing technology*. Wiley, 2002.
- [7] N. Sabri, S. Aljunid, M. Salim, R. Ahmad, and R. Kamaruddin, "Toward optical sensors: Review and applications," in *Journal of Physics: Conference Series*, 2013, vol. 423, no. 1, p. 012064: IOP Publishing.
- [8] D. A. Krohn, "Intensity modulated fiber optic sensors overview," in *Fiber Optic and Laser Sensors IV*, 1987, vol. 718, pp. 2-11: International Society for Optics and Photonics.
- [9] Y.-J. J. O. F. T. Rao, "Recent progress in fiber-optic extrinsic Fabry–Perot interferometric sensors," vol. 12, no. 3, pp. 227-237, 2006.
- [10] P. Lu *et al.*, "Distributed optical fiber sensing: Review and perspective," vol. 6, no. 4, p. 041302, 2019.
- [11] A. D. Kersey and A. Dandridge, "Distributed and multiplexed fiber-optic sensors," in *Optical Fiber Sensors*, 1988, p. WDD1: Optical Society of America.
- [12] P. Roriz, A. Ramos, J. L. Santos, and J. A. J. P. S. Simões, "Fiber optic intensity-modulated sensors: A review in biomechanics," vol. 2, no. 4, pp. 315-330, 2012.
- [13] Y. Qiu, Q.-b. Wang, H.-t. Zhao, J.-a. Chen, and Y.-y. J. J. o. S. J. U. Wang, "Review on composite structural health

- monitoring based on fiber Bragg grating sensing principle," vol. 18, no. 2, pp. 129-139, 2013.
- [14] M. Islam, M. M. Ali, M.-H. Lai, K.-S. Lim, and H. J. S. Ahmad, "Chronology of Fabry-Perot interferometer fiber-optic sensors and their applications: a review," vol. 14, no. 4, pp. 7451-7488, 2014.
- [15] J. Nedoma, M. Fajkus, and R. J. P. E. Martinek, "Measurement of electric current using optical fibers: A Review," vol. 93, no. 11, pp. 140-145, 2017.
- [16] E. J. R. S. Milton, "Review article principles of field spectroscopy," vol. 8, no. 12, pp. 1807-1827, 1987.
- [17] C. Muehlethaler, M. Leona, and J. R. J. A. C. Lombardi, "Review of surface enhanced Raman scattering applications in forensic science," vol. 88, no. 1, pp. 152-169, 2016.
- [18] S. Andonov and M. Cundeva-Blajer, "Calibration for industry 4.0 metrology: touchless calibration," in *Journal of Physics: Conference Series*, 2018, vol. 1065, no. 7.
- [19] V. Majstorovic, S. Stojadinovic, S. Zivkovic, D. Djurdjanovic, Z. Jakovljevic, and N. J. P. C. Gligorijevic, "Cyber-physical manufacturing metrology model (CPM3) for sculptured surfaces–turbine blade application," vol. 63, pp. 658-663, 2017.
- [20] M. J. O. E. Johnson, "Fiber displacement sensors for metrology and control," vol. 24, no. 6, pp. 961-1, 1985.
- [21] T. J. I. T. o. C. Calvin, Hybrids, and M. Technology, "Quality control techniques for" zero defects", " vol. 6, no. 3, pp. 323-328, 1983.
- [22] C. Boller and N. Meyendorf, "State-of-the-art in Structural Health monitoring for aeronautics," in *Proceedings of the International Symposium on NDT in Aerospace*, 2008.
- [23] G. Wild, "Optical fiber Bragg grating sensors applied to gas turbine engine instrumentation and monitoring," in *2013 IEEE Sensors Applications Symposium Proceedings*, 2013, pp. 188-192: IEEE.
- [24] S. Heath and M. Imregun, "A survey of blade tip-timing measurement techniques for turbomachinery vibration," 1998.

- [25] I. García, J. Beloki, J. Zubia, G. Aldabaldetrekú, M. A. Illarramendi, and F. J. S. Jiménez, "An optical fiber bundle sensor for tip clearance and tip timing measurements in a turbine rig," vol. 13, no. 6, pp. 7385-7398, 2013.
- [26] D. Wisler, "Loss reduction in axial-flow compressors through low-speed model testing," 1985.
- [27] M. W. Wiseman and T.-H. Guo, "An investigation of life extending control techniques for gas turbine engines," in *Proceedings of the 2001 American Control Conference.(Cat. No. 01CH37148)*, 2001, vol. 5, pp. 3706-3707: IEEE.
- [28] N. Kishi and E. Yamashita, "A simple coupled-mode analysis method for multiple-core optical fiber and coupled dielectric waveguide structures," *IEEE Transactions on Microwave Theory and Techniques*, vol. 36, no. 12, pp. 1861-1868, 1988.
- [29] K. J. Melcher and J. A. Kypuros, "Toward a fast-response active turbine tip clearance control," 2003.
- [30] J. L. Geisheimer and T. Holst, "Metrology considerations for calibrating turbine tip clearance sensors," in *Proceedings of the XIX Biannual Symposium on Measuring Techniques in Turbomachinery Transonic and Supersonic Flow in Cascades and Turbomachines, Rhodes-St-Genève, Belgium*, 2007, pp. 7-8.
- [31] A. Kempe, S. Schlamp, T. Rösger, and K. Haffner, "Spatial and temporal high-resolution optical tip-clearance probe for harsh environments," in *Proceedings of the 13th International Symposium on Applications of Laser Techniques to Fluid Mechanics, Lisbon, Portugal*, 2006, pp. 26-29: Citeseer.
- [32] A. W. Snyder, "Coupled-Mode Theory for Optical Fibers," *Journal of the Optical Society of America*, vol. 62, no. 11, pp. 1267-1277, 1972/11/01 1972.
- [33] V. Georgiev *et al.*, "The blade flutter measurement based on the blade tip timing method," in *Proceedings of the 15th WSEAS international conference on Systems, Corfu Island, Greece*, 2011, pp. 14-16.
- [34] S. Wu, Z. Zhao, Z. Yang, S. Tian, L. Yang, and X. Chen, "Physical constraints fused equiangular tight frame method for

- Blade Tip Timing sensor arrangement," *Measurement*, vol. 145, pp. 841-851, 2019/10/01/ 2019.
- [35] A. J. I. J. o. R. M. Sheard, "Blade by blade tip clearance measurement," vol. 2011, 2011.
- [36] L. Du, X. Zhu, J. J. S. m. Zhe, and structures, "A high sensitivity inductive sensor for blade tip clearance measurement," vol. 23, no. 6, p. 065018, 2014.
- [37] B. Yu, T. Zhang, H. Ke, and T. J. I. A. Zhang, "Research on the Tip Clearance Measuring Method Based on AC Discharge," vol. 8, pp. 60355-60363, 2020.
- [38] A. Schicht, S. Schwarzer, L.-P. J. I. T. o. I. Schmidt, and Measurement, "Tip clearance measurement technique for stationary gas turbines using an autofocusing millimeter-wave synthetic aperture radar," vol. 61, no. 6, pp. 1778-1785, 2012.
- [39] M. Violetti, A. K. Skrivervik, Q. Xu, and M. Hafner, "New microwave sensing system for blade tip clearance measurement in gas turbines," in *SENSORS, 2012 IEEE*, 2012, pp. 1-4: Ieee.
- [40] A. Kempe, S. Schlamp, T. Rösigen, and K. J. O. l. Haffner, "Low-coherence interferometric tip-clearance probe," vol. 28, no. 15, pp. 1323-1325, 2003.
- [41] T. Pfister, L. Büttner, J. Czarske, H. Krain, R. J. M. S. Schodl, and Technology, "Turbo machine tip clearance and vibration measurements using a fibre optic laser Doppler position sensor," vol. 17, no. 7, p. 1693, 2006.
- [42] I. García *et al.*, "Different configurations of a reflective intensity-modulated optical sensor to avoid modal noise in tip-clearance measurements," vol. 33, no. 12, pp. 2663-2669, 2015.
- [43] I. García, J. Zubia, J. Beloki, J. Arrue, G. Durana, and G. J. S. Aldabaldetrekue, "Optical tip clearance measurements as a tool for rotating disk characterization," vol. 17, no. 1, p. 165, 2017.
- [44] H. Cao, Y. Chen, Z. Zhou, G. J. S. Zhang, and A. A. Physical, "Theoretical and experimental study on the optical fiber bundle displacement sensors," vol. 136, no. 2, pp. 580-587, 2007.
- [45] M. Yasin, S. Harun, H. Abdul-Rashid, A. J. O. Zaidan, and A. M.-R. COMMUNICATIONS, "Performance of optical

- displacement sensor using a pair type bundled fiber from a theoretical and experimental perspective," vol. 1, no. 11, pp. 549-553, 2007.
- [46] H. Huang and U. J. A. o. Tata, "Simulation, implementation, and analysis of an optical fiber bundle distance sensor with single mode illumination," vol. 47, no. 9, pp. 1302-1309, 2008.
- [47] L. Bergougnoux, J. Misguich-Ripault, and J.-L. J. R. o. s. i. Firpo, "Characterization of an optical fiber bundle sensor," vol. 69, no. 5, pp. 1985-1990, 1998.
- [48] S. Cao, F. Duan, Z. Fang, and Y. Ma, "Research on optical fiber bundle displacement sensor with multi-grouped receiving fibers," in *Advanced Laser Technologies 2005*, 2006, vol. 6344, p. 63442Y: International Society for Optics and Photonics.
- [49] S. Cao, F. Duan, and Y. Zhang, "Measurement of rotating blade tip clearance with fibre-optic probe," in *Journal of Physics: Conference Series*, 2006, vol. 48, no. 1, p. 873: IOP Publishing.
- [50] H. Guo, F. Duan, G. Wu, and J. J. R. o. S. I. Zhang, "Blade tip clearance measurement of the turbine engines based on a multi-mode fiber coupled laser ranging system," vol. 85, no. 11, p. 115105, 2014.
- [51] D.-c. Ye, F.-j. Duan, H.-t. Guo, Y. Li, and K. J. O. E. Wang, "Turbine blade tip clearance measurement using a skewed dual-beam fiber optic sensor," vol. 51, no. 8, p. 081514, 2012.
- [52] I. García, R. Przysowa, J. Amorebieta, and J. J. S. Zubia, "Tip-clearance measurement in the first stage of the compressor of an aircraft engine," vol. 16, no. 11, p. 1897, 2016.
- [53] R. Fernández-Bello *et al.*, "Performance Comparison of Three Fibre-Based Reflective Optical Sensors for Aero Engine Monitorization," vol. 19, no. 10, p. 2244, 2019.
- [54] H. A. Rahman, N. M. Isa, and S. W. J. I. S. J. Harun, "Modeling the Concentric Fiber Optic Bundle Displacement Sensor Using a Quasi-Gaussian Beam Approach," vol. 15, no. 9, pp. 4777-4781, 2015.
- [55] J. J. M. Brandão Faria and O. T. Letters, "Modeling the Y-branched optical fiber bundle displacement sensor using a

- quasi-Gaussian beam approach," vol. 25, no. 2, pp. 138-141, 2000.
- [56] M. Yu-zhen, Z. Yong-kui, L. Guo-ping, and L. Hua-guan, "Tip clearance optical measurement for rotating blades," in *MSIE 2011*, 2011, pp. 1206-1208: IEEE.
- [57] G. Webb, P. J. Vardanega, and C. R. J. J. o. B. E. Middleton, "Categories of SHM deployments: technologies and capabilities," vol. 20, no. 11, p. 04014118, 2015.
- [58] E. J. S. S. T. Nyfors and Applications, "Industrial microwave sensors—A review," vol. 1, no. 1, pp. 23-43, 2000.
- [59] K. K. K. Annamdas and V. G. M. Annamdas, "Review on developments in fiber optical sensors and applications," in *Fiber Optic Sensors and Applications VII*, 2010, vol. 7677, p. 76770R: International Society for Optics and Photonics.
- [60] G. Rodriguez, J. R. Casas, S. J. S. M. Villalba, and Maintenance, "SHM by DOFS in civil engineering: A review," vol. 2, no. 4, pp. 357-382, 2015.
- [61] J. Chen, B. Liu, and H. J. F. o. O. i. C. Zhang, "Review of fiber Bragg grating sensor technology," vol. 4, no. 2, pp. 204-212, 2011.
- [62] Y. J. J. o. A. P. Wang, "Review of long period fiber gratings written by CO₂ laser," vol. 108, no. 8, p. 11, 2010.
- [63] L. Li, L. Xia, Z. Xie, and D. J. O. e. Liu, "All-fiber Mach-Zehnder interferometers for sensing applications," vol. 20, no. 10, pp. 11109-11120, 2012.
- [64] R. Kashyap and B. J. j. o. L. T. Nayar, "An all single-mode fiber Michelson interferometer sensor," vol. 1, no. 4, pp. 619-624, 1983.
- [65] K. McKenzie, D. A. Shaddock, D. E. McClelland, B. C. Buchler, and P. K. J. P. r. l. Lam, "Experimental demonstration of a squeezing-enhanced power-recycled Michelson interferometer for gravitational wave detection," vol. 88, no. 23, p. 231102, 2002.
- [66] K. Saitoh and S. J. J. o. L. T. Matsuo, "Multicore fiber technology," vol. 34, no. 1, pp. 55-66, 2016.

- [67] Y. Sasaki, K. Takenaga, S. Matsuo, K. Aikawa, and K. J. O. F. T. Saitoh, "Few-mode multicore fibers for long-haul transmission line," vol. 35, pp. 19-27, 2017.
- [68] J. Villatoro, E. Antonio-Lopez, A. Schülzgen, and R. J. O. L. Amezcua-Correa, "Miniature multicore optical fiber vibration sensor," vol. 42, no. 10, pp. 2022-2025, 2017.
- [69] N. Kishi, E. J. I. t. o. m. t. Yamashita, and techniques, "A simple coupled-mode analysis method for multiple-core optical fiber and coupled dielectric waveguide structures," vol. 36, no. 12, pp. 1861-1868, 1988.
- [70] A. W. J. J. Snyder, "Coupled-mode theory for optical fibers," vol. 62, no. 11, pp. 1267-1277, 1972.
- [71] J. Hudgings, L. Molter, and M. J. I. j. o. q. e. Dutta, "Design and modeling of passive optical switches and power dividers using non-planar coupled fiber arrays," vol. 36, no. 12, pp. 1438-1444, 2000.
- [72] A. Perez-Leija, J. Hernandez-Herrejon, H. Moya-Cessa, A. Szameit, and D. N. J. P. R. A. Christodoulides, "Generating photon-encoded W states in multiport waveguide-array systems," vol. 87, no. 1, p. 013842, 2013.
- [73] W.-P. J. J. A. Huang, "Coupled-mode theory for optical waveguides: an overview," vol. 11, no. 3, pp. 963-983, 1994.
- [74] F. Y. Chan, A. P. T. Lau, and H.-Y. J. O. e. Tam, "Mode coupling dynamics and communication strategies for multi-core fiber systems," vol. 20, no. 4, pp. 4548-4563, 2012.
- [75] Y. Chunxia, D. Hui, D. Wei, X. J. S. Chaowei, and A. A. Physical, "Weakly-coupled multicore optical fiber taper-based high-temperature sensor," vol. 280, pp. 139-144, 2018.
- [76] C. Xia, N. Bai, I. Ozdur, X. Zhou, and G. J. O. e. Li, "Supermodes for optical transmission," vol. 19, no. 17, pp. 16653-16664, 2011.
- [77] C. Xia *et al.*, "Supermodes in coupled multi-core waveguide structures," vol. 22, no. 2, pp. 196-207, 2015.
- [78] "Revisiting twin-core fiber sensors for high-temperature measurements," *Applied Optics*, vol. 51, no. 25, pp. 6227-6232, 2012/09/01 2012.

- [79] J. Villatoro *et al.*, "Accurate strain sensing based on super-mode interference in strongly coupled multi-core optical fibres," vol. 7, no. 1, pp. 1-7, 2017.
- [80] G. Coviello, V. Finazzi, J. Villatoro, and V. J. O. e. Pruneri, "Thermally stabilized PCF-based sensor for temperature measurements up to 1000° C," vol. 17, no. 24, pp. 21551-21559, 2009.
- [81] J. E. Antonio-Lopez, Z. S. Eznaveh, P. LiKamWa, A. Schülzgen, and R. J. O. l. Amezcua-Correa, "Multicore fiber sensor for high-temperature applications up to 1000° C," vol. 39, no. 15, pp. 4309-4312, 2014.
- [82] A. Van Newkirk, E. Antonio-Lopez, G. Salceda-Delgado, R. Amezcua-Correa, and A. J. O. L. Schülzgen, "Optimization of multicore fiber for high-temperature sensing," vol. 39, no. 16, pp. 4812-4815, 2014.
- [83] M. Han and A. J. O. l. Wang, "Temperature compensation of optical microresonators using a surface layer with negative thermo-optic coefficient," vol. 32, no. 13, pp. 1800-1802, 2007.
- [84] G. Adamovsky *et al.*, "Peculiarities of thermo-optic coefficient under different temperature regimes in optical fibers containing fiber Bragg gratings," vol. 285, no. 5, pp. 766-773, 2012.
- [85] H. Watanabe, N. Yamada, and M. J. I. j. o. t. Okaji, "Linear thermal expansion coefficient of silicon from 293 to 1000 K," vol. 25, no. 1, pp. 221-236, 2004.
- [86] M. Heiblum and J. J. I. J. o. Q. E. Harris, "Analysis of curved optical waveguides by conformal transformation," vol. 11, no. 2, pp. 75-83, 1975.
- [87] R. T. J. O. E. Schermer, "Mode scalability in bent optical fibers," vol. 15, no. 24, pp. 15674-15701, 2007.
- [88] R. T. Schermer and J. H. J. I. J. o. Q. E. Cole, "Improved bend loss formula verified for optical fiber by simulation and experiment," vol. 43, no. 10, pp. 899-909, 2007.
- [89] O. Arrizabalaga *et al.*, "High-performance vector bending and orientation distinguishing curvature sensor based on asymmetric coupled multi-core fibre," vol. 10, no. 1, pp. 1-10, 2020.

- [90] G. Salceda-Delgado, A. Van Newkirk, J. Antonio-Lopez, A. Martinez-Rios, A. Schülzgen, and R. A. J. O. l. Correa, "Compact fiber-optic curvature sensor based on super-mode interference in a seven-core fiber," vol. 40, no. 7, pp. 1468-1471, 2015.
- [91] J. Villatoro, A. Van Newkirk, E. Antonio-Lopez, J. Zubia, A. Schülzgen, and R. J. O. L. Amezcua-Correa, "Ultrasensitive vector bending sensor based on multicore optical fiber," vol. 41, no. 4, pp. 832-835, 2016.
- [92] G. Yin, F. Zhang, B. Xu, J. He, and Y. J. O. E. Wang, "Intensity-modulated bend sensor by using a twin core fiber: theoretical and experimental studies," vol. 28, no. 10, pp. 14850-14858, 2020.
- [93] H. Qu, G. Yan, and M. J. O. l. Skorobogatiy, "Interferometric fiber-optic bending/nano-displacement sensor using plastic dual-core fiber," vol. 39, no. 16, pp. 4835-4838, 2014.
- [94] J. Villatoro, V. P. Minkovich, and J. J. O. l. Zubia, "Photonic crystal fiber interferometric vector bending sensor," *Optics Letters*, vol. 40, no. 13, pp. 3113-3116, 2015.
- [95] A. Shrivastava and V. B. J. C. o. y. s. Gupta, "Methods for the determination of limit of detection and limit of quantitation of the analytical methods," vol. 2, no. 1, p. 21, 2011.
- [96] Y.-P. Wang and Y.-J. J. I. S. J. Rao, "A novel long period fiber grating sensor measuring curvature and determining bend-direction simultaneously," vol. 5, no. 5, pp. 839-843, 2005.

Section 2

Conclusions

In this section, the conclusions of the thesis are presented, as well as the future lines of investigation that are feasible as a result of it. The latter are divided in investigation lines focused on improving the performance of the devices described in this work and in new investigation lines in which they may be suitable. The scientific papers and conferences in which the results of the research have been published are included in this section as well.

2.1 OFDS

2.1.1 Conclusions

In the first line of research, two OFDSs designed and manufactured for TC measurements were described. Their operating principle was based on the modulation of the reflected light as a function of the distance to the blades, but their measurement conditions were significantly different due to the manner in which they were installed in the casings of the turbines. For the first case, the sensor head was aiming at the sealing lands of the blades, which decreased the reflected light and forced placing the sensor close to the blade tips in order to operate in Region 1. For the second case, the sensor head was aiming at the flat part of the blade, which was further from the casing but offered more surface for the light to be reflected. To operate under such conditions, the design of the sensor was upgraded so Region 1 could be larger and start at longer distances. In this manner, the sensor could be placed further from the blade tips, which improved the operation safety significantly. This last version of the OFDS enhanced the performance of the previous one significantly and fulfilled the requirements set by our partner CTA regarding the following aspects:

- Non-contact measurement so that the mechanical behavior of the blades is not compromised.
- Precision in the measurement of TC. For instance, for the last tests, The TC values over 20000 engine revolutions were registered showing a mean variability below 7 μm for each individual blade turn after turn, which is far below the demanded 25 μm .
- Use of the more sensitive Region 1. Compared to the first fiber bundle, in the second version, Region 1 was longer (3.5 mm vs 2 mm), started at longer distances (4.5 mm vs 2 mm) and showed higher sensitivity due to its steeper slope.

- Installation ease. This feature was very much appreciated by CTA technicians. The sensor head was easy to install in the casing, which is a very important feature, as it reduces significantly the time required for its installation and does not require special holes in the casing to be placed in it.
- Robustness. The sensor has been able to perform during the entire tests in real-field conditions without any performance issue.
- Cost-effectiveness of the sensing system. The interrogation system of the OFDS is made by off-the-shelf equipment. Regarding the fiber bundle, it is made of commercial multimode and single mode fibers.
- Versatility and safety improvements. The last version of the OFDS has been designed to operate in as many turbines as possible, avoiding in this manner the need of manufacturing ad-hoc fiber bundles for each case. Moreover, thanks to the arrangement of the fibers, it allows locating it further from the blade tips, which improves the safety.

2.1.2 Improvement/Evolution of the developed devices

The following lines of work are suggested in order to continue with this investigation line:

- To measure the TC simultaneously in 3 consecutive turbine stages (rotor+stator) in the wind tunnel, measuring the TC of each rotor in at least 3 different points of it. This measurement would be very challenging, as it would imply multiplying the hardware used for the tests so far and adapting the acquisition system to be able to acquire such amount of data simultaneously. The information provided by such test is very important for CTA, as it would allow

characterizing the TC behavior when several turbine stages are operating simultaneously.

- To design a mechanism to avoid the sensor head getting dirty because of contamination or residues coming from the combustion chamber with the aim of making it viable for tests in aeronautical engines in real operating conditions.
- Related with the previous point, in order to use the OFDS in real operating conditions, the fiber bundle has to be adapted to withstand operating temperatures between 700 °C and 1000 °C, which are common in turbines.
- Miniaturization of the hardware components of the measurement system to integrate them in a compact setup in order to make it easier to transport and handle.

2.1.3 New lines of investigation

Apart from the lines of work mentioned above, the OFDS could be used for the following applications:

- With the OFDS in this work, the radial vibrations of the blades (TC) have been measured and analyzed, and as it has been mentioned, the same signal could be used for measuring the tangential vibrations of the blades (TT). However, it would be interesting to develop a sensing system capable of measuring axial vibrations of the blades, as there is not an effective solution yet for this purpose.
- Use the OFDS for other potential applications that involve the characterization of rotating elements as disks, or the measurement of eccentricity of shafts or axles. Such measurements may be interesting for several sectors such as car industry, for instance.

2.2 MCF-based sensors

2.2.1 Conclusions

In the second line of the research, several MCF-based sensing solutions were developed after describing their operating principle. By exploiting it, MCF-based sensors for the measurement of temperature, bending, vibrations and curvature were designed and manufactured. Such solutions made use of different operating configurations (single or cascaded MCF segments of identical or different lengths) and MCF geometries (7cMCF or 3cMCF) in order to pursue the optimum performance. The MCF-based sensors reported in this thesis showed the following characteristics:

- High sensitivity sensors: The sensors showed high sensitivity for the measurement of the parameter under test. Moreover, in specific cases as those in which an asymmetric MCF was used, the devices proved to be direction sensitive as well.
- Easy and fast to manufacture, and easily reproducible: Only a precision cleaver and fusion splicer are required to manufacture such devices.
- Simple interrogation setup: The setup for the interrogation of these devices is very simple and cost-effective, as it only requires a broadband light source, a circulator (or optic coupler), a spectrometer and a PD. All of these components are off-the-shelf equipment.
- Capability to measure multiple parameters: As MCFs are sensitive to multiple parameters; a MCF-based sensor for each of them can be developed. However, as these fibers are sensitive to multiple parameters at the same time, they have to be fixed or packaged in a manner that certifies that the effect in the spectrum is only due to the parameter of interest.

- Easily customizable devices: The shape of the spectrum in these devices is easily configurable by modifying the length and configuration of the MCF (reflection or transmission operation, single or cascaded segments...). In this manner, it is easy to manufacture multiple devices with easily distinguishable spectra in order to multiplex them for multipoint measurements.

2.2.2 Improvement/Evolution of the developed devices

As it has been pointed out above, MCFs have appealing characteristics for the development of sensing solutions. Thanks to that, the following lines of work are suggested in order to continue with this investigation line:

- Development of MCF-based sensing solutions for the measurement of other parameters that are of interest for the industry such as force, strain, dynamic pressure, shape sensing...
- To design specific MCF geometries aimed at maximizing their sensitivity for the measurement of a specific parameter of interest. Analogous to the mathematical approach that in this document has been used to predict the most sensitive MCF geometry for temperature measurements, by modifying certain parameters of the MCF such as the diameter of the cores, distance between cores, etc., ad-hoc structures can be designed for each parameter.
- To develop a system that allows multiplexing MCFs for multipoint sensing: By cascading multiple MCF segments in the same SMF and being able to interrogate or identify them unequivocally, a significantly high spatial resolution could be achieved, especially if the segments are short, which could be considered quasi-distributed sensing.

- Measurement of more than one parameter with the same MCF segment: As it has been demonstrated in this thesis, MCFs can sense with wavelength shift or power variation. With the appropriate configuration, each of these parameters could be used for the measurement of different parameters simultaneously with the same MCF segment. For instance, the same device could use wavelength shift to measure temperature and power variations for vibration sensing.
- To embed the MCF in different materials for SHM: In this manner, the inside of the piece or structure under test could be analyzed in detail in order to detect air bubbles or manufacturing defects.
- Cladding shapes: Some of the MCF sensors shown in this work, especially those based on asymmetric MCFs, require specific alignments in order to operate properly. To make this alignment easier, MCFs could be manufactured with shaped claddings to indicate the correct alignment.
- Commercial sensors: Some of the sensors presented in this work have been packaged to withstand harsh environments and real-field working conditions, and their interrogation is easy and cost-effective. The latter could be integrated in a compact box in order to make it easier to transport and handle, and offer the complete system (MCF sensor + interrogation setup) commercially.

2.2.3 New lines of investigation

The following research lines could be developed:

- Design of filters and couplers based on MCF segments: By using segments of certain geometries and lengths, MCFs can act as ad-hoc band pass or notch filters that allow the coupled power to be maximized or cancelled at specific wavelengths.

Such characteristics may be appealing for research areas as telecommunications.

- Manipulation of the cores: By inscribing FBGs or modifying in a controlled manner the refractive index in a certain core or cores, the response of each of the modified MCF segments could be identified unequivocally and used for multipoint sensing.

2.3 Contributions of the thesis

During the thesis, the results of the research have been published in international journals and presented in several conferences as follows (in chronological order from newest to oldest):

2.3.1 Publications

Summary of the research articles that have been published in international journals:

1. **Amorebieta, J.**; Ortega-Gomez, A.; Durana, G.; Fernández, R.; Antonio-Lopez, E.; Schülzgen, A.; Zubia, J.; Amezcua-Correa, R.; Villatoro, J. (2020). Highly sensitive multicore fiber accelerometer for low frequency vibration sensing. *Scientific Reports*, 10 (1), 1-11 (Q1 in Multidisciplinary sciences in 2019 with an Impact Factor of 3.998, statistics of 2020 not available yet).
2. Villatoro, J.; **Amorebieta, J.**; Ortega-Gomez, A.; Antonio-Lopez, E.; Zubia, J.; Schülzgen, A.; Amezcua-Correa, R. (2020). Composed multicore fiber structure for direction-sensitive curvature monitoring. *APL Photonics*, 5 (7), 070801 (Q1 in Optics in 2019 with an Impact Factor of 4.864, statistics of 2020 not available yet).

3. **Amorebieta, J.**; Durana, G.; Ortega-Gomez, A.; Fernández, R.; Velasco, J.; Sáez de Ocáriz, I.; Zubia, J.; Antonio-López, E.; Schülzgen, A.; Amezcua-Correa, R.; Villatoro, J. (2019). Packaged multi-core fiber interferometer for high-temperature sensing. *Journal of Lightwave Technology*, *37* (10), 2328-2334 (Q1 in Optics in 2019 with an Impact Factor of 4.288).
4. Fernández, R.; **Amorebieta, J.**; Beloki, J.; Aldabaldetrekú, G.; García, I.; Zubia, J.; Durana, G. (2019). Performance Comparison of Three Fibre-Based Reflective Optical Sensors for Aero Engine Monitorization. *Sensors*, *19* (10), 2244 (Q1 in Instruments & Instrumentation in 2019 with an Impact Factor of 3.275).
5. Durana, G.; **Amorebieta, J.**; Fernandez, R.; Beloki, J.; Arrospide, E.; Garcia, I.; Zubia, J. (2018). Design, Fabrication and Testing of a High-Sensitive Fibre Sensor for Tip Clearance Measurements. *Sensors*, *18* (8), 2610 (Q1 in Instruments & Instrumentation in 2018 with an Impact Factor of 3.031).

2.3.2 Conferences

Summary of the conferences at which the research work has been presented:

1. **Amorebieta, J.**; Ortega-Gomez, A.; Durana, G.; Antonio-Lopez, E.; Schülzgen, A.; Zubia, J.; Amezcua-Correa, R.; Villatoro, J. "Highly Sensitive Supermode Interferometer for Low Frequency Vibration Monitoring". 27th International Conference on Optical Fiber Sensors OFS2020, Alexandria,

Virginia, USA. This conference has been postponed to June 2021 due to COVID.

2. **Amorebieta, J.**; Ortega-Gomez, A.; Durana, G.; Antonio-Lopez, E.; Schülzgen, A.; Zubia, J.; Amezcua-Correa, R.; Villatoro, J. “Highly sensitive orientation and amplitude discerning vector bending sensor based on asymmetric multicore fiber”. OSA Advanced Photonics, Montreal, Canada, July 13, 2020.
3. Garcia, I.; Durana, G.; **Amorebieta, J.**; Fernández, R.; Zubia, J. “Review of a Custom-Designed Optical Sensing System for Aero-Engine Applications”. The 9th EVI-GTI International Gas Turbine Instrumentation Conference, Graz, Austria, November 21, 2019.
4. **Amorebieta, J.**; Ortega-Gomez, A.; Amezcua-Correa, R.; Antonio-López, E.; Schülzgen, A.; Villatoro, J. “Novel twin cascaded multicore fiber-based structure for high sensitive multipurpose optical sensing”. 11^a Reunión Española de Optoelectrónica OPTOEL´19, Zaragoza, Spain, July 4, 2019.
5. **Amorebieta, J.**; Durana, G.; Ortega-Gomez, A.; Fernández, R.; Velasco, J.; Sáez de Ocáriz, I.; Zubia, J.; Antonio-López, E.; Schülzgen, A.; Amezcua-Correa, R.; Villatoro, J. “Strongly coupled multi-core fiber-based interferometer for high temperature sensing”. SPIE Optics+Optoelectronics, Prague, Czech Republic, April 15, 2019.
6. **Amorebieta, J.**; Fernández, R.; Durana, G.; Beloki, J.; Zubia, J. “Optical Fibre-Based Reflective Displacement Sensing System for High Sensitivity Blade Tip-Clearance

Measurements”. OSA Advanced Photonics Congress, Zurich, Switzerland, July 2, 2018.

7. Fernández, R.; **Amorebieta, J.**; Durana, G.; Beloki, J.; Zubia, J. “Performance comparison among three optical fibre-based displacement sensors for Blade Tip Clearance measurements”. 5th IEEE International Workshop on Metrology for AeroSpace (MetroAeroSpace), Rome, Italy, June 20, 2018.
8. **Amorebieta, J.**; Garcia, I.; Durana, G.; Aldabaldetrekua, G.; Zubia, J.; Sáez-Ocáriz, I. “Optical fibre-based reflective displacement sensor: computer modelling and application to impact detection in aeronautical structures”. SPIE Optical Metrology, Munich, Germany, June 26, 2017.

Section 3

Appendix: Published papers

Article 1

Title:

Design, fabrication and testing of a high-sensitive fibre sensor for tip clearance measurements

D.O.I.:

10.3390/s18082610

Authors:

Durana, G.; **Amorebieta, J.**; Fernandez, R.; Beloki, J.; Arrospide, E.; Garcia, I.; Zubia, J.

Journal and publication information:

Sensors, 18 (8), 2610 (2018)

Cited 3 times



Indicators of the Journal in 2018:

Impact factor: 3.031

Q1 in Instruments & Instrumentation (15/61)

Article

Design, Fabrication and Testing of a High-Sensitive Fibre Sensor for Tip Clearance Measurements

Gaizka Durana ^{1,*} , Josu Amorebieta ¹, Ruben Fernandez ¹, Josu Beloki ², Eneko Arrospide ³ , Iker Garcia ¹ and Joseba Zubia ¹

¹ Communications Engineering Department, University of the Basque Country (UPV/EHU), Ingeniero Torres Quevedo Plaza 1, E-48013 Bilbao, Spain; josu.amorebieta@ehu.eus (J.A.); ruben.fernandez@ehu.eus (R.F.); ikergeb@gmail.com (I.G.); joseba.zubia@ehu.eus (J.Z.)

² Aeronautical Technologies Centre, Bizkaia Technological Park, E-48170 Zamudio, Spain; josu.beloki@ctabef.com

³ Applied Mathematics Department, University of the Basque Country (UPV/EHU), Ingeniero Torres Quevedo Plaza 1, E-48013 Bilbao, Spain; eneko.arrospide@ehu.eus

* Correspondence: gaizka.durana@ehu.eus; Tel.: +34-94-601-4128

Received: 4 July 2018; Accepted: 2 August 2018; Published: 9 August 2018



Abstract: A highly sensitive fibre bundle-based reflective optical sensor has been designed and fabricated for Tip Clearance measurements in a turbine rig. The sensor offers high spatial and temporal resolution. The sensor probe consists of a single-mode transmitting fibre and two concentric rings of receiving multimode fibres that collect reflected light in a differential detection gain configuration, yielding a highly linear calibration curve for distance measurements. The clearance measurement range is approximately 2 mm around the central point fixed at 3.2 mm from the probe tip, and the sensitivity of the probe is 61.73 mm^{-1} . The fibre bundle has been designed to ensure that the distance security specifications required for the experimental program of the turbine are met. The optical sensor has operated under demanding conditions set by the blade and casing design. The experimental results obtained so far are promising and lead us to think that the optical sensor has great potential for online clearance measurements with high precision.

Keywords: tip clearance; optical fibre sensor; aircraft turbine

1. Introduction

In aeronautics, Tip Clearance (TC) refers to the gap existing between the blade tip and its surrounding case. Since the invention of the gas turbine engine, intense research has been conducted on reducing TC, as this parameter, of great concern for engine designers, is intimately related to engine efficiency and represents the driving force of most new architectures and innovative technological improvements for future aircraft applications. Whereas high TC values allow an amount of air to flow without generating useful work, a lack of clearance accelerates blade tip and shroud wear over time due mainly to rubs, and can put engine integrity at risk [1]. The clearance varies with the operation point of the mission profile (take-off, cruise and landing) as well as with the engine aging [2,3]. TC changes are caused by two types of loads, namely engine and flight loads. The former encompasses centrifugal, thermal, internal engine pressure, and thrust loads, whereas the latter comprises inertial (gravitational), aerodynamic (external pressure) and gyroscopic loads [4]. At cruise, a rule of thumb equates 0.25 mm of reduced clearance to a reduction of 1% in specific fuel consumption. Therefore, some of the most relevant benefits of reducing the TC include efficiency increase as well as increased payload and mission range capabilities [1,5]. In addition, aircraft noise and emissions are reduced, along with the subsequent environmental benefits involved [6,7]. It seems obvious that an accurate and real-time

measurement technology is necessary. In contrast to power-system turbines where common clearance values range from 2 to 8 mm, in aircraft turbines, TC is typically lower than 3 mm and a resolution better than 25 μm is usually required [8–10].

Currently, there are several traditional methods for TC measurements that include capacitive, eddy current, microwave, and discharging probe sensors (electromechanical). The former are popular due to their simplicity, low cost, and robustness, but they suffer from low spatial resolution, short measurement range, and require calibration [11–13]. Eddy current sensing is also a common technique for TC measurements, and it has about the same accuracy as capacitive probes [14,15]. It provides non-contact measurements at the expense of requiring magnetic materials for the blades. Additionally, the magnetic disturbance of the turbine engine may interfere with their output signal, and they are highly sensitive to temperature and blade tip shape. Microwave sensors are robust and insensitive to contamination, but the hollow waveguides at submillimeter wavelengths are impractical, and the corresponding circuitry complex [16,17]. Finally, electromechanical systems belong to the oldest tip clearance measurement systems [18]. They benefit from their high resolution over the entire measurement range, but their main drawbacks are that they only measure the clearance of the longest blade and the slow response time.

Optical sensors may overcome many of the previous drawbacks as they offer high sensitivity and resolution, immunity to electromagnetic interference, non-contact measurement and information about every blade [19–22]. However, among the different optical technologies (i.e., triangulation [23,24], OCT [22], time-of-flight measurements [25], laser Doppler velocimetry [26] and reflective intensity modulation [27]) employed for TC measurements at turbo machines, many of them do not fully satisfy the requirements of future closed-loop Active Clearance Control (ACC) systems [5]. For example, laser Doppler position probes offer high resolution, but the complexity of the probe limits the application of the system. In the case of the Optical Coherence Tomography (OCT), the measurement rate is limited by the speed of mechanical scanning, or in the case of triangulation, by the detector frame rate and minimum exposure time. Finally, the resolution of reflective intensity modulation-based sensor probes—compared to the rest of optical methods mentioned previously—is low due to the modal noise at the endface of the transmitting fibre.

In this paper, we report on the design and fabrication of a highly sensitive fibre bundle-based reflective optical sensor that has been tested in an aircraft turbine rig. The content of the paper has been structured as follows: first, a brief description of the operation principle is given, explaining the general sensor design and defining the working region of interest that will allow to maximize the sensitivity of the sensor. Afterwards the experimental program followed at the Aeronautical Technologies centre's (CTA's) transonic wind tunnel is explicated. Then, the most relevant results are presented and discussed. Finally, some conclusions are drawn from the previous discussion.

2. Materials and Methods

2.1. Sensor Design and Working Region of Interest

The schematic diagram of the sensor's operation is shown in Figure 1a. The fibre bundle is the principal element of the system. To avoid modal noise at the output [28], a central single-mode fibre is used as transmitting fibre of red laser light (wavelength of light: 660 nm), which after exiting the fibre bundle and being reflected by the target object located at a distance d from the fibre bundle tip, is partially gathered by two concentric rings of multimode optical fibres arranged around the central transmitting fibre; the inner ring consists of 5 optical fibres (fibre bunch 1; core diameters of 200 μm and Numerical Aperture (NA) of 0.2), whereas the outer ring consists of 17 optical fibres (fibre bunch 2; core diameters of 300 μm and NA of 0.2). The light collected by fibre bunches 1 and 2 is measured as a voltage level at photodetectors 1 and 2, respectively (V_1 and V_2). If we plot the ratio of V_2 to V_1 as a function of distance d , we get the characteristic calibration curve shown in Figure 1b. The reason of using two photodetectors is aimed at minimizing the undesirable effects caused by intensity fluctuations in the light source and reflectivity variations on the target surface. As both

voltage signals contain the same disturbance, the ratio V_2/V_1 gets rid of it and therefore becomes a pure function of the distance to the illuminated target surface d [27,29,30].

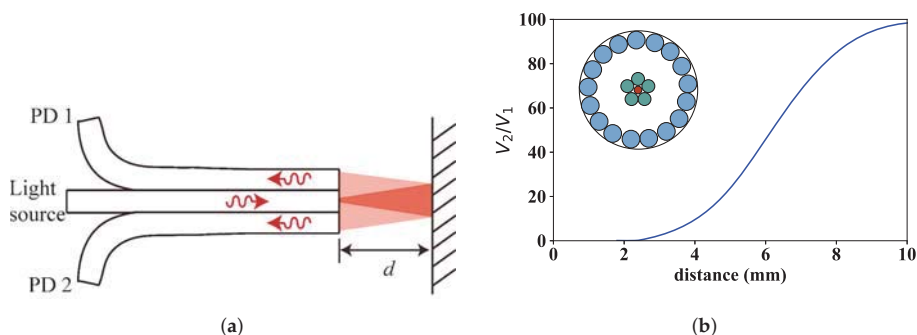


Figure 1. Fibre optic intensity sensor for TC measurements: (a) illustration of the fibre bundle based sensor; and (b) signal response (V_2/V_1) as a function of the distance d to a mirror. The drawing included in the plot shows the cross-section of the fibre bundle, where the single-mode transmitting fibre is in the centre and the two rings of receiving multimode fibres are arranged concentrically around it.

The signal response presents two regions of interest for distance sensing with a characteristic linear variation of the signal with distance. Those regions are at both sides of the peak signal and are designated as “front slope” and “back slope”, respectively. Figure 1b only shows the front slope, which exhibits clear advantages in terms of sensitivity, protection against noise and temperature fluctuations, in comparison to the back slope [31]. In practice, however, for distance security reasons typical TC values found in turbine rigs makes it necessary to operate in the back slope of the sensor, resulting in a lower signal sensitivity and higher dependency on the type of surface and on the temperature. Additionally, a post-processing of the raw signal is often necessary to get reliable results [27]. In the present work, we set out to operate in the front slope through the design of a new fibre bundle that guarantees a safe operation without compromising the physical integrity of the sensor head keeping it away from the blades. Indeed, in previous works, we used a fibre bundle with a measurement range for the front slope that clearly was too short (from 1 mm to 1.6 mm), and therefore required using the back slope to avoid placing the fibre bundle tip too close to the blades. The new bundle design (number of fibres, fibre type composition and geometrical fibre arrangement) takes into account all this, and, as a result, is able to shift the front slope to bigger probing distances (4–8 mm, see Figure 1b).

Regarding the achievable sensitivity in the front slope, differential gain of the photodetectors have been considered to increase it as much as possible provided that the gain configuration of the transimpedance amplifier of each photodetector does not compromise the minimum bandwidth required by the target application. In our particular case, for a turbine with 92 blades spinning at a maximum of 6000 revolutions per minute (rpm), even at the highest gain configuration the bandwidth available is enough to receive a signal with clearly identifiable individual blades. Figure 2 shows simulation results of four different gain configurations $G_1 - G_2$ of the photodetectors (G_1 for photodetector 1 (PD1) and G_2 for photodetector 2 (PD2), both given in dB units with respect to the reference gain value of 0.75×10^3 V/A) obtained by a custom designed program for bundle behaviour simulation. As can be clearly observed, the gain increase of the second photodetector with respect to the first one yields not only a higher ratio of V_2 to V_1 , but also a steeper calibration curve than in the case of the symmetric configuration ($G_1 = G_2$). Therefore, for maximum sensitivity, we have set the gain configuration to 10–40.

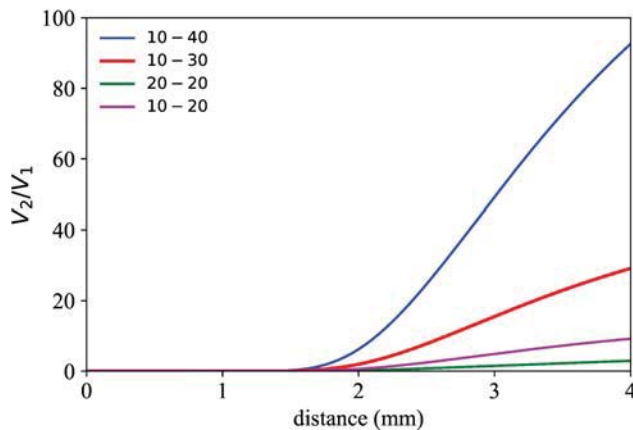


Figure 2. Simulated calibration curves of the fibre bundle in region I for different gain configurations ($G_1 - G_2$) of the two photodetectors.

2.2. Calibration Curve

Once the measurement system has been defined, the next step consists in calibrating the optical sensor using as target object a spare blade from the tested turbine rig. The schematic drawing of the side view of the experimental set-up is shown in Figure 3a.

It is important to point out that, in the laboratory calibration tests, the transmitting fibre did not face the flat platform of the blade—as would be desirable to maximize the amount of reflected light gathered back by the bundle—but the very narrow sealing lands of the blade (around 0.7 mm in width) to simulate the real turbine configuration that the sensor head met when installed in the turbine rig. Figure 3b shows a close-up picture of the sensor head during the calibration process. Please note that even perfectly facing the transmitting fibre to the narrow sealing lands yielded a very low reflected signal that required setting the optical power to maximum value, in this case 50 mW. Therefore, the setting of 50 mW laser power and 10–40 gain configuration of the photodetectors always resulted in light intensity levels at each of the photodetectors below the saturation value, and the created voltage values spanned over the full voltage scale (0–5 V), ensuring a good use of the 16-bit resolution of the A/D converter. The large working distance set by the front slope of the fibre bundle also contributed to the low coupling efficiency of reflected light into the fibre bundle. Both simulated and measured calibration curves are shown in Figure 3c.

It is worth mentioning the great similarity between both curves in the distance range from 2 to 4 mm with very small differences between them, and with a clear linear increase of the rate of the voltage quotient with distance. The best linear fit (shown in the inset of Figure 3c) to the experimental data has a Pearson's correlation of 0.997 in the distance range from 2.8 mm to 4 mm with a sensitivity slope of 61.73 mm^{-1} . Within this distance range of interest, Table 1 shows, for different values of V_2/V_1 ranging between 30 and 100, the difference between the experimentally measured distance value and the corresponding value obtained from the simulation. The result is given as a percentage of the corresponding experimental value. The discrepancy between experiment and simulation never exceeds 1.5% (at $V_2/V_1 = 34.1$). It is also interesting to draw attention to the shift to lower distance values occurring in the front slope when moving from an object with specular reflection (target presented in Figure 1) to another one with diffuse reflection (blade shown in Figure 3). This can be easily understood with simple geometric and ray tracing models [32].

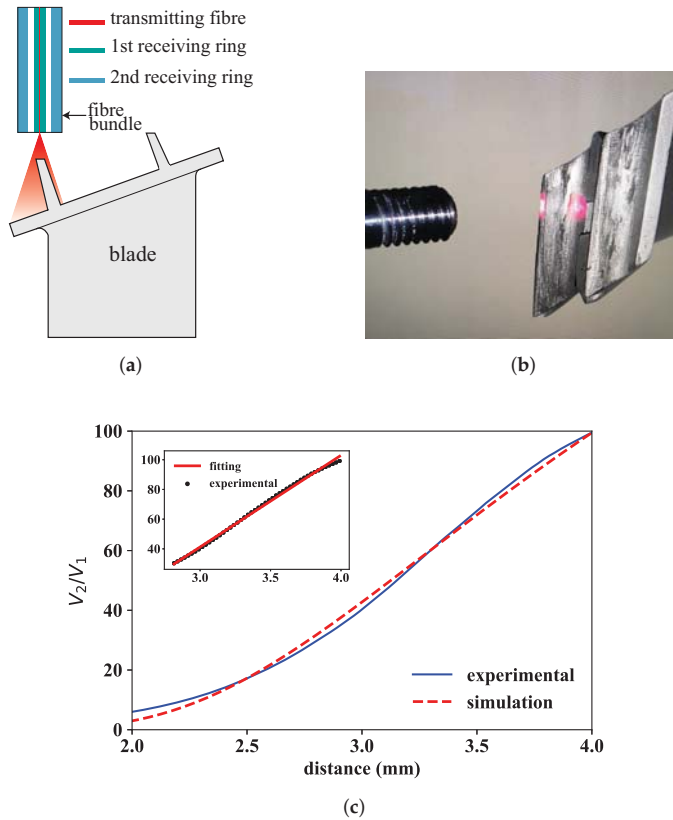


Figure 3. Laboratory calibration of a typical blade from the turbine rig: (a) schematic representation of the optical probe tip relative to the spare blade; (b) close-up picture of fibre bundle and blade; and (c) simulated and measured calibration curves. The inset shows the linear fit to the experimental data in the region of interest ($2.8 \text{ mm} < z < 4 \text{ mm}$).

Table 1. Comparison of measured and simulated data in the distance region of interest.

V_2/V_1	$d_{\text{sim}}, \text{ mm}$	$d_{\text{exp}}, \text{ mm}$	Difference, %
30.329	2.778	2.815	1.31
45.930	3.055	3.090	1.13
59.443	3.289	3.290	0.11
75.959	3.543	3.540	0.83
90.551	3.831	3.790	1.08
99.171	3.992	3.990	0.06

2.3. Experimental Program

The performance of the optical sensor was tested in the transonic wind tunnel at CTA. The rotating-turbine-test facility is a continuous transonic-flow-test bed with an atmospheric inlet/outlet. The level of pressure/vacuum, the temperature and the mass flow are individually regulated, so that the rig is operated to meet realistic Mach and Reynolds numbers allowing to transfer the results to real gas turbines.

The supply and exit air conditions in the test section are achieved by two centrifugal compressor and vacuum groups, which are, respectively, run by electrical motors of 3.7MW and 5.0MW. Two vacuum pumps are used to achieve altitude conditions of sub-atmospheric pressure down

to 12.5 kPa. A two-stage compressor group is used to control the pressure ratio and flow temperature and thus the Mach number of the flow within the circuit. The top mass flow rate achievable is 18 kg/s, with a maximum supply pressure up to 450 kPa, and a temperature regulation from atmospheric up to 450 K. Prior to entering the turbine, the air flows through a settling chamber that removes any swirl and axial velocity non-uniformity. The turbine power is transmitted by a single shaft (up to 7800 rpm) to a dynamometer. The test section has a section of 1 m. A schematic diagram of the facility is shown in Figure 4.

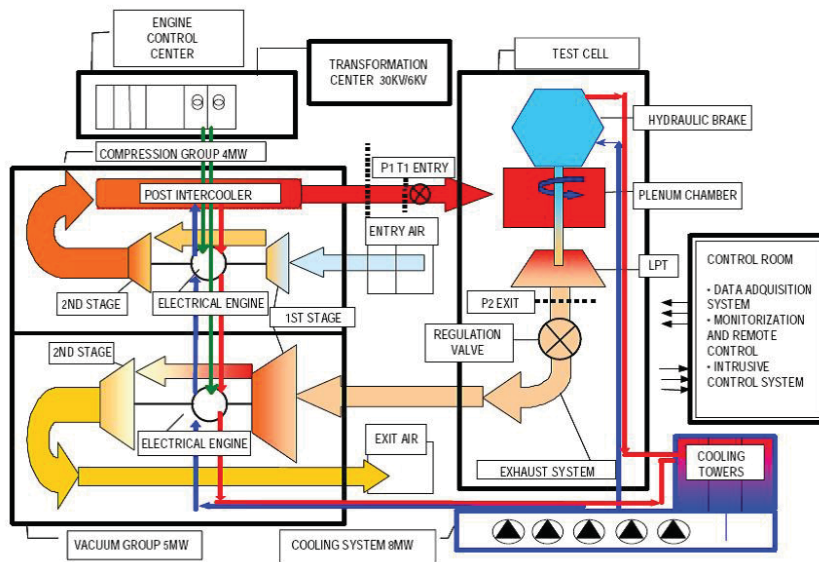


Figure 4. Schematic diagram of the rotating-turbine-test facility at CTA.

The rig corresponds to a single stage of a turbine rig with 92 blades. As already commented previously, the measurement requirements were really demanding because, for the extremely narrow sealing lands of the blades that defined the reflecting surface, the distance of about 3.2 mm from where the end of the probe was finally set, to the reflecting surface caused a low reflected signal level at the receiving rings to happen. An additional challenge that posed the coupling of the optical probe to the casing of the turbine was that the optical probe was not perfectly faced to the sealing lands when the turbine was at rest (0 rpm), so that the reflected signal was too low to get reliable calibration data that would allow building the calibration curve for the actual measurements. For that reason, the laboratory calibration curve was accepted as valid for the turbine rig measurements since it was carried out with a spare blade of the same turbine stage under test. As shown in the Results Section, the good news is that, at different workload conditions of the turbine rig, the optical probe was able to receive enough reflected signal for reliable tip clearance measurements. This improvement in the level of reflected signal was a consequence of the several vibrations that tend to suffer rotor blades causing them not only to deform but also to get a better alignment of the reflecting surface with respect to the optical probe.

Figure 5 shows a schematic representation of the final arrangement of the bundle embedded in the casing of the turbine. The optical probe was attached to a micrometer-driven adapter that was inserted in a radial hole of the casing and fixed to it with four screws. The micrometer allowed to set a certain distance—3.2 mm in this particular case—between the probe tip and the sealing lands of one of the blades to set the operation point at the middle of the linear region shown in Figure 3c. For this particular configuration, the optical probe tip resulted to be within the abradable layer. The abradable

is a soft protective wear material that is mounted on the casing wall aligned with the blades to create a good sealing, and avoid gas leakage and improve combustion efficiency. As TC values are commonly referenced to the abradable coating, below, we consider this case. Therefore, according to turbine design blueprints, the TC is obtained subtracting 2.74 mm to the actual sensor measurement (distance from probe tip to reflecting surface):

$$TC(\text{mm}) = \text{sensor measurement} (\text{mm}) - 2.74 \quad (1)$$

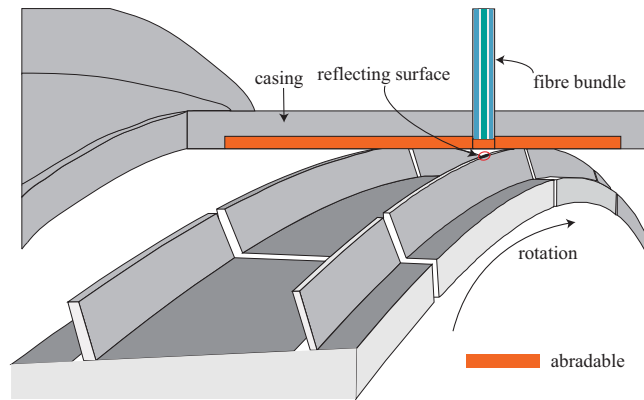


Figure 5. Schematic representation of the optical probe (not to scale) installed in the turbine rig at CTA.

Figure 6 shows a schematic illustration of the optical probe configuration within the casing. The optical signal of each of the two photodetectors is acquired with 16-bit resolution at a sampling rate of 2 MS/s, which results in a detailed map of all the blades with unambiguous identification of each of them, extending further the information provided by classical electromechanical systems that limit the TC information to the longest blade, and with a much lower data refresh frequency. The data acquisition and processing was done with a custom-made LabVIEW program that allows online and offline working modes. In online mode, the TC values of the different blades are monitored live at a configurable refresh rate, whereas, in offline mode, the data are stored in a hard disk for later processing. The latter mode is particularly interesting for long acquisition times where the amount of data created is huge and a thorough data analysis is required.

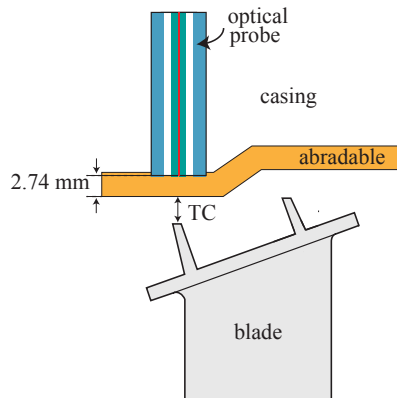


Figure 6. Optical probe placement within the casing.

3. Results and Discussion

All tests were carried out at CTA's facilities where different Working Points (WP) of the engine were repeated during several days. Each engine revolution was identified both with a blade of a particular reflection pattern and a stable non-vibrating Once per Revolution (OPR) signal obtained from the shaft. The raw data (V_2/V_1) from the optical sensor were converted to distance value using the linear calibration curve $f(V_2/V_1)$ obtained in the laboratory calibration tests (see Section 2.2). As an example, Figure 7 shows the sensor response of 13 blades after applying the calibration curve without any type of data post-processing. The first feature worth observing is the sharp minima that define the gap between consecutive blades.

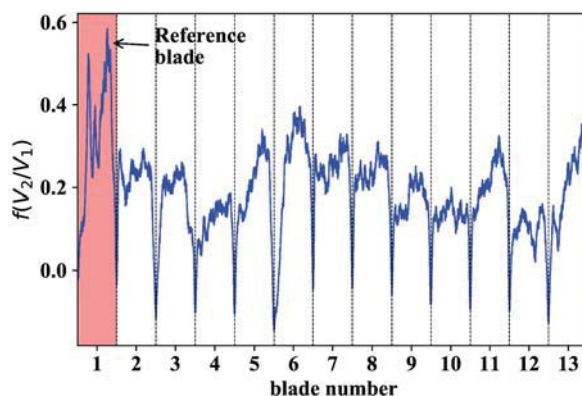


Figure 7. Typical signal response V_2/V_1 after applying the corresponding calibration curve. The blade highlighted in red refers to the blade with a higher reflection pattern. The dashed vertical lines correspond to local minima defining the limit between adjacent blades.

It is also worth mentioning that the signal pattern corresponding to each blade was highly reproducible over time, regardless of the operation point of the engine. The response curve of each of the 92 blades followed a certain pattern that might be classified according to one of the three types presented in Figure 8 (curves shown on the left-hand side of Figure 8). To give a consistent definition of the TC, for each blade, we started selecting a variable percentage (from 0% to 100%) of the corresponding dataset around the central data sample, and analyzed the evolution followed by the average value. The curves on the right-hand side of Figure 8 show the variability of the given TC definition for each of the three blade types. It comes out that, regardless of the type of response curve considered, the average value variation always was below a tenth of a millimetre. Therefore, it was decided to define the TC of each blade as the average value of the corresponding dataset at the 50% selection level around the central sample.

With the given definition of TC in mind, Figure 9 shows the TC map corresponding to a certain engine WP at 4258 rpm. It is worth noticing that the TC of every blade is different. Of particular importance are blades number 16, 38, 43, 51 and 69 as their TC values suggest that they are close to the abradable surface and they should be monitored to keep them under control. Regarding the stability of the test, the vertical error bars represent the variability of the TC values over time. Even in the worst case (blade number 85), the TC variability expressed as a single standard deviation value is approximately of 20 μm within the same WP, and the average value over the 92 blades is below 5 μm . All this suggests that we are dealing with stable TC experiments.

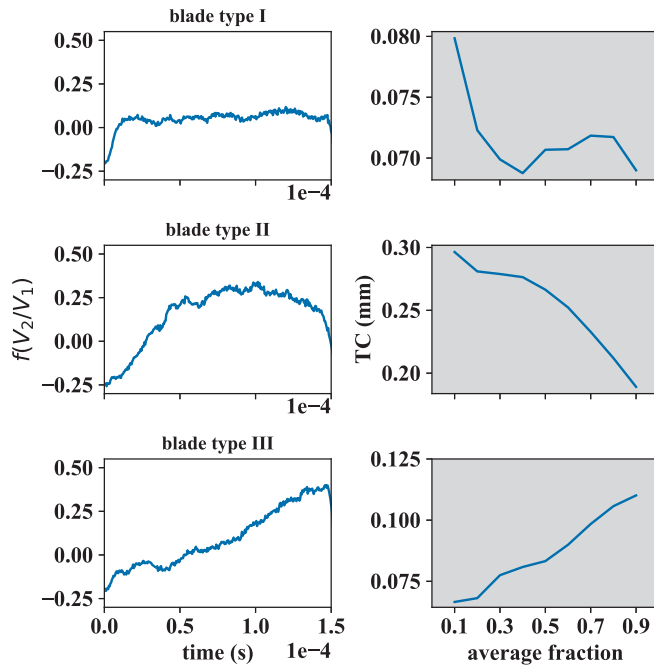


Figure 8. (Left) Types of blade signals found in the 92 blade turbine rig after applying the calibration curve; and (Right) evolution of TC definition with the selected fraction of blade data for each blade type.

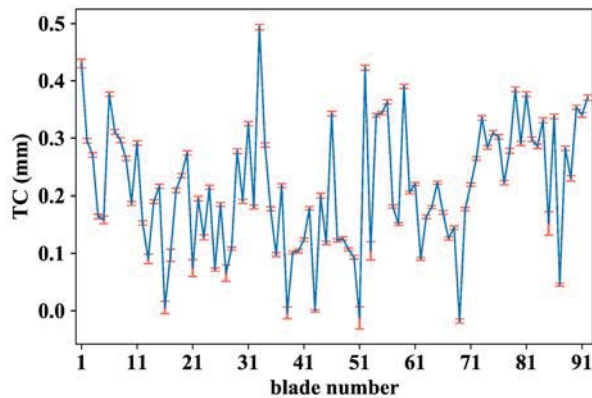


Figure 9. TC values of each blade at 4258 rpm with error bars that account for the TC standard deviation over 1100 revolutions.

The TC maps of all blades corresponding to three different WPs in ascending order of rpm are shown in the polar plot of Figure 10. Each TC map is represented as a curve of a particular color. On the other hand, each blade is expressed as a single point where the polar angle θ_i defines the blade number $i - \theta_i = 360^\circ / 92 * i$ for $i \in [1, 92]$ —and the corresponding TC value is given by the radial distance. Observe that TC values of individual blades decrease as engine rotational speed increases, a fact that can be attributed to the centrifugal and thermal loads acting on static and rotating components of the turbine. It is also interesting to point out that blades 43 and 51 still continue to be decisive in

determining the TC values of the turbine, in the same way as in the case of the WP at 4258 rpm shown in Figure 9. If we define the turbine TC as the minimum blade TC among all blades, as expected, the TC decreases from 0.002 mm to -0.005 mm when going from WP 1 (5466 rpm) to WP 3 (6005 rpm).

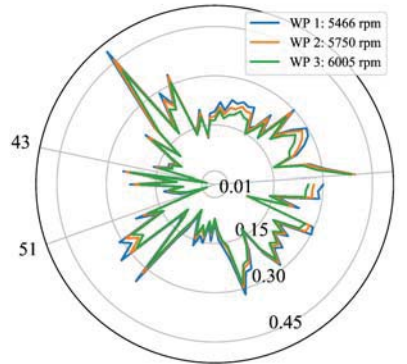


Figure 10. TC values of each of the 92 blades at three different WPs.

Another interesting point to consider is the analysis of the TC evolution when the turbine rpm ramp up before arriving at the first WP. Blue data points shown in Figure 11 are representative of this case. Contrary to what is expected for the general case in which the TC diminishes when rotor speed increases (as already shown in Figure 10), during the warming-up lapse of time, the clearance increases with rpm values. This might be explained on the basis that, when speed increases, the centrifugal load of the rotor as well as the rapid heating of the blades cause the rotating elements to grow outwards, but the case expands at a faster rate during this process.

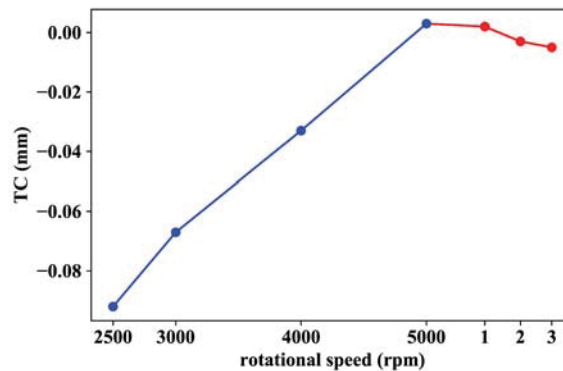


Figure 11. TC behaviour before (blue data points) and after (red data points) setting the first WP. The red data points refer to WPs 1, 2 and 3 shown in Figure 10: WP 1 \rightarrow 5466 rpm; WP 2 \rightarrow 5750 rpm; and WP 3 \rightarrow 6005 rpm.

This observation brings us to conclude that temperature ramping occurring in the wind tunnel before the first operation point is reached might be associated with the observed TC increase with rotational speed. In addition, the blade-case rubbing experienced during the whole warming-up process (negative TC values of blue data points in Figure 11) may be justified if we consider that the centrifugal load on the blades applies from the first moment before the casing starts to expand.

However, once the operation temperature has been reached and the casing has expanded to its equilibrium value (first red data point in Figure 11: WP 1 \rightarrow 5466 rpm), the clearance starts to decrease with rotational speed as expected.

4. Conclusions

A highly sensitive optical fibre bundle-based sensor prototype was designed and fabricated based on a custom simulation program developed within the research group. The manufactured optical sensor probe allowed measuring TC values in a turbine rig of an aircraft engine at the wind tunnel of the CTA. The optical measurements rely on collecting reflected light from each of the blades using two concentrically arranged rings of optical fibres and converting the gathered light intensities into voltage levels that are eventually divided with respect to each other to get rid of the disturbances (light intensity fluctuations, reflectivity variations, etc.) and retain a pure function of the distance from the fibre bundle tip to each blade. This curve has two characteristic working regions of interest with linear behaviour, the so-called front slope and back slope. The added value of the present work with respect to previous works resides in shifting the highly sensitive front slope curve to longer distance values to meet the distance security specifications set for the experimental program of the turbine, a fact that enables establishing the working point around the central part of this sharply sloped curve section instead of using the less sensitive back slope section of the response function. Additionally, the sensitivity has been further improved using differential gain of the two photodetectors associated to their corresponding receiving fibre rings. Altogether, the sensitivity of the optical sensor is 61.73 mm^{-1} , in contrast to the value of -0.0733 mm^{-1} published by other authors [33]. It is also worth mentioning that the optical sensor has proved to be capable of measuring the TC in very unfavourable conditions set by the specific blade and casing design that prevented the sensor from receiving an appreciable level of reflected signal. In such demanding scenario, the calibration curve used for the actual measurements was obtained in the laboratory using a spare blade of the turbine as it was impossible to get reliable calibration data from the turbine at rest. The results derived from the experimental program carried out on a turbine rig at CTA's facilities show a high resolution and highly sensitive measurement tool for inspection of individual blades that provides engineers with valuable information on turbine performance. The results of the optical fibre-based sensor presented in this paper opens up the possibility of widening its applicability to other fields of interest.

Author Contributions: G.D., J.A., J.B., and J.Z. conceived and designed the experiments; J.A. and I.G. developed the software to design the sensor probe; G.D. and J.Z. manufactured the fibre bundle; J.A., R.F., and E.A. performed the sensor calibration; J.A., R.F., G.D., and J.B. carried out the experiments; G.D., J.A., R.F., and J.B. analysed the data; G.D., J.A., and I.G. wrote the paper; and J.Z. supervised the whole project.

Funding: This work was funded in part by the Fondo Europeo de Desarrollo Regional (FEDER), in part by the Ministerio de Economía y Competitividad under project TEC2015-638263-C03-1-R, and in part by the Gobierno Vasco/Eusko Jaurlaritz IT933-16 and ELKARTEK (KK-2016/0030, KK-2017/00033, KK-2017/00089 and KK-2016/0059). The work of Josu Amorebieta is supported in part by a PhD fellowship from the Universidad del País Vasco/Euskal Herriko Unibertsitatea (UPV/EHU), Vicerrectorado de Euskera y Formación Continua.

Conflicts of Interest: The authors declare no conflict of interest.

References

1. Wiseman, M.W.; Guo, T.H. An investigation of life extending control techniques for gas turbine engines. In Proceedings of the 2001 American Control Conference. (Cat. No.01CH37148), Arlington, VA, USA, 25–27 June 2001; Volume 5, pp. 3706–3707. [[CrossRef](#)]
2. Kempe, A.; Schlamp, S.; Rösgen, T.; Haffner, K. Spatial and Temporal High-Resolution Optical Tip-Clearance Probe for Harsh Environments. In Proceedings of the 13th International Symposium on Applications of Laser Techniques to Fluid Mechanics, Lisbon, Portugal, 26–29 June 2006; Number 1155.
3. Guo, T.H. Active Turbine Tip Clearance Control Research. In Proceedings of the 5th NASA GRC Propulsion Control and Diagnostics (PCD) Workshop, Cleveland, OH, USA, 16–17 September 2015.

4. Lattime, S.B.; Steinetz, B.M.; Robbie, M.G. Test Rig for Evaluating Active Turbine Blade Tip Clearance Control Concepts. *J. Propul. Power* **2005**, *21*, 552–563. [[CrossRef](#)]
5. Lattime, S.B.; Steinetz, B.M. High-Pressure-Turbine Clearance Control Systems: Current Practices and Future Directions. *J. Propul. Power* **2004**, *20*, 302–311. [[CrossRef](#)]
6. Miller, K.; Key, N.; Fulayter, R. Tip Clearance Effects on the Final Stage of an HPC. In Proceedings of the 45th AIAA/ASME/SAE/ASEE Joint Propulsion Conference & Exhibit, Denver, CO, USA, 2–5 August 2009. [[CrossRef](#)]
7. Neuhaus, L.; Neise, W. Active Control to Improve the Aerodynamic Performance and Reduce the Tip Clearance Noise of Axial Turbomachines. In Proceedings of the 11th AIAA/CEAS Aeroacoustics Conference, Monterey, CA, USA, 23–25 May 2005. [[CrossRef](#)]
8. Geisheimer, J.; Holst, T. Metrology considerations for calibrating turbine tip clearance sensors. In Proceedings of the XIX Biannual Symposium on Measuring Techniques in Turbomachinery, Rhodes-St-Genève, Belgium, 7–8 April 2008.
9. Guo, H.; Duan, F.; Wu, G.; Zhang, J. Blade tip clearance measurement of the turbine engines based on a multi-mode fiber coupled laser ranging System. *Rev. Sci. Instrum.* **2014**, *85*, doi:10.1063/1.4901601. [[CrossRef](#)] [[PubMed](#)]
10. Geisheimer, J.; Holst, T. Novel sensors to enable close-loop active clearance control in gas turbine engines. In Proceedings of the SPIE Micro- and Nanotechnology Sensors, Systems, and Applications VI, Baltimore, MD, USA, 5–9 May 2014; Volume 9083, Number 908310. [[CrossRef](#)]
11. Sheard, A. Blade by Blade Tip Clearance Measurement. *Int. J. Rotating Mach.* **2011**, *2011*. [[CrossRef](#)]
12. Haase, W.C.; Haase, Z.S. High-Speed, capacitance-based tip clearance sensing. In Proceedings of the 2013 IEEE Aerospace Conference, Big Sky, MT, USA, 2–9 March 2013; pp. 1–8. [[CrossRef](#)]
13. Ye, D.C.; Duan, F.J.; Guo, H.T.; Li, Y.; Wang, K. Turbine blade tip clearance measurement using a skewed dual-beam fiber optic sensor. *Opt. Eng.* **2012**, *51*, 081514, doi:10.1117/1.OE.51.8.081514. [[CrossRef](#)]
14. Sheard, A.; O'Donnell, S.; Stringfellow, J. High Temperature Proximity Measurement in Aero and Industrial Turbomachinery. *J. Eng. Gas Turbines Power* **1999**, *121*, 167–173. [[CrossRef](#)]
15. Roeseler, C.; von Flotow, A.; Tappert, P. Monitoring blade passage in turbomachinery through the engine case (no holes). In Proceedings of the IEEE Aerospace Conference, Big Sky, MT, USA, 9–16 March 2002; Volume 6, pp. 3125–3129. [[CrossRef](#)]
16. Chivers, J.W.H. Microwave Interferometer. U.S. Patent 4,359,683, 16 November 1982.
17. Woolcock, S.C.; Brown, E.G. Checking the Location of Moving Parts in a Machine. U.S. Patent 4,346,383, 24 August 1982.
18. Davidson, D.P.; DeRose, R.D.; Wennerstrom, A.J. The Measurement of Turbomachinery Stator-to-Drum Running Clearances. In *Volume 1: Turbomachinery, Proceedings of the ASME 1983 International Gas Turbine Conference and Exhibit, Phoenix, AZ, USA, 27–31 March 1983*; ASME: New York, NY, USA, 1983; p. V001T01A054. [[CrossRef](#)]
19. López-Higuera, J.M. (Ed.) *Handbook of Optical Fibre Sensing Technology*; Wiley: Hoboken, NJ, USA, 2002.
20. García, I.; Zubia, J.; Durana, G.; Aldabaldetrekú, G.; Illarramendi, M.A.; Villatoro, J. Optical Fiber Sensors for Aircraft Structural Health Monitoring. *Sensors* **2015**, *15*, 15494–15519. [[CrossRef](#)] [[PubMed](#)]
21. Zhang, X.; Yang, L. Research on displacement sensor of two-circle reflective coaxial fiber bundle. In Proceedings of the 2008 IEEE/ASME International Conference on Advanced Intelligent Mechatronics, Xi'an, China, 2–5 July 2008; pp. 211–216. [[CrossRef](#)]
22. Kempe, A.; Schlamp, S.; Rösgen, T.; Haffner, K. Low-coherence interferometric tip-clearance probe. *Opt. Lett.* **2003**, *28*, 1323–1325. [[CrossRef](#)] [[PubMed](#)]
23. Barranger, J.P.; Ford, M.J. Laser-Optical Blade Tip Clearance Measurement System. *J. Eng. Power* **1981**, *103*, 457–460. [[CrossRef](#)]
24. Matsuda, Y.; Tagashira, T. Optical Blade-Tip Clearance Sensor for Non-Metal Gas Turbine Blade. *J. Gas Turbine Soc. Jpn.* **2001**, *29*, 479–484.
25. Dhadwal, H.S.; Kurkov, A.P. Dual-Laser Probe Measurement of Blade-Tip Clearance. *J. Turbomach.* **1999**, *121*, 481–485. [[CrossRef](#)]
26. Pfister, T.; Büttner, L.; Czarske, J.; Krain, H.; Schodl, R. Turbo machine tip clearance and vibration measurements using a fibre optic laser Doppler position Sensor. *Meas. Sci. Technol.* **2006**, *17*, 1693–1705. [[CrossRef](#)]

27. García, I.; Beloki, J.; Zubia, J.; Aldabaldetrek, G.; Illarramendi, M.A.; Jiménez, F. An Optical Fiber Bundle Sensor for Tip Clearance and Tip Timing Measurements in a Turbine Rig. *Sensors* **2013**, *13*, 7385–7398. [[CrossRef](#)] [[PubMed](#)]
28. García, I.; Zubia, J.; Berganza, A.; Beloki, J.; Arrue, J.; Illarramendi, M.A.; Mateo, J.; Vázquez, C. Different Configurations of a Reflective Intensity-Modulated Optical Sensor to Avoid Modal Noise in Tip-Clearance Measurements. *J. Lightwave Technol.* **2015**, *33*, 2663–2669. [[CrossRef](#)]
29. Cao, S.Z.; Duan, F.J.; Zhang, Y.G. Measurement of Rotating Blade Tip Clearance with Fibre-Optic Probe. *J. Phys. Conf. Ser.* **2006**, *48*, 873, doi:10.1088/1742-6596/48/1/165. [[CrossRef](#)]
30. Yu-zhen, M.; Yong-kui, Z.; Guo-ping, L.; Hua-guan, L. Tip clearance optical measurement for rotating blades. In Proceedings of the MSIE, Harbin, China, 8–11 January 2011; pp. 1206–1208. [[CrossRef](#)]
31. García, I.; Przysowa, R.; Amorebieta, J.; Zubia, J. Tip-Clearance Measurement in the First Stage of the Compressor of an Aircraft Engine. *Sensors* **2016**, *16*, 1897, doi:10.3390/s16111897. [[CrossRef](#)] [[PubMed](#)]
32. Shimamoto, A.; Tanaka, K. Geometrical analysis of an optical fiber bundle displacement sensor. *Appl. Opt.* **1996**, *35*, 6767–6774. [[CrossRef](#)] [[PubMed](#)]
33. Binghui, J.; Lei, H. An Optical Fiber Measurement System for Blade Tip Clearance Engine. *Int. J. Aerosp. Eng.* **2017**, *2017*, 4168150, doi:10.1155/2017/4168150. [[CrossRef](#)]



© 2018 by the authors. Licensee MDPI, Basel, Switzerland. This article is an open access article distributed under the terms and conditions of the Creative Commons Attribution (CC BY) license (<http://creativecommons.org/licenses/by/4.0/>).

Article 2

Title:

Packaged multi-core interferometer for high temperature sensing

D.O.I.:

10.1109/JLT.2019.2903595

Authors:

Amorebieta, J.; Durana, G.; Ortega-Gomez, A.; Fernández, R.; Velasco, J.; Sáez de Ocáriz, I.; Zubia, J.; Antonio-López, E.; Schülzgen, A.; Amezcua-Correa, R.; Villatoro, J.

Journal and publication information:

Journal of Lightwave Technology, 37 (10), 2328-2334 (2019)

Cited 12 times

Indicators of the Journal in 2019:

Impact factor: 4.288

Q1 in Optics (14/97)

Packaged Multi-Core Fiber Interferometer for High-Temperature Sensing

Josu Amorebieta ¹, Gaizka Durana ¹, Angel Ortega-Gomez ¹, Rubén Fernández, Javier Velasco, Idurre Sáez de Ocariz, Joseba Zubia ¹, Jose Enrique Antonio-López, Axel Schülzgen ², *Fellow, OSA*, Rodrigo Amezcua-Correa, and Joel Villatoro

Abstract—A small size and compactly packaged optical sensor for high-temperature measurements is reported. The sensor consists of a short piece of multi-core fiber (MCF) spliced to the distal end of a single-mode fiber. The packaging consists of an inner ceramic shield that prevents bending, curvature, and vibration effects on the MCF, and an outer metallic shield that protects the device against impacts. The interaction between specific supermodes excited in the MCF creates an interference pattern that shifts linearly with the temperature. The sensor was calibrated in the range from 200 to 1000 °C and a K-type thermocouple was used as a reference. The average temperature sensitivity was found to be 24.8 pm/°C with a response time of 15 s. Our results indicate that our MCF interferometric thermometer is as accurate as an electronic one with the advantage that it is passive. Therefore, we believe that the proposed sensor is suitable for industrial applications.

Index Terms—High temperature measurement, mode interferometers, multi-core fibers, optical sensors, optical thermometers, supermodes.

I. INTRODUCTION

IN THE industrial sector, there are several environments and applications where high temperature is present. For example, in engine tests, metallurgical processes, in gas and oil facilities, etc. In such harsh environments, temperature can reach very

high values (up to 1000 °C, and even higher). Thus, accurate measurement of temperature is crucial.

Currently, the technology commonly accepted and well established for high temperature measurement is based on thermocouples [1]–[5]. However, due to their electronic nature, thermocouples may not be a viable solution for applications or environments where electromagnetic or microwave radiation is present. In such cases, optical fiber thermometers are a good alternative since they are totally passive.

Optical fibers exhibit an intrinsic sensitivity to temperature, which makes them ideal for temperature sensing. In fact, throughout the years, many different optical fiber temperature sensors have been demonstrated [6]–[10]. Most optical fiber thermometers operate in a limited temperature range. However, the use of specialty optical fibers and innovative approaches and techniques have allowed expanding the temperature range up to 1000 °C. Thus, optical fiber thermometers may reach the performance and capabilities of thermocouples and be a real alternative for high temperature sensing, hence for industrial applications.

The most common approach for high temperature sensing consists of using regenerated fiber Bragg gratings (rFBGs), also called chemical composition gratings [11]–[14]. The operating principle of such sensors is based on the thermo-optic effect that modifies the period of the grating. rFBG-based sensors have temperature sensitivity of around 10 pm/°C, and their response time is of several seconds [15]–[18]. The disadvantage of rFBGs sensors is their high cost, as their fabrication and interrogation require expensive setups, lasers, and picometer-resolution detectors.

Fabry-Perot interferometry has been widely studied for high temperature sensing as well. In this technique, the sensitive element is a cavity that can be fabricated from temperature-resistant materials such as pure glass or sapphire [19]–[24]. The advantages of the Fabry-Perot interferometers (FPI) include high sensitivity and small size. However, their performance is directly linked to the uniformity of the cavity, which is not easy to achieve.

Other alternatives for high temperature sensing are based on long period gratings (LPGs) [25]–[27] and different types of interferometers [28]–[31]. The drawback of LPGs is their sensitivity to the surrounding medium, which imposes proper isolation to measure temperature only. On the other hand, most interferometers provide relative temperature measurements, as they are

Manuscript received November 20, 2018; revised January 16, 2019 and February 20, 2019; accepted February 27, 2019. Date of publication March 7, 2019; date of current version April 17, 2019. This work was supported in part by the Fondo Europeo de Desarrollo Regional, in part by the Ministerio de Economía y Competitividad under Project TEC2015-638263-C03-1-R, and in part by the Gobierno Vasco/Eusko Jaurlaritza IT933-16 and ELKARTEK (KK/00033, KK-2017/00089, and KK-2018/00078). The work of J. Amorebieta was supported in part by a Ph.D. fellowship from the University of the Basque Country UPV/EHU, Vicerrectorado de Euskera y Formación Continua. (Corresponding author: Josu Amorebieta.)

J. Amorebieta, G. Durana, A. Ortega-Gomez, R. Fernández, and J. Zubia are with the Department of Communications Engineering, University of the Basque Country, E-48013 Bilbao, Spain (e-mail: josu.amorebieta@ehu.eus; gaizka.durana@ehu.eus; angel.ortega@ehu.eus; ruben.fernandez@ehu.eus; joseba.zubia@ehu.eus).

J. Velasco and I. Sáez de Ocariz are with the Science and Technology Department, Fundación Centro de Tecnologías Aeronáuticas, E-01510 Miñano Mayor, Spain (e-mail: javier.velasco@ctaero.com; idurre.saezdeocariz@ctaero.com).

J. E. Antonio-López, A. Schülzgen, and R. Amezcua-Correa are with the CREOL, The College of Optics and Photonics, University of Central Florida, Orlando, FL 32816 USA (e-mail: jealopez@creol.ucf.edu; axel@creol.ucf.edu; r.amezcua@creol.ucf.edu).

J. Villatoro is with the Department of Communications Engineering, University of the Basque Country, E-48013 Bilbao, Spain, and also with the IKERBASQUE-Basque Foundation for Science, E-48013 Bilbao, Spain (e-mail: agustinjoel.villatoro@ehu.eus).

Color versions of one or more of the figures in this paper are available online at <http://ieeexplore.ieee.org>.

Digital Object Identifier 10.1109/JLT.2019.2903595

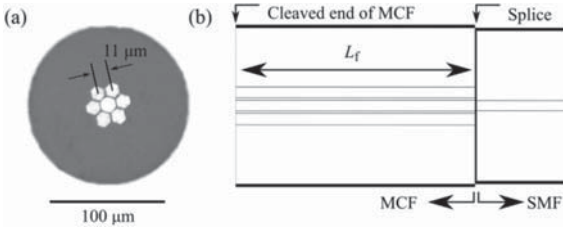


Fig. 1. (a) Picture of the cross-section of the MCF used to build the temperature sensor. (b) Schematic representation of the sensor architecture. L_f is the length of the MCF. The cleaved end reflects less than the 4% of the emitted light.

codified in the shift of interference patterns. As a result, LPG- and interferometer- based high temperature sensors have not reached the market yet.

As an alternative to the existing optical fiber thermometers for high temperature, in this work, we propose a sensor that may overcome the main limitations and drawbacks mentioned above. Our device consists of a short segment of MCF spliced to the distal end of a typical SMF. The fabrication of our device is easy, reproducible, and inexpensive. The temperature sensitive region of our device is the segment of MCF that can withstand high temperatures (up to 1000 °C) as demonstrated in [32]–[34]. In our case, the sensor operates in reflection mode. In addition, we have packaged our device with a double shielding (ceramic and metallic). The packaging eliminates the effects of strain, bending, curvature, or vibrations on the MCF interferometer as it is sensitive to such parameters [35]–[38].

The reflection spectrum of our device is sinusoidal and shifts when temperature changes. The interference pattern of our MCF sensor is easily traceable, thus, it is easy to establish a relationship between the absolute maximum of the interference pattern and temperature. With our packaged MCF sensor, temperatures up to 1000 °C, response times at different temperature gradients and its robustness against vibrations were measured. For comparison, similar experiments were also carried out with a bare MCF interferometer. The results suggest that the proposed packaging does not compromise the temperature sensitivity of our device. In addition, our packaged sensor is as accurate as a K-type thermocouple, which is widely used and accepted as reference in the industry.

II. OPERATION PRINCIPLE, DESIGN AND FABRICATION

In the device reported here, the MCF is the key element. The MCF, fabricated at the University of Central Florida (Orlando, USA), has a particular structure based on seven identical hexagonal cores. Six of them are concentrically arranged in a ring-like shape around a central one. The mean diameter and distance among adjacent axes is 9.2 μm and 11 μm , respectively, see Fig. 1(a). All the cores are made of germanium doped silica glass and are inlaid in pure silica cladding. The numerical aperture (NA) of each core is 0.14 at 1550 nm that is the same NA of a typical SMF. The outer diameter of the fiber is 130 μm .

A scheme of the MCF interferometer is shown in Fig. 1(b). The device consists of a short MCF segment fusion spliced to a

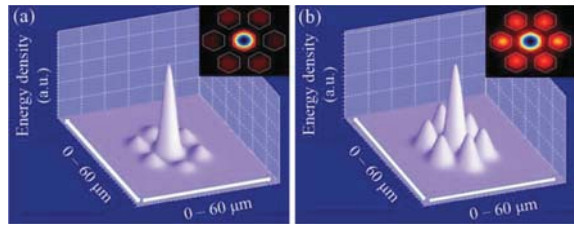


Fig. 2. Simulations of the 3D and 2D profiles of the two supermodes excited in the MCF. In (a) the supermode SP_{01} is shown, and in (b) the supermode SP_{02} . The inset 2D profiles have an area of $60 \times 60 \mu\text{m}^2$.

conventional SMF. A fiber fusion splicer (Fujikura 100 P+) was used to fabricate the device. Such a machine aligns precisely the single core of the SMF with the central core of the MCF. Due to that, the insertion loss of supermode interferometers is minimal (typically 0.1 dB or below) as reported in [35].

The MCF described above is called strongly-coupled multi-core fiber, which means its cores are close enough to each other to allow interaction among them. The modes supported by such an MCF are called supermodes [39], [40], which are the linear combination of individual LP modes of each core of the MCF. In our device, schematically shown in Fig. 1(b), the excitation of the MCF is with the LP_{01} (fundamental) mode of the SMF. This, combined with the axial symmetry of the SMF-MCF structure, causes only two specific supermodes to be excited in the MCF. The profiles of such supermodes are shown in Fig. 2.

The effective refractive index of each supermode is different, thus, a phase difference between them can be expected as they propagate through the length of the MCF (L_f). The phase difference ($\Delta\varphi$) will be $\Delta\varphi = 4\pi\Delta nL_f/\lambda$, where $\Delta n = n_2 - n_1$, with n_1 and n_2 being the indices of the supermodes SP_{01} and SP_{02} , respectively, and λ the wavelength of the light source. According to our simulations, the value of Δn was 7.8×10^{-4} at $\lambda = 1545$ nm. The phase difference will cause a coupling between both supermodes, which will generate a sequence of maximum and minimum values in the reflection spectrum of our MCF interferometer. When the reflection reaches a maximum value to a given wavelength, the interference is constructive, which means that the two supermodes are in phase and, therefore, their coupled power is maximum for that wavelength. The maximum values appear when the phase difference equals an integer multiple of 2π ($m2\pi$, where $m = 1, 2, 3, \dots$). Thus, by considering that the reflected light travels twice the length of the MCF ($2L_f$), the maxima are located at the following wavelengths:

$$\lambda_m = 2L_f\Delta n/m. \quad (1)$$

In general, in an optical fiber, the thermo-optic effect prevails over the thermal expansion effect. Thus, for temperature measurements, only the changes in the refractive index of the fiber core (or cores) are considered [28], [32]. In our case, such changes induce a variation in the effective indices of the interfering supermodes, and hence, a shift in the interference pattern. Therefore, by monitoring λ_m , the temperature around the MCF can be known. It is important to point out that with our MCF

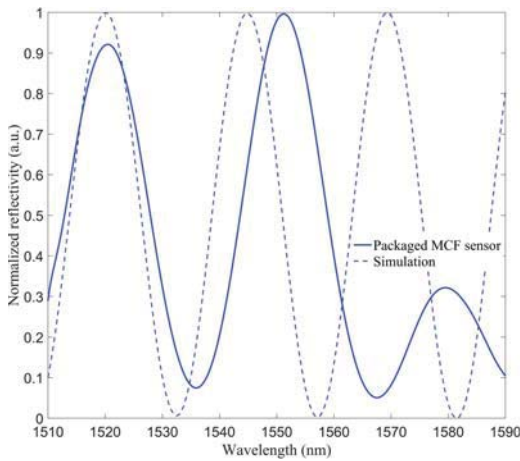


Fig. 3. Interference pattern obtained by simulation for a 2.54 cm-long MCF interferometer (dashed line) and with the fabricated device (solid line).

interferometer the measurement of temperature is absolute, as it will be codified in wavelength.

In order to measure the widest temperature range possible, the length of the MCF segment is crucial. On the one hand, the displacement of λ_m , which shifts around 30 pm/°C without any packaging [32], must not overlap with the maximum located at λ_{m+1} or λ_{m-1} . On the other hand, λ_m must be within the wavelength range of the sensor interrogator, which in our case was between 1510 and 1595 nm, at any temperature of the measuring range. Thus, to achieve the aforementioned requirements, two different simulation programs (Matlab MathWorks and Photon-Design) were used in which Eq. (1) was implemented with the parameters of the MCF and the desired initial position of λ_m established to obtain the MCF length. It was calculated to be 2.545 cm. However, due to the difficulty for obtaining an MCF segment of that precision with a conventional cleaver, we fabricated a device with $L_f = 2.54$ cm with an error of approximately 200 μm .

Fig. 3 shows the spectra of the designed and fabricated interferometers at room temperature. For the calculated MCF length, the difference between the maxima and minima (visibility) is of 0.9. The difference between the simulated and observed pattern is due to the impossibility of reproducing the ideal conditions of the simulation in real-life conditions, such as the fact that the simulation programs use a flat spectrum light source whereas the manufactured sensor uses a Gaussian-like emission light source. It can be noted that the peak at which simulated and manufactured sensor's patterns match is located at 1520 nm. As temperature increases, such a peak is expected to shift to longer wavelengths [32]. Hence, the peak located at 1520 nm (λ_m) was selected to be monitored and correlated with temperature.

In order to make the MCF interferometer sensitive exclusively to temperature, it was packaged as follows: The bare SMF-MCF structure, whose total length was approximately 15 cm, was protected with a double shielding. The first layer was a double bore thin ceramic tube (Omega Engineering TRX-005132-6). Each

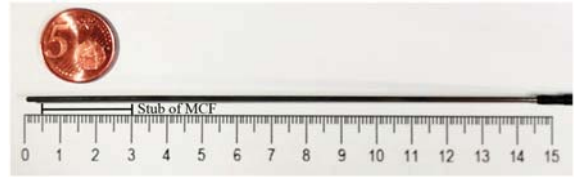


Fig. 4. Picture of the manufactured MCF sensor after being exposed to 1000 °C. Notice that the metallic tube has a blackening gradient that indicates the different temperatures on the tube. The position and length (2.54 cm) of the MCF segment are indicated. The gap between the tip of the metallic tube and the stub of MCF is long enough to avoid a Fabry-Perot cavity.

bore had a diameter of 127 $\mu\text{m} \pm 5\%$. In this manner, the MCF and part of the SMF were kept straight. Thus, bending effects on the interference pattern of the MCF were eliminated. The second layer was a stainless steel tube (Omega Engineering SS-116-6CLOSED) that covered the ceramic layer and provided physical protection against possible impact or shocks. A photograph of the final sensor prototype is shown in Fig. 4. As it can be noticed, the sensitive part of the sensor is only 2.54 cm long and located at the edge of the shielding. Thus, the sensor could be just about 3 cm long. The reason for the extra 12 cm is to protect the SMF due to the configuration of the furnace. The latter had a circular hole (slightly bigger than the sensor in diameter) that only in the deepest part reached temperatures of 1000 °C. This causes that the packaged sensor has to be vertically inserted completely. As it can be seen in the blackening gradient in Fig. 4, the area where the MCF is located is the area that has been exposed to the highest temperatures.

The interrogation of our MCF interferometer consisted of a broadband light source centered at 1550 nm, with Gaussian-like emission, a 50:50 coupler and a small spectrum analyser (I-MON512-USB, Ibsen Photonics). The data processing was made with an *ad hoc* program developed in Matlab MathWorks. The data processing approach was as follows: Raw spectra provided by the spectrum analyser were collected at different temperatures; then, the spectra were averaged and normalized. After that, a Savitzky-Golay filter was applied to every spectra in order to smooth them. Finally, the highest peak (λ_m), or absolute maximum of the interference pattern, was found. The wavelength at which the maximum was located was correlated with temperature, which was measured with a K-type thermocouple used for temperature calibration measurements (Herten, K-type, SN TCP187).

III. RESULTS AND DISCUSSION

The tests were performed at the Aeronautical Technologies Centre (CTA) facilities located in the Alava Technology Park (Spain). The heating/cooling processes were carried out with a programmable high temperature furnace (Isotech Pegasus Plus 1200). Before running the calibration measurements, a curing process was carried out to eliminate as much as possible the hysteresis effect of the sensor [28]. The calibration was performed repeatedly in the range from 200 to 1000 °C, in steps of 50 °C that lasted 70 minutes each. Thus, overall, each calibration lasted 100 hours approximately. The sampling rate was 1 Hz.

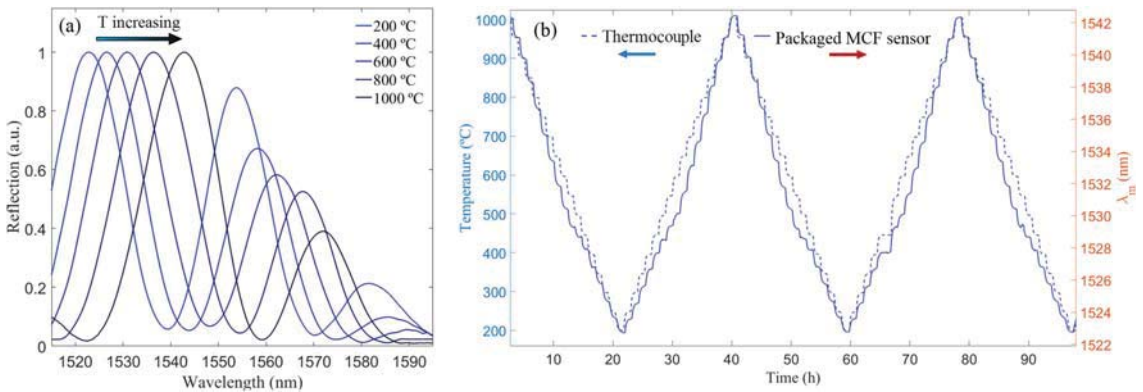


Fig. 5. (a) Spectra observed in the 200-1000 °C temperature range. (b) Time evolution of our packaged MCF sensor compared to that of the thermocouple. Colored arrows indicate the corresponding vertical axe of each curve.

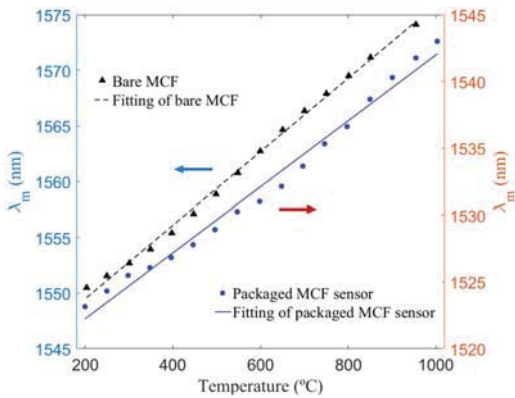


Fig. 6. Calibration curve of the packaged MCF sensor (solid dots, solid line) and 2.54 cm of bare MCF (triangles, dashed line). Colored arrows indicate the corresponding axe of each curve.

Fig. 5(a) shows the reflection spectra of our packaged MCF interferometer at different temperatures. It can be seen that the shift for the thermal range under study was around 20 nm. The position of the maximum peak as a function of time is shown in Fig. 5(b). For comparison, the time evolution of the temperature measurement provided by the thermocouple is also shown. From the monitored λ_m and temperature data, the calibration curve of the packaged MCF sensor was obtained, which is shown in Fig. 6. In order to evaluate the effect of the shielding on the temperature sensitivity of the packaged MCF sensor, the calibration curve obtained from a 2.54 cm-long bare MCF device that was subjected to an identical calibration process as the packaged MCF sensor is also shown in Fig. 6.

For the packaged MCF sensor, the Pearson squared correlation coefficient was found to be $R^2 = 0.9856$ and the uncertainty of $\sigma^2 = 0.611 \text{ nm}^2$ [41]. The correlation between temperature (in °C) and λ_m (in nm) that was obtained from the experiments was:

$$T = 39.929\lambda_m - 60525. \quad (2)$$

This indicates that the temperature sensitivity of the packaged MCF sensor was 24.8 pm/°C. From the calibration curve of the 2.54 cm-long bare MCF sensor shown in Fig. 6, we obtained a temperature sensitivity of 31.47 pm/°C. The latter agrees with that (29 pm/°C) of the MCF thermometer reported in [32] in the range between 100°C and 300°C, which was fabricated with bare MCF as well. Therefore, the packaging proposed here does not compromise the temperature sensitivity of the device. As a matter of fact, the main purpose of protecting the SMF and the MCF with a close-fitting ceramic tube was to keep the fibers tightly in the axial direction so that the measurements were strictly related to temperature and not affected by undesired effects of bending or vibrations, something that cannot be achieved when unprotected MCF is used. This may be the cause of the performance differences between the packaged MCF sensor and the bare MCF shown in Fig. 6 and the one reported in [32] where non-linear response to temperature was observed.

The response and recovery times of our packaged MCF temperature sensor and those of the device built with bare MCF were also evaluated as these are important parameters to be considered. The rising and falling times were measured several times at different temperature gradients. The measurements were carried out for 2 different thermal loops: from 25 °C to 550 °C, and back to 25 °C, and from 25 °C to 900 °C, and back to 25 °C. In each case, the response time of both optical devices and that of the K-type thermocouple were recorded. The response time ($\tau_{63\%}$), or time constant, is defined as the time required to reach 63.2% of an instantaneous change in temperature [42].

The results for the 25 °C–550 °C–25 °C loop are shown in Fig. 7. The results shown in Fig. 7 indicate that the shift of λ_m of the bare MCF device was more than expected according to the sensitivity obtained from its calibration curve shown in Fig. 6. This means that the shift of λ_m may not be strictly due to temperature as the MCF segment was also exposed to bending and/or vibrations induced by the furnace. The tracked peak of the packaged MCF sensor shifts 10.1 nm and shows a smoother and less noisy curve compared to that of the bare MCF. This shift agrees with the combination of the sensitivity of the sensor in

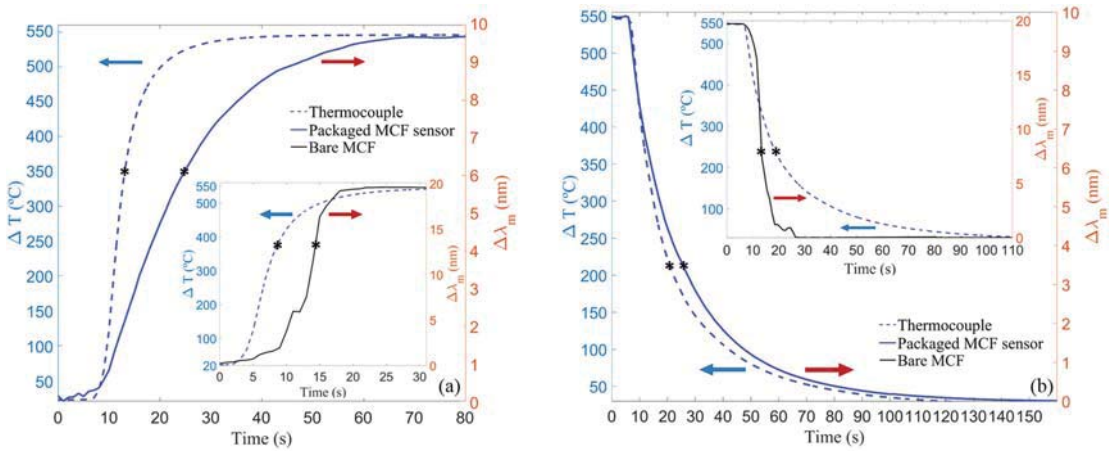


Fig. 7. Response times for (a) heating from 25 °C to 550 °C and for (b) cooling from 550 °C to 25 °C of a packaged and bare MCF sensors. For comparison, the response and recovering times of a commercial thermocouple are shown. Notice the non-uniform shape of the curves of the bare MCF compared to that of the packaged MCF. Colored arrows indicate the corresponding vertical axis of each curve. The black asterisk (*) in each curve represents the $\tau_{63\%}$ of each sensor.

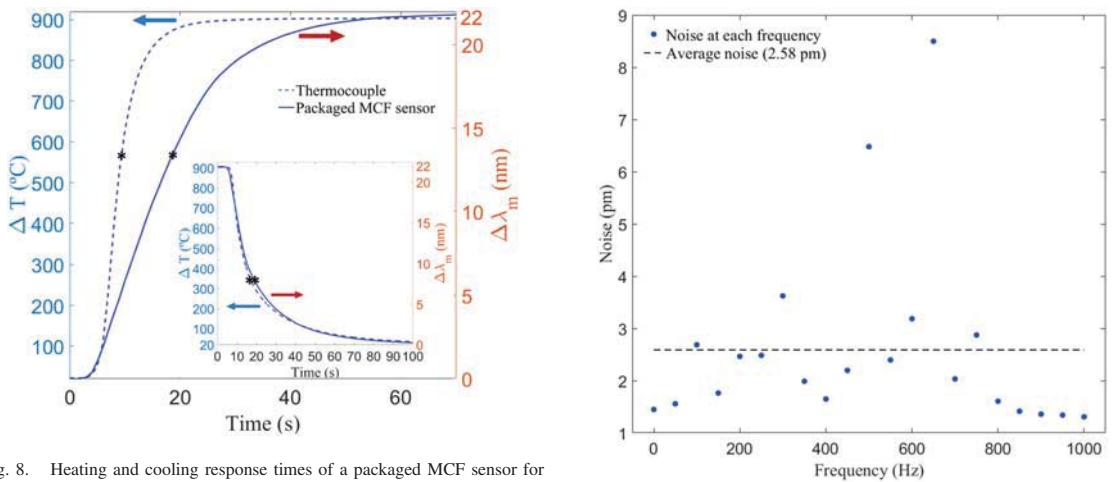


Fig. 8. Heating and cooling response times of a packaged MCF sensor for the 25 °C-900 °C-25 °C loop. Colored arrows indicate the corresponding axis of each curve. The black asterisk (*) in each curve represents the $\tau_{63\%}$ of each sensor.

TABLE I
RESPONSE TIMES (IN S) OF THE PACKAGED MCF SENSOR AND THE THERMOCOUPLE

Temperature gradient (°C)	25 - 550	550 - 25	25 - 900	900 - 25
Thermocouple	6	14	6	12
MCF sensor	17	20	15	14

the 200 °C–1000 °C calibrated range and the lower temperature sensitivity of the MCF below 100 °C as reported in [32].

For the results of the 25 °C-900 °C-25 °C loop shown in Fig. 8 only the curves of the packaged MCF sensor and the thermocouple are presented, since only the performance of these devices can be compared as their results are strictly related to temperature.

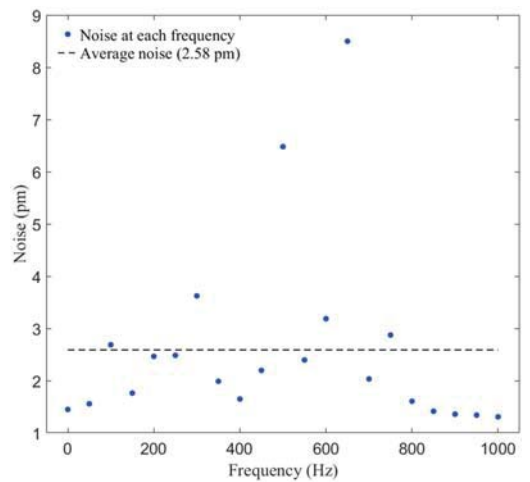


Fig. 9. Results of the effect of the vibrations in the measurements of λ_m at room temperature (25 °C). The biggest deviation (8.49 pm) happened at 650 Hz, where a resonance due to the 10 cm cantilever configuration took place.

The results shown in Fig. 7 and Fig. 8 are summarised in Table I. It can be noted that in all the cases, our packaged MCF temperature sensor responded slower than the thermocouple used as a reference. The results regarding the bare MCF are not shown in the table due to the fact that they are not related only to temperature, and therefore, not suitable for comparison.

In order to evaluate the effectiveness of the packaging in terms of protection against vibrations, the packaged MCF sensor was placed in a cantilever configuration and attached to a piezoelectric actuator (STr-35, Piezomechanik GmbH) whose maximum vibration amplitude was 6 μm . The length of the cantilever was 10 cm. The sensor was then subjected to vibrations at different frequencies. In all the cases, the voltage applied to the actuator

was the same (10 Vpp), and the measurements were carried out at room temperature (25 °C). The sensor was interrogated with the spectrum analyser mentioned above (I-MON512-USB, Ibsen Photonics) and the data processing approach was as follows: in two consecutive days 17000 raw spectra for each frequency were acquired and then, the maximum of each spectra (λ_m) was identified. These values were averaged for each point along with their standard deviation.

In Fig. 9, it can be seen that vibrations introduce an average noise of 2.58 pm in the measurement of λ_m . This turns into an uncertainty of 0.1 °C according to Eq. (2). Considering that the noise for the case of 0 Hz is intrinsic to the measurement system and not caused by vibrations, this means our MCF sensor is robust and practically immune to vibrations in a wide frequency range.

IV. CONCLUSIONS

In this work, we have reported on a sensitive and compactly packaged fiber optic temperature sensor that is robust against vibrations. The sensor is based on an MCF with strongly coupled cores. The sensor consists of a short segment of MCF (2.54 cm) spliced to a commonly used in telecommunications SMF. The fabrication of the device is simple, fast, inexpensive, and reproducible. The packaging of the sensor was conceived to make the MCF exclusively sensitive to temperature, hence independent to other parameters that may be present during temperature measurements, as for example, strain, bending, curvature, or vibrations.

The sensitive part of our sensor is the section of MCF. Temperature changes the effective indices of two supermodes that are excited in the MCF, causing a detectable shift in the interference pattern. The calibration of our MCF sensor was performed in the range from 200 to 1000 °C and a K-type thermocouple widely used and accepted in the conservative aeronautical industry was used as a reference. Results show that the packaged MCF sensor has a sensitivity of 24.8 pm/°C, high robustness against vibrations and a response time of 15 s. Thus, it may represent an attractive solution in several applications that require high temperature sensing, high resolution and sensitivity, small dimensions, and electromagnetic immunity. Some examples may include sensing in aeronautical engines, gas and oil facilities, etc.

The packaged MCF sensor can be customised for the aforementioned and other applications. In addition, its interrogation is carried out with commercially available sensor interrogators. Therefore, we believe that this prototype represents a substantial step forward in the direction of a commercially appealing optical temperature sensor.

REFERENCES

- [1] D. Bradley and K. J. Matthews, "Measurement of high gas temperatures with fine wire thermocouples," *J. Mech. Eng. Sci.*, vol. 10, no. 4, pp. 2328–305, Oct. 1968.
- [2] D. O'Sullivan and M. Cotterell, "Temperature measurement in single point turning," *J. Mater. Process. Technol.*, vol. 118, nos. 1–3, pp. 301–308, Dec. 2001.
- [3] M. Tagawa and Y. Ohta, "Two-thermocouple probe for fluctuating temperature measurement in combustion—Rational estimation of mean and fluctuating time constants," *Combustion Flame*, vol. 109, no. 4, pp. 549–560, Jun. 1997.
- [4] D. A. Stephenson, "Tool-work thermocouple temperature measurements—Theory and implementation issues," *J. Eng. Ind.*, vol. 115, no. 4, pp. 432–437, Nov. 1993.
- [5] L. Y. W. Lee, J. C. Chen, and R. A. Nelson, "Liquid-solid contact measurements using a surface thermocouple temperature probe in atmospheric pool boiling water," *Int. J. Heat Mass Transf.*, vol. 28, no. 8, pp. 1415–1423, Aug. 1985.
- [6] R. R. Dils, "High-temperature optical fiber thermometer," *J. Appl. Phys.*, vol. 54, no. 3, pp. 1198–1201, Nov. 1982.
- [7] V. Fericola and L. Crovini, "Digital optical fiber point sensor for high-temperature measurement," *J. Lightw. Technol.*, vol. 13, no. 7, pp. 1331–1334, Jul. 1995.
- [8] K. T. V. Grattan, A. W. Palmer, and Z. Zhang, "Development of a high-temperature fiber-optic thermometer probe using fluorescent decay," *Rev. Sci. Instrum.*, vol. 62, no. 5, pp. 1210–1213, May 1991.
- [9] Z. Zhang, K. T. V. Grattan, and A. W. Palmer, "Fiber-optic high-temperature sensor based on the fluorescence lifetime of alexandrite," *Rev. Sci. Instrum.*, vol. 63, no. 8, pp. 3869–3873, Apr. 1992.
- [10] G. Beheim, "Fiber-optic thermometer using semiconductor-etalon sensor," *Electron. Lett.*, vol. 22, no. 5, pp. 238–239, Feb. 1986.
- [11] M. Fokine and P. Holmberg, "Chemical composition gratings," presented at the OSA Tech. Dig. Adv. Photon. Conf., Barcelona, Spain, 2014, Paper SoW3B.4.
- [12] M. Fokine, "Formation of thermally stable chemical composition gratings in optical fibers," *J. Opt. Soc. Amer. B*, vol. 19, no. 8, pp. 1759–1765, 2002.
- [13] S. Bandyopadhyay, J. Canning, M. Stevenson, and K. Cook, "Ultrahigh-temperature regenerated gratings in boron-codoped germanosilicate optical fiber using 193 nm," *Opt. Lett.*, vol. 33, no. 16, pp. 1917–1919, Aug. 2008.
- [14] S. Trpkovski *et al.*, "High-temperature-resistant chemical composition Bragg gratings in Er³⁺-doped optical fiber," *Opt. Lett.*, vol. 30, no. 6, pp. 607–609, Mar. 2005.
- [15] D. Barrera, V. Finazzi, J. Villatoro, S. Sales, and V. Pruneri, "Packaged optical sensors based on regenerated fiber Bragg gratings for high temperature applications," *IEEE Sensors J.*, vol. 12, no. 1, pp. 107–112, Jan. 2012.
- [16] S. S. Chong, W. Y. Chong, S. W. Harun, and H. Ahmad, "Regenerated fiber Bragg grating fabricated on high germanium concentration photosensitive fiber for sensing at high temperature," *Opt. Laser Technol.*, vol. 44, no. 4, pp. 821–824, Jun. 2012.
- [17] S. J. Mihailov, "Fiber Bragg grating sensors for harsh environments," *Sensors*, vol. 12, no. 2, pp. 1898–1918, Feb. 2012.
- [18] S. Sales *et al.*, "Evaluation of new regenerated fiber Bragg grating high-temperature sensors in an ISO 834 fire test," *Fire Saf. J.*, vol. 71, pp. 332–339, Jan. 2015.
- [19] A. Wang *et al.*, "Sapphire-fiber-based intrinsic Fabry–Perot interferometer," *Opt. Lett.*, vol. 17, no. 14, pp. 1021–1023, Jul. 1992.
- [20] J. Wang *et al.*, "Multiplexed high temperature sensing with sapphire fiber air gap-based extrinsic Fabry–Perot interferometers," *Opt. Lett.*, vol. 35, no. 5, pp. 619–621, Mar. 2010.
- [21] Y. Zhu *et al.*, "Sapphire-fiber-based white-light interferometric sensor for high-temperature measurements," *Opt. Lett.*, vol. 30, no. 7, pp. 711–713, Apr. 2005.
- [22] C. Zhan *et al.*, "High temperature sensing using higher-order-mode rejected sapphire fiber gratings," *Opt. Memory Neural Netw.*, vol. 16, no. 4, pp. 204–210, Dec. 2007.
- [23] H. Y. Choi, K. S. Park, S. J. Park, U. C. Paek, B. H. Lee, and E. S. Choi, "Miniature fiber-optic high temperature sensor based on a hybrid structured Fabry-Perot interferometer," *Opt. Lett.*, vol. 33, no. 21, pp. 2455–2457, 2008.
- [24] T. Zhu *et al.*, "Fabry–Perot optical fiber tip sensor for high temperature measurement," *Opt. Commun.*, vol. 283, no. 19, pp. 3683–3685, Oct. 2010.
- [25] Y. Zhan *et al.*, "Fiber grating sensors for high-temperature measurement," *Opt. Laser Eng.*, vol. 46, no. 4, pp. 349–354, Jan. 2008.
- [26] V. M. Churikov, V. I. Kopp, and A. Z. Genack, "Chiral diffraction gratings in twisted microstructured fibers," *Opt. Lett.*, vol. 35, no. 3, pp. 342–344, 2010.
- [27] T. F. Morse, Y. He, and F. Luo, "An optical fiber sensor for the measurement of elevated temperatures," *IEICE Trans. Electron.*, vol. 83, no. 3, pp. 298–302, 2000.
- [28] G. Coviello *et al.*, "Thermally stabilized PCF-based sensor for temperature measurements up to 1000 °C," *Opt. Express*, vol. 17, no. 24, pp. 21551–21559, 2009.
- [29] D. Liu *et al.*, "Hollow core fiber based interferometer for high-temperature (1000 °C) measurement," *J. Lightw. Technol.*, vol. 36, no. 9, pp. 1583–1590, May 2018.

- [30] Z. Zhang *et al.*, "Hollow-core-fiber-based interferometer for high-temperature measurements," *IEEE Photon. J.*, vol. 9, no. 2, Apr. 2017, Art. no. 7101109.
- [31] T. Wang *et al.*, "A large range temperature sensor based on an angled fiber end," *Opt. Fiber Technol.*, vol. 45, pp. 19–23, Nov. 2018.
- [32] J. E. Antonio-Lopez *et al.*, "Multicore fiber sensor for high-temperature applications up to 1000 °C," *Opt. Lett.*, vol. 39, no. 15, pp. 4309–4312, Aug. 2014.
- [33] Y. Chunxia *et al.*, "Weakly-coupled multicore optical fiber taper-based high-temperature sensor," *Sens. Actuators A, Phys.*, vol. 280, pp. 139–144, Sep. 2018.
- [34] M. D. Wales *et al.*, "Multicore fiber temperature sensor with fast response times," *OSA Continuum*, vol. 1, no. 2, pp. 764–771, Oct. 2018.
- [35] J. Villatoro *et al.*, "Accurate strain sensing based on super-mode interference in strongly coupled multi-core optical fibers," *Sci. Rep.*, vol. 7, no. 1, pp. 4451–4457, Jun. 2017.
- [36] G. Salceda-Delgado *et al.*, "Compact fiber-optic curvature sensor based on super-mode interference in a seven-core fiber," *Opt. Lett.*, vol. 40, no. 7, pp. 1468–1471, Apr. 2015.
- [37] J. Villatoro *et al.*, "Miniature multicore optical fiber vibration sensor," *Opt. Lett.*, vol. 42, no. 10, pp. 2022–2025, May 2017.
- [38] J. Villatoro *et al.*, "Ultrasensitive vector bending sensor based on multicore optical fiber," *Opt. Lett.*, vol. 41, no. 4, pp. 832–835, 2016.
- [39] C. Xia *et al.*, "Supermodes for optical transmission," *Opt. Express*, vol. 19, no. 17, pp. 16653–16664, Aug. 2011.
- [40] C. Xia *et al.*, "Supermodes in coupled multi-core waveguide structures," *IEEE J. Sel. Topics Quantum Electron.*, vol. 22, no. 2, pp. 196–207, Mar.-Apr. 2008.
- [41] J. Taylor, "Uncertainty in the measurements of y ," in *An Introduction to Error Analysis: The Study of Uncertainties in Physical Measurements*, 2nd ed. Sausalito, CA, USA: Maple-Vail Book Manufacturing Group, 1997, pp. 186–188.
- [42] EGOLF (European Group of Organizations for Fire Testing, Inspection and Certification), Determination of the response time of thermocouples to be used for the measurement of air or gas phase temperature in reaction to fire testing, EGOLF Agreement EA 01: 2008, pp. 1–8, 2008.

Josu Amorebieta received the Master's degree in telecommunications engineering from the University of the Basque Country UPV/EHU, Bilbao, Spain, in 2016. He is currently working toward the Ph.D. degree with the Applied Photonics Group (APG-FAT), University of the Basque Country UPV/EHU. His current research interests include the optical fiber sensing utilizing special fibers for industry and aeronautics.

Gaizka Durana received the M.Sc. and Ph.D. degrees in solid-state physics and telecommunications engineering from the University of the Basque Country UPV/EHU, Bilbao, Spain, in 1999 and 2008, respectively. He is currently an Associate Professor with the Department of Communications Engineering, University of the Basque Country UPV/EHU. His research is focused on the manufacture of specialty polymer optical fibers and design, development, and application of fiber-based optical sensors.

Angel Ortega-Gomez received the Master's degree in telecommunications engineering from the University of the Malaga (UMA), Spain, in 2016. He is currently working toward the Ph.D. degree with the Applied Photonics Group (APG-FAT), University of the Basque Country UPV/EHU, Bilbao, Spain. His research is based on microstructure fibers sensors and Local Surface Plasmon Resonance (LSPR) effect applied on biosensors.

Rubén Fernández received the Electronics Engineer and Master's degrees in advanced electronics systems from the University of the Basque Country UPV/EHU, Bilbao, Spain. He is currently working toward the Ph.D. degree with the Applied Photonics Group (APG-FAT), University of the Basque Country UPV/EHU, Spain.

Javier Velasco is currently a Project Manager with the Aeronautical Technologies Center (CTA), Spain, and has been specialized during the last years in Industry 4.0. He has been working in several research projects focused on test control (load, vibration, and temperature), test automation, data acquisition, and monitoring technologies.

Idurre Sáez de Ocáriz, biography not available at the time of publication.

Joseba Zubia, biography not available at the time of publication.

Jose Enrique Antonio-López, biography not available at the time of publication.

Axel Schülzgen received the Ph.D. degree in physics from Humboldt-University of Berlin, Germany. Since 2009, he has been a Professor of Optics and Photonics with CREOL, The College of Optics and Photonics, University of Central Florida, Orlando, FL, USA. He is also an Adjunct Research Professor with the College of Optical Sciences, University of Arizona, Tucson, AZ, USA.

Dr. Schülzgen has published more than 120 papers in peer-reviewed journals and holds six patents. He is a Fellow of the Optical Society of America.

Rodrigo Amezcua-Correa, biography not available at the time of publication.

Joel Villatoro received the M.Sc. and Ph.D. degrees in optics from the National Institute for Astrophysics, Optics, and Electronics, Mexico. He is an Ikerbasque Research Professor with the University of the Basque Country UPV/EHU, Bilbao, Spain. His research interests include optical fiber sensors and real-world applications of photonic technology.

Article 3

Title:

Highly sensitive multicore fiber accelerometer for low frequency vibration sensing

D.O.I.:

<https://doi.org/10.1038/s41598-020-73178-x>

Authors:

Amorebieta, J.; Ortega-Gomez, A.; Durana, G.; Fernández, R.; Antonio-Lopez, E.; Schülzgen, A.; Zubia, J.; Amezcua-Correa, R.; Villatoro, J.

Journal and publication information:

Scientific Reports, 10 (1), 1-11 (2020)

Indicators of the Journal in 2020:

Not available

Indicators of the Journal in 2019:

Impact factor: 3.998

Q1 in Multidisciplinary sciences (17/71)



OPEN

Highly sensitive multicore fiber accelerometer for low frequency vibration sensing

Josu Amorebieta^{1✉}, Angel Ortega-Gomez¹, Gaizka Durana¹, Rubén Fernández¹, Enrique Antonio-Lopez², Axel Schülzgen², Joseba Zubia¹, Rodrigo Amezcua-Correa² & Joel Villatoro^{1,3✉}

We report on a compact, highly sensitive all-fiber accelerometer suitable for low frequency and low amplitude vibration sensing. The sensing elements in the device are two short segments of strongly coupled asymmetric multicore fiber (MCF) fusion spliced at 180° with respect to each other. Such segments of MCF are sandwiched between standard single mode fibers. The reflection spectrum of the device exhibits a narrow spectrum whose height and position in wavelength changes when it is subjected to vibrations. The interrogation of the accelerometer was carried out by a spectrometer and a photodetector to measure simultaneously wavelength shift and light power variations. The device was subjected to a wide range of vibration frequencies, from 1 mHz to 30 Hz, and accelerations from 0.76 mg to 29.64 mg, and performed linearly, with a sensitivity of 2.213 nW/mg. Therefore, we believe the accelerometer reported here may represent an alternative to existing electronic and optical accelerometers, especially for low frequency and amplitude vibrations, thanks to its compactness, simplicity, cost-effectiveness, implementation easiness and high sensitivity.

For a long time, accelerometers have been used to detect and measure vibrations with high sensitivity and precision. Thus, they have a wide variety of applications. For instance, in the heavy industry, accelerometers are used to monitor low-frequency vibrations in large rotating machineries or in oil pipes¹, or in structural health monitoring, to supervise the condition of pillars, bridges, etc.². They are also used in biomedicine and biomechanics³, and even in gravitational wave detectors⁴. Accelerometers are one of the key elements in seismology as well⁵, where they are used for the detection and monitoring of ground motions caused by earthquakes, volcanic eruptions, explosions, landslides, tsunamis, avalanches, etc. In these cases, accelerometers with high sensitivity for low amplitude vibrations are required.

The detection of vibrations with low frequencies is a very challenging field. For example, the frequency range of ground motions caused by natural events or explosions is between 0.1 and 20 Hz^{6,7}. For the case of tsunamis, such frequency range is even narrower, from 0.1 to 1 Hz⁸. Moreover, it is important to identify the ground motions accurately from the surrounding noise. Therefore, accelerometers for such applications must be highly sensitive and must be capable of measuring acceleration in a wide range. Additional requirements for accelerometers include simple operation, compactness, robustness, capability to operate in hostile or harsh environments and multi-point sensing^{9,10}. Finally, as natural events are usually unpredictable and spaced in time¹¹, such accelerometers must be reliable, long-lasting, and should require minimum or no maintenance.

So far, the most spread accelerometers for low frequencies are based on piezoelectric components¹², MEMS membranes¹³ or pendulums¹⁴ that move with vibrations, or have electrochemical nature¹⁵. Moreover, frequently, such operating principles are combined to enhance their overall performance⁷. The technology of electronic accelerometers is very mature and cost-effective. However, the harsh environments in which these accelerometers are commonly deployed, such as seabed or boreholes, may affect the lifetime of their elements. For such applications, accelerometers based on optical fibers are a good alternative. Fiber-based accelerometers have important advantages that include small size, electromagnetic immunity, as they do not require any electric component to operate, high resolution, remote and long-distance operation capabilities.

¹Department of Communications Engineering, University of the Basque Country UPV/EHU, 48013 Bilbao, Spain. ²CREOL -The College of Optics and Photonics, University of Central Florida, Orlando, FL 162700, USA. ³Ikerbasque-Basque Foundation for Science, 48011 Bilbao, Spain. ✉email: josu.amorebieta@ehu.es; agustinjoel.villatoro@ehu.es

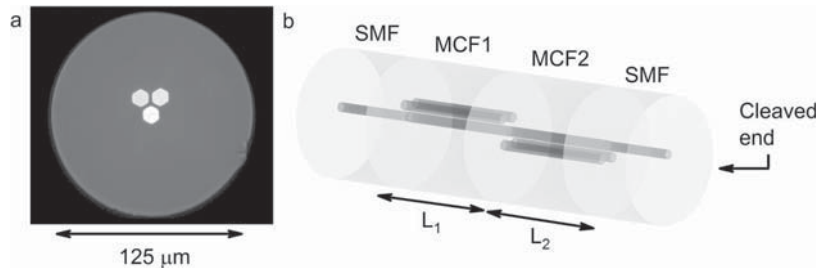


Figure 1. (a) Cross section of the asymmetric MCF. (b) Schematic layout of the device drawn with Blender v2.82 (<https://www.blender.org/>).

Among optical fiber accelerometers, those based on interferometry and fiber Bragg gratings (FBGs) are the most advanced configurations. Optical fiber interferometric accelerometers feature larger dynamic range, wider frequency response band and higher sensitivity compared to some electronic accelerometers^{16–18}. In fact, optical fiber interferometric seismometers capable of detecting vibrations of few mHz have been reported^{19,20}. However, they are bulky and their interrogation tends to be complex. FBG-based optical accelerometers are more compact. Moreover, they provide high sensitivity, large dynamic range and multiplexing ability²¹; and may operate in frequency response bands below 1 Hz^{22,23}. To reach such performance, they require sophisticated interrogation systems that entail picometer-resolution interrogators. In addition, they require elaborated packaging. As a consequence, FBG accelerometers are expensive.

In recent years, multicore fibers (MCFs) have drawn much attention as multipurpose sensing elements²⁴. As accelerometers, strongly coupled MCFs have proved to have much potential²⁵. Moreover, their capability to withstand and operate under elevated strain and temperature conditions has been reported as well^{26,27}, which is a demanded characteristic for harsh environments or outdoors implementations.

In this work, we report on a highly sensitive all-fiber optical accelerometer suitable for sensing vibrations of extremely low frequencies (down to 1 MHz) and low amplitudes. The device is compact and consists of two segments of MCF sandwiched between standard single mode fiber. The MCF segments have different lengths and are rotated 180° with respect to each other. Due to its architecture, the reflection spectrum of the device exhibits a narrow peak that shrinks when it is subjected to vibrations. To test the device, it was subjected to vibrations from 1 mHz to 30 Hz and accelerations from 0.76 to 29.64 mg. The performance of our device was compared and calibrated with a commercial electronic accelerometer. We believe that the simplicity and high performance of the MCF accelerometer reported here are appealing for several applications; particularly those where frequencies are low.

Sensor design, operating mechanism and fabrication

The MCF used to build the accelerometer was fabricated at the University of Central Florida (Orlando, USA). It is an asymmetric strongly coupled MCF consisting of three cores, where one of the cores is located at the geometrical center of the fiber, whereas the other two are surrounding it and arranged adjacently in a V-like configuration (Fig. 1a). Each core is made of Germanium doped silica, and has a mean diameter of 9 μm and a numerical aperture (NA) of 0.14 at 1550 nm to match with that of the SMF. The cores are separated 11.5 μm from each other and embedded in a pure silica cladding of 125 μm of diameter.

The architecture of the device is sketched in Fig. 1b. The sensor consists of two cascaded short segments of different lengths of MCF rotated 180° with respect to each other and sandwiched between two SMFs, resulting in a SMF-MCF1-MCF2-SMF structure. In this structure, the distal SMF has a cleaved end that acts as a low reflectivity mirror in order the device to be interrogated in reflection mode. The benefits of such structure will be discussed throughout this section.

The theoretical background of strongly coupled MCFs relies on the coupled mode theory (CMT)^{28–31}. According to it, if at least two waveguides are close enough to interact, a cyclical power transfer between the waveguides will take place due to the overlapping between the propagating modes through each of them. For conventional CMT, it is assumed that the propagating modes under study are orthogonal³². In the simplest case, if we assume two single mode waveguides named 1 and 2 that are so close to each other that the evanescent field from one guide penetrates into the other, there is a coupling between the two propagating modes. For waveguide 1, such propagation can be expressed as:

$$\frac{\partial a_1}{\partial z} = -j(\beta_1 + k_{1,1})a_1 - jk_{1,2}a_2 \quad (1)$$

where a is the amplitude of the mode in the waveguide indicated in the subindex, β is its corresponding propagation constant and the k parameters are the mutual and self-coupling coefficients between the orthogonal propagating modes in the waveguides 1 and 2, respectively, along the z axis where the propagation is taking place. Identical expression is valid for the propagation in waveguide 2 by substituting in Eq. (1) the subindex 1 for 2 and vice versa.

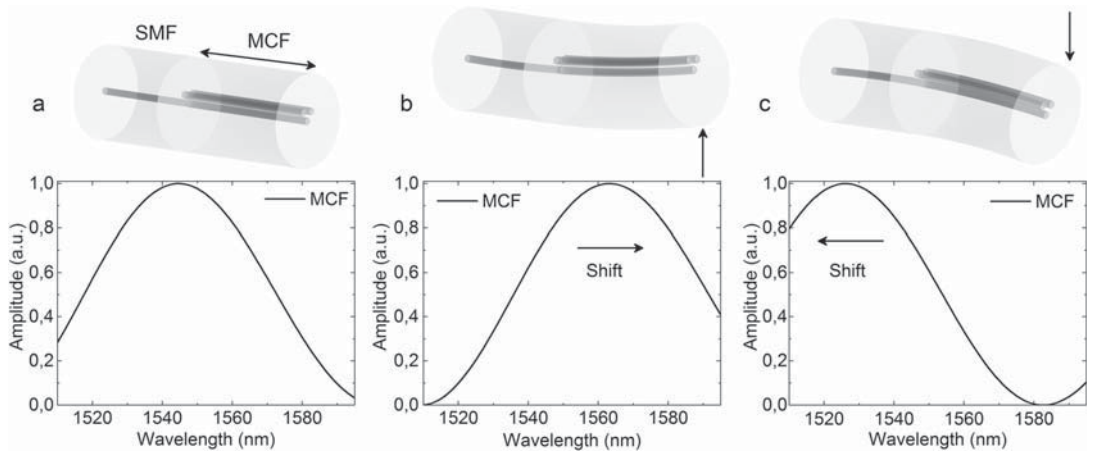


Figure 2. Simulated spectra for the cases in which a segment of MCF is (a) straight, (b) bent upwards and (c) bent downwards when the cores are positioned in a V-like configuration. The arrow indicates the bending direction and the wavelength shift in each case.

Now let us assume the boundary condition in which the amplitude of the mode a only exists in one of the waveguides at $z=0$. Thus, by applying the condition $a_1(0) = 1$ and $a_2(0) = 0$, it is possible to calculate the coupled power in any of the waveguides at any distance by calculating $P(z) = a(z) * a^*(z)$, where a^* refers to the conjugate amplitude of the mode. For such case, the normalized coupled power in the waveguide 1 at a certain propagation distance z , can be expressed as:

$$P_1(z) = \cos^2(Sz) + \cos^2(\gamma)\sin^2(Sz) \tag{2}$$

where $S = \sqrt{\delta^2 + k^2}$, $\delta = (\beta_1 - \beta_2)/2$ and $\tan(\gamma) = k/\delta$.

In strongly coupled MCFs, each of the cores acts as a waveguide. In such coupled structures, the propagating modes are called supermodes^{33,34}, which are the linear combination of the propagating modes through each of the individual waveguides. When such MCFs are excited in their central core by the incoming LP₀₁ mode from the SMF, the two orthogonal supermodes that have power in the central core are coupled. Such supermodes are named SP₀₁ and SP₀₂, and are specific for each MCF. Moreover, for strongly coupled MCFs as the one employed to manufacture this accelerometer, in which all the cores are identical in terms of size and physical properties, and the distance between the central and the neighboring cores remains unaltered, this supermode coupling provokes the power distribution among all the adjacent cores to be identical. Therefore, particularizing Eq. (2) for a stub of the MCF in Fig. 1a, the normalized coupled power in the central core can be expressed as:

$$P(z) = \cos^2\left(\frac{\sqrt{3\pi} \Delta n}{\lambda} z\right) + \frac{1}{3} \sin^2\left(\frac{\sqrt{3\pi} \Delta n}{\lambda} z\right) \tag{3}$$

where Δn is the difference between the effective refractive indexes of the two propagating coupled supermodes and depends on the physical characteristics of the MCF, λ is the excitation wavelength, and z is the distance at which the normalized power is being evaluated along the propagation axis. Therefore, the transmitted power will vary periodically, with a maximum at certain values of z and a minimum at others.

Now, if the length of MCF is fixed, let us say L , the transmission of an SMF-MCF-SMF structure can also be described by particularizing Eq. (3) for $z=L$. If such a structure is excited with a broadband source, the transmission spectrum will be periodic in wavelength according to the phase in Eq. (3).

When an MCF is bent, each core suffers different levels of strain, and their respective refractive indices vary accordingly^{35–39}, modifying the effective refractive indexes of the two propagating supermodes and therefore, the power coupling conditions, which will be reflected in the spectrum. In our case, this effect, added to the asymmetrical arrangement of the cores and their orientation, will cause detectable wavelength shift and coupled power variations that will have unique characteristics depending on the applied bending direction and amplitude, making the MCF ideal for direction-sensitive bending sensors. As demonstrated in⁴⁰, when the position of the cores and the applied bending are aligned as in Fig. 2, where the cores are orientated in a V-like configuration and the MCF is bent upwards and downwards, only wavelength shifts will be noticed in the spectrum; whereas if we rotate the fiber 90°, only coupled power variations will be noticed.

As a step forward of such operating principle, the accelerometer proposed in this work consists of two short segments of the aforementioned MCF (MCF1 and MCF2) of similar but different lengths (L_1 and L_2) that are cascaded and rotated 180° with respect to each other. For this configuration, Eq. (1) has to be applied to each segment. Hence, the normalized output power of the cascade is the product of the individual normalized power outputs of each MCF segment:

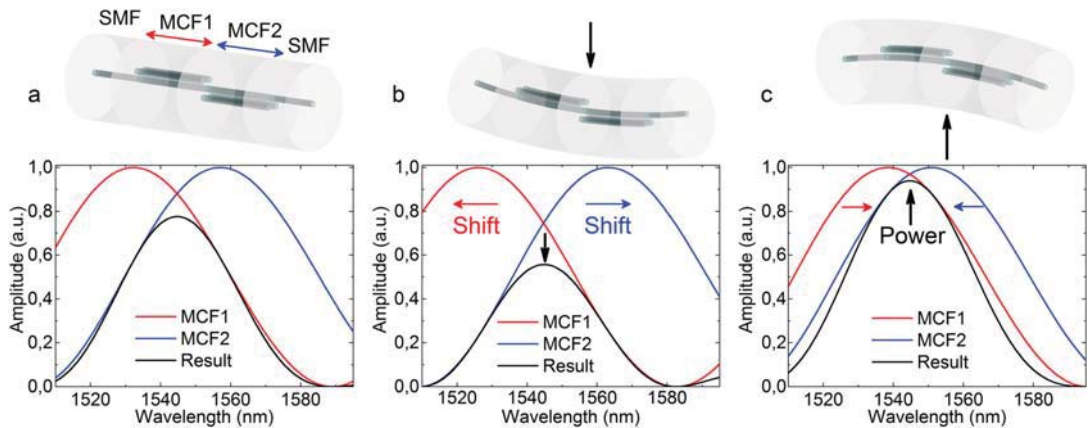


Figure 3. Simulated spectra of each of the MCF segments and the resulting spectra for the cases where the structure is (a) straight, (b) bent upwards and (c) bent downwards by its fusion splice point. The arrow indicates the bending direction, the wavelength shift or the power variation in each case. The cores of MCF1 are in a V-like configuration, whereas the ones in MCF2 are in an inverted V-like configuration.

$$P(L_1, L_2) = P_{MCF1}(L_1) * P_{MCF2}(L_2) \quad (4)$$

where the subindexes MCF1 and MCF2 are referred to each short MCF segment of lengths L_1 and L_2 , respectively. Thus, for $\theta = \sqrt{3\pi \Delta n} / \lambda$, the normalized output power in the central core after passing through the two MCF segments is as follows:

$$P(L_1, L_2) = \cos^2(\theta L_1) * \cos^2(\theta L_2) + \frac{1}{9} \sin^2(\theta L_1) * \sin^2(\theta L_2) + \frac{1}{3} \cos^2(\theta L_1) * \sin^2(\theta L_2) + \frac{1}{3} \cos^2(\theta L_2) * \sin^2(\theta L_1) \quad (5)$$

If we compare the predominant terms in Eqs. (3) and (5), in Eq. (3) it is a squared cosine whereas in Eq. (5) it can be considered a cosine raised to the fourth. Thus, a spectrum derived from Eq. (5) will have narrower peak or peaks than one from Eq. (3) for identical MCF lengths. Moreover, the visibility of a spectrum from Eq. (5) will be higher as well, as the contribution of the rest of the terms in the equation is less than the contribution of the term in Eq. (3), which makes the difference between adjacent maxima and minima to be lower in the latter. Hence, the advantages of cascading two MCF segments compared to a single MCF segment are narrower peaks in the spectrum and higher visibility, which facilitate tracking any change in it.

By operating in reflection mode, the normalized output power is the product of Eq. (5) by itself due to the back-and-forth path of the light through the SMF-MCF1-MCF2-SMF structure; so it can be assumed that the predominant term is a cosine raised to the eighth. Thus, this is an easy manner to improve the narrowness and visibility of the spectrum even more and the reason why this device operates in such configuration.

Regarding the fiber arrangement, by rotating the two MCF segments 180° with respect to each other, each of them will show contrary behavior in terms of wavelength shift and amplitude of the spectrum when they are bent due to their direction sensitive nature that has been explained previously. When the position of the cores of each MCF segment and the applied vertical bending are aligned as in Fig. 3, where one of the MCF segments has its cores oriented in a V-like configuration and the other MCF segment has its cores oriented in an inverted V-like configuration (or rotated 180°), only pronounced amplitude variations will take place in the spectrum. In order the device to perform as shown in Fig. 3, MCF segments of different lengths are compulsory to avoid any ambiguity in the measurement. If the lengths were identical, the spectra of both segments would be overlapped in idle state, being that situation the point at which the maximum reflected light power would take place. Each spectrum would shift in opposite directions when the structure was bent, but only power decreases would be recorded, resulting in the same or similar power readings for opposite bending directions. Such ambiguity or loss in sensitivity is avoided by using segments of different lengths, as for this case, the measured power increases and decreases accordingly with the applied bending direction compared to the power measurement in idle state. Such amplitude variations in the spectrum are proportional to power variations, and therefore, only a PD will be necessary to interrogate the device. Such simplicity makes this SMF-MCF1-MCF2-SMF structure appealing as a very sensitive and cost-effective accelerometer, as it does not require high performance or ad-hoc equipment to operate.

To manufacture a device with such characteristics, some design constraints were required to be considered: Its spectrum had to be confined within the interrogation window (from 1510 to 1595 nm, according to our interrogation setup) at any time and it must have a unique and well-defined peak with no secondary lobes. Such requirements are mandatory to minimize any sensitivity loss when measuring the reflected light power that is

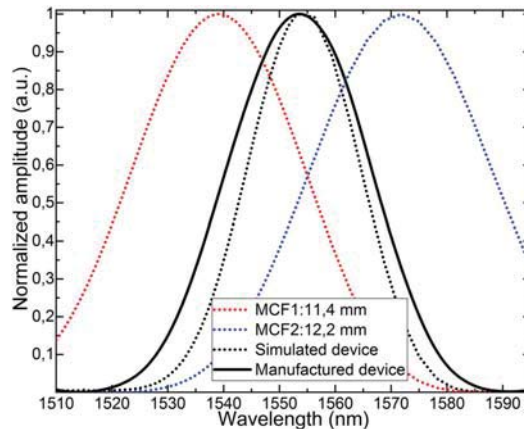


Figure 4. Normalized spectra of the simulated (black dashed line) and manufactured devices (black continuous line). Notice that the maxima of both curves is around 1554 nm and there are no secondary lobes. Simulated spectra of MCF segments of 11.4 mm (red dashed line) and 12.2 (blue dashed line) are shown as well. As indicated in Eq. (2) their product results in the black dashed line.

caused by adjacent lobes with opposite trends (one increases whereas the other decreases) in the same interrogation window, as shown in⁴⁰.

The best fitting lengths for the MCF segments that fulfilled the requirements were 11.4 mm and 12.2 mm, resulting in a compact device of 23.6 mm. To manufacture such device (illustrated in Fig. 1b), a precision fiber cleaver (Fujikura CT-105) and a specialty fiber fusion splicer (Fujikura 100P+) were used. On the one hand, the cleaver allowed us to cut MCF segments of the desired length with 10 μm precision. On the other hand, the splicer can align the central core of the MCF with the unique of the SMF with high precision and has a rotating mechanism and an imaging system that allows observing the end-face of the MCF. Once the MCF segments were rotated 180° with respect to each other, they were spliced, so the central cores of all the segments of the structure were aligned. The fabrication process of our device is inexpensive, fast, and reproducible.

The spectra of the simulated and the manufactured devices are shown in Fig. 4, along with the simulation for each of the MCF segments that comprise the structure. Such simulations were carried out with PhotonDesign simulation software. In such figure, it can be noticed that the curves corresponding to the manufactured and simulated devices agree well, and that the design constraints that included one well-defined and centered peak with no secondary lobes were achieved.

Results and discussion

The interrogation of the device is simple and was carried out with commercial equipment. It consists of a broadband light source (Safibra, s.r.o.) centered at 1550 nm and an InGaAs PD (Thorlabs PDA30B2). To interrogate the device in reflection mode, a fiber optic circulator was used. As it can be noticed in the simulations in Fig. 3, when the structure is bent by the point in which both MCFs are fusion spliced to each other and with that specific core orientation, only power variation will take place. However, when the physical device is subjected to the same effect, a slight wavelength shift is likely to happen as well apart from the amplitude variation. This is caused by two factors: in first place, the impossibility to apply the bending only and exactly at the fusion splice point; and in second place, the length difference of 0.8 mm between the MCF segments, which will cause a small variation in the shift of each against the same stimulus. Due to that, the device was also interrogated with a spectrometer (Ibsen Photonics I-MON-512 High Speed) to monitor the wavelength shift in the spectrum. Such measurement was used as an indicator of the relation between the direction of the applied bending and the position of the cores, as according to Fig. 3, small wavelength shifts would imply the accelerometer is operating as intended, as it is optimized to maximize the power variation.

To test the device, a horizontally fixed rectangular methacrylate thin plate was used. Underneath and at the center of it, an amplified piezoelectric actuator (Thorlabs APFH720 combined with Thorlabs MDT694B amplifier) was fixed so that the plate could vibrate only in the vertical plane. The piezoelectric actuator was connected to a function generator (Keysight Technologies 33220A) to generate signals of diverse amplitudes and frequencies. Then, the manufactured device was surface bonded with cyanoacrylate adhesive to the upper side of the plate, locating the MCF1-MCF2 splice at the center of it and just above the piezoelectric actuator, as it can be observed in the scheme of the experimental setup shown in Fig. 5. It was surface bonded with its cores oriented as in Fig. 3 to match the direction of vibration. Adjacent to the device, a commercial accelerometer (Pico Technology PP877 with Pico Technology TA096) was fixed for comparison and calibration purposes, as this electronic accelerometer provided the relation between the amplitude of the vibration and the acceleration. All the tests were carried out at room temperature (25 °C) and the raw signal of the time response of both devices was monitored and recorded.

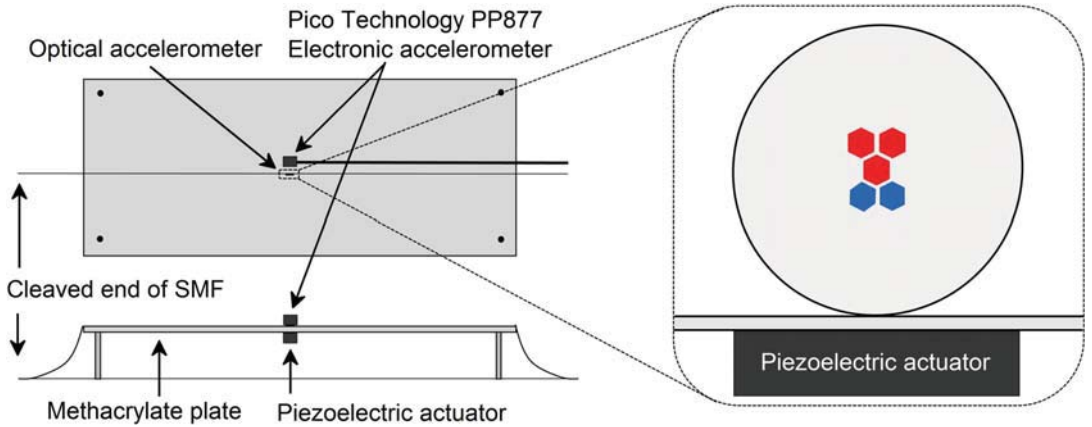


Figure 5. Schematic lateral and top views of the experimental setup drawn with Origin2019b (<https://www.originlab.com/>). The close-up shows how the manufactured optical accelerometer was surface bonded to the plate. Red cores belong to MCF1 whereas blue cores belong to MCF2. The red central core indicates MCF1 is in front of MCF2, as they share common central core. Adjacent to it, the Pico Technology PP877 electronic accelerometer was fixed.

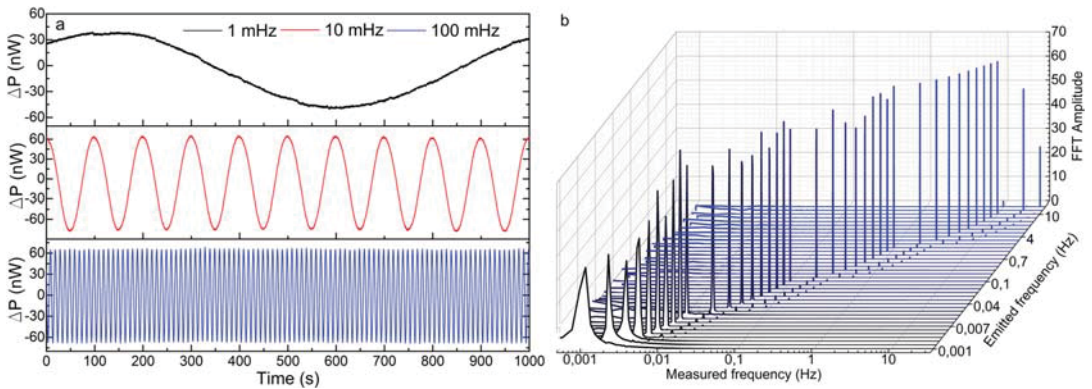


Figure 6. Results of the power measurements in the manufactured optical device. (a) Time response of three representative cases. (b) FFT amplitudes for frequencies from 30 Hz down to 1 MHz for a sinusoidal signal of 1 V_{pp}. The Measured frequency axis is in logarithmic scale.

According to the optical accelerometer, the time response signals in terms of wavelength at which the maxima in the spectrum takes place (λ) and measured power in the PD (P) were acquired. The value of such parameters with the device in idle state were taken as reference (λ_{ref} , P_{ref}) to obtain the wavelength shift ($\Delta\lambda = \lambda - \lambda_{ref}$) and power variation ($\Delta P = P - P_{ref}$), respectively. Subsequently, the FFT of such signals was done to obtain the amplitude of their corresponding frequency components and weights. The criteria to define the limit of detection (LoD) was set to be a signal to noise ratio (SNR) of 3 in the FFT amplitude of the most prominent component, which is commonly taken as a rule⁴¹.

The first test consisted in emitting a sinusoidal signal of 1 V_{pp} amplitude and varying its frequency from 30 Hz down to 1 MHz (the lowest frequency provided by the function generator) in several steps so that the LoD in terms of frequency of each device could be defined. The results are shown from Figs. 6 to 8. The manufactured device detected every vibration clearly down to 1 MHz in wavelength shift and power variation (see Figs. 6a and 7a). The small wavelength shift in Fig. 7a indicates that the device has been surface bonded with the proper core orientation to the plate, and explains the fact that the FFT amplitudes are lower for the wavelength shift measurements than those for the power variation. Nevertheless, even in this configuration aimed at maximizing the power variation, the device has detected such low vibrations by its wavelength shift as well, which is an indicator of its high sensitivity.

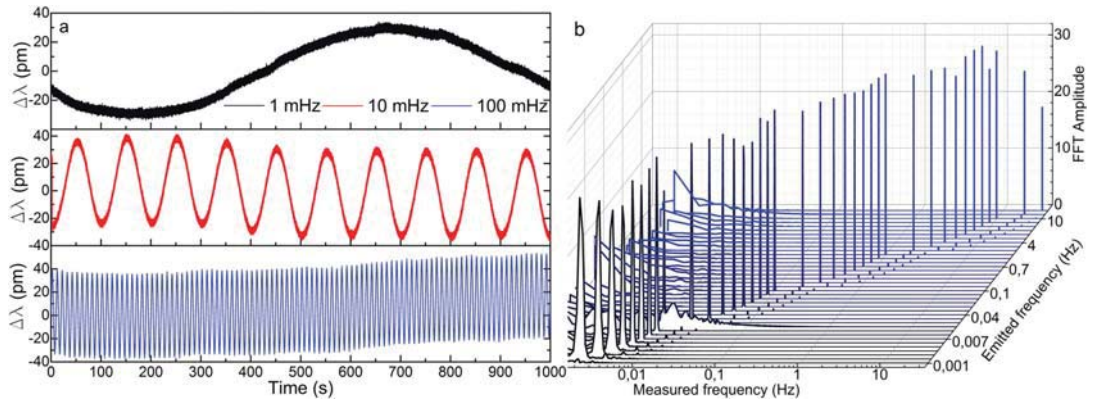


Figure 7. Results of the wavelength shift measurements in the manufactured optical device. (a) Time response of three representative cases. (b) FFT amplitudes for frequencies from 30 Hz down to 1 mHz for a sinusoidal signal of 1 Vpp. The Measured frequency axis is in logarithmic scale.

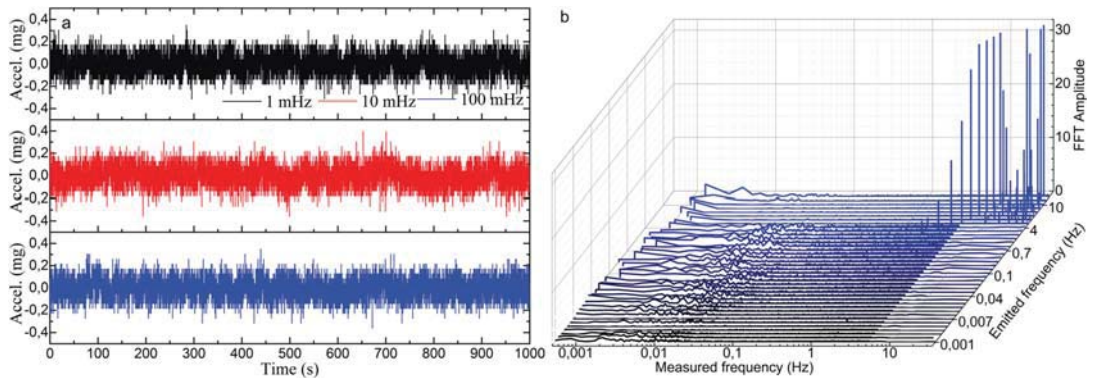


Figure 8. Results of the acceleration measurements in the electronic accelerometer. (a) Time response of three representative cases. (b) FFT amplitudes for frequencies from 30 Hz down to 1 mHz for a sinusoidal signal of 1 Vpp. The Measured frequency axis is in logarithmic scale.

Some other facts that should be highlighted from these results are the low variability and narrowness in amplitude and width, respectively, of the most prominent FFT component in all the cases (see Figs. 6b and 7b), with low level of the harmonic components. These characteristics are directly related to the purity of the acquired raw signal. This performance is critical for vibration measurements as it indicates that the device is practically insensitive to frequency variations if the same vibration amplitude is applied. This characteristic is noticeable if we pay attention to the time responses in Figs. 6a and 7a, where the recorded sinusoidal signal has practically the same amplitude in all the frequencies. According to the commercial accelerometer, it only detected vibrations of 2 Hz and above and with significantly noisier signal and with high level of harmonic components (see Fig. 8).

The second test consisted in emitting a sinusoidal signal of a fixed frequency (6 Hz) and varying its amplitude from 1 Vpp down to 10 mVpp (the lowest amplitude provided by the function generator) to define the LoD of each device in terms of amplitude of vibration, which is related to the acceleration of the oscillation movement. The time responses and FFT amplitudes of both devices are shown from Figs. 9 to 11. The optical device detected vibrations down to 10 mVpp above the established 3:1 SNR criteria. The noticeable progressive decrease in the amplitude of the signals in the time domain (see Figs. 9a and 10a) and the FFT (see Figs. 9b and 10b) is proportional to the diminishment of the amplitude of the emitted signal. In both cases, wavelength shift and power variations, the emitted signal can be clearly detected and the low level of the harmonic components is noticeable. Such results should be highlighted for the PD, whose FFT amplitudes are almost the double compared with the ones obtained by the spectrometer. In relation to the electronic accelerometer, according to the 3:1 SNR criteria, it detected the emitted signals from 1 Vpp down to 30 mVpp, which according to its calibration, covers an acceleration range from 29.64 to 0.76 mg. Its time response signals were significantly noisier (see Fig. 11a), and as a result of that, their corresponding FFT amplitudes were an order of magnitude below the ones of our MCF accelerometer (see Fig. 11b).

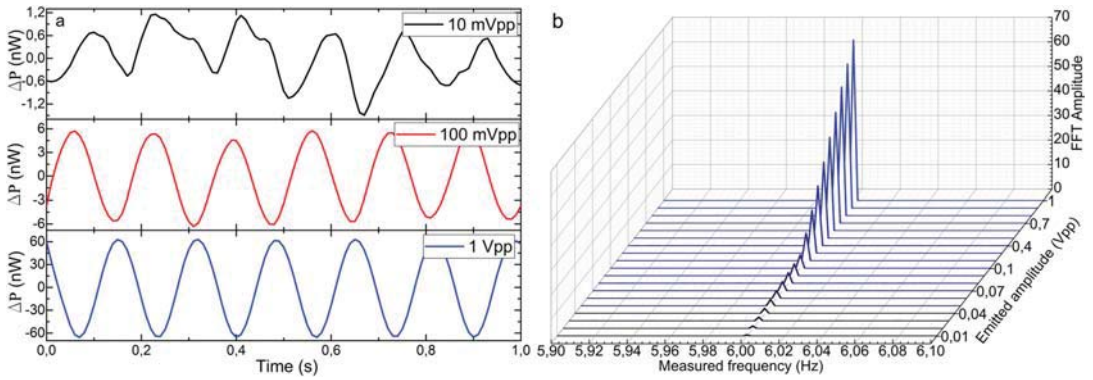


Figure 9. Results of the power variation measurements in the manufactured optical device. (a) Time response of three representative cases, and (b) FFT amplitudes for sinusoidal signals of 6 Hz and amplitudes from 1 Vpp down to 10 mVpp.

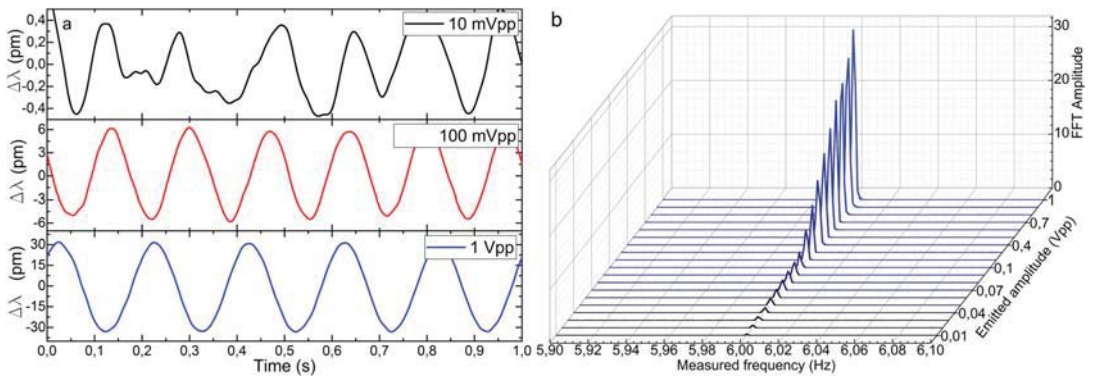


Figure 10. Results of the wavelength shift measurements in the manufactured optical device. (a) Time response of three representative cases, and (b) FFT amplitudes for sinusoidal signals of 6 Hz and amplitudes from 1 Vpp down to 10 mVpp.

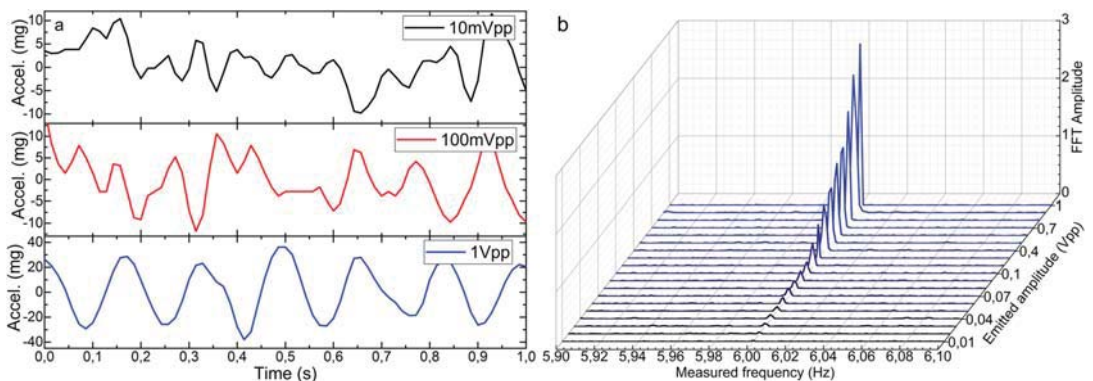


Figure 11. Results of the acceleration measurements in the electronic accelerometer. (a) Time response of three representative cases, and (b) FFT amplitudes for sinusoidal signals of 6 Hz and amplitudes from 1 Vpp down to 10 mVpp.

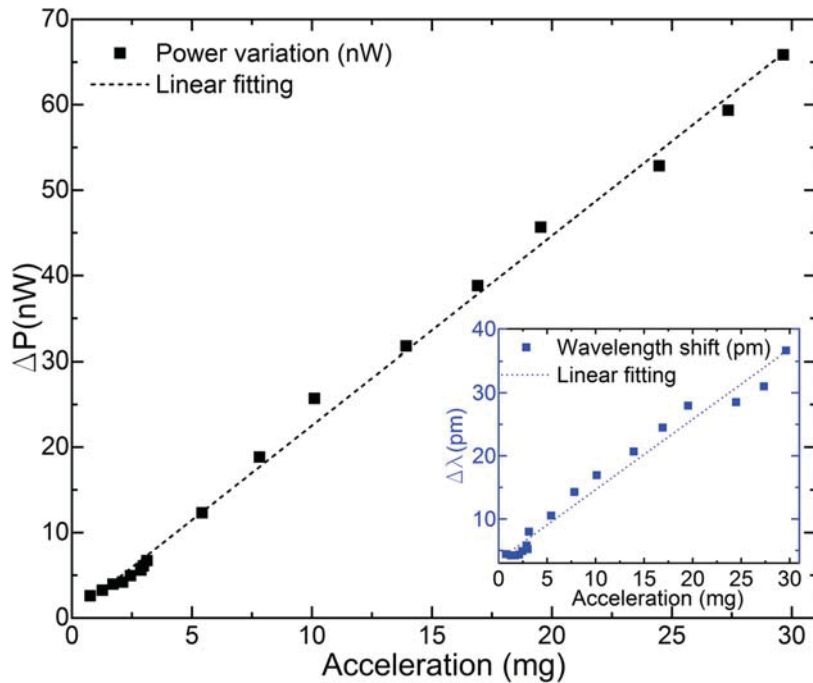


Figure 12. Calibration of the manufactured optical accelerometer in terms of power variation. The calibration of the device in terms of wavelength shift is shown in the inset.

The calibration resulting from these tests is shown in Fig. 12. The linear behavior of wavelength shift and power variations is significant, especially for the power variation measurements, where a sensitivity of 2.213 nW/mg with a Pearson squared correlation coefficient of $R^2 = 0.997$ and with a noise density of $1.083 \mu\text{g}/\sqrt{\text{Hz}}$ was obtained. As a result, the correlation between the power variation (ΔP) and the acceleration (in mg) is as expressed in Eq. (6):

$$a = 0.450\Delta P - 0.143 \quad (6)$$

Equation 6 is applicable for accelerations from 29.64 mg down to 0.76 mg, as this was the LoD of the electronic accelerometer. However, considering that the MCF accelerometer detected vibrations of amplitudes below 30 mVpp and its significant linear behavior, we believe that this equation could be extrapolated and be valid for vibrations down to the tested limit (10 mVpp) and below. If so, this would indicate our device is capable of detecting accelerations of up to 0.25 mg. For real-field implementation, the robustness of the proposed measurement system could be improved by using a reference PD to monitor the stability of the light source in order to avoid any unwanted effect due to light power fluctuation.

According to wavelength shift measurements, a sensitivity of 1.116 pm/mg with a Pearson squared correlation coefficient of $R^2 = 0.976$ was achieved. It should be pointed out that our MCF accelerometer was optimized to operate with power variation measurements, which implied low sensitivity in terms of wavelength shift. Thus, such result points out that the device was surface bonded as close as possible as depicted in Fig. 5 and that it operates as intended.

Conclusions

In this work, we have reported on a compact and highly sensitive all-fiber accelerometer based on two short segments of different lengths of asymmetric MCF. Such segments are rotated 180° with respect to each other and sandwiched between SMFs, creating a SMF-MCF1-MCF2-SMF structure. Its fabrication is fast, easily reproducible and customizable. Such configuration maximizes the change in the amplitude of the spectrum, which is related to power variation. Its interrogation is very simple and cost-effective, as it is made by few off-the-shelf equipment.

The manufactured device was subjected to vibrations of different amplitudes and frequencies, and its performance compared and calibrated with a commercial electronic accelerometer. It was found that our MCF accelerometer outperformed a commercial electronic accelerometer, as it was capable of detecting extremely low frequency vibrations down to 1 mHz with a sensitivity of 2.213 nW/mg, which makes it appealing for applications

in which these characteristics are demanded, such as in seismology. To the authors' best knowledge, this is the simplest optical fiber-based accelerometer that reaches this performance.

The MCF accelerometer proposed here is suitable for parallel multiplexing by means of an optical switch, which makes multi-point measurement feasible in order to cover large structures or areas. Thanks to the narrow reflection peaks provided by this SMF-MCF1-MCF2-SMF structure, several devices of this kind can be multiplexed in the same interrogation window. By modifying the length of the MCF segments in each device, the shape of the spectra and the location of the maxima can be customized individually, leading to an unambiguous identification of each. Moreover, the proposed structure may be embedded or surface bonded in oil pipelines or pillars, which facilitates its installation significantly, as it does not require expensive or complex setups. Lastly, we would like to highlight the potential of the device reported here to be direction sensitive by combining simultaneous analysis of wavelength shift and power variation. In this manner, the vibration as well as its direction could be identified accurately thanks to the effects observed in the spectrum.

Therefore, we believe that the MCF vibration sensor reported here may represent an alternative to conventional electronic and optical accelerometers thanks to its compactness, simplicity, high sensitivity, cost-effectiveness and versatility.

Received: 2 July 2020; Accepted: 14 September 2020

Published online: 30 September 2020

References

- Medeiros, K. A. R., Barbosa, C. R. H. & de Oliveira, E. C. Flow Measurement by piezoelectric accelerometers: application in the oil industry. *Pet. Sci. Technol.* **33**, 1402–1409. <https://doi.org/10.1080/10916466.2015.1044613> (2015).
- Sabato, A., Niezrecki, C. & Fortino, G. Wireless MEMS-based accelerometer sensor boards for structural vibration monitoring: a review. *IEEE Sens. J.* **17**, 226–235 (2017).
- Wixted, A. J. *et al.* Measurement of energy expenditure in elite athletes using MEMS-based triaxial accelerometers. *IEEE Sens. J.* **7**, 481–488 (2007).
- DeSalvo, R. Review: accelerometer development for use in gravitational wave-detection interferometers. *Bull. Seismol. Soc. Am.* **99**, 990–997. <https://doi.org/10.1785/0120080155> (2009).
- Evans, J. R. *et al.* Performance of several low-cost accelerometers. *Seismol. Res. Lett.* **85**, 147–158. <https://doi.org/10.1785/0220130091> (2014).
- Havskov, J. & Alguacil, G. *Instrumentation in Earthquake Seismology* Vol. 358 (Springer, Berlin, 2004).
- Deng, T., Chen, D., Wang, J., Chen, J. & He, W. A MEMS based electrochemical vibration sensor for seismic motion monitoring. *J. Microelectromech. Syst.* **23**, 92–99 (2014).
- Shindo, Y., Yoshikawa, T. & Mikada, H. *SENSORS, 2002 IEEE*, Vol. 1762 1767–1770.
- Shinohara, M. *et al.* Precise aftershock distribution of the 2007 Chuetsu-oki Earthquake obtained by using an ocean bottom seismometer network. *Earth Planets Space* **60**, 1121–1126. <https://doi.org/10.1186/BF03353147> (2008).
- Wang, H. F. *et al.* Ground motion response to an ML 4.3 earthquake using co-located distributed acoustic sensing and seismometer arrays. *Geophys. J. Int.* **213**, 2020–2036. <https://doi.org/10.1093/gji/ggy102> (2018).
- Hutton, K., Woessner, J. & Hauksson, E. Earthquake monitoring in southern California for seventy-seven years (1932–2008). *Bull. Seismol. Soc. Am.* **100**, 423–446. <https://doi.org/10.1785/0120090130> (2010).
- Levinzon, F. A. Ultra-low-noise seismic piezoelectric accelerometer with integral FET amplifier. *IEEE Sens. J.* **12**, 2262–2268 (2012).
- Zou, X., Thiruvengathanan, P. & Seshia, A. A. A seismic-grade resonant MEMS accelerometer. *J. Microelectromech. Syst.* **23**, 768–770 (2014).
- Bertolini, A., DeSalvo, R., Fidecaro, F. & Takamori, A. Monolithic folded pendulum accelerometers for seismic monitoring and active isolation systems. *IEEE Trans. Geosci. Remote Sens.* **44**, 273–276 (2006).
- Leugoud, R. & Kharlamov, A. Second generation of a rotational electrochemical seismometer using magnetohydrodynamic technology. *J. Seismol.* **16**, 587–593. <https://doi.org/10.1007/s10950-012-9290-y> (2012).
- Kamenev, O. T., Kulchin, Y. N., Petrov, Y. S., Khiznyak, R. V. & Romashko, R. V. Fiber-optic seismometer on the basis of Mach-Zehnder interferometer. *Sens. Actuator A Phys.* **244**, 133–137. <https://doi.org/10.1016/j.sna.2016.04.006> (2016).
- Chang, T. *et al.* Fiber optic interferometric seismometer with phase feedback control. *Opt. Express* **28**, 6102–6122. <https://doi.org/10.1364/OE.385703> (2020).
- Pisco, M. *et al.* Opto-mechanical lab-on-fibre seismic sensors detected the Norcia earthquake. *Sci. Rep.* **8**, 6680. <https://doi.org/10.1038/s41598-018-25082-8> (2018).
- Chen, J. *et al.* Ultra-low-frequency tri-component fiber optic interferometric accelerometer. *IEEE Sens. J.* **18**, 8367–8374 (2018).
- Bernard, P. *et al.* Onland and offshore extrinsic Fabry-Pérot optical seismometer at the end of a long fiber. *Seismol. Res. Lett.* **90**, 2205–2216. <https://doi.org/10.1785/0220190049> (2019).
- Laudati, A. *et al.* A fiber-optic Bragg grating seismic sensor. *IEEE Photonics Technol. Lett.* **19**, 1991–1993 (2007).
- Liu, F., Dai, Y., Karanja, M. J. & Yang, M. A low frequency FBG accelerometer with symmetrical bended spring plates. *Sensors* <https://doi.org/10.3390/s17010206> (2017).
- Antunes, P. F. D. C. *et al.* Optical fiber accelerometer system for structural dynamic monitoring. *IEEE Sens. J.* **9**, 1347–1354 (2009).
- Villatoro, J. *et al.* Composed multicore fiber structure for direction-sensitive curvature monitoring. *APL Photonics* **5**, 070801. <https://doi.org/10.1063/1.5128285> (2020).
- Villatoro, J., Antonio-Lopez, E., Zubia, J., Schülzgen, A. & Amezcua-Correa, R. Interferometer based on strongly coupled multicore optical fiber for accurate vibration sensing. *Opt. Express* **25**, 25734–25740. <https://doi.org/10.1364/OE.25.025734> (2017).
- Villatoro, J. *et al.* Accurate strain sensing based on super-mode interference in strongly coupled multi-core optical fibres. *Sci. Rep.* **7**, 4451. <https://doi.org/10.1038/s41598-017-04902-3> (2017).
- Amorebieta, J. *et al.* Packaged multi-core fiber interferometer for high-temperature sensing. *J. Lightwave Technol.* **37**, 2328–2334 (2019).
- Kishi, N. & Yamashita, E. A simple coupled-mode analysis method for multiple-core optical fiber and coupled dielectric waveguide structures. *IEEE Trans. Microw. Theory Tech.* **36**, 1861–1868. <https://doi.org/10.1109/22.17423> (1988).
- Snyder, A. W. Coupled-mode theory for optical fibers. *J. Opt. Soc. Am.* **62**, 1267–1277. <https://doi.org/10.1364/JOSA.62.001267> (1972).
- Hudgings, J., Molter, L. & Dutta, M. Design and modeling of passive optical switches and power dividers using non-planar coupled fiber arrays. *IEEE J. Quantum Electron.* **36**, 1438–1444 (2000).
- Perez-Leija, A., Hernandez-Herrejon, J. C., Moya-Cessa, H., Szameit, A. & Christodoulides, D. N. Generating photon-encoded SW Ψ states in multipoint waveguide-array systems. *Phys. Rev. A* **87**, 013842. <https://doi.org/10.1103/PhysRevA.87.013842> (2013).

32. Huang, W.-P. Coupled-mode theory for optical waveguides: an overview. *J. Opt. Soc. Am. A* **11**, 963–983. <https://doi.org/10.1364/JOSAA.11.000963> (1994).
33. Xia, C., Bai, N., Ozdur, I., Zhou, X. & Li, G. Supermodes for optical transmission. *Opt. Express* **19**, 16653–16664. <https://doi.org/10.1364/OE.19.016653> (2011).
34. Xia, C. *et al.* Supermodes in coupled multi-core waveguide structures. *IEEE J. Sel. Top. Quantum Electron.* **22**, 196–207 (2016).
35. Schermer, R. T. Mode scalability in bent optical fibers. *Opt. Express* **15**, 15674–15701. <https://doi.org/10.1364/OE.15.015674> (2007).
36. Schermer, R. T. & Cole, J. H. Improved bend loss formula verified for optical fiber by simulation and experiment. *IEEE J. Quantum Electron.* **43**, 899–909 (2007).
37. Heiblum, M. & Harris, J. Analysis of curved optical waveguides by conformal transformation. *IEEE J. Quantum Electron.* **11**, 75–83 (1975).
38. Yin, G., Zhang, F., Xu, B., He, J. & Wang, Y. Intensity-modulated bend sensor by using a twin core fiber: theoretical and experimental studies. *Opt. Express* **28**, 14850–14858. <https://doi.org/10.1364/OE.390054> (2020).
39. Arrizabalaga, O. *et al.* High-performance vector bending and orientation distinguishing curvature sensor based on asymmetric coupled multi-core fibre. *Sci. Rep.* **10**, 14058. <https://doi.org/10.1038/s41598-020-70999-8> (2020).
40. Villatoro, J. *et al.* Ultrasensitive vector bending sensor based on multicore optical fiber. *Opt. Lett.* **41**, 832–835. <https://doi.org/10.1364/OL.41.000832> (2016).
41. Shrivastava, A. & Gupta, V. Methods for the determination of limit of detection and limit of quantitation of the analytical methods. *Chron. Young Sci.* **2**, 21–25. <https://doi.org/10.4103/2229-5186.79345> (2011).

Acknowledgments

Ministerio de Economía y Competitividad; Ministerio de Ciencia, Innovación y Universidades; European Regional Development Fund (PGC2018-101997-B-I00 and RTI2018-094669-B-C31); Gobierno Vasco/Eusko Jaurlaritza (IT933-16); ELKARTEK KK-2019/00101 (μ 4Indust) and ELKARTEK KK-2019/00051 (SMART-RESNAK). The work of Angel Ortega-Gomez is funded by a PhD fellowship from the Spain Government. The work of Josu Amorebieta is funded by a PhD fellowship from the University of the Basque Country UPV/EHU.

Author contributions

J.A. collaborated in the theoretical approach, performed the experiments, processed and analyzed data and wrote the first draft. A.O.-G. did the simulations and the theoretical approach, J.V. conceived and fabricated the device, designed and supervised the experiments. A.S., E.A.-L. and R.A.C. conceived and fabricated the MCF. R.F. developed the data acquisition software. G.D. and J.Z. supervised the experiments. All authors discussed the experimental data, revised and approved the manuscript. JA and JV wrote the final version with inputs of all the authors.

Competing interests

The authors declare no competing interests.

Additional information

Correspondence and requests for materials should be addressed to J.A. or J.V.

Reprints and permissions information is available at www.nature.com/reprints.

Publisher's note Springer Nature remains neutral with regard to jurisdictional claims in published maps and institutional affiliations.



Open Access This article is licensed under a Creative Commons Attribution 4.0 International License, which permits use, sharing, adaptation, distribution and reproduction in any medium or format, as long as you give appropriate credit to the original author(s) and the source, provide a link to the Creative Commons licence, and indicate if changes were made. The images or other third party material in this article are included in the article's Creative Commons licence, unless indicated otherwise in a credit line to the material. If material is not included in the article's Creative Commons licence and your intended use is not permitted by statutory regulation or exceeds the permitted use, you will need to obtain permission directly from the copyright holder. To view a copy of this licence, visit <http://creativecommons.org/licenses/by/4.0/>.

© The Author(s) 2020

Article 4

Title:

Composed multicore fiber structure for direction-sensitive curvature monitoring

D.O.I.:

<https://doi.org/10.1063/1.5128285>

Authors:

Villatoro, J.; **Amorebieta, J.**; Ortega-Gomez, A.; Antonio-Lopez, E.; Zubia, J.; Schülzgen, A.; Amezcua-Correa, R.

Journal and publication information:

Invited paper

APL Photonics, 5 (7), 070801 (2020)

Cited 3 times

Indicators of the Journal in 2020:

Not available

Indicators of the Journal in 2019:

Impact factor: 4.864

Q1 in Optics (13/97)

Composed multicore fiber structure for direction-sensitive curvature monitoring

Cite as: APL Photon. 5, 070801 (2020); doi: 10.1063/1.5128285

Submitted: 18 September 2019 • Accepted: 7 June 2020 •

Published Online: 1 July 2020



Joel Villatoro,^{1,2,a)}  Josu Amorebieta,¹ Angel Ortega-Gomez,¹ Enrique Antonio-Lopez,³ Joseba Zubia,¹ 
Axel Schülzgen,³  and Rodrigo Amezcua-Correa³

AFFILIATIONS

¹Department of Communications Engineering, University of the Basque Country UPV/EHU, Torres Quevedo Plaza 1, E-48013 Bilbao, Spain

²IKERBASQUE—Basque Foundation for Science, E-48011 Bilbao, Spain

³CREOL, The College of Optics & Photonics, University of Central Florida, P.O. Box 162700, Orlando, Florida 32816-2700, USA

^{a)}Author to whom correspondence should be addressed: agustinjoel.villatoro@ehu.eus

ABSTRACT

The present work deals with a curvature sensor that consists of two segments of asymmetric multicore fiber (MCF) fusion spliced with standard single mode fiber (SMF). The MCF comprises three strongly coupled cores; one of such cores is at the geometrical center of the MCF. The two segments of MCF are short, have different lengths (less than 2 cm each), and are rotated 180° with respect to each other. The fabrication of the sensor was carried out with a fusion splicing machine that has the means for rotating optical fibers. It is demonstrated that the sensor behaves as two SMF–MCF–SMF structures in series, and consequently, it has enhanced sensitivity. The device proposed here can be used to sense the direction and amplitude of curvature by monitoring either wavelength shifts or intensity changes. In the latter case, high curvature sensitivity was observed. The device can also be used for the development of other highly sensitive sensors to monitor, for example, vibrations, force, pressure, or any other parameter that induces periodic or local curvature or bending to the MCF segments.

© 2020 Author(s). All article content, except where otherwise noted, is licensed under a Creative Commons Attribution (CC BY) license (<http://creativecommons.org/licenses/by/4.0/>). <https://doi.org/10.1063/1.5128285>

INTRODUCTION

Multicore fibers (MCFs) are revolutionary waveguides^{1,2} that have multiple individual cores sharing a common cladding. In general, MCFs have diameters similar to that of a standard telecommunications optical fiber. The cores of an MCF can be well isolated from each other to avoid interactions between them. In this manner, each core behaves as an independent waveguide. Completely the opposite is also possible; this means that the cores can be in close proximity to each other to allow coupling between them. In the latter case, the fiber is called coupled-core MCF and supports supermodes.³

The unique features of MCFs provide new alternatives for the development of innovative devices whose functionalities cannot be easily achieved with conventional optical fibers. For example, ultrathin lensless endoscopes⁴ for biomedical applications and minimal intrusive shape sensors have been demonstrated.^{5,6} MCFs with

coupled cores offer also new possibilities for the development of simple and compact devices that can be used to monitor vibrations and bending,^{7,8} among other parameters.

With regard to fiber optic curvature sensors, so far, a variety of configurations based on conventional fibers have been proposed and demonstrated (see Refs. 9–14). However, to the best of the authors' knowledge, such curvature sensors have not reached high readiness level. This suggests that it is important to investigate new alternatives to devise functional fiber optic curvature sensors.

MCFs with isolated cores offer multiple alternatives to build curvature sensors. For example, curvature sensors based on interferometers,^{15–18} twisted MCFs,¹⁹ or directional couplers²⁰ have been demonstrated. Some drawbacks of these sensors are the need of bulk optics to interrogate them, their insensitivity to the direction of curvature, their fragility as, in some cases, the MCF must be tapered, and the high insertion losses. Strongly coupled MCFs with

quasi-symmetric core distribution have also been demonstrated for direction-insensitive curvature sensing.^{21,22}

MCFs with a series of Bragg gratings^{23–25} or long period gratings^{26–28} in some or in all the cores can also be used to sense curvature. In fact, MCF curvature sensors based on Bragg gratings have reached a commercial level, but their high cost may limit their use to high-end applications. Some disadvantages of grating-based MCF curvature sensors include complex fabrication and expensive interrogation. Moreover, the curvature on some MCFs with gratings can induce coupling between cores. Such coupling can induce errors in the measurements of curvature.

Fiber optic curvature sensors have potential applications in shape sensing,^{6,14} that is why they have attracted considerable research interest in recent years. Ideally, a fiber optic curvature sensor must be cost effective and must provide the amplitude and the direction of curvature. In addition, the sensor must be sensitive, simple, reliable, and very small in diameter, so it can be integrated to devices, instruments, or structures. We believe that the fiber optic curvature sensors reported to date cannot provide all these desirable characteristics.

Here, we propose a highly sensitive curvature sensor based on a strongly coupled MCF. Our device is easy to fabricate and requires a simple (low cost) interrogation system. In addition, our sensor is able to provide the amplitude and direction of curvature even by monitoring intensity changes. To achieve the curvature sensor with the aforementioned features, we used two short segments of different lengths of an MCF that comprises three identical cores. The two MCF segments are fusion spliced and rotated 180° with respect to each other and are inserted in a conventional single mode fiber.

The structure reported here can also be used to devise other sensors to monitor any parameter that induces point or periodic curvature to the MCF. Some examples may include force, pressure, and vibration sensors or accelerometers.

SENSOR FABRICATION AND WORKING MECHANISM

In Fig. 1(a), we show the cross section of the MCF used to fabricate the sensor. The fiber has three coupled cores made of germanium-doped silica embedded in a cladding made of pure silica. The diameter of each core is approximately 9 μm, and the cores are separated from each other by 11 μm approximately. It can be noted that one core is at the geometrical center of the MCF. The numerical aperture of each core of the MCF is identical to that of an SMF (0.14). Due to the matching between the numerical apertures of both

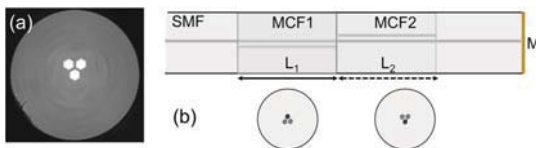


FIG. 1. (a) Micrograph of the MCF used to fabricate the samples. (b) Drawing of the device in which the two segments of MCF are rotated 180° with respect to each other. L_1 and L_2 are the lengths of the segments MCF1 and MCF2, respectively, and M is the mirror.

fibers, the insertion losses of our devices are low as demonstrated previously.^{7,21}

The architecture of our curvature sensor is shown in Fig. 1(b). Such a structure is fabricated by fusion splicing two segments of different lengths (typically less than 20 mm each) of the aforementioned MCF with a conventional SMF. The two segments of MCF are rotated 180° with respect to each other; the reason of this angle is explained below. A reflector or mirror at the distal end of the SMF allows the sensor to operate in reflection mode, which has the advantages described in the following.

The fabrication of the device shown in Fig. 1(b) can be carried out with a splicing machine that has means of rotating optical fibers. In our case, we used a specialty fiber splicer (a Fujikura FSM-100P+) in which an *ad hoc* splicing program was implemented. With such a program, the end face of the two segments of MCF was inspected to orient the cores before the splicing. In all cases, the splices were carried out with a cladding alignment method. Under such splicing conditions, the cores located in the geometrical center of the two segments of MCF and the unique core of the SMF were axially aligned and permanently joined together. The two segments of MCF were intentionally rotated 180° to achieve an SMF–MCF1–MCF2–SMF structure in which the two cores outside the center of the MCFs were upward in one part of the structure and downward in the other part. We will see that such a structure behaves as a dual supermode coupler in series.

To understand the working mechanism of the device shown in Fig. 1(b), we carried out simulations based on the finite difference method with commercial software (FimmWave and FimmProp by Photon Design) and different experiments. In Fig. 2, we show the propagation of two different wavelengths from the lead-in SMF to the lead-out SMF in an SMF–MCF1–MCF2–SMF structure with the dimensions described in the figure. It can be seen that at 1500 nm, the guided light does not reach the lead-out SMF. On the other hand, light at 1550 nm propagates with losses. Consequently, in the referred structure, maximum transmission can be expected at 1550 nm and minimum at 1500 nm.

In addition to the simulations, we analyzed mathematically our device by considering that it is composed of two parts. Let us

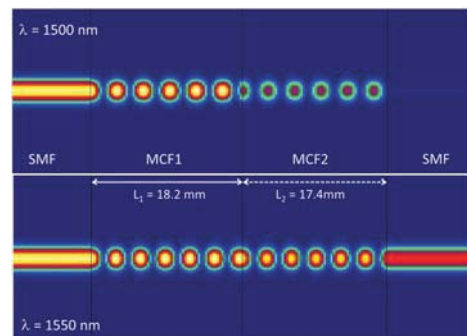


FIG. 2. Simulations of light propagation in an SMF–MCF1–MCF2–SMF structure. The following values were considered: $L_1 = 12.20$ mm and $L_2 = 11.40$ mm. The analyzed wavelengths are indicated.

consider first the case when $L_2 = 0$. In this case, we will have an SMF–MCF1–SMF structure. To predict the transmission intensity of such a structure, we have to consider the following situations: (i) The three cores of the MCF are identical, i.e., they have the same diameter and the same refractive index; (ii) the distance between the MCF cores is the same; (iii) the central core of the MCF is excited with the fundamental SMF mode, and (iv) the MCF is composed by evanescently coupled single-mode cores. In our case, the latter assumptions are valid in the 1200 nm–1600 nm wavelength range. Under these conditions, two supermodes are excited in the MCF. Such supermodes have non-zero intensity in the central core of the MCF.⁸

The transfer function of the SMF–MCF–SMF structure can be calculated by means of the coupled mode theory.²⁹ The transfer function is a periodic function of wavelength (λ) and can be expressed as^{30–32}

$$I_{1T}(\lambda, L_1) = 1 - (2/3)\sin^2\left(\sqrt{3}\pi\Delta n L_1/\lambda\right). \quad (1)$$

In Eq. (1), Δn is the effective refractive index difference between the two excited supermodes. Δn depends on the wavelength, refractive index, dimensions, and separation between the cores of the MCF. For the MCF shown in Fig. 1(a), Δn was found to be 4.66×10^{-4} . Now, if $L_1 = 0$, we will have an SMF–MCF2–SMF structure of length L_2 . The transfer function of such a structure can also be expressed by Eq. (1), but with L_2 instead of L_1 .

Let us now calculate the transfer function of an SMF–MCF–SMF structure when the SMF at the final extreme has a reflector or mirror on its face [see Fig. 1(b)]. In this case, the structure can be considered as two SMF–MCF–SMF structures in series. As demonstrated by several groups, the transfer function of two periodic fiber devices placed in series is the product of the individual transfer functions.^{33–36} Thus, if a single SMF–MCF–SMF structure with L_1 (or L_2) is interrogated in reflection, the transfer function is simply $I_{1R} = I_{1T}^2$ (or $I_{2R} = I_{2T}^2$).

If the device shown in Fig. 1(b) is excited with a broadband source, the reflection measured with a photodetector or spectrometer will be

$$R(\lambda) = I_s(\lambda)[I_{1T}(\lambda, L_1)I_{2T}(\lambda, L_2)]^2. \quad (2)$$

In Eq. (2), $I_s(\lambda)$ is the spectral power distribution of the excitation light source. In a practical situation, such a light source can be a narrow-band light emitting diodes (LED) whose spectral distribution is Gaussian.

RESULTS AND DISCUSSION

The interrogation of the device depicted in Fig. 1(b) is simple. In our case, we used a superluminescent light emitting diode (SLED) with peak emission at 1550 nm and a FWHM of 60 nm as the light source, a conventional fiber optic coupler (or circulator), and a photodetector or a miniature spectrometer (Ibsen I-MON-512) connected by a universal serial bus (USB) cable to a personal computer. Unless otherwise stated, in all our experiments, the cleaved end of the SMF segment after the MCF2 was used as a reflector. The reflectivity in this case was less than 4%.

In Fig. 3, we show the normalized reflection spectra of SMF–MCF–SMF structures in three different cases. The plots with dotted

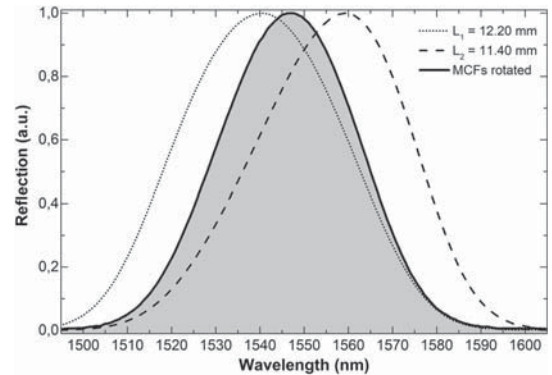


FIG. 3. Reflection spectra observed when the structure is SMF–MCF–SMF in which the lengths of MCFs are 12.20 mm (dashed line) and 11.4 mm (dotted line). The shadowed area beneath the solid line is the reflection spectrum observed when a 12.20 mm-long and an 11.40 mm-long segment of MCF are fusion spliced and rotated 180° with respect to each other.

and dashed lines correspond to the spectra of individual structures with $L_1 = 12.20$ mm and $L_2 = 11.40$ mm. As the lengths of the MCF segments are short, the periods of the reflection spectra are long, and thus, it is not possible to observe two consecutive maxima in the monitored wavelength range. The shadowed area beneath the solid line represents the reflection spectrum observed when two segments of MCF, one with $L_1 = 12.20$ mm and the other with $L_2 = 11.40$ mm, were spliced together, but one segment of MCF was rotated 180° with respect to the other. The reflection spectrum of the SMF–MCF1–MCF2–SMF structure coincides with the spectrum that is obtained when the spectra shown in dotted and dashed lines are multiplied and then normalized. It can be noted that the experimental results shown in Fig. 3 agree with the simulations described in Fig. 2. Therefore, we can conclude that the reflection of the device depicted in Fig. 1(b) can be calculated with Eq. (2) as it can be treated as two SMF–MCF–SMF structures in series.

To assess the performance of our composed MCF device as a curvature sensor, we carried out simulations, which are summarized in Fig. 4. In the figure, we show the reflection spectra of an SMF–MCF1–MCF2–SMF structure built with $L_1 = 17.4$ mm and $L_2 = 18.2$ mm at different values of curvature. It was assumed that the structure was bent in the MCF1–MCF2 junction and that both segments of MCF experienced the same curvature. The curvature was assumed to be applied in four different directions with respect to the orientations of the MCF cores. Any other orientation of the cores with respect to curvature will be contained between the four cases shown in Fig. 4. From the simulations, it can be concluded that the reflection intensity of our device will increase or decrease depending on the direction of curvature. This means that our device can distinguish the amplitude and direction of curvature.

To corroborate the above predictions, a simple setup, schematically shown in Fig. 5, was implemented. The SMF segments were secured with two fiber chucks that were mounted on respective

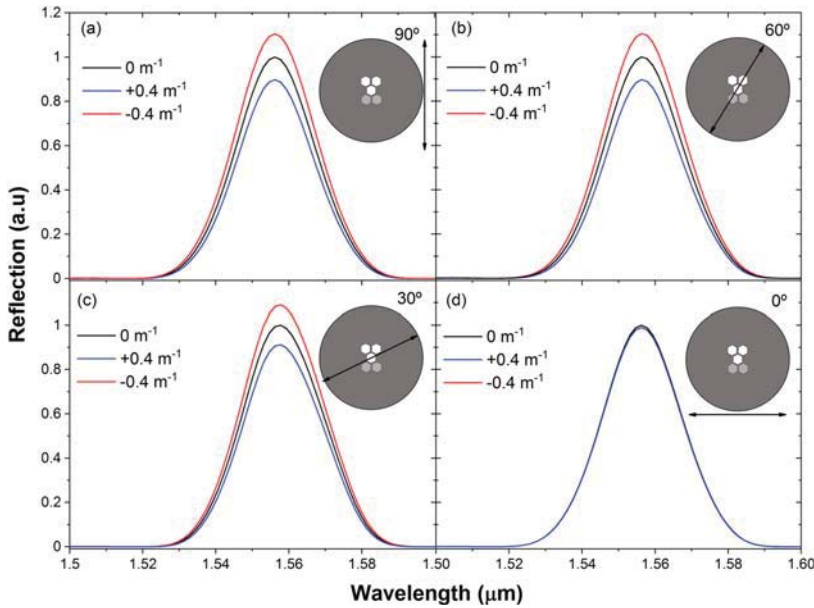


FIG. 4. Simulated reflection spectra of an SMF-MCF1-MCF2-SMF structure for different values of curvature when the orientations of the MCF cores are 90° (a), 60° (b), 30° (c), and 0° (d) with respect to the direction of curvature indicated by arrows. For the simulations, it was considered that $L_1 = 17.40$ mm and $L_2 = 18.20$ mm.

rotators (HFR001 from Thorlabs). The chuck rotators were separated by a fixed distance and were secured on an optical breadboard that was placed in a vertical position. A fiber chuck was used as a mass (20 g) to keep the tension of the fibers constant. The measurements of curvature were carried out at different orientations of the MCFs, between 0 and 180° in steps of 30°, with respect to curvature [see Fig. 5]. A translation stage with micrometer resolution was used to bend the structure in a controlled manner. The stage bent the device close to the MCF1-MCF2 junction. The value of curvature (C) on the device was calculated with the following equation: $C = 12h/d^2$ (see Ref. 12), where h is the displacement of the translation stage and d is the separation between the two fiber rotators.

In the setup described in the above paragraph, any displacement of the translation stage (or change of h) causes bending to the two segments of MCF. However, the effect on them was different

as the cores outside the center of the MCF had a different position with respect to the applied curvature. As demonstrated in Ref. 8, the asymmetric MCF used here is highly sensitive to bending. In addition, the direction of the bending can be distinguished when the MCF cores are oriented properly. Therefore, high sensitivity to curvature and capability to distinguish the direction of curvature were expected with an SMF-MCF1-MCF2-SMF structure. For this reason, we fabricated the structure as shown in Fig. 1(b) with the cores of the MCF1 and MCF2 segments rotated 180° with respect to each other.

A device fabricated with a segment of 17.4 mm of MCF fusion spliced to another segment of 18.2 mm was characterized in detail. As mentioned before, the cores of the MCF segments were in opposite orientation. Wavelength shifts and intensity changes were monitored at each value of curvature. In the former case, a spectrometer was used, while in the latter case, a low cost InGaAs photodiode (S154C from Thorlabs) was used. The light source was the same in all the measurements. The intensity of the reflected light when no curvature ($C = 0 \text{ m}^{-1}$) was applied to the device was considered as P and the changes caused by curvature as ΔP . At $C = 0 \text{ m}^{-1}$, the wavelength position of the peak reflection was considered to be λ_m and $I_R = 1$.

Figures 6(a) and 6(b) show the spectra observed when the curvature at two perpendicular directions was applied to the device described in the above paragraph. Figures 6(c) and 6(d) show the averaged curvature sensitivities that were measured in seven different orientations of the MCF. The core orientations with respect to curvature are illustrated in Figs. 4 and 5. Note that when the wavelength shift is larger, the changes in intensity are minimal and vice versa. The different values of sensitivities at different orientations of

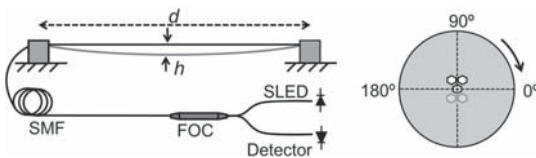


FIG. 5. Schematic diagram of the measuring setup and the sensor interrogation; h is the deflection of the device and d is the distance between the two supports. FOC is fiber optic coupler or circulator, SMF is single mode fiber, and SLED is superluminescent light emitting diode. The MCF core orientation with respect to the applied curvature is indicated.

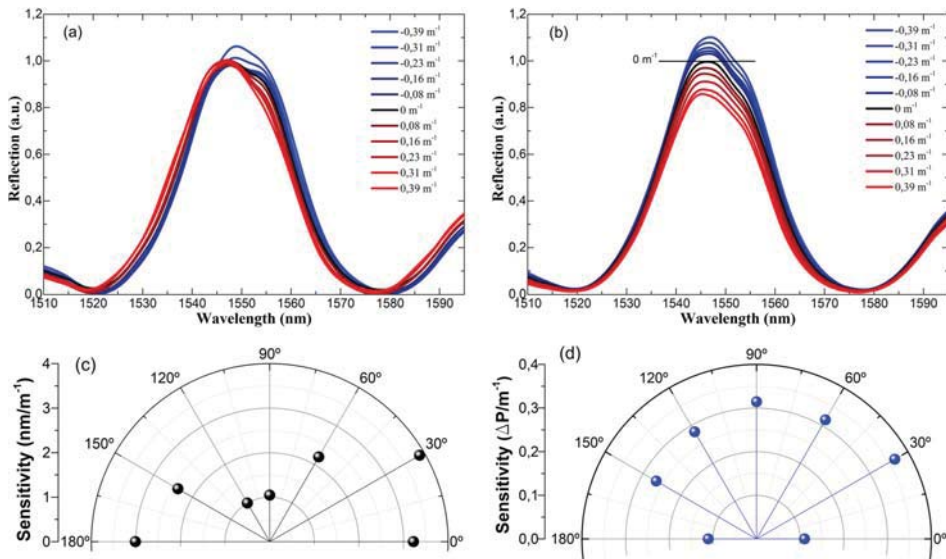


FIG. 6. [(a) and (b)] Reflection spectra at different curvatures observed when the position of the MCF was at 0° and 90° , respectively, according to Figs. 4(c) and 4(d). [(c) and (d)] Average curvature sensitivity measured by monitoring wavelength shift or intensity changes. In all cases, the MCF device had $L_1 = 17.40$ mm and $L_2 = 18.20$ mm.

the MCF cores with respect to curvature were expected due to the asymmetry of the device.

The discrepancy between simulations and experimental results with regard to shifts of the spectra may be due to the strain induced to the device and curvature of the SMF–MCF junctions, as these are inevitable in an experiment. In addition, during the measurements, the two segments of MCF may not experience exactly the same curvature. In the simulations, however, the two stubs of MCF were supposed to be exclusively subjected to the same curvature. Nonetheless, regardless of the orientation of the MCFs with respect to curvature, the wavelength position and height of the reflection peak (intensity) can be simultaneously tracked. Hence, it is possible to know the direction and amplitude of the curvature applied to the device.

The drastic changes in the reflection spectrum of the SMF–MCF1–MCF2–SMF structure when it is subjected to curvature can be explained with Eq. (2) and with the simulations shown in Fig. 4. Note that the structure is composed of two MCF segments that are highly sensitive to bending. Moreover, the reflection spectrum results from the multiplication of two spectra that move in opposite directions. This causes the height of the resulting reflection peak to increase or decrease. Consequently, the total intensity detected by using the photodetector increases or decreases depending on the direction of curvature.

In real-world applications, fiber optic curvature sensors are attached or integrated to structures or devices. Thus, to investigate the performance of our curvature sensor in more detail, the sample described in Fig. 3 was glued on a thin rectangular plastic beam that

was secured with two supports separated by a fixed distance. The orientation of the cores of the segments of MCF with respect to the plastic beam was approximately as that shown in Fig. 5. This means that a segment of MCF had two cores up and the other two cores down with respect to the direction of the curvature. Again, a translation stage with micrometer resolution was used to bend the beam upward (convex curvature) and downward (concave curvature) in a controlled manner. Other curvature orientations were not possible due to the geometry of the beam. The stage was located in the middle point of the distance between the two supports. The MCF1–MCF2 junction of the structure was located in the same position than the translation stage.

Figure 7 summarizes the behavior of our sensor when it was subjected to concave and convex curvatures. Note that the shift of the spectrum is to longer wavelengths in the former case and to shorter wavelengths in the latter case. The figure also shows the calibration curve for concave and convex curvatures. It can be noted that the response of our device in both cases is linear. From the calibration curve, the curvature sensitivities were calculated to be 791 pm/m^{-1} for concave curvature and 950 pm/m^{-1} for convex curvature. The discrepancy in the values of sensitivities of our device can be attributed to imperfections of the same, for example, the MCFs may not be exactly 180° with respect to each other. Strain applied to the MCFs and curvature of the SMF–MCF segments may also induce shifts to the reflection spectra.

In Fig. 8, we show the observed changes in $\Delta P/P$ for different values of concave and convex curvatures. It can be noted that when the device was subjected to concave curvature, the value of $\Delta P/P$

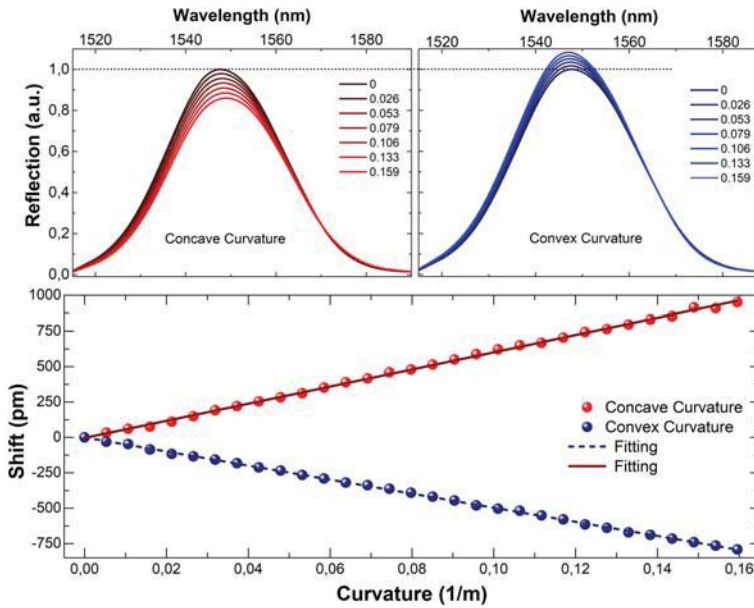


FIG. 7. Top: spectra observed when the beam shown in Fig. 5 was curved downward (left) and upward (right). The values of curvature (in m⁻¹) are indicated in the graphs. Bottom: calibration curves for concave and convex curvatures.

decreased, and it increased when the curvature on it was convex. Note also that the value of $\Delta P/P$ reached the baseline ($\Delta P/P = 0$) when the curvature was removed from the sensor. The calibration curves for concave and convex curvatures are also shown in Fig. 8. The sensitivities for concave and convex curvature were found to be almost identical, 4.66 dB/m⁻¹, which is slightly higher than those of

the intensity-modulated curvature sensors reported in Refs. 26, 37, and 38.

The results shown in Fig. 8 suggest that with our device and an inexpensive intensity-based interrogation system, it is possible to distinguish concave and convex curvatures as well as the amplitude of the applied curvature. If maximum sensitivity is needed in a particular curvature direction, the cores of the MCF can be oriented properly. We believe that these features cannot be achieved with other fiber optic curvature sensors reported so far in the literature.

CONCLUSIONS

In this work, we have reported on a simple MCF curvature sensor that comprises two short segments of strongly coupled MCF fusion spliced and rotated with respect to each other. The fabrication of the device only involves cleaving and fusion splicing; such processes are well established in the fiber optics industry. The sensor can be interrogated with a low power SLED and a miniature spectrometer or a simple photodetector. It was found that the sensor behaves as two SMF–MCF–SMF structures in series and the reflection spectrum exhibited a single, narrow peak whose height and position in wavelength can be simultaneously determined with high accuracy.

The proposed device was assessed as a curvature sensor. It was found that for this application, it is able to provide the amplitude and the direction of curvature no matter how the cores of the MCF are oriented with respect to the direction of curvature. Moreover, our sensor can be interrogated in two different manners. When the sensor was subjected to concave curvature, the reflection spectrum

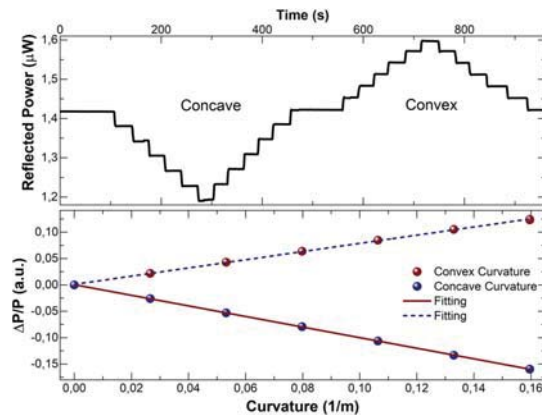


FIG. 8. Top: relative power changes as a function of time when the beam, hence the MCF segments, was bent downward (concave curvature) and upward (convex curvature). The step in each case is 0.0266 m⁻¹. Bottom: calibration curve.

shifted to red and the intensity decreased. However, when convex curvature was applied to the device, the shift was to blue and the intensity decreased.

The curvature sensitivity of the sensor reported here was found to be 4.66 dB/m^{-1} when intensity changes were correlated with curvature. Such sensitivity can be sufficient in several applications.

We believe that the composed MCF structure reported here can be used for different sensing applications. Vibrations, for example, can be translated to periodic concave and convex curvatures on the device and hence to periodic intensity changes. It also seems possible to sense pressure or lateral force as they can induce curvature to the MCF segments. Therefore, cost effective, highly sensitive force, pressure, or vibration (accelerometers) sensors can be devised with the platform proposed here.

ACKNOWLEDGMENTS

The authors acknowledge the financial support of the Spanish MINECO under Project Nos. PGC2018-101997-B-I00 and RTI2018-094669-B-C31 of the Eusko Jaurlaritz (Basque Government) under Project Nos. IT933-16 and ELKARTEK.

DATA AVAILABILITY

The data that support the findings of this study are available from the corresponding author upon reasonable request.

REFERENCES

- ¹K. Saitoh and S. Matsuo, *J. Lightwave Technol.* **34**, 55–66 (2016).
- ²E. M. Dianov, S. L. Semjonov, and I. A. Bufetov, *Quant. Electron.* **46**, 1 (2016).
- ³C. Xia, M. A. Eftekhari, R. A. Correa, J. E. Antonio-Lopez, A. Schülzgen, D. Christodoulides, and G. Li, *IEEE J. Sel. Top. Quantum Electron.* **22**, 196–207 (2015).
- ⁴S. Sivankutty, V. Tsvirkun, G. Bouwmans, D. Kogan, D. Oron, E. R. Andresen, and H. Rigneault, *Opt. Lett.* **41**, 3531–3534 (2016).
- ⁵R. G. Duncan, M. E. Froggatt, S. T. Kreger, R. J. Seeley, D. K. Gifford, A. K. Sang, and M. S. Wolfe, *Proc. SPIE* **6530**, 65301S (2007).
- ⁶J. P. Moore and M. D. Rogge, *Opt. Express* **20**, 2967–2973 (2012).
- ⁷J. Villatoro, E. Antonio-Lopez, A. Schülzgen, and R. Amezcua-Correa, *Opt. Lett.* **42**, 2022–2025 (2017).
- ⁸J. Villatoro, A. Van Newkirk, E. Antonio-Lopez, J. Zubia, A. Schülzgen, and R. Amezcua-Correa, *Opt. Lett.* **41**, 832–835 (2016).
- ⁹D. Monzon-Hernandez, A. Martinez-Rios, I. Torres-Gomez, and G. Salceda-Delgado, *Opt. Lett.* **36**, 4380–4382 (2011).
- ¹⁰Q. Wang and Y. Liu, *Measurement* **130**, 161–176 (2018).
- ¹¹J. A. Martin-Vela, J. M. Sierra-Hernandez, A. Martinez-Rios, J. M. Estudillo-Ayala, E. Gallegos-Arellano, D. Toral-Acosta, T. E. Porraz-Culebro, and D. Jauregui-Vazquez, *IEEE Photonics Technol. Lett.* **31**, 1265–1268 (2019).
- ¹²Y.-P. Wang and Y.-J. Rao, *IEEE Sens. J.* **5**, 839–843 (2005).
- ¹³D. Z. Stupar, J. S. Bajic, L. M. Manojlovic, M. P. Slankamenac, A. V. Joza, and M. B. Zivanov, *IEEE Sens. J.* **12**, 3424–3431 (2012).
- ¹⁴M. Jang, J. S. Kim, S. H. Um, S. Yang, and J. Kim, *Opt. Express* **27**, 2074–2084 (2019).
- ¹⁵L. Yuan, J. Yang, Z. Liu, and J. Sun, *Opt. Lett.* **31**, 2692–2694 (2006).
- ¹⁶H. Qu, G. F. Yan, and M. Skorobogatiy, *Opt. Lett.* **39**, 4835–4838 (2014).
- ¹⁷C. Li, T. Ning, C. Zhang, J. Li, C. Zhang, X. Wen, H. Lin, and L. Pei, *Sens. Actuators, A* **248**, 148–154 (2016).
- ¹⁸S. Zhang, A. Zhou, H. Guo, Y. Zhao, and L. Yuan, *OSA Continuum* **2**, 1953–1963 (2019).
- ¹⁹W. Chen, Z. Chen, Y. Qiu, L. Kong, H. Lin, C. Jia, H. Chen, and H. Li, *Appl. Opt.* **58**, 8776–8784 (2019).
- ²⁰J. R. Guzman-Sepulveda and D. A. May-Arrijo, *Opt. Express* **21**, 11853–11861 (2013).
- ²¹G. Salceda-Delgado, A. Van Newkirk, J. E. Antonio-Lopez, A. Martinez-Rios, A. Schülzgen, and R. Amezcua Correa, *Opt. Lett.* **40**, 1468–1471 (2015).
- ²²A. V. Newkirk, J. E. Antonio-Lopez, A. Velazquez-Benitez, J. Albert, R. Amezcua-Correa, and A. Schülzgen, *Opt. Lett.* **40**, 5188–5191 (2015).
- ²³G. M. H. Flockhart, W. N. MacPherson, J. S. Barton, J. D. C. Jones, L. Zhang, and I. Bennion, *Opt. Lett.* **28**, 387–389 (2003).
- ²⁴D. Barrera, I. Gasulla, and S. Sales, *J. Lightwave Technol.* **33**, 2445–2450 (2014).
- ²⁵D. Zheng, J. Madrigal, H. Chen, D. Barrera, and S. Sales, *Opt. Lett.* **42**, 3710–3713 (2017).
- ²⁶P. Saffari, T. Allsop, A. Adebayo, D. Webb, R. Haynes, and M. M. Roth, *Opt. Lett.* **39**, 3508–3511 (2014).
- ²⁷S. Wang, W. Zhang, L. Chen, Y. Zhang, P. Geng, Y. Zhang, T. Yan, L. Yu, W. Hu, and Y. Li, *Opt. Lett.* **42**, 4938–4941 (2017).
- ²⁸D. Barrera, J. Madrigal, and S. Sales, *J. Lightwave Technol.* **36**, 1063–1068 (2018).
- ²⁹A. W. Snyder, *J. Opt. Soc. Am.* **62**, 1267–1277 (1972).
- ³⁰N. Kishi and E. Yamashita, *IEEE Trans. Microwave Theory Tech.* **36**, 1861–1868 (1988).
- ³¹J. Hudgings, L. Molter, and M. Dutta, *IEEE J. Quantum Electron.* **36**, 1438–1444 (2000).
- ³²A. Perez-Leija, J. Hernandez-Herreon, H. Moya-Cessa, A. Szameit, and D. N. Christodoulides, *Phys. Rev. A* **87**, 013842 (2013).
- ³³R. P. Murphy, S. W. James, and R. P. Tatam, *J. Lightwave Technol.* **25**, 825–829 (2007).
- ³⁴A. Varguez-Flores, G. Beltran-Perez, S. Munoz-Aguirre, and J. Castillo-Mixcoatl, *J. Lightwave Technol.* **27**, 5365–5369 (2009).
- ³⁵D. Barrera, J. Villatoro, V. P. Finazzi, G. A. Cardenas-Sevilla, V. P. Minkovitch, S. Sales, and V. Pruneri, *J. Lightwave Technol.* **28**, 3542–3547 (2010).
- ³⁶H. Liao, P. Lu, X. Fu, X. Jiang, W. Ni, D. Liu, and J. Zhang, *Opt. Express* **25**, 26898–26909 (2017).
- ³⁷Y. Fu, H. Di, and R. Liu, *Opt. Laser Technol.* **42**, 594–599 (2010).
- ³⁸J. Shi, F. Yang, D. Yan, D. Xu, C. Guo, H. Bai, W. Xu, Y. Wu, J. Bai, S. Zhang, T. Liu, and J. Yao, *Opt. Express* **27**, 23585–23592 (2019).

eman ta zabal zazu



Universidad
del País Vasco

Euskal Herriko
Unibertsitatea



Aplikazio industrialetarako sentsore fotoniko aurreratuak

Josu Amorebieta Herrero



2021

Aplikazio industrialetara zuzendutako sentso-re fotoniko aurreratuak

Josu Amorebieta Herrerok aurkeztua

Ingeniaritzan Doktoretza

eman ta zabal zazu



Universidad
del País Vasco

Euskal Herriko
Unibertsitatea

Euskal Herriko Unibertsitatea UPV/EHU_n

Komunikazio Ingeniaritza Saila

Zuzendariak

Gaizka Durana Apaolaza

Agustín Joel Villatoro Bernardo

Bilbo, 2021

A los que estáis,

Y especialmente a los que no estáis ya con nosotros.

Después de todo lo que nos ha pasado,
¿quién se hubiera imaginado que llegaríamos hasta aquí?

Soy feliz por encima de mis posibilidades

ESKER ONAK

Nire esker onak eman nahi ditut tesian parte hartu duten pertsona eta erakunde guztiek emandako laguntza eta konfiantzagatik. Lehenik eta behin, Joseba Zubia irakasleari eskerrak eman nahi dizkiot APG/FAT Fotonika Aplikatuko Taldeko kide izateko aukera eman didalako eta uneoro transmititu didan baikortasun eta animoagatik. Bigarrenik, Gaizka Durana eta Joel Villatoro zuzendari eta aholkulariei eskerrak eman nahi nizkieke ikerketan eman didaten orientazio eta askatasunaren arteko konbinazioagatik, nire ikerketarako gaitasuna hobetzen nabarmen lagundu baitute, nire ustez. Azkenik, baina niretzat garrantzi-maila berdinean, eskerrak eman nahi dizkiet APG/FAT Fotonika Aplikatuko Taldeko kideei, haiekin igaro baititut azken urte hauek. Beti laguntzeko prest egon dira, modu desinteresatuan eta norabide egokian aholkuak emanez. Beraien familiaren parte sentiarazi naute.

Walter Margulis irakasleari eskerrak eman nahi nizkioke ere RISEn lan egiten uzteagatik pandemiak eragindako inguruabar gogorra kontuan hartuta. Oso denbora eraikitzailea izan da niretzat, lan metodologia eta kultura desberdinen inguruan ikaragarri ikasi eta pertsona oso bereziak ezagutu nituen.

Aurrekoaz gain, nire hurbileko familiari eskerrak eman nahi nizkioke honaino iristeko aukera emateagatik. Hona iristeko gainditu behar izan ditugun arazoak eta oztopoak guk ezagutzen ditugu soilik. Bizitzan hainbeste gauza atzeratu edo galdu ditut haien ondorioz, eta behin edo bitan baino gehiago amore ematea pentsarazi didaten esperientziak bizitzera bultzatu gaituzte. Badirudi azkenean

tunelaren amaieran argia ikusten ari garela, ez hain aspaldi ezinezkoa zirudiena. Eskerrik asko bihotz-bihotzez.

Azkenik, ezin ditut eskerrak bukatu nire lagunak aipatu gabe, beti egon direlako niretzat momentu txarreetan ere, eta ez hondoratzen lagundu baitidate. Lan hau eurena ere bada.

LABURPENA

Sentsore fotonikoak, eta batez ere zuntz optikoetan oinarritutakoak, heldutasun puntu batera iritsi dira non industria-ingurune batzuetarako alternatiba errealista bihurtu diren sentsore tradizionalekin alderatuta duten moldakortasun eta errendimendu handiagoari esker. Hau dela eta, sentsore optiko sentikor eta fidagarrien eskaera nabarmen handitu da alor desberdin ugarietan erabiltzeko, hala nola biomedikuntza, automobilgintza, aeronautika, gas eta petrolio industrian, adibidez.

Lan honetan, aplikazio industrialetara zuzendutako sentsore optiko desberdinak erakusten dira. Sentsore hauek aplikazio aeronautikoetarako diseinatuta daude bereziki, baina ez daude haietara mugatuta; eta neurketaren izaeraren arabera funtzionamendu-printzipio desberdinetan oinarritzen dira. Gailu bakoitzaren diseinua, fabrikazioa eta euren errendimenduaren emaitzak biltzen dituen prozesua zehatz-mehatz azaltzen da lan honetan.

Tesi hau argitaratutako artikuluen laburpen gisa egituratuta dago. Dokumentua sintesi atal baten bitartez hasten da. Bertan, ikerketa gaiaren sarrera, marko teorikoaren eta horretarako erabilitako tresna metodologikoen deskribapena, hipotesien definizioa eta haien bitartez lortu nahi diren helburuak azaltzen dira. Emaitzen laburpena eta eztabaida atal honen barne daude ere.

Lehen zati honetan deskribatutako ikerketa bi lerro desberdinetan banatuta dago: lehenengoan, aeronautika-turbinetarako zuntz optikoetan oinarritutako desplazamendu-sentsoreak garatzeko prozesua deskribatzen da. Ikerketa hori eta haren emaitzak eranskineko **1. artikuluan** daude. Bigarren zatian, sendoki akoplatutako nukleo anitzez osatutako zuntz optikoetan oinarritutako hainbat sentsore deskribatzen dira. Azken hauek

hainbat parametro desberdin neurtzeko diseinatu dira, hala nola temperatura edo bibrazioak. Gailu bakoitzera iristeko prozesua eta dagozkien emaitzak eranskineko **2., 3. eta 4. artikuluetan** daude.

2. atalean, tesian zehar egindako ikerketen ondorioak laburbiltzen dira, baita horien ondorioz ireki diren etorkizuneko ikerketa-ildoak ere. Horrez gain, tesian zehar egindako ekarpenak, argitaratutako artikulua eta kongresuak ere barne daude.

Eranskinean, tesi hau artikuluen laburpen gisa aurkeztea ahalbidetu duten argitaratutako artikulua biltzen dira.

Aurkibidea

Sintesia	1
1.1 Sarrera.....	3
1.1.1 Ikerketaren testuingurua.....	3
1.1.2 Zuntz optikoetan oinarritutako sentsoreak.....	5
1.1.1.1 Ikuspegi orokorra.....	5
1.1.1.2 Sailkapenak	8
1.1.3 Tesiaren motibazioa.....	10
1.2 Zuntz optikoetan oinarritutako desplazamendu-sentsore optikoa (OFDS).....	11
1.2.1 Sarrera eta ikerketaren testuingurua.....	12
1.2.2 Esparru teorikoa eta baliabide metodologikoak.....	15
1.2.2.1 Tip Clearance (TC) eta Tip Timing (TT) terminoen definizioa	15
1.2.2.2 TCa eta TTA neurtzeko teknologiak.....	18
1.2.2.3 Zuntz optikoetan oinarritutako TC- eta TT-sentsoreak.....	19
1.2.2 Hipotesia eta helburuak.....	21
1.2.2.1 Errendimendu betekizunak.....	21
1.2.2.2 Eredu matematikoa.....	27
1.2.3 Laburpena eta emaitzak	31
1.2.3.1 Besoen zigilatze-puntari zuzenduta.....	31
1.2.3.2 Besoen datum-ari zuzenduta	37
1.3. Sendoki akoplatutako nukleo anitzez osatutako zuntz optikoetan (MCF) oinarritutako sentsoreak.....	45
1.3.1 Sarrera eta ikerketaren testuingurua.....	45
1.3.1.1 Industriarentzat interesa duten parametroak.....	45
1.3.1.2 Sentsore optiko estrintsekoak	46
1.3.2 Alor teorikoa eta tresna metodologikoak.....	49
1.3.2.1 Sendoki akoplatutako MCFen eredu matematikoa..	49
1.3.2.2 Fabrikazio-tresnak eta galdeketa-konfigurazioa	56

1.3.3 Hipotesia eta helburuak	57
1.3.4 Laburpena eta emaitzak	58
1.3.4.1 Temperatura-sentsoreak	58
1.3.4.1.1 Sentikortasun handiko 7cMCFan oinarritutako sentsorea	58
1.3.4.1.2 Sentikortasun handiko 3cMCFan oinarritutako sentsore iraunkorra	64
1.3.4.2 Noranzko guztietarako tolestura-bektore sentsorea.	73
1.3.4.3 Azelerometroa	82
1.3.4.4 Noranzko sentikortasuna duen kurbatura-sentsorea	91
Bibliografia	93
Ondorioak	103
2.1 OFDS	105
2.1.1 Ondorioak	105
2.1.2 Aurkeztutako gailuen hobekuntza/garapena	106
2.1.3 Ikerketa-lerro berriak	107
2.2 MCFtan oinarritutako sentsoreak	108
2.2.1 Ondorioak	108
2.2.2 Aurkeztutako gailuen hobekuntza/garapena	109
2.2.3 Ikerketa-lerro berriak	110
2.3 Tesiaren ekarpenak	111
2.3.1 Argitalpenak	111
2.3.2 Hitzaldiak	112
Eranskina: Argitaratutako lanak	115
1. artikulua	117
2. artikulua	133
3. artikulua	143
4. artikulua	157

Irudien aurkibidea

1. irudia: Zuntz optikoen funtzionamendu-printzipioa.	6
2. irudia: Zuntz optikoan oinarritutako detekzio-sistema baten eskema.	7
3. irudia: Jet-motako motor baten etapen eskema. Jeff Dahl, CC BY-SA 4.0, Wikimedia Commons-en bitartez.	14
4. irudia: a) Konpresore baten <i>blisk</i> batean aire-fluxuaren norabidea (gezi beltza), eta besoek jasaten dituzten bibrazioen norabideak kolorezko geziez adierazita. b) Presio baxuko turbina bateko beso baten gainean eragiten dituzten bibrazio-mota desberdinen norabideak kolore desberdineko geziez adierazita.	15
5. irudia: Presio baxuko turbina-etapa batetan TCaren xehetasuna.	16
6. irudia: TTaren definizioaren irudikapen eskematikoa.	17
7. irudia: Intentsitatearen modulazioan oinarritutako sentsoaren erantzun-kurba tipikoak zuntz-antolaketa desberdinetarako. Kolore gorriak eta urdinak zuntz igorle eta hartzaileak adierazten dituzte, hurrenez hurren.....	21
8. irudia: a) Probak egiteko erabili den haize-tunela. Errotorearen kokapena puntu-lerro gorritz osatutako laukizuzenak adierazten du. b) Haize-tunelean turbina-etapa baten muntaketaren xehetasuna.	22
9. irudia: a) Errotore baten 3D eredua. Puntu gorriak estalkian zunda sartzeko egin den zuloaren posizioa adierazten du. Puntu-lerro beltzak sentsoarea norantz zuzenduta dagoen adierazten du. b) Zunda optikoa estalkian egindako zuloan nola sartu eta haize-tuneleko karkasan nola instalatu denaren xehetasuna.....	23
10. irudia: Turbinaren beso baten punta generiko baten 3D eredua.	24

11. irudia: Lan honetan TCaren neurketarako garatutako OFDSaren geometria generikoa.	26
12. irudia: Argi-izpiek definitutako geometriaren eskema.	27
13. irudia: Neurketarako baldintzen irudikapen eskematikoa.....	32
14. irudia: Zunda-puntaren amaierako argazkia eta fabrikatutako zuntz-sortaren eskema.....	33
15. irudia: 1. eskualderako kalibrazio-kurba simulatua eta esperimentala.	34
16. irudia: a) Zunda optikoa turbinan muntatzeko erabilitako egokitzailea. b) Zunda optikoaren xehetasuna egokitzailearen babes-hodiaren barruan.....	34
17. irudia: Karkasan instalatutako zunda optikoaren kokapena eta TCaren definizioa.....	35
18. irudia: Probetan zehar eskuratutako seinaleen adibidea. Gorriz nabarmendutako zatia erreferentzia gisa erabili zen islapen eredu berezia zuen besoari dagokio.	36
19. irudia: Beso bakoitzari dagozkion TC eta desbiderapen estandarraren balioak 4258 rpm-ko WPan 1100 bira eman ondoren.	37
20. irudia: Hobetutako zunda optikoaren mutur bakoitzeko argazkia eta eskema.	39
21. irudia: OFDS guztiaren eskema, hura osatzen duen hardware elementu nagusienak adieraziz.....	39
22. irudia: Probetan erabilitako gailuen eskalatutako zeharkako sekzioen irudikapen eskematikoa.	40
23. irudia: Karkasan zehar sentsoreak nola instalatu zirenaren irudikapen eskematikoa.....	40

24. irudia: Sentsoreen erantzuna-kurbak. Grisez adierazitako eremuak, sentsoreen lan-eremua adierazten dute turbinaren probetan zehar.	41
25. irudia. 55. besoaren seinalea hiru sentsoreen arabera. Horiekin batera, seinale ideala ere adierazten da.	42
26. irudia: Nolabaiteko irregulartasunak dituzten besoen uhin-formen adibidea. Proben ondoren egindako besoen ikuskapenean, portaeraren jatorria erakutsi zen. a) Beltzez margotutako zati bat duen beso eta b) urradura bat duen beso baten kasua.....	43
27. irudia: Beso bakoitzari dagokion TC balioa eta desbiderapen estandarra 3627 rpm-ko puntuan 20000 bira eta gero.....	43
28. irudia. Mikroskopiaarekin ateratako argazkiak: a) hobetutako OFDSa eta b) 1. artikuluko OFDSa.	44
29. irudia: Desakoplatuta dauden uhin-gida biren eskema.	49
30. irudia: Akoplatuta dauden gida biren eskema.	50
31. irudia: Aztertu diren MCFen egitura generikoaren eskema.	53
32. irudia: MCF generiko baterako nukleo zentral eta ondoko nukleoetan dagoen potentzia akoplatu normalizatuaren bilakaera igorritako uhin-luzeraren funtzio gisa.	55
33. irudia: SMF berebean seriean jarritako n MCF segmentuen eskema.	56
34. irudia: Galdeketa-konfigurazioaren eskema.	57
35. irudia: a) 7cMCFaren sekzioaren argazkia eta b) tenperatura-sentsorearen eskema.	59
36. irudia: 7cMCFak dituen supermodu ortogonal akoplatuak. a) SP_{01} eta b) SP_{02}	59
37. irudia: Fabrikatutako eta simulatutako gailuen espektroak. ...	61

38. irudia: Proben ondoren egindako fabrikatutako tenperatura-sentsorearen argazkia.	62
39. irudia: Espektroaren bilakaera tenperaturaren arabera.	63
40. irudia: Paketatutako sentsorearen eta 7cMCF biluziaren kalibrazio-kurbak eta egokitzapen linealak.	63
41. irudia: 3cMCFaren sekzioa.	65
42. irudia: 3cMCFak dituen supermodu ortogonal akoplatuak. a) SP ₀₁ eta b) SP ₀₂	65
43. irudia: Fabrikatutako laginen eskemak eta giro-tenperaturan (T=25 °C) dagozkien espektroak.	67
44. irudia: Δn ren tenperaturarekiko simulazioak 7cMCFrentzako (triangelu beltzak) eta 3cMCFrentzako (zirkulu beltzak).	68
45. irudia: a) Espektroaren bilakaera tenperaturaren arabera eta b) Paketatutako 25 mm-ko 3cMCFko gailuaren kalibrazio kurba.	69
46. irudia: Hobetutako gailuaren (goian) eta 2. artikuluko gailuaren (behean) argazkiak probak egin ondoren.	71
47. irudia: Tenperaturaren araberrako espektroen bilakaera a) 3cMCF eta b) 7cMCFa duten gailuetan.	72
48. irudia: 3cMCFan (zirkulu beltzak) eta 7cMCFan oinarritutako (triangelu beltzak) sentsoreen kalibrazio-kurbak.	72
49. irudia: Sentsorearen egituraren eskema.	74
50. irudia: 3cMCFa duten 8 mm-ko fabrikatutako eta simulatutako gailuen espektroak.	77
51. irudia: a) tolestura aplikatzeko konfigurazioaren eskema eta b) 3cMCF-aren biraketaren noranzkoa, ebaluatutako puntuak eta aplikatutako tolestura norabidea adierazita daudelarik.	78
52. irudia: Bildutako espektroak eta neurtutako parametroen denboraren araberrako eboluzioaren bi ziklo sentsorea geziak	

adierazten duen norabidean tolestu zenean eta 3cMCFa a) b) 90° eta c) d) 270° hasierako 0° posizioarekiko biratu zenean, hurrenez hurren.	79
53. irudia: Bildutako espektroak eta neurtutako parametroen denboraren arabera eboluzioaren bi ziklo sentsorea geziak adierazten duen norabidean tolestu zenean eta 3cMCFa a) b) 180° eta c) d) 360° hasierako 0° posizioarekiko biratu zenean, hurrenez hurren.	80
54. irudia: Uhin-luzeraren desplazamendua eta argi-potentziaren aldakuntzaren sentsibilitatea eta dagokien desbiderapen estandarrek zuntzaren posizio bakoitzerako.	81
55. irudia: Sentsibilitate eta desbideratze estandarren irudikapen polar normalizatua balio absolutuan.	82
56. irudia: Gailuaren eskema.	83
57. irudia: 3cMCFko segmentu bakoitzaren espektro simulatuak eta haien arteko emaitza egitura elkarketatik a) zuzen, b) gorantz eta c) beherantz okertzen denean. Geziek kasu bakoitzaren okerduraren norabidea, uhin-luzeraren desplazamendua edo potentzia-aldaketa adierazten dute. MCF1en nukleoak V moduko konfigurazioan daude, eta MCF2koak alderantzizko V itxurako konfigurazioan daude....	84
58. irudia: Simulatutako (marradun lerro beltza) eta fabrikatutako gailuen (lerro beltza) espektro normalizatuak. Bi kurben maximoa 1554 nm inguruan dago eta ez dago bigarren mailako lobulurik. 11.4 mm-ko (marradun lerro gorria) eta 12.2 mm-ko (marradun lerro urdina) segmentuen espektro simulatuak ere agertzen dira. 44. ekuazioan adierazten den moduan, euren arteko produktuaren emaitza marradun lerro beltza da.	85
59. irudia: Esperimentuaren alboko eta goiko bista eskematikoak. Lehen planoan, fabrikatutako azelerometro optikoa plakaren gainazalera nola itsatsi zen erakusten da. Nukleo gorriak MCF1renak dira eta urdinak MCF2koak. Nukleo zentral gorriak MCF1 MCF2ren	

aurrean dagoela adierazten du, nukleo zentral komuna partekatzen baitute.	86
60. irudia: Potentzia neurketen emaitzak fabrikatutako gailu optikoan. a) Hiru kasu adierazgarrienen erantzuna denboraren arabera. b) FFT anplitudeak 30 Hz-tik 1 mHz-ra bitarteko frekuentzientzat 1 Vpp-ko seinale sinusoidalerako. Neurtutako maiztasunaren ardatza eskala logaritmikoan dago.....	87
61. irudia: Uhin-luzeraren desplazamenduaren emaitzak fabrikatutako gailu optikoan. a) Hiru kasu adierazgarrienen erantzuna denboraren arabera. b) FFT anplitudeak 30 Hz-tik 1 mHz-ra bitarteko frekuentzientzat 1 Vpp-ko seinale sinusoidalerako. Neurtutako maiztasunaren ardatza eskala logaritmikoan dago.	87
62. irudia: Azelerazioaren emaitzak azelerometro elektronikoan. a) Hiru kasu adierazgarrienen erantzuna denboraren arabera. b) FFT anplitudeak 30 Hz-tik 1 mHz-ra bitarteko frekuentzientzat 1 Vpp-ko seinale sinusoidalerako. Neurtutako maiztasunaren ardatza eskala logaritmikoan dago.....	88
63. irudia: Potentzia neurketen emaitzak fabrikatutako gailu optikoan. a) Hiru kasu adierazgarrienen erantzuna denboraren arabera, eta b) FFT anplitudeak 6 Hz-eko eta 1 Vpp-tik 10 mVpp-ra doan anplitudea duen igorritako seinale sinusoidal batentzat...	89
64: irudia: Uhin-luzeraren desplazamenduaren emaitzak fabrikatutako gailu optikoan. a) Hiru kasu adierazgarrienen erantzuna denboraren arabera, eta b) FFT anplitudeak 6 Hz-eko eta 1 Vpp-tik 10 mVpp-ra doan anplitudea duen igorritako seinale sinusoidal batentzat.	89
65. irudia: : Azelerazioaren emaitzak azelerometro elektronikoan. a) Hiru kasu adierazgarrienen erantzuna denboraren arabera, eta b) FFT anplitudeak 6 Hz-eko eta 1 Vpp-tik 10 mVpp-ra doan anplitudea duen igorritako seinale sinusoidal batentzat.....	89
66: irudia: Fabrikatutako azelerometro optikoaren kalibrazioa.	90

67. irudia: 3. artikuluko (lerro urdina) eta 4. artikuluko (lerro beltza) fabrikatutako gailuen espektroak.....	92
68. irudia: Neurketen konfigurazioaren diagrama eskematikoa.	93
69: irudia: Kurbatura desberdinetarako espektroak gailuaren posizioa a) 0° eta b) 90° zirenean, hurrenez hurren.....	93
70. irudia: Batez-besteko kurbaturaren sentikortasunaren irudikapen polarra a) uhin-luzeraren desplazamenduari eta b) intentsitate-aldaketei dagokienez.....	94

Taulen aurkibidea

1. taula: Emaitzen laburpena	67
2. taula: Emaitzen laburpena	73

1. atala

Sintesia

Atal honetan ikerketaren ikuspegi orokorra azaltzen da. Tesiaren testuinguruari eta motibazioari buruzko sarrera bat egin eta gero, tesi-lanean zehar landutako bi ikerketa-lerro nagusien deskribapen zehatzak ematen dira. Lehenengo ikerketa-lerroari dagokionez, aeronautikaren sektorean turbinen monitorizaziorako zuntz optikoetan oinarritutako desplazamendu-sentsore baten diseinu, fabrikazio eta aplikazioa sakonki aztertzen da. Bigarren ikerketa-lerroan, sendoki akoplatutako nukleo anitzez osatutako zuntz optikoak abiapuntutzat hartuta, industriarentzat interesgarriak izan litezkeen zenbait sensore optiko aurkezten eta eztabaidatzen dira. Sentsoreok parametro fisiko desberdinak detektatzeko diseinatuak izan dira.

1.1 Sarrera

1.1.1 Ikerketaren testuingurua

Industriaren helburua kostu txikiagoko eta errendimendu hobetua duten produktuak diseinatu eta ekoiztea da. Beraz, fabrikazioak optimizatzeko balio duten mekanismoen bilaketek interes handia daukate. Horretarako, produkzio-prozesuaren urrats guztietan, prototipoen probetatik hasita produkzio-lerroetara heldu arte, kalitate-kontrol proba zehatzak egiten dira. Kalitate-proba horiek egiteko, industriak sentzore sendo, fidagarri eta sentikorren beharrezkoak du, berebiziko garrantzia duten hainbat parametro denbora errealean kontrolatzeko helburuarekin. Horiei esker, fabrikazio-prozesu guztiari buruzko informazio kritikoa lor daiteke, zehaztasunez kontrolatzeko eta ezaugarritzeko balioko duena. Adibidez, prototipoen diseinuetan egon daitezkeen akatsak detektatu eta zuzentzeko produkzio-lerroetara bidali baino lehen, produkzio-katean dauden elementu guztiek fabrikazioan zehar baldintza berdinak dituztela egiaztatzeko, edo industria bakoitzak ezartzen dituen estandar zorrotzak betetzen direla ziurtatzeko erabil daitezke. Beraz, agerikoak dira sentzore-sistema fidagarri eta sentikorren instalazioak ekartzen dituen onurak kalitatearen hobekuntza eta ekonomia aurreztei dagokienez.

Aipatutako prozesuak kontrolatzeko, industrian ohikoa da teknologia helduetan oinarritutako detekzio-sistemak aurkitzea. Izan ere, fidagarriak, iraupen luzekoak eta kostu eraginkorrekoak direla frogatu izan da denboran zehar. Teknologia horiek normalean izaera elektriko edo elektronikoko osagaietan oinarrituta daude. Azken horien funtzionamendu-mekanismoa inguruneko sarrera fisiko bat neurtzean oinarritzen da, jasotako informazioa gizaki batek edo makina batek interpretatu dezakeen seinale elektriko batean bihurtzeko. Horien eredu garbia termopareak eta galgak dira, besteak

beste [1]. Izaera elektriko horrek kasu askotan arazorik sortzen ez badu ere, kezkarako arrazoi bihur daiteke arriskutsuak eta segurtasun neurri zorrotzak behar dituzten lan-inguruneetan, adibidez gas eta petrolio instalazioetan, zentral nuklearretan, egitura aeronautikoetan, eta abar. Interferentzia elektromagnetiko bortitzek sentso horien jardun normalean zailtasunak eragin ditzakete. Bestalde, tenperatura altuek ere fidagarritasun-mailan negatiboki intziditzen dute.

Aipatutako mugapen horiek gainditzeko bidean, teknologia fotonikoan oinarritutako soluzioak aukera interesgarria bihurtu dira sentso elektrikoaren osagarri gisa, bai eta horien ordezkari gisa ere zenbait kasutan. Sentso fotonikoetan oinarritako partikula fotoia da, edo argi-kuantua. Fisikaren ikuspegitik, fotoiek ez dute masarik geldi daudenean, ez dute elkarrekintzarik elektroiekin, eta baldintza zehatz batzuetan soilik elkarrengaitan dute beste fotoi batzuekin. Hori dela eta, fotoien portaera aurreikus eta kontrola daiteke oinarritako lege fisiko batzuei jarraituz, nahiz eta eremu elektromagnetiko edo magnetiko, erradiazio edo tenperatura altuak dituzten inguruneetan egon [2]. Sentso fotonikoak oso sentikorak dira parametro ugariaren neurketan, hala nola tentsioa, presioa, tenperatura, eta abar. Ezaugarri hauei esker potentzial handia dute, ingurune etsaietan instalatu eta lan egiteko ezinbesteko baldintzak baitira [3]. Sentso fotonikoak, argia gidatzeko elementu desberdinez baliatuz (elementu optikoak, laserrak, zuntz optikoak, eta abar), gai dira jomugako parametro fisiko edo kimikoren bat zehaztasunez neurtzeko argiaren ezaugarriaren batean (edo batzuetan) gertatzen diren aldaketak aztertuz. Teknologia fotoniko desberdinak lehen aldiz agertu zirenean garestiak ziren arren, hauen etengabeko garapenak eta hobekuntzak kostua pixkanaka jaitea eragin dute, gaur egun ekonomikoki aukera bideragarria bihurtu arte. Horren ondorioz, fotonikak aurrerapen handia bizitzen ari da izaera desberdineko aplikazio-eremu ugarietan. Adibidez, sentsoez gain, komunikazio, informazio biltegi eta datu-prozesaketa eremuetara ere

hedatu da. Beraz, fotonikan oinarritutako gailuek garrantzi handia lortzen ari dira industrian, eta gaur egun posible da teknologia honetan oinarritutako sensorizazio-sistema komertzialak aurkitzea hainbat produkzio-prozesutan, hala nola, bereizmen handiko metrologian eta laser bidezko kalibratze-sistematan [4].

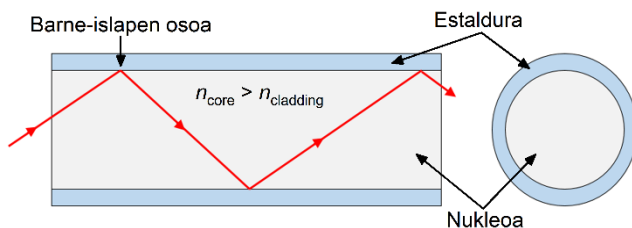
Fotonikan oinarritutako detekzio-soluzio desberdinen artean, zuntz optikoa deritzon teknologian oinarritutakoak nabarmendu behar dira. Historikoki, teknologia hori komunikazio-sareen gaitasunak hobetzeko jaio zen. Hala ere, industria horretatik eratorritako berrikuntza asko detekzio-sistematan aplikatzen joan izan dira, eta hau gertatu izan den neurrian, zuntz optikoetan oinarritutako detekzio-soluzioen gaineko interesak ere goraka egin du. Izan ere, gaur egun zuntz optikoaren teknologiak heldutasun puntu interesgarria lortu du, eskain dezakeen errentagarritasunaren eta errendimenduaren arteko konpromiso-mailari begiratzen badiogu. Puntu honetan gogoratu beharra dago sentzore fotonikoek, arestian aipatutako sentzore tradizionalen aldean, ingurune etsaietan jarduteko duten abantaila. Aipatutako guztiagatik, industriari interes handia erakutsi du ekoizpen-prozesuetan edo kalitate-kontrolerako probetan sentzore fotonikoak integratzeko, eta bereziki zuntz optikoan oinarritutakoak dira interesgarriak, zuntzaren teknologiak eskaintzen dituen abantaila ugarietarako.

1.1.2 Zuntz optikoetan oinarritutako sentzoreak

1.1.1.1 Ikuspegi orokorra

Zuntz optikoa giza ile baten tamainaren pareko uhin-gida dielektriko zirkular eta malgu bat da. Zuntzaren materialari dagokionez, normalean silizez eginda dagoen arren, polimeroz egindakoa ere interes praktikoa handikoa da. Bere oinarritzko egiturari dagokionez, nukleo batez eta hau inguratzen duen estaldura zentrukide batez

osatuta dago. Funtzionamendu-printzipioa barne-islapen osoan oinarritzen da, argi-iturri batek (laser bat edo diodo argi igorle bat) igorritako argia nukleoan zehar eraginkortasun handiz hedatzea ahalbidetzen duena hain zuzen ere (ikus 1. irudia). Argiaren hedapena nukleora soilik mugatzeko, azken honen errefrakzio-indizea (n_{core}) estaldurak duena baino handiagoa izan behar du (n_{cladding}) [5].

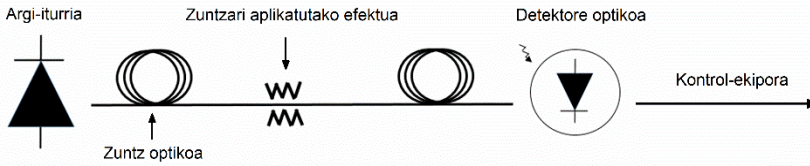


1. irudia: Zuntz optikoen funtzionamendu-printzipioa.

Ezaugarri guzti horiei esker, zuntz optikoak sarri erabili dira argia modu oso eraginkorren transmititzeko. Gainera, kable elektrikoekin alderatuta, zuntz optikoek banda-zabalera handiagoa eskaintzen dute, potentzia-galera txikiagoak eragiten dituzte, eta esparru elektrikoan hain arruntak diren interferentzia-arazoei aurre egiten diete. Horrezaz gain, elementu-sentsore gisa ere oso baliagarriak direla frogatu dute, parametro fisiko eta kimiko ugariren aurrean sentikortasun-maila handia dutela erakutsi baitute, argiaren propietate bat edo besteri eraginez (argi-intentsitatea, polarizazioa, fasea, eta abar).

Konfigurazio sinpleenean, zuntz optikoetan oinarritutako sentsoreek, zuntz optikoaz gain, argi iturri bat eta galdeketa-gailu bat dituzte bere oinarritzko osagaien artean. Zuntzari eragiten dion efektu fisikoaren intentsitate-mailaren arabera, zuntzean zehar hedatzen den argiaren propietate bat edo beste era proportzionalen modulatzeko da. Argiaren gainean eragindako transformazio hori galdeketa-gailura iristen da, eta bertan korrante elektrikoan bihurtzen da kontrol-ekipoan bere prozesaketari ekin ahal izateko. (ikus 2. irudia). Oinarritzko eskema horretatik abiatuta, neurketa-

sistemen konfigurazio konplexuagoak eraiki daitezke hainbat sensoreren erantzuna multiplexatu edo anitz parametroren aldibereko neurketa egin nahi denean.



2. irudia: Zuntz optikoan oinarritutako detekzio-sistema baten eskema.

Beraz, zuntz optikoetan oinarritutako sentsoerek abantaila ugari dituzte, hala nola tamaina eta pisu txikia, instalatzeko erraztasuna, konfigurazio sinpletasuna, materialen barnean integratzeko edo gainazaletara itsasteko gaitasuna eta immunitate elektromagnetikoa. Horrez gain, distantzia luzetan seinaleak bidaltzeko gaitasuna dute galera handirik sortu gabe eta inolako energia hornidurarik behar gabe, multiplexazioa onartzen dute aldi berean sentsoere kopuru handiak erabiltzeko eta ingurune etsaietan (goi tentsioko lineak, ingurune erradiaktiboak, tenperatura altuak, substantzia korrosiboak, eta abar) erabiltzeko egokiak dira.

Hala ere, sentsoere elektronikoak baino garestiagoak izan ohi dira eta galdeketa egiteko ekipamendua sentsoere elektronikoena baino konplexuagoa izan ohi da, nahiz eta azken ezaugarri hau azken hamarkadetan nabarmen hobetu den. Gainera, neurketa-testuinguruaren arabera, zuntz optikoa kaltetu edo hautsi ez dadin, instalazio-metodo eta prozedura zehatzak behar dituzte, eta galdeketa-sistemek erabiltzen hasi aurretik oinarritzko trebakuntza eskatzen dute.

Beraz, sentsoere sistema bat planifikatzerako orduan, sentsoere egokia eta sentsoere-teknologia egokia hautatzea funtsezkoa da. Horretarako, kasu bakoitza modu independentean aztertu behar da. Tesi honen ikerketaren esparruan, zuntz optikoaren erabilerak abantaila handiak eskaintzen ditu, dokumentu honetan zehar azalduko den moduan.

1.1.2.2 Sailkapenak

Zuntz optikoetan oinarritutako sentsoreak modu desberdinetan sailka daitezke. Ohikoak diren sailkapen batzuk laburbilduko ditugu jarraian.

Neurtuko diren magnitudeen izaeraren arabera sailkapen hau egin daiteke: mekanikoak, elektromagnetikoak, kimikoak, fluidoen fluxuak neurtzeko direnak, termikoak eta biomedikoak [6].

Beste sailkapen bat sentsore intrintsekoak eta estrintsekoak bereiziz egin daiteke [7]. Alde batetik, sentsore intrintsekoetan, argiaren aldaketa edo modulazioa zuntz barruko efektu batek eragiten du. Normalean, efektu horiek xurgapena, dispersioa edo fluoreszentzia izaten dira [8]. Beste alde batetik, sentsore estrintsekoetan, argiaren aldaketa edo modulazioa zuntzetik kanpo dagoen efektu batek (edo zenbaitek) eragiten du. Sentsore hauen bidez bibrazioa, biraketa, desplazamendua, abiadura, azelerazioa, momentua eta bihurtura bezalako parametroak zehaztasun handiz neur daitezke [9].

Banaketa espazialaren arabera, sentsore optikoak hiru mota desberdinetan sailka daitezke. Puntu bakarreko sentsoreek zuntzaren puntu diskretu batean ematen dute neurketa, banatuko sentsoreek zuntz osoan zehar neurketak emateko gai diren bitartean [10]. Erdibideko irtenbide gisa, kuasibanatutako sentsoreak aurki daitezke [11]. Sentsore horiek hainbat sentsoreren erantzuna multiplexatuz sortzen dira, sentsore bakoitzaren neurketa lortuz. Zenbait kasutan, neurketaren bereizmen espazialaren beharrianak oso zorrotzak ez direnean, puntu anitzeko sentsoreek banatuko sentsoreek baino aukera hobea dira, merkeagoak baitira eta funtzionamendu errazagoa baitute.

Argian modulutzen den parametroaren arabera, honako sailkapen hau egin daiteke:

1. Intentsitatearen modulazioan oinarritutako sentsoreak: zuntzean zehar doan argiaren intentsitatearen aldaketan oinarritutakoak dira. Sortzen den aldaketa eta zuntzari aplikatutako efektuaren intentsitate-maila elkarren proportzionalak dira. Sentsore hauek komertzialki erakargarriak dira, errentagarritasunaren eta sinpletasunaren arteko konbinazio ona eskaintzen baitute [12].
2. Uhin-luzeraren modulazioan oinarritutako sentsoreak: sentsore hauek zuntzean hedatzen den argiaren uhin-luzeraren desplazamenduaren azterketan oinarritzen dira. Azken hori zuntzari aplikatutako zenbait faktorek eragiten dute. Sentsore hauen abantaila nagusienetakoa zuntz bakar batean multiplexatzeko eta egitura handietan erraz instalatzeko edota integratzeko gaitasuna da, hala nola urtegieta, hegazkinetan, zubietan, eta abar. Ezaugarri horiek erakargarri egiten ditu Egitura-Osasanaren Jarraipena (ingelesez Structural Health Monitoring edo SHM) egiteko aplikazioetan [13]. Ziur aski sentsore horien arteko ezagunenak zuntz optikoan grabatutako Bragg sareetan (ingelesez Fibre Bragg Grating edo FBG) oinarritutakoak dira. FBGak teknologia heldu batetan oinarrituta dago, urtetan zehar komertzialki eskuragarri egon dena.
3. Fasearen modulazioan oinarritutako sentsoreak: teknika interferometrikoak erabiltzen dira bi argi-izpi koherenteren arteko elkarrekintzan sortzen den fase-aldaketa antzemateko. Era honetako sentsoreetan, izpietako bat erreferentzia gisa erabiltzen den bitartean, beste izpia neurtu nahi den efektuaren eraginpean dago. Eskema horrek neurketari sentikortasun handia ematen dio, nahiz eta konfigurazio konplexuak eta lerrokatze zehatzak behar izaten diren era egokian funtziona dezaten [14]. Mota honetako sentsorerik ohikoenak Mach-Zehnder, Michelson, Fabry-Perot eta Sagnac interferometroetan oinarritzen dira.

4. Polarizazioaren modulazioan oinarritutako sentsoareak: Efektu magneto-optikoa bezalako fenomenoen eraginez, zuntzaren barnean hedatzen den argiaren polarizazioaren aldaketa neurtzean oinarritzen dira. Ohikoa da korronea edo presioa bezalako magnitudeak neurtzeko erabiltzea [15].
5. Espektroaren modulazioan oinarritutako sentsoareak: sentsoare hauek espektroskopian oinarritzen dira, eta beraien funtzionamendu-printzipioa transmititutako espektroaren aldaketak aztertzean oinarritzen da [16].
6. Argiaren sakabanaketaren modulazioan oinarritutako sentsoareak: Raman, Brillouin edo Rayleigh bezalako efektuak erabiltzen dira sakabanatutako argiaren azterketa egiteko. Honen bitartez, neurtu nahi den parametroaren anplitude edota posizioa detekta daitezke [17].

1.1.3 Tesiaren motibazioa

Tesi honen ikerketaren helburu orokorra zuntz optikoetan oinarritutako sentsoare berriak diseinatzea eta fabrikatzea da; sinpleak, sendoak, funtzionatzeko errazak eta gaur egunean indarrean dauden soluzio optikoak edo elektronikoak baino errendimendu hobea eskaintzeko gai direnak. Lan honetan deskribatutako gailuak puntu bakarreko edo puntu anitzeko sentsoare gisa funtzionatzeko garatu dira, industriaren testuinguru ugarran ahalik eta malgutasun handienarekin implementatzeko.

Lan honetan aurkezten diren sentsoareak aplikazio konkretu bakoitzaren neurketa-eskakizun espezifikotara moldatu dira. Hori dela eta, lan honetan agertzen diren sentsoareak funtzionamendu-printzipio desberdinetan oinarritzen dira eta konfigurazio desberdinak dituzte neurtuko den magnitudearen eta implementazio-

testuinguruaren arabera, betiere beraien errendimendua optimizatzeko helburu argiarekin.

Tesi honetan bi sentzore mota desberdin diseinatu, fabrikatu eta probatu dira. Alde batetik, turbina eta konpresore aeronautikoetan funtzionatzeko diseinatutako desplazamendu-sentsore optikoa dago. Kasu honetan neurketak kontakturik gabe gertatu behar direnez, islatutako argiaren intentsitatean oinarritutako sentzorea garatu da. Beste alde batetik, industriarako interesgarriak diren hainbat parametro (tenperatura, bibrazioak, kurbadura, eta abar) neurtzeko sentzore optikoak azaltzen dira. Azken sentzore horiek funtzionamendu-printzipio bera partekatzen badute ere, kasu konkretu bakoitzean sentzorearen konfigurazioa neurketa-baldintza bakoitzera moldatu izan da errendimendua optimizatzeko asmoz.

1.2 Zuntz optikoetan oinarritutako desplazamendu-sentsore optikoa (OFDS)

Atal honetan, neurrira diseinatutako zuntz optikoetan oinarritutako desplazamendu-sentsore optiko (OFDS) bat garatzeko prozesu osoa aurkezten da. Sentzore hau motor aeronautikoetan denbora errealean *Tip Clearance* deritzon parametroaren neurketa egiteko erabiliko da. Prozesuaren deskribapena aplikazio honetarako eskakizunak definituz hasten da. Jarraian sentzorea haize-tunel batetan dagoen eskalan egindako turbina batetan probatzen da, eta azkenik lortutako datu gordinen prozesamendua eta analisisa dator. Horrezaz gain, sentzorearen funtzionamendu-printzipioaren ikuspegi matematikoa ere azaltzen da, bai eta sentzorearen errendimenduaren ebaluazioa ere sentzore komertzial baten ikuspuntutik begiratuta.

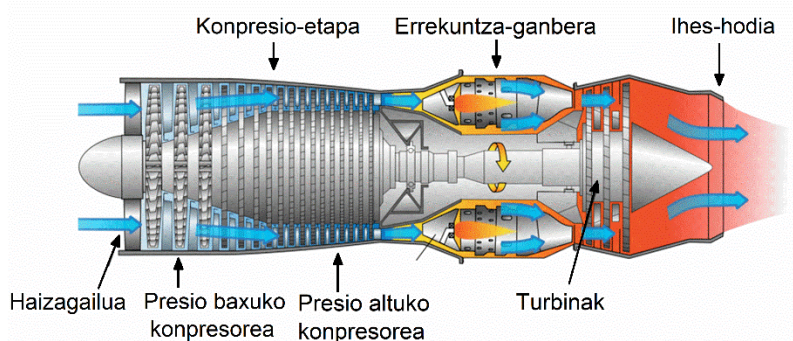
1.2.1 Sarrera eta ikerketaren testuingurua

Atal honetan azaldutako ikerketaren helburua sentsore optiko oso sentikor, sinple eta sendoak garatzea da, distantzia edota desplazamendua bereizmen handiarekin neurtzeko gai dena. Neurketa horiek oso garrantzitsuak dira sektoreentzat, sentsore horiek normalean metrologia eta kalibrazioetarako erabiltzen baitira 4.0 industriaren barruan [18, 19]. Azken horien adibide anitz kalitatearen balioztatze-prozeduretan aurki daitezke, aurreproduktzio prozesuetatik hasita, produktzio-osteko prozesuetara arte. Adibidez, automobilgintzan edo makina-erremintaren sektorean ugari aplikatzen dira, fabrikatutako artikuluen neurriak dagozkien simulazio-ereduekin alderatzeko, batik bat. OFDSeK ematen duten neurketaren kalitate-maila esanguratsuaz gain [20], beste zenbait abantaila interesgarri eskaintzen dituzte industria ingurunean inplementatzeko, hala nola abiadura handiko neurketak, temperatura-tarte zabaletan funtzionatzeko gaitasuna eta moldagarritasuna. Ezaugarri guzti horien konbinazioak OFDSak erakargarri bihurtzen ditu "zero akats" jomugako ekoizpena lortzeko [21].

Metrologiak zeresan handia duen sektoreen artean, industria aeronautikoa da ziurrenik erreferentzia nagusia errendimendu eta fidagarritasunari dagokionez, eskakizun zorrotzenak baititu. Sektore hori oso zorrotza izan ohi da fabrikazio eta balioztatze-prozesuei dagokienez, eta, horren ondorioz, teknologia helduak erabiltzen dituzte, hots, fidagarritasun eta errendimendua urtetan zehar egiaztatuta dutenak. Horien barne termopareak edo tentsio galgak aurki ditzakegu, besteak beste. Sentsore hauek normalean osagai aeronautikoak ezaugarritu eta euren egituren osasunaren egiaztatzeko erabiltzen dira, elementu horiek kalte batzuk jasan ditzaten diseinatu baitira beren errendimenduan eraginik izan gabe [22]. Hori dela eta, ikuskapen zorrotzak egin behar dira balizko kalte horiek segurtasun-marjinen barruan mantentzeko. Testuinguru

horretan, ikuskapenaren kalitate-estandarrak betetzeko eta aldi berean ikuskatze-prozesurako behar den denbora murrizteko gai diren sentsoreak bilatzen dira. Azken honen arrazoia konpainien eta fabrikatzaileen etekinak handitzea da, osagaiak baliozkotzeko behar den denbora edota hegazkinak lurrean dauden denbora laburtu baitezakete. Horregatik guztiagatik, baldintza zorrotz horiek betetzeko eta aeronautika bezalako industria kontserbadore batean alternatiba errealista bihurtzeko gai den OFDS bat garatzea erronka handia da.

Hegazkin bat osatzen duten osagai ugarien artean, motorrak osagai kritiko eta garestienak dira ziurrenik. 3. irudian ikus daitekeen moduan, elkarren jarraian muntatutako hainbat etapaz osatuta daude. Aire-fluxuaren norabideari erreparatzen badiogu, lehenengo fasea haizagailua da. Bere helburua bultzatzen duen airearen zati bat motorraren barrualdera bideratzea da, presio baxuko konpresorera bidaliz. Presio baxuko eta presio altuko konpresoreek bigarren etapa osatzen dute, eta hauen eginkizuna airearen presioa handitzea da, errekontzaren eraginkortasuna proportzionalki handitu dadin. Hirugarren etapa errekontza-ganbera da, non erregaia eta bigarren etapatik datorren presio altuko airea nahasten diren. Azkenik, laugarren etapa kokatzen da. Presio altuko eta baxuko turbinek osatzen dute, airearen fluxutik energia-zati bat erauzteaz arduratzen direnak haizagailua eta konpresoreak biraka iraun dezaten.

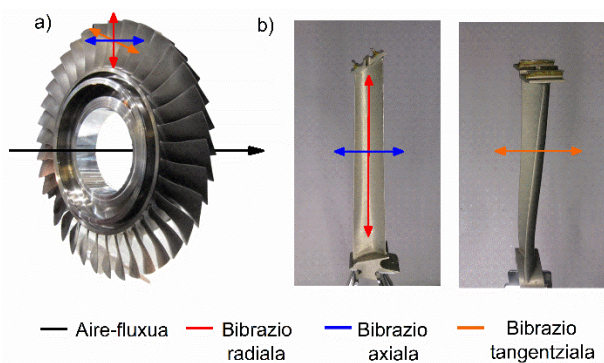


3. irudia: Jet-motako motor baten etapen eskema. Jeff Dahl, CC BY-SA 4.0, Wikimedia Commons-en bitartez.

Normalean, turbina eta konpresoreen etapak besodun diskoek (ingelesez *bladed disk* edo *blisk*) osatzen dituzte, hau da, disko batek eta bertan ahokatutako beso-serie batek. Izaera honetako motor baten funtzionamenduan hainbat parametro kontrolatu behar dira, hala nola tenperatura, bibrazioak, presioa, biraketa-abiadura, etab. [23]. Horien artean, *blisk*-etan besoen bibrazioak ezaugarritzea berebiziko garrantzia du, motorraren eraginkortasunarekin eta segurtasunarekin lotura zuzena baitu. Gainera, oraingoz, motor-fabrikatzaileak honen inguruan dituzten beharrian guztiak asetzen dituen teknologia bat ez da existitzen.

Blisk bat abiadura handian biratzen ari denean, besoek jasan ditzaketen bibrazioak hiru motakoak izan daitezke: erradialak, tangentialak eta axialak (ikus 4. irudia). Bibrazio erradialek besoaren luzeran aldaketak eragiten dituzte eta, beraz, besoak motorraren estalkitik gertuago edo urrunago egotea eragiten dute. Distantzia horri (besoaren muturraren eta estalkiaren barne-gainazalaren artekoa) *Tip Clearance* (TC) deritzo, eta oso parametro esanguratsua da motorraren segurtasunerako eta eraginkortasunerako. Besoen bibrazio tangentialak airearen fluxuarekiko norabide perpendikularrean gertatzen dira, eta *Tip Timing* (TT) izeneko teknikaren bidez ezaugarritu ahal dira [24]. Metodo hori erabiliz, besoen bibrazioen amplitudea eta maiztasuna

banan-banan kalkulatzeko eta neurtzeko ahalbidetzen da. Horretarako, ezinbestekoa da beso bakoitzaren iritsiera-denbora neurtzea eta konparatzea idealki izan beharko zuenarekin. TCaren eta TTaren izaerak direla eta, sentso berbera erabil liteke parametro biak neurtzeko [25]. Azkenik, bibrazio axialak airearen fluxuaren norabide berean gertatzen dira. Nahiz eta bibrazio horiek motorren errendimendurako garrantzitsuak izan, ikerketa-lan honen eremutik kanpo daude.



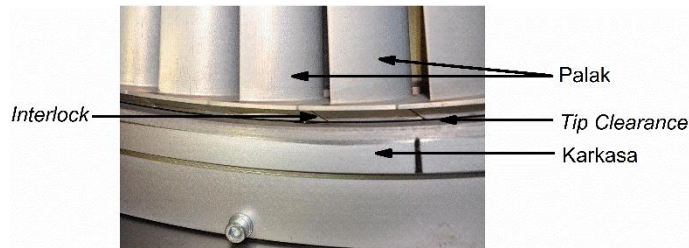
4. irudia: a) Kompresore baten *blisk* batean aire-fluxuaren norabidea (gezi beltza), eta besoek jasaten dituzten bibrazioen norabideak kolorezko geziez adierazita. b) Presio baxuko turbina bateko beso baten gainean eragiten dituzten bibrazio-mota desberdinen norabideak kolore desberdineko geziez adierazita.

1.2.2 Esparru teorikoa eta baliabide metodologikoak

1.2.2.1 *Tip Clearance* (TC) eta *Tip Timing* (TT) terminoen definizioa

Aurreko atalean aipatu den bezala, beso baten TCa, norabide erradialean besoaren muturretik motorren karkasarainoko distantziari deritzo (ikus 5. irudia). Lasaiara horrek airearen fluxuan ihes bat sortzen du, motorren funtzionamenduari laguntzen ez diona eta, beraz, eraginkortasuna murrizten duena [26]. Parametro honen garrantzia hain da handia ezen, 0.25 mm gutxitzen bada,

erregai-kontsumoa %1 murriztea eta ihes-gasen temperatura 10 °C-tan jaitea eragiten duen, motorreko osagaien bizitza luzatuko lukeena [27]. Zifra horiek lehen begiratuan txikiak direla diruditen arren, pandemiaren aurretiko aire-trafikoaren datu globalak hartzen baditugu abiapuntutzat, urtean 167 milioi dolar inguru aurreztea ekarriko luke [28]. COVID-19 pandemiaren ondorioz, batetik hegazkin-konpainia askoren egoera ekonomiko zaila, eta bestetik pandemia aurreko hegaldi-kopurura itzultzeko prozesua motela izango dela ikusita, datu horiek kontuan hartzeko modukoak dirudite. Abantaila ekonomikoez gain, ingurumenarentzako onurak ere aipatu beharrekoak dira, gas eta zarata-igorpenek sortutako kutsadura murriztuko litzatekeelako.



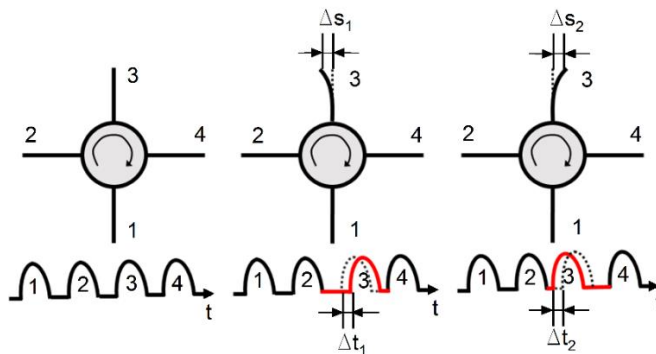
5. irudia: Presio baxuko turbina-etapa batetan TCaren xehetasuna.

Arestian aipatutako ezaugarrien konbinazioa dela eta, oso interesgarria da industriarentzat TCa ahalik eta txikiena duen sistema bat integratzea, beti ere segurtasun distantzia minimo baten gainetik funtzionatuz, besoek estalkia gehiegi urratzeagatik gerta litekeen beso-hauste baten ondoriozko istripu larria ekiditeko. Halako sistemak TC Kontrol Sistema Aktiboak gisa ezagutzen dira, eta TCaren balioa aldatzea ahalbidetzen dute karkasaren espantsio termikoa kontuan hartuz. Horretarako, aire-fluxuaren zati bat karkasara birbideratzen da balbula espezifiko batzuen bitartez, TCa uneoro optimizatu ahal izateko eta, beraz, motorraren eraginkortasuna handitzeko [29].

2 eta 8 mm bitarteko TC balioak energia sortzeko erabiltzen diren turbinetan ohikoak diren arren, motor aeronautikoen TC balioak

gutxitan dira 3 mm baino handiagoak [30]. TC balio horiek motorraren funtzionamendu-erregimenaren arabekoak dira batez ere (aireratzea, gurutzaldi-abiadura edo lurreratzea), eta, orokorrean, TC balioak motorraren biraketa-abiadurarekin alderantziz proportzionalak direla esan daiteke: abiadura handitzen den heinean, TCa murriztu egiten da eta alderantziz. Hala ere, hori ez da TCan eragina duen faktore bakarra, osagaien zahartzeak ere garrantzia baitu [31, 32].

TCak motorraren eraginkortasunari buruzko informazioa ematen duen bitartean, TT izenarekin ezagutzen den teknikak *blisk*-en osasun-egoerari buruzko informazioa eskaintzen du [24]. Horretarako, teknika horrek besoen bibrazio tangentialak ezaugarritzen ditu, nekeak eragindako balizko akatsak aurreikustea ahalbidetzen duena [33]. Azken hau informazio erabakigarria da motor fidagarri eta seguruagoak diseinatu eta garatzeko. TTak besoen okerduren anplitudea eta maiztasuna zehaztea ahalbidetzen du besoen sensorearen posiziora iristeko behar duten denbora neurtuz eta puntu horretara iristeko beharko luketen denbora teorikoarekin alderatuz. Iritsiera denbora teorikoa besoen inolako bibrazio gabe daudeneko kasuan puntu berberera iristeko behar duten denbora da (ikus 6. irudia).



6. irudia: TTaren definizioaren irudikapen eskematikoa.

TTa neurtzeko, hainbat sentsore instalatu behar dira estalkian elkarren segidan biraketa noranzkoari jarraituz, beso bakoitzaren bibrazioa bere biraketa bidearen atal zehatz batean zehar jarraitzeko [34]. Neurtutako iritsiera denboraren eta dagokion balio teorikoaren arteko aldea jakinda, bai eta biraketa-abiadura eta turbinaren erradioa ere, besoen bibrazioen anplitudea kalkula daiteke. Datu horiek prozesatuz gero, motorraren beste zenbait parametro garrantzitsu ere ezagutu daitezke, hala nola besoen bibrazioen maiztasuna, diskoaren diametro-noduluen kopurua, etab.

1.2.2.2 TCa eta TTa neurtzeko teknologiak

TC eta TT neurketak besoek abiadura handian biratzen ari diren testuinguruan egin behar dira. Beraz, kontakturik gabeko neurketak emateko gai diren sentsoreak behar dira besoen mugimendu naturalean eraginik ez izateko edo nolabait haien mugimendua ez baldintzatzeko. Horretarako, motore aeronautikoen fabrikatzaileek kontaktu gabeko neurketa sentsore-mota anitz garatu dituzte, teknologia desberdinetan oinarrituta daudenak. Horien artean, kapazitiboak, induktiboak eta mikrouhinetan eta zuntz optikoetan oinarritutako sentsoreak nabarmendu behar dira.

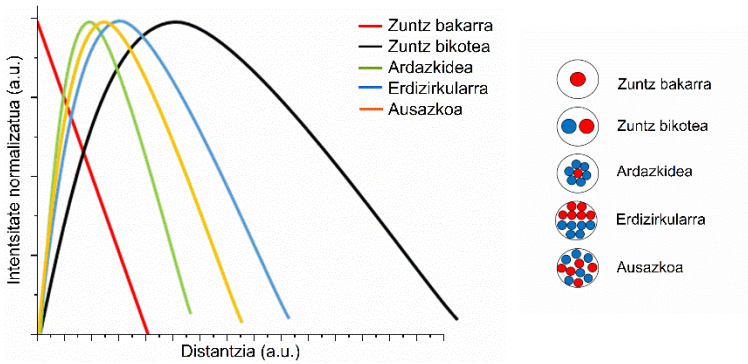
Sentsore kapazitiboak TC sentsorerik hedatuenak dira ziur aski, eskaintzen duten sinpletasun, sendotasun eta errentagarritasunari esker. Haien eragozpen nagusiak bereizmen espazial baxua, banda-zabalera txikia eta funtzionamendu tarte txikiak dira. Horrez gain, ondo funtzionatzeko, besoak material eroalez eginda egon behar dira [35]. Sentsore induktiboak arinak eta errentagarriak dira, eta bitartean oztoporen bat dagoenean ere neurtzeko gai dira. Hala ere, haien konfigurazioa konplexua izan ohi da, kalibrazio-kurba aldez aurretik ezagutu beharreko faktore askoren menpe baitago, hala nola temperatura, besoaren forma edo ardatzaren biraketa-abiadura [36]. Deskarga-zundetan oinarritutako sentsoreak aurreko teknologiaren

moldaketa arrunt bat dira. Horrelako sentsoreek besoak material eroalez osatua izatera behartzen dituzte, eta *blisk*-ean beso guztien artean gertatzen den TC baliorik baxuena soilik ematen dute [37]. Mikrouhin-sentsoreak tenperatura altuetan zehaztasun handiz funtzionatzeko gai dira, eta turbinaren errekontza hondakinek ez daukate inolako eraginik haiengan. Teknologia horren eragozpen nagusia prezioa da, seinaleak prozesatzeko ekipamendu konplexu eta astunak behar baititu behar bezala funtzionatzeko [38, 39]. Aipatutako eragozpenetariko asko zuntz optikoetan oinarritutako sentsoreek gaindi ditzakete, banda-zabalera, bereizmen eta sentikortasun handiak eskaintzen baitituzte [25]. Horrez gain, moldakortasun handia dute eta ez dute konfigurazio konplexurik behar funtzionatzeko. Hala ere, beraien eragozpen nagusia daukaten errekontza hondakinekiko sentikortasun handia da, argia aztertuz funtzionatzen baitute. Beraz, zunda-burua kutsatuta badago, haien errendimenduan eragina izan dezake. Oztopo hori konpondu behar da mota honetako sentsoreak denbora luzez errekontza ematen den turbinetan erabili ahal izateko. Hala ere, lan honetako testuinguruan, non probak errekontza gabeko haize-tunel batean egin diren, sentsore optikoak dira soluziorik onena, ez baitago tunel barruan errendimenduan eragina izan dezakeen errekontza hondakinik.

1.2.2.3 Zuntz optikoetan oinarritutako TC- eta TT-sentsoreak

Zuntz optikoetan oinarritutako sentsoreen artean, hiru konfigurazio nagusi daude distantzia-neurketa zehatzak egiteko: sentsore interferometrikoak, Doppler efektuan oinarritutako sentsoreak eta islatutako argiaren intentsitate-modulazioan oinarritutako sentsoreak. Sentsore interferometrikoek bereizmen eta sentikortasun handia eskaintzen dute, nahiz eta, ondo funtzionatzeko, normalean argi-iturri koherentea eta konfigurazio optiko oso egonkorra izan behar duten [40]. Baldintza horiek konplikatu egiten dute era

horretako sentsoreak bibrazioen eraginpean dauden turbinetan instalatzea. Doppler efektuan oinarritutako sentsoreen funtzionamendua, besoen biraketazko mugimenduak islatutako argiaren maiztasunean eragiten duen aldaketa aztertzean datza, seinalea prozesatu ondoren distantzia baloreetara itzul daitekeena hain zuzen ere [41]. Bereizmen eta sentikortasun handia eskaintzen dute, nahiz eta beharrezkoak diren elementu desberdinak garestiak diren. Azkenik, islatutako argiaren intentsitate-modulazioan oinarritutakoak bi zuntz mota behar ditu, bata igorlea eta bestea hartzailea. Zuntz igorleak igorritako argia besoaren kontra talka egin eta gero, argi islatuaren zati bat zuntz hartzaileek biltzen dute. Bildutako argiaren intentsitatea aztertuz, sentsoretik besomuturrerainoko distantzia era zehatzean determina daiteke [42]. Sentsore hauek oso errazak eta moldakorak dira. Izan ere, haien errendimendua optimizatzeko edo erantzun-kurba zehatz bat lortzeko, erraz egoki daitezke, bertan dauden zuntz igorle eta hartzaileen antolamendua aldatuz. Mota horretako sentsore-konfigurazio arruntenean laburpena 7. irudian erakusten da, dagozkien erantzun-kurbekin batera. Igorle eta hartzaile gisa funtzionatzen duen zuntz bakarraren kasuan izan ezik, jokabide ia-linealeko bi eskualde desberdin antzeman daitezke erantzun-kurban: lehenengo eskualdeak (hemendik aurrera 1. eskualdea deituko dena) malda positiboa du, eta bigarren eskualdeak (hemendik aurrera 2. eskualdea deituko dena) berriz, malda negatiboa. 1. eskualdeak sentikortasun eta linealtasun handiagoa erakusten du 2. eskualdearekin alderatuta, nahiz eta lehenengoaren kasuan erregimen linealean lan egiteko distantzia-tartea nabarmen txikiagoa izan.



7. irudia: Intentsitatearen modulazioan oinarritutako sentsoreen erantzun-kurba tipikoak zuntz-antolaketa desberdinetarako. Kolore gorriak eta urdinak zuntz igorle eta hartzaileak adierazten dituzte, hurrenez hurren.

Aipatutako konfigurazio optikoetako bat hautatzea neurketa-eskakizunen arabera izango da. Lan honen kasuan, neurketa-baldintzak jarraian azaltzen dira.

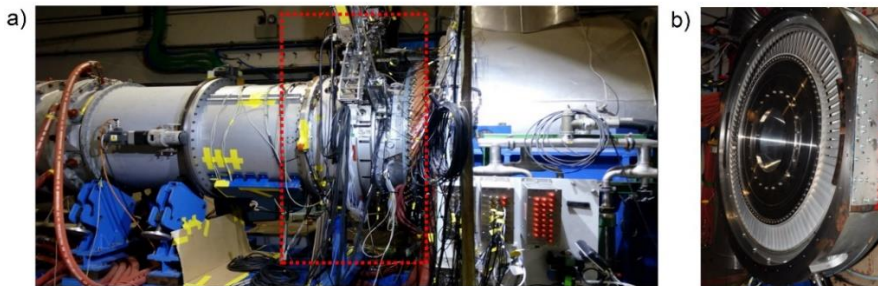
1.2.2 Hipotesia eta helburuak

1.2.2.1 Errendimendu betekizunak

Ikerketa honetan erabilitako OFDSa, gure ikerketa kolaboratzaile den Centro de Tecnologías Aeronáuticas (CTA) zentroak definitutako zehaztapenen arabera diseinatu zen. CTAREN instalazioak Zamudion (Bizkaia) dagoen Bizkaiko Zientzia eta Teknologia Parkean daude, APG/FAT Fotonika Aplikatuko Taldeko laborategitik 20 km ingurura, ikerketa-kideen arteko komunikazioa eta berrelikadura nabarmen erraztu zituena. Bertako instalazioetan haize-tunel bat dago, non motor aeronautikoen eskalan egindako turbinak fabrikatzen eta probatzen diren.

Aurreko paragrafoan aipatutako haize-tunela etengabeko aire fluxu transonikoa duen proba-bankua da, non presioa, tenperatura eta masa-fluxua bezalako parametroak banaka kontrola daitezkeen.

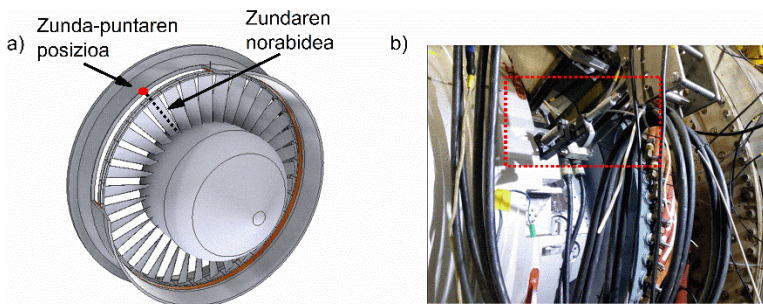
Modu horretan, Mach eta Reynolds zenbakiak modu independentean alda daitezke motorraren aireratze, gurutzaldi-abiadura eta lurreratze baldintzak ahalik eta hoberen simulatzeko. Haize-tunelak metro bateko diametroa du eta 7800 rpm-ra biratzeko gai den ardatz bakarra du (ikus 8. irudia). Aire hornitzeko, 3.7 eta 5 MW-ko bi energia konpresore elektriko erabiltzen dira. Konpresore horiek gehienez 18 kg/s-ko masa-emaria eta 4.5 barreko presioa hornitzeko gai dira. Horrez gain, tunelaren barruan, temperatura giro temperaturatik 160 °C-ra arte doi daiteke. Aipatzekoa da haize-tunela 800 presio-seinale eta 200 temperatura-seinale lortzeko ere prestatuta dagoela, baita ardatzaren biraketa-abiadura ezagutzeko aukera ematen duen *Once Per Revolution* (OPR) seinalea neurtzeko ere [43]. Lehen esan den bezala, sentsoreak probatu diren haize-tunelian ez dago errekuntzarik. Horrenbestez, testuinguru honetan, teknologia optikoa da TCaren neurketetarako aukerarik egokiena, zuntz optikoak erabiltzearen abantaila guztiak aporetza baitaitezke sentsorearen puntan kutsaduraren eragozpen kritikorik gabe. Garrantzitsua da OFDSa beirazko zuntzez egitea, 160 °C-tan polimerozko zuntz optikoen funtzionamendu-eremutik kanpo baitago. Horrez gain, beiraz egindako zuntzak aukeratzeko arrazoi gehigarria, temperatura altuagoetan ere erabilgarria izango den OFDSa garatzeko asmoa da.



8. irudia: a) Probak egiteko erabili den haize-tunela. Errotorearen kokapena puntu-lerro gorri osatutako laukizuzenak adierazten du. b) Haize-tunelian turbina-etapa baten muntaketaren xehetasuna.

Motor aeronautiko batetan, errekuntza ganbera eta gero, elkarren jarraian muntatuko turbina talde bat aurki daiteke. Horietako bakoitza errotore eta estatore batez osatuta dago. Estatorea karkasara finkatuta eta besoz osatua dago, eta bere helburua airearen fluxuaren abiadura handitzea eta errotorera birbideratzea da. Errotorea ardatzera finkatuta dago eta abiadura handian biratzen ari diren besoez osatuta dago. Bere helburua estatoretik datorren aire fluxutik energia ateratzea da. Turbina-karkasaren barneko gainazala material urragarri batez estalita dago. Geruza hori besoen biraketaren ondorioz higatu egiten da. Izan ere, turbinaren besoak estalkitik ahalik eta hurbilen biratzeko diseinatuta daude, karkasaren eta besoen artean ahalik eta estankotasun hoberena lortzeko.

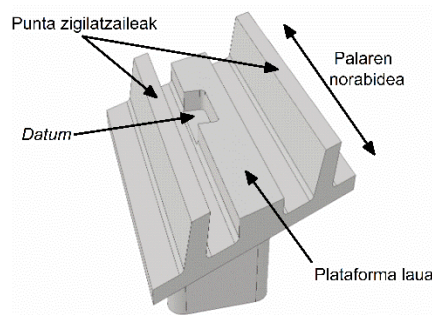
CTAko haize-tunelean, turbinen etapa desberdinak probatzen dira. TC neurketak egiteko, sentsoreak estalkian erradialki instalatuta daude errotorearen zentrorantz begira eta biratzen ari diren besoekin lerrokatuta (ikus 9. irudia). Besoek jasaten dituzten bibrazioak kontuan hartuta, sentsoreak instalatzeko karkasan egin behar diren zulo txikiak zehazki egin behar dira lerrokatzea bermatzeko eta sentsorearen errendimendua optimizatzeko.



9. irudia: a) Errotore baten 3D eredua. Puntu gorriak estalkian zunda sartzeko egin den zuloaren posizioa adierazten du. Puntu-lerro beltzak sentsorea norantz zuzenduta dagoen adierazten du. b) Zunda optikoa estalkian egindako zuloan nola sartu eta haize-tuneleko karkasan nola instalatu denaren xehetasuna.

Bsoen punten diseinuak turbina bakoitzerako eta turbinaren etapa bakoitzerako ere espezifikoak dira. Hortaz, ohikoa da tamaina eta

forma aldetik besoen punta desberdinak izatea turbina beraren fase desberdinetan. Normalean, besoen puntak punta zigilatzaile biren artean kokatutako gainazal lau-mehe batez osatuta daude. Punta zigilatzaileak bi ertz zorrotz eta mehe dira (1 mm-tik beherako zabalera dute), eta karkasan jarritako urratzeko materialetik ahalik eta gertuen egoteko edota marratu ahal izateko diseinatuta daude. Punta bien arteko plataforma lauak, berriz, besoen fabrikazio-prozesuaren kalitatearen ebaluazioa egiteko markatzaile gisa jokatzeko du (ikus 10. irudia).



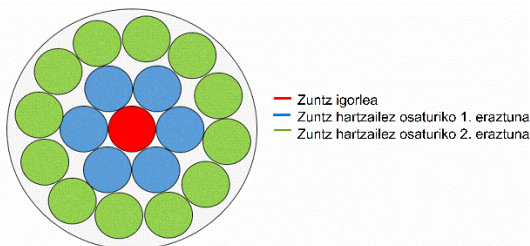
10. irudia: Turbinaren beso baten punta generiko baten 3D eredua.

OFDSak hornitutako neurketak CTArako baliozkoak eta baliagarriak izan daitezzen, proba guztietan bete beharreko errendimendu baldintza batzuk zehaztu zituzten:

- Ukipenik gabeko neurketa egin besoen portaera mekanikoa ez oztopatzeko.
- Gutxienez 25 μm -tako TC zehaztasuna neurketetan.
- Bereizmen handia. Sentsorea besoak banan-banan detektatzeko gai izan behar da, banan-banan aztertu eta ezohiko balioak dituztenak zalantzarik gabe identifikatzeko.
- Sentikortasun eta bereizmen handia neurketetan, besoetako inperfekzio edo akatsak antzeman ahal izateko.
- Gutxienez 1 mm-ko luzera duen eskualde lineala erantzun-kurban. Behin betiko interes-tartea probatuko den turbinak definituko du.

- Sentsorearen sendotasuna neurketak burutuko diren ingurune erasokorrari aurre egiteko, batez ere bibrazioei dagokienez.
- Instalaziorako sinpletasun eta erraztasuna. Zuntz-sortaz ez ezik, gainerako hardwareak ahalik eta arruntena izan beharko lirateke, erraz eta azkar ordezkatu ahal izateko, hondatu edo apurtzen badira.
- Errentagarritasun ekonomikoa produktu komertziala garatzeko asmoarekin. Zuntz-sortaz aparte, ez luke neurrirra egindako beste hardwarerik egon behar, eta zuntz-sorta ere zuntz estandarrez osatua egon beharko litzateke.

Aipatutako betebeharrak guztiak kontuan hartuta, TCaren neurketarako OFDS bat diseinatzeko orduan, islatutako argiaren intentsitate-modulazioan oinarritutako sentsore optikoak egokienak zirela erabaki zen. Sentsore mota horiek duten konfigurazio anitzetan (ikus 7. irudia), zuntz ardazkideen antolamendua hautatu zen. Nahiz eta konfigurazio hori ez den onena erantzun-kurbaren luzerari dagokionez [44], duen simetria zirkularra dela eta, errorearen besoekin lerrotzeko arazoak ekiditen da. Hau oso ezaugarri garrantzitsua da, estalkian instalazioa nabarmen errazten duelako, CTaren eskakizunetarako bati erantzun egokia emanez. Horrez gain, zuntz hartzailez osatutako eraztun zentrokide independenteetan oinarritutako konfigurazioa aukeratu zen (ikus 11. irudia). Modu honetan, bi eraztunetatik jasotako seinale diferentziala kontuan hartuz, besoen islagarritasunean egondako aldaketak, argi iturrian izandako gorabeherak edo potentzia optikoaren galerak izan ditzaketek efektuak leundu edo gutxi daitezke.



11. irudia: Lan honetan TCaren neurketarako garatutako OFDSaren geometria generikoa.

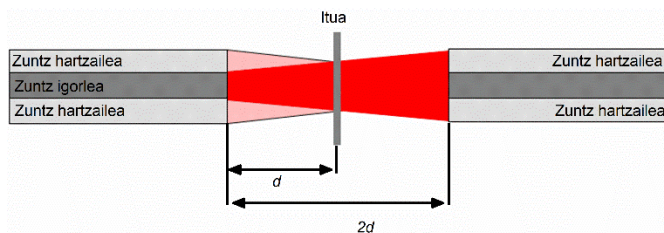
Literatura espezializatuan erraza da distantzia neurtzeko mota horretako sentsoare asko aurkitzea [45-48]. Sentso horietako gehienak laborategian probatu dira ispilu bat gainazal islatzaile gisa hartuta, eta horietako batzuk espezifikoki egokitu dira ingurune kontrolatuetan dauden turbina-simulagailuetan funtzionatzeko [49-51]. Hala ere, oso gutxi probatu dira benetako motor baten baldintzapean. Kasu gutxi horietan, erantzun-kurbaren 2. eskualdean jardun zuten, hau da, 1. eskualdea baino luzeagoa dena baina bereizmen eta sentikortasun gutxiago eskaintzen dituen [25]; edo 1. eskualdean jardun zuten egoera oso zehatz eta berezietan, non TC aldaketa oso txikiak espero ziren [52]. Horrez gain, kasu horietan, neurketak ez ziren denbora errealean egin, baizik eta emaitzak lortzeko seinalea postprozesatu behar izan zen, denbora errealeko prebentziozko mantentze-sistema gisa aritzeko gaitasuna mugatuz.

Muga guzti horiek gainditzeko, lan honetan, 1. eskualdean funtzionatzeko eta denbora errealean TCa neurtu eta haren balioak emateko gai den OFDSaren diseinua deskribatzen da, 2. eskualdearen erabilera soilik egoera ez hain zorrotzetarako edo konparazio gisa utziz. Zuntz optikoaren sorta diseinatzeko erabili den eredu matematikoa beheko atalean azaltzen da, baita OFDS guztiaren hardware konfigurazioa ere. Ikerketa honi buruzko informazio osoa eta bere emaitzen laburpena eranskinen **1. artikuluan**, 1.2.3 atalean eta [53] erreferentzian agertzen dira, hain zuzen ere.

1.2.2.2 Eredu matematikoa

OFDSeko zuntz-sortaren erantzun-iragarpenik zehatzena lortzeko, funtsezko parametroa zuntz igorlearentzat (TF) aukeratutako hedapen-eredua da. Intentsitate-modulazioan oinarritutako OFDStan non zuntzak axialki lerrokatuta eta guztiz argiztatuta dauden neurketa guztian zehar, argiaren hedapen gausstarraren eredua iragarpen zehatzak egiteko balio du. Hala ere, zuntz hartzaileen argiztapena partziala den OFDSetarako, lan honetan gertatzen den bezala, argiaren hedapen gausstarraren ereduak ez du hainbesteko zehaztasunik eskaintzen eta hedapen kuasi-gausstarraren ereduak ezarritako hurbiltze matematikoa beharrezkoa da [44, 54]. Azken horrek Gausen eredua moldatu egiten du perturbazio-parametro deiturikoak sartzeko [55], bi izpien hedapen-ereduen arteko desberdintasuna adierazten dutenak.

Izpien hedapen-ereduaren adierazpen matematikoak zuntzaren irteeran definitzen den distantziaren arabera eremu optikoaren erradio efektiboa definitzen du ($q(d)$). TF eta zuntz hartzailearen (RF) muturrak plano berean daudela kontuan izanik, optika geometrikoaren bidez, d distantzia jakin batean islatutako eta ondoren bildutako argia distantzia bikoitzera ($2d$) kokatutako zuntz bakar batek biltzen duenaren baliokidea dela ziurta daiteke (ikus 12. irudia).



12. irudia: Argi-izpien definitutako geometriaren eskema.

Beraz, zuntzaren irteerako eremu optikoaren erradio efektiboa honela adieraz daiteke:

$$q(2d) = \sigma r_T \left[1 + \zeta \left(\frac{2d}{r_T} \right)^n \tan(\arcsin(NA)) \right] \quad (1)$$

non r_T eta NA TFaren nukleoaren erradioa eta zenbakizko irekidura diren, hurrenez hurren, eta σ , ζ eta η argi iturriaren eta TFaren ezaugarriekin erlazioa duten argiaren intentsitatearen banaketa erregulatzen duten hiru parametroak diren [44]. TF eta RF bakar baten kasurako, jasotako argi-intentsitate osoaren kalkulua RFaren nukleoaren azalera osoan zehar integratuz lortzen da. Integral horren emaitza honela idatz daiteke:

$$P(d) = \frac{\delta P_0 r_R^2}{q^2(2d)} \exp \left[\frac{-\rho^2}{q^2(2d)} \right] \quad (2)$$

Bertan, $f = [r_R^2/q^2(2d)] \exp[-\rho^2/q^2(2d)]$ adierazpenari zuntz bikote baten berezko modulazio funtzioa deitzen badiogu, 2. ekuazioa honela laburbil daiteke:

$$P(d) = \delta P_0 f(r_T, r_R, NA, \rho, d) \quad (3)$$

non δ ituaren gainazaleko islapen mailaren adierazle, P_0 TFtik ateratzen den potentzia, r_R RFren nukleoaren erradioa eta ρ RF eta TF ardatzen arteko distantzia diren. Arestian azaldu den bezala, zuntz-sorta diseinatzeko aukeratu den banaketa ardazkidearen ondorioz, RFz osatutako eraztun bakoitzak zuntz-mota berdinen kopuru finitua du (n_R) eta TF bakarra dago (ikus 11. irudia). Honen ondorioz, eraztun bakoitzaren TF-RF arteko elkarreragin bakoitzaren batuketa-eredua kontuan hartu behar da:

$$P(d) = \sum_{i=1}^{n_R} P_{i(d)} = \delta P_0 \sum_{i=1}^{n_R} f(r_T, r_R, NA, \rho_i, d) = \delta P_0 F(r_T, r_R, n_R, NA, \rho_i, d) \quad (4)$$

non $F = \sum_{i=1}^{n_R} f(r_T, r_R, n_R, \rho_i, NA, d)$ zuntz-sorta baten berezko modulazioaren funtzio gisa definitzen den. 4. ekuaziotik ondoriozta

daitekeenez, bildutako potentziak gainazaleko islapenarekiko eta igorritako potentziarekiko menpekotasun handia du TF bakarraren eta RFz osatutako eraztun baten konfigurazioan. Menpekotasun hori gutxitzeko edo ekiditeko, zuntzez osatutako bi eraztun zentrokidetan oinarritutako banaketa ezarri zen eraztun bakoitzetik bildutako argiaren arteko erlazioa lortzeko.

$$Ratio = \frac{P_1}{P_2} = \frac{\delta P_0 F_1}{\delta P_0 F_2} = \frac{F_1}{F_2} \quad (5)$$

non 1 eta 2 azpiindizedun terminoek barneko eta kanpoko eraztunekin erlazionatuta dauden, hurrenez hurren. 5. ekuaziotik ondoriozta daitekeenez, konfigurazio hau erabiliz, islagarritasunarekiko eta igorritako potentziarekiko menpekotasuna ekiditen da. Horrez gain, kontuan hartuta F_n agertzen diren r_T , r_R , n_R eta NA parametroak zuntz-sorta osatzen duten zuntzek determinatzen dituztela, berezko modulazio funtzioa ρ zuntzen ardatzen arteko distantzian eta d ituarekiko distantziaren menpe egongo dira. TCrako neurtu nahi den balioa d denez, zuntz-sortaren diseinuaren funtsezko parametroa ρ dela ondoriozta daiteke. Behin ρ finkatuta, bildutako potentziaren ratioa iturako distantziaren araberakoa izango da soilik (d).

Eraztun bakoitzetik bildutako argi-intentsitatea anplifikatu eta tentsiora bihurtzeko, RFz osatutako eraztun bakoitza irabazi aldakorreko (G) fotodetektore batera (PD) konektatu zen: PD1 barneko RF eraztunera eta PD2 kanpoko RF eraztunera, hurrenez hurren. PD bakoitzak laserrak igorritako uhin-luzeraren araberako sentikortasun-balio zehatz bat du ($R(\lambda)$) eta hautatutako irabaziaren araberako transinpedantzia-balio espezifikoko bat ($T(G)$).

$$V_{PD} = R(\lambda) * T(G) * P(d) \quad (6)$$

Era honetan, bi eraztun zentrokideren konfiguraziorako, bi eraztunen arteko tentsioaren erlazioa honela adieraz daiteke:

$$Ratio = \frac{R(\lambda) * T_2(G) * F_2(d)}{R(\lambda) * T_1(G) * F_1(d)} = \frac{T_2(G) * F_2(d)}{T_1(G) * F_1(d)} = K * \frac{F_2(d)}{F_1(d)} \quad (7)$$

non 1 eta 2 azpiindizea duten terminoak barneko eta kanpoko eraztunekin erlazionatuta dauden, hurrenez hurren. Igorritako uhin-luzera berdina denez bi eraztunetarako, sentikortasun-balioari buruzko terminoa ($R(\lambda)$) sinplifika daiteke. 7. ekuaziotik ondoriozta daiteke ratioa eraztunetara konektatutako PDen irabazien arteko zatiduraren (K) eta bi F funtzioen arteko zatiduraren arabera izango dela, azken hau zuntzetatik itura dagoen distantziaren (d) menpe soilik dagoena. Horrek esan nahi du argi-iturrien gorabeherek, zuntzean dauden galerek edota besoen islagarritasunaren aldaketek ratioan ez dutela eraginik izango [49, 56]. Era honetan, neurtutako tentsioen eta distantziaren arteko erlazioa erraztasunez ezar daiteke.

Aipatutako hurbiltze matematikoa Matlab MathWorks-en inplementatu zen zuntz, geometria eta PDen irabazi desberdinak zuten OFDSen erantzun-kurbak simulatzeko, CTA gure bazkidearen eskakizunak betetzen zituen, bizitza errealean fabrikatu eta haize-tunelean neurketak egiteko erabil zitekeen konfigurazioa lortzeko. Horretarako, OFDSaren zenbait propietate finkatu ziren, hala nola 660 nm-tako laserra erabiltzea, zuntz-sorta maila-indizeko zuntz optikoez eginda egotea ($\sigma = 1$) eta TFa SMF ($NA = 0,12$ eta $r_T = 2,15 \mu\text{m}$) izatea 660 nm-tan. Ezaugarri horiek praktikotasunagatik erabaki ziren: TF gisa SMF bat erabiliz, potentzia banaketan eragina izan dezakeen edozein zarata modal edo pikarda txikiak agertzea ekiditen da [42], eta ikusgai den uhin-luzera bat erabiliz, sentsoreak nora apuntatzen duen egiazta daiteke. Gainera, ezaugarri horiek dituzten osagaien prezioa txikiagoa da uhin-luzera luzeagoentzako moldatuta dagoenekin alderatuta, eta horrek sentsorizazio-sistema merketu egiten du.

Hurrengo atalean erakutsiko den bezala, lan honetan garatutako simulazio-programak zuntz-sortak diseinatzeko eta hauen erantzun-kurbak fabrikatu aurretik aurreikusteko oso tresna indartsua eta erabilgarria dela frogatu zuen, azken honek emandako emaitzak CTAk emandako zehaztapenen arabera fabrikatu ziren gailu fisikoek emandakoengatik gertu egon baitziren.

Gainontzeko neurketa sistemari dagokionez, honako hauek osatzen dute: zuntz bati akoplatuta dagoen 660 nm-tako uhin-luzera duen laser iturri bat (Thorlabs S4FC), RFz osaturiko eraztun bakoitzerako irabazi aldakorreko PD bat (Thorlabs PDA100A-EC), eta tentsio-datuak abiadura handian eskuratzeko txartel bat (National Instruments 6366 USB, 2 MS/s), USB bidez ordenagailu eramangarri batera konektatzen dena (HP Elitebook 840 g3). Datuak prozesatzeko, neurrira egindako LabVIEW programa bat garatu zen. Programa horri esker, TCaren balioak denbora errealean ikusi eta seinale gordina disko zurrunean gorde ahal izan da. Azken hau iraupen luzeko probetarako ezaugarri garrantzitsu bat da, datu-kopuru handiko fitxategiak sortzen baitira, GB tamainakoak.

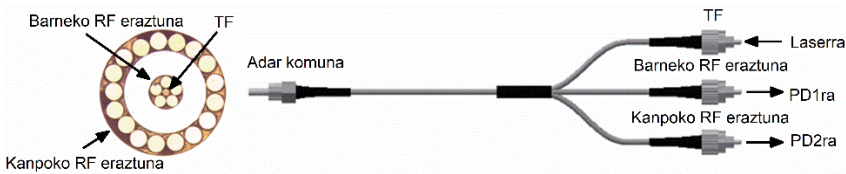
1.2.3 Laburpena eta emaitzak

1.2.3.1 Besoen zigitatze-puntari zuzenduta

*Puntu honetan, “Design, Fabrication and Testing of a High-Sensitive Fibre Sensor for Tip Clearance Measurements” artikulua laburpen bat azaltzen da. Artikulu hau Sensors aldizkarian argitaratu zen 2018ko abuztuan eta tesiaren eranskinaren atalean dago **1. artikulua** gisa xehetasun gehiago kontsultatzeko.*

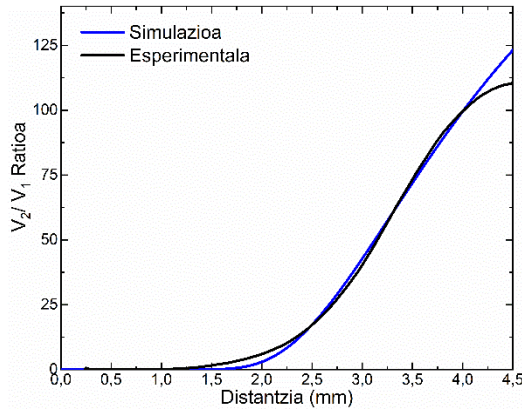
Simulazio-programak emandako emaitzen eta ezaugarrien arabera konfiguratu zen eta 1. eskualdean funtzionatzen zuen lehen OFDSa 92 besoz osatutako turbina batean inplementatu zen. Turbina horrek

40 dB-tan ezarri zen barneko eta kanpoko eraztunetarako, hurrenez hurren, PDeK duten saturazio-balioaren azpitik mantentzeko eta eskuratzeko-txartelaren tentsio eskala osoan zehar (0-5 V) tentsio-balioak sortzeko.



14. irudia: Zunda-puntaren amaierako argazkia eta fabrikatutako zuntz-sortaren eskema.

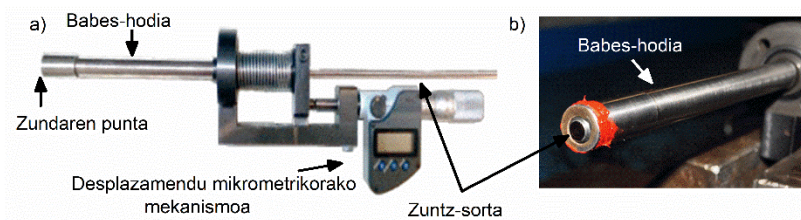
OFDSaren kalibrazioa laborategian egin zen, turbinaren ordeko beso baten zigilatze-punta itu gisa hartuta, turbinan egingo ziren neurketa-baldintzetatik ahalik eta hurbilen egoteko. Kalibrazioa laborategira eramatearen arrazoiak zuntz-sorta eta zigilatze-punten arteko lerrokatzea turbina abiadura handian biratzen ari zenean soilik emango zelako zen. Turbina geldirik zegoenean ez zegoen inolako lerrokatzarik, eta horrek ezinezkoa egiten zuen sentsorea bertan kalibratzea karkasan instalatu ondoren. 1. eskualderako, kalibrazio esperimentalean lortutako kurbaren eta simulazio-programak emandakoaren arteko alde txikia 15. irudian ageri da, non antzeman daitekeen bi kurben arteko aldea ez dela inoiz %1.5 baino handiagoa.



15. irudia: 1. eskualderako kalibrazio-kurba simulatua eta esperimental.

15. irudian agertzen den kurba esperimentalaren egokitzapen lineala 2.8 mm-tan hasten da, eta 4 mm-taraino hedatzen da, 0.997-ko Pearsonen korrelazio koefizientearekin eta 61.73 mm^{-1} -ko sentikortasunarekin.

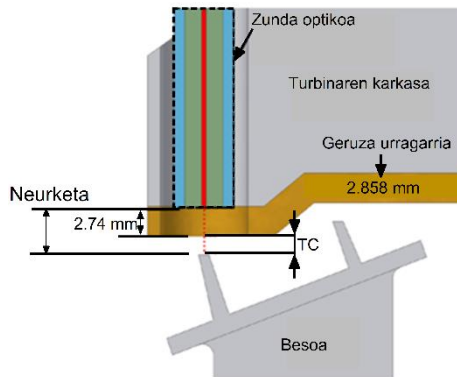
Zunda optikoa turbinan instalatzeko, mikrometro batez gidatutako egokitzaille batean sartu zen (ikus 16. irudia). Horren ondoren, egokitzaillea estalkian sartu eta finkatu zen helburu horretarako egindako zulo erradiala erabiliz (ikus 9b. irudia).



16. irudia: a) Zunda optikoa turbinan muntatzeko erabilitako egokitzaille. b) Zunda optikoaren xehetasuna egokitzaillearen babes-hodiaren barruan..

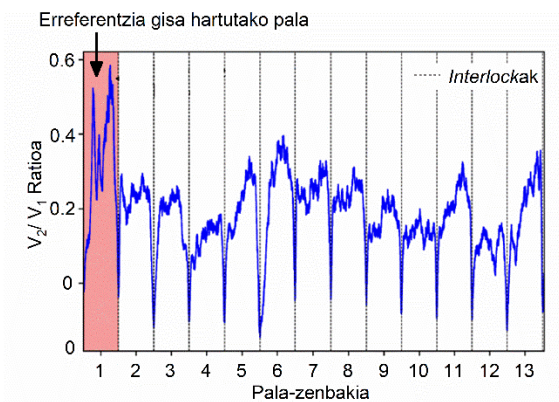
Guzti horri (egokitzaillea eta 1. eskualdearen funtzionamendutartearen kokapena) esker, sentsorea geruza urragarriaren barruan kokatu zen, besoen puntetatik 3.2 mm-tako distantziara. Distantzia hori erantzun-kurbaren 1. eskualdeko erdiko puntuarekin bat egiten du (ikus 15. irudia). Konfigurazio horri esker, batetik eskualde linealean funtzionatzea, eta bestetik bai besoak baita zunda optikoa

ere babestea, bermatzen zen. TC balioak estaldurak duen material hondagarriaren amaierarekiko ematen direnez, TC balioa sentsorearen neurketari 2.74 mm kenduz kalkulatu zen (zundaren puntatik gainazal islatzailera arteko distantzia), 17. irudian erakusten den moduan.



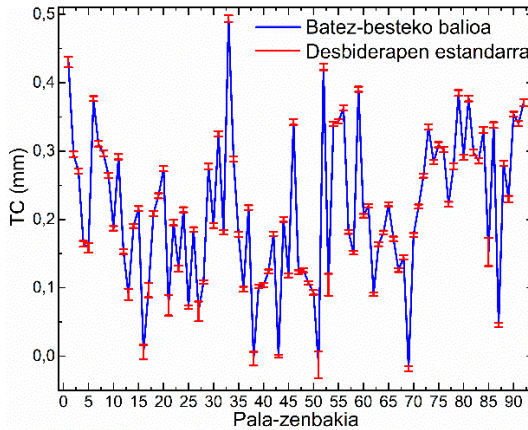
17. irudia: Karkasan instalatutako zunda optikoaren kokapena eta TCaren definizioa.

Probak turbinaren Lan-Puntu desberdinetarako (WP edo Working Point ingelesez) egin ziren eta egun desberdinetan zehar errepikatu ziren. WP bakoitzerako, haize-tuneleko biraketa-abiadura, presioa eta abar bezalako parametroak aldatu zituzten CTako teknikariek, motorraren intereseko egoera zehatzak simulatzeko. Motorraren bira bakoitza bi metodo desberdinekin neurtu zen besoak egokiro identifikatzeko helburuarekin: erreferentzia gisa hartu zen islapeneredu berezi bateko beso baten bidez, eta ardatzetik lortutako bibrazio gabeko seinale egonkor (OPR) baten bidez. Proba osoan zehar, errotorean dauden 92 besoen seinale-ereduak banan-banan identifikatu ziren, baita haien arteko tartea ere (*interlockak*) (ikus 18. irudia).



18. irudia: Probetan zehar eskuratutako seinaleen adibidea. Gorriz nabarmendutako zatia erreferentzia gisa erabili zen islapen eredu berezia zuen besoari dagokio.

Beso bakoitza banan-banan aztertzeko, TCa beso bakoitzaren datu-multzo osoaren erdiko laginetik hasita, inguruko %50-en laginez osaturiko datu-multzoaren batez-besteko balioa bezala definitu zen. Definizio horren arabera, kasurik okerreanean ere, TCaren aldakortasuna 20 μm -takoa zen gutxi-gorabehera WP beraren barruan, eta 92 besoen batez-besteko balioa 5 μm -tik beherakoa. Horrez gain, TC balio oso txikiak edo ezohiko balioak zituzten besoak identifikatzea posible izan zen, besoen fabrikazio edo instalazio-prozesuan akatsen bat zegoela adieraz zezakeena eta turbinaren segurtasunerako arriskutsua izan zitekeena. 19. irudian adierazitakoa azken honen adibide bat da, 4258 rpm-ko WPari dagokionez, 16, 38, 43, 51 eta 69. besoek duten TC balioek gainazal urragarritik gertu zeudela adierazten baitzuten eta beraz, arretaz kontrolatu behar zirela.



19. irudia: Beso bakoitzari dagozkion TC eta desbiderapen estandarraren balioak 4258 rpm-ko WPan 1100 bira eman ondoren.

OFDS honek ematen duen bereizmen eta sentsibilitate handiari esker, besoen analisi individualizatua ahalbidetu zen, bai eta TCaren eta errotorearen biraketa-abiadura alderantziz proportzionalak direla frogatu ere: bata handitzen den neurrian, bestea txikitzen da, eta alderantziz. Gertakari hori turbinaren osagai estatiko eta birakarietan eragina duten karga zentrifugo eta termikoei egotz dakiok.

Horrez gain, lan honen emaitzak baliagarriak izan ziren CTarentzat turbinaren TCa karakterizatzeko eta guretzako simulazio-programa balioztatzeko, simulatutako eta fabrikatutako gailuen kalibratze-kurbak antzekotasun handia baitzuten, programaren zehaztasuna eta fidagarritasuna berretsiz. Horri esker, testuinguru zehatzetarako oso sentikorrek diren neurrira egindako OFDSak diseinatzeko aukera ireki zen, behean deskribatzen den moduan.

1.2.3.2 Besoen *datum*-ari zuzenduta

Puntu honetan, "Performance Comparison of Three Fibre-Based Reflective Optical Sensors for Aero Engine Monitorization" artikulua laburpen bat azaltzen da. Artikulu hori Sensors

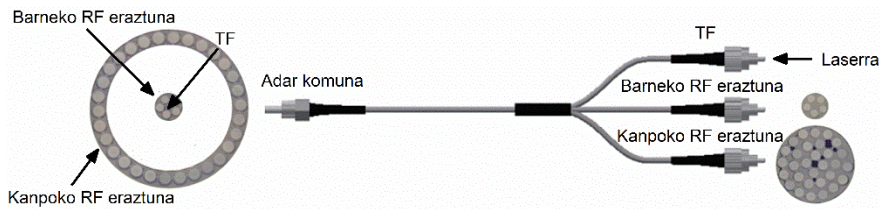
aldizkarian argitaratu zen 2019ko maiatzean eta [53]. erreferentzia da xehetasun gehiago kontsultatzeko.

Aurreko atalean deskribatutako gailuaren aurrerapauso gisa eta simulazio-programaren baliozkotasuna berresteko, OFDS hobetu bat diseinatu zen turbina berri baten TCa neurtzeko CTAn. [53]n azaltzen zen bezala, OFDS berri baten beharra 94 besoz osatutako turbina berri baten TCaren neurketaren beharrizanei dagokie. Turbina honetan, TCa **1. artikuluko** baino handiagoa izango zela esperoenez, **1. artikuluko** OFDSa sentikortasun baxuagoa duen 2. eskualdean funtzionatzera behartuko baitzuen.

Egoera hau aprobetxatuz, OFDS berria hobekuntza bereizgarri batzuekin diseinatu zen aurrekoarekin alderatuta:

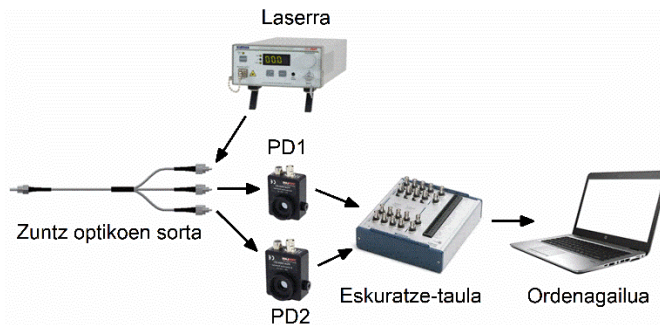
- 1. eskualde luzeagoa: modu honetan, OFDSak eremu lineal luzeagoa izango du funtzionatzeko. Ezaugarri honi esker, TC desberdinak dituzten turbinetan jardun ahalko du, kasu bakoitzerako OFDSen diseinu espezifikoaren beharra saihestuz.
- Urrunago hasten den 1. eskualdea: Modu honetan, zunda optikoaren muturra besoen puntatik urrunago eta beraz karkasa barruan koka liteke, segurtasun-maila handiagoa bermatuz.
- Malda eta anplitude handiko 1. eskualdea, sentsibilitate handiagoa eskaintzen duenak, ahalik eta bereizmen eta zehaztasun handiena lortzeko asmoarekin.
- OFDSaren tamainak **1. artikuluko** berdina izan behar du estalkian egindako zuloetan sar dadin. Zulo horiek **1. artikuluko** tamaina berdina zuten, turbina honetarako espero ziren TC balioak handiagoak zirela jakin aurretik egin baitziren. Hori dela eta, zuntz-sortaren diametroari dagokionez, tamaina mugatuta zegoen. Beraz, OFDS hau tamaina estandarreko zuloetan jarduteko gai eta aldi berean errendimendu hobea emateko gai izan behar du.

1. artikuluan erabilitako simulazio-programa berbera erabili zen sentzore berri hau diseinatzeko. Horren arabera, aipatutako baldintza guztiak betetzen zituen OFDSa aurreko probetan erabilitakoaren berdina zen, zuntz-sortaren kanpoko eraztuneko erradioaren eta bertan dagoen zuntz kopuruaren salbuespenarekin. OFDS hobetu honetan, kanpoko eraztunak 1800 μm -tako erradioa zuen eta 30 zuntzek osatzen zuten (ikus 20. irudia).



20. irudia: Hobetutako zunda optikoaren mutur bakoitzeko argazkia eta eskema.

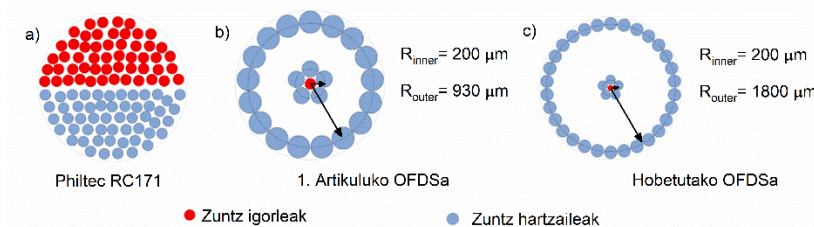
Gainerako sistemari dagokionez, aurreko probetako hardware bera erabili zen (laser iturria: Thorlabs S4FC, PDak: Thorlabs PDA100A-EC, eskuratzetxartela: National Instruments 6366 USB eta ordenagailu eramangarria: HP Elitebook 840 g3) (ikus 21. irudia).



21. irudia: OFDS guztiaren eskema, hura osatzen duen hardware elementu nagusienak adieraziz.

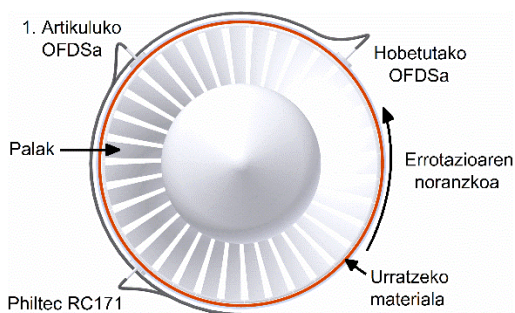
Errendimenduak konparatzeko, proba hauetan beste bi OFDS instalatu ziren turbinaren estalkian. Lehenengoa sentzore komertzial bat zen (Philtex RC171 modeloa), zuntzak ausaz bananduta dituen eredu erdizirkularrean antolatutako hainbat zuntz igorle eta hartzailez osatua. Bigarren sentzorea **1. artikuluko** OFDSa zen,

baina 2. eskualdean jardutera behartua neurketaren baldintzak zirela eta. Proba hauetan erabilitako hiru OFDSen zeharkako sekzioen eskemak 22. irudian agertzen dira.



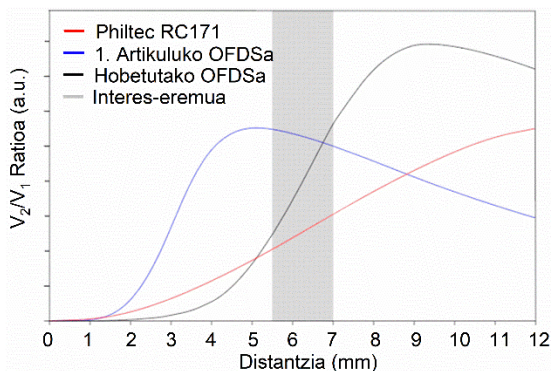
22. irudia: Probetan erabilitako gailuen eskalatutako zeharkako sekzioen irudikapen eskematikoa.

Hiru sentsoerak mikrometroz gidatutako egokitzazaleetan sartu ziren 16. irudian bezala eta karkasan instalatu ziren 23. irudian adierazten den moduan. **1. artikuluan** agertzen den funtzionamendu baldintzetan ez bezala, non sentsoerak zigilatze puntetara zuzenduta zeuden, proba hauetan karkasako zuloak sentsoerak besoaren plataforma lauera begira egon zitezzen egin ziren (ikus 10. irudia). Azken honek islatutako argia nabarmen handitu zuen eta kalibrazioa bertan egitea ahalbidetu zuen karkasan instalatu ondoren. Islatutako argiaren handitzeari esker, laser iturria 50:50 zatitzaile optiko baten bidez partekatu zen diseinatutako OFDS bien artean, sentsoerak komertzialak bere argi-iturria integraturik baitzuen. Eskuratzetxartel berbera hiru gailuen datuak biltzeko erabili zen.



23. irudia: Karkasan zehar sentsoerak nola instalatu zirenen irudikapen eskematikoa.

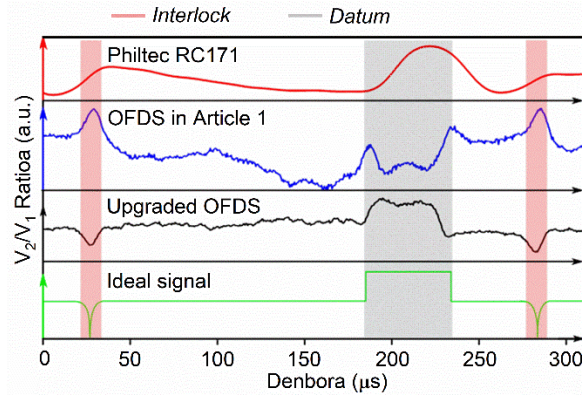
Sentsore guztien kalibrazio-kurbak 24. irudian agertzen dira. Bertan, antzeman daiteke intereseko lan-eremurako hobetutako OFDSak 1. Eskualdean funtzionatzen duela, lehen OFDSak 2. Eskualdean funtzionatzera behartuta dagoen bitartean. Hobetutako OFDSak 1. Eskualde aldapatsuagoa duela erraz nabari daiteke. Gailu komertzialari dagokionez, duen malda txikiagoko 1. Eskualdean funtzionatzen du.



24. irudia: Sentsoreen erantzuna-kurbak. Grisez adierazitako eremuak, sentsoreen lan-eremua adierazten dute turbinaren probetan zehar.

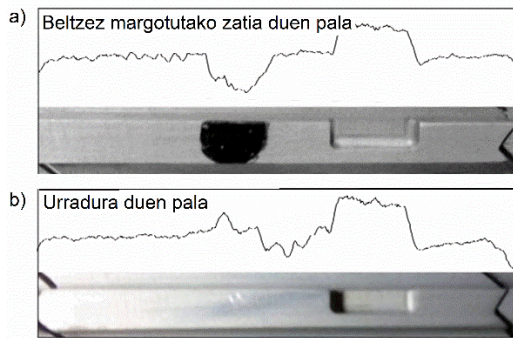
Probek egun bakoitzeko zortzi eta hamar ordu bitartean iraun zuten eta bi astetan zehar errepikatu ziren. Aurreko proben antzera, lan-puntu guztiak eta OPR seinalea grabatu ziren sinkronizazio eta besoen identifikaziorako.

Emaitzek adierazten duten moduan, diseinatutako OFDS pertsonalizatuek beso bakoitzaren igarotzea zehatz-mehatz identifikatu eta ezaugarri zehatzak antzemateko gai izan ziren, hala nola, *datumak* eta besoen arteko tartekak (*interlockak*). Azken horiek ez ziren sentsore komertzialean antzeman, seinale atzeratu eta leuna ematen baitzuen, gertaerak identifikatzea eta sinkronizatzea zailtzen zutena. Horren adibide gisa, 25. irudian, hiru sentsoreen bidez eskuratutako 55. besoaren seinalea (besoaren seinale estandartzat har litekeena) eta seinale ideala erakusten dira.



25. irudia. 55. besoaren seinalea hiru sentsoreen arabera. Horiakin batera, seinale ideala ere adierazten da.

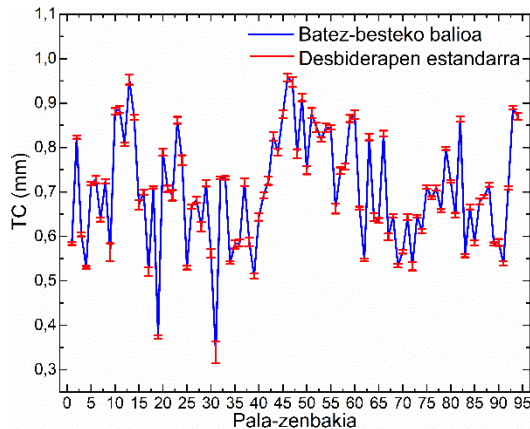
Diseinatutako bi OFDS pertsonalizatuen artean, bertsio berri honen sentsibilitate eta bereizmen handiagoa eskaintzen duen, bere seinalea besoaren forma fisikoarekin erraz lotu ahal baitzen eta seinale idealekin askoz ere gertuago baitzegoen. Bere uhin-formaren goranzko eta beheranzko ertz gogorrek *datum*-aren mugak zehazki zehaztea ahalbidetu zuten eta, beraz, besoaren iritsiera-denbora, TT teknikaerako ezaugarri interesgarria izan daitekeena (ikus 6. irudia). Horrez gain, sentsibilitate hobekuntzari esker, TCaz aparte, turbinaren portaeraren parametro estatistiko osagarriak lortu ziren, hala nola aldiuneko abiadura. Besoetan ustekabeko ezaugarriak identifikatzea ere ahalbidetu zuen, eskuratutako seinalearen forma beso estandarrekoarekin alderatuz (25. irudian agertzen dena). Gaitasun hau oso garrantzitsua da hutsegite eta funtzionamendu okerrak ekiditeko edota fabrikazioko-akatsak hautemateko (ikus 26. irudia).



26. irudia: Nolabaiteko irregulartasunak dituzten besoeh uhin-formen adibidea. Proben ondoren egindako besoeh ikuskapenean, portaeraren jatorria erakutsi zen.

a) Beltzez margotutako zati bat duen beso eta b) urradura bat duen beso baten kasua.

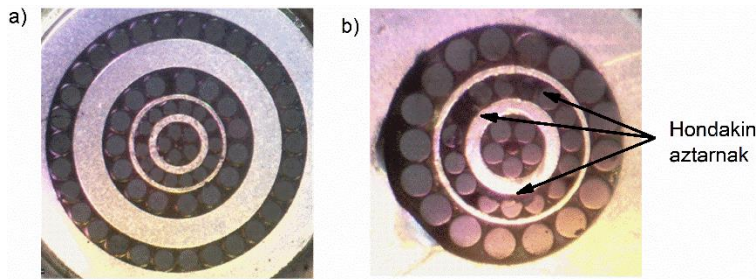
TCari dagokionez, OFDS bertsio berri hau oso seinale egonkorra emateko gai izan zen. Adibidez, 27. irudian, 3627 rpm-ko WP baten TC balioak erakusten dira. TC balioen aldagarritasuna denboran zehar (20000 motor-biren ondoren) eta WP beraren barruan, errore-barra bertikal gisa agertzen dena, 20 μm -takoa da kasurik okerreanean, eta 94 besoetan neurtutako TCaren batez-besteko balioa 7 μm -tik beherakoa.



27. irudia: Beso bakoitzari dagokion TC balioa eta desbiderapen estandarra 3627 rpm-ko puntuan 20000 bira eta gero.

Lan honen emaitzek behin-betiko baieztatu zuten garatutako simulazio-programaren baliozkotasuna TCa neurtzeko OFDS oso

sentikorrek diseinatu eta fabrikatzeko. Gainera, OFDS hau moldakortasun handiagoa eskaintzeko diseinatu zen turbina desberdinetan erabili ahal izateko, 1. eskualdeak duen luzera eta hein dinamiko handiari esker. Ezaugarri horiek, 1. eskualdea distantzia luzeagoetan hastearekin batera, sentsorearen burua besoen puntetatik urrunago eta urratzeko materialetik kanpo kokatzea ahalbidetzen du, errendimendua honda dezaketen besoen puntan eta sentsore buruaren arteko talka-arriskua, eta zunda-burua zikintzeko arriskua minimizatuz. Azken hori frogatzeko, pertsonalizatutako bi OFDSak mikroskopioan aztertu ziren proben ondoren. Ikuskerapean, hobetutako OFDSa kutsadura-hondakinik gabe zegoela ikusi zen. Era berean, **1. artikuluko** OFDSak zenbait zatitan hondakinak zituen, bere errendimendua honda zezaketenak hondagarriaren barruan eta besoetatik gertuago kokatu behar izatearen ondorioz (ikus 28. irudia).



28. irudia. Mikroskopioarekin ateratako argazkiak: a) hobetutako OFDSa eta b) **1. artikuluko** OFDSa.

1.3. Sendoki akoplatutako nukleo anitzez osatutako zuntz optikoetan (MCF) oinarritutako sentsoreak

Atal honetan, temperatura, okerdura, azelerazioa eta abar bezalako parametro desberdinak hautemateko sendoki akoplatutako MCFtan oinarritutako sentsore optiko ugari deskribatzen dira. Horretarako, zuntz horien funtzionamendu-printzipioa azaldu eta ustiatzen da sentikortasun handiko gailuak garatzeko.

1.3.1 Sarrera eta ikerketaren testuingurua

1.3.1.1 Industriarentzat interesa duten parametroak

Arestian azaldu den bezala, atal honetan deskribatuko diren sentsore estrintsekoetan, argiaren ezaugarri batzuen aldaketa edo modulazioa zuntzaz kanpoko efektu batek eragiten du. Horren ondorioz, sentsore-mota hauek temperatura, okerdura edo azelerazioa bezalako parametroak neurtzeko erabiltzen dira, adibidez. Sentsore hauek garatzeko interesa mantendu egin da urteetan zehar, aipatutako parametro guztiak oso garrantzitsuak baitira industria prozesuak kontrolatzeko edo SHMrako [57, 58], non ohikoa den fidagarriak eta errentagarriak frogatu diren teknologia helduetan oinarritutako detekzio-sistemak aurkitzea. Normalean, sentsore hauek izaera elektronikoko gailuetan oinarritzen dira, hala nola termopareetan, galgetan, eta abar. Hala ere, sentsore horiek normalean ingurune latzetan edota erradiazio edo erradioaktibitate-maila altuko inguruneetan instalatzen direla kontuan hartuta, korrosioa edo interferentziak jasan behar dituzte, funtzionamendu okerra edo bizi-iraupenaren gutxitzea ekar ditzakeena. Gainera, baliteke haien izaera elektrikoa edo elektronikoagatik aukerarik onena ez izatea gas edo likido sukoiak dituzten inguruetan inplementatzeko. Arazo

honetarako irtenbideetako bat gailuak babestean datza, sentsibilitatea galtzea eragin dezakeena.

Aipatutako desabantailak gainditu, sentsibilitate eta bereizmen handia, inplementatze-erraztasuna, errentagarritasuna eta abar eskaintzeko gai diren gailuak bilatzeak teknologia berriak bultzatu ditu. Testuinguru honetan, zuntz optikoetan oinarritutako detekzio-sistemak aukera erakargarri bihurtu dira aurreko ataletan zehatz-mehatz azaldu diren ezaugarriei esker, eta gero eta garrantzi handiagoa lortzen hasi dira industria sentso-re eta SHMrako alternatiba errealista gisa [59, 60].

1.3.1.2 Sentso-re optiko estrintsekoak

Sentso-re optiko estrintsekoen artean, uhin-luzeraren alterazio edo modulazioan, edo igorritako argiaren fasean oinarritutakoak dira soluziorik hedatuena. Izan ere, teknika horiek hain dira helduak, non haietan oinarritutako hainbat sentso-re komertzialki aurki daitezkeen.

Hedatuena eta helduena dagoen tekniketako bat FBG-arena da. Laburbilduz, zuntz optikoaren nukleoaren errefrakzio-indizearen aldizkako aldakuntza sortzean datza, igorritako argiaren uhin-luzera batzuk soilik islatu eta besteak transmiti ditzan. FBG-ek kanpoko edozein efektu jasaten dutenean, egindako sarearen periodoa aldatu egiten da, islatutako uhin-luzeraren desplazamendua eragiten duena. Beraz, uhin-luzeraren desplazamendu hori kanpoko efektuarekin erraz lotu daiteke. FBG-ak asko garatu dira eta oso ezagunak dira, temperatura eta tentsioak neurtzeko batez ere, oso sentikorrak direlako. Gaur egun, aplikazioaren arabera, konfigurazio anitzetan aurki daitezke, hala nola, okertuak, fasez aldatuak, txiribilduak, apodatuak eta abar [61]. FBG- teknika moldaketa bat, berez kategoriatzat har litekeena, aldi luzeko sareena da (LPG). LPG-etan, sarearen periodoa uhin-luzera baino askoz ere handiagoa da (100 mikrometroen ordenekoa, milimetro bateraino), erantzun askoz ere

zabalagoak lortzeko erabil daitekeena. Honen ondorioz, FBGak baino askoz errazago fabrikatzen dira [62]. FBG eta LPGen eragozpen nagusiak hauek dira: biek beren ingurunearekiko berezko sentsibilitatea daukate, isolamendu edo konpentsazio-mekanismo egokiak ezartzera behartzen dituen elkarreragin gurutzatua ekiditeko eta soilik intereseko parametroarekiko sentikorrek izateko; eta haien instalazioek laser eta galdetzaile garestiak behar dituzte.

Fabry-Perot interferometroak (FPI) ohiko aukera dira ere hezetasuna, temperatura eta abar neurtzeko sentsore estrintsekoak garatzeko [14]. Beren funtzionamendu-printzipioa islapen handiko gainazal bien arteko tarte optiko txiki batean oinarritzen da, haren luzera proportzionalki aldatzen dena kanpoko efektua aplikatzen zaionean. Horren ondorioz, uhin-optikoak tarte optikoarekin erresonantzian daudenean bakarrik igaro daitezke, hau da, banda zabaleko argi iturria erabiltzen bada, haren uhin-luzera jakin batzuk soilik igaroko dira. Era horretan, tartetik irteten diren uhin-luzeren desplazamendua erraz lotu daiteke aplikatutako efektuarekin. FPIak oso sentikorrek dira, nahiz eta hauen eragozpen nagusia tarte uniformeak errepikatzeko zailtasuna den.

Mach Zehnder (MZI) eta Michelson interferometroak hainbat parametro neurtzeko erabiltzen dira, hala nola, errefrakzio-indizeak, temperatura, gasak, kurbatura, etab. [63, 64]. MZIEk aplikatutako efektua iturri bakarretik datorren argia zatituz eratorritako bi izpi kolimatuen arteko desfase erlatiboa neurtuz kuantifikatzen dute. Izpietako bat erreferentzia gisa erabiltzen da, eta bestea, berriz, neurtu nahi den efektuaren menpe uzten da. Michelson interferometroetan, igorritako argia bi besoetan banatzen da eta, MZietan bezala, horietako bat erreferentzia gisa erabiltzen da eta bestea neurketetarako. Argi-izpi horietako bakoitza islatu eta izpi-zatitzaileantz joaten da berriz, izpi bien anplitudeak konbinatzen dituen superposizio-printzipioa erabiliz. Interferentziaren patroia aztertuz, aplikatutako efektua zehaztasun handiz neur daiteke.

Michelson interferometroek hainbat aplikazio dituzte, batez ere astronomian, uhin grabitatorioen detektagailuetan, eta abar [65]. MZI eta Michelson interferometroak oso sentikorak diren arren, haien eragozpen nagusia behar dituzten sistema konplexuak dira, ispiluen lerrokatze eta konfigurazio oso zehatzak behar baitituzte behar bezala funtziona dezaten, arazoak sor ditzaketenak industrialdeetan edo atari zabalean instalatzeko.

Azken urteetan, zuntz optiko espezializatuen garapenak zuntz optikoen bidez neurtzeko alternatiba berriak eskaini ditu. Aurrerapen horiek esanguratsuak izan dira batez ere MCFei esker, estalki arrunt batean txertatutako nukleo anitzez osatuta dauden zuntzak direnak. Nukleoan antolamendu geometrikoaren arabera, bi talde bereiz daitezke: akoplamendu ahul eta sendoko MCFak [66], hain zuzen ere. Alde batetik, nukleoak elkarrengandik nahiko urrun badaude, elkarketa ia nulua dago eta desakoplatuta daudela onar daiteke. Zuntz horiek telekomunikazioetarako erabili ohi dira, euskarri fisiko berean kanal independente anitz izatea onartzen baitute [67]. Bestalde, nukleoak elkarren artean elkarrengandiko adina gertu daudenean, sendoki akoplatutako MCFak deitzen zaie, nukleoan artean elkarketa handia baitago, argiaren akoplamendu periodikoa gauzatzen duena. Akoplamendu hori oso sentikorra da zuntzari aplikatutako efektu mekanikoen aurrean. Beraz, arraio honegatik zuntz mota hauek sentsoreetarako ustiatzen dira [68].

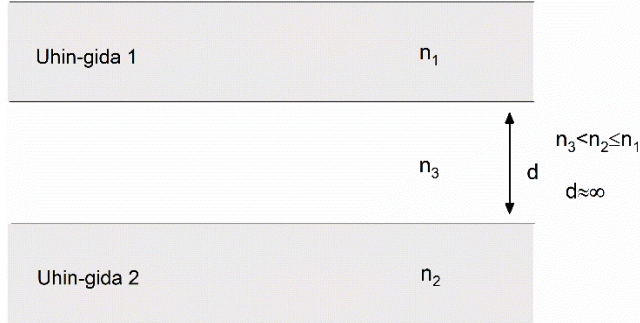
Arestian aipatutako gainontzeko soluzio optikoekin alderatuta, sendoki akoplatutako MCFek abantaila esanguratsuak eskaintzen dituzte sentsore optiko estrintsekoak garatzeko. Adibidez, ez dute konfigurazio konplexurik behar funtzionatzeko (zuntz horren segmentu labur bat, zirkulagailu bat, espektrometro edo fotodetektore bat eta banda zabaleko argi iturri bat besterik ez), ez dute lerrokatze zehatzik behar, ezta neurritara egindako osagai garestirik ere ez, eta maneiatzeko errazak dira. Arrazoi horiengatik,

zuntz mota hauek aukeratu dira tesian agertzen diren gailuak garatzeko.

1.3.2 Alor teorikoa eta tresna metodologikoak

1.3.2.1 Sendoki akoplatutako MCFen eredu matematikoa

Sendoki akoplatutako MCFen eredu matematikoa literaturan asko garatu den Modu Akoplatuaren Teoriaren bidez (CMT) deskriba daiteke [69-73]. Horren arabera, kasurik errazenean, elkarren artean elkarreragiteko adina urrun dauden modu bakarreko uhin-gida bi (1 eta 2 izenekoak) daudenean (ikus 29. irudia), uhin-gida bakoitzaren modua independenteki propagatuko da. Kasu horretan, uhin-gida bakoitzean propagatzen den moduaren anplitudea honela adieraz daiteke:



29. irudia: Desakoplatuta dauden uhin-gida biren eskema.

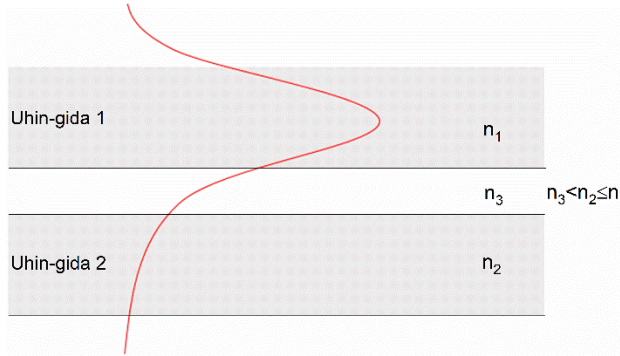
$$\frac{\partial a_1}{\partial z} = -j\beta_1 a_1 \quad (8)$$

$$\frac{\partial a_2}{\partial z} = -j\beta_2 a_2 \quad (9)$$

non a uhin-gida bakoitzean zehar propagatzen den zeharkako eremu elektrikoaren anplitudea den, β moduaren propagazio-konstantea

den, z propagazioaren norabidea eta 1 eta 2 azpiindizeek uhin-gida bakoitzari erreferentzia egiten dioten.

Hala ere, uhin-gidak elkarrengandik nahiko hurbil badaude gida baten eremu ebaneszentea bestean barneratzeko, propagatzen ari diren bi moduen arteko akoplamendua dago (ikus 30. irudia). Kasu horretan, moduen anplitudea honela adieraz daiteke:



30. irudia: Akoplatuta dauden gida biren eskema.

$$\frac{\partial a_1}{\partial z} = -j(\beta_1 + k_{11})a_1 - jk_{12}a_2 \quad (10)$$

$$\frac{\partial a_2}{\partial z} = -j(\beta_2 + k_{22})a_2 - jk_{21}a_1 \quad (11)$$

non k parametroak 1 eta 2 uhin-gidetan propagatzen ari diren moduen arteko elkar eta auto-akoplamenduko koefizienteak diren, hurrenez hurren. Galerarik gabeko sistema batean gaudela eta uhin-gidak uniformeak direla suposatzen badugu, propagazio-konstanteak eta akoplamendu-koefizienteak z -rekiko independenteak dira [70], eta honako sinplifikazioak aplikatu daitezke:

$$P(z) = |a_1|^2 + |a_2|^2 \quad (12)$$

$$k_{12} = k_{21}^* = k \quad (13)$$

10. eta 11. ekuazioetatik fasea faktore komun gisa hartzen bada, honela adieraz daitezke:

$$\frac{\partial \hat{a}_1}{\partial z} = -j\delta \hat{a}_1 - jk \hat{a}_2 \quad (14)$$

$$\frac{\partial \hat{a}_2}{\partial z} = -j\delta \hat{a}_2 - jk \hat{a}_1 \quad (15)$$

non

$$\delta = \frac{\beta_1 + k_{11} - \beta_2 - k_{22}}{2} \approx \frac{\beta'_1 - \beta'_2}{2} = \frac{\Delta\beta}{2} \quad (16)$$

Beraz, 14. eta 15. ekuazioek osatzen duten sistema matrize moduan idatz daiteke:

$$\frac{dA}{dz} = -j\bar{H}A \quad (17)$$

non

$$A = \begin{bmatrix} \hat{a}_1 \\ \hat{a}_2 \end{bmatrix} \quad (18)$$

$$\bar{H} = \begin{bmatrix} \delta & k \\ k & -\delta \end{bmatrix} \quad (19)$$

Moduen anplitudeak z propagazio-ardatzarekiko kalkulatzeko, hau da baita helburua uhin-gida eta distantzia jakin batean akoplatuta dagoen potentzia-kopurua kalkulatu ahal izateko, 17. ekuazioa transferentzia matrize gisa ordenatu eta adieraz daiteke:

$$A(z) = T(z)A(0) \quad (20)$$

non T matrizearen elementuak hurrengoak diren:

$$t_{11} = t_{22}^* = \cos(Sz) - j \cos(\eta) \sin(Sz) \quad (21)$$

$$t_{12} = t_{21} = -j \sin(\eta) \sin(Sz) \quad (22)$$

non

$$\tan(\eta) = \frac{k}{\delta} \quad (23)$$

$$S = \sqrt{\delta^2 + k^2} \quad (24)$$

$$\beta_0 = \frac{\beta_1 + k_{11} + \beta_2 + k_{22}}{2} \quad (25)$$

20. ekuaziotik, uhin-gida bakoitzeko potentzia normalizatua honako adierazpen hau aplikatuz lor daiteke:

$$P_i(z) = a_i(z) * a_i^*(z) \quad (26)$$

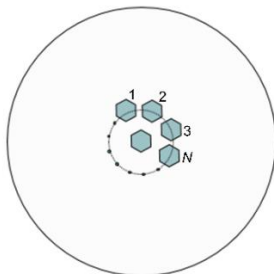
Beraz, uhin-gida bat bakarrik $z = 0$ puntuan kitzikatuta dagoen egoerarako ($a_1(0) = 1$ eta $a_2(0) = 0$, adibidez, 30. irudiaren arabera), uhin-gida bakoitzean z propagazio-ardatzaren arabera akoplatuta dagoen potentzia normalizatua honela adieraz daiteke:

$$P_1(z) = \cos^2(Sz) + \cos^2(\eta) \sin^2(Sz) \quad (27)$$

$$P_2(z) = \sin^2(\eta) \sin^2(Sz) \quad (28)$$

Zabal dezagun eredu hau uhin-gida zentral eta N ($N > 1$) uhin-gida berdin eta antolamendu zirkularrean banatuta duen egitura batera,

non nukleoak elkarrengatik adina gertu dauden. Geometria hori dokumentu honetako gailuak garatzeko erabilitako sendoki akoplatutako MCFen berdina da (ikus 31. irudia) eta, beraz, bere ondorioak aplikagarriak dira [74].



31. irudia: Aztertu diren MCFen egitura generikoaren eskema.

Horrelako MCFetan, hurrengo onarpenak egiten dira: nukleo guztiak tamaina eta propietate fisiko berdinak dituzte, LP_{01} oinarrizko modua soilik onartzen duten uhin-gida indibidualak dira eta elkarrengandik nahiko hurbil daude gida bakoitzean propagatzen den modua besteetan propagatzen denarekin gainjartzeko, nukleoaren arteko potentzia-akoplamentu ziklikoa eraginez [75]. Bertan lortutako moduak, supermoduak (SP) deiturikoak, uhin-gidetan propagatzen diren moduen arteko konbinazio lineala dira [76, 77]. Lan honetan egin den bezala, horrelako MCFak bere nukleo zentralean SMF estandar batetik datorren LP_{01} moduaz kitzikatzen direnean, CMTaren arabera, nukleo zentralean potentzia duten bi supermodu ortogonalak akoplatuta egongo dira [73]. Supermodu horiek SP_{01} eta SP_{02} izena dute, hurrenez hurren, eta MCF geometria bakoitzerako espezifikoa dira.

Kasu honen soluzio analitikoa 17. ekuazioan agertzen den bi uhin-gidaren kasukoaren antzekoa da baina potentziaren akoplamentuan parte hartzen duten nukleo guztien arteko interakzioa kontuan izanik:

$$\frac{dA(z)}{dz} = -j\bar{H}A(z) \quad (29)$$

non $A(z) = [A_1(z) \ A_2(z) \ \dots \ A_N(z)]^T$ zutabe-bektorea den, T transposizioa adierazten duen eta H $N \times N$ matrizea den. 29. ekuazioan dagoen sistema arestian deskribatutako bi uhin-giden kasuaren moduan garatu ondoren, erdiko (a_0) eta ondoko nukleoetan (a_i) propagatzen diren moduen anplitudeak honela adieraz daitezke:

$$a_0(z) = \frac{S \cos \frac{Sz}{2} + j\Delta\beta(z) \sin \frac{Sz}{2}}{S} e^{-j\beta_0 z} \quad (30)$$

$$a_i(z) = -j \frac{\Delta\beta}{S} e^{-j\beta_0 z} \sin\left(\frac{Sz}{2}\right) e^{\frac{-j\Delta\beta}{2z}} \quad (31)$$

non S honela definitu ahal den:

$$S = \sqrt{N\Delta\beta^2 + \Delta\beta^2} = \Delta\beta\sqrt{N+1} \quad (32)$$

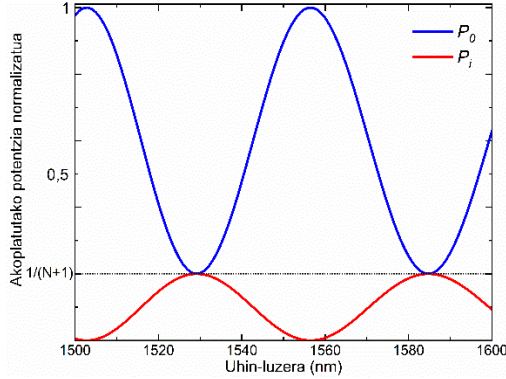
non $\Delta\beta$ honela definitzen den:

$$\Delta\beta = \frac{2\pi\Delta n}{\lambda} \quad (33)$$

non Δn propagatzen ari diren SP akoplatu eta ortogonalen errefrakzio-indize eraginkorren arteko aldea den eta λ kitzikatzen den uhin-luzera den. $\Delta\beta$ -ren definizio hau 30. eta 31. ekuazioei aplikatzen bazaie, MCFen nukleo zentral (P_0) eta ondoko nukleo bakoitzean (P_i) akoplatutako potentzia normalizatu generikoak (26. ekuazioan adierazitakoaren arabera kalkulatu) honela adieraz daitezke:

$$P_0(z) = \cos^2\left(\sqrt{N+1} \frac{\pi\Delta n}{\lambda} z\right) + \frac{1}{N+1} \sin^2\left(\sqrt{N+1} \frac{\pi\Delta n}{\lambda} z\right) \quad (34)$$

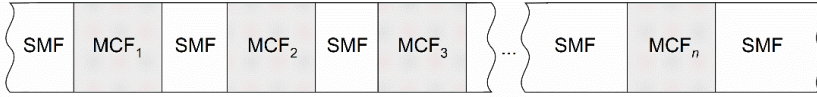
$$P_i(z) = \frac{1}{N+1} \sin^2 \left(\sqrt{N+1} \frac{\pi \Delta n}{\lambda} z \right) \quad (35)$$



32. irudia: MCF generiko baterako nukleo zentral eta ondoko nukleoetan dagoen potentzia akoplatu normalizatuaren bilakaera igorritako uhin-luzeraren funtzio gisa.

34. ekuaziotik eta 32. iruditik nukleo zentrolean potentzia periodikoki aldatuko dela ondoriozta daiteke, maximoa z edota λ balio jakin batzuetan lortuz eta minimoa beste batzuetan, baina argi-kopuru jakin bat egongo da beti nukleo honetan, $[1/(N+1), 1]$ tartean oszilatuko duena. Ondoko nukleo bakoitzari dagokionez, akoplatutako potentzia zentrolean dagoen osagarria izango da. Honek esan nahi du honelako MCFetan $\delta \neq 0$ dela. Nukleo guztiak berdina direnez eta, beraz, β berdina dutenez, fenomeno honen eragingarria nukleoaren banaketa dela onar daiteke [70]. Arestian aipatu den bezala, gertakari hau $N > 1$ kasurako gertatzen da soilik, $N=1$ kasuarentzat potentzia nukleo batetik bestera guztiz transferitzen baita [78].

SMF berebieran mota bereko n MCF segmentu-kopuru zehaztugabea dagoen kasurako (ikus 33. irudia), katearen amaieran, segmentu bakoitzaren nukleo zentrolean dagoen akoplatutako potentzia normalizatuaren arteko produktua izango da.



33. irudia: SMF berean seriean jarritako n MCF segmentuen eskema.

$$P_{cascade}(z) = \prod_{j=1}^n P_j(z) \quad (36)$$

Horrela, 33. irudiko kaskada-egitura batek espektroan segmentu bakar batek baino puntu goren estuagoa eta ikuspen handiagoa emango du karratura dauden *cos* eta *sin* terminoen ondorioz eta nukleo zentrolean seriean jarritako elementu kopuruarekiko proportzionalki dagoen argi-kopuru txikiagoa dela eta, hurrenez hurren. Honek, espektroaren edozein aldaketa jarraitzea nabarmen errazten du baina ez du sentibilitatea hobetuko, faseak ez baitu aldaketarik.

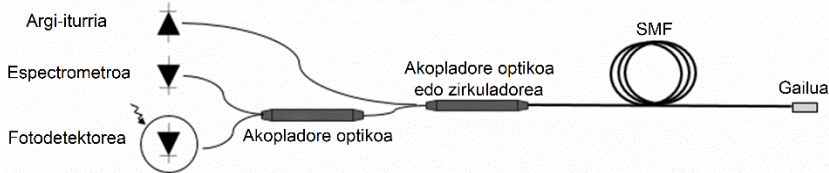
34. eta 36. ekuazioak lan honetan erakutsitako MCFtan oinarritutako sentsoreak diseinatzeko erabili ziren. Ekuazio horiek MCFen geometria eta konfigurazio desberdinetara egokituz, zuntzen espektroa simulatu ahal izan zen, haren forma zehatza lortzeko aukera ematen duten parametroen balioa optimizatzeko, hala nola MCF segmentuen luzera.

1.3.2.2 Fabrikazio-tresnak eta galdeketa-konfigurazioa

Ondorengo ataletan agertzen diren gailu guztiak fabrikatzeko, zehaztasun handiko zuntz-ebakitzaile bat eta zuntz-fusionatzaile bat erabili ziren. Lehenengoak, Fujikura CT-105ak, 10 μm -ko zehaztasuna lortzen du MCF segmentuak ebakitzean, ezaugarri garrantzitsua dena espektro zehatzak lortzerako orduan aurreko puntuan aipatu den bezala. Bigarrenak, Fujikura 100P+ak, MCFaren nukleo zentrala SMFak duen bakarrarekin lerroka dezake zehaztasun handiz, sartze-galera arruntak 0,1 dB edo txikiagoak izan

daitezen [79]. Horrez gain, makina honek biraketa-mekanismoa eta zuntzen muturreko aurpegia behatzea ahalbidetzen duen irudi-sistema bat ditu, orientazio zehatzak behar dituzten MCF-MCF fusioak behar diren kasuetarako erabilgarriak direnak.

Jarraian deskribatuko diren gailuen galdeketa-konfigurazioari dagokionez, konfigurazio bera partekatzen dute. Ekipamendu komertzialarekin osatutako sistema sinplea da, ahalik eta errentagarritasun handiena izateko. Banda zabaleko argi iturri gisa diodo superluminisente bat erabili da (Safibra, s.r.o.) 1550 nm-ean maximoa duena eta 40 nm inguruko FWHM duena, eta akopladore optiko (edo zirkuladore) arrunt bat. Islatutako argia aztertzeko, miniaturazko espektrometro bat (Ibsen Photonics I-MON-512 High Speed, 1510-1595 nm bitarteko galdeketa leihoa duena) edota InGaAs PD bat (Thorlabs PDA30B2) erabili ziren gailuaren edo neurketaren eskakizunen arabera. Aldi berean uhin-luzeraren desplazamendua eta potentzia-aldaketak neurtu behar ziren kasuetan, bi detektagailuak akopladore optiko baten bidez konektatu ziren (ikus 34. irudia).



34. irudia: Galdeketa-konfigurazioaren eskema.

1.3.3 Hipotesia eta helburuak

Helburua MCFtan oinarritutako sentore optiko berri eta oso sentikorrak garatzea da, goian deskribatutako funtzionamendu-printzipioaz baliatuz eta industrian interesgarriak diren parametro desberdinak neurtzeko. Horretarako, sentore bakoitzak konfigurazio

berezia du bere errendimendua optimizatzeko. Ikerketa honen emaitzak hurrengo ataletan eta **2.**, **3.** eta **4. artikuluetan** agertzen dira.

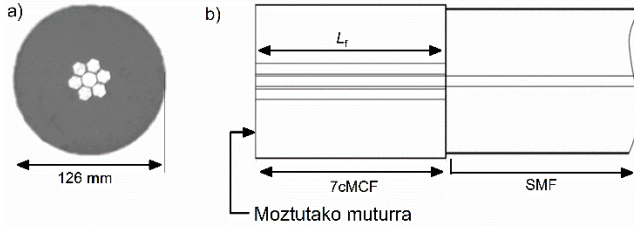
1.3.4 Laburpena eta emaitzak

1.3.4.1 Tenperatura-sentsoreak

1.3.4.1.1 Sentikortasun handiko 7cMCFan oinarritutako sentsorea

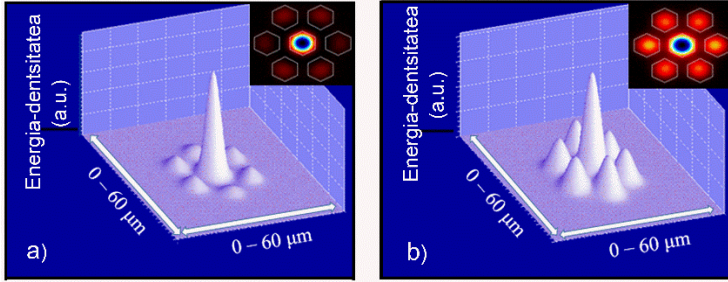
*Puntu honetan, “Packaged multi-core fiber interferometer for high temperature sensing” artikulua laburpena azaltzen da. Artikulu hau Journal of Lightwave Technology aldizkarian argitaratu zuen 2019ko martxoan eta tesiaren eranskinaren atalean dago **2. artikulua** gisa xehetasun gehiago kontsultatzeko.*

Ikerketan zehar garatutako MCFtan oinarritutako lehenengo gailua tenperatura-sentsore bat izan zen, ingurune latzak jasateko babestua haieran instalatzeko prestatua. Gailu honek duen MCFa University of Central Floridan (Orlando, AEB) fabrikatu zen, eta zazpi nukleo hexagonal berdina dituen egitura berezi bat du (7cMCF). Horietako sei zentroideki antolatuta daude eraztun itxuran nukleo zentralaren inguruan bat. Ondoko ardatzen arteko batez besteko diametroa eta distantzia $9.2\ \mu\text{m}$ eta $11\ \mu\text{m}$ dira, hurrenez hurren, eta zuntzaren kanpoko diametroa $126\ \mu\text{m}$ -koa da (ikus 35a irudia). Nukleo guztiak germanioz dopatutako silizeko beiraz eginak daude eta silizeko estaldura hutsean daude txertatuta. Horietako bakoitzaren NA 0.14-koa da $1550\ \text{nm}$ -tan, hau da, uhin-luzera horretako SMF tipiko batek duen NA bera. 7cMCFan oinarritutako gailuaren eskema 35b irudian ageri da. Bere egitura oso sinplea da: MCF segmentu labur bat (tenperaturarekiko sentikortasuna duen elementua) SMF arrunt batera bere nukleo zentralaren bitartez fusionatuta.



35. irudia: a) 7cMCFaren sekzioaren argazkia eta b) temperatura-sentsorearen eskema.

CMTaren arabera [73], 7cMCF honetan, akoplaturik dauden bi supermodu ortogonalak 36. irudian agertzen dira:



36. irudia: 7cMCFak dituen supermodu ortogonal akoplatuak. a) SP_{01} eta b) SP_{02} .

34. ekuazioa zuntz honetara partikularizatzeko, kontuan hartu behar da gailuak islapen-moduan funtzionatzen duela, eta horrek esan nahi du argiak MCFan joan-etorriko ibilbidea egiten duela. Beraz, L_f luzerako MCF segmentu fisiko baterako, argiak $2L_f$ bidaiatzen du. Hau kontuan hartuta, gailu honetan nukleo zentrolean dagoen akoplatutako potentzia normalizatua honela adieraz daiteke:

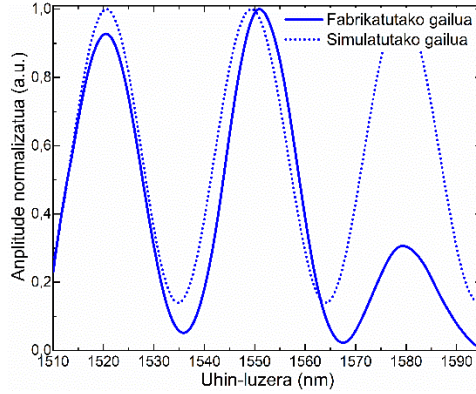
$$P_0(z = 2L_f) = \cos^2\left(\sqrt{7} \frac{\pi \Delta n}{\lambda} 2L_f\right) + \frac{1}{7} \sin^2\left(\sqrt{7} \frac{\pi \Delta n}{\lambda} 2L_f\right) \quad (37)$$

Espektroaren maximoa \cos -en faseak 2π -ren multiplo oso bat ($m2\pi$) berdintzen duenean gertatuko da. Beraz, maximoak uhin-luzera hauetan kokatuko dira:

$$\lambda_m = \frac{\sqrt{7}}{m} \Delta n 2L_f \quad (38)$$

Oro har, zuntz optikoetan, efektu termo-optikoa espantsio termikoaren efektuari gailentzen zaio. Beraz, temperatura neurtzeko, zuntzaren nukleoaren (edo nukleoaren) errefrakzio-indizearen aldaketak soilik hartu ahal dira kontuan [80, 81]. Gure kasuan, aldaketa horiek supermoduen indize eraginkorren aldaketa eragiten dute eta, horren ondorioz, espektroaren aldaketa. Gailu honetan, temperatura neurketak absolutuak dira, uhin-luzeran kodifikatuta daudelako, beraz, λ_m monitorizatuz, MCFaren inguruko temperatura erraztasunez jakin daiteke.

Ahalik eta temperatura tarterik zabalena neurtzeko, espektroak bi ezaugarri bete behar zituen. Alde batetik, λ_m ren desplazamendua 7cMCF honetarako, 30 pm/°C inguruko sentsibilitate termikoa duena inolako babesik gabe [81], ezin da alboko maximoekin gainjarri (λ_{m+1} edo λ_{m-1} etan dauden maximoak) neurketan anbiguotasuna ekiditeko. Bestalde, λ_m galdeketa leihoaren barruan egon behar da (1510 eta 1595 nm-en artean) uneoro. 37. ekuazioaren arabera, MCFaren luzera alda daitekeen parametro bakarra denez, gainerakoak zuntzak berak finkatzen baititu, baldintza horiek betetzen zituen luzera lortzeko, Matlab MathWorks eta PhotonDesign software programak erabili ziren. Simulazioen arabera, horiek betetzen zituen luzerarik egokiena 2.545 cm-koa izan zen. Hala ere, fabrikazioa azkarrago eta errazagoa izateko, 2.54 cm-ko luzera erabiltzea erabaki zen. Simulatutako eta fabrikatutako gailuen espektroak 37. irudian ageri dira.



37. irudia: Fabrikatutako eta simulatutako gailuen espektroak.

Maximoak kokatzen diren uhin-luzerak oso hurbil daude simulatutako eta fabrikatutako espektroetan. Tenperatura igo ahala, maximoak uhin-luzera luzeetara desplazatuko direla espero da [82]. Beraz, 1520 nm-tan kokatutako maximoa (λ_m) monitorizatzeke eta tenperaturarekin korrelatzeko hautatu zan. Bi kurben arteko anplitudeen aldea argi-iturriagatik gauzatuta dago, errealitatean erabilitakoa eta simulazioan implementatutakoa forma desberdinak baitituzte.

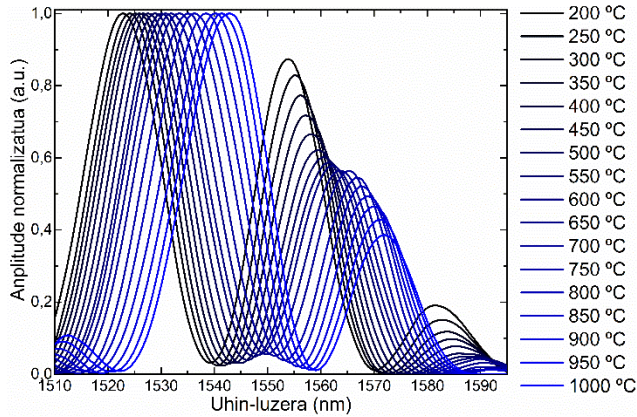
MCF sentsorea soilik tenperaturarekiko sentikorra izan dadin, honela paketatu zen: SMF-MCF egitura, 15 cm inguruko luzera zuena, geruza bikoitz batekin babestu zen. Lehenengo geruza zeramikako hodi mehe bat zen (Omega Engineering TRX-005132-6), 127 μm -ko diametroko zuloa zuena, SMF-MCF egitura zuzen mantentzeko eta MCFaren okerdurak sortutako efektuak ezabatzeko. Bigarren geruza zeramikako hodia estaltzen zuen altzairu herdoilgaitzeko hodi bat zen (Omega Engineering SS-116-6CLOSED), inpaktu edo zikinkeraren aurkako babes emateko. 38. irudian sentsorearen prototipoaren argazkia ageri da. Ohar daitekeenez, sentsorearen zati sentikorrak 2.54 cm-ko luzera besterik ez du, eta babesaren hodiaren puntaren ertzetik hurbil baina nahiko bereizita dago Fabry-Perot tarte baten sorrera ekiditeko. Beraz, sentsoreak 3 cm inguruko luzera izan dezake. Hodi metalikoarekin babestutako 12 cm gehigarrien arrazoia

probetarako erabili zen labearren konfigurazioa da (Isotech Pegasus Plus 1200). Azken honek zulo zirkular bertikal bat zuen (sentsorearen diametroa baino zertxobait handiagoa), 15 cm-ko luzera zuena, punturik sakonenean soilik 1000 °C-ko tenperatura lortzen zuena, paketatutako sentsore osoa bertikalki sartzeraz behartzen zuena.



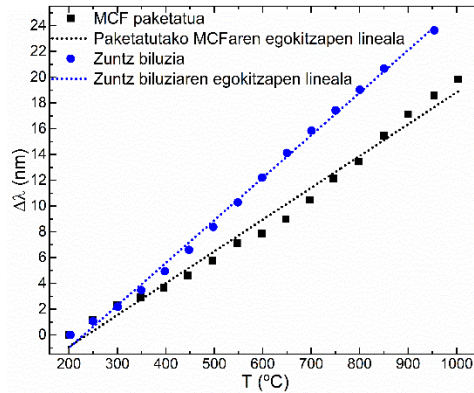
38. irudia: Proben ondoren egindako fabrikatutako tenperatura-sentsorearen argazkia.

Probak Arabako Teknologia Parkean (Araba) kokatutako Centro de Tecnologías Aeronáuticasen (CTA) instalazioetan egin ziren. Kalibrazioa egin aurretik, derrigorrezko ontze-prozesua egin zen sentsorearen histeresi-efektua ahalik eta gehien ezabatzeko [80]. Horren ondoren, kalibrazioa 200 eta 1000 °C tartean behin eta berriz egin zen, 70 minutu iraun zuten 50 °C-ko urratsetan. Orokorrean, kalibrazio-ziklo bakoitzak 100 ordu iraun zituen gutxi-gorabehera. Prozesu horretan, λ_m tenperaturarekin erlazionatu zen tenperatura kalibrazioetan erabiltzen den K motako termopare baten bidez (Herten, K motakoa, SN TCP187). MCF sentsorearen espektroaren tenperaturarekiko bilakaera 39. irudian erakusten da.



39. irudia: Espektroaren bilakaera temperaturaren arabera.

Babes-geruzek temperaturaren sentikortasunean duten eragina ebaluatzeko, biluzik utzitako 2.54 cm-ko MCF segmentu bat kalibratio-prozesu berdinerara ezarri zan. Bi MCF gailuen kalibratio kurbak 40. irudian agertzen dira.



40. irudia: Paketatutako sensorearen eta 7cMCF biluziaren kalibratio-kurbak eta egokitzapen linealak.

Paketatutako MCF sensoreari dagokionez, Pearson koadratuko korrelazio koefizientea $R^2=0.9856$ -koa zela kalkulatu zen. Esperimentuetatik kalkulaturako temperatura ($^{\circ}\text{C}$ -tan) eta λ_m ren (nm-tan) arteko korrelazioa hurrengoia izan zen:

$$T = 39,929\lambda_m - 60525 \quad (39)$$

Honek paketatutako MCF sentsorearen temperatura-sentikortasuna $24,8 \text{ pm}/^{\circ}\text{C}$ -koa zela adierazten du. 40. irudian agertzen den 2.54 cm luzerako MCF biluziaren kalibrazio-kurbaren arabera, $31.47 \text{ pm}/^{\circ}\text{C}$ -ko sentsibilitatea lortu zen. Hori dela eta, pentsa liteke paketatzeak gailuaren temperaturaren sentsibilitatean eragina duela, baina ez duela modu nabarmenean jaisten, emaitzak temperaturak soilik eragiten dituztela bermatzen duenaren abantailarekin. Azken hori ez da gertatzen 7cMCF biluzian, temperaturaz gain bibrazio eta tolesturak jasaten baititu, maximoaren desplazamenduan eragina dutenak.

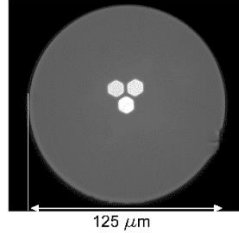
Lan honen bitartez MCF sentsore sinple, merke eta errepikatzeko erraza dena erakutsi zen, oso sentikor, trinko eta sendoa dena. Sentsore hau aukera erakargarria izan daiteke temperatura altuak neurtzeko, dituen bereizmen eta sentsibilitate handiei, dimentsio txiki eta immunitate elektromagnetikoari esker, hauek baitira eskatzen diren ezaugarriak zenbait aplikaziotan, hala nola, motor aeronautikoetarako, gas eta olio instalazioetarako, etab.

1.3.4.1.2 Sentikortasun handiko 3cMCFan oinarritutako sentsore iraunkorra

2. artikuluan erakutsitako lanaren aurrerapauso gisa, MCFan oinarritutako termometro hobetu bat garatu zen, eremu termiko zabalagoetan funtziona zezakeena, paketatze askoz sendoagoa eta sentsibilitate handiagoak zituena.

Lan honetan bi MCF desberdin erabili ziren. Biak University of Central Floridan fabrikatu ziren. Lehenengoa **2. artikulurako** erabilitako 7cMCFa izan zen, goiko atalean jadanik deskribatu dena. Bigarrena sendoki akoplatutako hiru nukleoz osatutako MCF asimetrikoa da (3cMCF): nukleoetako bat zuntzaren zentro geometrikoan kokatzen da, eta beste biak bere inguruan V itxurako konfigurazioan antolatuta (ikus 41. irudia). Nukleo bakoitza

germanioz dopatutako silizez egina dago, batez-besteko 9 μm -ko diametroarekin eta 0.14-ko N Arekin 1550 nm-tan SMFarekin bat egiteko. Nukleoak 11.5 μm bereizita daude elkarrengandik eta 125 μm -ko diametroa duen silize puruko estaldura batean sartuta daude.

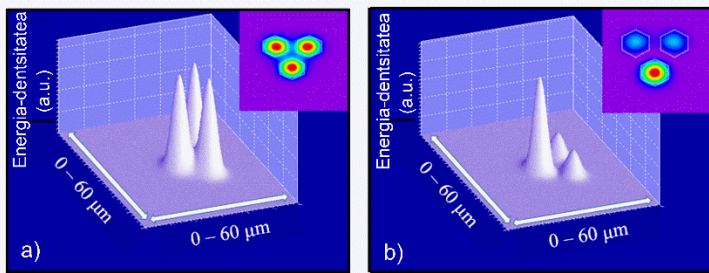


41. irudia: 3cMCFaren sekzioa.

34. ekuazioaren arabera, zuntz honetarako nukleo zentrolean dagoen akoplatutako potentzia normalizatuaren partikularizazioa honela adieraz daiteke:

$$P_0(z) = \cos^2\left(\sqrt{3} \frac{\pi\Delta n}{\lambda} z\right) + \frac{1}{3} \sin^2\left(\sqrt{3} \frac{\pi\Delta n}{\lambda} z\right) \quad (40)$$

Eta CMTaren arabera [73], akoplaturik dauden bi supermodu ortogonalak 42. irudian ageri dira:



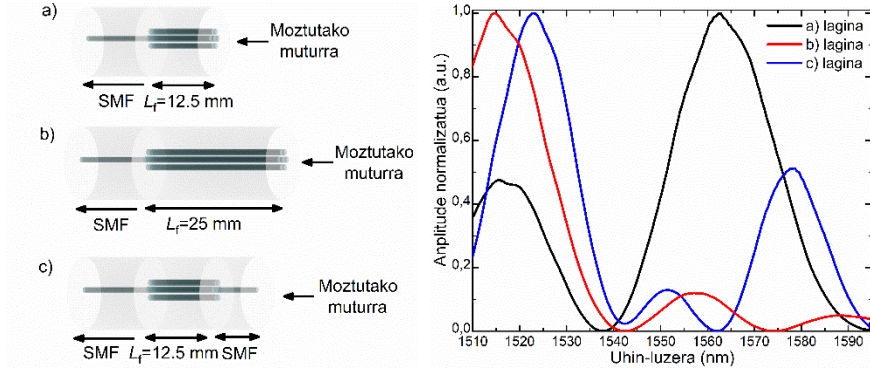
42. irudia: 3cMCFak dituen supermodu ortogonal akoplatuak. a) SP_{01} eta b) SP_{02} .

MCFen temperaturarekiko sentikortasuna ikertzeko, temperaturaren araberrako deribatu partziala aplikatu behar zaio 34. ekuazioari.

$$\frac{\partial \lambda_m}{\partial T} = \frac{L_f}{m} \sqrt{N+1} \left(\frac{\partial \Delta n}{\partial T} * (1 + \alpha \Delta T) + \Delta n \alpha \right) \quad (41)$$

non $L = L_f * (1 + \alpha \Delta T)$, L_f MCFaren luzera giro-tenperaturaren da ($T_f = 25 \text{ }^\circ\text{C}$), α termo-espantsioaren koefizientea da eta ΔT giro-tenperaturarekiko tenperaturaren aldaketa da ($T - T_f$). 41. ekuaziotik, onar daiteke sentsibilitate termikoan eragina duten parametro esanguratsuenak Δn eta L_f direla, α MCFaren materialaren propietate fisikoekin lotuta baitago, eta hauek berdinak direnez ikertu diren bi MCFetarako, propietate hauek finkatuta daude. Alde batetik, Δn eta, beraz, $\partial \Delta n / \partial T$, SPekin erlazionatuta daude eta, beraz, MCFaren geometriarekin eta propietate fisikoekin erlazionatuta ere bai, hala nola, nukleo kopuruarekin, horien banaketarekin, etab. Bestalde, L_f MCF segmentuak giro-tenperaturaren duen luzera da. Nahiz eta 41. ekuazioan, sentsibilitate termikoa L_f rekiko proportzionala dela pentsa daitekeen arren, sentsibilitatean duen eragina garrantzi gabekotzat jo daiteke, L_f/m erlazioa finkoa baita MCFaren hasierako luzera kontuan hartu gabe. Beraz, ondoriozta daiteke MCF segmentuaren hasierako luzerak eragin txikia duela sentsibilitate termikoan.

Hasierako luzerak sentsibilitate termikoan eragin nabarmenik ez duela egiaztatzeko, luzera desberdinetako 7cMCFz osatutako hiru gailu fabrikatu ziren (ikus 43. irudia), eta 200 $^\circ\text{C}$ -tik eta 500 $^\circ\text{C}$ -ra arteko tenperatura zikloetara jarri ziren 100 $^\circ\text{C}$ -ko urratsetan. Fabrikatutako eta probatutako konfigurazioak honako hauek izan ziren: 1) 12.5 mm-ko 7cMCFko segmentua duen lagina (43a irudia), 2) 25 mm-ko 7cMCFko segmentua duen lagina (43b irudia) eta 3) 12.5 mm-ko 7cMCFko kaskadan jarritako segmentu bi dituen lagina. (ikus 43c irudia).



43. irudia: Fabrikatutako laginen eskemak eta giro-tenperaturan ($T=25\text{ }^{\circ}\text{C}$) dagozkien espektroak.

43c irudiko egiturari dagokionez, SMF-MCF-SMF egitura batek osatzen du. Islatze-funtzionamendua dela eta, SMF segmentuaren mutur ebakiak ispilu gisa jokatzen zuen. Konfigurazio honen bidez, argiak joan-etorriko ibilbidea egiten du egituran, MCF segmentutik bi aldiz igaroz. Horrela, MCF segmentu bakarrarekin, egitura bikia erraz fabrika daiteke. Funtzionamendu-konfigurazio honetarako, 36. ekuazioa partikularizatu behar da. Partikularizazioaren ondorioz, egitura honen irteeran nukleo zentrolean dagoen potentzia akoplatu normalizatua honela adieraz daiteke:

$$P_0(z = L_f) = \cos^4\left(\sqrt{7} \frac{\pi\Delta n}{\lambda} L_f\right) + \frac{2}{7} \cos^2\left(\sqrt{7} \frac{\pi\Delta n}{\lambda} L_f\right) * \sin^2\left(\sqrt{7} \frac{\pi\Delta n}{\lambda} L_f\right) + \frac{1}{49} \sin^4\left(\sqrt{7} \frac{\pi\Delta n}{\lambda} L_f\right) \quad (42)$$

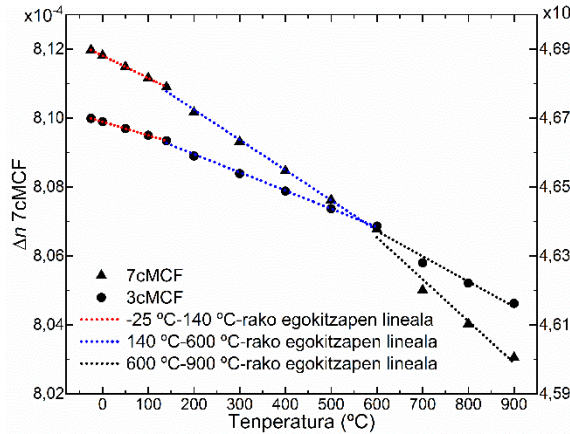
MCF segmentuak soilik tenperaturarekiko sentikorrak izan daitezten eta zuzen egoteko, ale bakoitza zeramikako hodi batean sartu zen (Omega TRX-005132-6). Ontze-prozesuaren ondoren, gailuek arestian aipatutako tenperatura zikloak jasan zituzten. Proba horien emaitzak 1. taulan laburbiltzen dira:

1. taula: Emaitzen laburpena

MCF luzera (L_f)	12.5 mm	25 mm	12.5 mm-ko bikia
Sentikortasuna (pm/ $^{\circ}\text{C}$)	20.38	22.22	21.16

1. taulatik ondoriozta daiteke MCFaren hasierako luzerek edota elementu horiek kaskadan jartzeak eragin ia nulua dutela temperaturaren neurketetarako sentikortasunean. Ondorio hau 34. eta 36. ekuazioetako adierazpen matematikoetatik ondoriozta zitekeen, haietako fasea berdina baitzen hasierako luzera edo gailuaren konfigurazioa (segmentu bakunak edo kaskadan jarritakoak) kontuan hartu gabe. Hala ere, horrek ez du esan nahi L_{fk} MCFetan oinarritutako termometro optikoen diseinurako kanpoan uzteko parametroa denik, espektroaren forma eta λ_m ren kokapena definitzen duen diseinu-faktore garrantzitsua baita, **2. artikuluan** eta 43. irudian frogatu den bezala.

Δn_k sentzibilitate termikoan duen eragina aztertzeko, PhotonDesignen bidez temperaturarekiko duen aldaketa simulatu zen erabiltzen ari ziren bi MCFentzako (ikus 44. irudia). Horretarako, materialaren errefrakzio-indizea honela definitu zen: $n = n_f + \gamma \Delta T$ [83], non n_f nukleoen errefrakzio-indizea den 25 °C-tan, eta γ koefiziente termo-optikoa den [82]. Hauen ez-linealtasuna kontuan hartu zen -25 °C eta 900 °C arteko simulazioetarako [84, 85].

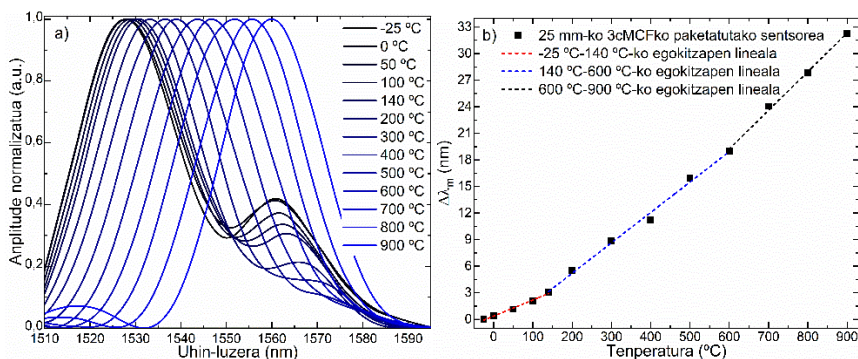


44. irudia: Δn ren temperaturarekiko simulazioak 7cMCFrentzako (triangelu beltzak) eta 3cMCFrentzako (zirkulu beltzak).

2. artikuluan frogatu den moduan, λ_{mk} duen temperaturarekiko desplazamendu proportzionalak (temperatura handitu ahala, λ_m uhin-

luzera luzeagoetara desplazatuko da eta alderantziz) esan nahi du 41. ekuazioan dagoen $(\partial\Delta n/\partial T * (1 + \alpha\Delta T) + \Delta n\alpha)$ terminoa positiboa dela. 44. ekuaziotik, Δn beti positiboa dela antzeman daiteke, baina bere malda $(\partial\Delta n/\partial T$ eran adierazita) negatiboa dela ikertzen ari diren bi MCFentzako. Honek esan nahi du $\partial\Delta n/\partial T * (1 + \alpha\Delta T) < \Delta n\alpha$, eta horren ondorioz, bi termino horien arteko aldea handitzen den heinean, sentsibilitate termikoa handitzen dela suposa daiteke. Beraz, 42. iruditik atera daitekeen ondorioa 3cMCFak duen temperaturarekiko sentikortasuna 7cMCFak duena baino handiagoa dela da, Δn baxuagoa duelako eta baita bere malda txikiagoa delako ikertzen ari garen temperatura-eremuan.

Aurreko paragrafoan esandakoa demostratzeko asmoz, **2. artikuluan** agertzen den paketatze berdina duen gailu bat fabrikatu zen baina 25 mm-ko 3cMCFko segmentua zuena, eta -25 °C-tik 900 °C-ra doan temperatura-ziklo mailakatu batzuetarako probatu zena. Probak egin aurretik, gailuak **2. artikuluan** egindako ontze-prozesua jasan zuen histeresia ekiditeko. Horren ondoren, aipatutako temperatura-zikloak jasan zituen. 45. irudian espektroaren bilakaera temperaturaren arabera eta haren kalibrazioaren emaitzak agertzen dira.



45. irudia: a) Espektroaren bilakaera temperaturaren arabera eta b) Paketatutako 25 mm-ko 3cMCFko gailuaren kalibrazio kurba.

Gailu honek **2. artikuluan** adierazitakoa baino sentsibilitate handiagoa erakutsi zuen paketatze eta funtzionamendu-konfigurazio

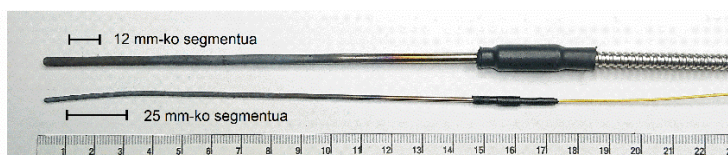
berarekin, 43.61 pm/°C-ko sentikortasuna lortuz 600 °C eta 900 °C tartean (**2. artikuluko** gailuak 24.8 pm/°C-ko sentikortasuna lortu zuten). Hori dela eta, ondoriozta daiteke MCFtan oinarritutako termometro sentikorrek diseinatzeko parametrorik esanguratsuena Δn dela, eta aztertzen ari diren bi MCFen artean, 3cMCFa sentikorrakoa dela eta, beraz, termometro optiko hobetua fabrikatzeko aukeratu behar den zuntza dela.

Sentsorea fabrikatzeko, espektroaren formaren betebeharreko kondizioak **2. artikuluan** azaldutako berdinak ziren. Hala ere, 3cMCFa erabiliz, baldintzak betetzen dituen MCFaren luzerarik egokiena 12 mm-koa izan zen, hau da, **2. artikuluan** erabili behar izan zen MCFaren erdia baino gutxiago (2.54 cm). Hau abantaila gehigarria da zeren gailuak material gutxiago behar baitu.

Paketatzeari dagokienez, **2. artikuluko** gailuaren eragozpenetako bat hauxe zen: altzairu herdoilgaitzeko estalki metalikoak tenperatura altuak jasaten zituenean, okertu egiten zen eta ez zuen jatorrizko formara itzultzen. Hau inguru latzetan jarduteko balizko arazoa da, barneko zuntza haustea ekar baitezake. Eragozpen kritiko hori gainditzeko, paketatzea hobetu zen ingurune latzetan eta tenperatura altuetan jarduteko sendoagoa izan dadin. Gailu honen paketatzeak zuntz optikoa estaltzen zuten hiru geruzek osatzen zuten. Lehenengo geruza aurreko gailuetako berdina zen eta zeramikako hodi batek osatzen zuten (Omega TRX-005132-6) MCFa zuzen mantentzeko eta, beraz, tenperaturarekiko soilik sentikorra izan dadin. Bigarren geruza Inconel hodi mehe batek osatzen zuten (INC-116-6-OPEN), bere barneko diametroa zeramikako hodiaren kanpoko diametroa baino zertxobait handiagoa zena. Honen helburua zeramikako hodiari zurruntasuna ematea eta hausturak saihestea zen, azken honek inpaktuen aurrean hauskortasun handia erakusten baitu. Hirugarren geruza Inconel hodi lodi batez osatuta zegoen (INC-18-6 CLOSED), sendotasun gehigarria emateko. **2. artikuluan** ez bezala, Inconel altzairu herdoilgaitzaren ordeztu erabiltzearen

arrazoia, Inconelek tenperatura altuagoak jasateko duen gaitasunagatik izan da. Paketatze honekin, azken prototipoak 14 cm inguruko luzera zuen (ikus 46. irudia). **2. artikuluan** gertatzen zen bezala, gailuaren zati sentikorrek 1.2 cm-ko luzera besterik ez zuen eta puntan kokatuta zegoen, baina era berean puntatik urrun Fabry-Perot tartea sortzea saihesteko. 14 cm-ko paketatzea kalibrazioan erabilitako labeengatik izan zen (Fluke 9103 eta Fluke 9150). Azken hauek 15 cm inguruko zulo bertikala zuten, eta punturik sakonenean soilik lortzen zuten tenperatura altuetara iristea.

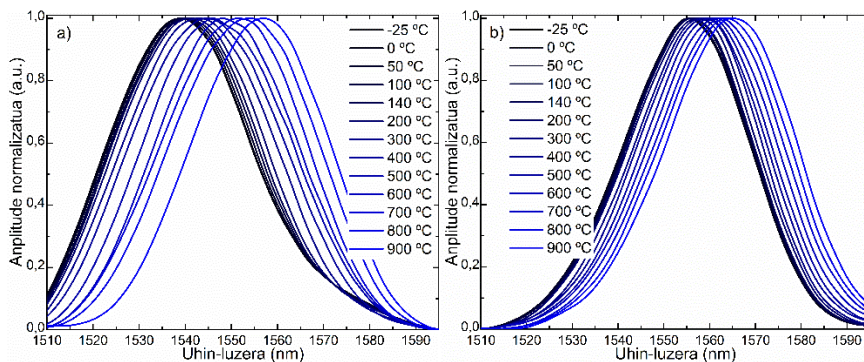
Azkenik, ingurune latzetarako ahalik eta sendoen izan dadin, gailutik galdeketa-sistemara doan SMFa geruza bikoitz batekin babestu zen. Lehenengoa hodi batek (Thorlabs FT030) osatzen zuen, kanpoko PVCko jaka eta Kevlar hariak zituen. Bigarren geruza altzairu herdoilgaitzeko jaka batez osatuta zegoen (Thorlabs FT05SS), babes gehigarria ematen zuena eta zuntzaren zehar nahi ez den argi ikusgaiaren edo Iren sarrera saihesten zuena.



46. irudia: Hobetutako gailuaren (goian) eta **2. artikuluko** gailuaren (behean) argazkiak probak egin ondoren.

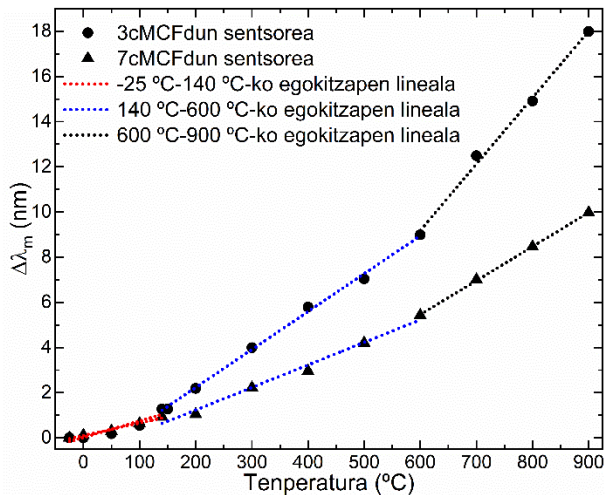
46. irudian paketatzeren onurak aitor daitezke. Erraz antzematen da **2. artikuluko** gailua nabarmen okertu dela hainbat tenperatura-ziklo jasan ondoren, eta horrek bizitza-esperantza eragina izan dezake. Bertsio berrituak, berriz, zuzen jarraitzen du.

Konparatzeko, ezaugarri fisiko eta paketatze berdina duen gailu berdina bat fabrikatu zen, baina 7cMCFrekin. Kalibratu aurretik, bi gailuek **2. artikuluan** deskribatutako ontze-prozesua jasan zuten histeresia ekiditeko. Horren ondoren, 45. irudiko gailuaren mailakako tenperatura-ziklo berdinak jasan zituzten. Horiei dagozkien espektroen bilakaerak 47. irudian agertzen dira.



47. irudia: Temperaturaren araberako espektroen bilakaera a) 3cMCF eta b) 7cMCFa duten gailuetan.

Sentsore iraunkor hauen kalibrazio-kurbak 48. irudian agertu eta 2. taulan laburbiltzen dira. Emaitzek erakusten dute 3cMCFak duen gailuak sentsibilitate termiko handiagoa duela 7cMCFa duen gailuak baino temperatura-tarte guztietan, ia sentikortasun-maila bikoitza lortuz 200 °C eta 900 °C tartean.



48. irudia: 3cMCFan (zirkulu beltzak) eta 7cMCFan oinarritutako (triangelu beltzak) sentsoreen kalibrazio-kurbak.

2. taula: Emaitzen laburpena

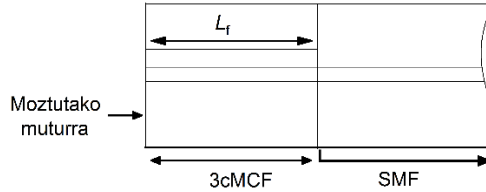
		-25 °C-140 °C	200 °C-600 °C	600 °C-900 °C
3cMCF	Korrelazioa	T=117.61 λ_m +5.74	T=59.445 λ_m +67.693	T=33.83 λ_m +290.09
	Sentikortasuna (pm/°C)	7.302	16.785	29.426
	R^2	0.926	0.9989	0.997
7cMCF	Korrelazioa	T=177.31 λ_m -17.193	T=86.72 λ_m +129.17	T=66.295 λ_m +238.47
	Sentikortasuna y (pm/°C)	5.531	9.983	15.081
	R^2	0.99	0.992	0.999

Hemen azaldutako emaitzek sendoki akoplatutako MCFen oinarriak ulertzearen garrantzia azpimarratzen dute, horiek ustiatzeari esker MCF geometria egokia hautatuz soilik sentikortasun handiagoa lortu ahal baita. Lan honetan, egitate honetaz baliatu gara temperatura neurtzeko: paketatze sendoagoa ahalbidetu du, blindajearen ondorioz gauzatutako sentikortasunaren-galera MCFak emandako sentsibilitatearen hazkuntzarekin konpentsatu baita. Gainera, hemen azaldutako oinarriek aukera ematen dute neurrira egindako sentsibilitate optimizatuak edota hobetuak dituzten MCF egiturak eta geometriak diseinatu eta fabrikatzeko temperatura, tentsioa edo okerdura bezalako beste edozein parametro neurtzeko. Baita iragazkiak edo etengailuak diseinatzeko, kasu horietako guztientzako diseinu-prozedura hemen azaldutakoaren analogoa baita.

1.3.4.2 Noranzko guztietarako tolestura-bektore sentsorea

Atal honetan, tolestura-bektore sentsore simple eta trinkoa erakusten da, tolesturaren edozein norabide eta anplitudea antzemateko gai dena. Gailu hau fabrikatzeko, aurreko lanean agertzen zen 3cMCF beraren segmentu labur bat ($L_f=8$ mm) erabili zen (ikus 41. irudia),

islapen-era funtzionatzen duen SMF-MCF egitura sinplea sortuz. Sentsorea uhin-luzeraren aldaketarekin eta argi-potentziaren aldaketekin galdekatu zen aldi berean. Modu honetan, tolesturaren norabidea eta anplitudea era nahasezinean neurtu ahal ziren, horren arabera espektroaren anplitudea aldatu eta desplazatzen baitzen MCFa tolesten zenean.



49. irudia: Sentsorearen egituraren eskema.

Egitura honetarako eta 3cMCFrako, akoplatutako potentzia 4. ekuazioan bezala adieraz daiteke, baina $z=2L_f$ kasurako egokituta:

$$P_0(z = 2L_f) = \cos^2\left(\sqrt{3} \frac{\pi\Delta n}{\lambda} 2L_f\right) + \frac{1}{3} \sin^2\left(\sqrt{3} \frac{\pi\Delta n}{\lambda} 2L_f\right) \quad (43)$$

Zuntz honetan akoplaturik dauden SP ortogonalak 42. irudian agertzen diren berberak dira.

Askotan frogatu den bezala, zuntz optikoen nukleoaren errefrakzio-indizea aldatu egiten da zuntza okertzen denean [86-89]. MCFetan, zenbait nukleo edo nukleok beste batzuek baino tentsio handiagoa izango dute okertze-plano eta anplitude berdina jasaten dituztenean, eta, honen ondorioz, supermoduen errefrakzio-indize eraginkorrak proportzionalki aldatuko dira. 43. ekuazioaren arabera, efektu horiek aldaketak dakarte normalizatutako akoplatutako potentzia baldintzetan, eta, beraz, sortzen den espektroan.

Sendoki akoplatutako MCFen artean, antolamendu simetrikoa dutenetan, tolestura-planoaren efektua beti izango da berdina okertze-norabidea edozein delarik ere. Hori dela eta, zuntz horiek gai dira aplikatutako tolestura bereizteko, baina ez bere norabidea [90]. Hala ere, MCF asimetrikoetarako, hots, 3cMCFaren modukoak

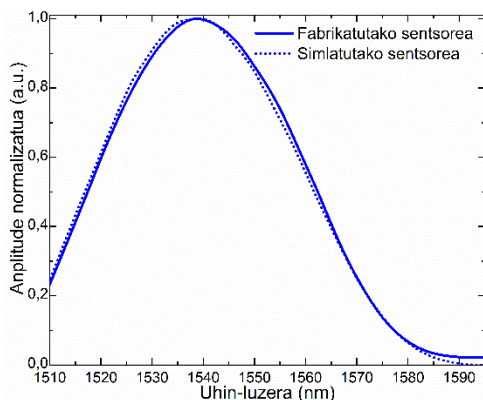
direnentzako, espektroan ikusgai izango den okertzearen eragina nukleoaren orientazioaren, tolesturaren norabidearen, nukleoan antolamenduaren eta geometriaren arabera izango da. MCF mota hauek tolestuta daudenean, nukleo bakoitzaren errefrakzio-indizearen aldakuntza okertze-planoaren eta berarekiko duen orientazioaren arabera izango da [91, 92]. Nukleoak asimetriki antolatuta daudenez, bakoitzak tentsio maila desberdinak ditu tolestura-plano eta erradio beraren aurrean, bakoitzaren errefrakzio-indizea modu independentean aldatzea eragiten duena. Egoera horrek supermoduen propagazioari eragiten dio zuzenean, eta, horren ondorioz, espektroa aldatzen da. Hau da MCF asimetrikoak noranzkoa detektatzen duten tolestura-sentsoreak egiteko hautagai onak bihurtzen dituen, potentzia normalizatuaren aldakuntza direkzio bakoitzerako espezifikoak izango baita, SMF-MCF egituraren espektroan antzeman daitezkeen aldaketak sortuko dituen uhin-luzeraren desplazamenduan edota argiaren potentziaren aldakuntzan aplikatutako okertze-norabidearen arabera.

Espektroan horrelako aldaketak eragiten dituzten tolestura-norabideak detektatu eta neurtzeko, bi aldagai horietako bat bakarrik monitorizatu, printzipioz, tolestura-norabidea eta anplitudea anbiguotasunik gabe 180° -tan neurtzea posible da. Tarte horretan, neurtutako aldagaiaren sentsibilitatea bakarra izango da tolestura-plano bakoitzerako eta, beraz, bere neurketa (uhin-luzera luzeago eta laburragoetara desplazatzea edo islatutako argi-potentzia handitzea eta txikitzea) aplikatutako tolesturarekin inolako zalantzarik gabe lotu liteke. Hala ere, gainerako 180° -etarako, aldagaiaren neurketa horiek aurreko 180° -ko bezalakoak izango dira, eta ondorioz, tolesturaren bi norabidek monitorizatutako aldagaian neurtutako aldaketa bera eragingo dute.

Anbiguotasun hori ezaba daiteke aldagai biak aldi berean neurtuz (uhin-luzeraren desplazamendua eta argi-potentziaren aldakuntza), bakoitzak sentikortasun berezia erakusten baitu tolestura-norabide

bakoitzerako. Modu honetan, lehenengo aldagaiaren neurketak bi irtenbide posible emango ditu (tolesturaren bi norabide), eta bigarren aldagaia anbiguotasun hori ebazteko gakoa izango da. Adibidez, demagun uhin-luzera desplazamendu jakin bat neurtu dela. Arestian azaldu den bezala, tolestura norabide desberdin bik eragin dezakete aldaketa hori. Une horretan, argi-indarraren neurketa anbiguotasuna ezabatzeko gakoa izango da, izan ere, posible den soluzio batean (uhin-luzera aldatzea eragiten duten tolestura norabideetako batean), neurtutako argi-indarra handituko baita, beste norabidean gutxitzen den heinean. Horrek bi aldagaietan aldi berean aldaketa horiek eragiten dituen tolestura-norabide posible bakarra uzten du. Prozedura berdina aldagaiak alderantzikatuz egin daiteke: argiaren potentziaren neurketa erabiliz posible diren bi soluzio emateko eta uhin-luzeraren desplazamendua anbiguotasuna ezabatzeko. Hori dela eta, bi aldagaien aldibereko neurketa konbinatuz, anbiguotasuna ebatz daiteke eta tolestura norabidea 360° -tan neur daiteke, gailua okerduraren noranzkoarekiko sentikor bihurtuz (noranzko guztietarako). Horretarako, 34. irudian agertzen den galdeketaren konfigurazioa ezarri zen, bi parametroak aldi berean neurtzeko.

Jokabide hori frogatzeko, uneoro espektrometroaren galdeketa eremuan (1510 eta 1595 nm tartean) dagoen eta bigarren mailako maximorik ez dituen espektro bat emateko gai den MCF segmentuaren (L_f) luzera bat behar zen. Azken hau derrigorrezkoa da galdeketa-eremu berean islatutako argi indarra neurtzerakoan kontrako joerak dituzten aldameneko lobuluek eragiten duten sentsibilitate-galera minimizatzeko (bata handitzen da bestea gutxitzen denean), [91]-an agertzen den bezala. Aipatutako eskakizunak betetzen zituen L_f a lortzeko, PhotonDesign simulazio-softwarea erabili zen, eta simulazio-emaitzek MCF luzerarik egokiena 8 mm-koa zela adierazi zuten. Simulatutako eta fabrikatutako gailuen espektroen arteko antz handia 50. irudian erakusten da.



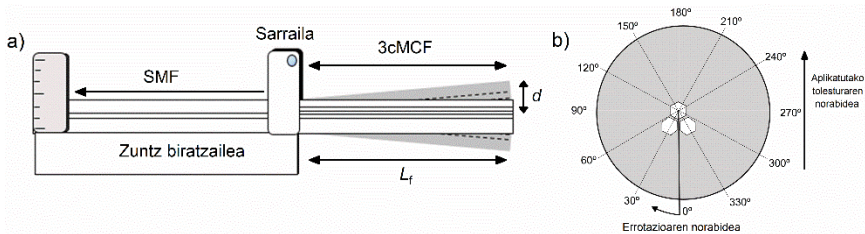
50. irudia: 3cMCFa duten 8 mm-ko fabrikatutako eta simulatutako gailuen espektroak.

Sentsorea horizontalki finkatu zen zuntz biragailu batean (Thorlabs HFR007). Horrela, MCF segmentua kantilera konfigurazioan ezarri zen (ikus 51a. irudia). Konfigurazio horri esker, MCFari aplikatutako tolestura-planoa zehazki hautatu ahal zen. Zuntza mutur batean finkatu zen zuntz biragailuaren txaloarekin SMF-MCF fusio-puntuan, beste muturra askatuta utziz, 51a irudian erakusten den moduan. MCFaren luzera kantilera konfigurazioan (L_f) 8 mm-koa zenez, zuzen zegoen tolesturarik aplikatzen ez zenean. Egoera horretan, erreferentzia-posizioa izango zen nukleoaren orientazioa ezartzeko (0° 51b irudian), bereizmen handiko kamera (Dyno-Lite AM4116T) jarri zen MCFaren aurrean nukleoaren orientazioa ikuskatzeko. Erreferentzia gisa erabiltzea erabaki zen hasierako nukleoaren orientazioa, nukleoak alderantzizko V itxurako konfigurazioan zeudenean izan zen, 51b irudian adierazten den moduan.

MCFak bere nukleoak orientazio horretan zituenean, zeramikako hodi mehe bat ezarri zen bere aurrean (Omega Engineering TRX-005132-6), zeinaren zuloaren barruko diametroa ($127 \mu\text{m}$) MCFaren diametroa baino zertxobait handiagoa zena ($125 \mu\text{m}$). Desplazamendu mikrometrikoko plataforma baten bidez (Thorlabs RB13M), MCFa eta hodia lerrotatu ziren. Lerrotatze horri esker,

zuntza aurrerapauso mikrometrikotan desplazatu zen, MCFaren mutur soltearen 0.5 mm zeramikako hodian sartu arte. MCFaren diametroaren eta zeramikako hodiaren arteko desberdintasun estuari esker, MCFa ondo enkaxatu zen hartan, zuntzaren malgutasuna saihestuz.

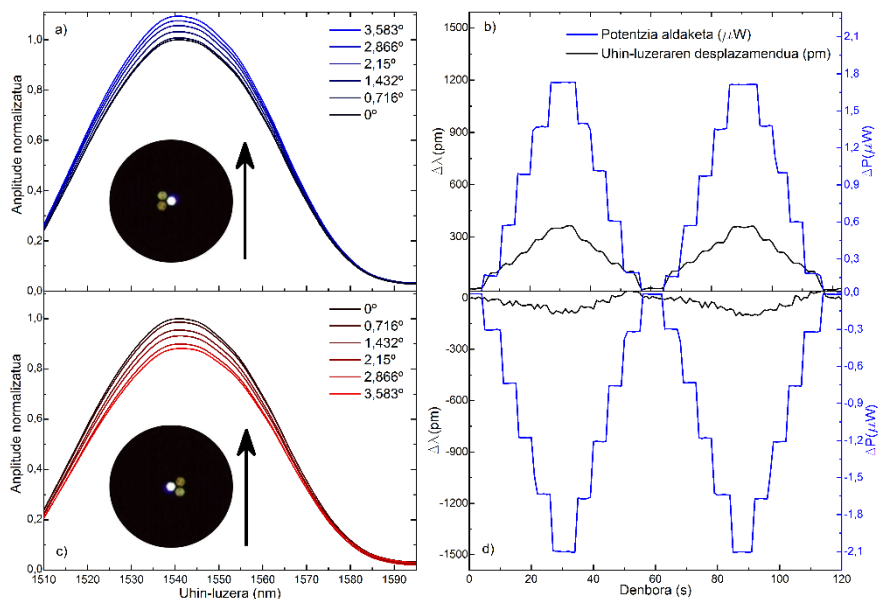
Horren ondoren, zeramikako hodia zehaztasun handiko plataforma batean finkatu zen (Thorlabs LTS150), bertikalki gorantz eta beherantz zehaztasun handiz mugitzeko, plataforma horrek gutxieneko $0.1 \mu\text{m}$ -ko mugimendu lorgarria baitu, fabrikatzailearen arabera. Modu honetan, hodia gora eta behera mugitzen zenean, zuntza tolestu eta triangelu bat sortzen zen, zeinen aldeak zuntzaren benetako posizioa, hasierako posizio horizontala (L_f) eta d desplazamendu bertikala ziren, 51a irudian adierazten den moduan. Zuntzari tolestura aplikatzeko mekanismo hau ugari erabili denaren antzekoa da [89, 91, 93, 94]. 51. irudiaren arabera, tolestura-anguluaren graduak $\sin \theta = d/L_f$ ekuazioaren bidez kalkulatu ziren. Horren arabera, d ren goranzko edo beherako pauso bakoitza $100 \mu\text{m}$ -koa zenez, urrats bakoitzean aplikatutako tolestura 0.716° -koa zela esan nahi zuen 3.583° -ra iritsi arte. Prozesu hau MCFaren biraketaren 30° bakoitzeko guztietan errepikatu zen 51b irudian adierazitako norabidean, bere ardatzaren inguruan biraketa osoa 5 aldiz osatu arte.



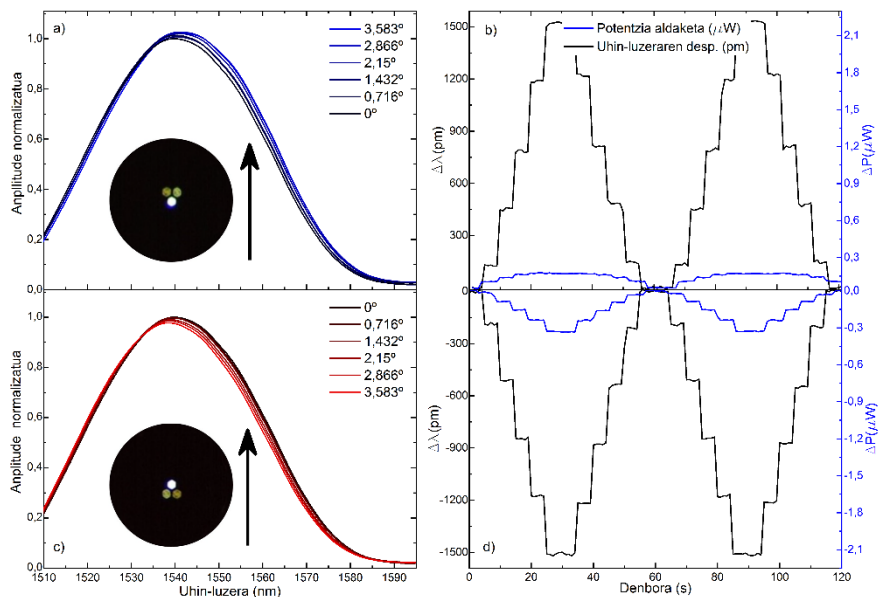
51. irudia: a) tolestura aplikatzeko konfigurazioaren eskema eta b) 3cMCF-aren biraketaren noranzkoa, ebaluatutako puntuak eta aplikatutako tolestura norabidea adierazita daudelarik.

Bildutako espektroen konparazioa eta dagokien uhin-luzeraren desplazamenduaren eta argi-potentziaren aldakuntzaren arteko

neurketa 3cMCFak flexio-plano beraren aurka kontrako nukleoen orientazioak dituen bi kasuak erakusten dira 52. eta 53. irudietan. Kontuan izan aplikatutako tolestura-norabide eta angelu berdinetarako, espektroen aldaketak batez ere argi-potentziaren aldakuntzetatik (ikus 52. irudia) batez ere uhin-luzeraren desplazamendura (ikus 53. irudia) doazela ziklo batetik bestera seinale oso egonkorrekin. Bilakaera hori progresiboki gertatu zen erlojuaren biraketaren noranzkoan. Beraz, tarteko posizio bakoitzean, uhin-luzeraren desplazamendu eta argi-potentziaren aldaketaren arteko konbinazio lineal espezifikoa ikusi zen.



52. irudia: Bildutako espektroak eta neurtutako parametroen denboraren araberrako eboluzioaren bi ziklo sentsorea geziak adierazten duen norabidean tolestu zenean eta 3cMCFa a) b) 90° eta c) d) 270° hasierako 0° posizioarekiko biratu zenean, hurrenez hurren.

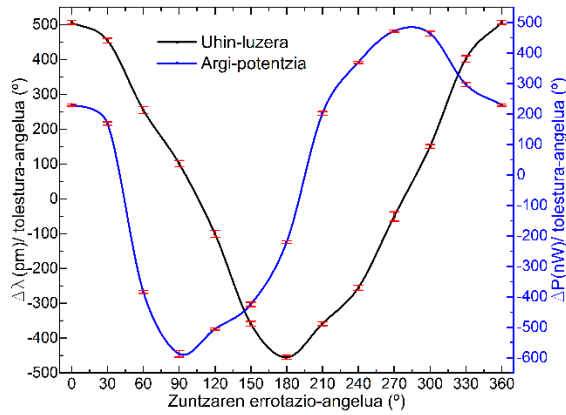


53. irudia: Bildutako espektroak eta neurtutako parametroen denboraren arabera eboluzioaren bi ziklo sentsorea geziak adierazten duen norabidean tolestu zenean eta 3cMCFa a) b) 180° eta c) d) 360° hasierako 0° posizioarekiko biratu zenean, hurrenez hurren.

Jokabide espektral hori aztertuta, ondoriozta daiteke bi aldagaien (uhin-luzeraren desplazamendua eta argi-potentziaren aldakuntzak) neurketa konbinatuz, gailu hau edozein tolestura-norabide neurtzeko gai dela 360°-tan eta tolestura-anplitude angeluak neurtzeko gai dela ere bai 3.583°-ra arte, 3cMCFaren oinarritzko orientazio bakoitzean joera eta sentsibilitate bakarrak aitortu baitaitezke. Gainera, emaitza horiek iradokitzen dute erabili aurretik egin beharreko nukleoaren eta tolestura-norabidearen arteko lerrokatze zehatza ez dela beharrezkoa MCFan oinarritutako tolestura-bektore sentsore hau erabiltzeko.

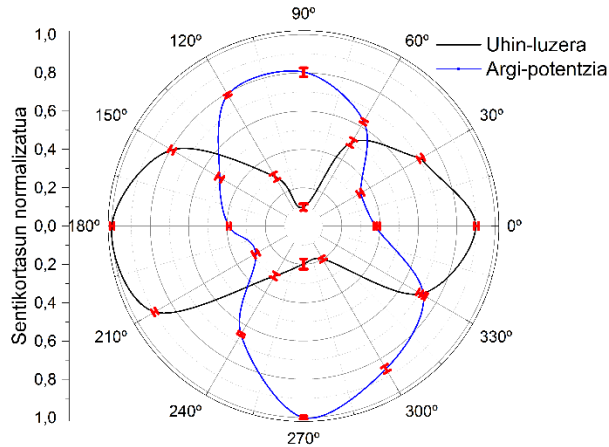
Uhin-luzeraren desplazamenduari eta argi-potentziaren aldaketari dagokienez, dagozkien tolestura-sentsibilitate eta desbideratze estandarrak 54. irudian laburbiltzen dira aplikatutako tolestura eta 3cMCFaren orientazio guztietarako. Sentikortasun maximoak $506.72 \pm 5.5 \text{ pm}/^\circ$ eta $587.5 \pm 11.08 \text{ nW}/^\circ$ izan ziren, uhin-luzera eta argi-

potentziaren aldaketarako, hurrenez hurren. Balio horiek uhin-luzeraren desplazamendurako 0.01° -ko ziurgabetasuna adierazten dute neurketan eta 0.018° -ko ziurgabetasuna potentzia aldakuntzarako. Parametro bakoitzaren joera eta sentsibilitate konbinazio bakarra dago puntu bakoitzean, eta horrek anbiguotasunik gabeko tolestura-norabidearen eta anplitudearen detekzioa ahalbidetzen du. 52. eta 53. irudietako emaitzetatik aurreikusi ahal zen moduan, bi kurbak beraien artean 90° defasatuta daudela antzeman daiteke.



54. irudia: Uhin-luzeraren desplazamendua eta argi-potentziaren aldakuntzaren sentsibilitatea eta dagokien desbiderapen estandarrak zuntzaren posizio bakoitzerako.

55. irudia 54. irudiko emaitzen irudikapen polar normalizatua da, balio absolutuan. Islapen-espektroaren desplazamendua maximoa denean, argi-potentziaren aldaketa minimoa da, eta alderantziz. Beste orientazioetan, berriz, potentzia-aldakuntzaren eta uhin-luzeraren desplazamenduaren arteko konbinazio espezifikoak antzeman daiteke.



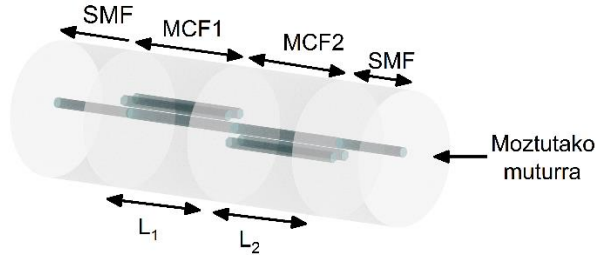
55. irudia: Sentsibilitate eta desbideratze estandarren irudikapen polar normalizatua balio absolutuan.

Aldi bereko uhin-luzeraren desplazamendua eta argi-potentziaren aldakuntzaren neurketak konbinatuz, 3cMCFz osaturiko 8 mm-ko sentore sinplea garatu zen, tolesturaren norabidea eta anplitudea 360°-tan zehaztasunez antzemateko gai dena. Gailu honek ez du lerrokadura zehatzik behar, eta tolestura-angelu txiki zen handiak neurtzeko gai da, 1° azpitik 3.583°-ra arte.

1.3.4.3 Azelerometroa

*Puntu honetan, “Highly sensitive multicore fiber accelerometer for low frequency vibration sensing” artikulua en laburpen bat azaltzen da. Artikulu hau Scientific Reports aldizkarian argitaratu zan 2020ko irailean eta tesiaren eranskinaren atalean dago **3. artikulua** gisa xehetasun gehiago kontsultatzeko.*

Atal honetan, luzera desberdineko (L_1 eta L_2 , hurrenez hurren) eta 180° biratuta dauden 3cMCFren bi segmentuz (MCF1 eta MCF2 izenekoak) osatutako azelerometroa erakusten da. 3cMCFren segmentuak modu bakarreko zuntz estandarren artean daude, islapen-konfigurazioan funtzionatzen duen SMF-MCF1-MCF2-SMF egitura sortuz (ikus 56. irudia).



56. irudia: Gailuaren eskema.

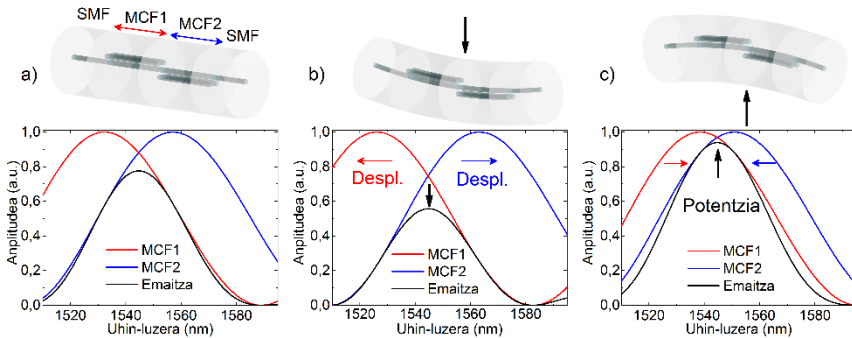
3cMCFz osatutako kaskada-konfigurazio honetarako, 36. ekuazioaren arabera, irteeran dagoen potentzia segmentu bakoitzaren irteeran dagoen potentzia normalizatuaren arteko produktua da:

$$\begin{aligned}
 P_0(L_1, L_2) = & \cos^2\left(\sqrt{3} \frac{\pi\Delta n}{\lambda} L_1\right) * \cos^2\left(\sqrt{3} \frac{\pi\Delta n}{\lambda} L_2\right) + \\
 & + \frac{1}{9} \sin^2\left(\sqrt{3} \frac{\pi\Delta n}{\lambda} L_1\right) * \sin^2\left(\sqrt{3} \frac{\pi\Delta n}{\lambda} L_2\right) + \frac{1}{3} \cos^2\left(\sqrt{3} \frac{\pi\Delta n}{\lambda} L_1\right) * \sin^2\left(\sqrt{3} \frac{\pi\Delta n}{\lambda} L_2\right) + \\
 & + \frac{1}{3} \cos^2\left(\sqrt{3} \frac{\pi\Delta n}{\lambda} L_2\right) * \sin^2\left(\sqrt{3} \frac{\pi\Delta n}{\lambda} L_1\right)
 \end{aligned} \quad (44)$$

Honela, arestian esan bezala, islapen-konfigurazioan funtzionatzen duen kaskada-egiturak segmentu bakar batek baino puntu goren estuagoa eta ikuspen handiagoak emango ditu, espektroaren edozein aldaketa jarraitzeak erraztuko dutenek.

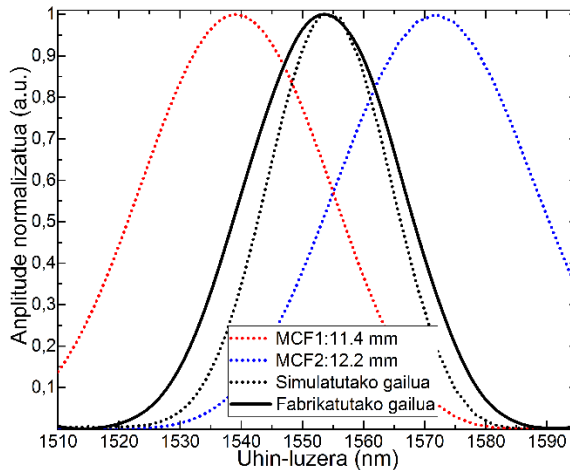
Zuntzen antolamenduari dagokionez, 3cMCFren bi segmentuak 180° biratuz elkarren artean, haietako bakoitzak kontrako portaera erakutsiko du uhin-luzeraren desplazamenduari eta espektroaren anplitudeari dagokionez, aurreko atalean eta [91]-n azaltzen den norabidearekiko izaera sentikorra dela eta zuntz mota hau okertzen denean. 3cMCF segmentu bakoitzaren nukleoaren posizioa eta aplikatutako tolestura 57. irudian bezala lerrokatuta daudenean, non MCF segmentuetako batek nukleoak V bezalako konfigurazioan orientatuta dituen eta besteak alderantzizko V moduko konfigurazioan orientatuta dituen (edo 180° biratuta), anplitudearen aldakuntzak bakarrik gertatuko dira espektroan. Gailuak 57. irudian

bezala funtziona dezan, luzera desberdineko MCF segmentuak derrigorrezkoak dira neurketan anbiguotasuna ekiditeko. Luzerak berdinak izango balira, bi segmentuen espektroak gainjarrita egongo lirateke efekturik aplikatzen ez denean, puntu hori islatutako argi-potentzia maximoa gertatuko den momentua izanik. Espektrorako bakoitza kontrako noranzkoetan aldatuko zen egitura okertzen denean, baina potentziaren jaisierak bakarrik erregistratuko lirateke, potentzia-irakurketa berdinak edo antzekoak lortuz kontrako noranzko okerdurentzako. Luzera desberdinetako segmentuak erabiliz, berriz, anbiguotasun edo sentsibilitate galera hori saihesten da, izan ere, kasu honetan, neurtutako potentzia hazi eta murriztu egingo da aplikatutako okerduraren norabidearen arabera geldirik dagoen neurketarekin alderatuta. Espektrorako anplitude-aldaketak potentzia-aldaketekiko proportzionalak dira, eta, beraz, PD bat besterik ez da beharrezkoa izango gailuaren galdeketa egiteko. Sinpletasun honek SMF-MCF1-MCF2-SMF egitura hau erakargarri bihurtzen du azelerometro oso sentikor eta errentagarriak egiteko, funtzionatzeko ez baitu neurrira egindako ekipamendu berezirik behar.



57. irudia: 3MCFko segmentu bakoitzaren espektrorako simulatuak eta haien arteko emaitza egitura elkarketatik a) zuzen, b) gorantz eta c) beherantz okertzen denean. Geziek kasu bakoitzaren okerduraren norabidea, uhin-luzeraren desplazamendua edo potentzia-aldaketa adierazten dute. MCF1en nukleoak V moduko konfigurazioan daude, eta MCF2koak alderantzizko V itxurako konfigurazioan daude.

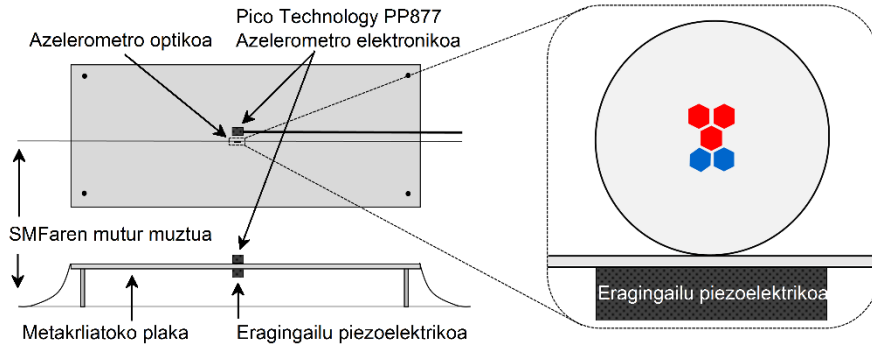
Ezaugarri horiek dituen gailua fabrikatzeko, diseinuaren betebeharrak batzuk kontuan hartu behar ziren: bere espektroa galdeketa-leihoan egon behar zen (1510 eta 1595 nm tartean) edozein unetan eta puntu goren bakarra eta ondo zehaztuta eduki behar du, bigarren mailako lobulu gabe. Eskakizun hauek derrigorrezkoak dira kontrako joerak dituzten bigarren mailako lobuluek eragiten duten sentsibilitate-galera minimizatzeko argi-potentzia islatua neurtzerakoan (bata handitzen da eta bestea gutxitzen da), [91]-n erakusten den moduan. Eskakizun hauek betetzen zituzten MCF segmentuen luzera egokienak 11.4 mm eta 12.2 mm izan ziren, 23.6 mm-ko gailu trinkoa lortuz. Simulatutako eta fabrikatutako gailuen espektroak 58. irudian agertzen dira, egitura osatzen duten MCF segmentu bakoitzaren simulazioekin batera. Simulazio hauek PhotonDesign softwarearekin egin ziren.



58. irudia: Simulatutako (marradun lerro beltza) eta fabrikatutako gailuen (lerro beltza) espektro normalizatuak. Bi kurben maximoa 1554 nm inguruan dago eta ez dago bigarren mailako lobulurik. 11.4 mm-ko (marradun lerro gorria) eta 12.2 mm-ko (marradun lerro urdina) segmentuen espektro simulatuak ere agertzen dira. 44. ekuazioan adierazten den moduan, euren arteko produktuaren emaitza marradun lerro beltza da.

Gailua probatzeko, horizontalki finkatutako laukizuzeneko formako metakrilatoko plaka mehe bat erabili zen. Haren azpi eta erdian, eragingailu piezoelektriko bat (Thorlabs APFH720 Thorlabs

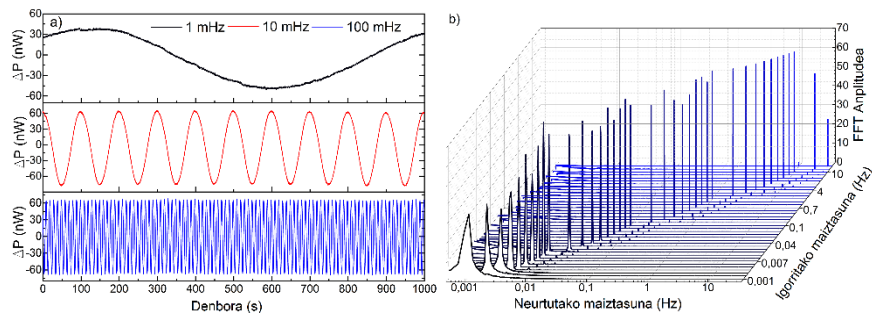
MDT694B anplifikadorearekin konbinatuta) finkatu zen, plakak plano bertikalean soilik bibratu ahal izateko. Eragingailu piezoelektrikoa funtzio-sorgailu batera konektatu zen (Keysight Technologies 33220A) anplitude eta maiztasun anitzeko seinaleak sortzeko. Horren ondoren, fabrikatutako gailua plakaren goiko gainazalera itsatsi zen zianoakrilatozko itsasgarri batekin, MCF1-MCF2-en arteko elkartzepuntua eragingailu piezoelektrikoaren gainean kokatuz, 59. irudian agertzen den konfigurazio esperimentalaren eskeman ikus daitekeen bezala. 57. irudian bezala orientaturik itsatsi zen gailua gainazalera, nukleoaren orientazioa bibrazioaren norabidearekin bat etortzeko. Gailuaren ondoan, azelerometro komertzial bat itsatsi zen (Pico Technology PP877 Pico Technology TA096rekin batera), azelerometro elektronikoa honek bibrazioaren anplitudearen eta azelerazioaren arteko erlazioa ematen baitzuen. Galdeketa-sistema 34. irudiko konfigurazioarekin egin zen.



59. irudia: Esperimentuaren alboko eta goiko bista eskematikoak. Lehen planoan, fabrikatutako azelerometro optikoa plakaren gainazalera nola itsatsi zen erakusten da. Nukleo gorriak MCF1renak dira eta urdinak MCF2koak. Nukleo zentral gorriak MCF1 MCF2ren aurrean dagoela adierazten du, nukleo zentral komuna partekatzen baitute.

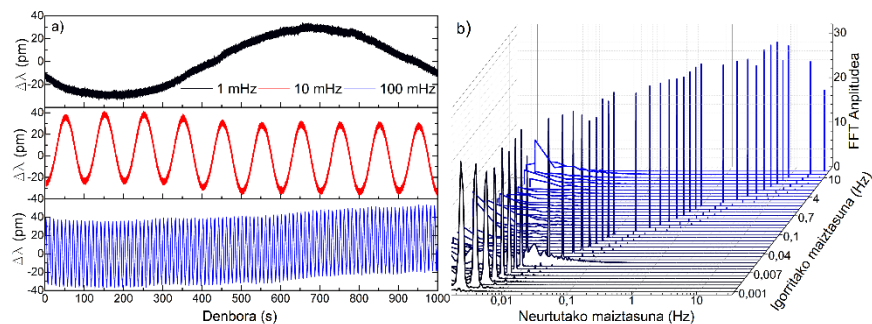
Lehenengo proba 1 Vpp anplitudeko seinale sinusoidalak igortzean eta beren maiztasuna 30 Hz-tik 1 mHz-ra (funtzio sorgailuak ematen duen maiztasunik baxuena) hainbat urratsetan aldatzean zitzan, gailuen detekzio-muga (LoD) maiztasunari dagokionez definitzeko. Fabrikatutako gailuak 1 mHz-ra arteko bibrazio guztiak hauteman

zituen argi eta garbi bai uhin-luzeraren desplazamendu bai argipotentziaren aldaketan (ikus 60. eta 61. irudiak). 61. irudiko uhin-luzeraren desplazamendu txikiak gailua nukleoen orientazio egokiarekin plakara itsatsi zela adierazten du, eta bere FFT anplitudeak potentzia aldaketarenak baino txikiagoak direnaren zergatia azaltzen du. Hala ere, potentziaren aldaketa maximizatzea helburu duen konfigurazio honetan ere, gailuak halako maiztasun txikiak antzeman ditu uhin-luzeraren desplazamenduaren bitartez ere, duen sentzibilitate handiaren erakusle dena. Azelerometro komertzialari dagokionez, 2 Hz-tik gorako bibrazioak soilik hauteman zituen, seinale nabarmen zatatsukoak eta harmonikoen maila altuak zituztenak (ikus 62. irudia).



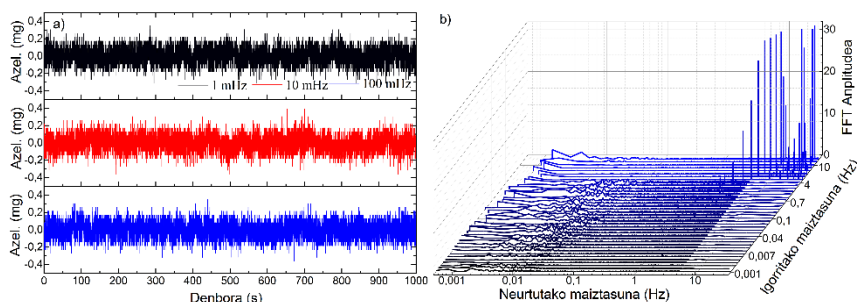
60. irudia: Potentzia neurketen emaitzak fabrikatutako gailu optikoan. a) Hiru kasu adierazgarrienen erantzuna denboraren arabera. b) FFT anplitudeak 30 Hz-tik 1 mHz-ra bitarteko frekuentzientzat 1 V_{pp}-ko seinale sinusoidalera.

Neurututako maiztasunaren ardatza eskala logaritmikoan dago.



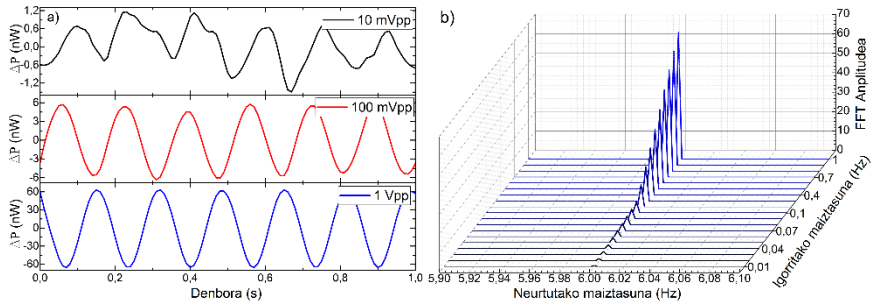
61. irudia: Uhin-luzeraren desplazamenduaren emaitzak fabrikatutako gailu optikoan. a) Hiru kasu adierazgarrienen erantzuna denboraren arabera. b) FFT

amplitudeak 30 Hz-tik 1 mHz-ra bitarteko frekuentzientzat 1 Vpp-ko seinale sinusoidalerako. Neurtutako maiztasunaren ardatza eskala logaritmikoan dago.

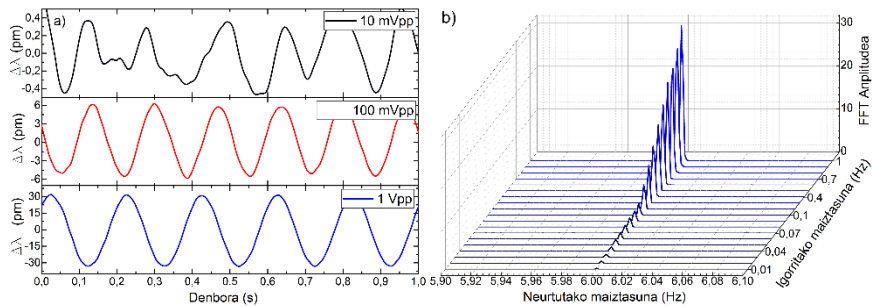


62. irudia: Azelerazioaren emaitzak azelerometro elektronikoan. a) Hiru kasu adierazgarrienen erantzuna denboraren arabera. b) FFT amplitudeak 30 Hz-tik 1 mHz-ra bitarteko frekuentzientzat 1 Vpp-ko seinale sinusoidalerako. Neurtutako maiztasunaren ardatza eskala logaritmikoan dago.

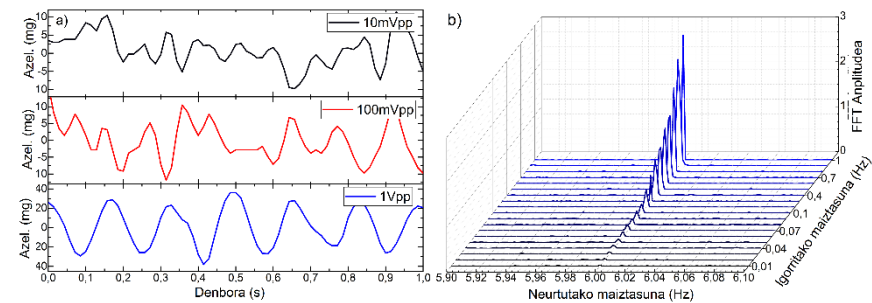
Bigarren proba maiztasun finkodun (6 Hz) seinale sinusoidal bat igortzean eta honen amplitudea 1 Vpp-tik 10 mVpp-ra (funtzio-sorgailuak ematen duen amplitudearik txikiena) aldatzean zitzan, gailu bakoitzaren LoDa bibrazioen amplitudearen arabera definitzeko, oszilazio mugimenduaren azelerazioarekin lotura duena. Bi gailuen denbora-erantzunak eta FFT amplitudeak 63. iruditik 65. irudira agertzen dira. Gailu optikoak 10 mVpp-ra arteko bibrazioak antzeman zituen 3:1 SNR irizpideen gainetik, normalean arau gisa hartzen dena [95]. Ikus daitekeen denboraren domeinuko (ikus 63a eta 64a. irudiak) eta FFTaren (ikus 63b eta 64b. irudiak) seinaleen amplitudearen jaitziera progresiboa igorritako seinalearen amplitudearen txikitzearekiko proportzionala da. Bi kasuetan (uhin-luzeraren desplazamendua eta potentzia aldatetak), igorritako seinalea argi antzeman daiteke eta harmonikoen maila baxua nabaria da. Azelerometro komertzialari dagokionez, 30 mVpp-rainoko seinaleak soilik hauteman zituen (ikus 65. irudia).



63. irudia: Potentzia neurketen emaitzak fabrikatutako gailu optikoan. a) Hiru kasu adierazgarrienen erantzuna denboraren arabera, eta b) FFT anplitudeak 6 Hz-eko eta 1 Vpp-tik 10 mVpp-ra doan anplitudea duen igorritako seinale sinusoidal batentzat.

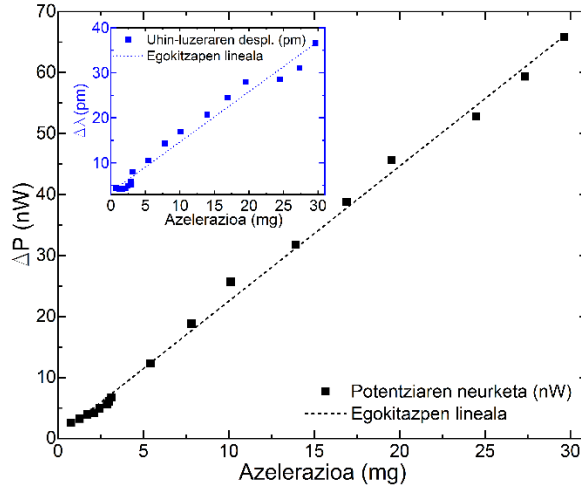


64. irudia: Uhin-luzeraren desplazamenduaren emaitzak fabrikatutako gailu optikoan. a) Hiru kasu adierazgarrienen erantzuna denboraren arabera, eta b) FFT anplitudeak 6 Hz-eko eta 1 Vpp-tik 10 mVpp-ra doan anplitudea duen igorritako seinale sinusoidal batentzat.



65. irudia: Azelerazioaren emaitzak azelerometro elektronikoan. a) Hiru kasu adierazgarrienen erantzuna denboraren arabera, eta b) FFT anplitudeak 6 Hz-eko eta 1 Vpp-tik 10 mVpp-ra doan anplitudea duen igorritako seinale sinusoidal batentzat.

Proba hauen ondorioz lortutako kalibrazioa 66. irudian ageri da.



66: irudia: Fabrikatutako azelerometro optikoaren kalibrazioa.

Uhin-luzeraren desplazamenduaren eta potentziaren aldaketaren portaera lineala adierazgarria da, batez ere azken honetan, non 2.213 nW/mg-ko sentsibilitatea lortu zen 0.997-ko Pearsonen korrelazio koefiziente karratuarekin ($R^2=0.997$) eta 1.083 $\mu\text{g}/\sqrt{\text{Hz}}$ -ko zarata-dentsitatearekin. Beraz, potentziaren aldaketa (ΔP) eta azelerazioaren (mg-tan) arteko korrelazioa honela adieraz daiteke:

$$a = 0.450\Delta P - 0.143 \quad (45)$$

Uhin-luzeraren desplazamendu-neurketen arabera, 1.116 pm/mg-ko sentsibilitatea lortu zen 0.976-ko Pearsonen korrelazio koefiziente karratuarekin ($R^2=0.976$). Azpimarratu behar da MCFan oinarritutako azelerometro hau potentziaren aldaketaren neurketekin funtzionatzeko optimizatu dela, uhin-luzeraren desplazamenduari dagokionez sentsibilitate txikia suposatzen duena. Beraz, emaitza hauek gailua 59. irudian irudikatutako modutik oso gertu jarri zela adierazten dute, eta gailua nahi den bezala funtzionatzen duela adierazten du.

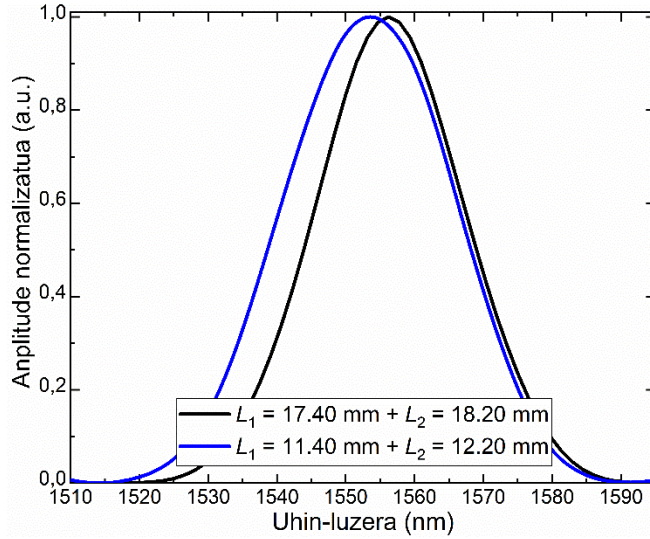
Lan honetan, zuntzez osatutako azelerometro trinko eta oso sentikorra erakusten da. Bere egitura espektroaren anplitudearen

aldaketa optimizatzeko diseinatuta dago, potentziaren aldaketarekin lotuta dagoena. Konfigurazio honi esker, bere galdeketa-sistema oso erraza da, ekipamendu gutxi eta sinplez egina eta errentagarritasun altua duena. Gailua 1 mHz-rainoko maiztasun baxuko bibrazioak hautemateko gai izan zen 2.213 nW/mg-ko sentsibilitatearekin, erakargarria izan daitekeena ezaugarri horiek eskatzen dituzten aplikazioetan, hala nola sismologian.

1.3.4.4 Noranzko sentikortasuna duen kurbatura-sentsorea

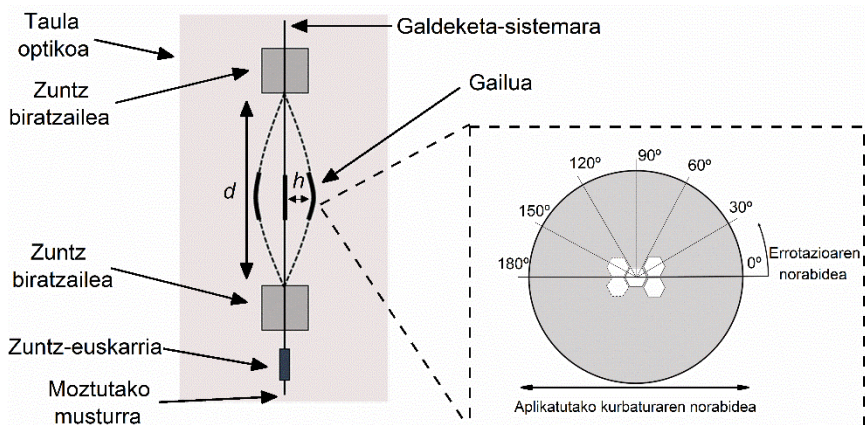
*Puntu honetan, “Composed multicore fiber structure for direction-sensitive curvature monitoring” artikulua laburpena azaltzen da. Artikulu hau APL Photonics aldizkarian argitaratu zan 2020ko uztailan eta tesiaren eranskinaren atalean dago **4. artikulua** gisa xehetasun gehiago kontsultatzeko.*

Atal honetan, **3. artikuluko** sentsorearen arkitektura eta galdeketa-konfigurazio bera erabili ziren kurbatura neurtzeko (ikus 56. irudia). Hala ere, kasu honetan, SMF-MCF1-MCF2-SMF egitura $L_1 = 17.4$ mm-ko eta $L_2 = 18.2$ mm-ko segmentuekin egin zen, **3. artikuluan** baino puntu goren zorrotz eta estuagoa lortzeko espektroan (ikus 67. irudia). Nukleo zentrolean akoplatutako potentziaren adierazpena aurreko gailuaren berbera da (44. ekuazioa), baita galdeketaren konfigurazioa ere (ikus 34. irudia).



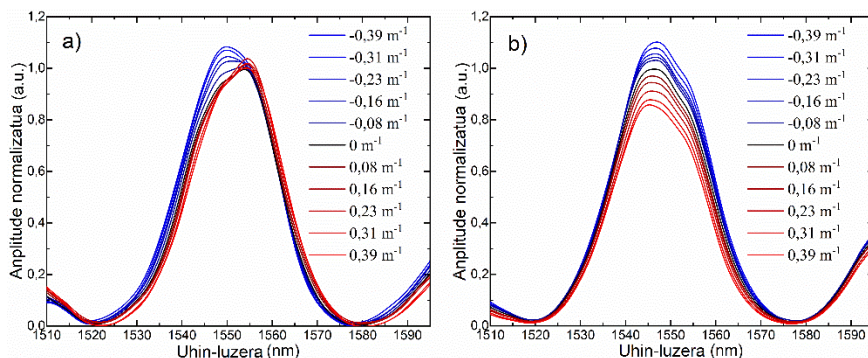
67. irudia: **3. artikuluko** (lerro urdina) eta **4. artikuluko** (lerro beltza) fabrikatutako gailuen espektroak.

Gailua kurbatzeko, muturretako SMFetatik eutsi zen lehenik eta behin. Horren ondoren, SMFak biragailuetan (Thorlabs HFR001) muntatutako bi zuntz-euskarrien bidez tinkatu ziren eta posizio bertikalean kokatutako taula optiko batean finkatu zen gailu osoa. Beste zuntz-euskarri bat erantsi zen beheago zegoen SMFaren amaieran masa gisa aritzeko (20 g) eta grabitatearen bidez zuntzaren tentsioa konstante mantentzeko. Kurbaduraren neurketak gailuko 3cMCF segmentuen orientazio desberdinetarako egin ziren, 0° eta 180° artean 30° -ko urratsetan (ikus 68. irudia) eta mikrometroko bereizmena duen translazio-etapa bat erabili zen egitura bere MCF1-MCF2 elkartze-puntutik okertzeko. Gailuaren kurbaduraren balioa (C) ondoko ekuazioarekin kalkulatu zen: $C = 12h/d^2$ [96], non h translazio-etaparen desplazamendua den eta d bi zuntz-biratzailen arteko distantzia den.

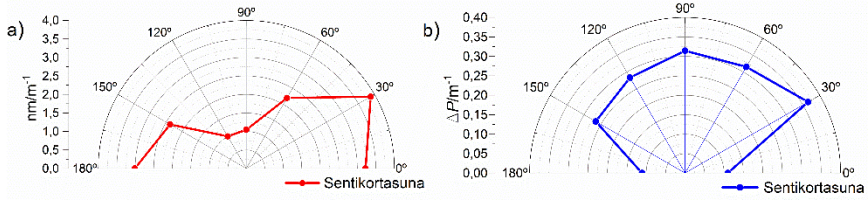


68. irudia: Neurketen konfigurazioaren diagrama eskematikoa.

69. irudian, gailuari bi norabide perpendikularreko kurbadura aplikatu zitzaizkionean ikusitako espektroak erakusten dira (0° eta 90° orientazioak 68. irudiaren arabera). Kontuan izan behar da uhin-luzeraren desplazamendua handiagoa denean intentsitate aldaketak minimoak direla eta alderantziz. Jokabide hau gailuaren arkitekturarengatik eta bertan zeuden 3mCFCen asimetriagatik espero zen, **3. artikuluan** erakutsi den moduan.

69. irudia: Kurbatura desberdinetarako espektroak gailuaren posizioa a) 0° eta b) 90° zirenean, hurrenez hurren.

70. irudian 68. irudian adierazitako gailuaren zazpi orientazio desberdinetan neurtutako batez-besteko kurbadura-sentsibilitateak erakusten dira.



70. irudia: Batez-besteko kurbaduraren sentikortasunaren irudikapen polarra a) uhin-luzeraren desplazamenduari eta b) intentsitate-aldaketei dagokienez.

Beraz, lan honetan, kurbaduraren anplitudea eta norabidea emateko gai den gailu oso sentikor bat erakutsi da. Hemen deskribatutako sentsorearen kurbaduraren sentsibilitatea 4.66 dB/m^{-1} -koa izan da intentsitate-aldaketak kurbadurarekin erlazionatu direnean.

Bibliografia

- [1] J. S. Wilson, *Sensor technology handbook*. Elsevier, 2004.
- [2] S. L. Chuang, *Physics of photonic devices*. John Wiley & Sons, 2012.
- [3] M. Zhang *et al.*, "photonic sensors review progress of optical fiber sensors and its application in harsh environment," vol. 1, no. 1, pp. 84-89, 2011.
- [4] G. E. J. P. E. Sommargren, "A new laser measurement system for precision metrology," vol. 9, no. 4, pp. 179-184, 1987.
- [5] E. Udd and W. B. Spillman Jr, *Fiber optic sensors: an introduction for engineers and scientists*. John Wiley & Sons, 2011.
- [6] J. M. López-Higuera, *Handbook of optical fibre sensing technology*. Wiley, 2002.
- [7] N. Sabri, S. Aljunid, M. Salim, R. Ahmad, and R. Kamaruddin, "Toward optical sensors: Review and applications," in *Journal of Physics: Conference Series*, 2013, vol. 423, no. 1, p. 012064: IOP Publishing.
- [8] D. A. Krohn, "Intensity modulated fiber optic sensors overview," in *Fiber Optic and Laser Sensors IV*, 1987, vol. 718, pp. 2-11: International Society for Optics and Photonics.
- [9] Y.-J. J. O. F. T. Rao, "Recent progress in fiber-optic extrinsic Fabry–Perot interferometric sensors," vol. 12, no. 3, pp. 227-237, 2006.
- [10] P. Lu *et al.*, "Distributed optical fiber sensing: Review and perspective," vol. 6, no. 4, p. 041302, 2019.
- [11] A. D. Kersey and A. Dandridge, "Distributed and multiplexed fiber-optic sensors," in *Optical Fiber Sensors*, 1988, p. WDD1: Optical Society of America.
- [12] P. Roriz, A. Ramos, J. L. Santos, and J. A. J. P. S. Simões, "Fiber optic intensity-modulated sensors: A review in biomechanics," vol. 2, no. 4, pp. 315-330, 2012.
- [13] Y. Qiu, Q.-b. Wang, H.-t. Zhao, J.-a. Chen, and Y.-y. J. J. o. S. J. U. Wang, "Review on composite structural health

- monitoring based on fiber Bragg grating sensing principle," vol. 18, no. 2, pp. 129-139, 2013.
- [14] M. Islam, M. M. Ali, M.-H. Lai, K.-S. Lim, and H. J. S. Ahmad, "Chronology of Fabry-Perot interferometer fiber-optic sensors and their applications: a review," vol. 14, no. 4, pp. 7451-7488, 2014.
- [15] J. Nedoma, M. Fajkus, and R. J. P. E. Martinek, "Measurement of electric current using optical fibers: A Review," vol. 93, no. 11, pp. 140-145, 2017.
- [16] E. J. R. S. Milton, "Review article principles of field spectroscopy," vol. 8, no. 12, pp. 1807-1827, 1987.
- [17] C. Muehlethaler, M. Leona, and J. R. J. A. C. Lombardi, "Review of surface enhanced Raman scattering applications in forensic science," vol. 88, no. 1, pp. 152-169, 2016.
- [18] S. Andonov and M. Cundeva-Blajer, "Calibration for industry 4.0 metrology: touchless calibration," in *Journal of Physics: Conference Series*, 2018, vol. 1065, no. 7.
- [19] V. Majstorovic, S. Stojadinovic, S. Zivkovic, D. Djurdjanovic, Z. Jakovljevic, and N. J. P. C. Gligorijevic, "Cyber-physical manufacturing metrology model (CPM3) for sculptured surfaces–turbine blade application," vol. 63, pp. 658-663, 2017.
- [20] M. J. O. E. Johnson, "Fiber displacement sensors for metrology and control," vol. 24, no. 6, pp. 961-1, 1985.
- [21] T. J. I. T. o. C. Calvin, Hybrids, and M. Technology, "Quality control techniques for" zero defects", " vol. 6, no. 3, pp. 323-328, 1983.
- [22] C. Boller and N. Meyendorf, "State-of-the-art in Structural Health monitoring for aeronautics," in *Proceedings of the International Symposium on NDT in Aerospace*, 2008.
- [23] G. Wild, "Optical fiber Bragg grating sensors applied to gas turbine engine instrumentation and monitoring," in *2013 IEEE Sensors Applications Symposium Proceedings*, 2013, pp. 188-192: IEEE.
- [24] S. Heath and M. Imregun, "A survey of blade tip-timing measurement techniques for turbomachinery vibration," 1998.

- [25] I. García, J. Beloki, J. Zubia, G. Aldabaldetrekú, M. A. Illarramendi, and F. J. S. Jiménez, "An optical fiber bundle sensor for tip clearance and tip timing measurements in a turbine rig," vol. 13, no. 6, pp. 7385-7398, 2013.
- [26] D. Wisler, "Loss reduction in axial-flow compressors through low-speed model testing," 1985.
- [27] M. W. Wiseman and T.-H. Guo, "An investigation of life extending control techniques for gas turbine engines," in *Proceedings of the 2001 American Control Conference.(Cat. No. 01CH37148)*, 2001, vol. 5, pp. 3706-3707: IEEE.
- [28] N. Kishi and E. Yamashita, "A simple coupled-mode analysis method for multiple-core optical fiber and coupled dielectric waveguide structures," *IEEE Transactions on Microwave Theory and Techniques*, vol. 36, no. 12, pp. 1861-1868, 1988.
- [29] K. J. Melcher and J. A. Kypuros, "Toward a fast-response active turbine tip clearance control," 2003.
- [30] J. L. Geisheimer and T. Holst, "Metrology considerations for calibrating turbine tip clearance sensors," in *Proceedings of the XIX Biannual Symposium on Measuring Techniques in Turbomachinery Transonic and Supersonic Flow in Cascades and Turbomachines, Rhodes-St-Genève, Belgium*, 2007, pp. 7-8.
- [31] A. Kempe, S. Schlamp, T. Rösger, and K. Haffner, "Spatial and temporal high-resolution optical tip-clearance probe for harsh environments," in *Proceedings of the 13th International Symposium on Applications of Laser Techniques to Fluid Mechanics, Lisbon, Portugal*, 2006, pp. 26-29: Citeseer.
- [32] A. W. Snyder, "Coupled-Mode Theory for Optical Fibers," *Journal of the Optical Society of America*, vol. 62, no. 11, pp. 1267-1277, 1972/11/01 1972.
- [33] V. Georgiev *et al.*, "The blade flutter measurement based on the blade tip timing method," in *Proceedings of the 15th WSEAS international conference on Systems, Corfu Island, Greece*, 2011, pp. 14-16.
- [34] S. Wu, Z. Zhao, Z. Yang, S. Tian, L. Yang, and X. Chen, "Physical constraints fused equiangular tight frame method for

- Blade Tip Timing sensor arrangement," *Measurement*, vol. 145, pp. 841-851, 2019/10/01/ 2019.
- [35] A. J. I. J. o. R. M. Sheard, "Blade by blade tip clearance measurement," vol. 2011, 2011.
- [36] L. Du, X. Zhu, J. J. S. m. Zhe, and structures, "A high sensitivity inductive sensor for blade tip clearance measurement," vol. 23, no. 6, p. 065018, 2014.
- [37] B. Yu, T. Zhang, H. Ke, and T. J. I. A. Zhang, "Research on the Tip Clearance Measuring Method Based on AC Discharge," vol. 8, pp. 60355-60363, 2020.
- [38] A. Schicht, S. Schwarzer, L.-P. J. I. T. o. I. Schmidt, and Measurement, "Tip clearance measurement technique for stationary gas turbines using an autofocusing millimeter-wave synthetic aperture radar," vol. 61, no. 6, pp. 1778-1785, 2012.
- [39] M. Violetti, A. K. Skrivervik, Q. Xu, and M. Hafner, "New microwave sensing system for blade tip clearance measurement in gas turbines," in *SENSORS, 2012 IEEE*, 2012, pp. 1-4: Ieee.
- [40] A. Kempe, S. Schlamp, T. Rösger, and K. J. O. l. Haffner, "Low-coherence interferometric tip-clearance probe," vol. 28, no. 15, pp. 1323-1325, 2003.
- [41] T. Pfister, L. Büttner, J. Czarske, H. Krain, R. J. M. S. Schodl, and Technology, "Turbo machine tip clearance and vibration measurements using a fibre optic laser Doppler position sensor," vol. 17, no. 7, p. 1693, 2006.
- [42] I. García *et al.*, "Different configurations of a reflective intensity-modulated optical sensor to avoid modal noise in tip-clearance measurements," vol. 33, no. 12, pp. 2663-2669, 2015.
- [43] I. García, J. Zubia, J. Beloki, J. Arrue, G. Durana, and G. J. S. Aldabaldetrekue, "Optical tip clearance measurements as a tool for rotating disk characterization," vol. 17, no. 1, p. 165, 2017.
- [44] H. Cao, Y. Chen, Z. Zhou, G. J. S. Zhang, and A. A. Physical, "Theoretical and experimental study on the optical fiber bundle displacement sensors," vol. 136, no. 2, pp. 580-587, 2007.
- [45] M. Yasin, S. Harun, H. Abdul-Rashid, A. J. O. Zaidan, and A. M.-R. COMMUNICATIONS, "Performance of optical

- displacement sensor using a pair type bundled fiber from a theoretical and experimental perspective," vol. 1, no. 11, pp. 549-553, 2007.
- [46] H. Huang and U. J. A. o. Tata, "Simulation, implementation, and analysis of an optical fiber bundle distance sensor with single mode illumination," vol. 47, no. 9, pp. 1302-1309, 2008.
- [47] L. Bergougnoux, J. Misguich-Ripault, and J.-L. J. R. o. s. i. Firpo, "Characterization of an optical fiber bundle sensor," vol. 69, no. 5, pp. 1985-1990, 1998.
- [48] S. Cao, F. Duan, Z. Fang, and Y. Ma, "Research on optical fiber bundle displacement sensor with multi-grouped receiving fibers," in *Advanced Laser Technologies 2005*, 2006, vol. 6344, p. 63442Y: International Society for Optics and Photonics.
- [49] S. Cao, F. Duan, and Y. Zhang, "Measurement of rotating blade tip clearance with fibre-optic probe," in *Journal of Physics: Conference Series*, 2006, vol. 48, no. 1, p. 873: IOP Publishing.
- [50] H. Guo, F. Duan, G. Wu, and J. J. R. o. S. I. Zhang, "Blade tip clearance measurement of the turbine engines based on a multi-mode fiber coupled laser ranging system," vol. 85, no. 11, p. 115105, 2014.
- [51] D.-c. Ye, F.-j. Duan, H.-t. Guo, Y. Li, and K. J. O. E. Wang, "Turbine blade tip clearance measurement using a skewed dual-beam fiber optic sensor," vol. 51, no. 8, p. 081514, 2012.
- [52] I. García, R. Przysowa, J. Amorebieta, and J. J. S. Zubia, "Tip-clearance measurement in the first stage of the compressor of an aircraft engine," vol. 16, no. 11, p. 1897, 2016.
- [53] R. Fernández-Bello *et al.*, "Performance Comparison of Three Fibre-Based Reflective Optical Sensors for Aero Engine Monitorization," vol. 19, no. 10, p. 2244, 2019.
- [54] H. A. Rahman, N. M. Isa, and S. W. J. I. S. J. Harun, "Modeling the Concentric Fiber Optic Bundle Displacement Sensor Using a Quasi-Gaussian Beam Approach," vol. 15, no. 9, pp. 4777-4781, 2015.
- [55] J. J. M. Brandão Faria and O. T. Letters, "Modeling the Y-branched optical fiber bundle displacement sensor using a

- quasi-Gaussian beam approach," vol. 25, no. 2, pp. 138-141, 2000.
- [56] M. Yu-zhen, Z. Yong-kui, L. Guo-ping, and L. Hua-guan, "Tip clearance optical measurement for rotating blades," in *MSIE 2011*, 2011, pp. 1206-1208: IEEE.
- [57] G. Webb, P. J. Vardanega, and C. R. J. J. o. B. E. Middleton, "Categories of SHM deployments: technologies and capabilities," vol. 20, no. 11, p. 04014118, 2015.
- [58] E. J. S. S. T. Nyfors and Applications, "Industrial microwave sensors—A review," vol. 1, no. 1, pp. 23-43, 2000.
- [59] K. K. K. Annamdas and V. G. M. Annamdas, "Review on developments in fiber optical sensors and applications," in *Fiber Optic Sensors and Applications VII*, 2010, vol. 7677, p. 76770R: International Society for Optics and Photonics.
- [60] G. Rodriguez, J. R. Casas, S. J. S. M. Villalba, and Maintenance, "SHM by DOFS in civil engineering: A review," vol. 2, no. 4, pp. 357-382, 2015.
- [61] J. Chen, B. Liu, and H. J. F. o. O. i. C. Zhang, "Review of fiber Bragg grating sensor technology," vol. 4, no. 2, pp. 204-212, 2011.
- [62] Y. J. J. o. A. P. Wang, "Review of long period fiber gratings written by CO₂ laser," vol. 108, no. 8, p. 11, 2010.
- [63] L. Li, L. Xia, Z. Xie, and D. J. O. e. Liu, "All-fiber Mach-Zehnder interferometers for sensing applications," vol. 20, no. 10, pp. 11109-11120, 2012.
- [64] R. Kashyap and B. J. j. o. L. T. Nayar, "An all single-mode fiber Michelson interferometer sensor," vol. 1, no. 4, pp. 619-624, 1983.
- [65] K. McKenzie, D. A. Shaddock, D. E. McClelland, B. C. Buchler, and P. K. J. P. r. l. Lam, "Experimental demonstration of a squeezing-enhanced power-recycled Michelson interferometer for gravitational wave detection," vol. 88, no. 23, p. 231102, 2002.
- [66] K. Saitoh and S. J. J. o. L. T. Matsuo, "Multicore fiber technology," vol. 34, no. 1, pp. 55-66, 2016.

- [67] Y. Sasaki, K. Takenaga, S. Matsuo, K. Aikawa, and K. J. O. F. T. Saitoh, "Few-mode multicore fibers for long-haul transmission line," vol. 35, pp. 19-27, 2017.
- [68] J. Villatoro, E. Antonio-Lopez, A. Schülzgen, and R. J. O. L. Amezcua-Correa, "Miniature multicore optical fiber vibration sensor," vol. 42, no. 10, pp. 2022-2025, 2017.
- [69] N. Kishi, E. J. I. t. o. m. t. Yamashita, and techniques, "A simple coupled-mode analysis method for multiple-core optical fiber and coupled dielectric waveguide structures," vol. 36, no. 12, pp. 1861-1868, 1988.
- [70] A. W. J. J. Snyder, "Coupled-mode theory for optical fibers," vol. 62, no. 11, pp. 1267-1277, 1972.
- [71] J. Hudgings, L. Molter, and M. J. I. j. o. q. e. Dutta, "Design and modeling of passive optical switches and power dividers using non-planar coupled fiber arrays," vol. 36, no. 12, pp. 1438-1444, 2000.
- [72] A. Perez-Leija, J. Hernandez-Herrejon, H. Moya-Cessa, A. Szameit, and D. N. J. P. R. A. Christodoulides, "Generating photon-encoded W states in multiport waveguide-array systems," vol. 87, no. 1, p. 013842, 2013.
- [73] W.-P. J. J. A. Huang, "Coupled-mode theory for optical waveguides: an overview," vol. 11, no. 3, pp. 963-983, 1994.
- [74] F. Y. Chan, A. P. T. Lau, and H.-Y. J. O. e. Tam, "Mode coupling dynamics and communication strategies for multi-core fiber systems," vol. 20, no. 4, pp. 4548-4563, 2012.
- [75] Y. Chunxia, D. Hui, D. Wei, X. J. S. Chaowei, and A. A. Physical, "Weakly-coupled multicore optical fiber taper-based high-temperature sensor," vol. 280, pp. 139-144, 2018.
- [76] C. Xia, N. Bai, I. Ozdur, X. Zhou, and G. J. O. e. Li, "Supermodes for optical transmission," vol. 19, no. 17, pp. 16653-16664, 2011.
- [77] C. Xia *et al.*, "Supermodes in coupled multi-core waveguide structures," vol. 22, no. 2, pp. 196-207, 2015.
- [78] "Revisiting twin-core fiber sensors for high-temperature measurements," *Applied Optics*, vol. 51, no. 25, pp. 6227-6232, 2012/09/01 2012.

- [79] J. Villatoro *et al.*, "Accurate strain sensing based on super-mode interference in strongly coupled multi-core optical fibres," vol. 7, no. 1, pp. 1-7, 2017.
- [80] G. Coviello, V. Finazzi, J. Villatoro, and V. J. O. e. Pruneri, "Thermally stabilized PCF-based sensor for temperature measurements up to 1000° C," vol. 17, no. 24, pp. 21551-21559, 2009.
- [81] J. E. Antonio-Lopez, Z. S. Eznaveh, P. LiKamWa, A. Schülzgen, and R. J. O. l. Amezcua-Correa, "Multicore fiber sensor for high-temperature applications up to 1000° C," vol. 39, no. 15, pp. 4309-4312, 2014.
- [82] A. Van Newkirk, E. Antonio-Lopez, G. Salceda-Delgado, R. Amezcua-Correa, and A. J. O. L. Schülzgen, "Optimization of multicore fiber for high-temperature sensing," vol. 39, no. 16, pp. 4812-4815, 2014.
- [83] M. Han and A. J. O. l. Wang, "Temperature compensation of optical microresonators using a surface layer with negative thermo-optic coefficient," vol. 32, no. 13, pp. 1800-1802, 2007.
- [84] G. Adamovsky *et al.*, "Peculiarities of thermo-optic coefficient under different temperature regimes in optical fibers containing fiber Bragg gratings," vol. 285, no. 5, pp. 766-773, 2012.
- [85] H. Watanabe, N. Yamada, and M. J. I. j. o. t. Okaji, "Linear thermal expansion coefficient of silicon from 293 to 1000 K," vol. 25, no. 1, pp. 221-236, 2004.
- [86] M. Heiblum and J. J. I. J. o. Q. E. Harris, "Analysis of curved optical waveguides by conformal transformation," vol. 11, no. 2, pp. 75-83, 1975.
- [87] R. T. J. O. E. Schermer, "Mode scalability in bent optical fibers," vol. 15, no. 24, pp. 15674-15701, 2007.
- [88] R. T. Schermer and J. H. J. I. J. o. Q. E. Cole, "Improved bend loss formula verified for optical fiber by simulation and experiment," vol. 43, no. 10, pp. 899-909, 2007.
- [89] O. Arrizabalaga *et al.*, "High-performance vector bending and orientation distinguishing curvature sensor based on asymmetric coupled multi-core fibre," vol. 10, no. 1, pp. 1-10, 2020.

- [90] G. Salceda-Delgado, A. Van Newkirk, J. Antonio-Lopez, A. Martinez-Rios, A. Schülzgen, and R. A. J. O. l. Correa, "Compact fiber-optic curvature sensor based on super-mode interference in a seven-core fiber," vol. 40, no. 7, pp. 1468-1471, 2015.
- [91] J. Villatoro, A. Van Newkirk, E. Antonio-Lopez, J. Zubia, A. Schülzgen, and R. J. O. L. Amezcua-Correa, "Ultrasensitive vector bending sensor based on multicore optical fiber," vol. 41, no. 4, pp. 832-835, 2016.
- [92] G. Yin, F. Zhang, B. Xu, J. He, and Y. J. O. E. Wang, "Intensity-modulated bend sensor by using a twin core fiber: theoretical and experimental studies," vol. 28, no. 10, pp. 14850-14858, 2020.
- [93] H. Qu, G. Yan, and M. J. O. l. Skorobogatiy, "Interferometric fiber-optic bending/nano-displacement sensor using plastic dual-core fiber," vol. 39, no. 16, pp. 4835-4838, 2014.
- [94] J. Villatoro, V. P. Minkovich, and J. J. O. l. Zubia, "Photonic crystal fiber interferometric vector bending sensor," *Optics Letters*, vol. 40, no. 13, pp. 3113-3116, 2015.
- [95] A. Shrivastava and V. B. J. C. o. y. s. Gupta, "Methods for the determination of limit of detection and limit of quantitation of the analytical methods," vol. 2, no. 1, p. 21, 2011.
- [96] Y.-P. Wang and Y.-J. J. I. S. J. Rao, "A novel long period fiber grating sensor measuring curvature and determining bend-direction simultaneously," vol. 5, no. 5, pp. 839-843, 2005.

2. atala

Ondorioak

Atal honetan tesiaren ondorioak aurkezten dira, baita horren ondorioz bideragarriak diren etorkizuneko ikerketa-ildoak ere. Azken hauek lan honetan azaldutako gailuen errendimendua hobetzera bideratutako ikerketa-lerroetan eta egokiak izan daitezkeen ikerketa-lerro berrietan banatuta daude. Ikerketaren emaitzak biltzen dituzten argitaratutako artikuluko zientifikoak eta kongresuak atal honetan daude ere.

2.1 OFDS

2.1.1 Ondorioak

Lehen ikerketa-lerroan, TCaren neurketarako diseinatu eta fabrikatutako bi OFDS deskribatu dira. Haien funtzionamendu-printzipioa besoen distantziaren arabera islatutako argiaren modulazioan oinarritzen zen. Hala ere, neurketa-baldintzak nabarmen desberdinak ziren sentsoreak turbinen karkasetan instalatzeko orduan. Lehenengo kasuan, sentsorearen buruak besoen zigilatze-puntetara zuzenduta zeuden, islatutako argia murriztu, sentsorea besoen puntetatik gertu jartzera eta 1. Eskualdean funtzionatzera behartzen zuena. Bigarren kasuan, besoaren zati lauari begira zeuden sentsoreak. Plataforma hau karkasatik urrunago zegoen baina argia islatzeko azalera gehiago eskaintzen zuen. Baldintza horietan funtzionatzeko, sentsorearen diseinua berritu egin zen, 1. Eskualdea handituz eta distantzia luzeagoetan hasteko. Modu honetan, sentsorea besoen puntetatik urrunago jar zitekeen, segurtasuna nabarmen hobetu zezakeena. OFDSaren azken bertsio honek aurrekoaren errendimendua nabarmen hobetu zuen eta CTA gure bazkideak ezarritako hurrengo baldintzak bete zituen:

- Kontakturik gabeko neurketa, besoen portaera mekanikoa arriskuan egon ez dadin.
- Zehaztasuna TCaren neurketan. Adibidez, azken probetan, 20000 motor biren ondoren lortutako TC balioak 7 μ m-tik beherako batez-besteko aldakortasuna zuten beso bakoitzeko, eskatutako 25 μ m-ak baino nabarmen beherakoa den balioa.
- 1. Eskualde sentikorragoaren erabilera. Lehen zuntz-sortarekin alderatuta, bigarren bertsioan, 1. Eskualdea luzeagoa zen (3.5 mm vs 2 mm), distantzia luzeagoetan hasten zen (4.5 mm vs 2 mm) eta sentsibilitate handiagoa erakusten zuen bere malda handiagoari esker.

- Instalatzeko erraztasuna. Ezaugarri hau asko estimatu zuten CTako teknikariek sentsore-burua erraz instala zitekeelako karkasan. Azken hau ezaugarri oso garrantzitsua da, izan ere, instalatzeko behar den denbora nabarmen murrizten duelako eta karkasan instalatzeko ez duelako zulo berezien beharrik.
- Sendotasuna. Sentsoreak gai izan dira proba osoetan zehar baldintza errealetan funtzionatzeko errendimendu arazorik izan gabe.
- Sistemaren errentagarritasuna. OFDSaren galdeketa-sistema ekipamendu arruntez osatuta dago. Zuntz-sortari dagokionez, zuntz komertzialez egina dago.
- Moldakortasun eta segurtasunaren hobekuntza. OFDSaren azken bertsioa ahalik eta turbina gehienetan funtzionatzeko diseinatu da, kasu bakoitzerako neurritara egindako zuntz-sortak fabrikatzearen beharra saihestuz. Gainera, zuntzen antolaketari esker, besoen puntetatik urrunago kokatu ahal da, segurtasuna hobetzen duena.

2.1.2 Aurkeztutako gailuen hobekuntza/garapena

Ondorengo lan-ildoak iradokitzen dira ikerketa-lerro honekin jarraitzeko:

- Haizearen tunelean jarraian jarritako 3 turbina etapatan (errotorea+estatorea) TCa aldi berean neurtzea, errotore bakoitzaren TCa gutxienez 3 puntu desberdinetan neurtuz. Neurketa hau erronka oso handia izango litzateke, orain arte probetan erabilitako hardwarea biderkatzea eta eskuraketa-sistema egokitzera behartuko lukeelako datu kopuru hori aldi berean eskuratu ahal izateko. Proba horiek ematen duten informazioa oso garrantzitsua da CTarentzat, TCaren portaera hainbat turbina-etapa aldi berean funtzionatzen dutenean karakterizatzeko aukera emango lukeelako.

- Sentsore-burua kutsadura edo errekontza-ganberatik datozen hondakinetatik babesteko mekanismo bat diseinatzea, errekontza dagoen motor aeronautikoek dauzkaten funtzionamendu-baldintzetan probak egiteko bideragarria izan dadin.
- Aurreko puntuarekin lotuta, OFDSa funtzionamendu-baldintza errealetan erabiltzeko, zuntz-sorta egokitu egin behar da turbinetan ohikoak diren 700 °C eta 1000 °C arteko tenperaturak jasateko.
- Neurketa sistemako hardware osagaiak miniaturizatzea konfigurazio trinko batean integratzeko, bere garraiatzea eta maneiatzea errazteko.

2.1.3 Ikerketa-lerro berriak

Arestian aipatutako lan-ildoak ez ezik, OFDSa aplikazio hauetarako erabil liteke:

- Lan honetan garatutako OFDSarekin, besoen bibrazio erradialak (TC) neurtu eta aztertu dira, eta aipatu den bezala, seinale bera erabil liteke besoen bibrazio tangentialak (TT) neurtzeko. Hala ere, interesgarria litzateke besoen bibrazio axialak neurtzeko gai den sentsore-sistema bat garatzea, oraindik ez baitago horretarako irtenbide eraginkorrik.
- OFDSa erabili diskoak bezalako biraketa-elementuen karakterizazioa, edo ardatzen eszentrikotasuna neurtzea eskatzen duten beste aplikazio batzuetarako. Neurketa horiek interesgarriak izan daitezke sektore askotan, hala nola automobilgintzarako.

2.2 MCFtan oinarritutako sentsoreak

2.2.1 Ondorioak

Bigarren ikerketa-lerroan, MCFtan oinarritutako sentsore ugari garatu ziren haien funtzionamendu-printzipioa deskribatu ondoren. Hortaz baliauz, tenperatura, tolestura, bibrazioak eta kurbatura neurtzeko MCFtan oinarritutako sentsoreak diseinatu eta fabrikatu ziren. Soluzio horiek konfigurazio desberdinak (luzera berdina edo desberdina, MCF segmentu bat edo bi jarraian, eta abar) eta MCF geometria desberdinak (7cMCF edo 3cMCF) erabili zituzten ahalik eta errendimendurik onena lortzeko. Tesi honetan zehar erakutsitako MCFtan oinarritutako sentsoreek ezaugarri hauek zituzten:

- Sentsibilitate handiko sentsoreak: sentsoreek sentsibilitate handia erakutsi zuten probatutako parametroa neurtzeko. Gainera, MCF asimetrikoa erabiltzen zen kasu zehatzetan gailuak norabidearekiko sentikortasuna frogatu zuten ere.
- Fabrikatzeko erraztasuna eta azkartasuna, eta errepikatzeko erraztasuna: zehaztasun handiko zuntz-ebakitzaila bat eta fusionatzaile bat soilik behar dira soilik horrelako gailuak fabrikatzeko.
- Galdeketa-konfigurazio sinplea: gailu hauen galdeketarako konfigurazioa oso erraza eta errentagarria da, banda zabaleko argi iturri bat, zirkulagailu bat (edo akopladore optiko bat), espektrometro bat eta PD bat besterik ez baititu eskatzen. Osagai horiek guztiak ekipamendu arruntak dira.
- Parametro anitz neurtzeko gaitasuna: MCFak parametro anitzekiko sentikorak direnez; horietako bakoitzerako MCFtan oinarritutako sentsore espezifikoa gara daiteke. Hala ere, zuntz horiek parametro anitzekiko sentikorak direnez, finkatu edo paketatutako behar dira, espektroan ikusitako eragina intereseko parametroagatik soilik dela ziurtatzeko.

- Pertsonalizatzeko erraztasuna duten gailuak: espektroaren forma erraz moldatu ahal da MCFaren luzera eta konfigurazioa aldatuz (islapen edo transmisioan funtzionatuz, segmentu bakarreko edo kaskadan jarritako segmentuak erabiliz, eta abar). Modu honetan, erraz bereizten diren espektroak dituzten gailu ugari fabrikatzea erraza da, interesgarria dena puntu anitzeko neurketen multiplexaziorako.

2.2.2 Aurkeztutako gailuen hobekuntza/garapena

Gorago adierazi den moduan, MCFek ezaugarri erakargarriak dituzte sentsoreak garatzeko. Horri esker, ikerketa-lan honekin jarraitzeko honako lan-ildoak iradokitzen dira:

- Industriarako interesgarriak diren beste parametro batzuk neurtzeko MCFtan oinarritutako detekzio-sistemak garatzea, hala nola, indarra, tentsioa, presio dinamikoa, forma, eta abar.
- Intereseko parametro zehatz bat neurtzeko sentsibilitatea maximizatzen bideratutako MCF geometria zehatzak diseinatzea. Dokumentu honetan tenperatura neurtzeko MCFen geometriarik sentikorrena iragartzeko erabili den ikuspegi matematiko berbera erabiliz, MCFen zenbait parametro aldatuta, hala nola, nukleoen diametroa, nukleoen arteko distantzia, etab. parametro bakoitzerako neurria egindako diseinuak egin daitezke.
- Puntu anitzeko detekziorako MCFen multiplexazioa ahalbidetzen duen sistema garatu SMF berean MCF segmentu ugari kaskadan jarri eta zalantzarik gabe identifikatu ahal izateko. Honela, bereizmen espazial handia lortuko litzateke, batez ere segmentuak laburrak badira, ia banatutako sentsore sistema bat lez jo daitekeena.

- MCF segmentu berarekin parametro bat baino gehiago neurtzea: Tesi honetan frogatu den bezala, MCFek uhin-luzeraren desplazamenduarekin edo potentziaren aldaketarekin neur dezakete. Konfigurazio egokiarekin, MCF segmentu berarekin parametro horietako bakoitza parametro desberdinak neurtzeko erabil liteke aldi berean. Adibidez, gailu berak uhin-luzeraren desplazamendua erabil lezake temperatura neurtzeko eta potentziaren aldakuntzak bibrazioak hautemateko.
- MCFak SHMrako material desberdinetan txertatu: modu horretan, aztertzen ari den piezaren edo egituraren barrualdea zehatz-mehatz azertu ahal izango da, aire burbuilak edo fabrikazio-akatsak hautemateko.
- Estalkien formak: Lan honetan agertzen diren MCF sentsore batzuek, batez ere MCF asimetrikoetan oinarritutakoek, lerrokatze zehatzak behar dituzte behar bezala funtzionatzeko. Lerrokatze hori errazteko, MCFak forma zehatzeko estaldurekin fabrika litezke lerrokatze zuzena errazteko.
- Sentsore komertzialak: lan honetan aurkeztutako sentsore batzuk ingurune eta lan-baldintza latzei aurre egiteko paketatu dira, eta haien galdeketa erraza eta errentagarria da. Beraz, sentsoreak kutxa trinko batean sar litezke, errazago garraiatzeko eta maneiatzeko, sistema osoa (MCF sentsorea+galdeketa-ekipamendua) komertzialki eskaintzeko.

2.2.3 Ikerketa-lerro berriak

Ondorengo ikerketa lerroak gara litezke:

- MCF segmentuetan oinarritutako iragazkien eta akopladoreen diseinua: geometria eta luzera jakin batzuetako segmentuak erabilita, MCFek neurrira egindako banda-iragazkiak edo *notch* iragazkiak izan daitezke, uztartutako

potentzia uhin-luzera zehatzetan maximizatu edo bertan behera uztea ahalbidetzen dutenak. Ezaugarri horiek erakargarriak izan daitezke telekomunikazioak bezalako ikerketa-arloetarako.

- Nukleoan manipulazioa: FBGak inskribatuz edo errefrakzio-indizea zenbait nukleotan modu kontrolatuan aldatuz, modifikatutako MCF segmentu bakoitzaren erantzuna zalantzarik gabe identifika daiteke eta puntu anitzeko detekzioarako erabil liteke.

2.3 Tesiaren ekarpenak

Tesian zehar, ikerketaren emaitzak nazioarteko aldizkarietan argitaratu eta kongresuetan aurkeztu dira ondoren adierazten den bezala (berrietik zaharrenean ordena kronologikoan):

2.3.1 Argitalpenak

Nazioarteko aldizkarietan argitaratutako ikerketa-artikuluen zerrenda:

1. **Amorebieta, J.**; Ortega-Gomez, A.; Durana, G.; Fernández, R.; Antonio-Lopez, E.; Schülzgen, A.; Zubia, J.; Amezcua-Correa, R.; Villatoro, J. (2020). Highly sensitive multicore fiber accelerometer for low frequency vibration sensing. *Scientific Reports*, 10 (1), 1-11 (Q1 Diziplina anitzeko zientziak sailean 2019an 3.998-ko Eragin-Faktorearekin, 2020-ko estatistikak ez daude eskuragarri oraingoz).
2. Villatoro, J.; **Amorebieta, J.**; Ortega-Gomez, A.; Antonio-Lopez, E.; Zubia, J.; Schülzgen, A.; Amezcua-Correa, R. (2020). Composed multicore fiber structure for direction-sensitive curvature monitoring. *APL Photonics*, 5 (7), 070801

(Q1 Optika sailean 2019an 4.864-ko Eragin-Faktorearekin, 2020ko estatistikak ez daude eskuragarri oraingoz).

3. **Amorebieta, J.**; Durana, G.; Ortega-Gomez, A.; Fernández, R.; Velasco, J.; Sáez de Ocáriz, I.; Zubia, J.; Antonio-López, E.; Schülzgen, A.; Amezcua-Correa, R.; Villatoro, J. (2019). Packed multi-core fiber interferometer for high-temperature sensing. *Journal of Lightwave Technology*, *37* (10), 2328-2334 (Q1 Optika sailean 2019an 4.288-ko Eragin-Faktorearekin).
4. Fernández, R.; **Amorebieta, J.**; Beloki, J.; Aldabaldetrekua, G.; García, I.; Zubia, J.; Durana, G. (2019). Performance Comparison of Three Fibre-Based Reflective Optical Sensors for Aero Engine Monitorization. *Sensors*, *19* (10), 2244 (Q1 Instrumentuak & Instrumentazioa sailean 2019an 3.275-ko Eragin-Faktorearekin).
5. Durana, G.; **Amorebieta, J.**; Fernandez, R.; Beloki, J.; Arrospide, E.; Garcia, I.; Zubia, J. (2018). Design, Fabrication and Testing of a High-Sensitive Fibre Sensor for Tip Clearance Measurements. *Sensors*, *18* (8), 2610 (Q1 Instrumentuak & Instrumentazioa sailean 2019an 3.031-ko Eragin-Faktorearekin).

2.3.2 Hitzaldiak

Ikerketa-lana aurkeztu den kongresuen zerrenda:

1. **Amorebieta, J.**; Ortega-Gomez, A.; Durana, G.; Antonio-Lopez, E.; Schülzgen, A.; Zubia, J.; Amezcua-Correa, R.; Villatoro, J. "Highly Sensitive Supermode Interferometer for Low Frequency Vibration Monitoring". 27th International

Conference on Optical Fiber Sensors OFS2020, Alexandria, Virginia, AEB. Konferentzia hau 2021eko ekainera atzeratu da COVID dela eta.

2. **Amorebieta, J.**; Ortega-Gomez, A.; Durana, G.; Antonio-Lopez, E.; Schülzgen, A.; Zubia, J.; Amezcua-Correa, R.; Villatoro, J. “Highly sensitive orientation and amplitude discerning vector bending sensor based on asymmetric multicore fiber”. OSA Advanced Photonics, Montreal, Kanada, Uztailak 13, 2020.
3. Garcia, I.; Durana, G.; **Amorebieta, J.**; Fernández, R.; Zubia, J. “Review of a Custom-Designed Optical Sensing System for Aero-Engine Applications”. The 9th EVI-GTI International Gas Turbine Instrumentation Conference, Graz, Austria, Azaroak 21, 2019.
4. **Amorebieta, J.**; Ortega-Gomez, A.; Amezcua-Correa, R.; Antonio-López, E.; Schülzgen, A.; Villatoro, J. “Novel twin cascaded multicore fiber-based structure for high sensitive multipurpose optical sensing”. 11^a Reunión Española de Optoelectrónica OPTOEL´19, Zaragoza, Espainia, Uztailak 4, 2019.
5. **Amorebieta, J.**; Durana, G.; Ortega-Gomez, A.; Fernández, R.; Velasco, J.; Sáez de Ocáriz, I.; Zubia, J.; Antonio-López, E.; Schülzgen, A.; Amezcua-Correa, R.; Villatoro, J. “Strongly coupled multi-core fiber-based interferometer for high temperature sensing”. SPIE Optics+Optoelectronics, Praga, Txekiar Errepublika, Apirilak 15, 2019.
6. **Amorebieta, J.**; Fernández, R.; Durana, G.; Beloki, J.; Zubia, J. “Optical Fibre-Based Reflective Displacement

Sensing System for High Sensitivity Blade Tip-Clearance Measurements”. OSA Advanced Photonics Congress, Zurich, Suitza, Uztailak 2, 2018.

7. Fernández, R.; **Amorebieta, J.**; Durana, G.; Beloki, J.; Zubia, J. “Performance comparison among three optical fibre-based displacement sensors for Blade Tip Clearance measurements”. 5th IEEE International Workshop on Metrology for AeroSpace (MetroAeroSpace), Roma, Italia, Ekainak 20, 2018.
8. **Amorebieta, J.**; Garcia, I.; Durana, G.; Aldabaldetrekua, G.; Zubia, J.; Sáez-Ocáriz, I. “Optical fibre-based reflective displacement sensor: computer modelling and application to impact detection in aeronautical structures”. SPIE Optical Metrology, Munich, Alemania, Ekainak 26, 2017.

3. atala

Eranskina: Argitaratutako lanak

1. artikulua

Titulua:

Design, fabrication and testing of a high-sensitive fibre sensor for tip clearance measurements

D.O.I.:

10.3390/s18082610

Egileak:

Durana, G.; **Amorebieta, J.**; Fernandez, R.; Beloki, J.; Arrospide, E.; Garcia, I.; Zubia, J.

Aldizkari eta argitalpenaren informazioa:

Sensors, 18 (8), 2610 (2018)

3 aldiz aipatua



Aldizkariaren adierazleak 2018an:

Eragin-faktorea: 3.031

Q1 Instrumentuak & Instrumentazioa sailean (15/61)

Article

Design, Fabrication and Testing of a High-Sensitive Fibre Sensor for Tip Clearance Measurements

Gaizka Durana ^{1,*} , Josu Amorebieta ¹, Ruben Fernandez ¹, Josu Beloki ², Eneko Arrospide ³ , Iker Garcia ¹ and Joseba Zubia ¹

¹ Communications Engineering Department, University of the Basque Country (UPV/EHU), Ingeniero Torres Quevedo Plaza 1, E-48013 Bilbao, Spain; josu.amorebieta@ehu.eus (J.A.); ruben.fernandez@ehu.eus (R.F.); ikergeb@gmail.com (I.G.); joseba.zubia@ehu.eus (J.Z.)

² Aeronautical Technologies Centre, Bizkaia Technological Park, E-48170 Zamudio, Spain; josu.beloki@ctabef.com

³ Applied Mathematics Department, University of the Basque Country (UPV/EHU), Ingeniero Torres Quevedo Plaza 1, E-48013 Bilbao, Spain; eneko.arrospide@ehu.eus

* Correspondence: gaizka.durana@ehu.eus; Tel.: +34-94-601-4128

Received: 4 July 2018; Accepted: 2 August 2018; Published: 9 August 2018



Abstract: A highly sensitive fibre bundle-based reflective optical sensor has been designed and fabricated for Tip Clearance measurements in a turbine rig. The sensor offers high spatial and temporal resolution. The sensor probe consists of a single-mode transmitting fibre and two concentric rings of receiving multimode fibres that collect reflected light in a differential detection gain configuration, yielding a highly linear calibration curve for distance measurements. The clearance measurement range is approximately 2 mm around the central point fixed at 3.2 mm from the probe tip, and the sensitivity of the probe is 61.73 mm^{-1} . The fibre bundle has been designed to ensure that the distance security specifications required for the experimental program of the turbine are met. The optical sensor has operated under demanding conditions set by the blade and casing design. The experimental results obtained so far are promising and lead us to think that the optical sensor has great potential for online clearance measurements with high precision.

Keywords: tip clearance; optical fibre sensor; aircraft turbine

1. Introduction

In aeronautics, Tip Clearance (TC) refers to the gap existing between the blade tip and its surrounding case. Since the invention of the gas turbine engine, intense research has been conducted on reducing TC, as this parameter, of great concern for engine designers, is intimately related to engine efficiency and represents the driving force of most new architectures and innovative technological improvements for future aircraft applications. Whereas high TC values allow an amount of air to flow without generating useful work, a lack of clearance accelerates blade tip and shroud wear over time due mainly to rubs, and can put engine integrity at risk [1]. The clearance varies with the operation point of the mission profile (take-off, cruise and landing) as well as with the engine aging [2,3]. TC changes are caused by two types of loads, namely engine and flight loads. The former encompasses centrifugal, thermal, internal engine pressure, and thrust loads, whereas the latter comprises inertial (gravitational), aerodynamic (external pressure) and gyroscopic loads [4]. At cruise, a rule of thumb equates 0.25 mm of reduced clearance to a reduction of 1% in specific fuel consumption. Therefore, some of the most relevant benefits of reducing the TC include efficiency increase as well as increased payload and mission range capabilities [1,5]. In addition, aircraft noise and emissions are reduced, along with the subsequent environmental benefits involved [6,7]. It seems obvious that an accurate and real-time

measurement technology is necessary. In contrast to power-system turbines where common clearance values range from 2 to 8 mm, in aircraft turbines, TC is typically lower than 3 mm and a resolution better than 25 μm is usually required [8–10].

Currently, there are several traditional methods for TC measurements that include capacitive, eddy current, microwave, and discharging probe sensors (electromechanical). The former are popular due to their simplicity, low cost, and robustness, but they suffer from low spatial resolution, short measurement range, and require calibration [11–13]. Eddy current sensing is also a common technique for TC measurements, and it has about the same accuracy as capacitive probes [14,15]. It provides non-contact measurements at the expense of requiring magnetic materials for the blades. Additionally, the magnetic disturbance of the turbine engine may interfere with their output signal, and they are highly sensitive to temperature and blade tip shape. Microwave sensors are robust and insensitive to contamination, but the hollow waveguides at submillimeter wavelengths are impractical, and the corresponding circuitry complex [16,17]. Finally, electromechanical systems belong to the oldest tip clearance measurement systems [18]. They benefit from their high resolution over the entire measurement range, but their main drawbacks are that they only measure the clearance of the longest blade and the slow response time.

Optical sensors may overcome many of the previous drawbacks as they offer high sensitivity and resolution, immunity to electromagnetic interference, non-contact measurement and information about every blade [19–22]. However, among the different optical technologies (i.e., triangulation [23,24], OCT [22], time-of-flight measurements [25], laser Doppler velocimetry [26] and reflective intensity modulation [27]) employed for TC measurements at turbo machines, many of them do not fully satisfy the requirements of future closed-loop Active Clearance Control (ACC) systems [5]. For example, laser Doppler position probes offer high resolution, but the complexity of the probe limits the application of the system. In the case of the Optical Coherence Tomography (OCT), the measurement rate is limited by the speed of mechanical scanning, or in the case of triangulation, by the detector frame rate and minimum exposure time. Finally, the resolution of reflective intensity modulation-based sensor probes—compared to the rest of optical methods mentioned previously—is low due to the modal noise at the endface of the transmitting fibre.

In this paper, we report on the design and fabrication of a highly sensitive fibre bundle-based reflective optical sensor that has been tested in an aircraft turbine rig. The content of the paper has been structured as follows: first, a brief description of the operation principle is given, explaining the general sensor design and defining the working region of interest that will allow to maximize the sensitivity of the sensor. Afterwards the experimental program followed at the Aeronautical Technologies centre's (CTA's) transonic wind tunnel is explicated. Then, the most relevant results are presented and discussed. Finally, some conclusions are drawn from the previous discussion.

2. Materials and Methods

2.1. Sensor Design and Working Region of Interest

The schematic diagram of the sensor's operation is shown in Figure 1a. The fibre bundle is the principal element of the system. To avoid modal noise at the output [28], a central single-mode fibre is used as transmitting fibre of red laser light (wavelength of light: 660 nm), which after exiting the fibre bundle and being reflected by the target object located at a distance d from the fibre bundle tip, is partially gathered by two concentric rings of multimode optical fibres arranged around the central transmitting fibre; the inner ring consists of 5 optical fibres (fibre bunch 1; core diameters of 200 μm and Numerical Aperture (NA) of 0.2), whereas the outer ring consists of 17 optical fibres (fibre bunch 2; core diameters of 300 μm and NA of 0.2). The light collected by fibre bunches 1 and 2 is measured as a voltage level at photodetectors 1 and 2, respectively (V_1 and V_2). If we plot the ratio of V_2 to V_1 as a function of distance d , we get the characteristic calibration curve shown in Figure 1b. The reason of using two photodetectors is aimed at minimizing the undesirable effects caused by intensity fluctuations in the light source and reflectivity variations on the target surface. As both

voltage signals contain the same disturbance, the ratio V_2/V_1 gets rid of it and therefore becomes a pure function of the distance to the illuminated target surface d [27,29,30].

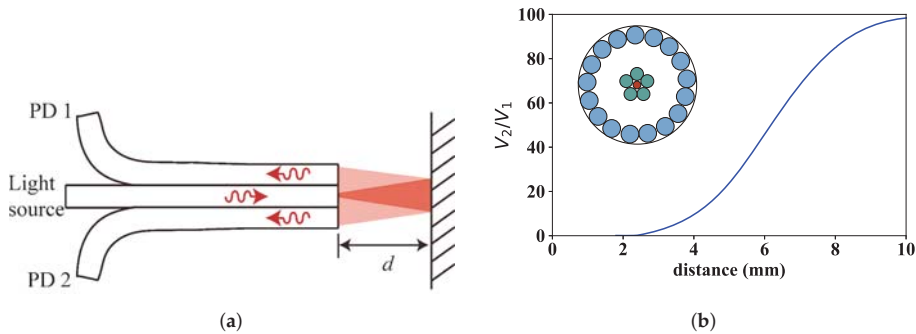


Figure 1. Fibre optic intensity sensor for TC measurements: (a) illustration of the fibre bundle based sensor; and (b) signal response (V_2/V_1) as a function of the distance d to a mirror. The drawing included in the plot shows the cross-section of the fibre bundle, where the single-mode transmitting fibre is in the centre and the two rings of receiving multimode fibres are arranged concentrically around it.

The signal response presents two regions of interest for distance sensing with a characteristic linear variation of the signal with distance. Those regions are at both sides of the peak signal and are designated as “front slope” and “back slope”, respectively. Figure 1b only shows the front slope, which exhibits clear advantages in terms of sensitivity, protection against noise and temperature fluctuations, in comparison to the back slope [31]. In practice, however, for distance security reasons typical TC values found in turbine rigs makes it necessary to operate in the back slope of the sensor, resulting in a lower signal sensitivity and higher dependency on the type of surface and on the temperature. Additionally, a post-processing of the raw signal is often necessary to get reliable results [27]. In the present work, we set out to operate in the front slope through the design of a new fibre bundle that guarantees a safe operation without compromising the physical integrity of the sensor head keeping it away from the blades. Indeed, in previous works, we used a fibre bundle with a measurement range for the front slope that clearly was too short (from 1 mm to 1.6 mm), and therefore required using the back slope to avoid placing the fibre bundle tip too close to the blades. The new bundle design (number of fibres, fibre type composition and geometrical fibre arrangement) takes into account all this, and, as a result, is able to shift the front slope to bigger probing distances (4–8 mm, see Figure 1b).

Regarding the achievable sensitivity in the front slope, differential gain of the photodetectors have been considered to increase it as much as possible provided that the gain configuration of the transimpedance amplifier of each photodetector does not compromise the minimum bandwidth required by the target application. In our particular case, for a turbine with 92 blades spinning at a maximum of 6000 revolutions per minute (rpm), even at the highest gain configuration the bandwidth available is enough to receive a signal with clearly identifiable individual blades. Figure 2 shows simulation results of four different gain configurations $G_1 - G_2$ of the photodetectors (G_1 for photodetector 1 (PD1) and G_2 for photodetector 2 (PD2), both given in dB units with respect to the reference gain value of 0.75×10^3 V/A) obtained by a custom designed program for bundle behaviour simulation. As can be clearly observed, the gain increase of the second photodetector with respect to the first one yields not only a higher ratio of V_2 to V_1 , but also a steeper calibration curve than in the case of the symmetric configuration ($G_1 = G_2$). Therefore, for maximum sensitivity, we have set the gain configuration to 10–40.

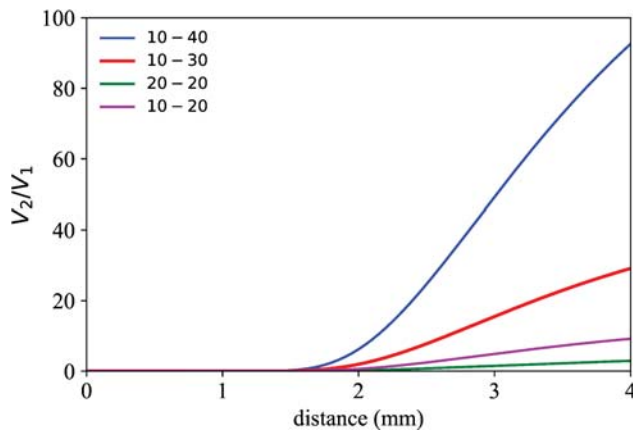


Figure 2. Simulated calibration curves of the fibre bundle in region I for different gain configurations ($G_1 - G_2$) of the two photodetectors.

2.2. Calibration Curve

Once the measurement system has been defined, the next step consists in calibrating the optical sensor using as target object a spare blade from the tested turbine rig. The schematic drawing of the side view of the experimental set-up is shown in Figure 3a.

It is important to point out that, in the laboratory calibration tests, the transmitting fibre did not face the flat platform of the blade—as would be desirable to maximize the amount of reflected light gathered back by the bundle—but the very narrow sealing lands of the blade (around 0.7 mm in width) to simulate the real turbine configuration that the sensor head met when installed in the turbine rig. Figure 3b shows a close-up picture of the sensor head during the calibration process. Please note that even perfectly facing the transmitting fibre to the narrow sealing lands yielded a very low reflected signal that required setting the optical power to maximum value, in this case 50 mW. Therefore, the setting of 50 mW laser power and 10–40 gain configuration of the photodetectors always resulted in light intensity levels at each of the photodetectors below the saturation value, and the created voltage values spanned over the full voltage scale (0–5 V), ensuring a good use of the 16-bit resolution of the A/D converter. The large working distance set by the front slope of the fibre bundle also contributed to the low coupling efficiency of reflected light into the fibre bundle. Both simulated and measured calibration curves are shown in Figure 3c.

It is worth mentioning the great similarity between both curves in the distance range from 2 to 4 mm with very small differences between them, and with a clear linear increase of the rate of the voltage quotient with distance. The best linear fit (shown in the inset of Figure 3c) to the experimental data has a Pearson’s correlation of 0.997 in the distance range from 2.8 mm to 4 mm with a sensitivity slope of 61.73 mm^{-1} . Within this distance range of interest, Table 1 shows, for different values of V_2/V_1 ranging between 30 and 100, the difference between the experimentally measured distance value and the corresponding value obtained from the simulation. The result is given as a percentage of the corresponding experimental value. The discrepancy between experiment and simulation never exceeds 1.5% (at $V_2/V_1 = 34.1$). It is also interesting to draw attention to the shift to lower distance values occurring in the front slope when moving from an object with specular reflection (target presented in Figure 1) to another one with diffuse reflection (blade shown in Figure 3). This can be easily understood with simple geometric and ray tracing models [32].

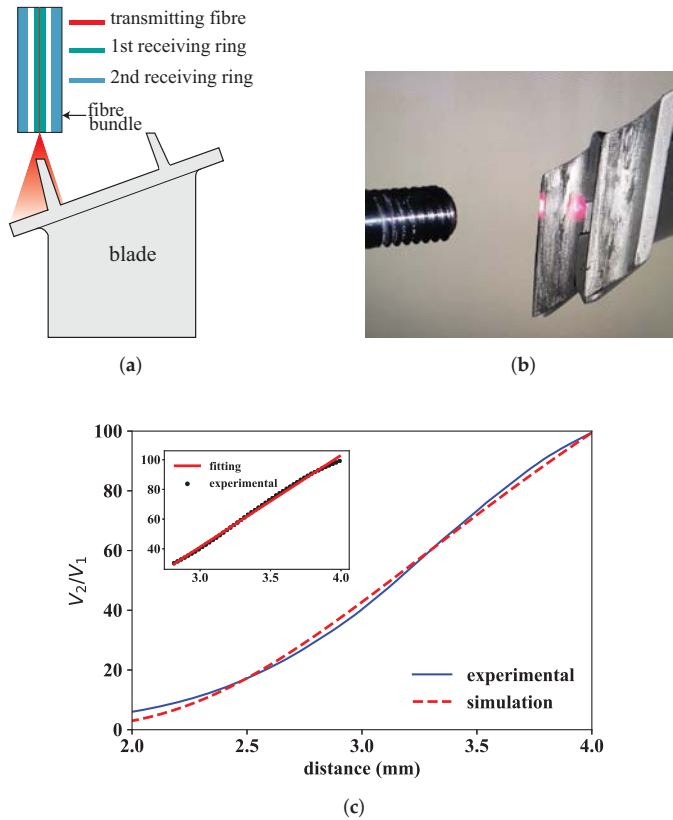


Figure 3. Laboratory calibration of a typical blade from the turbine rig: (a) schematic representation of the optical probe tip relative to the spare blade; (b) close-up picture of fibre bundle and blade; and (c) simulated and measured calibration curves. The inset shows the linear fit to the experimental data in the region of interest ($2.8 \text{ mm} < z < 4 \text{ mm}$).

Table 1. Comparison of measured and simulated data in the distance region of interest.

V_2/V_1	$d_{sim}, \text{ mm}$	$d_{exp}, \text{ mm}$	Difference, %
30.329	2.778	2.815	1.31
45.930	3.055	3.090	1.13
59.443	3.289	3.290	0.11
75.959	3.543	3.540	0.83
90.551	3.831	3.790	1.08
99.171	3.992	3.990	0.06

2.3. Experimental Program

The performance of the optical sensor was tested in the transonic wind tunnel at CTA. The rotating-turbine-test facility is a continuous transonic-flow-test bed with an atmospheric inlet/outlet. The level of pressure/vacuum, the temperature and the mass flow are individually regulated, so that the rig is operated to meet realistic Mach and Reynolds numbers allowing to transfer the results to real gas turbines.

The supply and exit air conditions in the test section are achieved by two centrifugal compressor and vacuum groups, which are, respectively, run by electrical motors of 3.7MW and 5.0MW. Two vacuum pumps are used to achieve altitude conditions of sub-atmospheric pressure down

to 12.5 kPa. A two-stage compressor group is used to control the pressure ratio and flow temperature and thus the Mach number of the flow within the circuit. The top mass flow rate achievable is 18 kg/s, with a maximum supply pressure up to 450 kPa, and a temperature regulation from atmospheric up to 450 K. Prior to entering the turbine, the air flows through a settling chamber that removes any swirl and axial velocity non-uniformity. The turbine power is transmitted by a single shaft (up to 7800 rpm) to a dynamometer. The test section has a section of 1 m. A schematic diagram of the facility is shown in Figure 4.

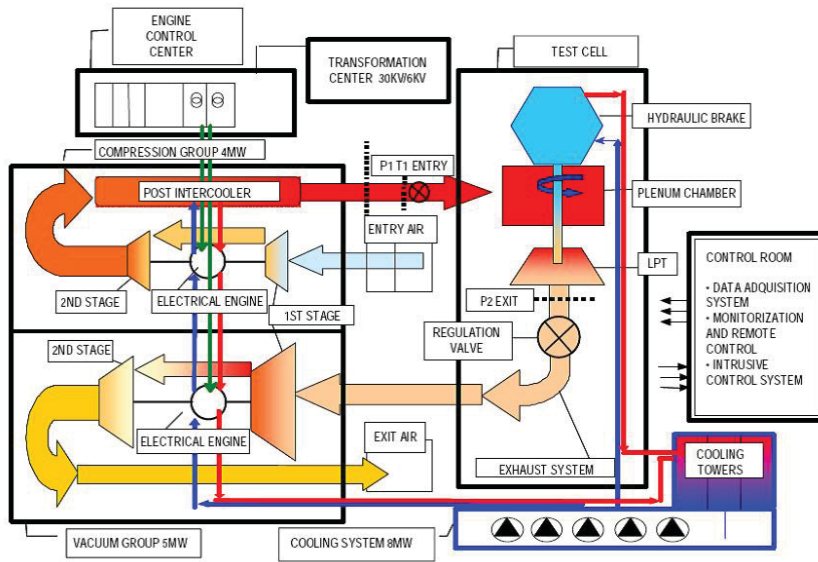


Figure 4. Schematic diagram of the rotating-turbine-test facility at CTA.

The rig corresponds to a single stage of a turbine rig with 92 blades. As already commented previously, the measurement requirements were really demanding because, for the extremely narrow sealing lands of the blades that defined the reflecting surface, the distance of about 3.2 mm from where the end of the probe was finally set, to the reflecting surface caused a low reflected signal level at the receiving rings to happen. An additional challenge that posed the coupling of the optical probe to the casing of the turbine was that the optical probe was not perfectly faced to the sealing lands when the turbine was at rest (0 rpm), so that the reflected signal was too low to get reliable calibration data that would allow building the calibration curve for the actual measurements. For that reason, the laboratory calibration curve was accepted as valid for the turbine rig measurements since it was carried out with a spare blade of the same turbine stage under test. As shown in the Results Section, the good news is that, at different workload conditions of the turbine rig, the optical probe was able to receive enough reflected signal for reliable tip clearance measurements. This improvement in the level of reflected signal was a consequence of the several vibrations that tend to suffer rotor blades causing them not only to deform but also to get a better alignment of the reflecting surface with respect to the optical probe.

Figure 5 shows a schematic representation of the final arrangement of the bundle embedded in the casing of the turbine. The optical probe was attached to a micrometer-driven adapter that was inserted in a radial hole of the casing and fixed to it with four screws. The micrometer allowed to set a certain distance—3.2 mm in this particular case—between the probe tip and the sealing lands of one of the blades to set the operation point at the middle of the linear region shown in Figure 3c. For this particular configuration, the optical probe tip resulted to be within the abradable layer. The abradable

is a soft protective wear material that is mounted on the casing wall aligned with the blades to create a good sealing, and avoid gas leakage and improve combustion efficiency. As TC values are commonly referenced to the abradable coating, below, we consider this case. Therefore, according to turbine design blueprints, the TC is obtained subtracting 2.74 mm to the actual sensor measurement (distance from probe tip to reflecting surface):

$$TC(\text{mm}) = \text{sensor measurement} (\text{mm}) - 2.74 \quad (1)$$

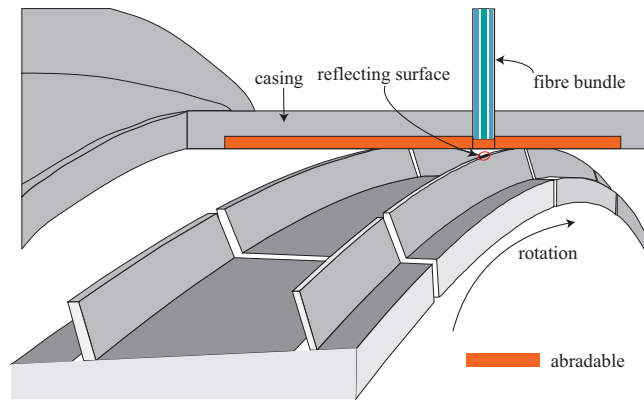


Figure 5. Schematic representation of the optical probe (not to scale) installed in the turbine rig at CTA.

Figure 6 shows a schematic illustration of the optical probe configuration within the casing. The optical signal of each of the two photodetectors is acquired with 16-bit resolution at a sampling rate of 2 MS/s, which results in a detailed map of all the blades with unambiguous identification of each of them, extending further the information provided by classical electromechanical systems that limit the TC information to the longest blade, and with a much lower data refresh frequency. The data acquisition and processing was done with a custom-made LabVIEW program that allows online and offline working modes. In online mode, the TC values of the different blades are monitored live at a configurable refresh rate, whereas, in offline mode, the data are stored in a hard disk for later processing. The latter mode is particularly interesting for long acquisition times where the amount of data created is huge and a thorough data analysis is required.

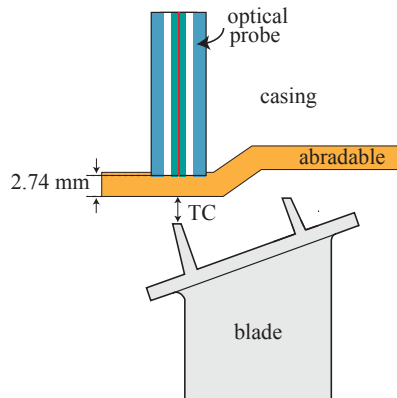


Figure 6. Optical probe placement within the casing.

3. Results and Discussion

All tests were carried out at CTA's facilities where different Working Points (WP) of the engine were repeated during several days. Each engine revolution was identified both with a blade of a particular reflection pattern and a stable non-vibrating Once per Revolution (OPR) signal obtained from the shaft. The raw data (V_2/V_1) from the optical sensor were converted to distance value using the linear calibration curve $f(V_2/V_1)$ obtained in the laboratory calibration tests (see Section 2.2). As an example, Figure 7 shows the sensor response of 13 blades after applying the calibration curve without any type of data post-processing. The first feature worth observing is the sharp minima that define the gap between consecutive blades.

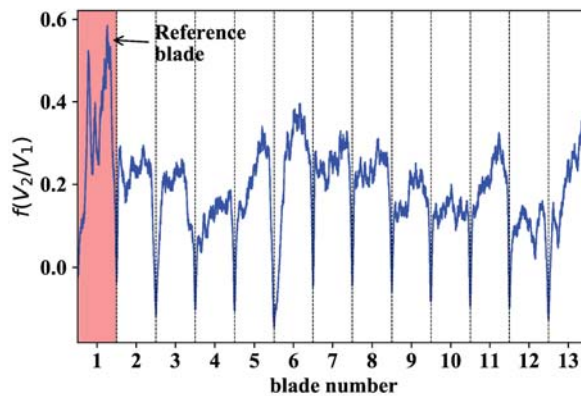


Figure 7. Typical signal response V_2/V_1 after applying the corresponding calibration curve. The blade highlighted in red refers to the blade with a higher reflection pattern. The dashed vertical lines correspond to local minima defining the limit between adjacent blades.

It is also worth mentioning that the signal pattern corresponding to each blade was highly reproducible over time, regardless of the operation point of the engine. The response curve of each of the 92 blades followed a certain pattern that might be classified according to one of the three types presented in Figure 8 (curves shown on the left-hand side of Figure 8). To give a consistent definition of the TC, for each blade, we started selecting a variable percentage (from 0% to 100%) of the corresponding dataset around the central data sample, and analyzed the evolution followed by the average value. The curves on the right-hand side of Figure 8 show the variability of the given TC definition for each of the three blade types. It comes out that, regardless of the type of response curve considered, the average value variation always was below a tenth of a millimetre. Therefore, it was decided to define the TC of each blade as the average value of the corresponding dataset at the 50% selection level around the central sample.

With the given definition of TC in mind, Figure 9 shows the TC map corresponding to a certain engine WP at 4258 rpm. It is worth noticing that the TC of every blade is different. Of particular importance are blades number 16, 38, 43, 51 and 69 as their TC values suggest that they are close to the abradable surface and they should be monitored to keep them under control. Regarding the stability of the test, the vertical error bars represent the variability of the TC values over time. Even in the worst case (blade number 85), the TC variability expressed as a single standard deviation value is approximately of 20 μm within the same WP, and the average value over the 92 blades is below 5 μm . All this suggests that we are dealing with stable TC experiments.

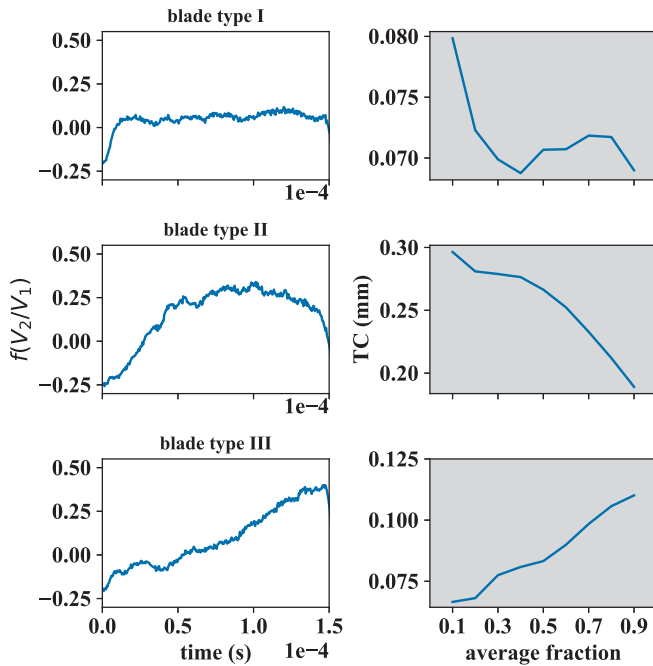


Figure 8. (Left) Types of blade signals found in the 92 blade turbine rig after applying the calibration curve; and (Right) evolution of TC definition with the selected fraction of blade data for each blade type.

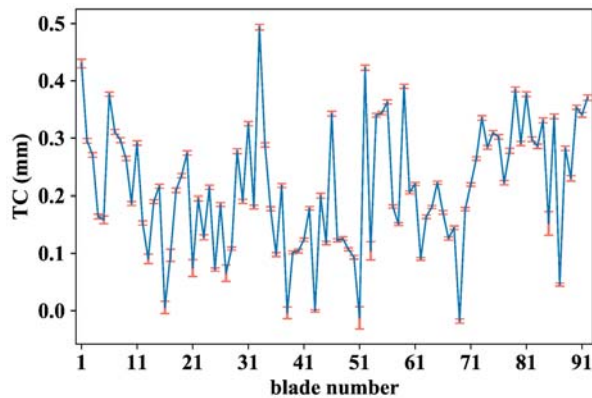


Figure 9. TC values of each blade at 4258 rpm with error bars that account for the TC standard deviation over 1100 revolutions.

The TC maps of all blades corresponding to three different WPs in ascending order of rpm are shown in the polar plot of Figure 10. Each TC map is represented as a curve of a particular color. On the other hand, each blade is expressed as a single point where the polar angle θ_i defines the blade number $i - \theta_i = 360^\circ / 92 * i$ for $i \in [1, 92]$ —and the corresponding TC value is given by the radial distance. Observe that TC values of individual blades decrease as engine rotational speed increases, a fact that can be attributed to the centrifugal and thermal loads acting on static and rotating components of the turbine. It is also interesting to point out that blades 43 and 51 still continue to be decisive in

determining the TC values of the turbine, in the same way as in the case of the WP at 4258 rpm shown in Figure 9. If we define the turbine TC as the minimum blade TC among all blades, as expected, the TC decreases from 0.002 mm to -0.005 mm when going from WP 1 (5466 rpm) to WP 3 (6005 rpm).

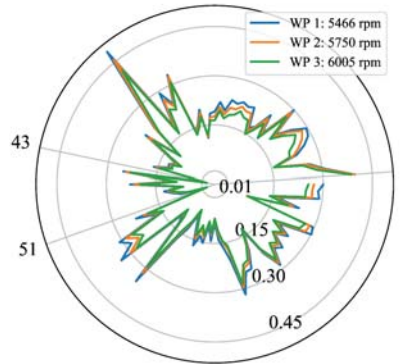


Figure 10. TC values of each of the 92 blades at three different WPs.

Another interesting point to consider is the analysis of the TC evolution when the turbine rpm ramp up before arriving at the first WP. Blue data points shown in Figure 11 are representative of this case. Contrary to what is expected for the general case in which the TC diminishes when rotor speed increases (as already shown in Figure 10), during the warming-up lapse of time, the clearance increases with rpm values. This might be explained on the basis that, when speed increases, the centrifugal load of the rotor as well as the rapid heating of the blades cause the rotating elements to grow outwards, but the case expands at a faster rate during this process.

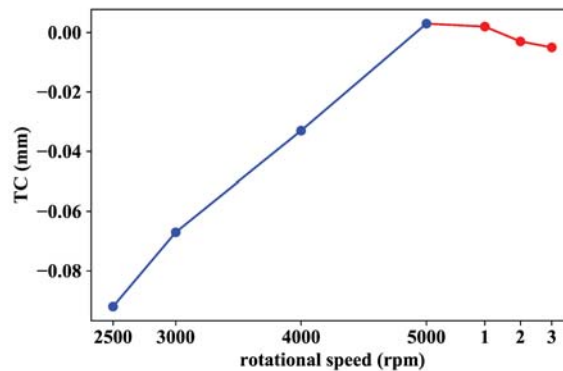


Figure 11. TC behaviour before (blue data points) and after (red data points) setting the first WP. The red data points refer to WPs 1, 2 and 3 shown in Figure 10: WP 1 \rightarrow 5466 rpm; WP 2 \rightarrow 5750 rpm; and WP 3 \rightarrow 6005 rpm.

This observation brings us to conclude that temperature ramping occurring in the wind tunnel before the first operation point is reached might be associated with the observed TC increase with rotational speed. In addition, the blade-case rubbing experienced during the whole warming-up process (negative TC values of blue data points in Figure 11) may be justified if we consider that the centrifugal load on the blades applies from the first moment before the casing starts to expand.

However, once the operation temperature has been reached and the casing has expanded to its equilibrium value (first red data point in Figure 11: WP 1 \rightarrow 5466 rpm), the clearance starts to decrease with rotational speed as expected.

4. Conclusions

A highly sensitive optical fibre bundle-based sensor prototype was designed and fabricated based on a custom simulation program developed within the research group. The manufactured optical sensor probe allowed measuring TC values in a turbine rig of an aircraft engine at the wind tunnel of the CTA. The optical measurements rely on collecting reflected light from each of the blades using two concentrically arranged rings of optical fibres and converting the gathered light intensities into voltage levels that are eventually divided with respect to each other to get rid of the disturbances (light intensity fluctuations, reflectivity variations, etc.) and retain a pure function of the distance from the fibre bundle tip to each blade. This curve has two characteristic working regions of interest with linear behaviour, the so-called front slope and back slope. The added value of the present work with respect to previous works resides in shifting the highly sensitive front slope curve to longer distance values to meet the distance security specifications set for the experimental program of the turbine, a fact that enables establishing the working point around the central part of this sharply sloped curve section instead of using the less sensitive back slope section of the response function. Additionally, the sensitivity has been further improved using differential gain of the two photodetectors associated to their corresponding receiving fibre rings. Altogether, the sensitivity of the optical sensor is 61.73 mm^{-1} , in contrast to the value of -0.0733 mm^{-1} published by other authors [33]. It is also worth mentioning that the optical sensor has proved to be capable of measuring the TC in very unfavourable conditions set by the specific blade and casing design that prevented the sensor from receiving an appreciable level of reflected signal. In such demanding scenario, the calibration curve used for the actual measurements was obtained in the laboratory using a spare blade of the turbine as it was impossible to get reliable calibration data from the turbine at rest. The results derived from the experimental program carried out on a turbine rig at CTA's facilities show a high resolution and highly sensitive measurement tool for inspection of individual blades that provides engineers with valuable information on turbine performance. The results of the optical fibre-based sensor presented in this paper opens up the possibility of widening its applicability to other fields of interest.

Author Contributions: G.D., J.A., J.B., and J.Z. conceived and designed the experiments; J.A. and I.G. developed the software to design the sensor probe; G.D. and J.Z. manufactured the fibre bundle; J.A., R.F., and E.A. performed the sensor calibration; J.A., R.F., G.D., and J.B. carried out the experiments; G.D., J.A., R.F., and J.B. analysed the data; G.D., J.A., and I.G. wrote the paper; and J.Z. supervised the whole project.

Funding: This work was funded in part by the Fondo Europeo de Desarrollo Regional (FEDER), in part by the Ministerio de Economía y Competitividad under project TEC2015-638263-C03-1-R, and in part by the Gobierno Vasco/Eusko Jaurlaritz IT933-16 and ELKARTEK (KK-2016/0030, KK-2017/00033, KK-2017/00089 and KK-2016/0059). The work of Josu Amorebieta is supported in part by a PhD fellowship from the Universidad del País Vasco/Euskal Herriko Unibertsitatea (UPV/EHU), Vicerrectorado de Euskera y Formación Continua.

Conflicts of Interest: The authors declare no conflict of interest.

References

1. Wiseman, M.W.; Guo, T.H. An investigation of life extending control techniques for gas turbine engines. In Proceedings of the 2001 American Control Conference. (Cat. No.01CH37148), Arlington, VA, USA, 25–27 June 2001; Volume 5, pp. 3706–3707. [[CrossRef](#)]
2. Kempe, A.; Schlamp, S.; Rösgen, T.; Haffner, K. Spatial and Temporal High-Resolution Optical Tip-Clearance Probe for Harsh Environments. In Proceedings of the 13th International Symposium on Applications of Laser Techniques to Fluid Mechanics, Lisbon, Portugal, 26–29 June 2006; Number 1155.
3. Guo, T.H. Active Turbine Tip Clearance Control Research. In Proceedings of the 5th NASA GRC Propulsion Control and Diagnostics (PCD) Workshop, Cleveland, OH, USA, 16–17 September 2015.

4. Lattime, S.B.; Steinetz, B.M.; Robbie, M.G. Test Rig for Evaluating Active Turbine Blade Tip Clearance Control Concepts. *J. Propul. Power* **2005**, *21*, 552–563. [[CrossRef](#)]
5. Lattime, S.B.; Steinetz, B.M. High-Pressure-Turbine Clearance Control Systems: Current Practices and Future Directions. *J. Propul. Power* **2004**, *20*, 302–311. [[CrossRef](#)]
6. Miller, K.; Key, N.; Fulayter, R. Tip Clearance Effects on the Final Stage of an HPC. In Proceedings of the 45th AIAA/ASME/SAE/ASEE Joint Propulsion Conference & Exhibit, Denver, CO, USA, 2–5 August 2009. [[CrossRef](#)]
7. Neuhaus, L.; Neise, W. Active Control to Improve the Aerodynamic Performance and Reduce the Tip Clearance Noise of Axial Turbomachines. In Proceedings of the 11th AIAA/CEAS Aeroacoustics Conference, Monterey, CA, USA, 23–25 May 2005. [[CrossRef](#)]
8. Geisheimer, J.; Holst, T. Metrology considerations for calibrating turbine tip clearance sensors. In Proceedings of the XIX Biannual Symposium on Measuring Techniques in Turbomachinery, Rhodes-St-Genève, Belgium, 7–8 April 2008.
9. Guo, H.; Duan, F.; Wu, G.; Zhang, J. Blade tip clearance measurement of the turbine engines based on a multi-mode fiber coupled laser ranging System. *Rev. Sci. Instrum.* **2014**, *85*, doi:10.1063/1.4901601. [[CrossRef](#)] [[PubMed](#)]
10. Geisheimer, J.; Holst, T. Novel sensors to enable close-loop active clearance control in gas turbine engines. In Proceedings of the SPIE Micro- and Nanotechnology Sensors, Systems, and Applications VI, Baltimore, MD, USA, 5–9 May 2014; Volume 9083, Number 908310. [[CrossRef](#)]
11. Sheard, A. Blade by Blade Tip Clearance Measurement. *Int. J. Rotating Mach.* **2011**, *2011*. [[CrossRef](#)]
12. Haase, W.C.; Haase, Z.S. High-Speed, capacitance-based tip clearance sensing. In Proceedings of the 2013 IEEE Aerospace Conference, Big Sky, MT, USA, 2–9 March 2013; pp. 1–8. [[CrossRef](#)]
13. Ye, D.C.; Duan, F.J.; Guo, H.T.; Li, Y.; Wang, K. Turbine blade tip clearance measurement using a skewed dual-beam fiber optic sensor. *Opt. Eng.* **2012**, *51*, 081514, doi:10.1117/1.OE.51.8.081514. [[CrossRef](#)]
14. Sheard, A.; O'Donnell, S.; Stringfellow, J. High Temperature Proximity Measurement in Aero and Industrial Turbomachinery. *J. Eng. Gas Turbines Power* **1999**, *121*, 167–173. [[CrossRef](#)]
15. Roeseler, C.; von Flotow, A.; Tappert, P. Monitoring blade passage in turbomachinery through the engine case (no holes). In Proceedings of the IEEE Aerospace Conference, Big Sky, MT, USA, 9–16 March 2002; Volume 6, pp. 3125–3129. [[CrossRef](#)]
16. Chivers, J.W.H. Microwave Interferometer. U.S. Patent 4,359,683, 16 November 1982.
17. Woolcock, S.C.; Brown, E.G. Checking the Location of Moving Parts in a Machine. U.S. Patent 4,346,383, 24 August 1982.
18. Davidson, D.P.; DeRose, R.D.; Wennerstrom, A.J. The Measurement of Turbomachinery Stator-to-Drum Running Clearances. In *Volume 1: Turbomachinery, Proceedings of the ASME 1983 International Gas Turbine Conference and Exhibit, Phoenix, AZ, USA, 27–31 March 1983*; ASME: New York, NY, USA, 1983; p. V001T01A054. [[CrossRef](#)]
19. López-Higuera, J.M. (Ed.) *Handbook of Optical Fibre Sensing Technology*; Wiley: Hoboken, NJ, USA, 2002.
20. García, I.; Zubia, J.; Durana, G.; Aldabaldetrekú, G.; Illarramendi, M.A.; Villatoro, J. Optical Fiber Sensors for Aircraft Structural Health Monitoring. *Sensors* **2015**, *15*, 15494–15519. [[CrossRef](#)] [[PubMed](#)]
21. Zhang, X.; Yang, L. Research on displacement sensor of two-circle reflective coaxial fiber bundle. In Proceedings of the 2008 IEEE/ASME International Conference on Advanced Intelligent Mechatronics, Xi'an, China, 2–5 July 2008; pp. 211–216. [[CrossRef](#)]
22. Kempe, A.; Schlamp, S.; Rösgen, T.; Haffner, K. Low-coherence interferometric tip-clearance probe. *Opt. Lett.* **2003**, *28*, 1323–1325. [[CrossRef](#)] [[PubMed](#)]
23. Barranger, J.P.; Ford, M.J. Laser-Optical Blade Tip Clearance Measurement System. *J. Eng. Power* **1981**, *103*, 457–460. [[CrossRef](#)]
24. Matsuda, Y.; Tagashira, T. Optical Blade-Tip Clearance Sensor for Non-Metal Gas Turbine Blade. *J. Gas Turbine Soc. Jpn.* **2001**, *29*, 479–484.
25. Dhadwal, H.S.; Kurkov, A.P. Dual-Laser Probe Measurement of Blade-Tip Clearance. *J. Turbomach.* **1999**, *121*, 481–485. [[CrossRef](#)]
26. Pfister, T.; Büttner, L.; Czarske, J.; Krain, H.; Schodl, R. Turbo machine tip clearance and vibration measurements using a fibre optic laser Doppler position Sensor. *Meas. Sci. Technol.* **2006**, *17*, 1693–1705. [[CrossRef](#)]

27. García, I.; Beloki, J.; Zubia, J.; Aldabaldetrekú, G.; Illarramendi, M.A.; Jiménez, F. An Optical Fiber Bundle Sensor for Tip Clearance and Tip Timing Measurements in a Turbine Rig. *Sensors* **2013**, *13*, 7385–7398. [[CrossRef](#)] [[PubMed](#)]
28. García, I.; Zubia, J.; Berganza, A.; Beloki, J.; Arrue, J.; Illarramendi, M.A.; Mateo, J.; Vázquez, C. Different Configurations of a Reflective Intensity-Modulated Optical Sensor to Avoid Modal Noise in Tip-Clearance Measurements. *J. Lightwave Technol.* **2015**, *33*, 2663–2669. [[CrossRef](#)]
29. Cao, S.Z.; Duan, F.J.; Zhang, Y.G. Measurement of Rotating Blade Tip Clearance with Fibre-Optic Probe. *J. Phys. Conf. Ser.* **2006**, *48*, 873, doi:10.1088/1742-6596/48/1/165. [[CrossRef](#)]
30. Yu-zhen, M.; Yong-kui, Z.; Guo-ping, L.; Hua-guan, L. Tip clearance optical measurement for rotating blades. In Proceedings of the MSIE, Harbin, China, 8–11 January 2011; pp. 1206–1208. [[CrossRef](#)]
31. García, I.; Przysowa, R.; Amorebieta, J.; Zubia, J. Tip-Clearance Measurement in the First Stage of the Compressor of an Aircraft Engine. *Sensors* **2016**, *16*, 1897, doi:10.3390/s16111897. [[CrossRef](#)] [[PubMed](#)]
32. Shimamoto, A.; Tanaka, K. Geometrical analysis of an optical fiber bundle displacement sensor. *Appl. Opt.* **1996**, *35*, 6767–6774. [[CrossRef](#)] [[PubMed](#)]
33. Binghui, J.; Lei, H. An Optical Fiber Measurement System for Blade Tip Clearance Engine. *Int. J. Aerosp. Eng.* **2017**, *2017*, 4168150, doi:10.1155/2017/4168150. [[CrossRef](#)]



© 2018 by the authors. Licensee MDPI, Basel, Switzerland. This article is an open access article distributed under the terms and conditions of the Creative Commons Attribution (CC BY) license (<http://creativecommons.org/licenses/by/4.0/>).

2. artikulua

Titulua:

Packaged multi-core interferometer for high temperature sensing

D.O.I.:

10.1109/JLT.2019.2903595

Egileak:

Amorebieta, J.; Durana, G.; Ortega-Gomez, A.; Fernández, R.; Velasco, J.; Sáez de Ocáriz, I.; Zubia, J.; Antonio-López, E.; Schülzgen, A.; Amezcu-Correa, R.; Villatoro, J.

Aldizkari eta argitalpenaren informazioa:

Journal of Lightwave Technology, 37 (10), 2328-2334 (2019)

12 aldiz aipatua

Aldizkariaren adierazleak 2019an:

Eragin-faktorea: 4.288

Q1 Optika sailean (14/97)

Packaged Multi-Core Fiber Interferometer for High-Temperature Sensing

Josu Amorebieta ¹, Gaizka Durana ¹, Angel Ortega-Gomez ¹, Rubén Fernández, Javier Velasco, Idurre Sáez de Ocariz, Joseba Zubia ¹, Jose Enrique Antonio-López, Axel Schülzgen ², *Fellow, OSA*, Rodrigo Amezcua-Correa, and Joel Villatoro

Abstract—A small size and compactly packaged optical sensor for high-temperature measurements is reported. The sensor consists of a short piece of multi-core fiber (MCF) spliced to the distal end of a single-mode fiber. The packaging consists of an inner ceramic shield that prevents bending, curvature, and vibration effects on the MCF, and an outer metallic shield that protects the device against impacts. The interaction between specific supermodes excited in the MCF creates an interference pattern that shifts linearly with the temperature. The sensor was calibrated in the range from 200 to 1000 °C and a K-type thermocouple was used as a reference. The average temperature sensitivity was found to be 24.8 pm/°C with a response time of 15 s. Our results indicate that our MCF interferometric thermometer is as accurate as an electronic one with the advantage that it is passive. Therefore, we believe that the proposed sensor is suitable for industrial applications.

Index Terms—High temperature measurement, mode interferometers, multi-core fibers, optical sensors, optical thermometers, supermodes.

I. INTRODUCTION

IN THE industrial sector, there are several environments and applications where high temperature is present. For example, in engine tests, metallurgical processes, in gas and oil facilities, etc. In such harsh environments, temperature can reach very

high values (up to 1000 °C, and even higher). Thus, accurate measurement of temperature is crucial.

Currently, the technology commonly accepted and well established for high temperature measurement is based on thermocouples [1]–[5]. However, due to their electronic nature, thermocouples may not be a viable solution for applications or environments where electromagnetic or microwave radiation is present. In such cases, optical fiber thermometers are a good alternative since they are totally passive.

Optical fibers exhibit an intrinsic sensitivity to temperature, which makes them ideal for temperature sensing. In fact, throughout the years, many different optical fiber temperature sensors have been demonstrated [6]–[10]. Most optical fiber thermometers operate in a limited temperature range. However, the use of specialty optical fibers and innovative approaches and techniques have allowed expanding the temperature range up to 1000 °C. Thus, optical fiber thermometers may reach the performance and capabilities of thermocouples and be a real alternative for high temperature sensing, hence for industrial applications.

The most common approach for high temperature sensing consists of using regenerated fiber Bragg gratings (rFBGs), also called chemical composition gratings [11]–[14]. The operating principle of such sensors is based on the thermo-optic effect that modifies the period of the grating. rFBG-based sensors have temperature sensitivity of around 10 pm/°C, and their response time is of several seconds [15]–[18]. The disadvantage of rFBGs sensors is their high cost, as their fabrication and interrogation require expensive setups, lasers, and picometer-resolution detectors.

Fabry-Perot interferometry has been widely studied for high temperature sensing as well. In this technique, the sensitive element is a cavity that can be fabricated from temperature-resistant materials such as pure glass or sapphire [19]–[24]. The advantages of the Fabry-Perot interferometers (FPI) include high sensitivity and small size. However, their performance is directly linked to the uniformity of the cavity, which is not easy to achieve.

Other alternatives for high temperature sensing are based on long period gratings (LPGs) [25]–[27] and different types of interferometers [28]–[31]. The drawback of LPGs is their sensitivity to the surrounding medium, which imposes proper isolation to measure temperature only. On the other hand, most interferometers provide relative temperature measurements, as they are

Manuscript received November 20, 2018; revised January 16, 2019 and February 20, 2019; accepted February 27, 2019. Date of publication March 7, 2019; date of current version April 17, 2019. This work was supported in part by the Fondo Europeo de Desarrollo Regional, in part by the Ministerio de Economía y Competitividad under Project TEC2015-638263-C03-1-R, and in part by the Gobierno Vasco/Eusko Jaurlaritza IT933-16 and ELKARTEK (KK/00033, KK-2017/00089, and KK-2018/00078). The work of J. Amorebieta was supported in part by a Ph.D. fellowship from the University of the Basque Country UPV/EHU, Vicerrectorado de Euskera y Formación Continua. (*Corresponding author: Josu Amorebieta.*)

J. Amorebieta, G. Durana, A. Ortega-Gomez, R. Fernández, and J. Zubia are with the Department of Communications Engineering, University of the Basque Country, E-48013 Bilbao, Spain (e-mail: josu.amorebieta@ehu.eus; gaizka.durana@ehu.eus; angel.ortega@ehu.eus; ruben.fernandez@ehu.eus; joseba.zubia@ehu.eus).

J. Velasco and I. Sáez de Ocariz are with the Science and Technology Department, Fundación Centro de Tecnologías Aeronáuticas, E-01510 Miñano Mayor, Spain (e-mail: javier.velasco@ctaero.com; idurre.saezdeocariz@ctaero.com).

J. E. Antonio-López, A. Schülzgen, and R. Amezcua-Correa are with the CREOL, The College of Optics and Photonics, University of Central Florida, Orlando, FL 32816 USA (e-mail: jealopez@creol.ucf.edu; axel@creol.ucf.edu; r.amezcua@creol.ucf.edu).

J. Villatoro is with the Department of Communications Engineering, University of the Basque Country, E-48013 Bilbao, Spain, and also with the IKERBASQUE-Basque Foundation for Science, E-48013 Bilbao, Spain (e-mail: agustinjoe.villatoro@ehu.eus).

Color versions of one or more of the figures in this paper are available online at <http://ieeexplore.ieee.org>.

Digital Object Identifier 10.1109/JLT.2019.2903595

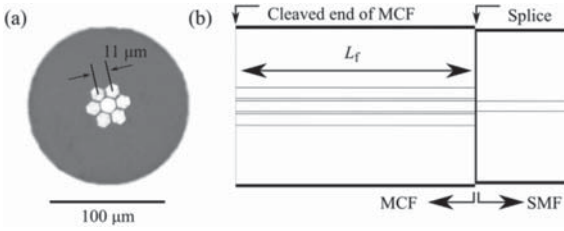


Fig. 1. (a) Picture of the cross-section of the MCF used to build the temperature sensor. (b) Schematic representation of the sensor architecture. L_f is the length of the MCF. The cleaved end reflects less than the 4% of the emitted light.

codified in the shift of interference patterns. As a result, LPG- and interferometer- based high temperature sensors have not reached the market yet.

As an alternative to the existing optical fiber thermometers for high temperature, in this work, we propose a sensor that may overcome the main limitations and drawbacks mentioned above. Our device consists of a short segment of MCF spliced to the distal end of a typical SMF. The fabrication of our device is easy, reproducible, and inexpensive. The temperature sensitive region of our device is the segment of MCF that can withstand high temperatures (up to 1000 °C) as demonstrated in [32]–[34]. In our case, the sensor operates in reflection mode. In addition, we have packaged our device with a double shielding (ceramic and metallic). The packaging eliminates the effects of strain, bending, curvature, or vibrations on the MCF interferometer as it is sensitive to such parameters [35]–[38].

The reflection spectrum of our device is sinusoidal and shifts when temperature changes. The interference pattern of our MCF sensor is easily traceable, thus, it is easy to establish a relationship between the absolute maximum of the interference pattern and temperature. With our packaged MCF sensor, temperatures up to 1000 °C, response times at different temperature gradients and its robustness against vibrations were measured. For comparison, similar experiments were also carried out with a bare MCF interferometer. The results suggest that the proposed packaging does not compromise the temperature sensitivity of our device. In addition, our packaged sensor is as accurate as a K-type thermocouple, which is widely used and accepted as reference in the industry.

II. OPERATION PRINCIPLE, DESIGN AND FABRICATION

In the device reported here, the MCF is the key element. The MCF, fabricated at the University of Central Florida (Orlando, USA), has a particular structure based on seven identical hexagonal cores. Six of them are concentrically arranged in a ring-like shape around a central one. The mean diameter and distance among adjacent axes is 9.2 μm and 11 μm, respectively, see Fig. 1(a). All the cores are made of germanium doped silica glass and are inlaid in pure silica cladding. The numerical aperture (NA) of each core is 0.14 at 1550 nm that is the same NA of a typical SMF. The outer diameter of the fiber is 130 μm.

A scheme of the MCF interferometer is shown in Fig. 1(b). The device consists of a short MCF segment fusion spliced to a

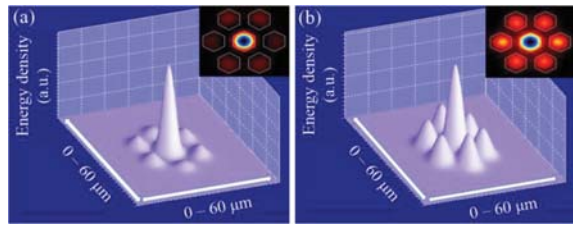


Fig. 2. Simulations of the 3D and 2D profiles of the two supermodes excited in the MCF. In (a) the supermode SP_{01} is shown, and in (b) the supermode SP_{02} . The inset 2D profiles have an area of $60 \times 60 \mu\text{m}^2$.

conventional SMF. A fiber fusion splicer (Fujikura 100 P+) was used to fabricate the device. Such a machine aligns precisely the single core of the SMF with the central core of the MCF. Due to that, the insertion loss of supermode interferometers is minimal (typically 0.1 dB or below) as reported in [35].

The MCF described above is called strongly-coupled multi-core fiber, which means its cores are close enough to each other to allow interaction among them. The modes supported by such an MCF are called supermodes [39], [40], which are the linear combination of individual LP modes of each core of the MCF. In our device, schematically shown in Fig. 1(b), the excitation of the MCF is with the LP_{01} (fundamental) mode of the SMF. This, combined with the axial symmetry of the SMF-MCF structure, causes only two specific supermodes to be excited in the MCF. The profiles of such supermodes are shown in Fig. 2.

The effective refractive index of each supermode is different, thus, a phase difference between them can be expected as they propagate through the length of the MCF (L_f). The phase difference ($\Delta\varphi$) will be $\Delta\varphi = 4\pi\Delta nL_f/\lambda$, where $\Delta n = n_2 - n_1$, with n_1 and n_2 being the indices of the supermodes SP_{01} and SP_{02} , respectively, and λ the wavelength of the light source. According to our simulations, the value of Δn was 7.8×10^{-4} at $\lambda = 1545$ nm. The phase difference will cause a coupling between both supermodes, which will generate a sequence of maximum and minimum values in the reflection spectrum of our MCF interferometer. When the reflection reaches a maximum value to a given wavelength, the interference is constructive, which means that the two supermodes are in phase and, therefore, their coupled power is maximum for that wavelength. The maximum values appear when the phase difference equals an integer multiple of 2π ($m2\pi$, where $m = 1, 2, 3, \dots$). Thus, by considering that the reflected light travels twice the length of the MCF ($2L_f$), the maxima are located at the following wavelengths:

$$\lambda_m = 2L_f\Delta n/m. \tag{1}$$

In general, in an optical fiber, the thermo-optic effect prevails over the thermal expansion effect. Thus, for temperature measurements, only the changes in the refractive index of the fiber core (or cores) are considered [28], [32]. In our case, such changes induce a variation in the effective indices of the interfering supermodes, and hence, a shift in the interference pattern. Therefore, by monitoring λ_m , the temperature around the MCF can be known. It is important to point out that with our MCF

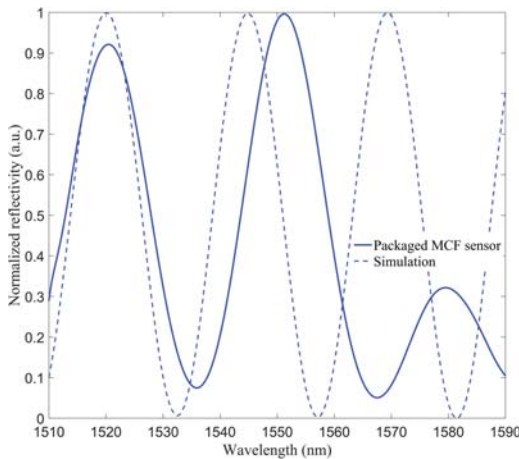


Fig. 3. Interference pattern obtained by simulation for a 2.54 cm-long MCF interferometer (dashed line) and with the fabricated device (solid line).

interferometer the measurement of temperature is absolute, as it will be codified in wavelength.

In order to measure the widest temperature range possible, the length of the MCF segment is crucial. On the one hand, the displacement of λ_m , which shifts around 30 pm/°C without any packaging [32], must not overlap with the maximum located at λ_{m+1} or λ_{m-1} . On the other hand, λ_m must be within the wavelength range of the sensor interrogator, which in our case was between 1510 and 1595 nm, at any temperature of the measuring range. Thus, to achieve the aforementioned requirements, two different simulation programs (Matlab MathWorks and Photon-Design) were used in which Eq. (1) was implemented with the parameters of the MCF and the desired initial position of λ_m established to obtain the MCF length. It was calculated to be 2.545 cm. However, due to the difficulty for obtaining an MCF segment of that precision with a conventional cleaver, we fabricated a device with $L_f = 2.54$ cm with an error of approximately 200 μm .

Fig. 3 shows the spectra of the designed and fabricated interferometers at room temperature. For the calculated MCF length, the difference between the maxima and minima (visibility) is of 0.9. The difference between the simulated and observed pattern is due to the impossibility of reproducing the ideal conditions of the simulation in real-life conditions, such as the fact that the simulation programs use a flat spectrum light source whereas the manufactured sensor uses a Gaussian-like emission light source. It can be noted that the peak at which simulated and manufactured sensor's patterns match is located at 1520 nm. As temperature increases, such a peak is expected to shift to longer wavelengths [32]. Hence, the peak located at 1520 nm (λ_m) was selected to be monitored and correlated with temperature.

In order to make the MCF interferometer sensitive exclusively to temperature, it was packaged as follows: The bare SMF-MCF structure, whose total length was approximately 15 cm, was protected with a double shielding. The first layer was a double bore thin ceramic tube (Omega Engineering TRX-005132-6). Each

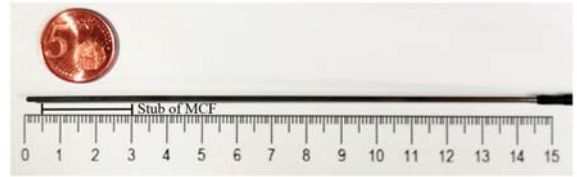


Fig. 4. Picture of the manufactured MCF sensor after being exposed to 1000 °C. Notice that the metallic tube has a blackening gradient that indicates the different temperatures on the tube. The position and length (2.54 cm) of the MCF segment are indicated. The gap between the tip of the metallic tube and the stub of MCF is long enough to avoid a Fabry-Perot cavity.

bore had a diameter of 127 $\mu\text{m} \pm 5\%$. In this manner, the MCF and part of the SMF were kept straight. Thus, bending effects on the interference pattern of the MCF were eliminated. The second layer was a stainless steel tube (Omega Engineering SS-116-6CLOSED) that covered the ceramic layer and provided physical protection against possible impact or shocks. A photograph of the final sensor prototype is shown in Fig. 4. As it can be noticed, the sensitive part of the sensor is only 2.54 cm long and located at the edge of the shielding. Thus, the sensor could be just about 3 cm long. The reason for the extra 12 cm is to protect the SMF due to the configuration of the furnace. The latter had a circular hole (slightly bigger than the sensor in diameter) that only in the deepest part reached temperatures of 1000 °C. This causes that the packaged sensor has to be vertically inserted completely. As it can be seen in the blackening gradient in Fig. 4, the area where the MCF is located is the area that has been exposed to the highest temperatures.

The interrogation of our MCF interferometer consisted of a broadband light source centered at 1550 nm, with Gaussian-like emission, a 50:50 coupler and a small spectrum analyser (I-MON512-USB, Ibsen Photonics). The data processing was made with an *ad hoc* program developed in Matlab MathWorks. The data processing approach was as follows: Raw spectra provided by the spectrum analyser were collected at different temperatures; then, the spectra were averaged and normalized. After that, a Savitzky-Golay filter was applied to every spectra in order to smooth them. Finally, the highest peak (λ_m), or absolute maximum of the interference pattern, was found. The wavelength at which the maximum was located was correlated with temperature, which was measured with a K-type thermocouple used for temperature calibration measurements (Herten, K-type, SN TCP187).

III. RESULTS AND DISCUSSION

The tests were performed at the Aeronautical Technologies Centre (CTA) facilities located in the Alava Technology Park (Spain). The heating/cooling processes were carried out with a programmable high temperature furnace (Isotech Pegasus Plus 1200). Before running the calibration measurements, a curing process was carried out to eliminate as much as possible the hysteresis effect of the sensor [28]. The calibration was performed repeatedly in the range from 200 to 1000 °C, in steps of 50 °C that lasted 70 minutes each. Thus, overall, each calibration lasted 100 hours approximately. The sampling rate was 1 Hz.

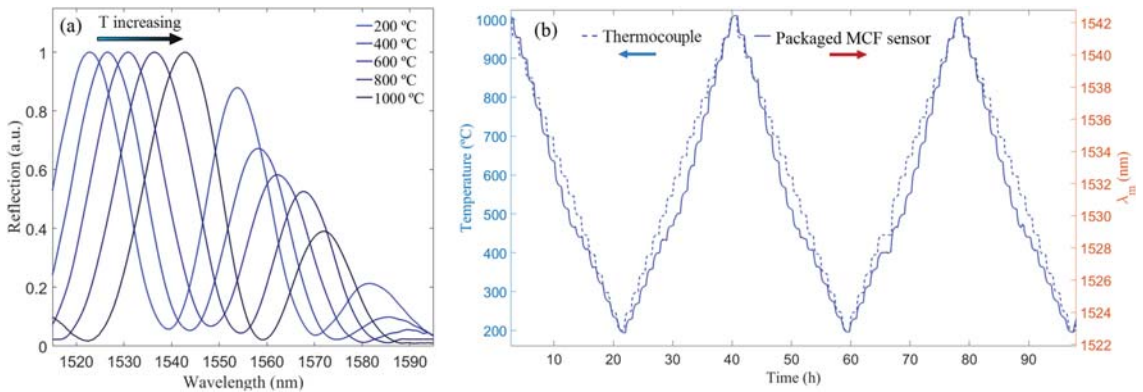


Fig. 5. (a) Spectra observed in the 200-1000 °C temperature range. (b) Time evolution of our packaged MCF sensor compared to that of the thermocouple. Colored arrows indicate the corresponding vertical axe of each curve.

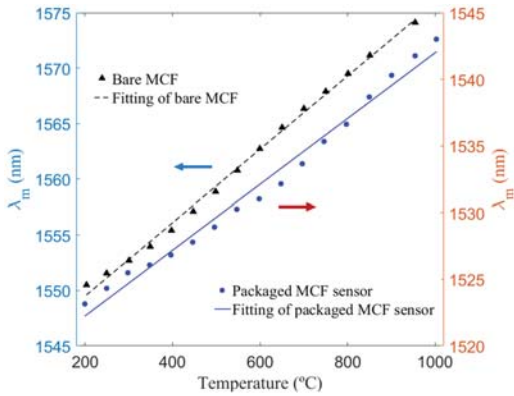


Fig. 6. Calibration curve of the packaged MCF sensor (solid dots, solid line) and 2.54 cm of bare MCF (triangles, dashed line). Colored arrows indicate the corresponding axe of each curve.

Fig. 5(a) shows the reflection spectra of our packaged MCF interferometer at different temperatures. It can be seen that the shift for the thermal range under study was around 20 nm. The position of the maximum peak as a function of time is shown in Fig. 5(b). For comparison, the time evolution of the temperature measurement provided by the thermocouple is also shown. From the monitored λ_m and temperature data, the calibration curve of the packaged MCF sensor was obtained, which is shown in Fig. 6. In order to evaluate the effect of the shielding on the temperature sensitivity of the packaged MCF sensor, the calibration curve obtained from a 2.54 cm-long bare MCF device that was subjected to an identical calibration process as the packaged MCF sensor is also shown in Fig. 6.

For the packaged MCF sensor, the Pearson squared correlation coefficient was found to be $R^2 = 0.9856$ and the uncertainty of $\sigma^2 = 0.611 \text{ nm}^2$ [41]. The correlation between temperature (in °C) and λ_m (in nm) that was obtained from the experiments was:

$$T = 39.929\lambda_m - 60525. \quad (2)$$

This indicates that the temperature sensitivity of the packaged MCF sensor was 24.8 pm/°C. From the calibration curve of the 2.54 cm-long bare MCF sensor shown in Fig. 6, we obtained a temperature sensitivity of 31.47 pm/°C. The latter agrees with that (29 pm/°C) of the MCF thermometer reported in [32] in the range between 100°C and 300°C, which was fabricated with bare MCF as well. Therefore, the packaging proposed here does not compromise the temperature sensitivity of the device. As a matter of fact, the main purpose of protecting the SMF and the MCF with a close-fitting ceramic tube was to keep the fibers tightly in the axial direction so that the measurements were strictly related to temperature and not affected by undesired effects of bending or vibrations, something that cannot be achieved when unprotected MCF is used. This may be the cause of the performance differences between the packaged MCF sensor and the bare MCF shown in Fig. 6 and the one reported in [32] where non-linear response to temperature was observed.

The response and recovery times of our packaged MCF temperature sensor and those of the device built with bare MCF were also evaluated as these are important parameters to be considered. The rising and falling times were measured several times at different temperature gradients. The measurements were carried out for 2 different thermal loops: from 25 °C to 550 °C, and back to 25 °C, and from 25 °C to 900 °C, and back to 25 °C. In each case, the response time of both optical devices and that of the K-type thermocouple were recorded. The response time ($\tau_{63\%}$), or time constant, is defined as the time required to reach 63.2% of an instantaneous change in temperature [42].

The results for the 25 °C–550 °C–25 °C loop are shown in Fig. 7. The results shown in Fig. 7 indicate that the shift of λ_m of the bare MCF device was more than expected according to the sensitivity obtained from its calibration curve shown in Fig. 6. This means that the shift of λ_m may not be strictly due to temperature as the MCF segment was also exposed to bending and/or vibrations induced by the furnace. The tracked peak of the packaged MCF sensor shifts 10.1 nm and shows a smoother and less noisy curve compared to that of the bare MCF. This shift agrees with the combination of the sensitivity of the sensor in

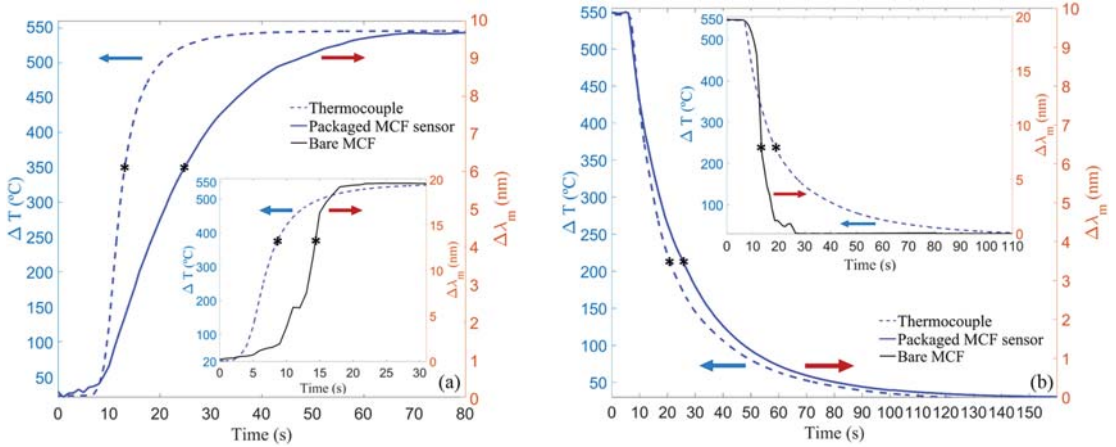


Fig. 7. Response times for (a) heating from 25 °C to 550 °C and for (b) cooling from 550 °C to 25 °C of a packaged and bare MCF sensors. For comparison, the response and recovering times of a commercial thermocouple are shown. Notice the non-uniform shape of the curves of the bare MCF compared to that of the packaged MCF. Colored arrows indicate the corresponding vertical axis of each curve. The black asterisk (*) in each curve represents the $\tau_{63\%}$ of each sensor.

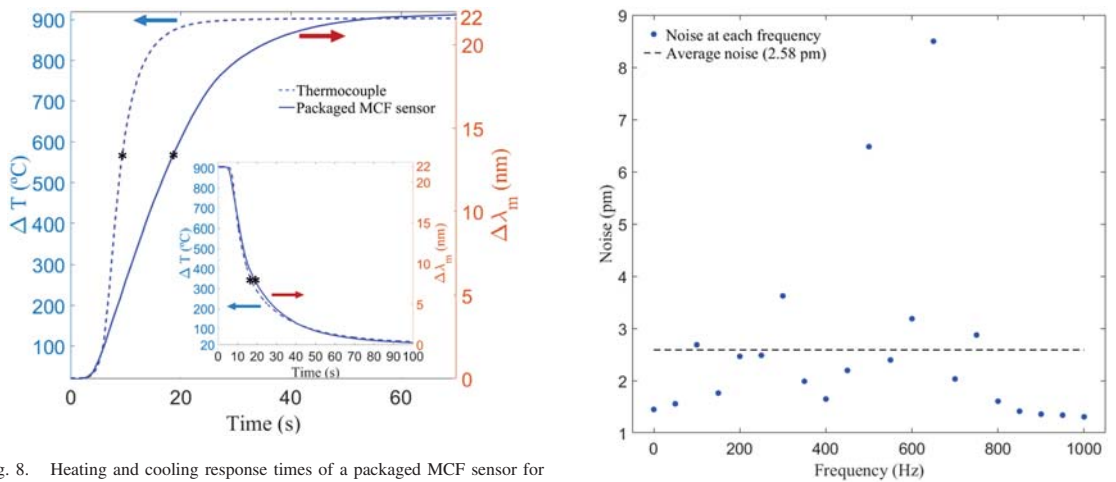


Fig. 8. Heating and cooling response times of a packaged MCF sensor for the 25 °C-900 °C-25 °C loop. Colored arrows indicate the corresponding axis of each curve. The black asterisk (*) in each curve represents the $\tau_{63\%}$ of each sensor.

TABLE I
RESPONSE TIMES (IN S) OF THE PACKAGED MCF SENSOR AND THE THERMOCOUPLE

Temperature gradient (°C)	25 - 550	550 - 25	25 - 900	900 - 25
Thermocouple	6	14	6	12
MCF sensor	17	20	15	14

the 200 °C–1000 °C calibrated range and the lower temperature sensitivity of the MCF below 100 °C as reported in [32].

For the results of the 25 °C-900 °C-25 °C loop shown in Fig. 8 only the curves of the packaged MCF sensor and the thermocouple are presented, since only the performance of these devices can be compared as their results are strictly related to temperature.

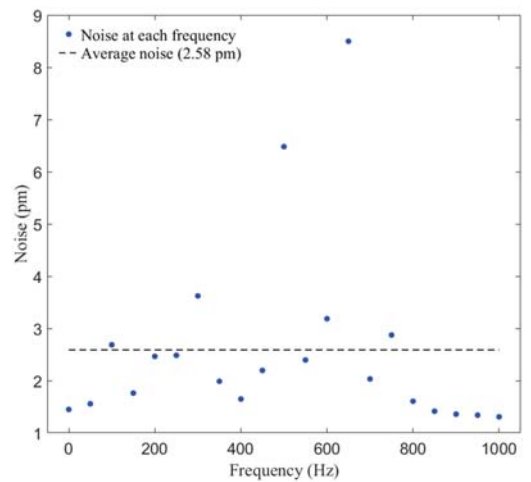


Fig. 9. Results of the effect of the vibrations in the measurements of λ_m at room temperature (25 °C). The biggest deviation (8.49 pm) happened at 650 Hz, where a resonance due to the 10 cm cantilever configuration took place.

The results shown in Fig. 7 and Fig. 8 are summarised in Table I. It can be noted that in all the cases, our packaged MCF temperature sensor responded slower than the thermocouple used as a reference. The results regarding the bare MCF are not shown in the table due to the fact that they are not related only to temperature, and therefore, not suitable for comparison.

In order to evaluate the effectiveness of the packaging in terms of protection against vibrations, the packaged MCF sensor was placed in a cantilever configuration and attached to a piezoelectric actuator (STr-35, Piezomechanik GmbH) whose maximum vibration amplitude was 6 μm . The length of the cantilever was 10 cm. The sensor was then subjected to vibrations at different frequencies. In all the cases, the voltage applied to the actuator

was the same (10 Vpp), and the measurements were carried out at room temperature (25 °C). The sensor was interrogated with the spectrum analyser mentioned above (I-MON512-USB, Ibsen Photonics) and the data processing approach was as follows: in two consecutive days 17000 raw spectra for each frequency were acquired and then, the maximum of each spectra (λ_m) was identified. These values were averaged for each point along with their standard deviation.

In Fig. 9, it can be seen that vibrations introduce an average noise of 2.58 pm in the measurement of λ_m . This turns into an uncertainty of 0.1 °C according to Eq. (2). Considering that the noise for the case of 0 Hz is intrinsic to the measurement system and not caused by vibrations, this means our MCF sensor is robust and practically immune to vibrations in a wide frequency range.

IV. CONCLUSIONS

In this work, we have reported on a sensitive and compactly packaged fiber optic temperature sensor that is robust against vibrations. The sensor is based on an MCF with strongly coupled cores. The sensor consists of a short segment of MCF (2.54 cm) spliced to a commonly used in telecommunications SMF. The fabrication of the device is simple, fast, inexpensive, and reproducible. The packaging of the sensor was conceived to make the MCF exclusively sensitive to temperature, hence independent to other parameters that may be present during temperature measurements, as for example, strain, bending, curvature, or vibrations.

The sensitive part of our sensor is the section of MCF. Temperature changes the effective indices of two supermodes that are excited in the MCF, causing a detectable shift in the interference pattern. The calibration of our MCF sensor was performed in the range from 200 to 1000 °C and a K-type thermocouple widely used and accepted in the conservative aeronautical industry was used as a reference. Results show that the packaged MCF sensor has a sensitivity of 24.8 pm/°C, high robustness against vibrations and a response time of 15 s. Thus, it may represent an attractive solution in several applications that require high temperature sensing, high resolution and sensitivity, small dimensions, and electromagnetic immunity. Some examples may include sensing in aeronautical engines, gas and oil facilities, etc.

The packaged MCF sensor can be customised for the aforementioned and other applications. In addition, its interrogation is carried out with commercially available sensor interrogators. Therefore, we believe that this prototype represents a substantial step forward in the direction of a commercially appealing optical temperature sensor.

REFERENCES

- [1] D. Bradley and K. J. Matthews, "Measurement of high gas temperatures with fine wire thermocouples," *J. Mech. Eng. Sci.*, vol. 10, no. 4, pp. 2328–305, Oct. 1968.
- [2] D. O'Sullivan and M. Cotterell, "Temperature measurement in single point turning," *J. Mater. Process. Technol.*, vol. 118, nos. 1–3, pp. 301–308, Dec. 2001.
- [3] M. Tagawa and Y. Ohta, "Two-thermocouple probe for fluctuating temperature measurement in combustion—Rational estimation of mean and fluctuating time constants," *Combustion Flame*, vol. 109, no. 4, pp. 549–560, Jun. 1997.
- [4] D. A. Stephenson, "Tool-work thermocouple temperature measurements—Theory and implementation issues," *J. Eng. Ind.*, vol. 115, no. 4, pp. 432–437, Nov. 1993.
- [5] L. Y. W. Lee, J. C. Chen, and R. A. Nelson, "Liquid-solid contact measurements using a surface thermocouple temperature probe in atmospheric pool boiling water," *Int. J. Heat Mass Transf.*, vol. 28, no. 8, pp. 1415–1423, Aug. 1985.
- [6] R. R. Dils, "High-temperature optical fiber thermometer," *J. Appl. Phys.*, vol. 54, no. 3, pp. 1198–1201, Nov. 1982.
- [7] V. Fericola and L. Crovini, "Digital optical fiber point sensor for high-temperature measurement," *J. Lightw. Technol.*, vol. 13, no. 7, pp. 1331–1334, Jul. 1995.
- [8] K. T. V. Grattan, A. W. Palmer, and Z. Zhang, "Development of a high-temperature fiber-optic thermometer probe using fluorescent decay," *Rev. Sci. Instrum.*, vol. 62, no. 5, pp. 1210–1213, May 1991.
- [9] Z. Zhang, K. T. V. Grattan, and A. W. Palmer, "Fiber-optic high-temperature sensor based on the fluorescence lifetime of alexandrite," *Rev. Sci. Instrum.*, vol. 63, no. 8, pp. 3869–3873, Apr. 1992.
- [10] G. Beheim, "Fiber-optic thermometer using semiconductor-etalon sensor," *Electron. Lett.*, vol. 22, no. 5, pp. 238–239, Feb. 1986.
- [11] M. Fokine and P. Holmberg, "Chemical composition gratings," presented at the OSA Tech. Dig. Adv. Photon. Conf., Barcelona, Spain, 2014, Paper SoW3B.4.
- [12] M. Fokine, "Formation of thermally stable chemical composition gratings in optical fibers," *J. Opt. Soc. Amer. B*, vol. 19, no. 8, pp. 1759–1765, 2002.
- [13] S. Bandyopadhyay, J. Canning, M. Stevenson, and K. Cook, "Ultra-high-temperature regenerated gratings in boron-codoped germanosilicate optical fiber using 193 nm," *Opt. Lett.*, vol. 33, no. 16, pp. 1917–1919, Aug. 2008.
- [14] S. Trpkovski *et al.*, "High-temperature-resistant chemical composition Bragg gratings in Er³⁺-doped optical fiber," *Opt. Lett.*, vol. 30, no. 6, pp. 607–609, Mar. 2005.
- [15] D. Barrera, V. Finazzi, J. Villatoro, S. Sales, and V. Pruneri, "Packaged optical sensors based on regenerated fiber Bragg gratings for high temperature applications," *IEEE Sensors J.*, vol. 12, no. 1, pp. 107–112, Jan. 2012.
- [16] S. S. Chong, W. Y. Chong, S. W. Harun, and H. Ahmad, "Regenerated fiber bragg grating fabricated on high germanium concentration photosensitive fiber for sensing at high temperature," *Opt. Laser Technol.*, vol. 44, no. 4, pp. 821–824, Jun. 2012.
- [17] S. J. Mihailov, "Fiber Bragg grating sensors for harsh environments," *Sensors*, vol. 12, no. 2, pp. 1898–1918, Feb. 2012.
- [18] S. Sales *et al.*, "Evaluation of new regenerated fiber Bragg grating high-temperature sensors in an ISO 834 fire test," *Fire Saf. J.*, vol. 71, pp. 332–339, Jan. 2015.
- [19] A. Wang *et al.*, "Sapphire-fiber-based intrinsic Fabry–Perot interferometer," *Opt. Lett.*, vol. 17, no. 14, pp. 1021–1023, Jul. 1992.
- [20] J. Wang *et al.*, "Multiplexed high temperature sensing with sapphire fiber air gap-based extrinsic Fabry–Perot interferometers," *Opt. Lett.*, vol. 35, no. 5, pp. 619–621, Mar. 2010.
- [21] Y. Zhu *et al.*, "Sapphire-fiber-based white-light interferometric sensor for high-temperature measurements," *Opt. Lett.*, vol. 30, no. 7, pp. 711–713, Apr. 2005.
- [22] C. Zhan *et al.*, "High temperature sensing using higher-order-mode rejected sapphire fiber gratings," *Opt. Memory Neural Netw.*, vol. 16, no. 4, pp. 204–210, Dec. 2007.
- [23] H. Y. Choi, K. S. Park, S. J. Park, U. C. Paek, B. H. Lee, and E. S. Choi, "Miniature fiber-optic high temperature sensor based on a hybrid structured Fabry-Perot interferometer," *Opt. Lett.*, vol. 33, no. 21, pp. 2455–2457, 2008.
- [24] T. Zhu *et al.*, "Fabry–Perot optical fiber tip sensor for high temperature measurement," *Opt. Commun.*, vol. 283, no. 19, pp. 3683–3685, Oct. 2010.
- [25] Y. Zhan *et al.*, "Fiber grating sensors for high-temperature measurement," *Opt. Laser Eng.*, vol. 46, no. 4, pp. 349–354, Jan. 2008.
- [26] V. M. Churikov, V. I. Kopp, and A. Z. Genack, "Chiral diffraction gratings in twisted microstructured fibers," *Opt. Lett.*, vol. 35, no. 3, pp. 342–344, 2010.
- [27] T. F. Morse, Y. He, and F. Luo, "An optical fiber sensor for the measurement of elevated temperatures," *IEICE Trans. Electron.*, vol. 83, no. 3, pp. 298–302, 2000.
- [28] G. Coviello *et al.*, "Thermally stabilized PCF-based sensor for temperature measurements up to 1000 °C," *Opt. Express*, vol. 17, no. 24, pp. 21551–21559, 2009.
- [29] D. Liu *et al.*, "Hollow core fiber based interferometer for high-temperature (1000 °C) measurement," *J. Lightw. Technol.*, vol. 36, no. 9, pp. 1583–1590, May 2018.

- [30] Z. Zhang *et al.*, "Hollow-core-fiber-based interferometer for high-temperature measurements," *IEEE Photon. J.*, vol. 9, no. 2, Apr. 2017, Art. no. 7101109.
- [31] T. Wang *et al.*, "A large range temperature sensor based on an angled fiber end," *Opt. Fiber Technol.*, vol. 45, pp. 19–23, Nov. 2018.
- [32] J. E. Antonio-Lopez *et al.*, "Multicore fiber sensor for high-temperature applications up to 1000 °C," *Opt. Lett.*, vol. 39, no. 15, pp. 4309–4312, Aug. 2014.
- [33] Y. Chunxia *et al.*, "Weakly-coupled multicore optical fiber taper-based high-temperature sensor," *Sens. Actuators A, Phys.*, vol. 280, pp. 139–144, Sep. 2018.
- [34] M. D. Wales *et al.*, "Multicore fiber temperature sensor with fast response times," *OSA Continuum*, vol. 1, no. 2, pp. 764–771, Oct. 2018.
- [35] J. Villatoro *et al.*, "Accurate strain sensing based on super-mode interference in strongly coupled multi-core optical fibers," *Sci. Rep.*, vol. 7, no. 1, pp. 4451–4457, Jun. 2017.
- [36] G. Salceda-Delgado *et al.*, "Compact fiber-optic curvature sensor based on super-mode interference in a seven-core fiber," *Opt. Lett.*, vol. 40, no. 7, pp. 1468–1471, Apr. 2015.
- [37] J. Villatoro *et al.*, "Miniature multicore optical fiber vibration sensor," *Opt. Lett.*, vol. 42, no. 10, pp. 2022–2025, May 2017.
- [38] J. Villatoro *et al.*, "Ultrasensitive vector bending sensor based on multicore optical fiber," *Opt. Lett.*, vol. 41, no. 4, pp. 832–835, 2016.
- [39] C. Xia *et al.*, "Supermodes for optical transmission," *Opt. Express*, vol. 19, no. 17, pp. 16653–16664, Aug. 2011.
- [40] C. Xia *et al.*, "Supermodes in coupled multi-core waveguide structures," *IEEE J. Sel. Topics Quantum Electron.*, vol. 22, no. 2, pp. 196–207, Mar.-Apr. 2008.
- [41] J. Taylor, "Uncertainty in the measurements of y ," in *An Introduction to Error Analysis: The Study of Uncertainties in Physical Measurements*, 2nd ed. Sausalito, CA, USA: Maple-Vail Book Manufacturing Group, 1997, pp. 186–188.
- [42] EGOLF (European Group of Organizations for Fire Testing, Inspection and Certification), Determination of the response time of thermocouples to be used for the measurement of air or gas phase temperature in reaction to fire testing, EGOLF Agreement EA 01: 2008, pp. 1–8, 2008.

Josu Amorebieta received the Master's degree in telecommunications engineering from the University of the Basque Country UPV/EHU, Bilbao, Spain, in 2016. He is currently working toward the Ph.D. degree with the Applied Photonics Group (APG-FAT), University of the Basque Country UPV/EHU. His current research interests include the optical fiber sensing utilizing special fibers for industry and aeronautics.

Gaizka Durana received the M.Sc. and Ph.D. degrees in solid-state physics and telecommunications engineering from the University of the Basque Country UPV/EHU, Bilbao, Spain, in 1999 and 2008, respectively. He is currently an Associate Professor with the Department of Communications Engineering, University of the Basque Country UPV/EHU. His research is focused on the manufacture of specialty polymer optical fibers and design, development, and application of fiber-based optical sensors.

Ángel Ortega-Gómez received the Master's degree in telecommunications engineering from the University of the Malaga (UMA), Spain, in 2016. He is currently working toward the Ph.D. degree with the Applied Photonics Group (APG-FAT), University of the Basque Country UPV/EHU, Bilbao, Spain. His research is based on microstructure fibers sensors and Local Surface Plasmon Resonance (LSPR) effect applied on biosensors.

Rubén Fernández received the Electronics Engineer and Master's degrees in advanced electronics systems from the University of the Basque Country UPV/EHU, Bilbao, Spain. He is currently working toward the Ph.D. degree with the Applied Photonics Group (APG-FAT), University of the Basque Country UPV/EHU, Spain.

Javier Velasco is currently a Project Manager with the Aeronautical Technologies Center (CTA), Spain, and has been specialized during the last years in Industry 4.0. He has been working in several research projects focused on test control (load, vibration, and temperature), test automation, data acquisition, and monitoring technologies.

Idurre Sáez de Ocáriz, biography not available at the time of publication.

Joseba Zubia, biography not available at the time of publication.

Jose Enrique Antonio-López, biography not available at the time of publication.

Axel Schülzgen received the Ph.D. degree in physics from Humboldt-University of Berlin, Germany. Since 2009, he has been a Professor of Optics and Photonics with CREOL, The College of Optics and Photonics, University of Central Florida, Orlando, FL, USA. He is also an Adjunct Research Professor with the College of Optical Sciences, University of Arizona, Tucson, AZ, USA.

Dr. Schülzgen has published more than 120 papers in peer-reviewed journals and holds six patents. He is a Fellow of the Optical Society of America.

Rodrigo Amezcua-Correa, biography not available at the time of publication.

Joel Villatoro received the M.Sc. and Ph.D. degrees in optics from the National Institute for Astrophysics, Optics, and Electronics, Mexico. He is an Ikerbasque Research Professor with the University of the Basque Country UPV/EHU, Bilbao, Spain. His research interests include optical fiber sensors and real-world applications of photonic technology.

3. artikulua

Titulua:

Highly sensitive multicore fiber accelerometer for low frequency vibration sensing

D.O.I.:

<https://doi.org/10.1038/s41598-020-73178-x>

Egileak:

Amorebieta, J.; Ortega-Gomez, A.; Durana, G.; Fernández, R.; Antonio-Lopez, E.; Schülzgen, A.; Zubia, J.; Amezcua-Correa, R.; Villatoro, J.

Aldizkari eta argitalpenaren informazioa:

Scientific Reports, 10 (1), 1-11 (2020)

Aldizkariaren adierazleak 2020an:

Oraingoz ez daude eskuragarri

Aldizkariaren adierazleak 2019an:

Eragin-faktorea: 3.998

Q1 Diziplina anitzeko zientziak sailean (17/71)



OPEN

Highly sensitive multicore fiber accelerometer for low frequency vibration sensing

Josu Amorebieta^{1✉}, Angel Ortega-Gomez¹, Gaizka Durana¹, Rubén Fernández¹, Enrique Antonio-Lopez², Axel Schülzgen², Joseba Zubia¹, Rodrigo Amezcua-Correa² & Joel Villatoro^{1,3✉}

We report on a compact, highly sensitive all-fiber accelerometer suitable for low frequency and low amplitude vibration sensing. The sensing elements in the device are two short segments of strongly coupled asymmetric multicore fiber (MCF) fusion spliced at 180° with respect to each other. Such segments of MCF are sandwiched between standard single mode fibers. The reflection spectrum of the device exhibits a narrow spectrum whose height and position in wavelength changes when it is subjected to vibrations. The interrogation of the accelerometer was carried out by a spectrometer and a photodetector to measure simultaneously wavelength shift and light power variations. The device was subjected to a wide range of vibration frequencies, from 1 mHz to 30 Hz, and accelerations from 0.76 mg to 29.64 mg, and performed linearly, with a sensitivity of 2.213 nW/mg. Therefore, we believe the accelerometer reported here may represent an alternative to existing electronic and optical accelerometers, especially for low frequency and amplitude vibrations, thanks to its compactness, simplicity, cost-effectiveness, implementation easiness and high sensitivity.

For a long time, accelerometers have been used to detect and measure vibrations with high sensitivity and precision. Thus, they have a wide variety of applications. For instance, in the heavy industry, accelerometers are used to monitor low-frequency vibrations in large rotating machineries or in oil pipes¹, or in structural health monitoring, to supervise the condition of pillars, bridges, etc.². They are also used in biomedicine and biomechanics³, and even in gravitational wave detectors⁴. Accelerometers are one of the key elements in seismology as well⁵, where they are used for the detection and monitoring of ground motions caused by earthquakes, volcanic eruptions, explosions, landslides, tsunamis, avalanches, etc. In these cases, accelerometers with high sensitivity for low amplitude vibrations are required.

The detection of vibrations with low frequencies is a very challenging field. For example, the frequency range of ground motions caused by natural events or explosions is between 0.1 and 20 Hz^{6,7}. For the case of tsunamis, such frequency range is even narrower, from 0.1 to 1 Hz⁸. Moreover, it is important to identify the ground motions accurately from the surrounding noise. Therefore, accelerometers for such applications must be highly sensitive and must be capable of measuring acceleration in a wide range. Additional requirements for accelerometers include simple operation, compactness, robustness, capability to operate in hostile or harsh environments and multi-point sensing^{9,10}. Finally, as natural events are usually unpredictable and spaced in time¹¹, such accelerometers must be reliable, long-lasting, and should require minimum or no maintenance.

So far, the most spread accelerometers for low frequencies are based on piezoelectric components¹², MEMS membranes¹³ or pendulums¹⁴ that move with vibrations, or have electrochemical nature¹⁵. Moreover, frequently, such operating principles are combined to enhance their overall performance⁷. The technology of electronic accelerometers is very mature and cost-effective. However, the harsh environments in which these accelerometers are commonly deployed, such as seabed or boreholes, may affect the lifetime of their elements. For such applications, accelerometers based on optical fibers are a good alternative. Fiber-based accelerometers have important advantages that include small size, electromagnetic immunity, as they do not require any electric component to operate, high resolution, remote and long-distance operation capabilities.

¹Department of Communications Engineering, University of the Basque Country UPV/EHU, 48013 Bilbao, Spain. ²CREOL -The College of Optics and Photonics, University of Central Florida, Orlando, FL 162700, USA. ³Ikerbasque-Basque Foundation for Science, 48011 Bilbao, Spain. ✉email: josu.amorebieta@ehu.eus; agustinjoel.villatoro@ehu.es

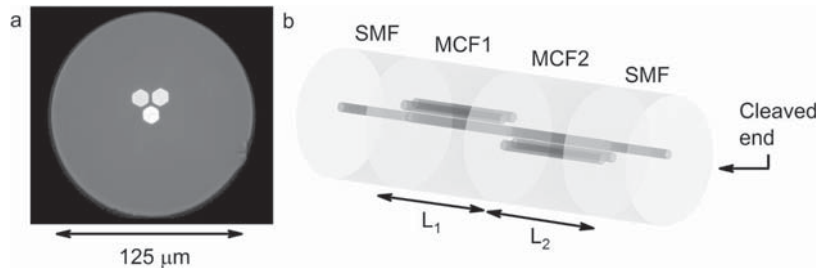


Figure 1. (a) Cross section of the asymmetric MCF. (b) Schematic layout of the device drawn with Blender v2.82 (<https://www.blender.org/>).

Among optical fiber accelerometers, those based on interferometry and fiber Bragg gratings (FBGs) are the most advanced configurations. Optical fiber interferometric accelerometers feature larger dynamic range, wider frequency response band and higher sensitivity compared to some electronic accelerometers^{16–18}. In fact, optical fiber interferometric seismometers capable of detecting vibrations of few mHz have been reported^{19,20}. However, they are bulky and their interrogation tends to be complex. FBG-based optical accelerometers are more compact. Moreover, they provide high sensitivity, large dynamic range and multiplexing ability²¹; and may operate in frequency response bands below 1 Hz^{22,23}. To reach such performance, they require sophisticated interrogation systems that entail picometer-resolution interrogators. In addition, they require elaborated packaging. As a consequence, FBG accelerometers are expensive.

In recent years, multicore fibers (MCFs) have drawn much attention as multipurpose sensing elements²⁴. As accelerometers, strongly coupled MCFs have proved to have much potential²⁵. Moreover, their capability to withstand and operate under elevated strain and temperature conditions has been reported as well^{26,27}, which is a demanded characteristic for harsh environments or outdoors implementations.

In this work, we report on a highly sensitive all-fiber optical accelerometer suitable for sensing vibrations of extremely low frequencies (down to 1 mHz) and low amplitudes. The device is compact and consists of two segments of MCF sandwiched between standard single mode fiber. The MCF segments have different lengths and are rotated 180° with respect to each other. Due to its architecture, the reflection spectrum of the device exhibits a narrow peak that shrinks when it is subjected to vibrations. To test the device, it was subjected to vibrations from 1 mHz to 30 Hz and accelerations from 0.76 to 29.64 mg. The performance of our device was compared and calibrated with a commercial electronic accelerometer. We believe that the simplicity and high performance of the MCF accelerometer reported here are appealing for several applications; particularly those where frequencies are low.

Sensor design, operating mechanism and fabrication

The MCF used to build the accelerometer was fabricated at the University of Central Florida (Orlando, USA). It is an asymmetric strongly coupled MCF consisting of three cores, where one of the cores is located at the geometrical center of the fiber, whereas the other two are surrounding it and arranged adjacently in a V-like configuration (Fig. 1a). Each core is made of Germanium doped silica, and has a mean diameter of 9 μm and a numerical aperture (NA) of 0.14 at 1550 nm to match with that of the SMF. The cores are separated 11.5 μm from each other and embedded in a pure silica cladding of 125 μm of diameter.

The architecture of the device is sketched in Fig. 1b. The sensor consists of two cascaded short segments of different lengths of MCF rotated 180° with respect to each other and sandwiched between two SMFs, resulting in a SMF-MCF1-MCF2-SMF structure. In this structure, the distal SMF has a cleaved end that acts as a low reflectivity mirror in order the device to be interrogated in reflection mode. The benefits of such structure will be discussed throughout this section.

The theoretical background of strongly coupled MCFs relies on the coupled mode theory (CMT)^{28–31}. According to it, if at least two waveguides are close enough to interact, a cyclical power transfer between the waveguides will take place due to the overlapping between the propagating modes through each of them. For conventional CMT, it is assumed that the propagating modes under study are orthogonal³². In the simplest case, if we assume two single mode waveguides named 1 and 2 that are so close to each other that the evanescent field from one guide penetrates into the other, there is a coupling between the two propagating modes. For waveguide 1, such propagation can be expressed as:

$$\frac{\partial a_1}{\partial z} = -j(\beta_1 + k_{1,1})a_1 - jk_{1,2}a_2 \quad (1)$$

where a is the amplitude of the mode in the waveguide indicated in the subindex, β is its corresponding propagation constant and the k parameters are the mutual and self-coupling coefficients between the orthogonal propagating modes in the waveguides 1 and 2, respectively, along the z axis where the propagation is taking place. Identical expression is valid for the propagation in waveguide 2 by substituting in Eq. (1) the subindex 1 for 2 and vice versa.

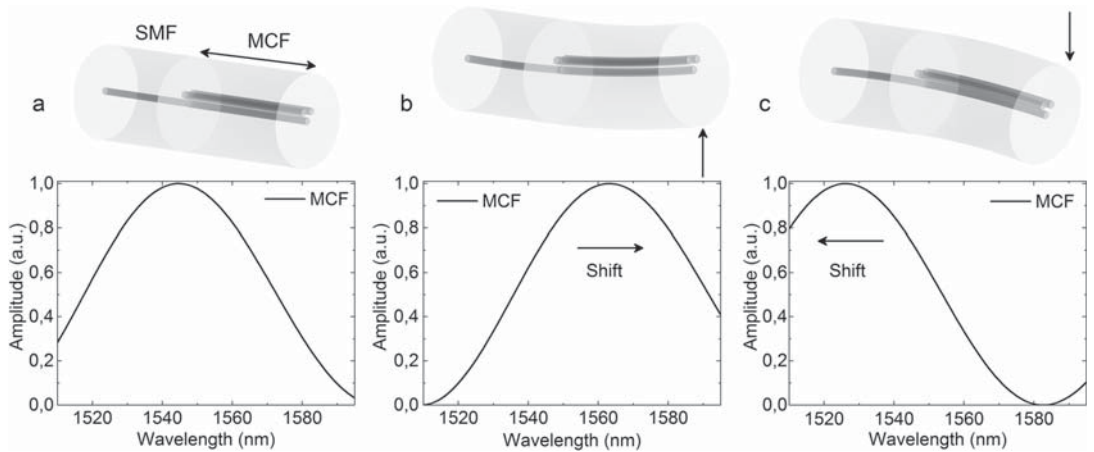


Figure 2. Simulated spectra for the cases in which a segment of MCF is (a) straight, (b) bent upwards and (c) bent downwards when the cores are positioned in a V-like configuration. The arrow indicates the bending direction and the wavelength shift in each case.

Now let us assume the boundary condition in which the amplitude of the mode a only exists in one of the waveguides at $z=0$. Thus, by applying the condition $a_1(0) = 1$ and $a_2(0) = 0$, it is possible to calculate the coupled power in any of the waveguides at any distance by calculating $P(z) = a(z) * a^*(z)$, where a^* refers to the conjugate amplitude of the mode. For such case, the normalized coupled power in the waveguide 1 at a certain propagation distance z , can be expressed as:

$$P_1(z) = \cos^2(Sz) + \cos^2(\gamma)\sin^2(Sz) \tag{2}$$

where $S = \sqrt{\delta^2 + k^2}$, $\delta = (\beta_1 - \beta_2)/2$ and $\tan(\gamma) = k/\delta$.

In strongly coupled MCFs, each of the cores acts as a waveguide. In such coupled structures, the propagating modes are called supermodes^{33,34}, which are the linear combination of the propagating modes through each of the individual waveguides. When such MCFs are excited in their central core by the incoming LP₀₁ mode from the SMF, the two orthogonal supermodes that have power in the central core are coupled. Such supermodes are named SP₀₁ and SP₀₂, and are specific for each MCF. Moreover, for strongly coupled MCFs as the one employed to manufacture this accelerometer, in which all the cores are identical in terms of size and physical properties, and the distance between the central and the neighboring cores remains unaltered, this supermode coupling provokes the power distribution among all the adjacent cores to be identical. Therefore, particularizing Eq. (2) for a stub of the MCF in Fig. 1a, the normalized coupled power in the central core can be expressed as:

$$P(z) = \cos^2\left(\frac{\sqrt{3\pi \Delta n}}{\lambda} z\right) + \frac{1}{3}\sin^2\left(\frac{\sqrt{3\pi \Delta n}}{\lambda} z\right) \tag{3}$$

where Δn is the difference between the effective refractive indexes of the two propagating coupled supermodes and depends on the physical characteristics of the MCF, λ is the excitation wavelength, and z is the distance at which the normalized power is being evaluated along the propagation axis. Therefore, the transmitted power will vary periodically, with a maximum at certain values of z and a minimum at others.

Now, if the length of MCF is fixed, let us say L , the transmission of an SMF-MCF-SMF structure can also be described by particularizing Eq. (3) for $z=L$. If such a structure is excited with a broadband source, the transmission spectrum will be periodic in wavelength according to the phase in Eq. (3).

When an MCF is bent, each core suffers different levels of strain, and their respective refractive indices vary accordingly^{35–39}, modifying the effective refractive indexes of the two propagating supermodes and therefore, the power coupling conditions, which will be reflected in the spectrum. In our case, this effect, added to the asymmetrical arrangement of the cores and their orientation, will cause detectable wavelength shift and coupled power variations that will have unique characteristics depending on the applied bending direction and amplitude, making the MCF ideal for direction-sensitive bending sensors. As demonstrated in⁴⁰, when the position of the cores and the applied bending are aligned as in Fig. 2, where the cores are orientated in a V-like configuration and the MCF is bent upwards and downwards, only wavelength shifts will be noticed in the spectrum; whereas if we rotate the fiber 90°, only coupled power variations will be noticed.

As a step forward of such operating principle, the accelerometer proposed in this work consists of two short segments of the aforementioned MCF (MCF1 and MCF2) of similar but different lengths (L_1 and L_2) that are cascaded and rotated 180° with respect to each other. For this configuration, Eq. (1) has to be applied to each segment. Hence, the normalized output power of the cascade is the product of the individual normalized power outputs of each MCF segment:

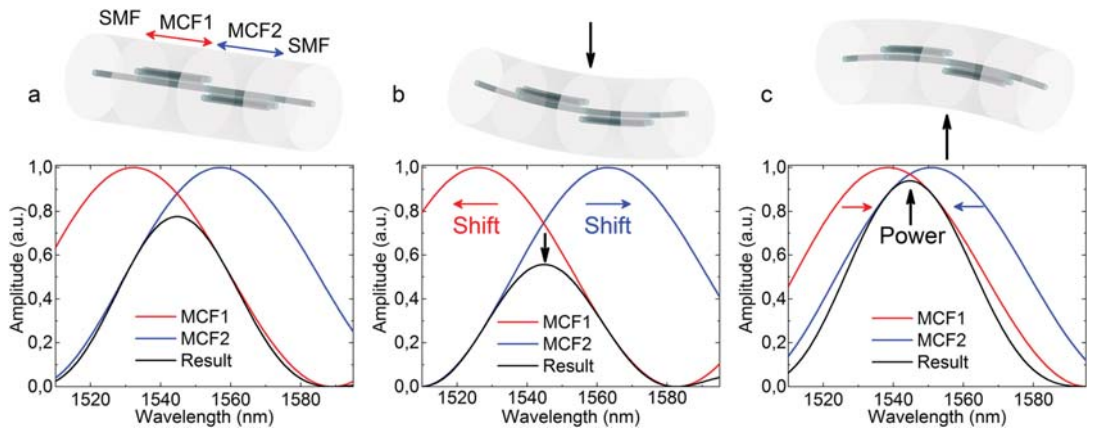


Figure 3. Simulated spectra of each of the MCF segments and the resulting spectra for the cases where the structure is (a) straight, (b) bent upwards and (c) bent downwards by its fusion splice point. The arrow indicates the bending direction, the wavelength shift or the power variation in each case. The cores of MCF1 are in a V-like configuration, whereas the ones in MCF2 are in an inverted V-like configuration.

$$P(L_1, L_2) = P_{MCF1}(L_1) * P_{MCF2}(L_2) \tag{4}$$

where the subindexes MCF1 and MCF2 are referred to each short MCF segment of lengths L_1 and L_2 , respectively. Thus, for $\theta = \sqrt{3\pi \Delta n} / \lambda$, the normalized output power in the central core after passing through the two MCF segments is as follows:

$$P(L_1, L_2) = \cos^2(\theta L_1) * \cos^2(\theta L_2) + \frac{1}{9} \sin^2(\theta L_1) * \sin^2(\theta L_2) + \frac{1}{3} \cos^2(\theta L_1) * \sin^2(\theta L_2) + \frac{1}{3} \cos^2(\theta L_2) * \sin^2(\theta L_1) \tag{5}$$

If we compare the predominant terms in Eqs. (3) and (5), in Eq. (3) it is a squared cosine whereas in Eq. (5) it can be considered a cosine raised to the fourth. Thus, a spectrum derived from Eq. (5) will have narrower peak or peaks than one from Eq. (3) for identical MCF lengths. Moreover, the visibility of a spectrum from Eq. (5) will be higher as well, as the contribution of the rest of the terms in the equation is less than the contribution of the term in Eq. (3), which makes the difference between adjacent maxima and minima to be lower in the latter. Hence, the advantages of cascading two MCF segments compared to a single MCF segment are narrower peaks in the spectrum and higher visibility, which facilitate tracking any change in it.

By operating in reflection mode, the normalized output power is the product of Eq. (5) by itself due to the back-and-forth path of the light through the SMF-MCF1-MCF2-SMF structure; so it can be assumed that the predominant term is a cosine raised to the eighth. Thus, this is an easy manner to improve the narrowness and visibility of the spectrum even more and the reason why this device operates in such configuration.

Regarding the fiber arrangement, by rotating the two MCF segments 180° with respect to each other, each of them will show contrary behavior in terms of wavelength shift and amplitude of the spectrum when they are bent due to their direction sensitive nature that has been explained previously. When the position of the cores of each MCF segment and the applied vertical bending are aligned as in Fig. 3, where one of the MCF segments has its cores oriented in a V-like configuration and the other MCF segment has its cores oriented in an inverted V-like configuration (or rotated 180°), only pronounced amplitude variations will take place in the spectrum. In order the device to perform as shown in Fig. 3, MCF segments of different lengths are compulsory to avoid any ambiguity in the measurement. If the lengths were identical, the spectra of both segments would be overlapped in idle state, being that situation the point at which the maximum reflected light power would take place. Each spectrum would shift in opposite directions when the structure was bent, but only power decreases would be recorded, resulting in the same or similar power readings for opposite bending directions. Such ambiguity or loss in sensitivity is avoided by using segments of different lengths, as for this case, the measured power increases and decreases accordingly with the applied bending direction compared to the power measurement in idle state. Such amplitude variations in the spectrum are proportional to power variations, and therefore, only a PD will be necessary to interrogate the device. Such simplicity makes this SMF-MCF1-MCF2-SMF structure appealing as a very sensitive and cost-effective accelerometer, as it does not require high performance or ad-hoc equipment to operate.

To manufacture a device with such characteristics, some design constraints were required to be considered: Its spectrum had to be confined within the interrogation window (from 1510 to 1595 nm, according to our interrogation setup) at any time and it must have a unique and well-defined peak with no secondary lobes. Such requirements are mandatory to minimize any sensitivity loss when measuring the reflected light power that is

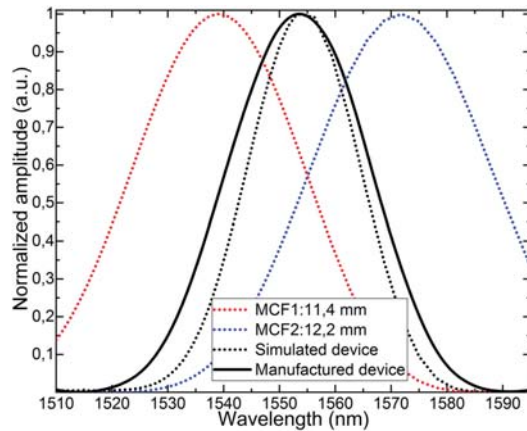


Figure 4. Normalized spectra of the simulated (black dashed line) and manufactured devices (black continuous line). Notice that the maxima of both curves is around 1554 nm and there are no secondary lobes. Simulated spectra of MCF segments of 11.4 mm (red dashed line) and 12.2 mm (blue dashed line) are shown as well. As indicated in Eq. (2) their product results in the black dashed line.

caused by adjacent lobes with opposite trends (one increases whereas the other decreases) in the same interrogation window, as shown in⁴⁰.

The best fitting lengths for the MCF segments that fulfilled the requirements were 11.4 mm and 12.2 mm, resulting in a compact device of 23.6 mm. To manufacture such device (illustrated in Fig. 1b), a precision fiber cleaver (Fujikura CT-105) and a specialty fiber fusion splicer (Fujikura 100P+) were used. On the one hand, the cleaver allowed us to cut MCF segments of the desired length with 10 μm precision. On the other hand, the splicer can align the central core of the MCF with the unique of the SMF with high precision and has a rotating mechanism and an imaging system that allows observing the end-face of the MCF. Once the MCF segments were rotated 180° with respect to each other, they were spliced, so the central cores of all the segments of the structure were aligned. The fabrication process of our device is inexpensive, fast, and reproducible.

The spectra of the simulated and the manufactured devices are shown in Fig. 4, along with the simulation for each of the MCF segments that comprise the structure. Such simulations were carried out with PhotonDesign simulation software. In such figure, it can be noticed that the curves corresponding to the manufactured and simulated devices agree well, and that the design constraints that included one well-defined and centered peak with no secondary lobes were achieved.

Results and discussion

The interrogation of the device is simple and was carried out with commercial equipment. It consists of a broadband light source (Safibra, s.r.o.) centered at 1550 nm and an InGaAs PD (Thorlabs PDA30B2). To interrogate the device in reflection mode, a fiber optic circulator was used. As it can be noticed in the simulations in Fig. 3, when the structure is bent by the point in which both MCFs are fusion spliced to each other and with that specific core orientation, only power variation will take place. However, when the physical device is subjected to the same effect, a slight wavelength shift is likely to happen as well apart from the amplitude variation. This is caused by two factors: in first place, the impossibility to apply the bending only and exactly at the fusion splice point; and in second place, the length difference of 0.8 mm between the MCF segments, which will cause a small variation in the shift of each against the same stimulus. Due to that, the device was also interrogated with a spectrometer (Ibsen Photonics I-MON-512 High Speed) to monitor the wavelength shift in the spectrum. Such measurement was used as an indicator of the relation between the direction of the applied bending and the position of the cores, as according to Fig. 3, small wavelength shifts would imply the accelerometer is operating as intended, as it is optimized to maximize the power variation.

To test the device, a horizontally fixed rectangular methacrylate thin plate was used. Underneath and at the center of it, an amplified piezoelectric actuator (Thorlabs APFH720 combined with Thorlabs MDT694B amplifier) was fixed so that the plate could vibrate only in the vertical plane. The piezoelectric actuator was connected to a function generator (Keysight Technologies 33220A) to generate signals of diverse amplitudes and frequencies. Then, the manufactured device was surface bonded with cyanoacrylate adhesive to the upper side of the plate, locating the MCF1-MCF2 splice at the center of it and just above the piezoelectric actuator, as it can be observed in the scheme of the experimental setup shown in Fig. 5. It was surface bonded with its cores oriented as in Fig. 3 to match the direction of vibration. Adjacent to the device, a commercial accelerometer (Pico Technology PP877 with Pico Technology TA096) was fixed for comparison and calibration purposes, as this electronic accelerometer provided the relation between the amplitude of the vibration and the acceleration. All the tests were carried out at room temperature (25 °C) and the raw signal of the time response of both devices was monitored and recorded.

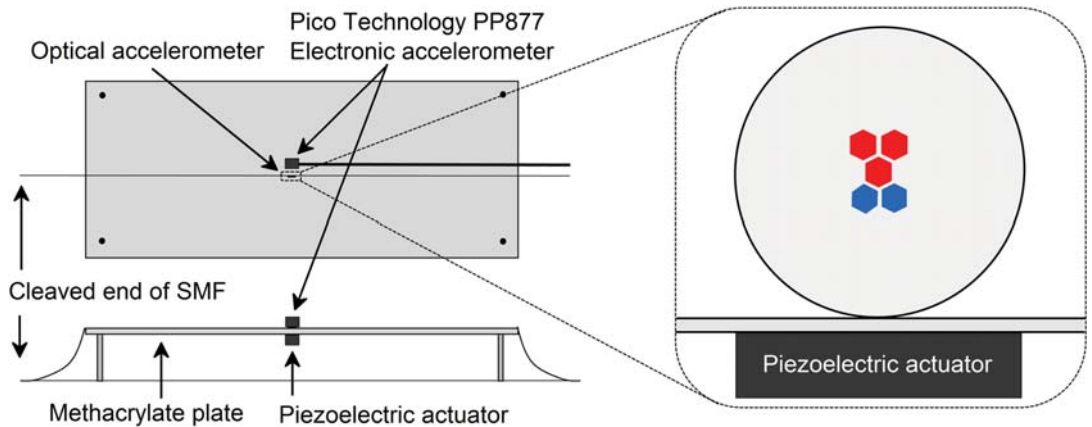


Figure 5. Schematic lateral and top views of the experimental setup drawn with Origin2019b (<https://www.originlab.com/>). The close-up shows how the manufactured optical accelerometer was surface bonded to the plate. Red cores belong to MCF1 whereas blue cores belong to MCF2. The red central core indicates MCF1 is in front of MCF2, as they share common central core. Adjacent to it, the Pico Technology PP877 electronic accelerometer was fixed.

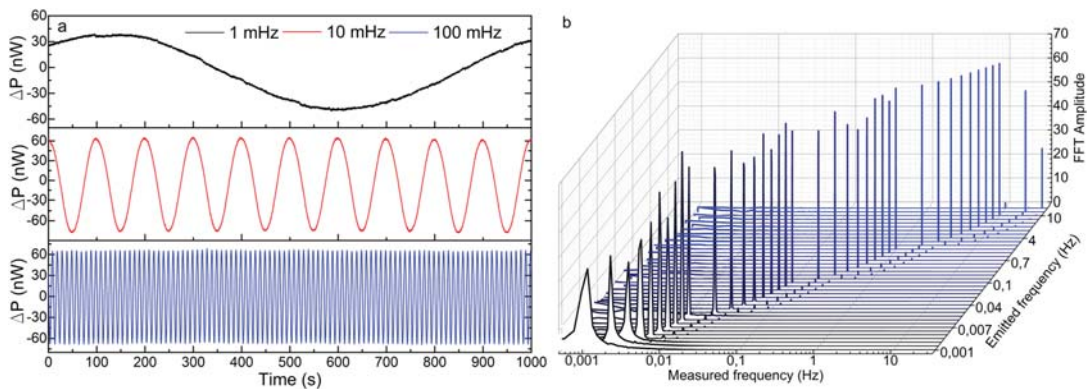


Figure 6. Results of the power measurements in the manufactured optical device. (a) Time response of three representative cases. (b) FFT amplitudes for frequencies from 30 Hz down to 1 MHz for a sinusoidal signal of 1 V_{pp}. The Measured frequency axis is in logarithmic scale.

According to the optical accelerometer, the time response signals in terms of wavelength at which the maxima in the spectrum takes place (λ) and measured power in the PD (P) were acquired. The value of such parameters with the device in idle state were taken as reference (λ_{ref} , P_{ref}) to obtain the wavelength shift ($\Delta\lambda = \lambda - \lambda_{ref}$) and power variation ($\Delta P = P - P_{ref}$), respectively. Subsequently, the FFT of such signals was done to obtain the amplitude of their corresponding frequency components and weights. The criteria to define the limit of detection (LoD) was set to be a signal to noise ratio (SNR) of 3 in the FFT amplitude of the most prominent component, which is commonly taken as a rule⁴¹.

The first test consisted in emitting a sinusoidal signal of 1 V_{pp} amplitude and varying its frequency from 30 Hz down to 1 MHz (the lowest frequency provided by the function generator) in several steps so that the LoD in terms of frequency of each device could be defined. The results are shown from Figs. 6 to 8. The manufactured device detected every vibration clearly down to 1 MHz in wavelength shift and power variation (see Figs. 6a and 7a). The small wavelength shift in Fig. 7a indicates that the device has been surface bonded with the proper core orientation to the plate, and explains the fact that the FFT amplitudes are lower for the wavelength shift measurements than those for the power variation. Nevertheless, even in this configuration aimed at maximizing the power variation, the device has detected such low vibrations by its wavelength shift as well, which is an indicator of its high sensitivity.

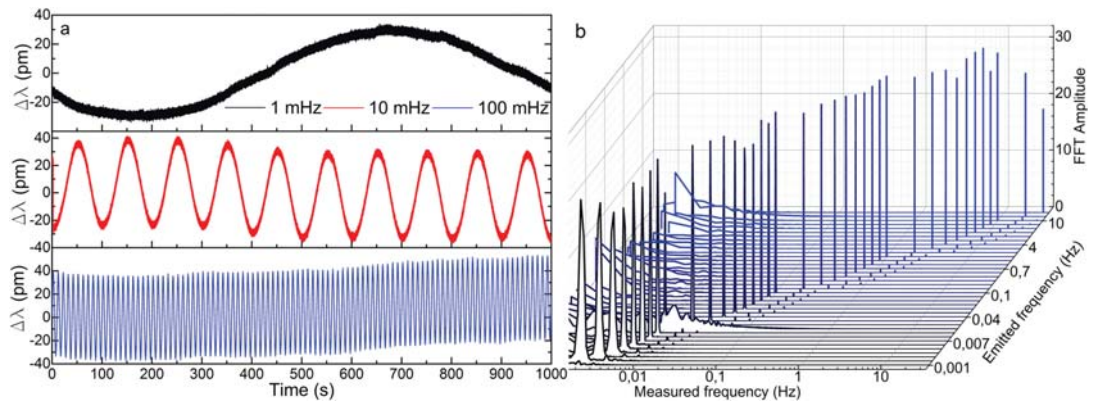


Figure 7. Results of the wavelength shift measurements in the manufactured optical device. (a) Time response of three representative cases. (b) FFT amplitudes for frequencies from 30 Hz down to 1 mHz for a sinusoidal signal of 1 Vpp. The Measured frequency axis is in logarithmic scale.

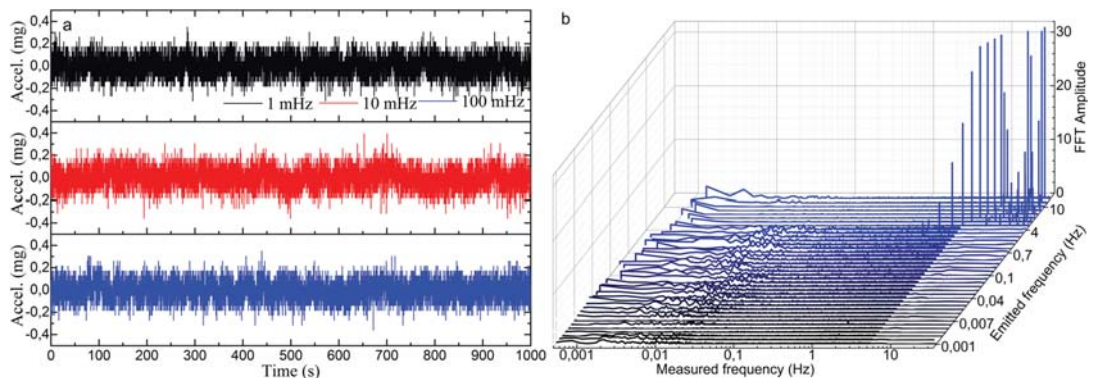


Figure 8. Results of the acceleration measurements in the electronic accelerometer. (a) Time response of three representative cases. (b) FFT amplitudes for frequencies from 30 Hz down to 1 mHz for a sinusoidal signal of 1 Vpp. The Measured frequency axis is in logarithmic scale.

Some other facts that should be highlighted from these results are the low variability and narrowness in amplitude and width, respectively, of the most prominent FFT component in all the cases (see Figs. 6b and 7b), with low level of the harmonic components. These characteristics are directly related to the purity of the acquired raw signal. This performance is critical for vibration measurements as it indicates that the device is practically insensitive to frequency variations if the same vibration amplitude is applied. This characteristic is noticeable if we pay attention to the time responses in Figs. 6a and 7a, where the recorded sinusoidal signal has practically the same amplitude in all the frequencies. According to the commercial accelerometer, it only detected vibrations of 2 Hz and above and with significantly noisier signal and with high level of harmonic components (see Fig. 8).

The second test consisted in emitting a sinusoidal signal of a fixed frequency (6 Hz) and varying its amplitude from 1 Vpp down to 10 mVpp (the lowest amplitude provided by the function generator) to define the LoD of each device in terms of amplitude of vibration, which is related to the acceleration of the oscillation movement. The time responses and FFT amplitudes of both devices are shown from Figs. 9 to 11. The optical device detected vibrations down to 10 mVpp above the established 3:1 SNR criteria. The noticeable progressive decrease in the amplitude of the signals in the time domain (see Figs. 9a and 10a) and the FFT (see Figs. 9b and 10b) is proportional to the diminishment of the amplitude of the emitted signal. In both cases, wavelength shift and power variations, the emitted signal can be clearly detected and the low level of the harmonic components is noticeable. Such results should be highlighted for the PD, whose FFT amplitudes are almost the double compared with the ones obtained by the spectrometer. In relation to the electronic accelerometer, according to the 3:1 SNR criteria, it detected the emitted signals from 1 Vpp down to 30 mVpp, which according to its calibration, covers an acceleration range from 29.64 to 0.76 mg. Its time response signals were significantly noisier (see Fig. 11a), and as a result of that, their corresponding FFT amplitudes were an order of magnitude below the ones of our MCF accelerometer (see Fig. 11b).

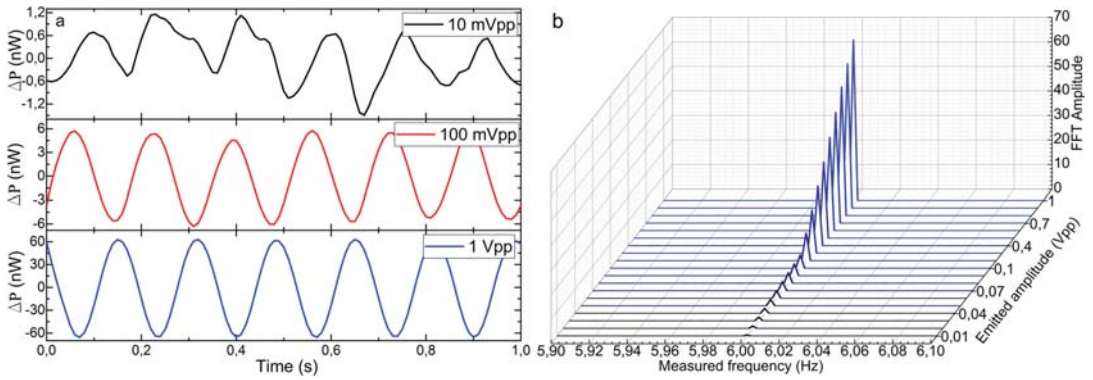


Figure 9. Results of the power variation measurements in the manufactured optical device. (a) Time response of three representative cases, and (b) FFT amplitudes for sinusoidal signals of 6 Hz and amplitudes from 1 Vpp down to 10 mVpp.

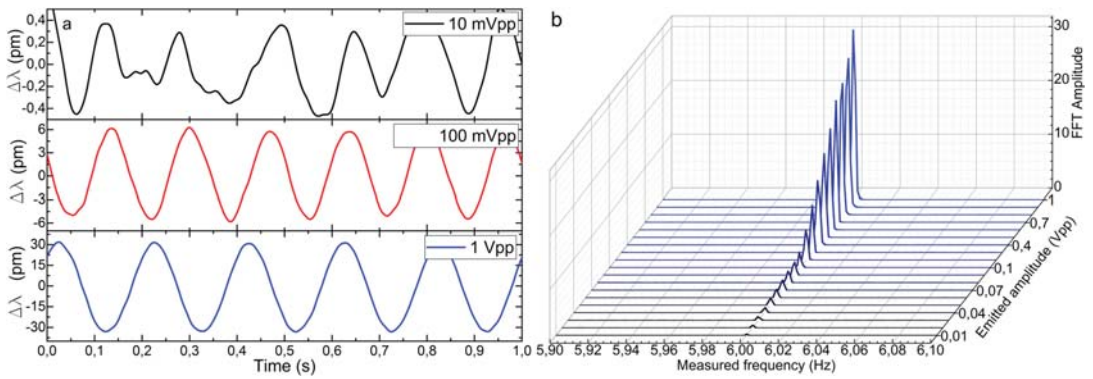


Figure 10. Results of the wavelength shift measurements in the manufactured optical device. (a) Time response of three representative cases, and (b) FFT amplitudes for sinusoidal signals of 6 Hz and amplitudes from 1 Vpp down to 10 mVpp.

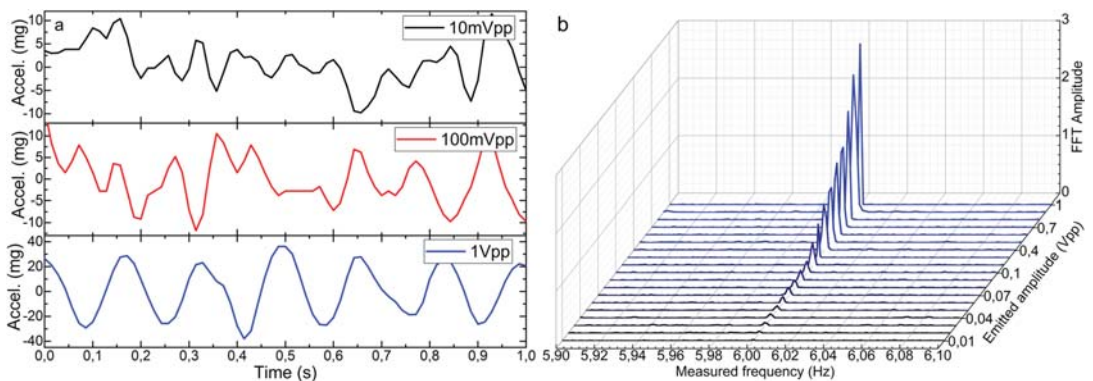


Figure 11. Results of the acceleration measurements in the electronic accelerometer. (a) Time response of three representative cases, and (b) FFT amplitudes for sinusoidal signals of 6 Hz and amplitudes from 1 Vpp down to 10 mVpp.

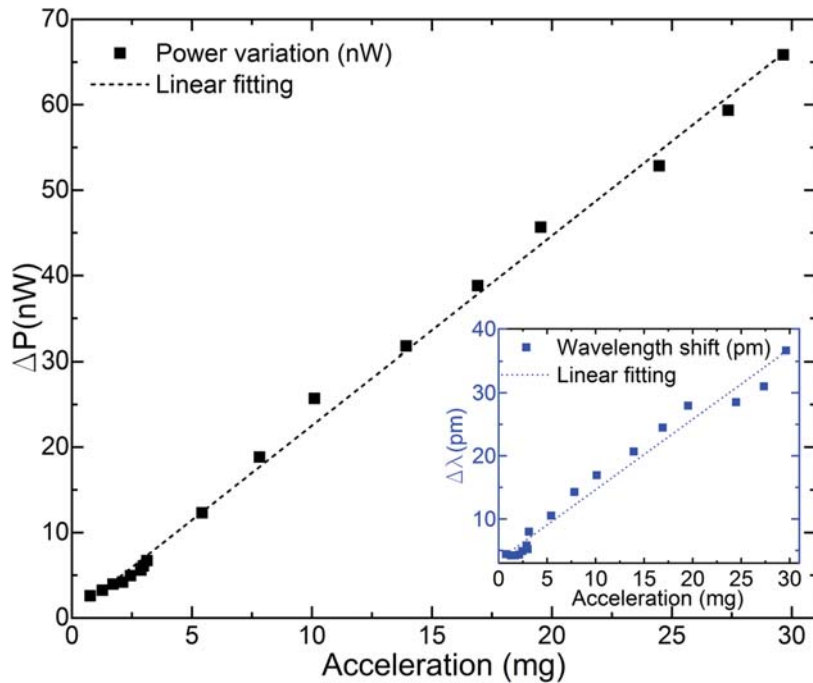


Figure 12. Calibration of the manufactured optical accelerometer in terms of power variation. The calibration of the device in terms of wavelength shift is shown in the inset.

The calibration resulting from these tests is shown in Fig. 12. The linear behavior of wavelength shift and power variations is significant, especially for the power variation measurements, where a sensitivity of 2.213 nW/mg with a Pearson squared correlation coefficient of $R^2 = 0.997$ and with a noise density of $1.083 \mu\text{g}/\sqrt{\text{Hz}}$ was obtained. As a result, the correlation between the power variation (ΔP) and the acceleration (in mg) is as expressed in Eq. (6):

$$a = 0.450\Delta P - 0.143 \quad (6)$$

Equation 6 is applicable for accelerations from 29.64 mg down to 0.76 mg, as this was the LoD of the electronic accelerometer. However, considering that the MCF accelerometer detected vibrations of amplitudes below 30 mVpp and its significant linear behavior, we believe that this equation could be extrapolated and be valid for vibrations down to the tested limit (10 mVpp) and below. If so, this would indicate our device is capable of detecting accelerations of up to 0.25 mg. For real-field implementation, the robustness of the proposed measurement system could be improved by using a reference PD to monitor the stability of the light source in order to avoid any unwanted effect due to light power fluctuation.

According to wavelength shift measurements, a sensitivity of 1.116 pm/mg with a Pearson squared correlation coefficient of $R^2 = 0.976$ was achieved. It should be pointed out that our MCF accelerometer was optimized to operate with power variation measurements, which implied low sensitivity in terms of wavelength shift. Thus, such result points out that the device was surface bonded as close as possible as depicted in Fig. 5 and that it operates as intended.

Conclusions

In this work, we have reported on a compact and highly sensitive all-fiber accelerometer based on two short segments of different lengths of asymmetric MCF. Such segments are rotated 180° with respect to each other and sandwiched between SMFs, creating a SMF-MCF1-MCF2-SMF structure. Its fabrication is fast, easily reproducible and customizable. Such configuration maximizes the change in the amplitude of the spectrum, which is related to power variation. Its interrogation is very simple and cost-effective, as it is made by few off-the-shelf equipment.

The manufactured device was subjected to vibrations of different amplitudes and frequencies, and its performance compared with a commercial electronic accelerometer. It was found that our MCF accelerometer outperformed a commercial electronic accelerometer, as it was capable of detecting extremely low frequency vibrations down to 1 mHz with a sensitivity of 2.213 nW/mg, which makes it appealing for applications

in which these characteristics are demanded, such as in seismology. To the authors' best knowledge, this is the simplest optical fiber-based accelerometer that reaches this performance.

The MCF accelerometer proposed here is suitable for parallel multiplexing by means of an optical switch, which makes multi-point measurement feasible in order to cover large structures or areas. Thanks to the narrow reflection peaks provided by this SMF-MCF1-MCF2-SMF structure, several devices of this kind can be multiplexed in the same interrogation window. By modifying the length of the MCF segments in each device, the shape of the spectra and the location of the maxima can be customized individually, leading to an unambiguous identification of each. Moreover, the proposed structure may be embedded or surface bonded in oil pipelines or pillars, which facilitates its installation significantly, as it does not require expensive or complex setups. Lastly, we would like to highlight the potential of the device reported here to be direction sensitive by combining simultaneous analysis of wavelength shift and power variation. In this manner, the vibration as well as its direction could be identified accurately thanks to the effects observed in the spectrum.

Therefore, we believe that the MCF vibration sensor reported here may represent an alternative to conventional electronic and optical accelerometers thanks to its compactness, simplicity, high sensitivity, cost-effectiveness and versatility.

Received: 2 July 2020; Accepted: 14 September 2020

Published online: 30 September 2020

References

- Medeiros, K. A. R., Barbosa, C. R. H. & de Oliveira, E. C. Flow Measurement by piezoelectric accelerometers: application in the oil industry. *Pet. Sci. Technol.* **33**, 1402–1409. <https://doi.org/10.1080/10916466.2015.1044613> (2015).
- Sabato, A., Niezrecki, C. & Fortino, G. Wireless MEMS-based accelerometer sensor boards for structural vibration monitoring: a review. *IEEE Sens. J.* **17**, 226–235 (2017).
- Wixted, A. J. *et al.* Measurement of energy expenditure in elite athletes using MEMS-based triaxial accelerometers. *IEEE Sens. J.* **7**, 481–488 (2007).
- DeSalvo, R. Review: accelerometer development for use in gravitational wave-detection interferometers. *Bull. Seismol. Soc. Am.* **99**, 990–997. <https://doi.org/10.1785/0120080155> (2009).
- Evans, J. R. *et al.* Performance of several low-cost accelerometers. *Seismol. Res. Lett.* **85**, 147–158. <https://doi.org/10.1785/0220130091> (2014).
- Havskov, J. & Alguacil, G. *Instrumentation in Earthquake Seismology* Vol. 358 (Springer, Berlin, 2004).
- Deng, T., Chen, D., Wang, J., Chen, J. & He, W. A MEMS based electrochemical vibration sensor for seismic motion monitoring. *J. Microelectromech. Syst.* **23**, 92–99 (2014).
- Shindo, Y., Yoshikawa, T. & Mikada, H. *SENSORS, 2002 IEEE*, Vol. 1762 1767–1770.
- Shinohara, M. *et al.* Precise aftershock distribution of the 2007 Chuetsu-oki Earthquake obtained by using an ocean bottom seismometer network. *Earth Planets Space* **60**, 1121–1126. <https://doi.org/10.1186/BF03353147> (2008).
- Wang, H. F. *et al.* Ground motion response to an ML 4.3 earthquake using co-located distributed acoustic sensing and seismometer arrays. *Geophys. J. Int.* **213**, 2020–2036. <https://doi.org/10.1093/gji/ggy102> (2018).
- Hutton, K., Woessner, J. & Hauksson, E. Earthquake monitoring in southern California for seventy-seven years (1932–2008). *Bull. Seismol. Soc. Am.* **100**, 423–446. <https://doi.org/10.1785/0120090130> (2010).
- Levinzon, F. A. Ultra-low-noise seismic piezoelectric accelerometer with integral FET amplifier. *IEEE Sens. J.* **12**, 2262–2268 (2012).
- Zou, X., Thiruvengathanan, P. & Seshia, A. A. A seismic-grade resonant MEMS accelerometer. *J. Microelectromech. Syst.* **23**, 768–770 (2014).
- Bertolini, A., DeSalvo, R., Fidecaro, F. & Takamori, A. Monolithic folded pendulum accelerometers for seismic monitoring and active isolation systems. *IEEE Trans. Geosci. Remote Sens.* **44**, 273–276 (2006).
- Leugoud, R. & Kharlamov, A. Second generation of a rotational electrochemical seismometer using magnetohydrodynamic technology. *J. Seismol.* **16**, 587–593. <https://doi.org/10.1007/s10950-012-9290-y> (2012).
- Kamenev, O. T., Kulchin, Y. N., Petrov, Y. S., Khiznyak, R. V. & Romashko, R. V. Fiber-optic seismometer on the basis of Mach-Zehnder interferometer. *Sens. Actuator A Phys.* **244**, 133–137. <https://doi.org/10.1016/j.sna.2016.04.006> (2016).
- Chang, T. *et al.* Fiber optic interferometric seismometer with phase feedback control. *Opt. Express* **28**, 6102–6122. <https://doi.org/10.1364/OE.385703> (2020).
- Pisco, M. *et al.* Opto-mechanical lab-on-fibre seismic sensors detected the Norcia earthquake. *Sci. Rep.* **8**, 6680. <https://doi.org/10.1038/s41598-018-25082-8> (2018).
- Chen, J. *et al.* Ultra-low-frequency tri-component fiber optic interferometric accelerometer. *IEEE Sens. J.* **18**, 8367–8374 (2018).
- Bernard, P. *et al.* Onland and offshore extrinsic Fabry-Pérot optical seismometer at the end of a long fiber. *Seismol. Res. Lett.* **90**, 2205–2216. <https://doi.org/10.1785/0220190049> (2019).
- Laudati, A. *et al.* A fiber-optic Bragg grating seismic sensor. *IEEE Photonics Technol. Lett.* **19**, 1991–1993 (2007).
- Liu, F., Dai, Y., Karanja, M. J. & Yang, M. A low frequency FBG accelerometer with symmetrical banded spring plates. *Sensors* <https://doi.org/10.3390/s17010206> (2017).
- Antunes, P. F. D. C. *et al.* Optical fiber accelerometer system for structural dynamic monitoring. *IEEE Sens. J.* **9**, 1347–1354 (2009).
- Villatoro, J. *et al.* Composed multicore fiber structure for direction-sensitive curvature monitoring. *APL Photonics* **5**, 070801. <https://doi.org/10.1063/1.5128285> (2020).
- Villatoro, J., Antonio-Lopez, E., Zubia, J., Schülzgen, A. & Amezcua-Correa, R. Interferometer based on strongly coupled multicore optical fiber for accurate vibration sensing. *Opt. Express* **25**, 25734–25740. <https://doi.org/10.1364/OE.25.025734> (2017).
- Villatoro, J. *et al.* Accurate strain sensing based on super-mode interference in strongly coupled multi-core optical fibres. *Sci. Rep.* **7**, 4451. <https://doi.org/10.1038/s41598-017-04902-3> (2017).
- Amorebieta, J. *et al.* Packaged multi-core fiber interferometer for high-temperature sensing. *J. Lightwave Technol.* **37**, 2328–2334 (2019).
- Kishi, N. & Yamashita, E. A simple coupled-mode analysis method for multiple-core optical fiber and coupled dielectric waveguide structures. *IEEE Trans. Microw. Theory Tech.* **36**, 1861–1868. <https://doi.org/10.1109/22.17423> (1988).
- Snyder, A. W. Coupled-mode theory for optical fibers. *J. Opt. Soc. Am.* **62**, 1267–1277. <https://doi.org/10.1364/JOSA.62.001267> (1972).
- Hudgings, J., Molter, L. & Dutta, M. Design and modeling of passive optical switches and power dividers using non-planar coupled fiber arrays. *IEEE J. Quantum Electron.* **36**, 1438–1444 (2000).
- Perez-Leija, A., Hernandez-Herrejon, J. C., Moya-Cessa, H., Szameit, A. & Christodoulides, D. N. Generating photon-encoded SW Ψ states in multiport waveguide-array systems. *Phys. Rev. A* **87**, 013842. <https://doi.org/10.1103/PhysRevA.87.013842> (2013).

32. Huang, W.-P. Coupled-mode theory for optical waveguides: an overview. *J. Opt. Soc. Am. A* **11**, 963–983. <https://doi.org/10.1364/JOSAA.11.000963> (1994).
33. Xia, C., Bai, N., Ozdur, I., Zhou, X. & Li, G. Supermodes for optical transmission. *Opt. Express* **19**, 16653–16664. <https://doi.org/10.1364/OE.19.016653> (2011).
34. Xia, C. *et al.* Supermodes in coupled multi-core waveguide structures. *IEEE J. Sel. Top. Quantum Electron.* **22**, 196–207 (2016).
35. Schermer, R. T. Mode scalability in bent optical fibers. *Opt. Express* **15**, 15674–15701. <https://doi.org/10.1364/OE.15.015674> (2007).
36. Schermer, R. T. & Cole, J. H. Improved bend loss formula verified for optical fiber by simulation and experiment. *IEEE J. Quantum Electron.* **43**, 899–909 (2007).
37. Heiblum, M. & Harris, J. Analysis of curved optical waveguides by conformal transformation. *IEEE J. Quantum Electron.* **11**, 75–83 (1975).
38. Yin, G., Zhang, F., Xu, B., He, J. & Wang, Y. Intensity-modulated bend sensor by using a twin core fiber: theoretical and experimental studies. *Opt. Express* **28**, 14850–14858. <https://doi.org/10.1364/OE.390054> (2020).
39. Arrizabalaga, O. *et al.* High-performance vector bending and orientation distinguishing curvature sensor based on asymmetric coupled multi-core fibre. *Sci. Rep.* **10**, 14058. <https://doi.org/10.1038/s41598-020-70999-8> (2020).
40. Villatoro, J. *et al.* Ultrasensitive vector bending sensor based on multicore optical fiber. *Opt. Lett.* **41**, 832–835. <https://doi.org/10.1364/OL.41.000832> (2016).
41. Shrivastava, A. & Gupta, V. Methods for the determination of limit of detection and limit of quantitation of the analytical methods. *Chron. Young Sci.* **2**, 21–25. <https://doi.org/10.4103/2229-5186.79345> (2011).

Acknowledgments

Ministerio de Economía y Competitividad; Ministerio de Ciencia, Innovación y Universidades; European Regional Development Fund (PGC2018-101997-B-I00 and RTI2018-094669-B-C31); Gobierno Vasco/Eusko Jaurlaritza (IT933-16); ELKARTEK KK-2019/00101 (μ 4Indust) and ELKARTEK KK-2019/00051 (SMART-RESNAK). The work of Angel Ortega-Gomez is funded by a PhD fellowship from the Spain Government. The work of Josu Amorebieta is funded by a PhD fellowship from the University of the Basque Country UPV/EHU.

Author contributions

J.A. collaborated in the theoretical approach, performed the experiments, processed and analyzed data and wrote the first draft. A.O.-G. did the simulations and the theoretical approach, J.V. conceived and fabricated the device, designed and supervised the experiments. A.S., E.A.-L. and R.A.C. conceived and fabricated the MCF. R.F. developed the data acquisition software. G.D. and J.Z. supervised the experiments. All authors discussed the experimental data, revised and approved the manuscript. JA and JV wrote the final version with inputs of all the authors.

Competing interests

The authors declare no competing interests.

Additional information

Correspondence and requests for materials should be addressed to J.A. or J.V.

Reprints and permissions information is available at www.nature.com/reprints.

Publisher's note Springer Nature remains neutral with regard to jurisdictional claims in published maps and institutional affiliations.



Open Access This article is licensed under a Creative Commons Attribution 4.0 International License, which permits use, sharing, adaptation, distribution and reproduction in any medium or format, as long as you give appropriate credit to the original author(s) and the source, provide a link to the Creative Commons licence, and indicate if changes were made. The images or other third party material in this article are included in the article's Creative Commons licence, unless indicated otherwise in a credit line to the material. If material is not included in the article's Creative Commons licence and your intended use is not permitted by statutory regulation or exceeds the permitted use, you will need to obtain permission directly from the copyright holder. To view a copy of this licence, visit <http://creativecommons.org/licenses/by/4.0/>.

© The Author(s) 2020

4. artikulua

Titulua:

Composed multicore fiber structure for direction-sensitive curvature monitoring

D.O.I.:

<https://doi.org/10.1063/1.5128285>

Egileak:

Villatoro, J.; **Amorebieta, J.**; Ortega-Gomez, A.; Antonio-Lopez, E.; Zubia, J.; Schülzgen, A.; Amezcua-Correa, R.

Aldizkari eta argitalpenaren informazioa:

APL Photonics, 5 (7), 070801 (2020)

3 aldiz aipatua

Aldizkariaren adierazleak 2020an:

Oraingoz ez daude eskuragarri

Aldizkariaren adierazleak 2019an:

Eragin-faktorea: 4.864

Q1 Optika sailean (13/97)

Composed multicore fiber structure for direction-sensitive curvature monitoring

Cite as: APL Photonics 5, 070801 (2020); <https://doi.org/10.1063/1.5128285>

Submitted: 18 September 2019 . Accepted: 07 June 2020 . Published Online: 01 July 2020

 Joel Villatoro,  Josu Amorebieta,  Angel Ortega-Gomez,  Enrique Antonio-Lopez,  Joseba Zubia,  Axel Schülzgen, and  Rodrigo Amezcua-Correa



View Online



Export Citation



CrossMark

ARTICLES YOU MAY BE INTERESTED IN

[Optical detection of the percolation threshold of nanoscale silver coatings with optical fiber gratings](#)


APL Photonics 5, 076101 (2020); <https://doi.org/10.1063/5.0011755>

[Highly sensitive magnetic field microsensor based on direct laser writing of fiber-tip optofluidic Fabry–Pérot cavity](#)

APL Photonics 5, 076112 (2020); <https://doi.org/10.1063/5.0012988>

[Integrated vortex beam emitter in the THz frequency range: Design and simulation](#)

APL Photonics 5, 076102 (2020); <https://doi.org/10.1063/5.0010546>



THE ADVANCED MATERIALS MANUFACTURER®

additive manufacturing epitaxial crystal growth cerium oxide polishing powder

deposition slugs OLED lighting spintronics solar energy

cerium nanowires thin films chalcogenides AuCu

GDC Li-ion battery electrolytes 99.999% ruthenium spheres

endofullerene copper nanoparticles diamond micropowder

COG MRB grade materials palladium catalysts flexible electronics

beta-barium borate borosilicate glass dysprosium pellets YBCO

pyrolytic graphite 3d graphene foam sodium tin oxide mesoporous silica

cerium substrates sapphire windows tungsten carbide InGaAs

barium fluoride carbon nanotubes lithium niobate scandium powder

gallium bump glassy carbon nanodiamonds

surface functionalized nanoparticles Au Bi Cd Co Cr Cu Fe Ga Ge Hf In Ir K La Li Mg Mn Mo Ni Pd Pt Pb Rh Ru Sb Se Si Sn Sr Ta Te Ti U V W Zn Zr

superconductors quantum dots

Al Be B C N O F Ne

Ar Ca Sc Ti V Cr Mn Fe Co Ni Cu Zn Ga Ge As Se Br Kr

Sr Y Zr Nb Mo Tc Ru Rh Pd Ag Cd In Sn Sb Te I Xe

Ra Ba La Ce Pr Nd Pm Sm Eu Gd Tb Dy Ho Er Tm Yb Lu

Rf Ac Th Pa U Np Pu Am Cm Bk Cf Es Fm Md No Lr

sputtering targets Si-IV semiconductors CVD precursors europium phosphors

alkali oxides laser crystals ultra high purity materials MOFs

rare earth metals photovoltaics refractory metals Ni/CVD

superconductors transparent ceramics ultra high purity silicon

Now Invent.™

The Next Generation of Material Science Catalogs

American Elements opens up a world of possibilities so you can **Now Invent!**

Over 15,000 certified high purity laboratory chemicals, metals, & advanced materials and a state-of-the-art Research Center. Printable GHS-compliant Safety Data Sheets. Thousands of new products. And much more. All on a secure multi-language "Mobile Responsive" platform.

perovskite crystals yttrium iron garnet alternative energy h-BN

gold nanocubes graphene oxide macromolecules photonics

rhodium sponge fiber optics beam splitters infrared dyes zeolites

fused quartz metalloenes platinum ink buckyballs Ti-6Al-4V

www.americanelements.com



Composed multicore fiber structure for direction-sensitive curvature monitoring

Cite as: *APL Photon.* **5**, 070801 (2020); doi: [10.1063/1.5128285](https://doi.org/10.1063/1.5128285)

Submitted: 18 September 2019 • Accepted: 7 June 2020 •

Published Online: 1 July 2020



Joel Villatoro,^{1,2,a)}  Josu Amorebieta,¹ Angel Ortega-Gomez,¹ Enrique Antonio-Lopez,³ Joseba Zubia,¹ 
Axel Schülzgen,³  and Rodrigo Amezcua-Correa³

AFFILIATIONS

¹Department of Communications Engineering, University of the Basque Country UPV/EHU, Torres Quevedo Plaza 1, E-48013 Bilbao, Spain

²IKERBASQUE—Basque Foundation for Science, E-48011 Bilbao, Spain

³CREOL, The College of Optics & Photonics, University of Central Florida, P.O. Box 162700, Orlando, Florida 32816-2700, USA

^{a)}Author to whom correspondence should be addressed: agustinjoel.villatoro@ehu.eus

ABSTRACT

The present work deals with a curvature sensor that consists of two segments of asymmetric multicore fiber (MCF) fusion spliced with standard single mode fiber (SMF). The MCF comprises three strongly coupled cores; one of such cores is at the geometrical center of the MCF. The two segments of MCF are short, have different lengths (less than 2 cm each), and are rotated 180° with respect to each other. The fabrication of the sensor was carried out with a fusion splicing machine that has the means for rotating optical fibers. It is demonstrated that the sensor behaves as two SMF–MCF–SMF structures in series, and consequently, it has enhanced sensitivity. The device proposed here can be used to sense the direction and amplitude of curvature by monitoring either wavelength shifts or intensity changes. In the latter case, high curvature sensitivity was observed. The device can also be used for the development of other highly sensitive sensors to monitor, for example, vibrations, force, pressure, or any other parameter that induces periodic or local curvature or bending to the MCF segments.

© 2020 Author(s). All article content, except where otherwise noted, is licensed under a Creative Commons Attribution (CC BY) license (<http://creativecommons.org/licenses/by/4.0/>). <https://doi.org/10.1063/1.5128285>

INTRODUCTION

Multicore fibers (MCFs) are revolutionary waveguides^{1,2} that have multiple individual cores sharing a common cladding. In general, MCFs have diameters similar to that of a standard telecommunications optical fiber. The cores of an MCF can be well isolated from each other to avoid interactions between them. In this manner, each core behaves as an independent waveguide. Completely the opposite is also possible; this means that the cores can be in close proximity to each other to allow coupling between them. In the latter case, the fiber is called coupled-core MCF and supports supermodes.³

The unique features of MCFs provide new alternatives for the development of innovative devices whose functionalities cannot be easily achieved with conventional optical fibers. For example, ultrathin lensless endoscopes⁴ for biomedical applications and minimal intrusive shape sensors have been demonstrated.^{5,6} MCFs with

coupled cores offer also new possibilities for the development of simple and compact devices that can be used to monitor vibrations and bending,^{7,8} among other parameters.

With regard to fiber optic curvature sensors, so far, a variety of configurations based on conventional fibers have been proposed and demonstrated (see Refs. 9–14). However, to the best of the authors' knowledge, such curvature sensors have not reached high readiness level. This suggests that it is important to investigate new alternatives to devise functional fiber optic curvature sensors.

MCFs with isolated cores offer multiple alternatives to build curvature sensors. For example, curvature sensors based on interferometers,^{15–18} twisted MCFs,¹⁹ or directional couplers²⁰ have been demonstrated. Some drawbacks of these sensors are the need of bulk optics to interrogate them, their insensitivity to the direction of curvature, their fragility as, in some cases, the MCF must be tapered, and the high insertion losses. Strongly coupled MCFs with

quasi-symmetric core distribution have also been demonstrated for direction-insensitive curvature sensing.^{21,22}

MCFs with a series of Bragg gratings^{23–25} or long period gratings^{26–28} in some or in all the cores can also be used to sense curvature. In fact, MCF curvature sensors based on Bragg gratings have reached a commercial level, but their high cost may limit their use to high-end applications. Some disadvantages of grating-based MCF curvature sensors include complex fabrication and expensive interrogation. Moreover, the curvature on some MCFs with gratings can induce coupling between cores. Such coupling can induce errors in the measurements of curvature.

Fiber optic curvature sensors have potential applications in shape sensing,^{6,14} that is why they have attracted considerable research interest in recent years. Ideally, a fiber optic curvature sensor must be cost effective and must provide the amplitude and the direction of curvature. In addition, the sensor must be sensitive, simple, reliable, and very small in diameter, so it can be integrated to devices, instruments, or structures. We believe that the fiber optic curvature sensors reported to date cannot provide all these desirable characteristics.

Here, we propose a highly sensitive curvature sensor based on a strongly coupled MCF. Our device is easy to fabricate and requires a simple (low cost) interrogation system. In addition, our sensor is able to provide the amplitude and direction of curvature even by monitoring intensity changes. To achieve the curvature sensor with the aforementioned features, we used two short segments of different lengths of an MCF that comprises three identical cores. The two MCF segments are fusion spliced and rotated 180° with respect to each other and are inserted in a conventional single mode fiber.

The structure reported here can also be used to devise other sensors to monitor any parameter that induces point or periodic curvature to the MCF. Some examples may include force, pressure, and vibration sensors or accelerometers.

SENSOR FABRICATION AND WORKING MECHANISM

In Fig. 1(a), we show the cross section of the MCF used to fabricate the sensor. The fiber has three coupled cores made of germanium-doped silica embedded in a cladding made of pure silica. The diameter of each core is approximately 9 μm, and the cores are separated from each other by 11 μm approximately. It can be noted that one core is at the geometrical center of the MCF. The numerical aperture of each core of the MCF is identical to that of an SMF (0.14). Due to the matching between the numerical apertures of both

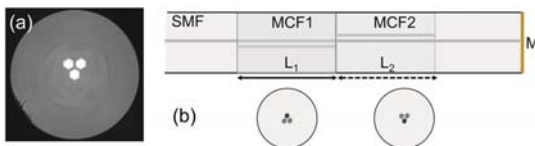


FIG. 1. (a) Micrograph of the MCF used to fabricate the samples. (b) Drawing of the device in which the two segments of MCF are rotated 180° with respect to each other. L_1 and L_2 are the lengths of the segments MCF1 and MCF2, respectively, and M is the mirror.

fibers, the insertion losses of our devices are low as demonstrated previously.^{7,21}

The architecture of our curvature sensor is shown in Fig. 1(b). Such a structure is fabricated by fusion splicing two segments of different lengths (typically less than 20 mm each) of the aforementioned MCF with a conventional SMF. The two segments of MCF are rotated 180° with respect to each other; the reason of this angle is explained below. A reflector or mirror at the distal end of the SMF allows the sensor to operate in reflection mode, which has the advantages described in the following.

The fabrication of the device shown in Fig. 1(b) can be carried out with a splicing machine that has means of rotating optical fibers. In our case, we used a specialty fiber splicer (a Fujikura FSM-100P+) in which an *ad hoc* splicing program was implemented. With such a program, the end face of the two segments of MCF was inspected to orient the cores before the splicing. In all cases, the splices were carried out with a cladding alignment method. Under such splicing conditions, the cores located in the geometrical center of the two segments of MCF and the unique core of the SMF were axially aligned and permanently joined together. The two segments of MCF were intentionally rotated 180° to achieve an SMF–MCF1–MCF2–SMF structure in which the two cores outside the center of the MCFs were upward in one part of the structure and downward in the other part. We will see that such a structure behaves as a dual supermode coupler in series.

To understand the working mechanism of the device shown in Fig. 1(b), we carried out simulations based on the finite difference method with commercial software (FimmWave and FimmProp by Photon Design) and different experiments. In Fig. 2, we show the propagation of two different wavelengths from the lead-in SMF to the lead-out SMF in an SMF–MCF1–MCF2–SMF structure with the dimensions described in the figure. It can be seen that at 1500 nm, the guided light does not reach the lead-out SMF. On the other hand, light at 1550 nm propagates with losses. Consequently, in the referred structure, maximum transmission can be expected at 1550 nm and minimum at 1500 nm.

In addition to the simulations, we analyzed mathematically our device by considering that it is composed of two parts. Let us

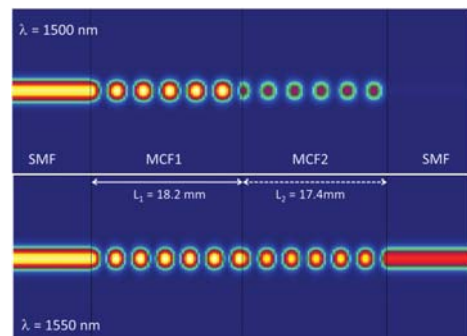


FIG. 2. Simulations of light propagation in an SMF–MCF1–MCF2–SMF structure. The following values were considered: $L_1 = 12.20$ mm and $L_2 = 11.40$ mm. The analyzed wavelengths are indicated.

consider first the case when $L_2 = 0$. In this case, we will have an SMF-MCF1-SMF structure. To predict the transmission intensity of such a structure, we have to consider the following situations: (i) The three cores of the MCF are identical, i.e., they have the same diameter and the same refractive index; (ii) the distance between the MCF cores is the same; (iii) the central core of the MCF is excited with the fundamental SMF mode, and (iv) the MCF is composed by evanescently coupled single-mode cores. In our case, the latter assumptions are valid in the 1200 nm–1600 nm wavelength range. Under these conditions, two supermodes are excited in the MCF. Such supermodes have non-zero intensity in the central core of the MCF.⁸

The transfer function of the SMF-MCF-SMF structure can be calculated by means of the coupled mode theory.²⁹ The transfer function is a periodic function of wavelength (λ) and can be expressed as^{30–32}

$$I_{1T}(\lambda, L_1) = 1 - (2/3)\sin^2\left(\sqrt{3}\pi\Delta nL_1/\lambda\right). \quad (1)$$

In Eq. (1), Δn is the effective refractive index difference between the two excited supermodes. Δn depends on the wavelength, refractive index, dimensions, and separation between the cores of the MCF. For the MCF shown in Fig. 1(a), Δn was found to be 4.66×10^{-4} . Now, if $L_1 = 0$, we will have an SMF-MCF2-SMF structure of length L_2 . The transfer function of such a structure can also be expressed by Eq. (1), but with L_2 instead of L_1 .

Let us now calculate the transfer function of an SMF-MCF-SMF structure when the SMF at the final extreme has a reflector or mirror on its face [see Fig. 1(b)]. In this case, the structure can be considered as two SMF-MCF-SMF structures in series. As demonstrated by several groups, the transfer function of two periodic fiber devices placed in series is the product of the individual transfer functions.^{33–36} Thus, if a single SMF-MCF-SMF structure with L_1 (or L_2) is interrogated in reflection, the transfer function is simply $I_{1R} = I_{1T}^2$ (or $I_{2R} = I_{2T}^2$).

If the device shown in Fig. 1(b) is excited with a broadband source, the reflection measured with a photodetector or spectrometer will be

$$R(\lambda) = I_s(\lambda)[I_{1T}(\lambda, L_1)I_{2T}(\lambda, L_2)]^2. \quad (2)$$

In Eq. (2), $I_s(\lambda)$ is the spectral power distribution of the excitation light source. In a practical situation, such a light source can be a narrow-band light emitting diodes (LED) whose spectral distribution is Gaussian.

RESULTS AND DISCUSSION

The interrogation of the device depicted in Fig. 1(b) is simple. In our case, we used a superluminescent light emitting diode (SLED) with peak emission at 1550 nm and a FWHM of 60 nm as the light source, a conventional fiber optic coupler (or circulator), and a photodetector or a miniature spectrometer (Ibsen I-MON-512) connected by a universal serial bus (USB) cable to a personal computer. Unless otherwise stated, in all our experiments, the cleaved end of the SMF segment after the MCF2 was used as a reflector. The reflectivity in this case was less than 4%.

In Fig. 3, we show the normalized reflection spectra of SMF-MCF-SMF structures in three different cases. The plots with dotted

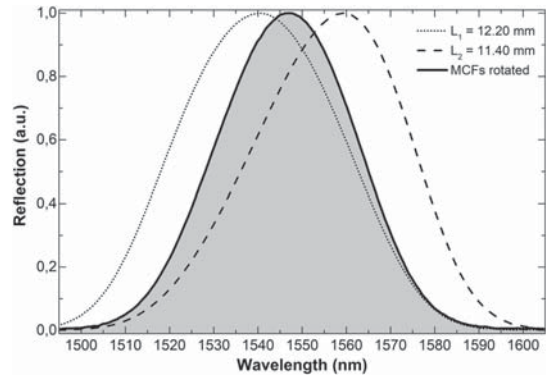


FIG. 3. Reflection spectra observed when the structure is SMF-MCF-SMF in which the lengths of MCFs are 12.20 mm (dashed line) and 11.4 mm (dotted line). The shadowed area beneath the solid line is the reflection spectrum observed when a 12.20 mm-long and an 11.40 mm-long segment of MCF are fusion spliced and rotated 180° with respect to each other.

and dashed lines correspond to the spectra of individual structures with $L_1 = 12.20$ mm and $L_2 = 11.40$ mm. As the lengths of the MCF segments are short, the periods of the reflection spectra are long, and thus, it is not possible to observe two consecutive maxima in the monitored wavelength range. The shadowed area beneath the solid line represents the reflection spectrum observed when two segments of MCF, one with $L_1 = 12.20$ mm and the other with $L_2 = 11.40$ mm, were spliced together, but one segment of MCF was rotated 180° with respect to the other. The reflection spectrum of the SMF-MCF1-MCF2-SMF structure coincides with the spectrum that is obtained when the spectra shown in dotted and dashed lines are multiplied and then normalized. It can be noted that the experimental results shown in Fig. 3 agree with the simulations described in Fig. 2. Therefore, we can conclude that the reflection of the device depicted in Fig. 1(b) can be calculated with Eq. (2) as it can be treated as two SMF-MCF-SMF structures in series.

To assess the performance of our composed MCF device as a curvature sensor, we carried out simulations, which are summarized in Fig. 4. In the figure, we show the reflection spectra of an SMF-MCF1-MCF2-SMF structure built with $L_1 = 17.4$ mm and $L_2 = 18.2$ mm at different values of curvature. It was assumed that the structure was bent in the MCF1-MCF2 junction and that both segments of MCF experienced the same curvature. The curvature was assumed to be applied in four different directions with respect to the orientations of the MCF cores. Any other orientation of the cores with respect to curvature will be contained between the four cases shown in Fig. 4. From the simulations, it can be concluded that the reflection intensity of our device will increase or decrease depending on the direction of curvature. This means that our device can distinguish the amplitude and direction of curvature.

To corroborate the above predictions, a simple setup, schematically shown in Fig. 5, was implemented. The SMF segments were secured with two fiber chucks that were mounted on respective

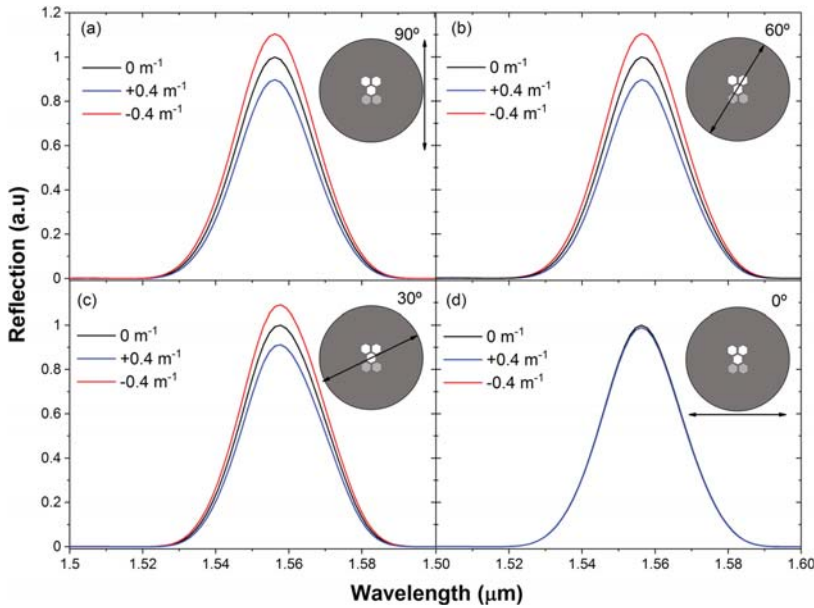


FIG. 4. Simulated reflection spectra of an SMF-MCF1-MCF2-SMF structure for different values of curvature when the orientations of the MCF cores are 90° (a), 60° (b), 30° (c), and 0° (d) with respect to the direction of curvature indicated by arrows. For the simulations, it was considered that $L_1 = 17.40$ mm and $L_2 = 18.20$ mm.

rotators (HFR001 from Thorlabs). The chuck rotators were separated by a fixed distance and were secured on an optical breadboard that was placed in a vertical position. A fiber chuck was used as a mass (20 g) to keep the tension of the fibers constant. The measurements of curvature were carried out at different orientations of the MCFs, between 0 and 180° in steps of 30°, with respect to curvature [see Fig. 5]. A translation stage with micrometer resolution was used to bend the structure in a controlled manner. The stage bent the device close to the MCF1-MCF2 junction. The value of curvature (C) on the device was calculated with the following equation: $C = 12h/d^2$ (see Ref. 12), where h is the displacement of the translation stage and d is the separation between the two fiber rotators.

In the setup described in the above paragraph, any displacement of the translation stage (or change of h) causes bending to the two segments of MCF. However, the effect on them was different

as the cores outside the center of the MCF had a different position with respect to the applied curvature. As demonstrated in Ref. 8, the asymmetric MCF used here is highly sensitive to bending. In addition, the direction of the bending can be distinguished when the MCF cores are oriented properly. Therefore, high sensitivity to curvature and capability to distinguish the direction of curvature were expected with an SMF-MCF1-MCF2-SMF structure. For this reason, we fabricated the structure as shown in Fig. 1(b) with the cores of the MCF1 and MCF2 segments rotated 180° with respect to each other.

A device fabricated with a segment of 17.4 mm of MCF fusion spliced to another segment of 18.2 mm was characterized in detail. As mentioned before, the cores of the MCF segments were in opposite orientation. Wavelength shifts and intensity changes were monitored at each value of curvature. In the former case, a spectrometer was used, while in the latter case, a low cost InGaAs photodiode (S154C from Thorlabs) was used. The light source was the same in all the measurements. The intensity of the reflected light when no curvature ($C = 0 \text{ m}^{-1}$) was applied to the device was considered as P and the changes caused by curvature as ΔP . At $C = 0 \text{ m}^{-1}$, the wavelength position of the peak reflection was considered to be λ_m and $I_R = 1$.

Figures 6(a) and 6(b) show the spectra observed when the curvature at two perpendicular directions was applied to the device described in the above paragraph. Figures 6(c) and 6(d) show the averaged curvature sensitivities that were measured in seven different orientations of the MCF. The core orientations with respect to curvature are illustrated in Figs. 4 and 5. Note that when the wavelength shift is larger, the changes in intensity are minimal and vice versa. The different values of sensitivities at different orientations of

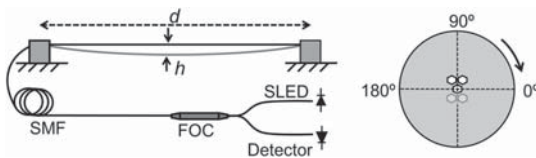


FIG. 5. Schematic diagram of the measuring setup and the sensor interrogation; h is the deflection of the device and d is the distance between the two supports. FOC is fiber optic coupler or circulator, SMF is single mode fiber, and SLED is superluminescent light emitting diode. The MCF core orientation with respect to the applied curvature is indicated.

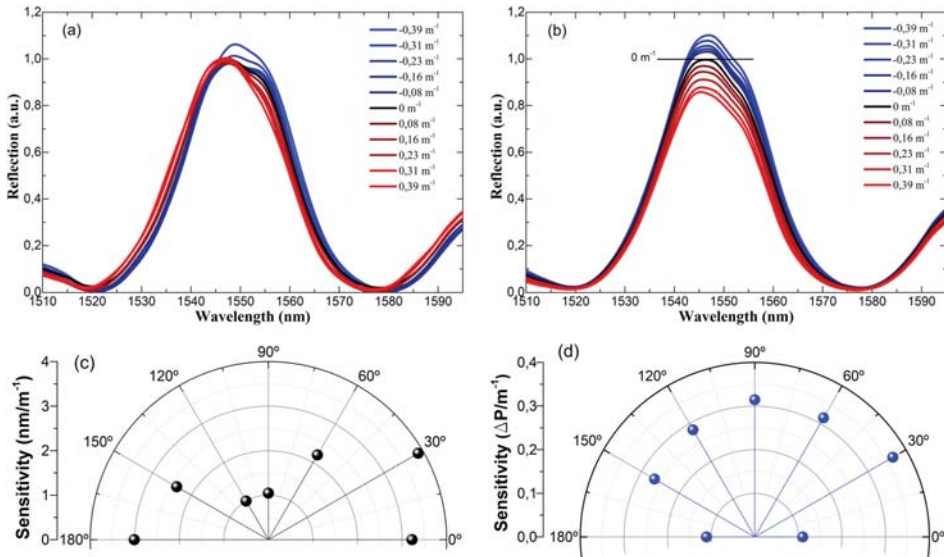


FIG. 6. [(a) and (b)] Reflection spectra at different curvatures observed when the position of the MCF was at 0° and 90° , respectively, according to Figs. 4(c) and 4(d). [(c) and (d)] Average curvature sensitivity measured by monitoring wavelength shift or intensity changes. In all cases, the MCF device had $L_1 = 17.40$ mm and $L_2 = 18.20$ mm.

the MCF cores with respect to curvature were expected due to the asymmetry of the device.

The discrepancy between simulations and experimental results with regard to shifts of the spectra may be due to the strain induced to the device and curvature of the SMF–MCF junctions, as these are inevitable in an experiment. In addition, during the measurements, the two segments of MCF may not experience exactly the same curvature. In the simulations, however, the two stubs of MCF were supposed to be exclusively subjected to the same curvature. Nonetheless, regardless of the orientation of the MCFs with respect to curvature, the wavelength position and height of the reflection peak (intensity) can be simultaneously tracked. Hence, it is possible to know the direction and amplitude of the curvature applied to the device.

The drastic changes in the reflection spectrum of the SMF–MCF1–MCF2–SMF structure when it is subjected to curvature can be explained with Eq. (2) and with the simulations shown in Fig. 4. Note that the structure is composed of two MCF segments that are highly sensitive to bending. Moreover, the reflection spectrum results from the multiplication of two spectra that move in opposite directions. This causes the height of the resulting reflection peak to increase or decrease. Consequently, the total intensity detected by using the photodetector increases or decreases depending on the direction of curvature.

In real-world applications, fiber optic curvature sensors are attached or integrated to structures or devices. Thus, to investigate the performance of our curvature sensor in more detail, the sample described in Fig. 3 was glued on a thin rectangular plastic beam that

was secured with two supports separated by a fixed distance. The orientation of the cores of the segments of MCF with respect to the plastic beam was approximately as that shown in Fig. 5. This means that a segment of MCF had two cores up and the other two cores down with respect to the direction of the curvature. Again, a translation stage with micrometer resolution was used to bend the beam upward (convex curvature) and downward (concave curvature) in a controlled manner. Other curvature orientations were not possible due to the geometry of the beam. The stage was located in the middle point of the distance between the two supports. The MCF1–MCF2 junction of the structure was located in the same position than the translation stage.

Figure 7 summarizes the behavior of our sensor when it was subjected to concave and convex curvatures. Note that the shift of the spectrum is to longer wavelengths in the former case and to shorter wavelengths in the latter case. The figure also shows the calibration curve for concave and convex curvatures. It can be noted that the response of our device in both cases is linear. From the calibration curve, the curvature sensitivities were calculated to be 791 pm/m^{-1} for concave curvature and 950 pm/m^{-1} for convex curvature. The discrepancy in the values of sensitivities of our device can be attributed to imperfections of the same, for example, the MCFs may not be exactly 180° with respect to each other. Strain applied to the MCFs and curvature of the SMF–MCF segments may also induce shifts to the reflection spectra.

In Fig. 8, we show the observed changes in $\Delta P/P$ for different values of concave and convex curvatures. It can be noted that when the device was subjected to concave curvature, the value of $\Delta P/P$

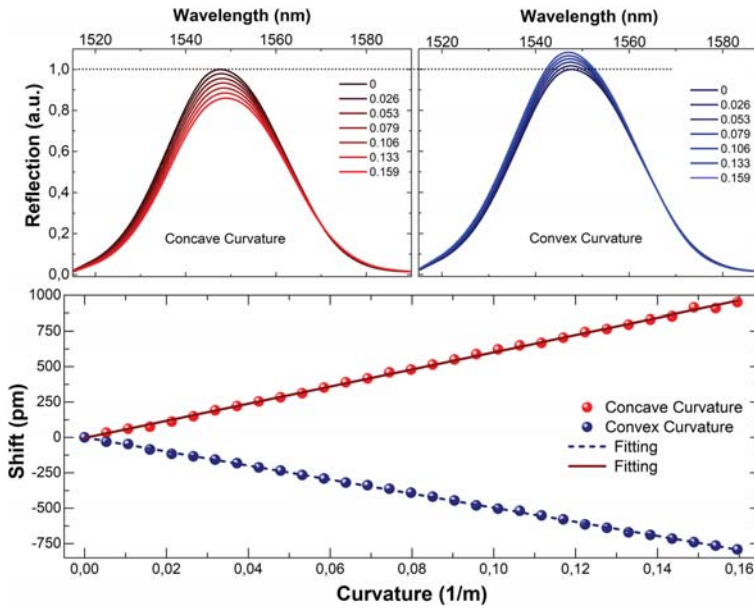


FIG. 7. Top: spectra observed when the beam shown in Fig. 5 was curved downward (left) and upward (right). The values of curvature (in m^{-1}) are indicated in the graphs. Bottom: calibration curves for concave and convex curvatures.

decreased, and it increased when the curvature on it was convex. Note also that the value of $\Delta P/P$ reached the baseline ($\Delta P/P = 0$) when the curvature was removed from the sensor. The calibration curves for concave and convex curvatures are also shown in Fig. 8. The sensitivities for concave and convex curvature were found to be almost identical, 4.66 dB/m^{-1} , which is slightly higher than those of

the intensity-modulated curvature sensors reported in Refs. 26, 37, and 38.

The results shown in Fig. 8 suggest that with our device and an inexpensive intensity-based interrogation system, it is possible to distinguish concave and convex curvatures as well as the amplitude of the applied curvature. If maximum sensitivity is needed in a particular curvature direction, the cores of the MCF can be oriented properly. We believe that these features cannot be achieved with other fiber optic curvature sensors reported so far in the literature.

CONCLUSIONS

In this work, we have reported on a simple MCF curvature sensor that comprises two short segments of strongly coupled MCF fusion spliced and rotated with respect to each other. The fabrication of the device only involves cleaving and fusion splicing; such processes are well established in the fiber optics industry. The sensor can be interrogated with a low power SLED and a miniature spectrometer or a simple photodetector. It was found that the sensor behaves as two SMF–MCF–SMF structures in series and the reflection spectrum exhibited a single, narrow peak whose height and position in wavelength can be simultaneously determined with high accuracy.

The proposed device was assessed as a curvature sensor. It was found that for this application, it is able to provide the amplitude and the direction of curvature no matter how the cores of the MCF are oriented with respect to the direction of curvature. Moreover, our sensor can be interrogated in two different manners. When the sensor was subjected to concave curvature, the reflection spectrum

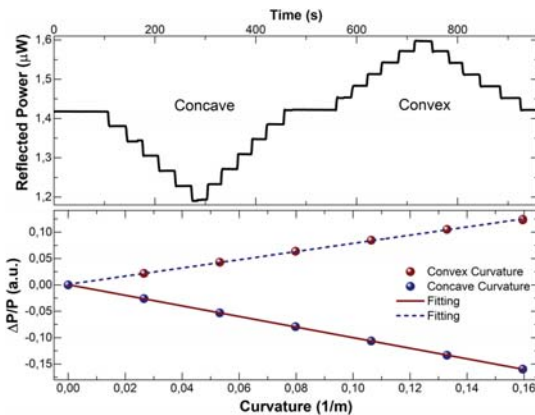


FIG. 8. Top: relative power changes as a function of time when the beam, hence the MCF segments, was bent downward (concave curvature) and upward (convex curvature). The step in each case is 0.0266 m^{-1} . Bottom: calibration curve.

shifted to red and the intensity decreased. However, when convex curvature was applied to the device, the shift was to blue and the intensity decreased.

The curvature sensitivity of the sensor reported here was found to be 4.66 dB/m^{-1} when intensity changes were correlated with curvature. Such sensitivity can be sufficient in several applications.

We believe that the composed MCF structure reported here can be used for different sensing applications. Vibrations, for example, can be translated to periodic concave and convex curvatures on the device and hence to periodic intensity changes. It also seems possible to sense pressure or lateral force as they can induce curvature to the MCF segments. Therefore, cost effective, highly sensitive force, pressure, or vibration (accelerometers) sensors can be devised with the platform proposed here.

ACKNOWLEDGMENTS

The authors acknowledge the financial support of the Spanish MINECO under Project Nos. PGC2018-101997-B-I00 and RTI2018-094669-B-C31 of the Eusko Jaurlaritz (Basque Government) under Project Nos. IT933-16 and ELKARTEK.

DATA AVAILABILITY

The data that support the findings of this study are available from the corresponding author upon reasonable request.

REFERENCES

- ¹K. Saitoh and S. Matsuo, *J. Lightwave Technol.* **34**, 55–66 (2016).
- ²E. M. Dianov, S. L. Semjonov, and I. A. Bufetov, *Quant. Electron.* **46**, 1 (2016).
- ³C. Xia, M. A. Eftekhar, R. A. Correa, J. E. Antonio-Lopez, A. Schülzgen, D. Christodoulides, and G. Li, *IEEE J. Sel. Top. Quantum Electron.* **22**, 196–207 (2015).
- ⁴S. Sivankutty, V. Tsvirkun, G. Bouwmans, D. Kogan, D. Oron, E. R. Andresen, and H. Rigneault, *Opt. Lett.* **41**, 3531–3534 (2016).
- ⁵R. G. Duncan, M. E. Froggatt, S. T. Kreger, R. J. Seeley, D. K. Gifford, A. K. Sang, and M. S. Wolfe, *Proc. SPIE* **6530**, 65301S (2007).
- ⁶J. P. Moore and M. D. Rogge, *Opt. Express* **20**, 2967–2973 (2012).
- ⁷J. Villatoro, E. Antonio-Lopez, A. Schülzgen, and R. Amezcua-Correa, *Opt. Lett.* **42**, 2022–2025 (2017).
- ⁸J. Villatoro, A. Van Newkirk, E. Antonio-Lopez, J. Zubia, A. Schülzgen, and R. Amezcua-Correa, *Opt. Lett.* **41**, 832–835 (2016).
- ⁹D. Monzon-Hernandez, A. Martinez-Rios, I. Torres-Gomez, and G. Salceda-Delgado, *Opt. Lett.* **36**, 4380–4382 (2011).
- ¹⁰Q. Wang and Y. Liu, *Measurement* **130**, 161–176 (2018).
- ¹¹J. A. Martin-Vela, J. M. Sierra-Hernandez, A. Martinez-Rios, J. M. Estudillo-Ayala, E. Gallegos-Arellano, D. Toral-Acosta, T. E. Porraz-Culebro, and D. Jauregui-Vazquez, *IEEE Photonics Technol. Lett.* **31**, 1265–1268 (2019).
- ¹²Y.-P. Wang and Y.-J. Rao, *IEEE Sens. J.* **5**, 839–843 (2005).
- ¹³D. Z. Stupar, J. S. Bajic, L. M. Manojlovic, M. P. Slankamenac, A. V. Joza, and M. B. Zivanov, *IEEE Sens. J.* **12**, 3424–3431 (2012).
- ¹⁴M. Jang, J. S. Kim, S. H. Um, S. Yang, and J. Kim, *Opt. Express* **27**, 2074–2084 (2019).
- ¹⁵L. Yuan, J. Yang, Z. Liu, and J. Sun, *Opt. Lett.* **31**, 2692–2694 (2006).
- ¹⁶H. Qu, G. F. Yan, and M. Skorobogatiy, *Opt. Lett.* **39**, 4835–4838 (2014).
- ¹⁷C. Li, T. Ning, C. Zhang, J. Li, C. Zhang, X. Wen, H. Lin, and L. Pei, *Sens. Actuators, A* **248**, 148–154 (2016).
- ¹⁸S. Zhang, A. Zhou, H. Guo, Y. Zhao, and L. Yuan, *OSA Continuum* **2**, 1953–1963 (2019).
- ¹⁹W. Chen, Z. Chen, Y. Qiu, L. Kong, H. Lin, C. Jia, H. Chen, and H. Li, *Appl. Opt.* **58**, 8776–8784 (2019).
- ²⁰J. R. Guzman-Sepulveda and D. A. May-Arrijo, *Opt. Express* **21**, 11853–11861 (2013).
- ²¹G. Salceda-Delgado, A. Van Newkirk, J. E. Antonio-Lopez, A. Martinez-Rios, A. Schülzgen, and R. Amezcua Correa, *Opt. Lett.* **40**, 1468–1471 (2015).
- ²²A. V. Newkirk, J. E. Antonio-Lopez, A. Velazquez-Benitez, J. Albert, R. Amezcua-Correa, and A. Schülzgen, *Opt. Lett.* **40**, 5188–5191 (2015).
- ²³G. M. H. Flockhart, W. N. MacPherson, J. S. Barton, J. D. C. Jones, L. Zhang, and I. Bennion, *Opt. Lett.* **28**, 387–389 (2003).
- ²⁴D. Barrera, I. Gasulla, and S. Sales, *J. Lightwave Technol.* **33**, 2445–2450 (2014).
- ²⁵D. Zheng, J. Madrigal, H. Chen, D. Barrera, and S. Sales, *Opt. Lett.* **42**, 3710–3713 (2017).
- ²⁶P. Saffari, T. Allsop, A. Adebayo, D. Webb, R. Haynes, and M. M. Roth, *Opt. Lett.* **39**, 3508–3511 (2014).
- ²⁷S. Wang, W. Zhang, L. Chen, Y. Zhang, P. Geng, Y. Zhang, T. Yan, L. Yu, W. Hu, and Y. Li, *Opt. Lett.* **42**, 4938–4941 (2017).
- ²⁸D. Barrera, J. Madrigal, and S. Sales, *J. Lightwave Technol.* **36**, 1063–1068 (2018).
- ²⁹A. W. Snyder, *J. Opt. Soc. Am.* **62**, 1267–1277 (1972).
- ³⁰N. Kishi and E. Yamashita, *IEEE Trans. Microwave Theory Tech.* **36**, 1861–1868 (1988).
- ³¹J. Hudgings, L. Molter, and M. Dutta, *IEEE J. Quantum Electron.* **36**, 1438–1444 (2000).
- ³²A. Perez-Leija, J. Hernandez-Herrejon, H. Moya-Cessa, A. Szameit, and D. N. Christodoulides, *Phys. Rev. A* **87**, 013842 (2013).
- ³³R. P. Murphy, S. W. James, and R. P. Tatam, *J. Lightwave Technol.* **25**, 825–829 (2007).
- ³⁴A. Varguez-Flores, G. Beltran-Perez, S. Munoz-Aguirre, and J. Castillo-Mixcoatl, *J. Lightwave Technol.* **27**, 5365–5369 (2009).
- ³⁵D. Barrera, J. Villatoro, V. P. Finazzi, G. A. Cardenas-Sevilla, V. P. Minkovich, S. Sales, and V. Pruneri, *J. Lightwave Technol.* **28**, 3542–3547 (2010).
- ³⁶H. Liao, P. Lu, X. Fu, X. Jiang, W. Ni, D. Liu, and J. Zhang, *Opt. Express* **25**, 26898–26909 (2017).
- ³⁷Y. Fu, H. Di, and R. Liu, *Opt. Laser Technol.* **42**, 594–599 (2010).
- ³⁸J. Shi, F. Yang, D. Yan, D. Xu, C. Guo, H. Bai, W. Xu, Y. Wu, J. Bai, S. Zhang, T. Liu, and J. Yao, *Opt. Express* **27**, 23585–23592 (2019).

eman ta zabal zazu



Universidad
del País Vasco

Euskal Herriko
Unibertsitatea

